



UNIVERSIDAD DE LA RIOJA

TESIS DOCTORAL

Título
Design and Synthesis of New Systems for Photoprotection and Solar Energy Storage
Autor/es
Raúl Losantos Cabello
Director/es
Pedro José Campos García y Diego Sampedro Ruiz
Facultad
Facultad de Ciencia y Tecnología
Titulación
Departamento
Química
Curso Académico



Design and Synthesis of New Systems for Photoprotection and Solar Energy Storage, tesis doctoral de Raúl Losantos Cabello, dirigida por Pedro José Campos García y Diego Sampedro Ruiz (publicada por la Universidad de La Rioja), se difunde bajo una Licencia Creative Commons Reconocimiento-NoComercial-SinObraDerivada 3.0 Unported. Permisos que vayan más allá de lo cubierto por esta licencia pueden solicitarse a los titulares del copyright.

© El autor
© Universidad de La Rioja, Servicio de Publicaciones, 2019
publicaciones.unirioja.es
E-mail: publicaciones@unirioja.es



**UNIVERSIDAD
DE LA RIOJA**

Facultad de Ciencia y Tecnología

Departamento de Química

Área de Química Orgánica

Grupo de Fotoquímica Orgánica

TESIS DOCTORAL

DESIGN AND SYNTHESIS OF NEW SYSTEMS FOR PHOTOPROTECTION AND SOLAR ENERGY STORAGE

Memoria presentada en la Universidad de La Rioja
para optar al grado de Doctor en Química por:

Raúl Losantos Cabello

Julio 2019



**UNIVERSIDAD
DE LA RIOJA**

Facultad de Ciencia y Tecnología

Departamento de Química

Área de Química Orgánica

Grupo de Fotoquímica Orgánica

D. PEDRO JOSÉ CAMPOS GARCÍA, Catedrático de Química Orgánica del Departamento de Química de la Universidad de La Rioja,

y **D. DIEGO SAMPEDRO RUIZ**, Profesor Titular de Química Orgánica del Departamento de Química de la Universidad de La Rioja.

CERTIFICAN:

Que la presente memoria, titulada "**Design and synthesis of new systems for photoprotection and solar energy storage**", ha sido realizada en el Departamento de Química de La Universidad de La Rioja bajo su dirección por el Licenciado en Química **D. RAÚL LOSANTOS CABELLO** y autorizan su presentación para que sea calificada como Tesis Doctoral.

Logroño, Julio de 2019

Fdo. Pedro J. Campos García

Fdo. Diego Sampedro Ruiz

"Learn from yesterday, live for today, hope for tomorrow. The important thing is not to stop questioning"

"A person who never made a mistake never tried anything new"

Albert Einstein

Table of contents

ABSTRACT	i
RESUMEN	iii
ABBREVIATIONS AND ACRONYMS	v
1. INTRODUCTION	1
1.1. History of photochemistry	3
1.2. Light-matter interaction	7
1.2.1. Electromagnetic radiation	7
1.2.2. Light absorption: Franck-Condon principle and Lambert-Beer law	9
1.2.3. Deactivation mechanisms	11
1.2.4. Photochemical processes	13
1.3. Sunscreens features	15
1.4. Bibliography	17
2. BACKGROUND	19
2.1. Solar Radiation	21
2.1.1. Effects of sunlight in humans and applications involving UV radiation	28
2.1.2. Natural photoprotection and photodamage reparation mechanisms	36
2.2. Need of extra protection: artificial sunscreens	39
2.2.1. Artificial sunscreens: action mechanisms and features	40
2.2.1.1. Physical filters: titanium dioxide and zinc oxide	41
2.2.1.2. Chemical filters: the most widely used	42
2.2.2. Current general concerns with sunscreens	48
2.3. Mycosporine-like aminoacids and gadusol	50
2.3.1. Location, structure, properties and biological roles	50
2.3.1.1. Photophysical properties	54
2.3.1.2. Photochemical properties	58
2.3.1.3. Other biological roles	61
2.3.2. Obtention from natural sources and synthetic attempts	62
2.3.3. Computational mechanistic approach	69
2.4. Bibliography	75
3. OBJECTIVES	81

Table of contents

4. DESIGN AND SYNTHESIS OF NEW MAA ANALOGUES	85
4.1. Computational screening: finding the core structure responsible of photoprotection	87
4.1.1. Static analysis to identify the best sunscreen core	88
4.1.2. Dynamic analysis	100
4.2. Synthesis and photochemical characterization of new MAA analogues	105
4.2.1 A synthetic entryway to new efficient sunscreens	105
4.2.1.1. Alkyl substituted derivatives	108
4.2.1.2. Oxygen substituted derivatives	110
4.2.1.3. Sulfur and selenium substituted derivatives	112
4.2.2. Photophysical and photochemical properties	116
4.3 Applications: further development and implementation attempts	128
4.4. Experimental section	131
4.4.1. Computational details	141
4.5. Bibliography	142
5. SPECTROSCOPIC CHARACTERIZATION OF SYNTHETIC MAA ANALOGUES	143
5.1. Spectroscopic study of MAA synthetic analogues	145
5.1.1. Spectroscopic techniques	146
5.1.1.1. Transient absorption spectroscopy	146
5.1.1.2. Time-resolved fluorescence upconversion	150
5.1.2. Time-resolved fluorescence upconversion and pump-probe experiments	153
5.2. Theoretical study of MAA synthetic analogues	162
5.3. Comparison with commercial sunscreens	175
5.4. Experimental section	180
5.4.1. Spectroscopic details	180
5.4.2. Computational details	181
5.5. Bibliography	183
6. SYNTHESIS AND CHARACTERIZATION OF NEW SUNSCREEN CANDIDATES	185
6.1. Chromone and chromenone derivatives	187
6.1.1 Synthesis of new derivatives	188
6.1.2. Photochemical and photophysical properties	191
6.1.3. Computational study of the photoprotection mechanism	195

Table of contents

6.2. Other cyclohexanedione derivatives	202
6.3. Experimental section and theoretical methods	205
6.3.1 Computational details	215
6.4. Bibliography	216
7. MOLECULAR ENERGY STORAGE SYSTEMS	217
7.1. MOST concept and relevant systems	219
7.2. Objectives in this section	228
7.3. Evaluation of MOST capabilities in different photoswitches	229
7.3.1. Computational screening of $\Delta H_{\text{storage}}$	229
7.3.2. Synthesis of promising derivatives	233
7.3.3. Photochemical study of the new hydantoin derivatives	235
7.3.4. Catalyzed back-conversion reaction	236
7.4. NBD/QC derivatives as MOST devices	238
7.4.1. Catalyst screening and preparation of supported materials	239
7.4.2 Heat release experiments	242
7.4.3 Computational exploration of the back-reaction mechanism	246
7.4.4. Contribution report	253
7.5. Azobenzene as MOST	254
7.5.1. Exploration of azobenzene on device tests	255
7.5.2. Catalyst screening for the back-conversion reaction	257
7.5.3. Computational exploration of the catalytic mechanism	259
7.5.4. Contribution report	265
7.6. Experimental section	266
7.6.1. Experimental details	266
7.6.2. Computational details	270
7.7. Bibliography	271
8. CONCLUSIONS / CONCLUSIONES	275
8.1. Conclusions	277
8.2. Conclusiones	279
Scientific Publications	281
Conference communications	282

Table of contents

9. GENERAL COMMENTS AND THEORETICAL METHODS	285
9.1. General comments	287
9.1.1. Characterization techniques	287
9.1.2. Lamps and photochemical techniques	288
9.2 Computational methods	291
9.2.1 CASSCF//CASPT2 strategy	291
9.2.2. Dynamic study	294
9.2.3. DFT	295
9.2.4. TD-DFT	296
9.3. Bibliography	297
APPENDIX A: ANNEX VI EUROPEAN REGULATION	I
APPENDIX B: SELECTED NMR SPECTRA	VII
APPENDIX C: X RAY DIFFRACTION	XXXI
APPENDIX D: CARTESIAN COORDINATES	XLIII

Abstract

This PhD. Thesis is focused on the rational design and obtention of new synthetic sunscreens and molecular energy storage systems. In particular, an evaluation of their photophysical and photochemical properties and diverse structural modifications to tune them was done.

The thesis is divided in different chapters. Firstly, an overview of the history of photochemistry and a brief explanation of the fundamental basis of photochemistry that will be crucial throughout this memory will be described in Chapter 1.

In the second chapter a general description of UV light exposition dangers and effects are explained together with the concerns and action mechanisms of the commercial sunscreens. Moreover, the obtention and properties of natural mycosporines (MAAs) which inspired this thesis are described.

In Chapter 4, a computational and synthetic design of MAA analogues is presented. The computational study clarifies the key features for photoprotection revealing a simpler scaffold which retains these skills. The development of a novel and versatile synthetic procedure allows for the synthesis of a series of analogues with proved and efficient photoprotective capabilities.

In Chapter 5, it is presented a spectroscopic analysis using femtosecond temporal resolution techniques to understand the relaxation mechanisms. Also, the influence of substitution is explored by computational methods.

Chapter 6 shows the preparation and characterization of other three families of UV filters together with a proposal for their deactivation mechanisms.

Finally, in Chapter 7 it is described the concept of molecular solar thermal energy storage (MOST) and three distinct types of system are explored. This work mainly focuses on the catalyzed back-conversion reaction and heat release measurements, obtaining a record system and the computational exploration of the ruling mechanisms.

Resumen

Esta tesis doctoral se centra en el diseño racional y la obtención de nuevos fotoprotectores de origen sintético y sistemas para almacenamiento de energía solar. En particular, se ha realizado la evaluación de sus propiedades fotofísicas y fotoquímicas y su ajuste a través de diversas modificaciones estructurales.

La tesis se divide en diferentes capítulos. Inicialmente se da una visión general de la historia de la fotoquímica y una breve explicación de conceptos fundamentales que se usarán a lo largo de la memoria.

En el segundo capítulo, se describen de manera general los peligros y efectos asociados a la exposición frente a luz UV junto con las preocupaciones y mecanismos de acción de los fotoprotectores comerciales. Además, se describen los métodos de obtención y propiedades de las micosporinas naturales (MAAs) que inspiran en gran medida este trabajo.

En el capítulo 4 se presenta el diseño computacional y sintético de análogos de MAAs. Este estudio computacional aclara las características clave en la fotoprotección revelando estructuras más sencillas que mantienen estas propiedades.

En el capítulo 5, se ha llevado a cabo un análisis espectroscópico por medio de técnicas con resolución temporal de femtosegundos para comprender los mecanismos de relajación. Además, la influencia de los sustituyentes se ha explorado por métodos teóricos.

El capítulo 6 muestra la preparación y caracterización de otras tres familias de filtros UV junto a una propuesta sobre sus mecanismos de desactivación.

Por último, en el capítulo 7 se describe el concepto de almacenamiento de energía termo-solar (MOST) y cómo se han explorado para ello tres tipos de sistemas distintos. Este trabajo se centra principalmente en la reacción de reversión catalizada y en medidas de liberación de calor, obteniéndose un sistema récord y explorando los mecanismos que rigen estas reacciones por medio de cálculos teóricos.

Abbreviations and acronyms

Abbreviations and acronyms

^{13}C-NMR	carbon nuclear magnetic resonance
^1H-NMR	proton nuclear magnetic resonance
A	absorbance
a.m.u.	atomic mass unit
AcOEt	ethyl acetate
AM	air mass coefficient
amino-CoPc	tetra amino cobalt phthalocyanine
AS/NZS	Australian/New Zealand Standard
BBO	beta barium borate
BHT	butylated hydroxytoluene
Boc	<i>tert</i> -butoxycarbonyl
BPH	benzophenone
C	concentration
ca.	approximately
CAN	cerium ammonium nitrate, $(\text{NH}_4)_2[\text{Ce}(\text{NO}_3)_6]$
CAS	coherent artifact signal
CASPT2	complete active space 2 nd order perturbation theory
CASSCF	complete active space self-consistent field
CE	chelated <i>enol</i>
CI	conical intersection
CIE	international commission on illumination
Colipa	European Cosmetic and Perfumery Association
CoPc	cobalt phthalocyanine

CoPc@C	cobalt phthalocyanine physisorbed onto charcoal
C_p	specific heat capacity
CSP	concentrating solar power
d	distance, path length
DAS	difference absorption spectrum
DC	derivative coupling vector
DFT	density functional theory
DHA	dihydroazulene
DHP	1,4-dihydropyridine
DMF	<i>N,N</i> -dimethylformamide
DMSO-d_6	deuterated dimethyl sulfoxide
DNA	deoxyribonucleic acid
DSC	differential scanning calorimetry
E	energy
$E_{1,1}$	specific extinction coefficient of 1% solution
e.g.	for example
eq.	equivalent
ESA	excited state absorption
ESHT	excited state proton transfer
f	focal distance
<i>f</i>	oscillator strength
FC	Franck-Condon point
FDA	Food and Drug Administration
GD	gradient difference vector
GSB	ground state bleaching

Abbreviations and acronyms

HOMO	highest occupied molecular orbital
HPLC	high performance liquid chromatography
<i>i</i>	imaginary
IC	internal conversion
ICD	International Statistical Classification of Diseases and Related Health Problems
I_R	intensity through reference blank
I_S	intensity through sample
ISC	intersystem crossing
ISO	International Organization for Standardization
JCIA	Japan Cosmetic Industry Association
LED	light-emitting diode
LIIC	linear interpolation on internal coordinates
LUMO	lowest unoccupied molecular orbital
MAA	Mycosporine-like aminoacid
MCSCF	multi configurational self-consistent field
MD	molecular dynamics
MECP	minimum energy crossing point
MED	minimum erythematol dose
MeOD	d_4 -methanol
MEP	minimum energy path
MLCT	metal-ligand charge transfer
MOST	molecular solar thermal
MP2	Møller-Plesset expansion truncated at second-order
MS-CASPT2	multistate CASPT2

MsCl	mesityl chloride
M_w	molecular weight
NAMD	non-adiabatic molecular dynamics
NBD	norbornadiene
NCE	non-chelated <i>enol</i>
NIR	near infrared radiation
NMR	nuclear magnetic resonance
OD	optical density
OD_w	optical density with irradiation
OD_{w/o}	optical density without irradiation
OPA	optical parametric amplifier
P	power of a radiation
PA	photoproduct absorption
PABA	<i>para</i> -aminobenzoic acid
PCM	polarizable continuum model
PES	potential energy surface
PMMA	poly(methyl methacrylate)
PPD	persistent pigment darkening
PTFE	polytetrafluoroethylene
<i>p</i>-TsOH	<i>para</i> -toluenesulfonic acid
PV	photovoltaics
QC	quadricyclane
ROS	reactive oxygen species
S₀	ground state
SE	stimulated emission

Abbreviations and acronyms

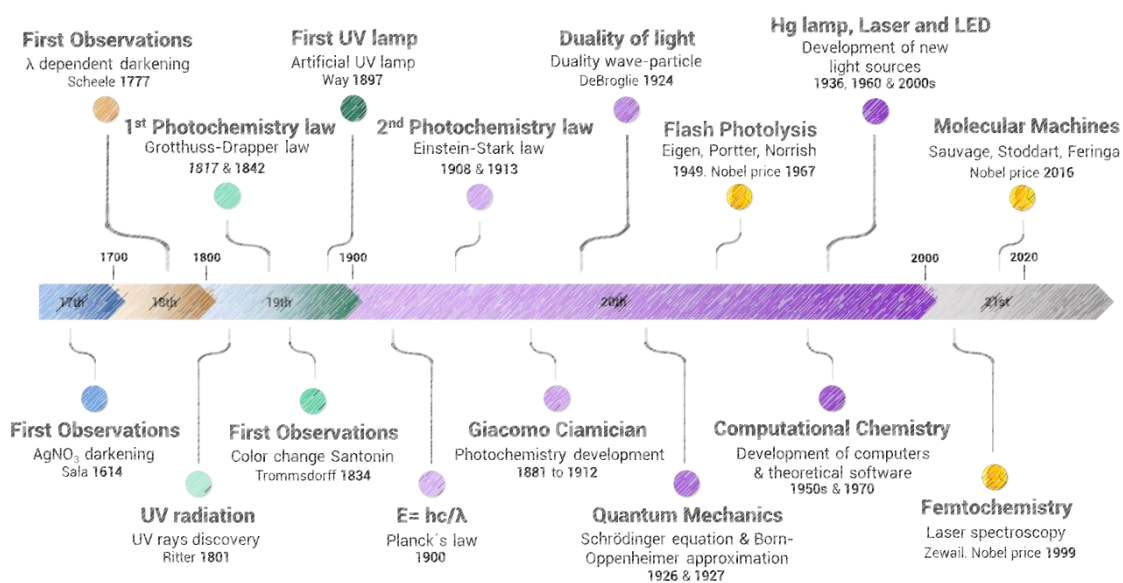
SED	standard erythemal dose
S_{er}	erythematic spectrum
SI	spectral irradiance
S_n	n th Singlet excited state
SO	spin-orbit coupling
SPF	solar protection factor
S_{PPD}	persistent pigment darkening spectrum
S_s	solar spectrum
T	transmittance, also temperature
T₁	triplet state
TA	transient absorption
TAS	transient absorption spectroscopy
TD-DFT	time dependent density functional theory
THF	tetrahydrofuran
TICT	twisted intramolecular charge transfer
TLC	thin layer chromatography
TOF	turnover frequency
TON	turnover number
TS	transition state
UV	ultraviolet radiation
UVA	ultraviolet A radiation
UVA-PF	ultraviolet A protection factor
UVB	ultraviolet B radiation
UVC	ultraviolet C radiation
UVI	UV index

Abbreviations and acronyms

UV-Vis	ultraviolet – visible, usually spectroscopy
VHF	vinylheptafulvene
Vis	visible radiation
VR	vibrational relaxation
ZPE	zero point energy
ΔG	Gibbs free energy difference
ΔH_{cat}	catalyzed back conversion enthalpy
$\Delta H_{\text{storage}}$	enthalpy difference between isomers in MOST systems
ΔH_{therm}	thermal back conversion enthalpy
ΔOD	time-dependent change of the optical density
ΔT	temperature difference
ϵ	molar extinction coefficient
ϵ_r	relative permittivity
λ	wavelength
τ	lifetime
φ	dihedral angle
ω_f	fluorescent emission in time-resolved measurements
ω_p	probe emission in time-resolved measurements
ω_s	upconversion signal in time-resolved fluorescence measurements

1. Introduction

Important Issues along Photochemistry History



1.1. History of photochemistry

Since the rise of ancient civilizations, the importance of light in life is known. It seems to be one of the driving forces of its evolution and its beginnings on Earth. Due to that, the sun surged as a veneration symbol in most of the ancient religions. From the classic Greece, where sunbathing was used to combat some health failures, the medicinal effects of light in humans are known. This type of therapy was called heliotherapy and is the precursor, in combination with some drugs, of the actual photodynamic therapy. Related to therapies using light, Niels Finsen treated patients with skin tuberculosis (*lupus vulgaris*) by visible light irradiation winning the Nobel Prize in 1903.^[1] Concerning this interest in how light interacts with the environment, surges photochemistry.

Photochemistry is the branch of chemistry that studies light induced effects in matter (atoms, molecules), dealing with chemical reactions and other physicochemical phenomena triggered by the absorption of light. In future references, photochemistry is only referred to molecular photochemistry. Molecules present different parts responsible for this absorption, the so-called chromophore. This term arises from the colorant industries referring to the colored nature of the obtained compounds.^[2] Photochemistry slowly emerged from the 17th to the 19th centuries but only was at the end of the 19th and along the 20th centuries when a great progress was achieved. Although nowadays the scientific basis of photochemistry is well known, it was only in the 1980s when it became a consolidated part of different scientific fields like chemistry or biology.

The first examples of photochemical reactions were observed accidentally and remained unexplained for years. One of the first evidences was the observation of darkening of silver nitrate salt by Sala in 1614.^[3] Related to this phenomenon, the difference of darkening in a silver chloride paper depending on the color (wavelength) of the incident light was also reported by Scheele in 1777.^[4] Here, the blue light produces a bigger darkening with respect to the red one. This fact was corroborated by Ritter, who found in 1801 that the rays beyond the violet ones (invisible rays) were even more efficient than the violet ones.^[5] These invisible rays were called "chemical rays" in order to discern them from the "heat rays" before the actual ultraviolet and infrared radiation terms, which were established in the 19th century. Other relevant observation also considered as one of the most significant at the beginning of photochemistry was the

color change of santonin promoted by light and described by Trommsdorff in 1834 being the first paper in photochemistry.^[6] This process was described only a few years ago as a photorearrangement.^[7] Thanks to these preliminary observations, scientists began to keep attention onto light as a new reagent with lots of possibilities. One of the most remarkable examples of that was the research done by Ciamician and Silber at the beginning of the 20th century in Bologna, using natural sunlight as radiation source and discovering a huge number of photoreactions that are used even nowadays.^[8] Also Ciamician described the possibility of employing photochemical devices exploiting solar energy as fuels to power the human civilization and called for their development more than a century ago.^[9]

The later development of photochemistry with respect to other branches of chemistry can be justified due to the absence of the physical principles, artificial light sources and spectroscopic techniques, which started their expansion during 20th century, especially after the Second World War. During the second half of the 20th century, physicists undertook the development of new spectroscopic techniques and light sources, which allowed an explosion in the progress of photochemistry, guided by physicists and chemists yielding in a multidisciplinary science as actually is.

The other key was the development by theoretical physicists during the first half of 20th century of the quantum mechanics, which allowed the explanation of a great number of physical phenomena, especially related to the interaction between light and matter. The energy associated with a light radiation could not present arbitrary values; they are distributed in some possible values so-called quants. According to this, light is quantized. The principle ruling this behavior is the Planck law, which correlates the energy (E) with the inverse of the radiation wavelength (λ) according to the following equation $E = hc/\lambda$, where h is the Planck's constant and c is the light speed.^[10]

Five years later, in 1905, a series of papers with the relativity theory, photoelectric effect,^[11] Brownian movement^[12] and the mass-energy equivalence were published by Einstein. These four papers had a great impact in physics and chemistry; they were called the *Annus Mirabilis* papers, supposing a change in the views on space, time, and matter. In chemistry, the Brownian movement supported the existence of atoms and was basic for the statistical mechanics supporting the actual kinetics models useful in reactivity studies. In addition, the explanation of the photoelectric effect considering the quantum theory is the effect behind the photovoltaics and was

crucial in the construction of light detectors, one of the key steps during the development of spectroscopic techniques.

In 1924, De Broglie postulated the dual nature of light, describing it as a particle, so-called photon, with an associated energy dependent on the associated wavelength by Planck's law, which is called wave-particle duality principle.^[13] At the same time surged the Schrödinger equation,^[14] becoming the most important postulate in the quantum mechanics field. Resolution of this equation yields in a function describing completely the molecule, the so-called wavefunction. As counterpoint, it can be solved exactly only for the hydrogen atom and for more complex systems, approximations are needed. The year after, in 1927, the Born-Oppenheimer approximation was published,^[15] allowing the wavefunction calculation splitting in two components, the contribution of nuclei and electrons, opening a new way to study polyatomic molecules and being one of the basis in the development of computational chemistry. At that moment, even with the main part of the physical laws ruling quantum mechanics developed, their implementation into the study of complex systems was delayed until the required calculation capacity to solve the complex mathematics behind this problem could be achieved. Together with the firsts processing machines, the firsts *ab initio* codes^[16] were developed in the seventies promoting an abrupt progress of computational chemistry.

Contemporaneously, the development of spectroscopic equipment and light sources experimented a great expansion. At the end of the nineteenth century, the only available light source was sunlight, with its inherent problematics, such as intensity and variability depending on weather, season and location. To avoid that irreproducibility, artificial light sources surged as a quantitative solution. J.T. Way patented the first example in 1857,^[17] being the low-pressure mercury lamp the first artificial UV radiation source. Other examples of these UV lamps were constructed increasing the mercury pressure; the high-pressure mercury lamp was reported in 1936 with a broad emission from 360 to 600 nm. Also, sodium lamps were built in 1932 and the high-power light emitting diodes (LED) that emerged in the 2000s.

Once different types of lamps were constructed, the spectroscopic techniques became technologically available and they grew up quickly. Especially significant were the evolution of ultrafast techniques, like the flash photolysis setup, established in 1949 by M. Eigen, G. Porter and R. G. W. Norrish, who won the Nobel Prize in Chemistry in 1967 for the development of this technique. The general concept of it is the

measurement of the optical density change produced in the sample after irradiation with a short pulse, related to the generation of transient species like radicals.^[18] It is important to note that only moderate rate photoreactions can be studied by this technique due to the time resolution of the pulses used, which are in the nanosecond to microsecond range. However, the study of ultrafast photochemical reactions (in the femtosecond time scale) started to be of interest with the passage of time. This means that novel laser systems with time response below the nanosecond time scale were required. Being in 1999 when Ahmed Zewail won the Nobel Prize in Chemistry for the study of transition states involved in chemical reactions using femtosecond spectroscopy. His pioneer work opened the doors for the study of chemical reactions across femtoseconds, so-called femtochemistry, allowing an easy obtention of information about photochemical processes.^[19]

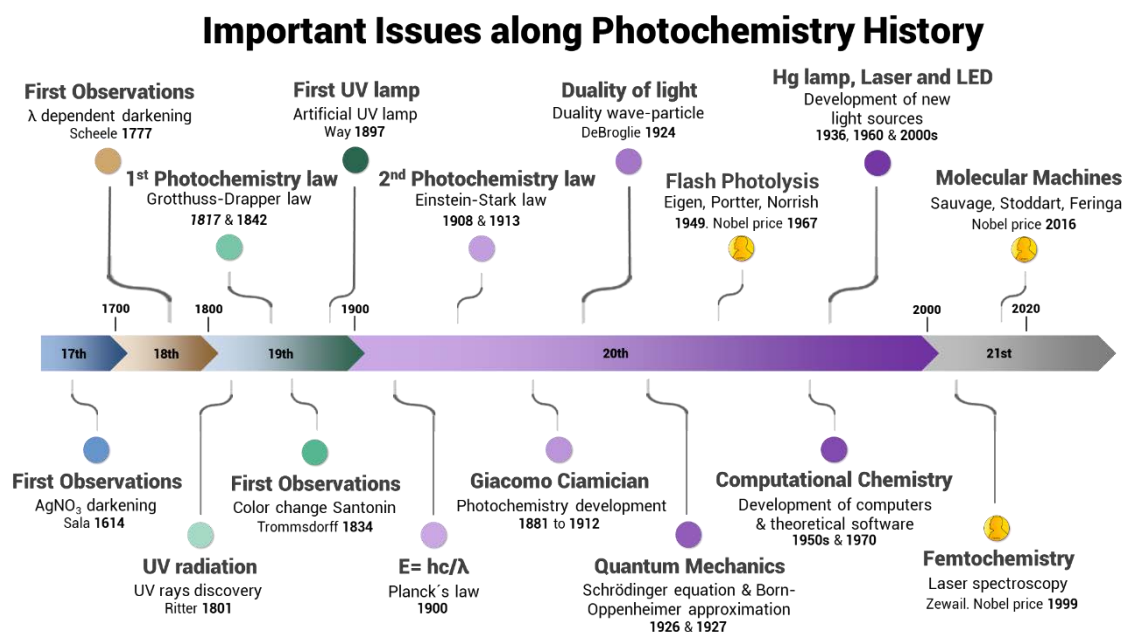


Figure 1.1. Chronology of most relevant issues along photochemistry history.

As summary, photochemistry is a young and multidisciplinary branch of chemistry which focus on the reactivity obtained after light absorption. Traditionally, UV radiation was used, but nowadays also visible light can be employed to cleavage different bond types through different processes such as sensitization, electron transfer or upconversion.^[20]

1.2. Light-matter interaction

As mentioned during the previous section, the interaction between light and matter aroused constant attention from humanity over centuries. However, during long time, the necessary knowledge to understand it was not developed.

There are two main principles ruling the photochemistry. Firstly, a basic rule formulated by Grotthuss in 1817^[21] and independently by Draper in 1842. The Grotthuss–Draper law states that only the light absorbed by a material sample can induce chemical transformations. The second law of photochemistry is the Stark–Einstein law, which states that for each photon of light absorbed by a chemical system, only one molecule is activated for a photochemical reaction. This is also known as the photoequivalence law and was derived by Einstein and Stark during the development of quantum theory of light.

These two rules seem to be basic nowadays, where “every photochemical or photophysical process is triggered by the absorption of one photon by one molecule” is properly assumed. However, this was a keystone in the knowledge of photochemical processes during the 20th century. Nevertheless, other concepts should be explained before exploring the photochemical reactivity.

1.2.1. Electromagnetic radiation

Color of molecules was an important sensorial feature, which strongly promoted the development of the chemical industry regarding the colorant production at the beginnings of the 19th century. What our vision senses as single colors is the impression of light that can still be decomposed into a spectral continuum of colors. The decomposition of radiation is the optical effect of dispersion exhibited by a prism or a grating when light passes through it. A spectrally pure light is characterized as a radiation of a defined wavelength (λ). All the possible radiations form the electromagnetic spectrum, which ranges along fifteen magnitude orders in the wavelength values together with their associated energy. As can be seen in Figure 1.2, the visible region only means a small portion of the global electromagnetic spectrum.

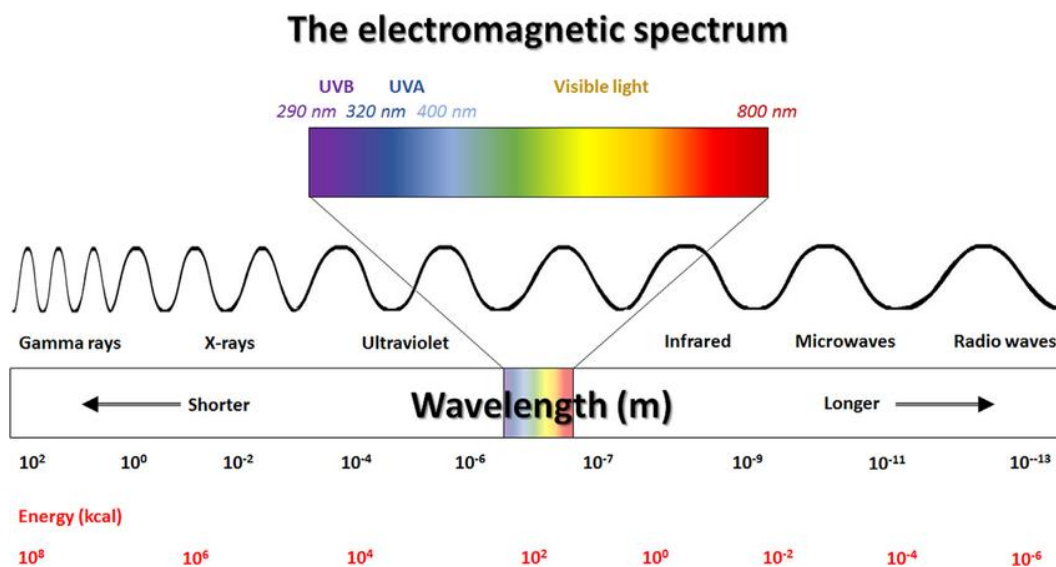


Figure 1.2. Different regions in electromagnetic spectrum.^[22]

The characteristic color of a chemical compound is due to its characteristic absorption of a fraction of the visible spectrum from the ambient white light, being the remaining reflected light, which determinates the color. In order to achieve photochemical transformations, the ultraviolet (UV) and visible (Vis) regions are the most interesting, because they have enough energy to produce electronic transitions and break chemical bonds. Concerning this thesis, the UV is the most relevant spectral region as being the fraction of solar radiation that can induce damaging effects on living organisms. This UV radiation can be divided in three smaller zones in terms of energy. The more energetic UVC ranges from 100 to 280 nm and can induce ionization and bond cleavage. The next zone is called UVB and ranges from 280 to 315 nm being a small band. The less energetic is the UVA radiation, ranging from 315 to 400 nm, being the most abundant of these three in Earth's surface.

In addition, each type of light in the electromagnetic spectrum^[23] has a different effect on living organisms or matter. Focusing on the aims of this work, which will be developed in next sections, the effects of different light types should be explained. The most relevant regions of the electromagnetic spectrum that could affect living organisms are mainly three, the UV, Vis, and near infrared (NIR), which are coming from the sun and they are not completely filtered by the atmosphere. NIR radiation only induces vibrational movements in molecules and as consequence it heats them up. Visible light is essential for living organisms like plants and animals, promoting photosynthesis and biosynthesis of some molecules, but without harmful effects.

Opposite to these, the UV light is the less abundant but the most harmful to organisms due to its capacity of promote photochemical reactions, which can produce species detrimental to health. Harmful effects will be described in more detail in the following Background section.

1.2.2. Light absorption: Franck-Condon principle and Lambert-Beer law

The absorption of light by a molecule could comprise radiation from microwave (causing rotation in the molecules), infrared (causes an increase of vibrational energy) to UV-Vis. Regarding the capacity of UV-Vis light of promote electronic transitions, these are the most used radiation wavelengths in photochemical processes. As mentioned before, the molecule or the part of a molecule which is the responsible of the light absorption is called chromophore. When this chromophore absorbs light, an electronic transition occurs from the ground state to more energetic excited states. This electronic reorganization takes place much faster than the nuclei movement, due to their larger mass. The Franck-Condon principle states that the electronic transitions befall faster than the nuclei or surrounding environment reorganization. Therefore, molecular geometry does not change during the light absorption process. Because of this, the electronic transitions can be called vertical transitions. The absorption process is usually represented by a vertical line, as seen in Figure 1.3.

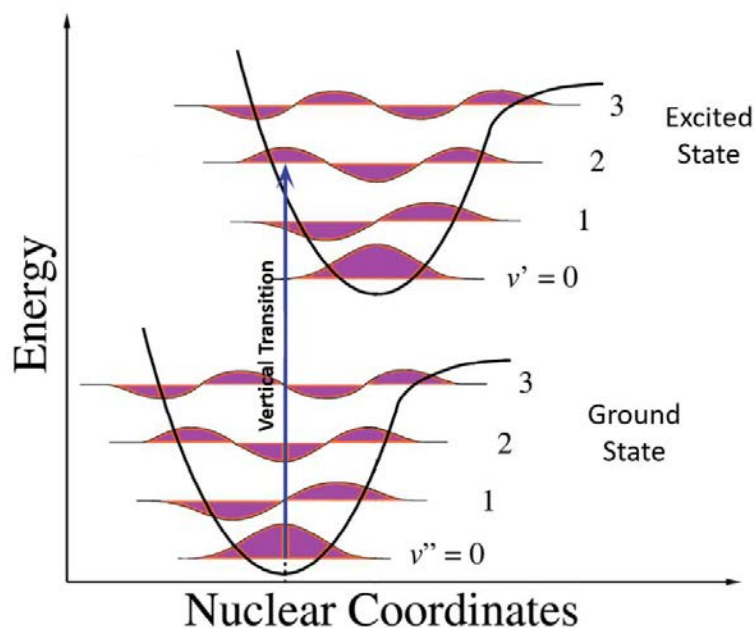



Figure 1.3. Potential energy surfaces with vibrational levels illustrating the Franck-Condon principle (adapted from Mark M. Somoza). 

As seen in Figure 1.3, the vertical transition usually not only involves the gap between the lower vibrational levels. Closer to reality, a transition from the $v'' = 0$ to a hot vibrational state in the excited state is the typical behavior.

Looking into the nature of the absorption, each system presents characteristic orbitals involved in the electronic transition. Independently from the orbitals involved, all absorptions are defined by its energy and strength. The energy is the gap between the ground state and the excited state. The strength of the absorption, the so-called oscillator strength, is directly proportional to the overlap of the vibrational wavefunctions of each state. Also, it is related to the square of the transition dipole moment generated between these involved states, taking into consideration the orbital overlapping. As it can be seen in Figure 1.3, the vertical transition from $v'' = 0$ overlaps with $v' = 2$ being this the vibrational excited state most probably populated during excitation.

Once defined the wavelength and the strength of the absorption, these spectral characteristics carry essential information about the electronic structure of the molecules and their concentration when dealing with dilute systems such as solutions. This correlation between concentration and the absorbed light amount can be done according to the Lambert-Beer law. In this law, the transmittance of the sample (T) is

the relation between the intensity transmitted through a sample solution (I_S) vs. a reference blank (I_R), being $T = I_S/I_R$.

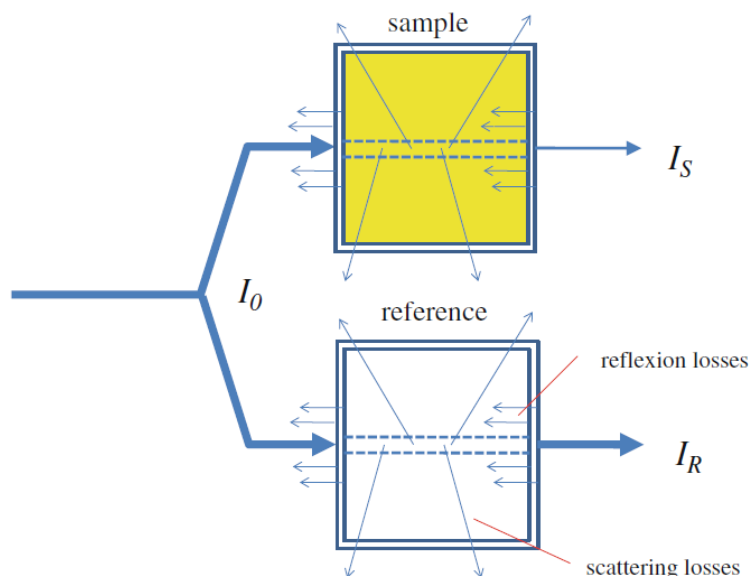


Figure 1.4. Schematic representation of a Transmittance measurement.^[24]

The transmittance exponentially depends on the distance and concentration of the sample according to $T = 10^{-\epsilon d M}$, being d the path length of the sample in cm, M the concentration in molarity and ϵ the molar extinction coefficient, which is specific for each compound. Also, absorbance was defined as $A = -\log T$, according to that, the Lambert-Beer law establish the correlation between the absorbance of the sample and its concentration according to the equation $A = \epsilon \cdot d \cdot M$.

1.2.3. Deactivation mechanisms

The first step in all photochemical processes is the absorption of a photon with the right energy. When light absorption occurs, the molecule is promoted to an excited state, which is in non-equilibrium conditions and some processes can take place to obtain a less energetic disposition, usually in the ground state. These processes can be easily represented in a Jablonski diagram, as shown in Figure 1.5. A general classification of the possible processes implies the presence of two groups, radiative

and non-radiative, depending on whether a photon emission takes place or not during the process.

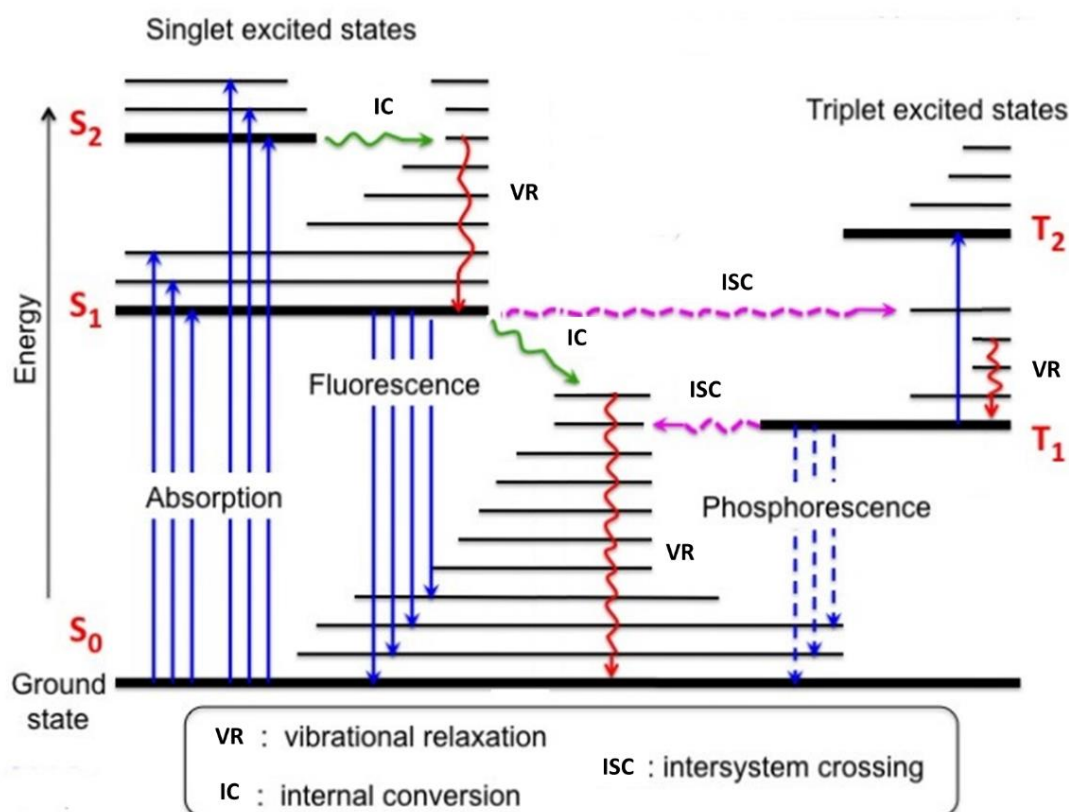


Figure 1.5. Jablonski diagram with the occurring processes after absorption. Straight arrows represent radiant processes and curve arrows depict the non-radiant ones. Note that IC in all cases is an isoenergetic process. Adapted from *J. Instrum.*^[25]

After the absorption, the exceeding energy can be dissipated by vibrational relaxation (VR). This is a fast transition through the different vibrational levels of one electronic state. Regarding the time scale for this process, it is an ultrafast relaxation in the order of few femtoseconds. However, if the vibrational levels of different electronic states are near in energy, a jump between electronic states can happen, leading to an internal conversion (IC). This non-radiative process implies a relaxation from a vibrational level of an electronic state to another vibrational level of an electronic state with lower energy (S_{n+1} , S_n), been a fundamental feature for this work. The time rate of internal conversion ranges from femtoseconds to picoseconds. Additionally, the system can decay to the ground state by fluorescence, emitting a photon with an energy correspondent to the difference between the involved states. It is important to remark that the fluorescent emission occurs between states with the same multiplicity, being

a singlet-to-singlet transition. This process usually involves a time constant in the picoseconds to nanoseconds range. In addition, these radiative emissions befall from the lowest excited state according to Kasha's rule.

Other states with different multiplicity can be populated during relaxation process. The Pauli Exclusion Principle, due to the unpaired electronic nature of the triplet state, does not allow the spin multiplicity change, but can take place due to vibronic coupling. This process implies an intersystem crossing (ISC). As this pathway implies a forbidden transition, the time scale strongly depends on the system. Once the triplet state is populated, a decay to the ground state can occur by phosphorescent emission. Alternatively, a singlet state could be populated, eventually emitting delayed fluorescence. In all these cases, even when a non-radiative deactivation takes place, the time rate for the triplet deactivation is longer than the other processes ranging from milliseconds to seconds.

1.2.4. Photochemical processes

The use of light as a reagent opens new reactive pathways, which normally are not allowed thermally due to the selection rules. This allows for a whole new reactivity. The main difference between thermal and photochemical reactivity yields in how the energy is transferred to the molecule. Thermally, the energy increases molecular vibrations and rotations of all the molecules in the sample, promoting molecular vibrations and translations. By light absorption, only a small portion of the molecules is electronically excited obtaining the desired photoreactivity. This energetic contribution allows, for example, endothermic reactions to proceed.

Concerning irradiation, the molecule enters a non-equilibrium state with an associated energy between +24 to +240 kcal/mol, which matches with near infrared, visible or ultraviolet (NIR, Vis and UV) radiation. This energy range allows the breaking of different bonds or major molecular rearrangements. These processes usually correspond with the promotion of an electron in a bonding (e.g. σ or π) or nonbonding orbital (e.g. n) to an antibonding one (e.g. σ^* , π^*).

A great number of photochemical reactions were described up to date, so a broad classification of the different types of processes should include the following:

- Abstraction reactions: Two types are relevant, the electron abstraction (ionization or electron transfer process) and proton abstraction (photoenolization).^[26]
- Photosubstitution: Substitution of aromatic compounds induced by light.^[27]
- Additions: Cycloadditions are the most common type of additions, also addition of singlet oxygen to double bonds.^[28] Biologically relevant are the formation of thymine dimers^[29] or singlet oxygen addition,^[30] which causes DNA damage.
- Rearrangements: isomerization, usually in *cis-trans* systems,^[31] e.g. azobenzene or stilbene; and intramolecular hydrogen transfer, as in oxybenzone.^[32]
- Dissociations: photofragmentation reactions as in 1,3-dicarbonyl compounds (Norrish type reaction),^[33] acyloximes^[34] or with C-I bonds.^[35]

1.3. Sunscreens features

As seen in the previous section 1.2.1, the UV radiation produces harmful effects in living organisms if they do not have the right protecting mechanisms against it. In humans there are some natural mechanisms, such as melanin production, but they are not enough to deal with the new life habits, involving an increased number of outdoor activities and sunbathing times. For that, the need of complementary protection arises as a key for avoid the contrary effects of excessive sun exposure.^[36]

Once seen all the possible deactivation processes and reactive paths after light absorption, the desirable features for a sunscreen molecule should be remarked. As expected, they mainly concern of what happen once light is absorbed and molecules reach the excited state. At this point, all the relaxation processes and some of the reactive paths explained before can occur. The first goal for a UV absorber to be used as sunscreen comprises the light absorption process. It should present a strong absorption (high molar extinction coefficient, ϵ) centered in the desired UV range, UVB and/or UVA regions (290 - 400 nm). Other targets arise when the molecule is in the excited state and concern how it dissipates the exceeding energy. At this stage, all the relaxation processes and the reactive paths can occur. In our concern, the selected molecule should not present photoreactivity, recovering the ground state by other non-reactive pathways. This feature is known as photostability, being related to the amount of light that can be absorbed by a molecule without forming other species. As exception of photoreactivity, some isomerization reactions are crucial in the deactivation mechanisms observed in some commercial and natural sunscreens, meaning non-destructive *E-Z* isomerization. How the molecule relaxes to the ground state is also a crucial step in terms of efficiency and it is related to the previously mentioned absence of photoreactivity. The aim is that the UV absorber dissipates the exceeding energy by internal conversion (IC) and by vibrational relaxation (VR), which implies a fast ground state recovery, avoiding the slower radiative mechanisms like fluorescence and phosphorescence. An undesired feature is also the intersystem crossing, as the population of triplet state yields in slower ground state recovery times and usually promotes radical formation. In addition, another feature required for an increased usability is the chemical and thermal stability. These features will be discussed in detail for the prepared compounds in the following chapters.

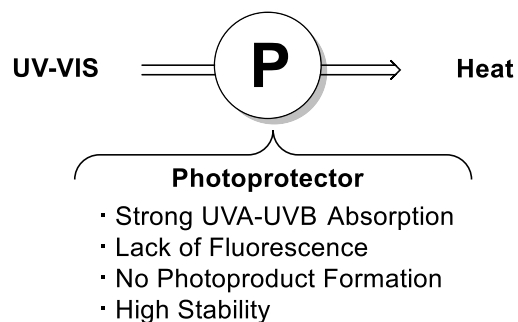


Figure 1.6. Ideal behavior for a sunscreen molecule (P).

To sum up, the desired features for an ideal sunscreen have been described,^[37] as can be seen in Figure 1.6:

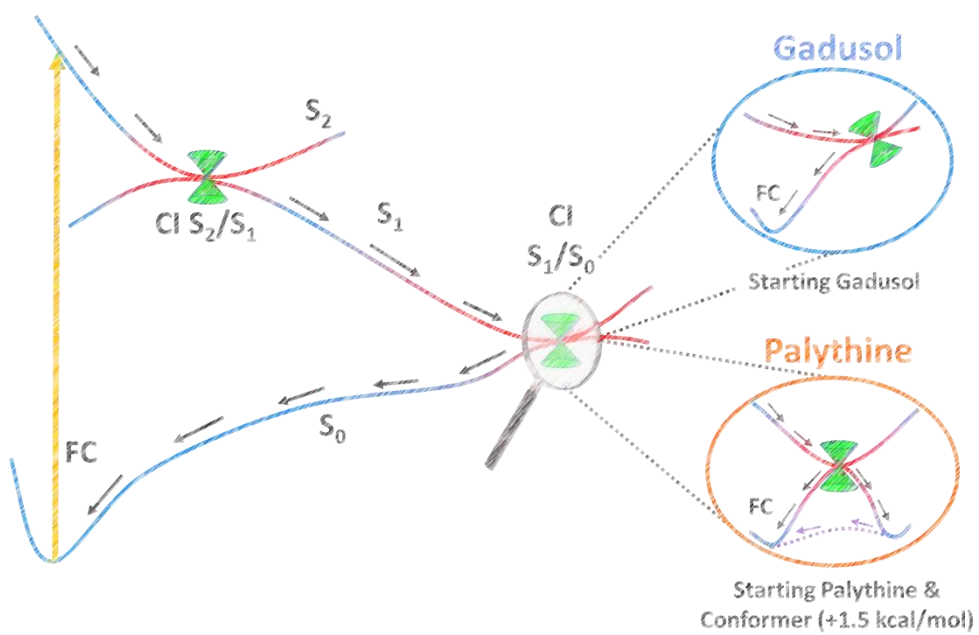
- Strong UVA-UVB absorption.
- Lack of radiative emission (fluorescence or phosphorescence), internal conversion and vibrational relaxation mechanism.
- High photostability, absence of photoreactivity or non-destructive one.
- Chemical and thermal stability.

1.4. Bibliography

- [1] N. R. Finsen, *Phototherapy*, Arnold Publishers, **1901**.
- [2] J. N. Chakraborty, in *Fundamentals and Practices in Colouration of Textiles*, Woodhead Publishing India, **2014**, pp. 12-21.
- [3] R. Hooykaas, *Religion and the rise of modern science*, Regent College Publishing, **2000**.
- [4] C. W. Scheele, J. R. Forster, J. Priestley, R. Kirwan, T. Bergman, *Chemical observations and experiments on air and fire*, J. Johnson Publishers, **1780**.
- [5] H. Berg; Johann Wilhelm Ritter, The founder of Scientific Electrochemistry, **2008**.
- [6] H. Trommsdorff, *Ann. Chem. Pharm.* **1834**.
- [7] A. Natarajan, C. K. Tsai, S. I. Khan, P. McCarren, K. N. Houk, M. A. Garcia-Garibay, *J. Am. Chem. Soc.* **2007**, *129*, 9846-9847.
- [8] G. Ciamician, M. Dennstedt, *Chem. Ber.* **1881**, *14*, 1153.
- [9] G. Ciamician, *Science* **1912**, *36*, 385.
- [10] M. Planck, *Verh. Deutsch. Phys. Ges.* **1900**, *2*, 202-204.
- [11] A. Einstein, *Ann. Phys.* **1905**, *322*, 132-148.
- [12] A. Einstein, *Ann. Phys.* **1905**, *322*, 549-560.
- [13] L. De Broglie, *Recherches sur la théorie des Quanta*, **1924**.
- [14] E. Schrödinger, *Ann. Phys.* **1926**, *384*, 361-376.
- [15] M. Born, R. Oppenheimer, *Ann. Phys.* **1927**, *389*, 457-484.
- [16] W. J. Hehre, W. A. Lathan, R. Ditchfield, M. D. Newton, J. A. Pople, *Gaussian 70 (Quantum Chemistry Program Exchange, Program No. 237)*, **1970**.
- [17] J. T. Way, British Patent N°1258, **1857**.
- [18] G. Porter, R. G. W. Norrish, *Proc. R. Soc. Lond. A. Math. Phys. Sci.* **1950**, *200*, 284-300.
- [19] A. Douhal, F. Lahmani, A. H. Zewail, *Chem. Phys.* **1996**, *207*, 477-498.
- [20] R. R. Islangulov, F. N. Castellano, *Angew. Chem. Int. Ed.* **2006**, *45*, 5957-5959.
- [21] T. Grotthuss, *Sitzungsberichte der kurländischen Gesellschaft für Literatur und Kunst* **1819**, *1*, 119 -189.
- [22] S. Giannakis, M. I. Polo López, D. Spuhler, J. A. Sánchez Pérez, P. Fernández Ibáñez, C. Pulgarin, *Appl. Catal. B* **2016**, *199*, 199-223.
- [23] ISO Standard, Definitions of Solar Irradiance Spectral Categories, ISO 21348, **2013**.
- [24] U. E. Steiner, in *Photodynamic Therapy: From Theory to Application* (Ed.: M. H. Abdel-Kader), Springer Berlin Heidelberg, **2014**, pp. 25-58.
- [25] N. Yahlali et al, *J. Instrum* **2012**, *7*, P02010-P02010.
- [26] B. Wardle, *Principles and Applications of Photochemistry*, WILEY, **2009**.
- [27] K. Mizuno, in *Photochemistry, Vol. 40*, The Royal Society of Chemistry, **2012**, pp. 106-145.
- [28] E. L. Clennan, M. E. Mehrsheikh-Mohammadi, *J. Am. Chem. Soc.* **1983**, *105*, 5932-5933.
- [29] B. Durbbeej, L. A. Eriksson, *J. Photochem. Photobiol. A* **2002**, *152*, 95-101.
- [30] L. F. Agnez-Lima, J. T. A. Melo, A. E. Silva, A. H. S. Oliveira, A. R. S. Timoteo, K. M. Lima-Bessa, G. R. Martinez, M. H. G. Medeiros, P. Di Mascio, R. S. Galhardo, C. F. M. Menck, *Mutat. Res. Rev. Mutat. Res.* **2012**, *751*, 15-28.
- [31] C. García-Iriepa, M. Marazzi, L. M. Frutos, D. Sampedro, *RSC Adv.* **2013**, *3*, 6241-6266.
- [32] C.-X. Li, W.-W. Guo, B.-B. Xie, G. Cui, *J. Chem. Phys.* **2016**, *145*, 074308.
- [33] W. Schwack, T. Rudolph, *J. Photochem. Photobiol. B* **1995**, *28*, 229-234.

- [34] R. Alonso, P. J. Campos, B. García, M. A. Rodríguez, *Org. Lett.* **2006**, *8*, 3521-3523.
- [35] E. Campos-Gómez, P. J. Campos, H. F. González, M. A. Rodríguez, *Tetrahedron* **2012**, *68*, 4292-4295.
- [36] G. Bens, *Sunlight, Vitamin D and Skin Cancer*, Springer-Verlag, **2014**.
- [37] R. Losantos, I. Funes-Ardoiz, J. Aguilera, E. Herrera-Ceballos, C. García-Iriepa, P. J. Campos, D. Sampedro, *Angew. Chem. Int. Ed.* **2017**, *56*, 2632-2635.

2. Background



2.1. Solar Radiation

Mainly there are three types of radiations that come to Earth from the sun, providing a huge amount of energy, which is constantly irradiating the Earth's surface. These three types of lights are the ultraviolet, visible, and infrared, which compose the solar spectrum. The infrared radiation (IR) represents a great part, around 48%, of the solar spectrum but it does not produce more effect in living organisms than heat it up by increasing their molecular vibrations. Visible light is essential for living organisms like plants and animals, promoting photosynthesis and biosynthesis of some biomolecules. It represents close to the 45% of the total radiation emitted by the sun without harmful effects. Opposite to these two, UV light despite being the less abundant, only ca. 6 - 7%, is the most harmful for organisms due to its capacity of promote photochemical reactions, which can produce species detrimental to health.

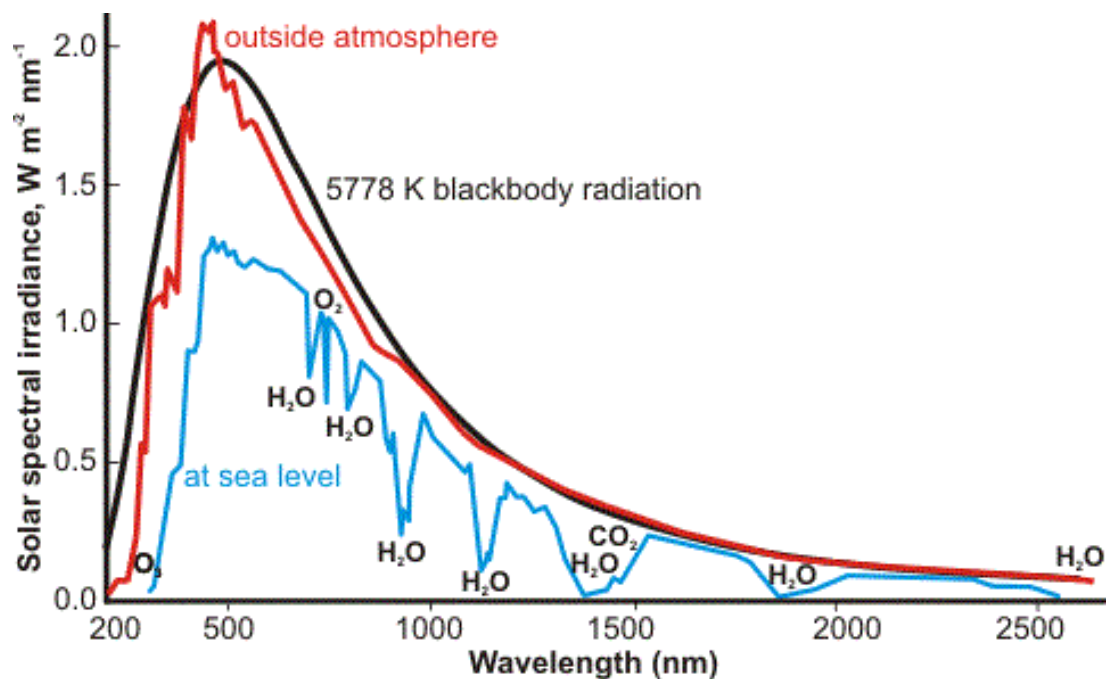


Figure 2.1. Irradiation of solar spectrum, at different altitudes (sea level and out of the atmosphere) and the different atmospheric absorptions.^[1]

Solar radiation exhibits a broad spectrum from 250 nm to more than 2000 nm, but it does not have a continuum and homogeneous distribution along the different wavelengths. The extraterrestrial radiation, red spectrum in Figure 2.1, approximately matches with the emission spectra of a blackbody at 5778 K, represented with a solid black line. Both, the blackbody and extraterrestrial radiation present a high amount of

2. Background

UVC and UVB radiation, which are the most energetic and could induce more types of reactivity in diverse systems or organisms. Fortunately, Earth presents an external cover, the atmosphere, which filters a great part of the damaging and more energetic radiations (Figure 2.2). However, this absorption occurs along all spectrum, but not homogeneously, being more considerable in the IR region where water, molecular oxygen and carbon dioxide exhibit their corresponding vibrational absorptions, being labeled in the sun spectra at sea level in Figure 2.1.

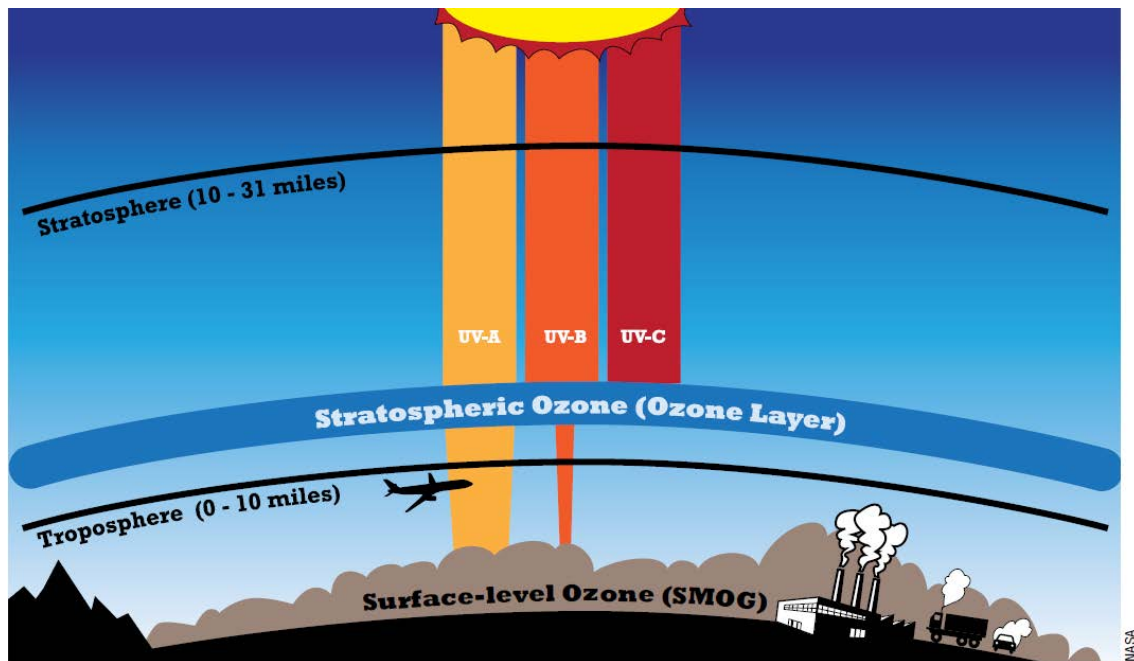


Figure 2.2. Atmospheric attenuation of the different types of UV radiation.^[2]

As can be observed in the previous figures, the totality of the UVC radiation is attenuated by the atmosphere, more concretely by the ozone molecules present in the ozone layer, which represent the Earth's primary protection against UV radiation. Although a great part of the UVB radiation is filtered off, around the 95% of the total, the remaining small fraction between 280 and 315 nm implies a risk for the living organisms. Contrary, the UVA radiation passes through the atmosphere and ozone layer with an unappreciable attenuation, only the 5% is removed. The deleterious effects of UV light will be addressed in the next section, but firstly some considerations about the solar spectrum and its quantification could be important for understanding the aims of this PhD.

It is well known that the sun constitutes an important energy source with a typical power flux on Earth's surface of 174 W m^{-2} , meaning 640 exajoules (EJ) in two hours of sunlight.^[3] To contextualize this amount of energy, it should be noted that the prefix "exa" denotes a factor of 10^{18} . In addition, the estimated global energy consumption, which actually is greater than 500 EJ/year could be covered with full exploitation of only 2 hours of sun irradiation (640 EJ), being a huge power energy source. The solar energy quantification should be done, equally to other light sources spectral calibration, using a spectroradiometer. This instrument, an example is shown in Figure 2.3, is a calibrated detector attached to an integrating sphere that homogenizes the studied light prior to its detection. Using the integrating sphere for spectroradiometric measurements is also essential due to the necessity to homogenize and collect the light from all the incoming directions onto the detector. The irradiance (S) of a light source is usually quantified in terms of $\text{W m}^{-2} \text{ nm}^{-1}$. The energy associated (P) is the integral of irradiance along wavelength, being $P = \int_{\lambda_1}^{\lambda_2} S I(\lambda) d\lambda$. By this way, the energy could be expressed in W m^{-2} or its different multiples or other energy units like joules per square meter (J m^{-2}).



Figure 2.3. Spectroradiometer composed by a big integrating sphere (left) and a detector (right), (commercial RadOMA equipment).

Regarding the amount of UV light that comes to the surface of Earth, the habitual irradiance is shown in Figure 2.1 showing maximum values around $1.3 \text{ W m}^{-2} \text{ nm}^{-1}$. As seems evident comparing both spectra (out atmosphere and sea level), some attenuation is occurring at all wavelengths, which is due to some absorptive and scattering interaction with the suspended particles, water vapor and other gases present in the atmosphere. For that, sunlight intensity is standardized in terms of the air mass coefficient (AM),^[4] which surged as a standard for comparison. This coefficient relates to the optical path length through Earth's atmosphere, which implies a complicate mathematical treatment to obtain the corresponding spectra. The most

2. Background

important factor is the light incidence angle, also correlated with the latitude. The typical values range from 0 (extraterrestrial spectra) to 38 in the pole (incidence angle close to 90°). In addition, typical values of 1 for equatorial zones and 1.5 for tropical latitudes are defined. Likewise, there are some computational approaches to predict the solar spectrum under different atmospheric conditions as can be seen in Figure 2.4.

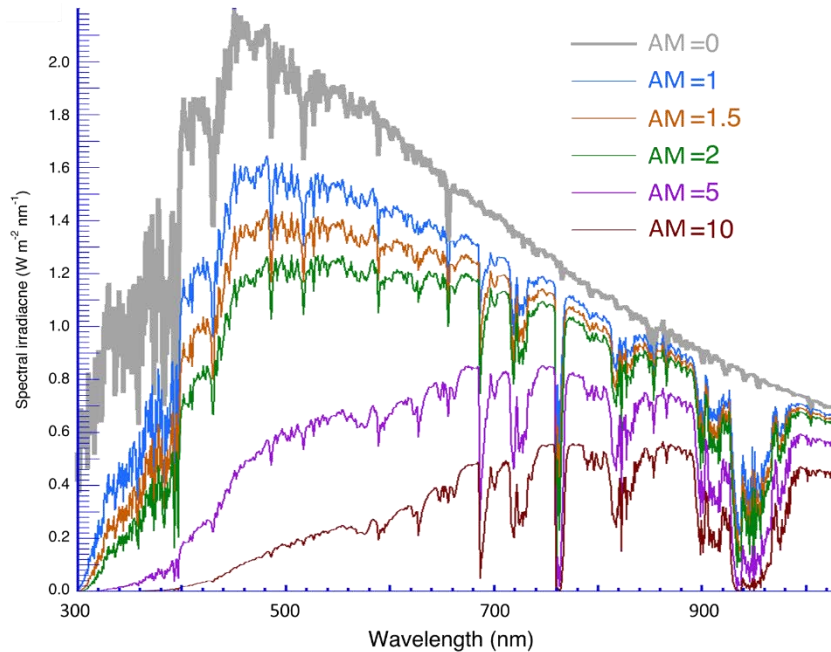


Figure 2.4. Variation of sun intensity at different latitudes.^[5]

The most relevant feature observed in Figure 2.4 is that the UV radiation passing through the atmosphere strongly depends on the atmosphere thickness that it should cross. Therefore, the UV radiation levels strongly depend on the latitude, being more intense in the equator and less in zones closer to the poles. Another relevant factor that is modifying the UV levels is the decrease in the concentration of the ozone in the atmosphere due to the reaction with emissions yielding on decomposition. That induces a lower attenuation of the UVB radiation increasing the incidence of skin problems, as it will be noted below.

Together with the irradiance characterization of the sun spectra, a simplified value is used to commonly refer to the amount of UV radiation of the sunlight and its sunburning effect. This value is the so-called UV index (UVI) and it is a standardized measurement of the sunburn capacity of the solar radiation using a linear scale with a minimum value of zero and not upper limit. In the 1990s, the values of this index changed being place dependent, but World Health Organization (WHO) looking for a

global measurement criterion, standardized it in 2002.^[6] This index is calculated as function of the solar irradiance weighted by the erythemal action reference spectra, being the integral of the weighted irradiance multiplied by a correction factor according to $UVI = k_{er} \int_{290}^{400} SI_{\lambda} s_{er}(\lambda) d\lambda$, where SI_{λ} is the spectral irradiance in $W m^{-2} nm^{-1}$ at the desired wavelength, $s_{er}(\lambda)$ is the erythemal action reference spectra and k_{er} is a constant equal to $40 m^2 W^{-1}$. The UVI should be round to the closer whole number and also associated with a color index, which represents the potential harmful effect of the radiation. The color index throws a simple and relevant message that can be seen in the Figure 2.5.

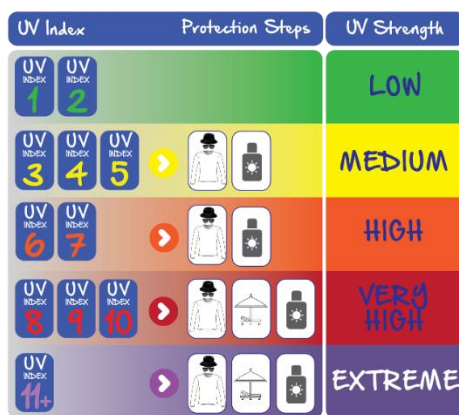


Figure 2.5. UV index and the recommended steps to be protected.^[7]

Related to the previous equation, which consider the erythemal action, surges the solar protection factor (SPF) to asset the efficiency of a cosmetic formulation protecting from the erythema. It considers the transmittance of sunlight through the sun care formulation. How to measure it and the different mathematical considerations will be described in detail in section 4.2.2. The SPF value ranges from one, where no radiation is attenuated, to highest values near to a hundred, where only 1% of the radiation is passing. For labeling in cosmetic formulations, the European commission tags SPF using a series of discrete values rounding to the following items: 6 and 10 as low protection; 15, 20 and 25 as medium; 30 and 50 as high and 50+ as very high protection level.

As previously stated, the intensity of UV radiation strongly depends on many factors. One of these factors is the latitude, which is related to the length of atmosphere that radiation crosses before reaching the surface. Other mentioned factor is the amount of ozone in the atmosphere that can block effectively the UVC and a great part

2. Background

of the UVB radiation. This factor is key in the increasing number of cutaneous affections in the last decades due to its diminution for the increasing pollution and emissions.

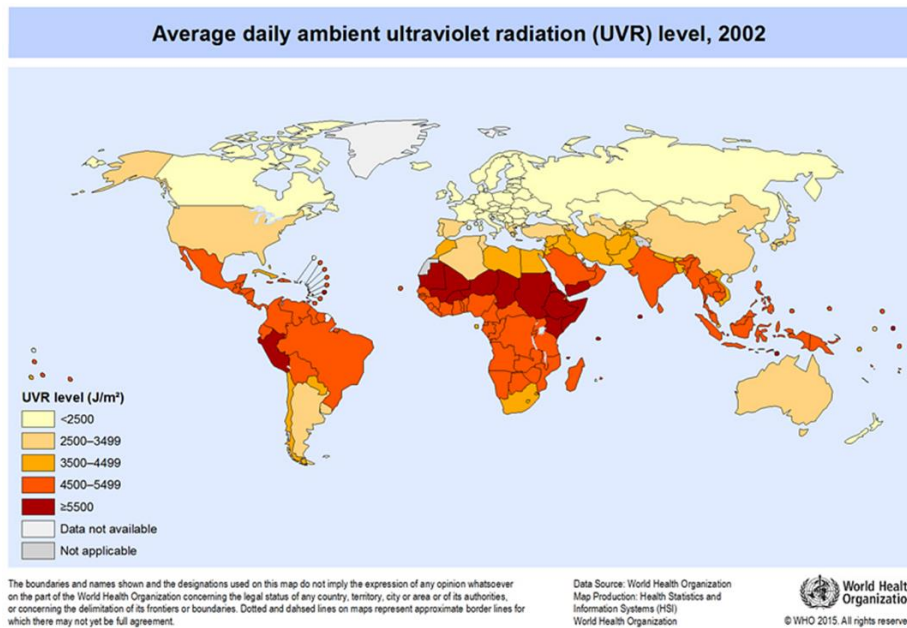


Figure 2.6. Map with solar irradiance distribution around the world in J m^{-2} , data from World Health Organization.

Other evident factor is the presence of clouds and other atmospheric phenomena like haze or fog, which also reduce the intensity of UV radiation due to the reflection and scattering processes. A usual danger occurs when people think that in these cases, there is no risk of sunburn and they do not take the right protection measures. The most important external protection measures, beyond the naturally present, will be explained in detail in the next section. Other factor is the altitude, as the described above for the air-mass coefficient. When increasing the altitude, the thickness of the atmosphere decreases and the UV radiation is less attenuated. In general terms, an increment of a thousand meters, yields in an augment on the UV intensity between 10 and 12%. Maybe the most relevant issue is the sun position or elevation. Due to that, the central hours are the most dangerous according to a higher intensity in the UV radiation, as can be seen in Figure 2.7.

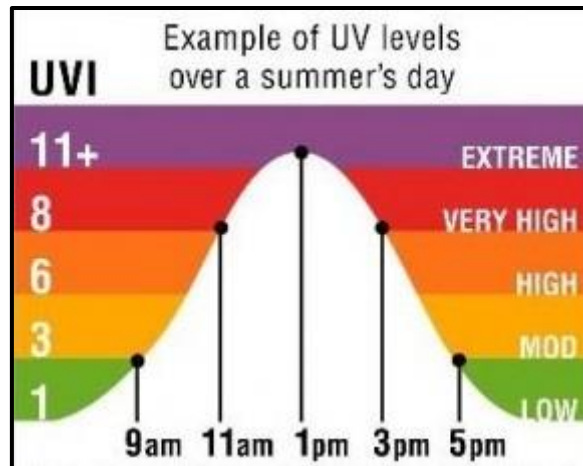


Figure 2.7. Variation along the day of the UV Index, data from New Zealand cancer society.

In addition, a similar behavior is observed in the UV intensity along the year, with an approximate Gaussian distribution presenting the highest values during summer months in the northern hemisphere.

The last important issue is the reflected radiation from all the surfaces around us, this is called albedo and supposes an increment ranging from 5% to almost an 80% of the radiation intensity.^[8] As example, snow is the most reflecting material in our surrounding media, offering a reflection of the UV radiation around an 80%. Also, sun can be reflected in the walls of buildings or the sand of the beach. Concerning the albedo, there are mathematical explanations about how much diffuse reflectance UV radiation can sunbath a person under different surrounding environments.^[9] In the following Figure 2.8, the typical reflection values of some materials are summarized.

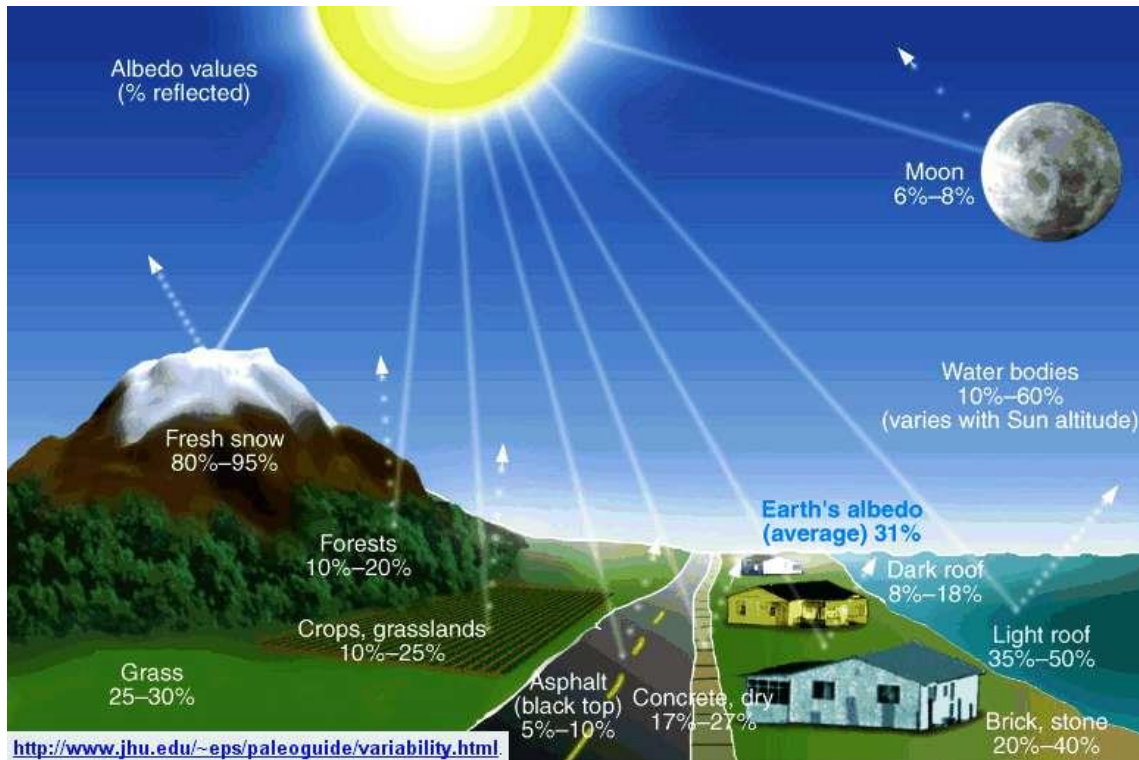


Figure 2.8. Albedo of different materials.

As observed in the previous figure, the albedo in snowy ambient is the strongest but also sand reflects around a 30% of the incident radiation on a beach. In addition, the averaged albedo on the Earth is the 31%, meaning that a third part of the incoming radiation comes back to the ambient after rising the surface.

2.1.1. Effects of sunlight in humans and applications involving UV radiation

It is well known that light was one of the driving forces in the development of life in the Earth, being essential for the plants that obtain glucose and organic molecules from CO_2 and water through the photosynthesis. This process was fundamental when the autotrophs were the most abundant organisms in the planet and the primitive atmosphere was richer in carbon dioxide. In turn, this contributed to the evolution to the actual atmosphere.

Ultraviolet light can interact with different molecules and with external tissues of the living organisms. It can promote many types of reactions; some are essential and beneficial for life, but many others are health detrimental. In this section, a global perspective about those beneficial and detrimental effects will be described in detail.

Firstly, the beneficial aspects of UV light will be summarized in the following lines. As said before, light played and plays an important role in the development of life and it is essential for most organisms. In this thesis, I will focus mainly in the interaction between humans and UV light, briefly resuming the effects in other types of organisms. The principal healthy effect on humans of the UV radiation is the production of vitamin D₃, which is a photoinduced reaction that proceeds in two steps.^[10] The first step consists of a six-electron conrotatory ring-opening electrocyclic reaction, which is a type of concerted reaction promoted by light and not allowed by the selection rules to undergo in thermal conditions. The obtained previtamin-D₃ quickly isomerizes to vitamin-D₃ by a proton rearrangement yielding the desired vitamin, being this last step an equilibrium displaced to the vitamin form at body temperature. This transformation is shown in Figure 2.9. In addition, solar radiation can decrease the bilirubin levels in blood due to a *cis-trans* isomerization where the photoisomer is easier metabolized.^[11]

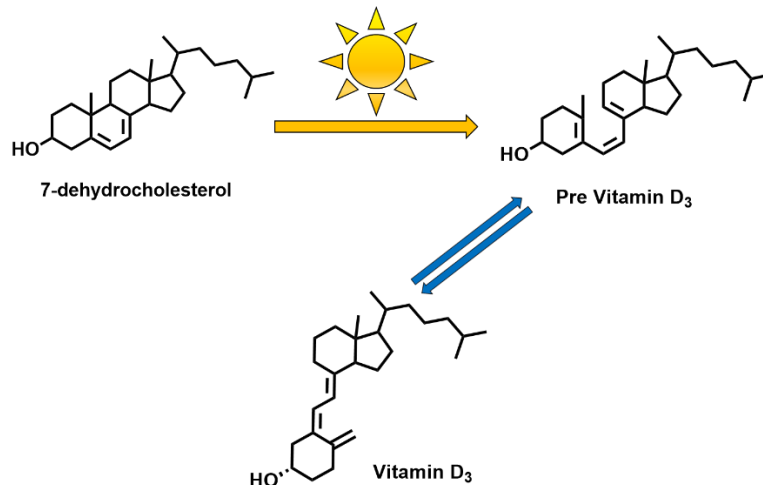


Figure 2.9. Photoinduced synthesis of Vitamin-D₃.

UV radiation also has an important role for other organisms. Some small insects can detect through their vision a proximal range of the UV radiation allowing their orientation, yielding in landmark navigation systems dependent on the intensity or direction of UV rays.^[12, 13]

2. Background

Other health-related application is the phototherapy. In this therapy, light contact is used for the treatment of some skin conditions, like psoriasis, where the UV exposure reduces the growth of the epithelial cells relieving the symptoms.^[14] Besides, some effects in the treatments of vitiligo were achieved.^[15] Other type of therapy using light is the photodynamic therapy, which is an effective treatment for some skin affections such as acne, some types of skin cancer or Bowen disease.^[16] This technique uses light in combination with a sensitizer, which transfers its energy to molecular oxygen generating singlet oxygen, which kills the surrounding cells. The sensitization process will be described in more detail in next sections.

There are many applications involving UV radiation. Some technical applications like forensic analysis use artificial UV light sources to detect hemoglobin or other substances in the crime scene. Another important application of UV in industry is the polymer curing, which uses a photochemical reaction to trigger the polymerization of a material for printing, decorating or coating different materials.^[17] As it is harmful for living organisms, the exposure to artificial UVC rays offers a sterilization procedure that is used in hospitals to destroy any microorganism due to UV light can penetrate the cell's membrane destroying the DNA and causing the cellular death.^[18]

All these applications alongside the biosynthesis of vitamin-D₃ and the different types of phototherapy rely on the beneficial or usable inputs of UV light.^[19]

As counterpoint, this radiation also presents a long list of detrimental effects for living organisms, and some aging effects also in materials that are exposed. The deleterious effects of UV radiation will be described in terms of how it affects the living organisms, especially humans where there are more studies and the effects are quantified.

The main part of the pigments used for coloring all type of materials or surfaces together with visible light absorb UV light. This light usually promotes their photolysis, which causes the loss of color due to the decomposition of the chromophore. This produces a fade of the colors that need the inclusion of a UV filter to avoid its decomposition. Related to this, sunlight also produces the breakdown of some polymers used as plastics, nylon or polystyrene.^[20] This weakens their structure facilitating the micronization causing an environmental risk due to the higher difficult to remove it and easier ingestion by marine species. Also, this effect can be complete, breaking the polymer, or partial, aging only the external surface.^[21] In this last case,

radiation affects the coating conferring an older aspect to the material. To avoid this effect, UV filters are incorporated to coating materials that must be exposed to light.

Looking into the harmful aspects for living organisms, all the effects described are applied to a great part of the organisms independently on its nature, mainly focus on humans. All the effects of sun exposition are cumulative, which is a major concern for being an increasing problem during last decades.

As expected, apart from the atmosphere, the skin is our first natural UV defense. The skin is a physical barrier, but it does not reflect all the incident radiation. Due to that, the body absorbs a great part of the incoming radiation. Fortunately, the absorbed radiation does not penetrate equally and does not produce the same changes in it. As can be seen in Figure 2.10 there are mainly two levels of penetration in skin.

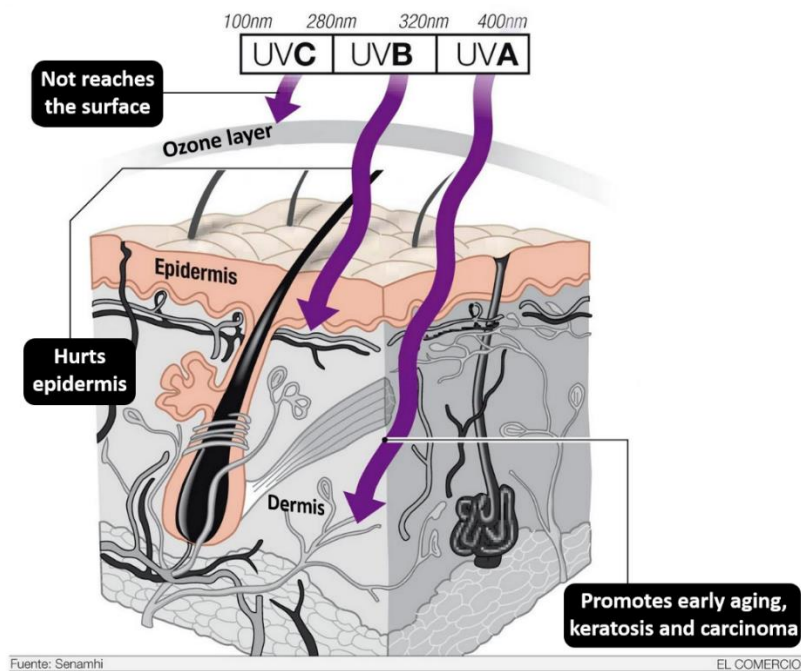


Figure 2.10. Skin penetration and typical effects of different UV radiations.

The UVB radiation only penetrates a few micrometers in the epidermis but it is the most dangerous due to its higher energy. This UVB radiation hurts the epidermis producing the so-called erythema or sunburn. Erythema is a temporary redness in the epidermis due to an excessive UVB exposition.^[22] There are different grades depending on how much tissue is burned, with deeper hurt more severe is the damage. An excessive and prolonged UVB exposition could yield in significant problems, promoting permanent damage in the skin. The gravest examples of these persistent problems are

melanoma and skin cancer.^[23] More details on these terms and how they are produced will be given below. In addition, photodermatoses and eye tissue damage are important effects especially promoted by UVB light.

The UVA radiation penetrates deeper, hundreds of micrometers reaching the dermis but being less harmful than UVB. Also they can produce skin cancer, but with a lower probability being skin aging the most common problem.^[24] The initial behavior of UVA exposure is the stimulation of melanocytes favoring the production of melanin. This is associated with an increase in the pigmentation, producing a darkening in the skin due to melanin accumulation. The other dominant effect is the production of oxidizing chemical species, such as free radicals or singlet oxygen. Usually these radical species are produced by sensitization when other molecules, cellular or external components like sunscreens, absorb the UVA radiation and their energy is transferred to the other molecule generating radicals by removing an electron. These reactive species can damage the cellular macromolecules; especially important is the damage to DNA and cancer. Additionally, the aging is induced by the photolysis of collagen, which produce a loss of elasticity and wrinkles in the skin.

As shown, the main effects of UVB and UVA radiation are the appearance of erythema and pigmentation, respectively. These two effects are not produced with the same efficiency along the whole UV range, being wavelength dependent. The efficiency of both processes is quantified at each wavelength using the corresponding reference action spectrum, the erythemal (s_{er}) (used in the calculation of UV index) and the persistent pigment darkening (PPD), whose values comes from the reference standard ISO 24443 for the calculation of solar protection factor (SPF). Both spectra can be seen in Figure 2.11.

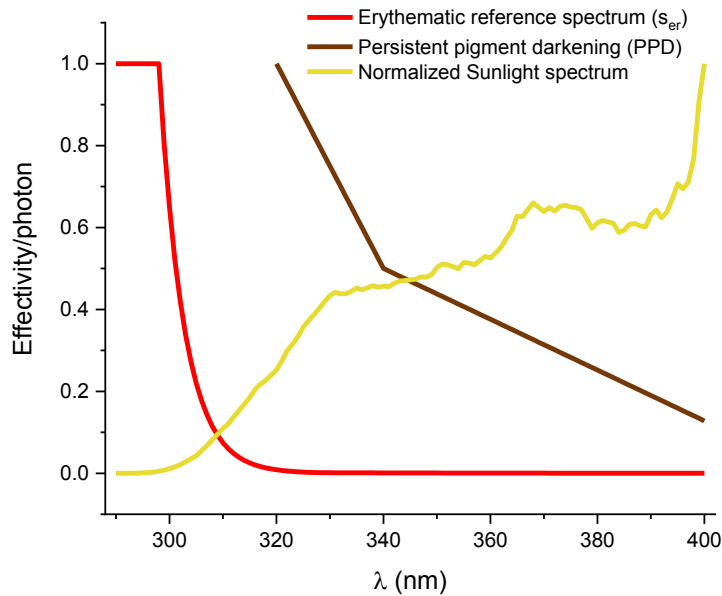


Figure 2.11. Sunlight together with Erythema and PPD action spectra.

From the erythemal action spectrum, two conclusions are clear. As expected, shortest wavelengths are the most dangerous, presenting a total effectiveness between 290 and 301 nm, it means that each photon induces erythema. In contrast, photons below 320 nm are not active for erythema, showing an efficiency below 1%. Regarding the PPD action spectrum, it starts in 320 nm decreasing to 50% at 340 nm, being the most efficient region, but in contrast with erythema, all photons contribute to pigmentation with an efficiency of at least 10%, so it presents a greater accumulative effect than erythema.

Therefore, considering these biological-dermatological effects of UV radiation, a new trend with a small modification in the delimiters arises. The typical delimiters for UVB (280 - 315 nm) and UVA (315 - 400 nm) were approved in the International Light Congress on 1912 considering photochemical issues.^[25] These new delimiters, despite not being officially recognized, are being increasingly used for all the photochemical community, not only for biologists and dermatologists. Then, this range considers UVB between 290 and 320 nm, and UVA between 320 and 400 nm and will be used along this memory.

As commented before, erythema is the first sign of an over-exposition to sunlight,^[26] it appears as a skin redness and begins a few hours after UV exposition. The amount of UV radiation determinates the importance and the severity of the

damage. Regarding the spectral characterization of sunlight and the erythemal action spectrum, a safe dose can be estimated. At this point, surges the minimum erythemal dose (MED) as the minimum amount of radiation needed to produce sunburn. The MED depends on the skin of each individual, but it is usually correlated with an *in-vitro* dose of 200 J m^{-2} of erythemal weighted sun exposure.^[27] Also, the standard erythemal dose (SED) is defined in the ISO 17166:1999 and CIE 125-1997 as 100 J m^{-2} .

In addition, the pigmentation increase is the visible sign of UVA exposure. In a moderate exposition, it stimulates uniformly the melanocytes and no marks or spots are observable. When an over-exposition is reached, the formation of cumulous of melanin and freckles become a sign of harmful effects. Also, skin aging due to radical formation and oxidative stress are the other consequences of UVA exposition.

Continuing with the detrimental effects, DNA damage can be produced by direct absorption of DNA molecules, which absorb UVB radiation. But also indirect damage occurs when other molecules (surrounding proteins or DNA bounded chromophores) absorbs UVA radiation and transfers energy to DNA in a sensitization process.^[28] The DNA is essential in cell life, controlling protein production and cellular growth. This DNA damage is produced in the nitrogenous bases, which can absorb UVB light efficiently undergoing some photoreactivity. Pyrimidinic bases, thymine and cytosine are the most reactive bases, presenting different types of photoreactivity.^[29] The most common is the [2+2] cycloaddition to form a cyclobutane dimer and the (6 - 4) adducts, that can occur as can be seen in Figure 2.12. In addition, sensitized reactivity could be achieved by energy transfer mechanisms, inducing similar reactivity than the obtained from direct irradiation. In this case, the necessary radiation to induce sensitized DNA damage is usually UVA and the sensitizers can be endogenous or exogenous molecules.^[30]

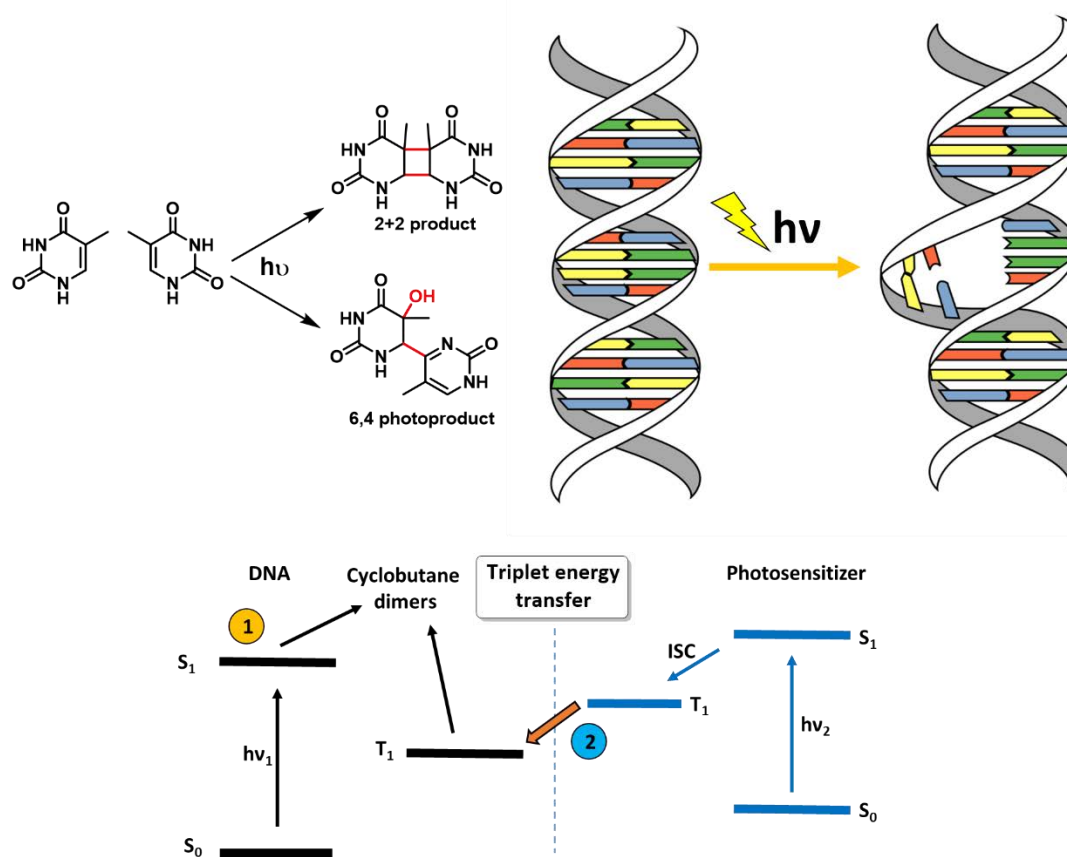


Figure 2.12. Main thymine photoproducts formation (top left). Schematic DNA damage by thymine dimers (top right). Direct (1) and sensitized (2) formation of cyclobutane dimers (bottom). Adapted from Cadet review.^[30]

The DNA damage is the most dangerous effect of UV radiation and usually yields in skin cancer, but cells have some protection mechanisms to repair that damage avoiding cellular death. A general description of these mechanisms will be presented in section 2.1.2.

The most harmful effects of UV light often begin with a mutation in DNA; this supposes a photocarcinogenesis event that usually derivate into a skin cancer. There are three main types of skin cancer, basal cell carcinoma, squamous cell carcinoma and melanoma. Being both types of carcinoma the most frequent cases,^[31] and the less aggressive, with a survival rate higher than 95% if it is detected early. The most harmful is melanoma,^[32] even presenting 10-fold lower incidence than the other skin carcinomas with only 5% incidence. It is becoming an increasing health problem due to its high growth in the last decades, especially relevant from the 1990s. Even being the most aggressive skin cancer, it presents a survival rate around 80% in Spain, due to this small localization and not too high trend to metastasis.

The effects of the UVA radiation at molecular level mainly concerns the generation of free radical species, like reactive oxygen species (ROS). This type of species are known to promote skin-aging process, due to their possible reactions with DNA.^[33] One of the most representative ROS is singlet oxygen, which is the most abundantly generated and a strong oxidizing agent.

In addition, other effects concerning the UV radiation exposure can be assessed. For example, the exposition of the eyes to UV light can produce ocular damages like conjunctivitis^[34] or more severe and permanent as cataract or cornea/retina damage.^[35] Immunosuppression effects can also be induced by UV light.

2.1.2. Natural photoprotection and photodamage repair mechanisms

As mentioned, the first natural barriers against UV radiation are the ozone layer and skin. Apart from them, organisms have developed their own photoprotection mechanisms to minimize UV-induced detrimental effects. One of the most important, due to its high risk for the organisms is the DNA damage. In humans this is partially solved by the scission of the damaged portions of DNA and the replication using the other strand as pattern.^[36, 37]

To avoid these detrimental effects, there are some metabolites which try to protect cells by absorbing light and averting irradiation of the more sensitive molecules, such as DNA.^[38] Indirect protection can be provided by pigments or antioxidants, such as carotenoids.^[39] Antioxidants provide protection by quenching UV-induced reactive oxygen species inside skin,^[40] playing an important role as scavengers, trapping free radicals and ROS, preventing the skin aging.^[41]

A very common strategy to avoid UV-damage is the presence or UV-induced synthesis of secondary metabolites that efficiently absorb potentially harmful light. These compounds should absorb light (mostly UV radiation) and dissipate the energy as heat preventing damage to the cells, so being natural sunscreens.

Several types of metabolites are known as UV blockers that protect living organisms against damaging light.^[42] Some examples can be seen in Figure 2.13.^[41, 43] Scytonemin is a very stable pigment found in some families of cyanobacteria, which

effectively shields the cells from UV and blue radiation.^[44] Melanins are the most widely extended pigment, being a group of water insoluble compounds, which present a broad UV absorption with a characteristic red-brown color.^[45] This type of compounds confers photoprotection to different living organisms, from fungi to superior animals. Also a similar behavior is observed with chromones or flavonoids, which present antimicrobial capabilities combined with a high UV absorptivity.^[46] Carotenoids indirectly protect cells by quenching photosensitized products and trapping free radicals rather than by direct absorption of UV light.^[47] Other examples of natural molecules^[48] that play a photoprotective role are the sargaquinoic acid,^[49] sinapoyl compounds,^[50, 51] myxoxanthophyll, zeaxanthin, canthaxanthin, echinenone, chlorophylls,^[52] and bacteriochlorophylla.^[53]

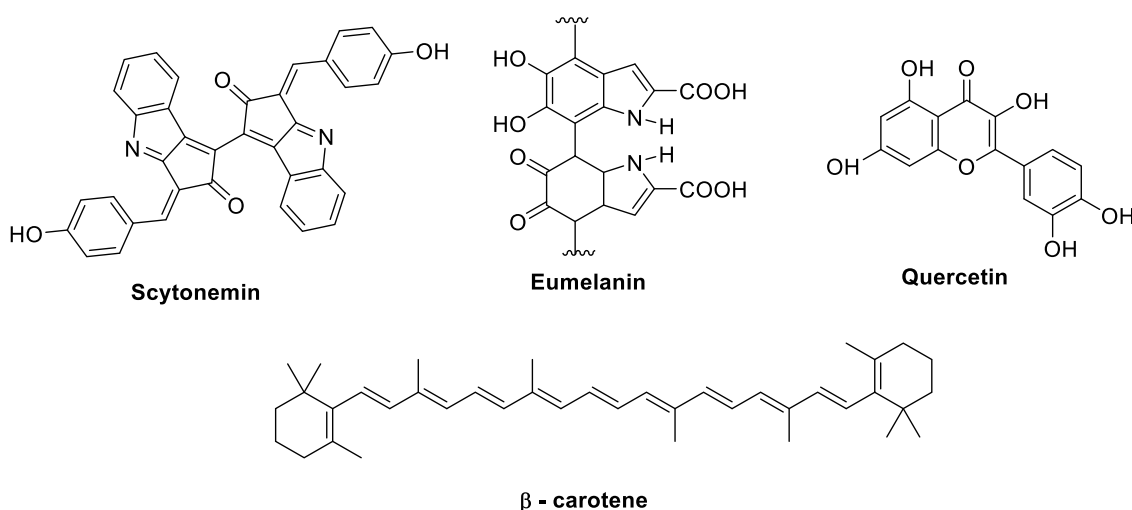


Figure 2.13. Some relevant natural sunscreens.

A special family within this group of natural pigments are the mycosporine-like aminoacids and the related gadusol, which were discovered at the end of the 1960s.^[54] These compounds will be described in detail in section 2.3. In addition, these derivatives present the strongest UV absorption in nature,^[55] being potential candidates to be used as artificial sunscreens.

As previously mentioned, living organisms have developed a series of repair mechanisms to minimize the effects of photodamage.^[56] DNA damage induced either directly or indirectly by sunlight is randomly distributed among the genome. Due to this random distribution, the biological consequences of DNA lesions are not of equal importance. As consequence, repair of a minority of lesions, as in the exons or in the transcribed strand, has much greater biological importance than repair of others in

the introns or non-transcribed strands. DNA repair systems focus on repairing these regions, such as transcribed strands, faster than others, in order to relieve phototoxic effects. Typical DNA reparation mechanisms are nucleotide excision, which removes the affected fragment repairing as if the damage had not occurred before. The main problem is the reparation speed, which is slow, taking more than 24 hours for removing of pyrimidine dimers from skin.^[57] Base excision removes the modified bases and releases them from the DNA backbone generating vacant sites. Also, it is very efficient in the removal of oxidation products, repairing them in about 6 hours.^[56] Other very efficient mechanism is the photoreactivation, which reuses the absorbed light to refuse aberrant covalent bonds in DNA.^[58] The responsible enzymes are photolyases that can repair quickly and efficiently the direct forms of photodamage inside human cells. Lesion bypass by polymerase is the last reparation mechanism, but it is not a reparation by itself.^[59] Instead, it prevents the replication of damaged DNA allowing restoration by other methods.

2.2. Need of extra protection: artificial sunscreens

All these mechanisms are working together to maintain living organisms safe from photodamage. Nevertheless, this protection in some cases is not enough to efficiently avoid the adverse effects of the increasing amount of UV radiation that we are exposed to. Thus, in the case of humans, extra protection is needed. Nowadays, humans practice many outdoor activities that implies a greater sun exposition with respect to some decades ago. Also, a greater time exposure and a known increase in the UV levels, especially in the UVB region due to the decreasing concentration of ozone should be considered.

Obviously, the first and the only fully effective protection mechanism is the non-exposition to sunlight. However, this is not a reasonable measure to asset, especially considering the need of a moderate UV exposition involved in different biological processes. Therefore, the most feasible efficient solution is to protect ourselves by a mechanical sunblock using clothes covering our skin, minimizing in this way the sun exposition. This is a partial solution due to the actual life habits, which includes sunbathing in the major part of outdoor activities.

With these social conditionings behind, the application of some products to improve the UV resistance of our skin is crucial to allow the maintenance of our sun habits in the safest way. For that, the widest extended solution is the utilization of topic formulations including artificial sunscreens, which cover the skin creating a film with the sunscreen agent incorporated in a cosmetic formulation.

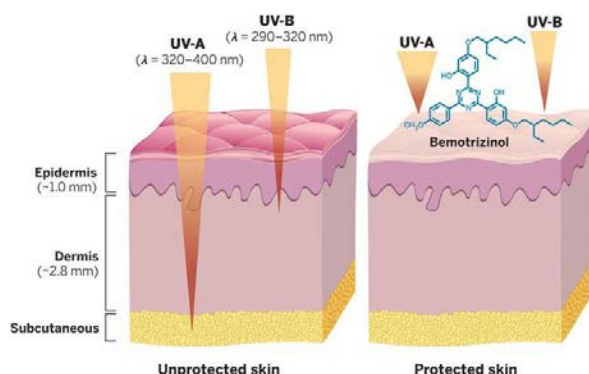


Figure 2.14. Light penetration through skin with (right) and without (left) sunscreen.^[60]

2.2.1. Artificial sunscreens: action mechanisms and features

These synthetic UV filters are chemical compounds that absorb or scatter UV light. Actually, many compounds that can absorb in the desired UV region are available, but not all can be used as sunscreens. The selected candidates should almost partially fulfill the desired capabilities, presenting a strong UVA - UVB absorption and a high photostability, which means absence of photoreactivity or a non-destructive one. Lack of emission (fluorescence or phosphorescence), internal conversion and vibrational relaxation mechanisms are desirable too, ideally in combination with chemical and thermal stability.

There are many different regulations concerning the use of sunscreens in cosmetics formulations. The Food and Drug Administration (FDA) in United States, Australian/New Zealand Standard (AS/NZS) in Australia, Japan Cosmetic Industry Association (JCIA) in Japan. Also the European Cosmetic and Perfumery Association (Colipa) rules it in Europe.^[61]

As it can be observed from the legislation on this field, there is not a global criterion in the regulation of the UV filters. In the United States, they are treated as drugs and a more restrictive protocol for new inclusions is applied. New compounds should pass the full set of clinical tests. Not all filters are allowed for all administrations, being only nine the filters globally approved in 2019. In Europe, actually there are 27 approved for their use in cosmetics. For the sake of comparison, in USA there are only 24, but not all of them are usable in Europe. For example, *para*-aminobenzoic acid (PABA) is still allowed by FDA but not anymore in Europe. A summary table containing all the approved sunscreens in Europe and their allowed loads in cosmetics is included in Appendix A.

Nowadays, the cosmetic used UV filters can be divided in two main and clearly differentiated groups. The division is not only made by their action mechanism, physical or chemical, but for their organic or inorganic composition too.

2.2.1.1. Physical filters: titanium dioxide and zinc oxide

Physical filters are a series of inorganic solids that can interact with UV radiation. The light interaction is mainly due to scattering, reflection and in a smaller contribution to absorption.^[62] The widest used in cosmetics are titanium dioxide (TiO₂) and zinc oxide (ZnO), due to their higher UV interaction.^[63] Also there are some others, like barium sulfate, mica or glass, which are used but not in cosmetics.^[64] The goodness of these derivatives as sunscreens could be attributed to different physical properties such as particle size, dispersion media, crystalline form and particle number (concentration). All these factors are adjusted to maximize the scattering and absorption of UV light. The most tunable factor is particle scale, which was studied in a broad range of sizes. The micronized TiO₂ and ZnO present in many sun care formulations show several practical problems. The most important are the difficulty on application, the possible staining on clothes and the deposit of a white residue over the skin, blocking skin pores acting as a comedogenic.^[65] Because of these practical problems and the more accessible nanomaterial preparation, nanoparticles of ZnO and TiO₂ began to be used during the last years.^[66] Decreasing the particle size to nanometric scale maintains or improves its capabilities as sunscreen, solving the main part of the practical issues found in the micronized materials. However, in the case of using nanosystems as sunscreens,^[67] some issues regarding safety were considered during the development of the nanoscale inorganic UV filters. The main problem considered is the potential epidermis penetration, due to the smaller particle size. During the last years, some conflicting evidences^[65] surged as to whether nanoparticles are small enough to penetrate the epidermis and to be absorbed into the human blood stream, causing toxicity with long-term use.^[68] However, the newest studies refused that theory as a result of the low epidermis penetration observed experimentally and the shedding of the epidermis cells, which avoids cellular penetration and prevents tissue accumulation.^[69] Also, penetration is difficult by the trend to form aggregates, increasing the effective particle size.^[66]

Looking into the physicochemical properties, nanometric titanium dioxide mainly absorbs in the UVB and ZnO does it in the UVA region, so together they can be used as a broad-spectrum filter, covering a great part of the UV region.^[64] Other phenomenon occurring when particle size is reduced is a decrease in the visible light

scattering and its blueshift, increasing its capacity of scattering interaction with UV light.

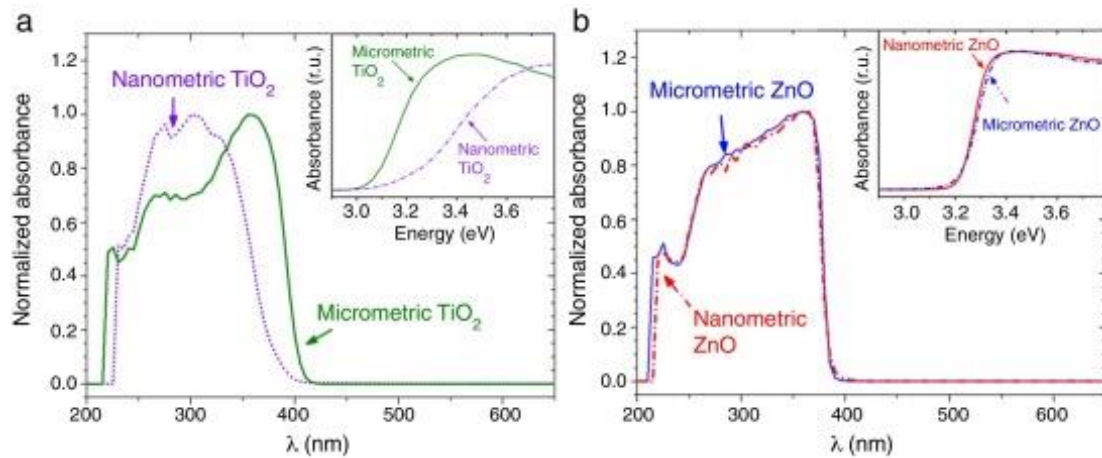


Figure 2.15. Comparative UV spectra for micrometric and nanometric TiO₂ (a) and ZnO (b).^[70]

According to the actual regulation in Europe, both physical filters can be included in sunscreen formulations with a maximum load of 25%, independently of the particle size. Even being 25% the allowed maximum load, typically lower values, 10 to 20% are employed in cosmetics to avoid aggregation problems in the formulation.

2.2.1.2. Chemical filters: the most widely used

The other type of sunscreens are chemical filters, being organic compounds with a protection mechanism based on their strong UV absorption. The mechanistic difference between both types is clear. In chemical filters, only absorption of light is representative, while in physical filters absorption together with reflection and scattering are possible. This difference lies in the aggregation state, inorganic filters are solid particles while organic filters are dissolved single molecules. Their absorption maxima depend on the chromophore, which is representative for each family of organic filters. Related to the position and spectral width, three distinct categories could be defined as UVB absorbers, UVA absorbers and broad-spectrum absorbers, which attenuate along the whole UV range (290 - 400 nm). This classification is also applied to physical filters, as mentioned in their description. Nevertheless, the most usual way to classify chemical filters is according to their molecular structure. This is the best classification criteria because chemical properties and photochemical features are

quite similar within the same family. In addition, most chemical filters are oil soluble; only a few exceptions are soluble in water.

In the following part, the most relevant chemical sunscreens together with a brief description of the known action mechanism and the relevant features concerning safety and possible problems will be described, along with the photochemically derived problems for the most representative families of chemical filters. For the most common families, a detailed analysis of the dynamics of their deactivation process is also commented in section 5.3.

PABA: *p*-aminobenzoic acid and derivatives

4-Aminobenzoic acid (also known as *para*-aminobenzoic acid or PABA) is one of the strongest UVB absorbers, with a $\lambda_{\text{max}} = 283 \text{ nm}$ and $\epsilon = 15300$, and one of the first compounds allowed for using as sunscreen in cosmetic formulations, being employed since 1930s alongside its esters and amino-alkylated forms.^[71] *Para*-aminobenzoates and other systems for which electron donating and withdrawing substituents are positioned *para* respectively, feature a twisted intramolecular charge transfer (TICT) state accessible upon photoexcitation, being the accessible deactivation pathway to ground state.^[72] PABA and its derivatives present an impressive photostability with a decomposition rate of 0.0001 min^{-1} , being the most photostable type of sunscreen.^[73] Also, PABA derivatives were incorporated in triazines yielding in strongly photostable molecules.

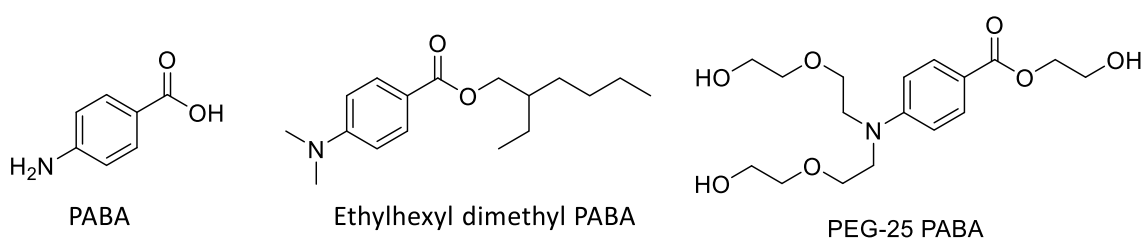


Figure 2.16. PABA and some approved derivatives.

In 2013, Colipa dismissed PABA (Commission Regulation (EU) N° 344/2013 of 4 April 2013) together with derivatives containing the free amino group. In other worldwide regulations, it still remains usable. However, its alkyl-ester derivatives are

still allowed in Europe, see Figure 2.16. This UV filter was dismissed due to its contact allergic and photoallergic potential.^[74] In addition, the two allowed derivatives, ethylhexyl dimethyl PABA and PEG-25 PABA, can be incorporated with loads of 8 and 10%, respectively.

Cinnamates: octinoxate and derivatives

These compounds present similar structures to PABA, also featuring a donor-acceptor system (Figure 2.17) with a double bond included between the carboxyl and phenyl groups, which increases the conjugation and redshifts around 20 nm the absorption maximum to a $\lambda_{\text{max}} = 311$ nm, in case of octinoxate. Together with this shift, the deactivation mechanism also changes completely. Here, is the double bond that allows a new *E-Z* isomerization pathway being the preferred relaxation channel.^[71, 75]

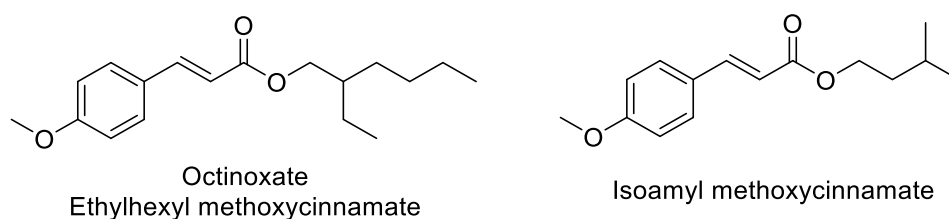


Figure 2.17. Cinnamate derivatives.

The most extended is ethylhexyl methoxycinnamate, so-called octinoxate or octyl methoxycinnamate, which can be used up to 10% in cosmetics. This *E-Z* isomerization upon irradiation yields in a photostationary state with a proportion of 40 - 60%. This mixture of isomers translates into a decrease in the total absorptivity of the sunscreen due to the lower absorption coefficient of the *cis* with respect to the *trans*-isomer.^[76]

There are a great number of experimental and computational studies regarding the excited state features and dynamics of these derivatives.^[77, 78] The *cis-trans* isomerization occurs through a $\pi-\pi^*$ excited state in the picosecond timescale.^[79] In this case, the decomposition rate constant is $k = 0.031 \text{ min}^{-1}$, which is three hundred times bigger than PABA.^[73] This photoinstability is mainly due to a [2+2] cycloaddition of the central double bond, forming a cyclobutane product, as happens in thymine dimers (Figure 2.12).

Dibenzoylmethanes: avobenzone

Avobenzone is the most employed UVA filter in the world. The deactivation pathway involves an intramolecular hydrogen bond in the 1,3-dicarbonylic system (Figure 2.18.a). The *enol* form is the most stable isomer and the *keto* is only formed upon irradiation and it is prone to degradation by triplet state population,^[80] with an energy close to 60 kcal/mol.^[81] Dibenzoyl methane derivatives present exceptionally high molar extinction coefficients ($\epsilon > 30000$) in *enol* form. Avobenzone is also reported to be relatively photolabile if it is improperly formulated in cosmetic vehicles. It is not as stable^[80, 82] as other sunscreens, for that, triplet–triplet quenchers have been introduced to stabilize it (a patent by L'Oréal uses octocrylene for its stabilization) and a number of emollients^[83] and active ingredients^[84] are purported to stabilize the more desirable *enol* form of the molecule.^[85] In formulation, a peculiar effect is observed, presenting worst SPF values in higher concentrations to the allowed 5%, being the only filter that presents this feature due to its photochemical instability.

Benzophenones: oxybenzone and derivatives

Benzophenones are the most numerous group of sunscreens, being approved around the world 10 different types, so-called BPH-1 to BPH-10. All benzophenones exhibit a hydroxyl group in *ortho* substitution from the *keto* moiety, see Figure 2.18.b. The excited state relaxation occurs through an excited state proton transfer (ESPT) between the hydroxyl group in the phenyl ring and the *keto* moiety.^[86] Some benzophenones could act as hormonal disruptors, the most studied ones are benzophenone 3 and 4. *In vitro* experiments using human breast cancer cells suggest that benzophenone 3 (oxybenzone) can exert both estrogenic^[87] and antiandrogenic^[88] effects. In humans, in a single-blinded and short-term clinical study, exposure to oxybenzone did not produce clinically relevant effects on hormonal homeostasis.^[89] In contrast, it was detected in urine of studied subjects in the United States and Denmark; however, it was not correlated with the use of sunscreens.^[90]

2. Background

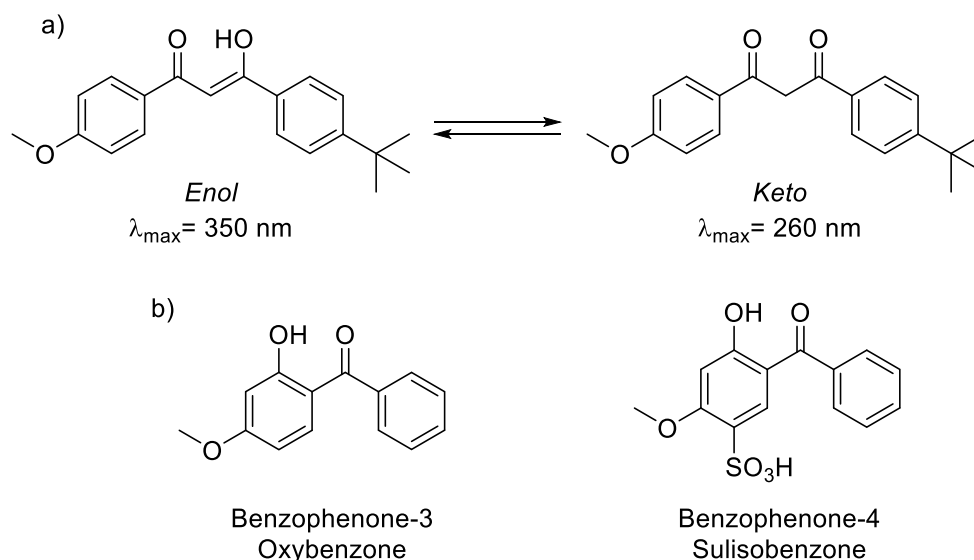


Figure 2.18. a) Tautomeric forms of avobenzone, b) two examples of benzophenones.

BPH-3 and BPH-4 can be used up to 10 and 5%, respectively. BPH-4 is one of the water-phase sunscreens, with a water solubility of 250 g/L.

Salicylates: ethylhexyl salicylate and derivatives

These derivatives based on salicylic acid started to be used in the 1950s. In these cases, an intramolecular excited state proton transfer is the responsible for the photoprotective capabilities.^[86] Providing an ultra-fast nonradiative relaxation channel to the ground state in few hundreds of femtoseconds.^[91] The most used one is the homomenthyl salicylate, so-called homosalate (top-left of Figure 2.20). Also, the intramolecular hydrogen bond induces a redshift in the absorption to ca. 300 nm instead of 260 nm in the *para* analogue. These compounds present low skin penetration and irritability. It is not common in Europe but remains as a reference in USA.^[92] Additionally, 5 and 10% of ethylhexyl salicylate and homomenthyl salicylate, respectively, could be incorporated in cosmetics formulations in Europe.

Triazine derivatives

Nowadays, triazine derivatives are the trendiest topic in the development of UV filters. These compounds present a stronger absorption due to the three chromophores present on the molecule, based on simpler previous sunscreens.^[93] In addition, these derivatives can be particularized in nanometric scale, as happens to tris-biphenyl triazine.^[94, 95] Usually 10% load is approved for cosmetics formulations, with the exception of ethylhexyltriazone with a 5%. In addition, they are the least studied from a photophysical and mechanistic point of view.^[93]

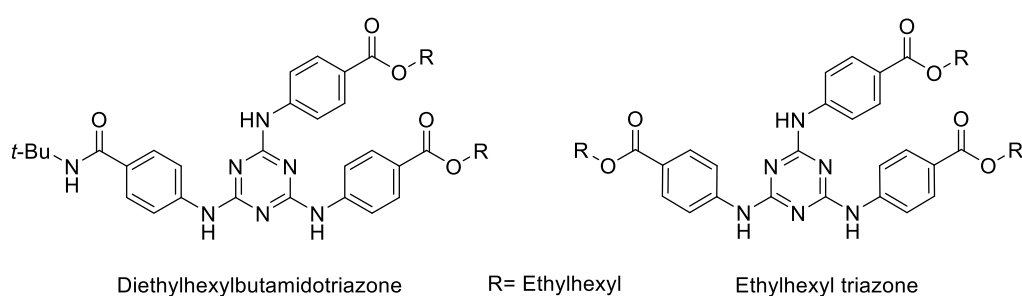


Figure 2.19. Triazine-based sunscreens.

Other derivatives

In addition to the previously described sunscreens, the most important of the remaining UV filters is octocrylene, being one of the most widely used sunscreen at present.^[96] It is a broad-spectrum (UVB - UVA) filter, photostable (0.0014 min^{-1}) and with a fast relaxation in ca. 2 ps.^[97] The mechanism behind remains unclear,^[86] but it seems to be a *cis-trans* isomerization. Nevertheless, it commonly acts as stabilizer for other sunscreens,^[98] typically avobenzene.^[84] Also some cases of photoallergy have been described.^[96] Octocrylene is an oil-phase sunscreen, which can be used up to 10% in Europe.

Camphor derivatives are others commercial sunscreens that owe their photoprotection mechanism to a reversible photoisomerization. 4-methyl benzylidene camphor (enzacamene) is the most extended. Due to it functions as an avobenzene photostabilizer, almost certainly by a triplet quenching mechanism.^[73] All camphor derivatives can be used in smaller amounts than other filters, ranging from 6 to 4%.

2. Background

In addition, imidazole and drometrizole derivatives are the least studied and employed sunscreens, see structures in Figure 2.20. Although, it can be used up to 10 and 15%, respectively.

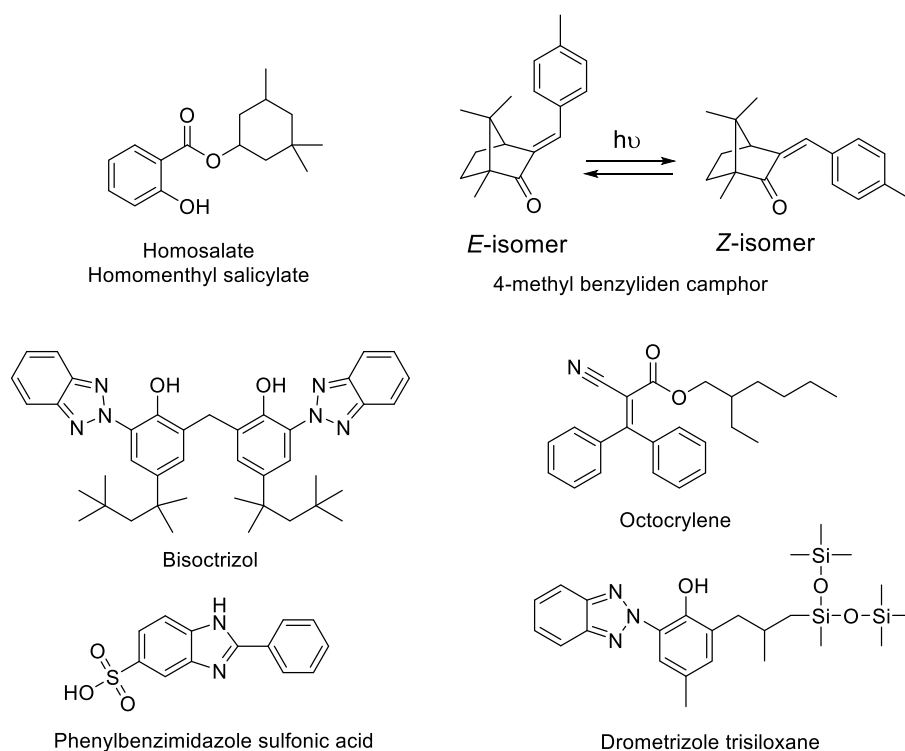


Figure 2.20. Salicylates and other families of sunscreens.

2.2.2. Current general concerns with sunscreens

At present, there are a changing number of sunscreens globally approved. These compounds are under a slow but constant revision and some dismisses occur frequently. An example of this is that European regulation has overcome close to twenty modifications in ten years.^[61] The principal concern about sunscreens is their safety; some of them have been proved as endocrine disruptors^[99] or conducting some photo allergies.^[100, 101] Others can produce triplet formation and could generate ROS, like avobenzene or oxybenzone.^[102] The problematic shown in some filters with the lower photostability, is partially solved by different methods.^[81] Increasing of the optical density and dispersion yields in a global enhancement of photostability, due to the major absorption in the external layers of the sunscreen film and the lower probability of photoreactivity between surrounding molecules. Addition of antioxidants or other UV filters to stabilize the reactive compounds, trapping excited states or reactive species.

Coating the pigments should stabilize according to the limited reactivity. Also triplet-triplet and singlet quenchers are acting as stabilizing agents.^[103] Other important issue regarding the physicochemical properties is the synergic effect when combining different UV filters; it can have stabilizing or boosting effects or detrimental for the final product result. As examples, avobenzene is stabilized in combination with oxybenzone, octocrylene,^[84] or encapsulation,^[104] but drastically decrease in presence of octinoxate,^[105] where the resulting photoproducts can promote photoallergic reactions as well.^[106]

Today there is no single sunscreen available that by itself can provide high SPF and broad-spectrum protection without aesthetic drawbacks. From a photochemical point of view, the main part of the commercial sunscreens does not fulfill the ideal features for an optimal UV filter as stated in section 1.3. Nevertheless, the different approaches previously shown partially solve the individual problems using it in combination with other emollients or UV filters. With the current state of UV filter technology, sunscreen products require the right combination of filters in the formulation to obtain both high efficacy in UV protection and optimal aesthetics to enhance compliance.^[84] Because of this, the development of new sunscreens represents a main concern especially for chemical companies, but also from an academic research point. The need of new and ideal sunscreens was also postulated as a milestone in its development.^[107] For that reason, natural sources could yield in proactive solutions to that problem, being an inspiration for the design of new efficient sunscreens.

Complementary to the cosmetic application, which is mainly described in this section, sunscreens are being used as additives in diverse materials, such as polymers, textiles or coatings.

2.3. Mycosporine-like aminoacids and gadusol

Mycosporines (also known as mycosporine-like aminoacids or MAAs) constitute a singular class of photoprotective compounds. These secondary metabolites are very water-soluble, low-molecular weight, colorless products that share a similar chemical structure. Their UV spectra show a single and strong absorption band in the 250 - 350 nm region. This fact, together with their high photostability and lack of luminescence contributes to the efficiency of these compounds as sunscreens in many types of organisms. In addition, gadusol is a related metabolite, seeming to be an evolutive precursor of MAAs, also being one of the simplest molecules with UV filter capabilities.

2.3.1. Location, structure, properties and biological roles

Mycosporine-like amino acids are present in many organisms in different parts of our planet. This type of UV-absorbing metabolites^[108] appears widespread among the fungal classes *Aphyllophorales*,^[109] *Basidiomycetes*,^[110] *Bacilliarophyta*,^[109] *Deuteromycetes*^[111] and *Zygomycetes*,^[110] but it is absent in *Agricales*^[112] and in the protozoan investigated.^[109] Likewise, these metabolites are found on the surfaces of apples exposed to solar radiation.^[113] More recently they have been also found and isolated from a broad array of marine species,^[114] ranging from algae,^[108] bacteria,^[115] symbionts like dinoflagellate algae associated with scleractinian corals,^[116] vertebrates,^[109] embryos of shrimp,^[117] lens tissues of fish^[118] and in the external mucus that covers samples of *Fungiidae*.^[119] However, they have not been detected in members of the genus *Ctenophora* and in certain holothurians.^[109]

Their abundance in a broad type of organisms suggests that these compounds have some properties making them useful for the organisms' life, being more than a residual metabolite. Analyzing the distribution around the planet of the species that feature these compounds, it is found that they are present in a broad range of latitudes, from temperate and tropical climates to the frozen Antarctica's oceans.^[108, 109, 114] Thus, these compounds appear in all type of ecosystems and organisms, but they are more

relevant in aquatic species, fungi, bacteria, algae and plants; and especially in the external parts of cells or epithelial cells in more complex organisms.

As mentioned, MAAs appear in a wide range of organisms and ecosystems. Interestingly, these compounds also present a very similar structure that contains a substituted cycle, specifically an aminocyclohexenone or an aminocyclohexenimine, a simplified scheme with these scaffolds can be seen in Figure 2.21. Fungal metabolites that present a UV absorption band at 310 - 320 nm possess exclusively the aminocyclohexenone ring and are commonly known as mycosporines. Mycosporines have a methoxy group in C2 position and feature a band with a maximum at 310 nm while nor-mycosporines have an hydroxyl group in C2 position and the maximum is shifted to 320 nm.^[120] This basic structure can be subsequently modified in different points, resulting in a diversity of more than 30 structures, considering both cyclic possibilities. In case of marine metabolites, their UV-absorption bands range wavelength maxima from 320 nm to ca. 360 nm and molar absorptions coefficients (ϵ) in the range from 28000 to 60000 M⁻¹ cm⁻¹.^[121] As mentioned, in this type of compounds two possible chromophores responsible for the UV absorption are described in Figure 2.22 and Figure 2.23. In fact, MAAs have been considered as the strongest UVA absorbing compounds in nature.

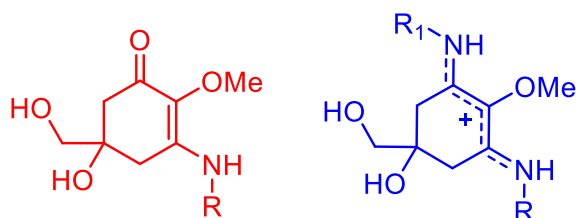


Figure 2.21. Basic structures of the two chromophores in MAAs, aminocyclohexenone (in red) and aminocyclohexenimine (in blue).

In fungi, the only amino acids present in mycosporines are serine (including its α -amino alcohol, serinol) and the related pairs glutamine-glutaminol and glutamic acid-glutamicol,^[110] with the exception of mycosporine alanine. The first isolated and elucidated structure was the mycosporine serinol, which was isolated from *Basidiomycetes Sterium hirutum*^[122] and elucidated in 1976. The mycosporine glutamicol isolated from *Botrytis cinera*^[111] presents a derivative of glutamic acid and appears both as open chain and as a cyclic ring form.

2. Background

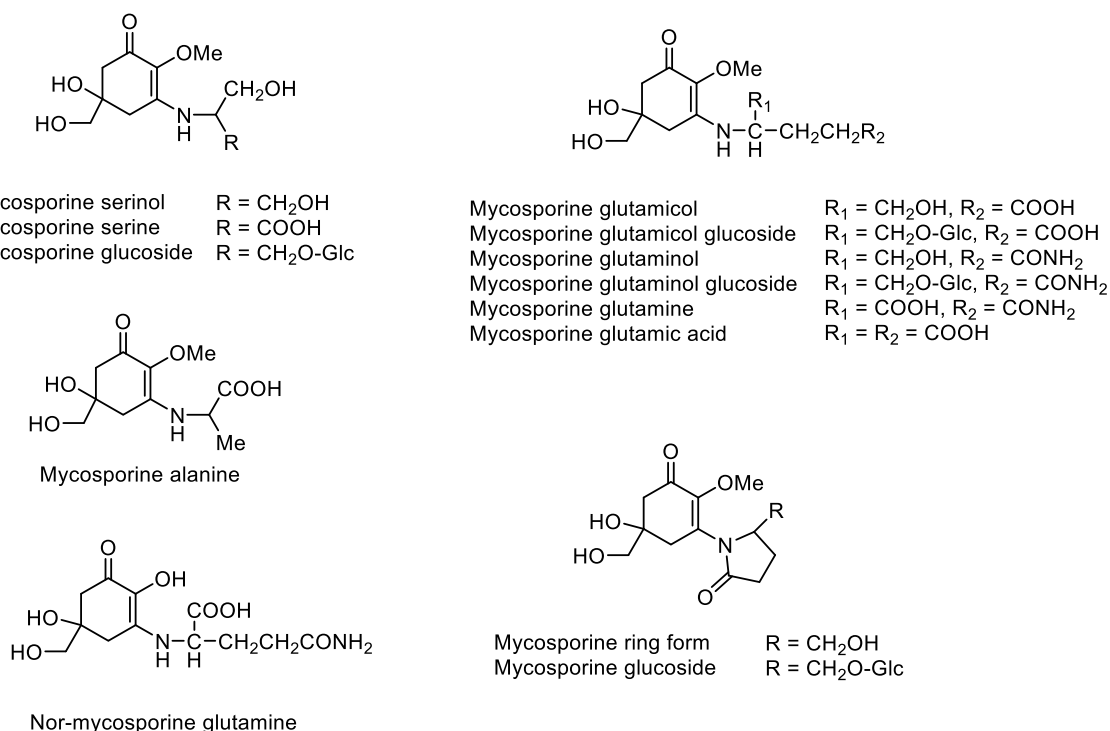


Figure 2.22. Structures of mycosporines present in fungi.

In contrast with fungal mycosporines, in marine organisms and algae the predominant structure is the aminocyclohexenimine ring, with only two exceptions of aminocyclohexenone (mycosporine taurine and mycosporine glycine). These metabolites are imine derivatives of mycosporines (enamine-imine) and they are also called mycosporine-like amino acids (MAAs). These compounds present a high absorption band centered between 320 and 360 nm. The most common amino acid in these compounds is glycine, but many variations are observed in all the isolated species, being around thirty the amount of MAAs found until now, as can be seen below.

2. Background

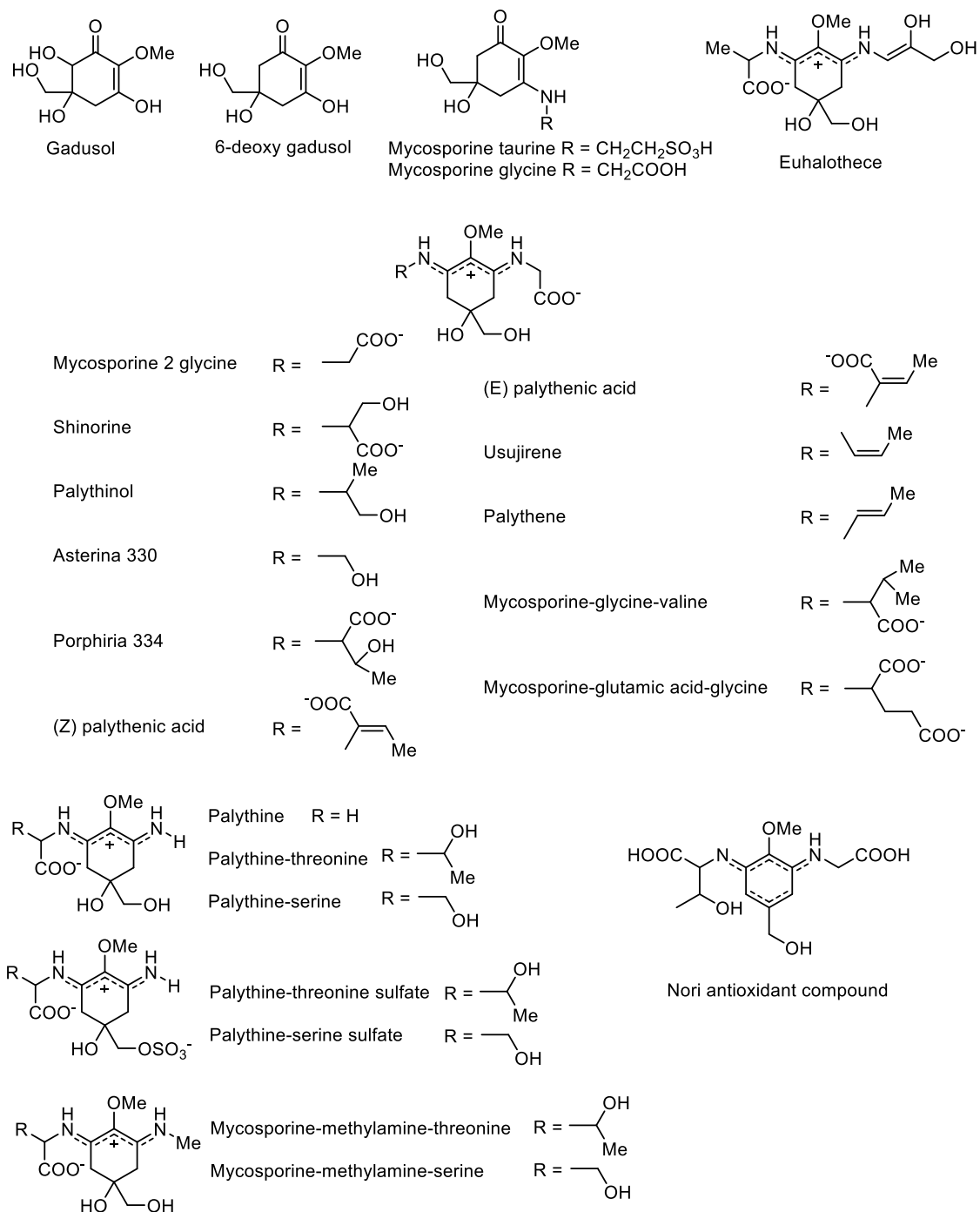


Figure 2.23. Gadusol, 6-deoxygadusol, oxo-mycosporines and imino-mycosporines present in marine organisms.

In many cases, MAAs appear in nature in combination with different amino acids. For instance, glycine is usually located at C3 when a second amino acid, an amino alcohol or an enamione may be located in C1. However, in some coral species, methylamine replaces glycine (mycosporine-methyl-amine-serine, mycosporine-methylamine-threonine). Occurring the same replacement by an amine group in

palythine, palythine-serine and palythine-threonine.^[123] Additionally, gadusol and 6-deoxygadusol have been found in some coral species.^[124] Finally, some MAAs may also contain sulfate esters,^[125] as happens to palythine-threonine sulfate and palythine-serine sulfate. Recently, a new rare MAA was isolated^[126] from the cyanobacterium *Euhalothece* (*Euhalothece*-362, *E*-*euhalothece*) and the Nori antioxidant compound was synthesized^[127] by heat treatment of porphyra-334,^[128] which promotes the dehydration of the residual hydroxyl group in C5 position.

The detailed structure of this type of compounds has been also obtained by diverse characterization techniques. There are some examples of X-ray diffraction studies on the total elucidation, specially of porphyra-334 and palythine.^[129]

2.3.1.1 Photophysical properties

Maybe the most relevant feature of MAAs is their high UV-absorbing capability, presenting a single band centered in the 310 – 360 nm range, which partially covers the UVA and UVB radiation zones being the harmful part of the solar emission. Also, MAAs exhibit a strong absorption with a molar absorptivity coefficient between 20000 and 40000 L cm⁻¹mol⁻¹ which may rise to over 50000 in the case of some examples such as palythene.^[121] Depending on the origin and as shown with the different possible structures, relevant differences between the compounds in algae and those found in fungi have been reported. In fungal metabolites, the chromophore (aminocyclohexenone) is less conjugated and in all cases it shows a maximum near 310 nm, practically without dependence on the substitution in the amino residue.^[54]

In marine MAAs (aminocyclohexenimine), a similar behavior is observed with an absorption maximum close to 320 nm for the non-conjugated-substituted imino-MAAs (palythine and derivatives) and ca. 360 nm for the conjugated-substituted ones (explained in more detail below). As expected in this case, substitution may be important due to the changes in chromophore's conjugation. This allows the modulation of the UV-Vis spectral properties in these compounds, yielding in a bathochromic shift when conjugation increases, being the typical behavior when a chromophore extends its conjugation. When a conjugated C=C bond is directly attached to the chromophore, as happens to the following pairs, the *Z*-isomer shows an hypsochromic shift relative to the *E*-isomer of 2 - 3 nm, as in usujirene and

palythene.^[130] A non-common behavior is found for the *E-Z*-palythenic acid pair, in which the *E*-isomer is 2 nm blue-shifted.^[131]

Also, in water solution, gadusol shifts the maximum reversibly from 268 nm to 296 nm and the intensity increases in going from acidic to neutral pH.^[132] Previously, the values of 269 ($12400 \text{ M}^{-1} \text{ cm}^{-1}$) and 264 nm ($12900 \text{ M}^{-1} \text{ cm}^{-1}$) were reported for the peak wavelength and maximal molar absorption coefficient, ϵ_{max} , of the band in acidic medium.^[133, 134] For the absorption band at higher pH, the informed values for ϵ_{max} range from 21800 to $22750 \text{ M}^{-1} \text{ cm}^{-1}$.^[133-135]

The effect of the pH on the absorption spectrum of gadusol has been ascribed to the deprotonation of the *enol* form of the molecule (gadusol) to give the resonance-stabilized enolate (see below Figure 2.26 with the corresponding structures).^[132, 133, 135]

As happened with gadusol, a key characteristic regarding the absorption is the pH dependence of these compounds due to their aminoacidic nature, where a zwitterionic character is expected. It is unclear what is the relevant *in vivo* form, if it is the anionic, the "neutral" or zwitterionic, or the protonated one. Trying to clarify this aspect porphyrin-334,^[136] shinorine and mycosporine glycine^[137] were studied at different pH values. It was found that in high acidic aqueous solution (pH 1 - 3) the absorption maximum of all these derivatives shows a hypsochromic shift of 2 - 6 nm. Under these conditions, the molar absorption coefficient also decreases with higher acidity. As other MAAs, porphyrin-334 and shinorine are a zwitterion that presents two acidic groups and one iminic nitrogen as shown in Figure 2.23. When the pH is below 3, the π delocalization is not possible due to the protonation of the non-bonding pair in the nitrogen atom. Subsequent protonation of the acidic groups may take place at lower pH values.

2. Background

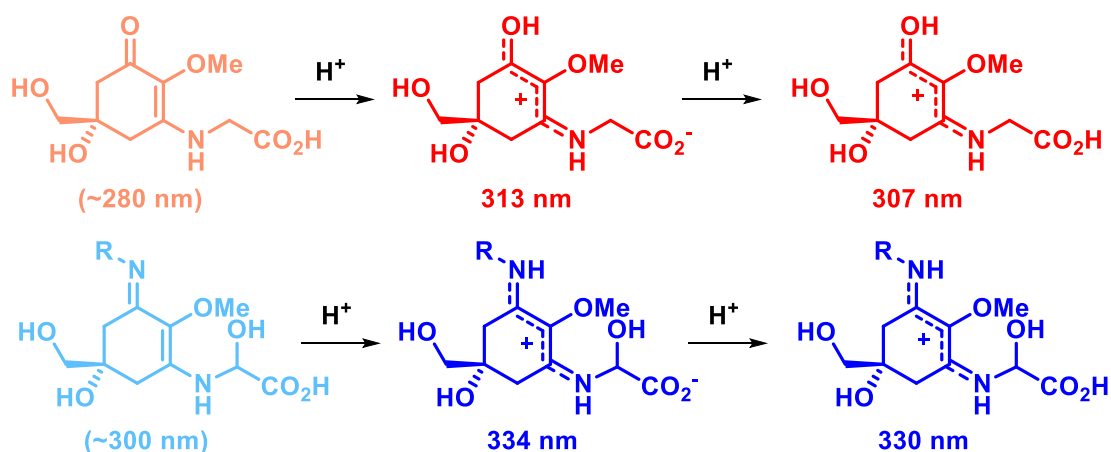


Figure 2.24. Molecular structures of mycosporine glycine (top in red) and shinorine (bottom in blue) at different pH values.

On the other hand, the absorption maximum and molar absorption coefficient of porphyra-334 do not change in alkaline solutions. This is reasonable, as both acidic groups do not alter the electronic properties of the chromophore, as they are not directly bonded to it. Likewise, the synthesis of the dimethyl ester of shinorine^[138] was further explored maintaining the same features as sunscreen, confirming the low influence of these acidic groups in the photoprotective role.

For porphyra-334, a value of 266 kcal/mol for the proton affinity^[129] was found, which is in the range of the gas phase proton affinity of certain artificial super-bases, so-called "proton sponges".^[139] This term refers to species with exceptionally high proton affinities that seems to be related to the high stability of this compound in very acidic water solutions. In contrast, under relatively low basic conditions of pH 12, it decomposes rapidly to give unknown products.^[136] The reasons behind this feature were explained in terms of positive charge delocalization along the chromophore, the two nitrogen atoms and the alkene moiety. This type of push-pull charge stabilization has been previously proposed for other types of compounds showing also high proton affinity.^[140] Significantly, this proton-capturing ability is comparable to other artificial systems specifically designed to behave like this.^[141] Other MAAs show also small solvent dependence in the UV absorption with changes within 2 - 4 nm in many of them.^[142, 143]

In contrast with the UV properties, fluorescence measurements for MAAs are only available for the most studied compounds, porphyra-334,^[128] shinorine^[144] and palythine.^[145] These three molecules were characterized by steady-state

spectrofluorometry in aqueous solutions under monochromatic irradiation at the absorption maximum and by time-correlated single photon counting for the determination of the singlet state lifetimes.

Porphyra-334 features an excited-state with a short lifetime of 0.4 ns without evidences of transient species after irradiation at the absorption maximum. The emission spectrum consists of a weak band centered at 395 nm which amounted a very low fluorescence quantum yield ($\Phi_F = 2.0 \times 10^{-4}$).^[123, 127] Detailed photophysical studies on shinorine also showed that, as porphyra-334, this metabolite efficiently dissipates light energy into heat.^[146] Shinorine also shows a very low fluorescence quantum yield ($\Phi_F = 1.6 \times 10^{-4}$) and a short fluorescence lifetime (0.35 ns). The emission spectrum exhibits a very weak maximum around 386 nm. The lack of measurable luminescence implies a very efficient deactivation pathway, only presenting a weak emission band attributed to an impurity and not to palythine.^[147]

Also, steady state fluorescence evidenced no net emission from gadusol in acid water by excitation at 268 nm or from gadusolate under neutral pH by excitation at 296 nm,^[132] so a radiative mechanism seems to be irrelevant in the energy dissipation path.

As happened with fluorescence studies, the triplet formation yield and the energy of the triplet state have been only determined for a few MAAs. Some laser-flash photolysis experiments have allowed the characterization of the excited triplet state of these same three compounds.^[142, 146, 147] Data for the triplet-triplet energy transfer from 1-naphthalene-methanol to porphyra-334 accounts for the low probability of triplets to generate reactive intermediates which might start further chemical reactions, in agreement with the previously reported lack of radical detection.^[148] The energy of the triplet state was estimated from the evaluation of the rate constants for the energy transfer processes with different donors with variable triplet energies. Thus, triplet energy for porphyra-334 in water solution is delimited to be $< 250 \text{ kJ mol}^{-1}$ whereas the triplet energy for palythine is approximately 330 kJ mol^{-1} .^[142, 147] The excited triplet state, however, could be assessed by sensitization with benzophenone or acetone, showing a low quantum efficiency ($\Phi_T < 0.05$) in all cases. Moreover, triplet lifetimes were determined in the same conditions. Porphyra-334 features a triplet state with a lifetime of 14 μs , while shinorine has a value of 11 μs and 9 μs were measured for palythine. In gadusol, no transient absorption was detected by direct laser flash photolysis of gadusolate.^[132] This contrasts with the production of stabilized triplets reported for β -carbon substituted α,β -unsaturated ketones.^[149] Nevertheless, in gadusolate the

formation of long-lived triplets is probably avoided under the competition with the ultrafast internal conversion.

In addition, photoacoustic calorimetry studies allowed for the quantification of non-radiative deactivation pathways of the excited state.^[146] For porphyra-334 and shinorine, it was found that around 98% of the absorbed energy was dissipated as heat to the environment. For palythine, photoacoustic calorimetry showed that around 90% of the light energy is transferred to the medium as heat.^[147] The photoacoustic signals for gadusolate, with laser excitation at 266 nm, matched exactly those from calorimetric studies, revealing that excited gadusolate promptly releases the complete amount of absorbed UV energy as heat to the surroundings. According to that, these compounds proved to have a non-radiative energy dissipation.

2.3.1.2 Photochemical properties

While some of the other roles, which will be described below, are probably speculative, the photoprotective capabilities of these compounds have been analyzed in detail since their discovery. The role in UV-photoprotection is supported by several characteristics that become MAAs into compounds capable of dealing in an efficient way with the potentially damaging effects of radiation. Firstly, MAAs evidence a strong UV absorption in the UVA - UVB region of the spectrum as described in the previous section. Secondly, these compounds also have a very low fluorescence emission. Nevertheless, a few natural compounds share these two properties. In the case of MAAs, these features are also accompanied by a high photostability that greatly increases their relevance.

Preliminary results on the photostability of MAAs were obtained through UV irradiation *in vivo* in biological samples.^[144, 150] Further detailed studies on diverse MAAs provided quantitative evidences on the high photostability of these compounds also *in vitro*. The photodegradation of aqueous solutions of porphyra-334 was explored by following the spectral changes as a function of time when irradiating with a medium-pressure mercury lamp.^[142] The photodecomposition quantum yield was determined to be $\Phi_R = 1.9 \times 10^{-4}$ under N₂ atmosphere and $\Phi_R = 3.4 \times 10^{-4}$ in oxygen-equilibrated aqueous solutions. On one hand, this MAA was found also to be very photostable. On the other hand, the small effect of oxygen in the photodecomposition quantum yield seems to

suggest a scarce contribution of the triplet state in the photochemistry of these compounds. In agreement with the results from photoacoustic calorimetry, shinorine and porphyrin-334 dissipate most of the absorbed energy as heat into the environment consistently with their very low photodecomposition quantum yields.^[144, 146] Palythine was also studied in order to confirm its photostability.^[147] Aqueous solutions over irradiation at 320 nm showed no significant changes in the absorbance or in the pH. The photodecomposition quantum yield for palythine was found to be $\Phi_R = 1.2 \times 10^{-5}$. In the case of gadusol, the photodecomposition quantum yields amounted $\Phi_R = 3.6 \times 10^{-2}$ for neutral gadusol at 254 nm and $\Phi_R = 1.4 \times 10^{-4}$ for gadusolate at 303 nm, without effect in presence of oxygen.^[132]

These results suggest that the photostability of MAAs is related to their core structure, aminocyclohexenone and especially of aminocyclohexenimine and the variability of substituents among different MAAs only have a minor effect on the photochemical properties, being these diverse decorating substituents in the basic core more related to the metabolic synthetic routes. The amino and alcohol groups directly bonded to the chromophore only redshifts the wavelength of absorption while keeping the photostability almost unchanged. The other substituents do not have any relevant influence in the chromophore. Acid, amino, and alcohol groups present in the lateral chains are probably originated in the biosynthetic routes and seem to have minor effects on the solubility. Interestingly, the photostability of these compounds is also maintained when incorporated in more complex structures. This is illustrated by mycosporine-glutaminolglucoside,^[151] a mycosporine metabolite present in several yeast species, which was also found to be very photostable ($\Phi_R = 1.2 \times 10^{-5}$) due to the mycosporine moiety.^[152]

However, some differences arise when the substituents are directly attached to the chromophore. Among the different isolated MAAs, this may happen to the pair palythine - usujirene, structures in Figure 2.23.^[145] In these two compounds, an additional double C=C bond is conjugated with the common chromophore. Thus, the absorption occurs at higher wavelengths: 360 nm for palythene and 357 nm for usujirene in contrast with the absorption at 320 nm of palythine, the equivalent MAA without the C=C bond. Besides the last evident effect of this extra double bond, a higher photoreactivity was also expected.

In a detailed study on the reactivity of these compounds, continuous irradiation of usujirene at 366 nm and HPLC quantitative analysis allowed the determination of a

photodecomposition quantum yield of $\Phi_R = 2.9 \times 10^{-5}$.^[153] However, the main part of the disappearance of usujirene was due to the *cis-trans* isomerization of the extra and exocyclic double bond to yield palythene with only a slightly lower quantum yield ($\Phi_{iso} = 1.7 \times 10^{-5}$). Thus, most of the reacting usujirene leads to the formation of palythene, which is the photostable isomer. Under these conditions, a photostationary state composed by palythene and usujirene (11:1) was found, explained by the higher stability of the *trans* C=C double bond in palythene. Thus, usujirene and palythene undergo photoisomerization as an additional reactivity in the excited state. This reactive pathway converts one isomer into the other affecting the mixture composition but maintaining the global photoprotective capabilities.

From a purely photochemical point of view, their photophysical properties imply that direct absorption of a photon populates excited electronic states of singlet multiplicity, which eventually decay to the ground state mainly through non-reactive and non-radiative pathways. However, it should be considered that other reactive possibilities might also influence the protection achieved *in vivo*. Among others, the photosensitized processes are accessible photodegradation routes due to the different sensitizers that can be available in biological media. For example, flavin-mediated photodegradation of mycosporine glutamine leads to the formation of an aminocyclohexenone and 2-hydroxyglutaric acid.^[120] This reactivity is pH independent but temperature and light wavelength play a decisive role. Thus, a mixture of photochemical and thermal degradation paths seems to be operating at the same time. Different sensitizers such as erythrosine, methylene blue or rose bengal (RB) are also effective.

Further comparative studies with up to seven different MAAs evidenced photosensitized decomposition in the presence of riboflavin and rose bengal.^[154] However, very different decomposition rates were observed when RB (an efficient singlet oxygen producer) and riboflavin (a photosensitizer) were used. A higher rate of photodecomposition was observed when riboflavin was present, this indicating that a type of photo-oxidation mechanism may be responsible for the degradation. Also, the requirement for a strong photosensitizer such as riboflavin and the low decomposition rates when other sensitizers are present further confirms the high photostability of MAAs even under indirect irradiation.

Several MAAs have been the subject of detailed analysis in photosensitization experiments, some of these results were summed up in the previous section 2.3.1.1.

Porphyra-334^[142] shinorine^[146] and palythine^[147] also forms triplets under sensitization with benzophenone and acetone, respectively.

The obtained values for the triplet state of these MAAs are relevant for the discussion of the complementary role that consists of avoiding the formation of pyrimidine dimers.^[155, 156] Thus, MAAs were proposed not only to protect against the UV damage by direct absorption and filtering of the light, but also through quenching of the excited state of thymine thus avoiding the formation of the dimers. However, as the value for the triplet energy of thymine in DNA was estimated to be 270 kJ/mol,^[157] it seems that this possibility could be ruled out in the case of palythine as no energy transfer seems possible from the thymine excited state. In contrast, porphyra-334, with a triplet energy of 250 kJ/mol, could quench the excited thymine and contribute to the photoprotection through this additional mechanism.

2.3.1.3. Other biological roles

The broad presence of MAAs in many organisms and ecosystems suggests a rather general and relevant biological role. Indeed, many different roles have been assigned to MAAs based on their unique features. For instance, it has been proposed that they could help in the control of the intracellular osmotic pressure, due to the fact that MAAs' biosynthesis can be induced by osmotic shock.^[158] However, it seems that the contribution of MAAs as compatible solutes is quantitatively small.^[159] Also, their intervention in sexual gametes has been invoked as high proportions of these compounds have been found in embryos of shrimp.^[117] According to this, MAAs concentration would be used as an indicator of ovarian maturation.^[160] Another possible function is their role as accessory pigments, precursors of photosynthetic pigments^[161] or with a photosynthetic role. However, recent studies conclude that MAA don't transfer efficiently energy to the chlorophyll A and, in conclusion, MAAs don't take part in photosynthesis.^[162]

Antioxidant effects were found in mycosporine-glycine^[163] in 1995. This compound is an efficient antioxidant that can protect biological systems by quenching oxygen. However, it seems that this property is not general for MAAs.^[163] Antioxidant properties may be in relation with the quench capacity of MAAs and their photoprotective role.^[162] Recently, the activity of mycosporine-glutaminol-glucoside

has also been studied.^[152] This compound is both an efficient antioxidant and photoprotective metabolite since it can act as a singlet oxygen quencher.

In case of gadusol, a considerable antioxidant capacity, redox properties similar to ascorbic acid and the ability to quench chain reactions induced by peroxy radicals were reported.^[160] These relations between MAAs and gadusol have induced the suggestion that gadusol may be the evolutionary precursor of MAAs. The stronger antioxidant capacity of gadusol, together with the photoprotection in more energetic regions of the UV spectrum could be linked to the characteristics of the early atmosphere, with strong UVC radiation and an increased oxidative nature. Gadusolate may undergo electron transfer reactions with different triplet sensitizers in water. In fact, the rose bengal triplet state is quenched by gadusolate through a collisional mechanism with a rate constant below the diffusion limit.^[132] This reductive quenching mechanism is considered to be responsible for the antioxidant capacity of gadusol *in vivo*.^[164] In living cells, the presence of critical compounds such as riboflavin and derivatives are related to DNA damage through photosensitized reactions. Gadusol is capable of efficiently contribute to diminish this potentially harmful reactions through quenching of the triplet of riboflavin.^[165]

2.3.2. Obtention from natural sources and synthetic attempts

The obtention of these compounds was committed classically from their natural sources, as urchins' eggs, algae, plankton and some families of bacteria. The sampling procedure depends on the polarity and chemical stability of the source and the composition. Commonly, the sample is treated with HPLC grade solvents for extracting the organic compounds present. Then, it is possible to follow three different procedures:^[166]

-For phytoplankton, lyophilized or filtered samples are poured in centrifuge tubes and methanol is added. After centrifugation, the decanted extracts are collected and filtered.

-Samples are soaked with small volumes of water overnight and in darkness, and then the first procedure is applied.

-If required, more aggressive conditions and solvents can be applied. Specifically, 25% aqueous methanol at 45°C through several cycles can be used until exhaustive extraction is achieved.

The obtained extracts for all procedures are evaporated to dryness and re-dissolved in a mobile phase consisting of a pH = 3 solution of trifluoroacetic acid and 0.2% ammonium hydroxide.

After recovery from natural sources, the methods used for the purification of these compounds are usually diverse chromatographic techniques. Gel permeation,^[116] ion exchange resins,^[167] norite A,^[128] and preparative TLC on silica gel^[168] have been used in different combinations to purify the samples. As other drugs, the characterization and structural elucidation is achieved by chemical degradation, spectroscopic techniques and X-ray analysis. As a general-purpose process, purification on Dowex 50W and carbon column followed by semi-preparative reverse-phase HPLC is usually a convenient method.

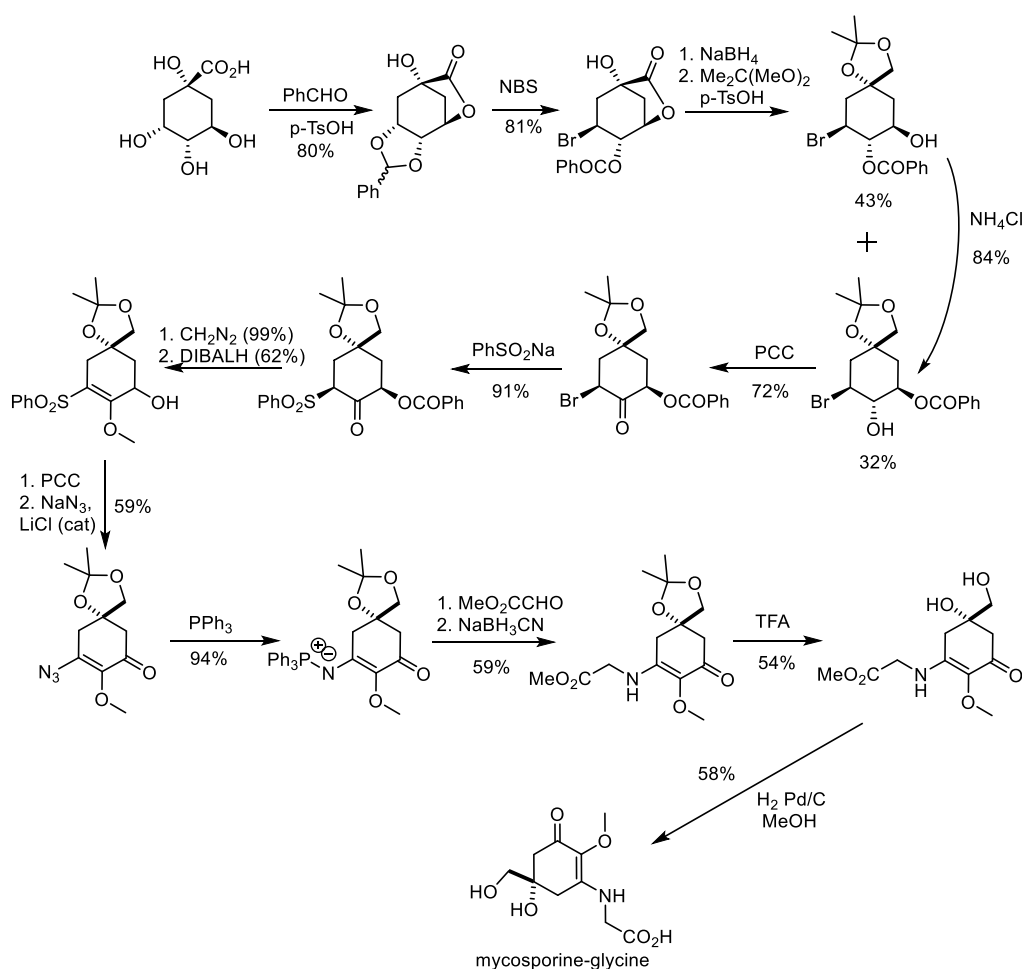
These general procedures of extraction and purification can be modified depending on the MAA or type of sample. Also, the mobile phase or the chromatographic column should be chosen according to the specific features of the sample and the metabolite.

Together with the natural extraction of MAAs, some synthetic approaches were committed trying to obtain these metabolites in a more efficient way. Extraction only offers the possibility of studying these compounds in small amounts. The main problematics of this procedure are the low efficiency,^[169] the big amount of starting material needed to afford an usable amount of sample and some instability. This is due to a dehydration process which involves the hydrolysis of the amine in C-3 and the elimination of hydroxyl group in C-5 position.^[145, 170] These reactions destroy the chromophore and prevent any further use of the resulting products. In contrast with that, all the studies on these compounds were performed using samples extracted from natural sources. However, some implementations attempts with natural extracts in cosmetic formulations were described,^[171, 172] but there are unviable for a real and large scale implementation. This fact was mentioned in several discussions along last years.^[171, 173]

In an attempt to solve these drawbacks, some genetic engineering with bacteria^[174] and many synthetic efforts have been made to obtain MAAs through a more

2. Background

efficient pathway. The genetic modification of bacteria supposed an improvement but the amount of MAAs obtained are still low, with yields around 1 - 3%.^[175] Unfortunately, lots of the synthetic efforts did not lead to any favorable results. In the literature, only two examples of a total synthesis for MAAs have appeared.^[176, 177] In both cases, the synthesis of MAAs was performed using quinic acid as starting material. The synthetic pathway is quite similar in both cases, involving about 15 steps with a very small total yield, about 1% with respect to the initial quinic acid. A schematic pathway for mycosporine-glycine obtention is shown in Scheme 2.1.



Scheme 2.1. Synthetic pathway described in 1995.^[177]

Considering the number of steps involved and the overall yield, these make the pathway an inefficient way to obtain large amounts of MAA and inhibits any attempt of implementation for these compounds in commercial applications.

On the other side and as previously described in section 2.3.1.2, the relevant photochemical properties of MAAs seem to be restricted to a very specific central core.

Thus, a structural simplification while keeping the important features may be reasonable.^[178] In this sense, some attempts in the field of aminocyclohexenone-MAAs have been reported.

The first attempts describing the preparation of this type of derivatives were reported by Dunlap in 1985^[179] and 1988.^[180] During the decades after these patent applications, a great number of synthetic proposals^[121, 181-183] were done but all have in common that none offered a feasible synthetic pathway to obtain the target compounds, even giving specific details.

Dunlap et al. proposed the most important in 1998,^[121] studying the effect of a series of substituents in different positions. This was carried out in three consecutive generations of compounds in which different structural modifications were included as shown in Figure 2.25.

The first generation was based on the use of pyrogallol to obtain compounds structurally related to mycosporine-glycine. Also this pathway is reported in a previous Dunlap patent^[184] which includes the synthesis of five-member ring analogues. Regarding the light absorption properties, UV absorption maximums in the range of 309 - 312 nm for monosubstituted amines and 318 - 322 nm in the case of secondary amines were found. However, these disubstituted aminoderivatives are not useful in practical applications due to their high instability, due to hydrolysis and oxidative decomposition.^[185] The influence of the C-2 substitution was also subject to exploration, removing of the 2-methoxy group to give aminocyclohexenones with absorbance maximum at shorter wavelengths, in the range of 290 - 296 nm. Also, with alkyl C-2 substitution a small red shift of *ca.* 5 nm can be achieved. The condensation products of 2-methyl analogues with secondary amines yielded redshifted bands (298 - 304 nm). All these modifications of mycosporines are under patent protection.^[181, 182]

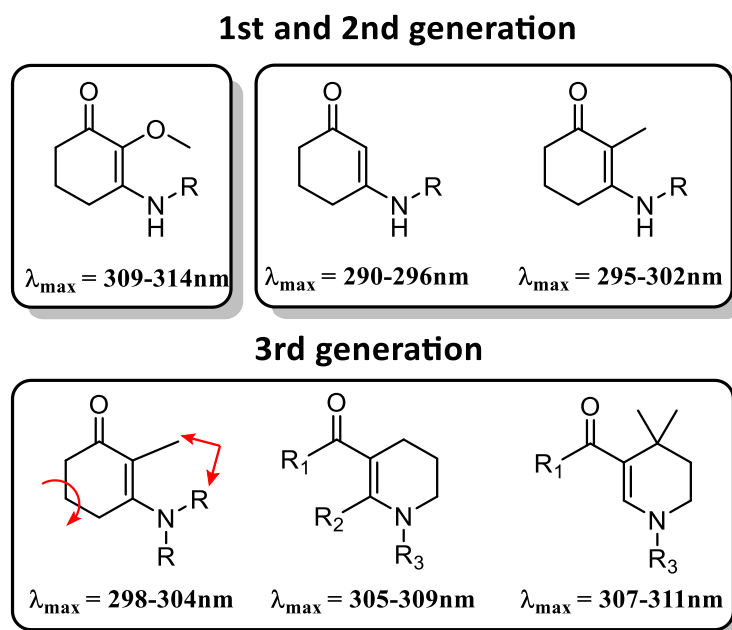
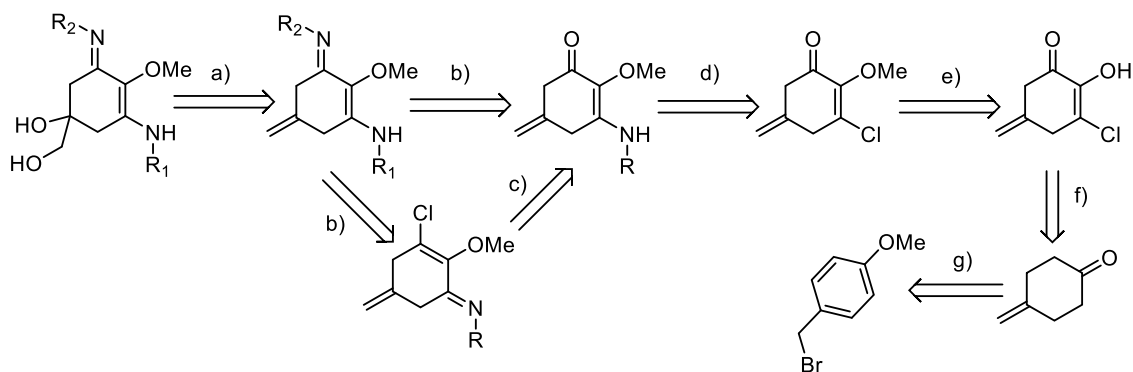


Figure 2.25. Development in the synthesis of mycosporines and fragments to modify (in red).

The third generation of MAA analogues reported by Dunlap implied the modification of the six-membered ring. This modification prevents the hydrolytic cleavage of the enaminone but, in contrast, the oxidative decomposition of the tetrahydropyridine ring can be relevant. This oxidation may be related to radical processes at the α -carbons and can be further limited by removal of the alkyl substituents at the 2-position in the tetrahydropyridine ring. Thus, the presence of *gem*-dimethyl groups is needed. These methyl groups block the radical processes responsible for the oxidation and restrict the rotation of the alkanoyl group, which in turn induces a bathochromic shift. This steric hindrance and the subsequent structure rigidity increase delocalization of the chromophore, extending the absorption band to 307 - 311 nm. This third generation of compounds is also protected under patent.^[182]

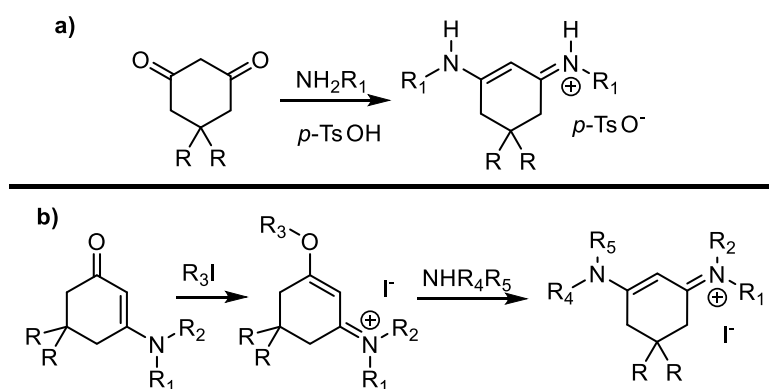
Other synthetic strategies and compounds are also under patent protection. In one of them, different aminocyclohexenones are proposed as drugs against oxidative stress.^[186] In some more recent patents,^[172, 183] the use of natural MAAs in cosmetic preparations is claimed. This implies the incorporation of natural MAAs in commercial applications. Although a synthetic methodology is suggested, only the retrosynthesis is provided, with no specific details of the preparation and involving seven or eight steps with only tentative reaction conditions as shown in Scheme 2.2.



Scheme 2.2. Retrosynthesis proposed in the W00239974A1 patent. a) OsO_4 or NaClO , and hydrolysis; b) Primary amine; c) Vilsmeier's reagent; d) Primary amine; e) Methylation; f) CuCl/water ; g) Sequential silylation, Birch reduction and protodesilylation.

Nevertheless, no examples of total synthesis of imino-mycosporines have been reported previously to the development of this work. Up to date, only the synthesis of aminocyclohexenones has been described and no examples of aminocyclohexenimines substituted in C-2 with any group different from hydrogen have appeared. This fact was already noted by Nguyen *et al.* in 2013.^[43]

In contrast with this lack of examples, some aminocyclohexenimines without substitution in C-2 have been proposed. Vinamidinium salts can be prepared by treatment of 1,3-cyclohexanedione with two equivalents of an aromatic amine in the presence of *p*-toluenesulfonic acid, Scheme 2.3.a.^[187] Also, aminocyclohexenones can be treated by an alkylating agent to yield 3-alkoxy-2-cyclohexen-1-ylidene salts which subsequently reacts with amines to give the vinamidinium salts, Scheme 2.3.b.^[188]



Scheme 2.3. Synthesis of rigid core vinamidinium salts.

2. Background

These compounds are proposed to be photostable due to their similarity to the iminoderivatives of MAAs, but no detailed information was reported.

2.3.3. Computational mechanistic approach

In comparison with the huge efforts made for the obtention and understanding of the biological roles of these compounds, it is curious the very few reports about chemical properties obtained by theoretical calculations on these (MAA and gadusol). Likewise, the main part of these computational studies is related to the elucidation of the chemical structures as a complement to experimental techniques. Some examples of this is the structural determination of porphyra-334 by NMR and using the density functional theory (DFT).^[129] As the right stereochemical assignment could not be achieved by attending exclusively to the experimental data, theoretical NMR signals for up to nine different tentative structures for porphyra-334 were computed, finding a good agreement between experimental and computational data.

Also the structures of palythine, palythanol, shinorine and asterine were studied by theoretical methods.^[189, 190] As previously mentioned, some calculations studying the proton affinity in mycosporines and MAAs were made in the last years.^[136, 137]

The most relevant computational approach to these systems was performed in 2011 and 2015, when the photochemistry of palythine^[191] and gadusol^[192] were studied. The experimental photophysical features found for palythine and gadusol in different solvents and pH values could be computationally explained using the high-level CASPT2//CASSCF strategy, together with the polarizable continuum medium (PCM) in order to include the solvent effects. These were the first studies concerning the mechanism behind the photoprotective role of these compounds. In case of palythine, an active space of 10 electrons in 7 orbitals was employed for the detailed photochemical analysis. With gadusol an active space of 16 electron in 12 orbitals was used. In both cases, the pH influence was considered computing the neutral (palythine and gadusol) and the charged species (protonated palythine and gadusolate) of the natural compounds, without simplification of the system, see Figure 2.26 with the corresponding structures.

2. Background

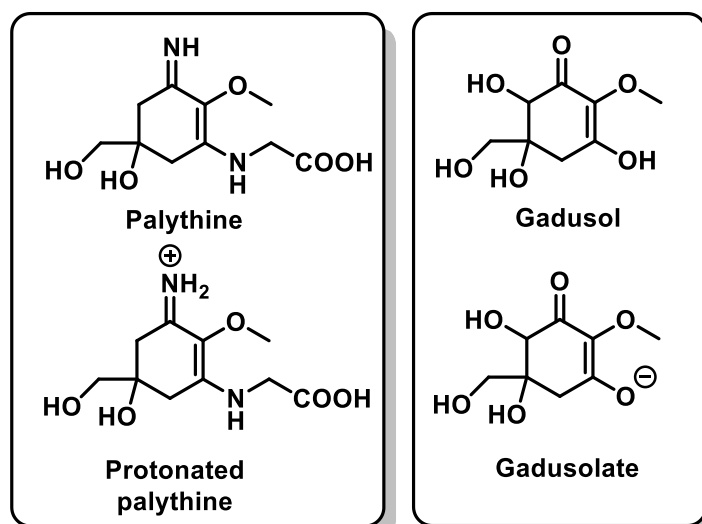


Figure 2.26. Palythine (left) and gadusol (right) in the both possible forms.

The computed UV spectra for both compounds showed that the charged forms must be the major species in neutral aqueous solutions. Even considering that, both forms in each compound supports their efficient photoprotective capabilities.

Firstly, the behavior exhibited by the neutral forms will be discussed. In both cases, the bright state corresponds to the second excited state (S_2), being related to a π - π^* transition. The first excited state (S_1) matched with a n - π^* transition, with a small oscillator strength. Also, in energy terms a blueshift of around 30 nm were obtained between the computed values ($\lambda_{\max} = 248$ nm, $f = 0.007$ for the neutral palythine and $\lambda_{\max} = 245$ nm, $f = 0.25$ for gadusol) and the experimental ones.

A further exploration of the minimum energy paths (MEPs) describing the relaxation from the Franck-Condon region to the ground state recovery for both neutral species proved the ultrafast deactivation of the excited state. Upon light absorption to S_2 an easy and fast (barrierless) relaxation in the excited states potential energy surfaces allows for the recovery of the starting materials. Thus, the light energy absorbed by the molecule is very efficiently dissipated as heat into the environment as observed experimentally. After light absorption and relaxation in the excited state potential energy surface, a region is reached in which the energies of at least two potential energy surfaces are similar. This is known as a conical intersection (CI) point and it is topologically defined as the geometry in which two potential energy surfaces have the same energy. From the CI point, population of the state of lowest energy is allowed and very fast. Thus, the decay from S_2 to S_1 and the ground state recovery takes

place at CI points in which the two involved states have the same energy. At this point, two different behaviors were reached. On one hand, the starting gadusol can be recovered unchanged. On the other hand, a conformer only slightly (+1.5 kcal/mol) more unstable of palythine is formed. This conformer will produce the more stable isomer once the thermal equilibration in the ground state takes place. A representation of this behavior can be seen in Figure 2.27.

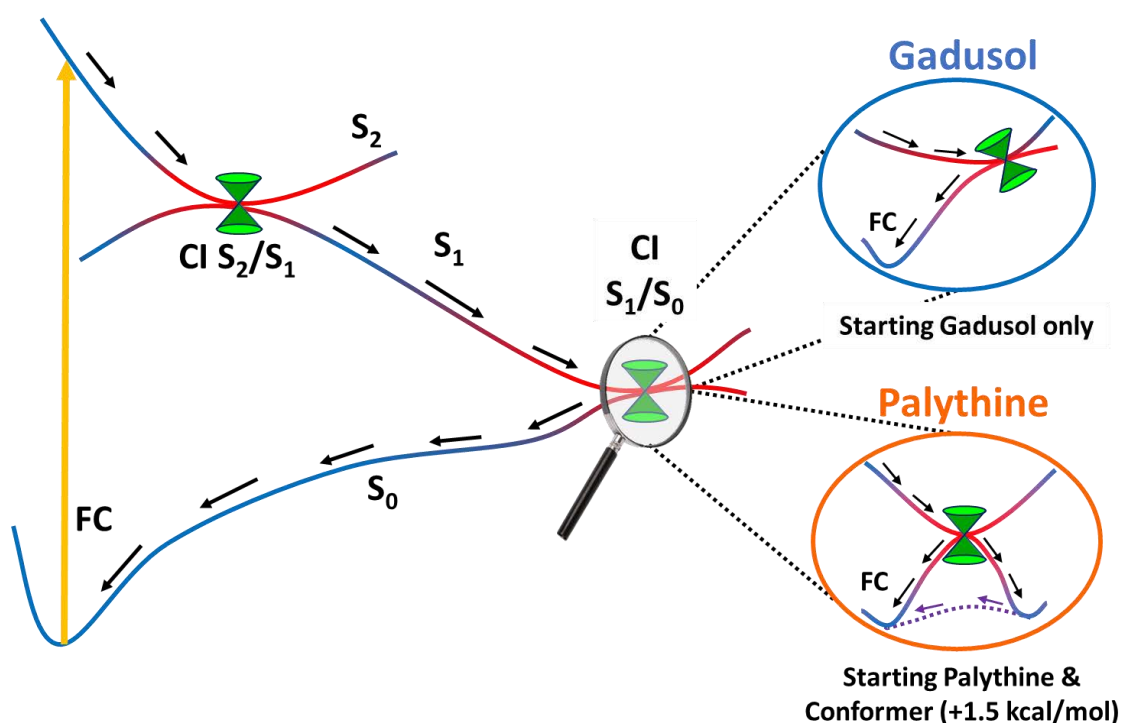


Figure 2.27. Schematic features along the PES for neutral species. Analysis of CI S_1/S_0 for Gadusol (blue) and Palythine (orange), showing the reactivity once reached ground state in both cases.

For comparison with neutral species, the analysis of the involved MEPs will be done. As previously mentioned, the most probable forms are the charged ones, which present a high similarity in their features. In the case of the protonated palythine and gadusolate the computed values of the UV spectra better match with the experimental, even with a considered blueshift of ca. 20 nm ($\lambda_{\max} = 274$ nm, $f = 0.94$ for the protonated palythine and $\lambda_{\max} = 273$ nm, $f = 0.97$ for gadusolate). The difference in palythine is relatively higher than the observed in gadusol, but then maintains the relative behavior between protonated and neutral forms. In both cases and in contrast with the neutral forms, the bright state corresponds to the first excited state S_1 matching with the π - π^* transition. In case of palythine, the n orbital is compromised due to nitrogen protonation and the n- π^* transition not possible.

2. Background

The computed MEP in this case is simpler than the previously obtained for the neutral forms; in this, the presence of a single Cl is enough to reach the ground state. The shape of the potential energy surfaces for protonated palythine and gadusolate can be seen in Figure 2.28.

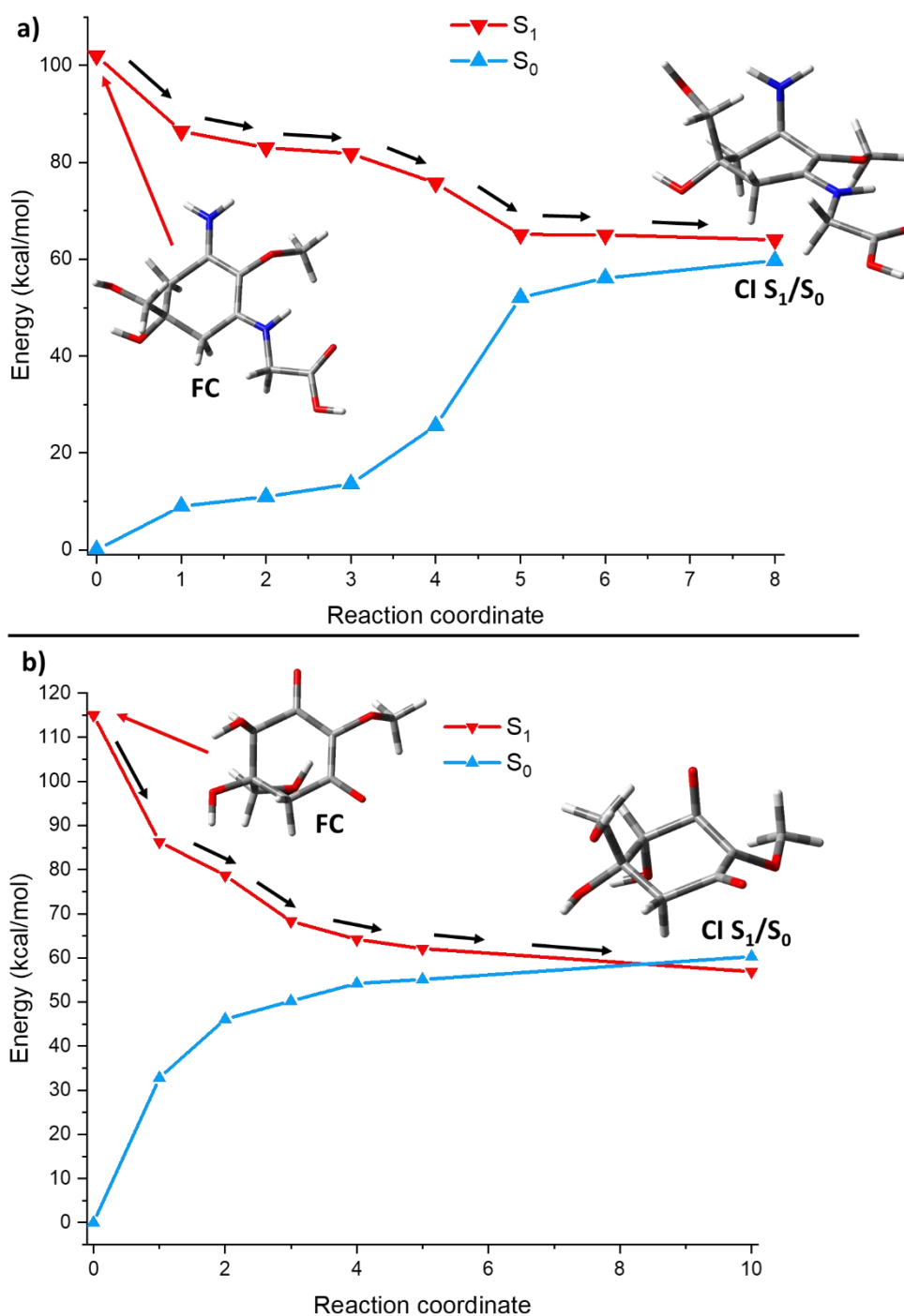


Figure 2.28. MEP of protonated palythine (a) and gadusolate (b).

As happens in neutral forms, a barrierless pathway is obtained in both systems, recovering the starting material after the relaxation to ground state; this process should be very efficient and extremely fast. In both cases, a conical intersection similar as found in the neutral compounds was reached, connecting S_1 with ground state and allowing an easy non-radiative relaxation pathway. A detailed comparison between the CIs found in gadusolate and the one found in protonated palythine should be done to understand the similarities along the relaxation process.

In protonated palythine (Figure 2.29, left), the S_1/S_0 CI features a main deformation corresponding with an out-of-plane movement of the imine moiety. At the same time, the adjacent carbon atoms approach to each other remaining the alkene moiety almost planar. Subsequent relaxation on the ground state following the vectors of the branching space recovers the starting material in all directions.

For gadusolate (Figure 2.29, right), the main molecular distortions are also the breakage of the π system and the out-of-plane movement of the oxygen atoms in the carbonyl and alkoxy groups of the chromophore. Then, deactivation in the ground state recovers also the initial structure.

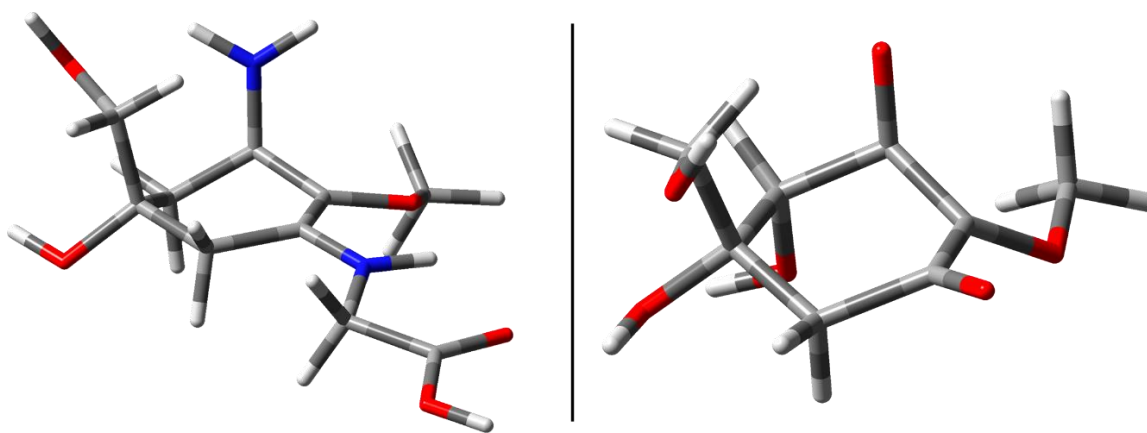


Figure 2.29. Conical intersection points for protonated palythine (left) and gadusolate (right).

Thus, in all cases, the final photoproduct formation implies the recovery of the starting material in agreement with the experimentally determined photostability. According to the observed mechanism, this out-of-plane deformation of the chromophore implies the appearance of a novel and clearly different photoprotection mechanism with respect to the previously described for commercial sunscreens. These results, beyond the mechanistic explanation of the experimental results, allow for the generalization of the relevant features required to generate an effective photoprotector.

Looking into the high similarity between both conical intersections and the main part of the described roles and features, the suggestion of gadusol being a precursor or synthetic intermediate in the biosynthesis of mycosporines, seems to be confirmed.

As previously described in section 1.3, the desired features for an ideal sunscreen are practically fulfilled in case of MAAs. These compounds present the highest UV absorption in nature,^[55] they lack radiative deactivation mechanisms, and they have an extremely efficient non-radiative deactivation pathway. These features combined with the obtained very low photodecomposition quantum yields, make the MAAs as very promising candidates to be further considered in the design of new sunscreens. Maybe the only drawback in these natural compounds could come from their difficult access and the chemical instability when it comes to the extraction of natural sources.

2.4. Bibliography

- [1] http://www1.lsbu.ac.uk/water/water_vibrational_spectrum.html.
- [2] M. Carlowicz, *ChemMatters* **2013**, 12-14.
- [3] J. Tsao, N. Lewis, G. Crabtree, Solar FAQs, US Department of Energy, USA, **2006**.
- [4] N. Heston, Design, Conjugated Polymers in Bulk Heterojunction Photovoltaic Devices, Doctoral dissertation, University of Florida, **2009**.
- [5] C. A. Gueymard, *Solar Energy* **2004**, 76, 423-453.
- [6] World Health Organization; Global Solar UV Index: A practical guide, **2002**.
- [7] http://www.weather.bm/helpdocs/UV_information.asp,
- [8] J. Turner, V. A. Parisi, *Int. J. Environ. Res. Public Health* **2018**, 15, 1507.
- [9] H. Ou-Yang, T. Shyr, *Photochem. Photobiol. Sci.* **2017**, 16, 1537-1545.
- [10] H. F. DeLuca, *BoneKEy Reports* 3, Article number: 479 **2014**.
- [11] A. F. McDonagh, in *Phototherapy in the newborn: an overview*, National Academy of Sciences, **1974**, pp. 56-73.
- [12] R. Moller, *J. Theor. Biol.* **2002**, 214, 619-631.
- [13] H. G. Krapp, *Curr. Biol.* **2007**, 17, R557-R560.
- [14] T. Colbourn, C. Mwansambo, *Lancet Glob Health* **2018**, 6, 1052-1053.
- [15] J. M. Bae, H. M. Jung, B. Y. Hong, J. H. Lee, W. J. Choi, J. H. Lee, G. M. Kim, *JAMA dermatol.* **2017**, 153, 666-674.
- [16] S. Choudhary, K. Nouri, M. L. Elsaie, *Lasers Med. Sci.* **2009**, 24, 971-980.
- [17] D. Kim, H. J. Park, K. Y. Lee, *Macromol. Res.* **2015**, 23, 944-951.
- [18] N. P. Tipnis, D. J. Burgess, *Int. J. Pharm.* **2018**, 544, 455-460.
- [19] R. K. Sivamani, L. A. Crane, R. P. Dellavalle, *Dermatol. Clin.* **2009**, 27, 149.
- [20] E. Yousif, R. Haddad, in *Photodegradation and photostabilization of polymers, especially polystyrene: review, Vol. 2*, SpringerPlus, **2013**, p. 398.
- [21] M. Zayat, P. Garcia-Parejo, D. Levy, *Chem. Soc. Rev.* **2007**, 36, 1270-1281.
- [22] L. R. Sklar, F. Almutawa, H. W. Lim, I. Hamzavi, *Photochem. Photobiol. Sci.* **2013**, 12, 54-64.
- [23] S. Lippens, E. Hoste, P. Vandenabeele, P. Agostinis, W. Declercq, *Apoptosis* **2009**, 14, 549-569.
- [24] M. Placzek, B. Przybilla, U. Kerkmann, S. Gaube, K. P. Gilbertz, *Br. J. Dermatol.* **2007**, 156, 843-847.
- [25] ISO Standard, Definitions of Solar Irradiance Spectral Categories, ISO 21348, **2013**.
- [26] J. D'Orazio, S. Jarrett, A. Amaro-Ortiz, T. Scott, *Int. J. Mol. Sci.* **2013**, 14, 12222-12248.
- [27] WHO, *Health and Environmental Effects of Ultraviolet Radiation*, **1995**.
- [28] R. Ben-Ishai, E. Ben-Hur, Y. Hornfeld, *Isr. J. Chem.* **1968**, 6, 769-775.
- [29] H. Ikehata, T. Ono, *J. Radiat. Res.* **2011**, 52, 115-125.
- [30] J. Cadet, S. Mouret, J.-L. Ravanat, T. Douki, *Photochem. Photobiol.* **2012**, 88, 1048-1065.
- [31] S. A. Gandhi, J. Kampp, *Med. Clin. North Am.* **2015**, 99, 1323-1335.
- [32] N. Matthews, W. Li, A. Qureshi, *Cutaneous Melanoma: Etiology and Therapy*, Codon Publications, Brisbane (AU), **2017**.
- [33] H. Kimura, A. Suzuki, *New Research on DNA Damage*, Nova Science Publishers, **2008**.
- [34] A. R. Young, *Prog. Biophys. Mol. Biol.* **2006**, 92, 80-85.
- [35] J. C. Yam, A. K. Kwok, *Int. Ophthalmol.* **2014**, 34, 383-400.

- [36] R. P. Rastogi, A. R. Kumar, M. B. Tyagi, R. P. Sinha, *J. Nucleic Acids* **2010**, 592980.
- [37] S. Kesari, S. J. Advani, J. D. Lawson, K. T. Kahle, K. Ng, B. Carter, C. C. Chen, *Future Oncol.* **2011**, *7*, 1335-1346.
- [38] Y. Wang, A. Casadevall, *Appl. Environ. Microbiol.* **1994**, 3864-3866.
- [39] A. J. Young, *Physiol. Plant.* **1991**, *83*, 702-708.
- [40] C. Oresajo, M. Yatskayer, A. Galdi, P. Foltis, S. Pillai, *J. Cosmet. Laser Ther.* **2010**, *12*, 157-162.
- [41] M. Cavinato, B. Waltenberger, G. Baraldo, C. V. C. Grade, H. Stuppner, P. Jansen-Dürr, *Biogerontology* **2017**, *18*, 499-516.
- [42] W. M. Bandaranayake, *Nat. Prod. Rep.* **2006**, *23*, 223-255.
- [43] K. H. Nguyen, M. Chellet-Krugler, N. Gouault, S. Tomasi, *Nat. Prod. Rep.* **2013**, *30*, 1490-1508.
- [44] F. Garcia-Pichel, R. W. Castenholz, *J. Phycol.* **1991**, *27*, 395-409.
- [45] M. J. Butler, A. W. Day, *Can. J. Microbiol.* **1998**, *44*, 1115-1136.
- [46] S. Khadem, R. J. Marles, *Molecules* **2011**, *17*, 191-206.
- [47] G. Britton, S. Liaaen-Jensen, H. Pfander, *Carotenoids Handbook*, Birkhäuser Verlag, Basel, **2004**.
- [48] N. Saewan, A. Jimtaisong, *J. Cosmet. Dermatol.* **2015**, *14*, 47-63.
- [49] R. Pallela, Y. Na-Young, S.-K. Kim, *Mar. Drugs* **2010**, *8*, 1189-1202.
- [50] J. Luo, Y. Liu, S. Yang, A. L. Flourat, F. Allais, K. Han, *J. Phys. Chem. Lett.* **2017**, *8*, 1025-1030.
- [51] M. D. Horbury, A. L. Flourat, S. E. Greenough, F. Allais, V. G. Stavros, *Chem. Commun.* **2018**, *54*, 936-939.
- [52] A. Derks, K. Schaven, D. Bruce, *Biochim. Biophys. Acta BBA - Bioenergetics* **2015**, *1847*, 468-485.
- [53] K. Rehakova, K. Capkova, P. Hrouzek, M. Koblizek, J. Dolezal, *Soil Biol. Biochem.* **2019**, *132*, 153-164.
- [54] J. I. Carreto, M. O. Carignan, *Mar. Drugs* **2011**, *9*, 387-446.
- [55] P. M. Agostino, V. S. Javalkote, R. Mazmouz, R. Pickford, P. R. Puranik, B. A. Neilan, *Appl. Environ. Microbiol.* **2016**, *82*, 5951.
- [56] N. Karaman-Jurukovska, D. B. Yarosh, in *Principles and Practice of Photoprotection* (Eds.: S. Q. Wang, H. W. Lim), Springer International Publishing, Cham, **2016**, pp. 377-386.
- [57] B. S. Tung, W. G. McGregor, Y. C. Wang, V. M. Maher, J. J. McCormick, *Mutat. Res.* **1996**, *362*, 65-74.
- [58] A. di Masi, in *Reference Module in Life Sciences*, Elsevier, **2017**.
- [59] T. Nohmi, *Annu. Rev. Microbiol.* **2006**, *60*, 231-253.
- [60] M. S. Reisch, *Chem. Eng. News* **2015**, *93*, 10-15.
- [61] Official Journal of the European Union, Cosmetic products Regulation EC N°1223/2009. , **2009**.
- [62] R. M. Sayre, N. Kollias, R. Roberts, A. Baqer, *J. Soc. Cosmet. Chem.* **1990**, *41*, 103-109.
- [63] P. Romanowski, R. Schueller, *Beginning cosmetic chemistry practical knowledge for the cosmetic industry*, Allured Books, Carol Stream, ILL., **2009**.
- [64] J. R. Villalobos-Hernandez, C. C. Muller-Goymann, *Curr. Drug Deliv.* **2006**, *3*, 405-415.
- [65] P. McSweeney, *Aust. Fam. Physician* **2016**, *45*, 397-399.
- [66] A. Nasir, S. Wang, A. Friedman, *Expert Rev. Dermatol.* **2011**, *6*, 437-439.
- [67] C. D. S. C. Coutinho, E. P. Dos Santos, C. R. E. Mansur, C. R. E. Mansur, *J. Nanosci. Nanotechnol.* **2015**, *15*, 9679-9688.

- [68] S. A. James, B. N. Feltis, M. D. de Jonge, M. Sridhar, J. A. Kimpton, M. Altissimo, S. Mayo, C. Zheng, A. Hastings, D. L. Howard, D. J. Paterson, P. F. A. Wright, G. F. Moorhead, T. W. Turney, J. Fu, *ACS Nano* **2013**, *7*, 10621-10635.
- [69] R. Jansen, U. Osterwalder, S. Q. Wang, M. Burnett, H. W. Lim, *J. Am. Acad. Dermatol.* **2013**, *69*, 867-884.
- [70] J. Jiménez Reinoso, P. Leret, C. M. Álvarez-Docio, A. del Campo, J. F. Fernández, *Bol. Soc. Esp. Ceram. Vidrio* **2016**, *55*, 55-62.
- [71] N. A. Shaath, *Photochem. Photobiol. Sci.* **2010**, *9*, 464-469.
- [72] N. d. N. Rodrigues, N. C. Cole-Filipiak, M. A. P. Turner, K. Krokidi, G. L. Thornton, G. W. Richings, N. D. M. Hine, V. G. Stavros, *Chem. Phys.* **2018**, *515*, 596-602.
- [73] C. A. Bonda, D. Lott, in *Principles and Practice of Photoprotection* (Eds.: S. Q. Wang, H. W. Lim), Springer International Publishing, Cham, **2016**, pp. 247-273.
- [74] T. Wong, D. Orton, *Clin. Dermatol.* **2011**, *29*, 306-310.
- [75] X.-P. Chang, C.-X. Li, B.-B. Xie, G. Cui, *J. Phys. Chem. A* **2015**, *119*, 11488-11497.
- [76] S. Pattanaargson, T. Munhapol, P. Hirunsupachot, P. Luangthongaram, *J. Photochem. Photobiol. A* **2004**, *161*, 269-274.
- [77] Y. Miyazaki, K. Yamamoto, J. Aoki, T. Ikeda, Y. Inokuchi, M. Ehara, T. Ebata, *J. Chem. Phys.* **2014**, *141*, 244313.
- [78] M. Promkatkaew, S. Suramitr, T. Karpkird, M. Ehara, S. Hannongbua, *Int. J. Quantum Chem* **2013**, *113*, 542-554.
- [79] E. M. M. Tan, M. Hilbers, W. J. Buma, *J. Phys. Chem. Lett.* **2014**, *5*, 2464-2468.
- [80] J. Kockler, M. Oelgemöller, S. Robertson, B. D. Glass, *J. Photochem. Photobiol. C* **2012**, *13*, 91-110.
- [81] G. Wypych, *Handbook of UV Degradation and Stabilization*, ChemTec Publishing, Toronto, **2015**.
- [82] J. J. Vallejo, M. Mesa, C. Gallardo, *J. Vitae* **2011**, *18*, 63-71.
- [83] S. Afonso, K. Horita, J. P. Sousa e Silva, I. F. Almeida, M. H. Amaral, P. A. Lobao, P. C. Costa, M. S. Miranda, J. C. Esteves da Silva, J. M. Sousa Lobo, *J. Photochem. Photobiol. B* **2014**, *140*, 36-40.
- [84] B. Herzog, M. Wehrle, K. Quass, *Photochem. Photobiol.* **2009**, *85*, 869-878.
- [85] P. C. V. Govindu, B. Hosamani, S. Moi, D. Venkatachalam, S. Asha, V. N. John, V. Sandeep, K. H. Gowd, *Photochem. Photobiol. Sci.* **2019**, *18*, 198-207.
- [86] L. A. Baker, S. E. Greenough, V. G. Stavros, *J. Phys. Chem. Lett.* **2016**, *7*, 4655-4665.
- [87] Y. Nakagawa, T. Suzuki, *Chem. Biol. Interact.* **2002**, *139*, 115-128.
- [88] M. Schlumpf, P. Schmid, S. Durrer, M. Conscience, K. Maerkel, M. Henseler, M. Gruetter, I. Herzog, S. Reolon, R. Ceccatelli, O. Faass, E. Stutz, H. Jarry, W. Wuttke, W. Lichtensteiger, *Toxicology* **2004**, *205*, 113-122.
- [89] N. R. Janjua, B. Mogensen, A. M. Andersson, J. H. Petersen, M. Henriksen, N. E. Skakkebaek, H. C. Wulf, *J. Investig. Dermatol.* **2004**, *123*, 57-61.
- [90] M. Schlumpf, B. Cotton, M. Conscience, V. Haller, B. Steinmann, W. Lichtensteiger, *Environ. Health Perspect.* **2001**, *109*, 239-244.
- [91] J. L. Herek, S. Pedersen, L. Bañares, A. H. Zewail, *J. Chem. Phys.* **1992**, *97*, 9046-9061.
- [92] K. Skotarczak, A. Osmola-Mankowska, M. Lodyga, A. Polanska, M. Mazur, Z. Adamski, *Eur. Rev. Med. Pharmacol. Sci.* **2015**, *19*, 98-112.
- [93] B. A. M. C. Santos, A. C. P. da Silva, M. L. Bello, A. S. Gonçalves, T. A. Gouvêa, R. F. Rodrigues, L. M. Cabral, C. R. Rodrigues, *J. Photochem. Photobiol. A* **2018**, *356*, 219-229.
- [94] D. Hüglin, *Chimia* **2016**, *70*, 496-501.
- [95] C. Couteau, E. Papparis, C. Chauvet, L. Coiffard, *Int. J. Pharm.* **2015**, *487*, 120-123.
- [96] A. C. de Groot, D. W. Roberts, *Contact Derm.* **2014**, *70*, 193-204.
- [97] L. A. Baker, M. D. Horbury, V. G. Stavros, *Opt. Express* **2016**, *24*, 10700-10709.

- [98] A. Kikuchi, Y. Hata, R. Kumasaka, Y. Nanbu, M. Yagi, *Photochem. Photobiol.* **2013**, *89*, 523-528.
- [99] I. Karlsson, E. Persson, J. Martensson, A. Borje, *Photochem. Photobiol.* **2012**, *88*, 904-912.
- [100] M. Avenel-Audran, H. Dutartre, A. Goossens, M. Jeanmougin, C. Comte, C. Bernier, L. Benkalfate, M. Michel, M. C. Ferrier-Lebouedec, M. Vigan, J. L. Bourrain, O. Outtas, J. L. Peyron, L. Martin, *Arch. Dermatol.* **2010**, *146*, 753-757.
- [101] F. Journe, M. C. Marguery, J. Rakotondrazafy, F. El Sayed, J. Bazex, *Acta Derm. Venereol.* **1999**, *79*, 211-213.
- [102] S. Tampucci, S. Buralassi, P. Chetoni, D. Monti, *Cosmetics* **2018**, *5*, 1-17.
- [103] V. Lhiaubet-Vallet, M. Marin, O. Jimenez, O. Gorchs, C. Trullas, M. A. Miranda, *Photochem. Photobiol. Sci.* **2010**, *9*, 552-558.
- [104] I. Hanno, C. Anselmi, K. Bouchemal, *Pharm. Res.* **2012**, *29*, 559-573.
- [105] R. M. Sayre, J. C. Dowdy, A. J. Gerwig, W. J. Shields, R. V. Lloyd, *Photochem. Photobiol.* **2005**, *81*, 452-456.
- [106] I. Karlsson, L. Hillerstrom, A. L. Stenfeldt, J. Martensson, A. Borje, *Chem. Res. Toxicol.* **2009**, *22*, 1881-1892.
- [107] U. Osterwalder, L. Hareng, in *Principles and Practice of Photoprotection* (Eds.: S. Q. Wang, H. W. Lim), Springer International Publishing, **2016**, pp. 179-197.
- [108] H. Nakamura, J. Kobayashi, Y. Hirata, *J. Chromatogr.* **1982**, *250*, 113.
- [109] D. Karentz, F. S. McEuen, M. C. Land, W. C. Dunlap, *Mar. Biol.* **1991**, *108*, 157.
- [110] N. Arpin, M. L. Bouillant, in *The Fungal Spore: Morphogenetic Controls* (Eds.: G. Turian, H. R. Hohl), Academic Press, London, **1981**, pp. 435-454.
- [111] N. Arpin, J. Favre-Bonvin, S. Thivend, *Tetrahedron Lett.* **1977**, *10*, 819.
- [112] G. Weste, *Austral. J. Bot.* **1970**, *18*, 11.
- [113] P. J. Brook, *N. Z. J. Bot* **1981**, *19*, 299.
- [114] M. L. Dionisio-Sese, M. Ishikura, T. Maruyama, S. Miyachi, *Mar. Biol.* **1997**, *128*, 455.
- [115] T. Arai, M. Nishijima, K. Adachi, H. Sano, *MBI Report*, Marine Biotechnology Institute, Tokio, **1992**.
- [116] W. D. Dunlap, B. E. Chalker, *Coral Reefs* **1986**, *5*, 155.
- [117] P. T. Grant, C. Middleton, P. A. Plack, R.H.Thompson, *Comp. Biochem. Physiol.* **1985**, *80B*, 755-759.
- [118] W. C. Dunlap, D. M. Williams, B. E. Chalker, A. T. Banaszak, *Comp. Biochem. Physiol.* **1989**, *93B*, 601.
- [119] J. H. Drollet, P. Glaziou, P. M. V. Martin, *Mar. Biol.* **1993**, *115*, 263.
- [120] J. Bernillon, M. L. Bouillant, J. L. Pittet, J. Favre-Bonvin, N. Arpin, *Phytochemistry* **1984**, *23*, 1083.
- [121] W. C. Dunlap, B. E. Chalker, W. M. Bandaranayake, J. J. W. Won, *Int. J. Cosmetic Sci.* **1998**, *20*, 41-51.
- [122] J. Favre-Bonvin, N. Arpin, C. Brevard, *Can. J. Chem.* **1976**, *54*, 1105.
- [123] T. Teai, P. Raharivelomanana, J. P. Bianchini, R. Faura, P. M. V. Martín, A. Cambon, *Tetrahedron Lett.* **1997**, *38*, 5799-5800.
- [124] E. M. Arbeloa, M. O. Carignan, F. H. Acuña, M. S. Churio, J. I. Carreto, *Comp. Biochem. Physiol. B: Biochem. Mol. Biol.* **2010**, *156*, 216-221.
- [125] J. J. Wu, B. E. Chalker, J. A. Rideout, *Tetrahedron Lett.* **1997**, *38*, 2525.
- [126] M. Volkmann, A. A. Gorbushina, L. Kedar, A. Oren, *FEMS Microbiol. Lett.* **2006**, *258*, 50.
- [127] M. Yoshiki, K. Tsuge, Y. Tsuruta, T. Yoshimura, K. Koganemaru, T. Sumi, T. Matsui, K. Matsumoto, *Food Chem.* **2009**, *113*, 1127.
- [128] S. Takano, A. Nakanishi, D. Uemura, Y. Hirata, *Chem. Lett.* **1979**, 419.
- [129] M. Klisch, P. Richter, D.-P. Häder, W. Bauer, *Helv. Chim. Acta* **2007**, *90*, 488-511.
- [130] T. Bjornland, *Monographs. Ocean. Methodology* **1997**, 578-594.

- [131] D. Uemura, C. Katayama, A. Wada, Y. Hirata, *Chem. Lett.* **1980**, 9, 755-756.
- [132] E. M. Arbeloa, S. G. Bertolotti, M. S. Churio, *Photochem. Photobiol. Sci.* **2011**, 10, 133.
- [133] P. T. Grant, P. A. Plack, R. H. Thomson, *Tetrahedron Lett.* **1980**, 21, 4043-4044.
- [134] W. M. Bandaranayake, D. J. Bourne, R. G. Sim, *Comp. Biochem. Physiol. B: Biochem. Mol. Biol.* **1997**, 118, 851-859.
- [135] P. A. Plack, N. W. Fraser, P. T. Grant, C. Middleton, A. I. Mitchell, R. H. Thomson, *Biochem. J.* **1981**, 199, 741-747.
- [136] Z. Zhang, Y. Tashiro, S. Matsukawa, H. Ogawa, *Fish. Sci.* **2005**, 71, 1382-1384.
- [137] K. Matsuyama, J. Matsumoto, S. Yamamoto, K. Nagasaki, Y. Inoue, M. Nishijima, T. Mori, *J. Phys. Chem. A* **2015**, 119, 12722-12729.
- [138] D. E. Orallo, M. F. Fangio, M. Poblet, M. O. Carignan, L. Bernal, J. I. Carreto, S. G. Bertolotti, M. S. Churio, *Photochem. Photobiol.* **2018**, 94, 829-833.
- [139] M. P. Vlasenko, V. A. Ozeryanskii, *J. Phys. Org. Chem.* **2017**, 30, e3609.
- [140] Y. Tao, W. Zou, E. Kraka, *Chem. Phys. Lett.* **2017**, 685, 251-258.
- [141] H. A. Staab, T. Saupe, *Angew. Chem. Int. Ed.* **1988**, 27, 865-879.
- [142] F. R. Conde, M. S. Churio, C. M. Previtali, *J. Photochem. Photobiol. B* **2000**, 56, 139-144.
- [143] A. H. Gröniger, D.-P., *Recent Res. Devel. Photochem. Photobiol.* **2000**, 4, 247-252.
- [144] N. L. Adams, J. M. Shick, *Photochem. Photobiol.* **1996**, 64, 149-158.
- [145] S. Takano, D. Uemura, Y. Hirata, *Tetrahedron Lett.* **1978**, 26, 2299-2300.
- [146] F. R. Conde, M. S. Churio, C. M. Previtali, *Photochem. Photobiol. Sci.* **2004**, 3, 960-967.
- [147] F. R. Conde, M. S. Churio, C. M. Previtali, *Photochem. Photobiol. Sci.* **2007**, 6, 669-674.
- [148] J. M. Shick, W. C. Dunlap, R. Buettner, in *Free Radicals in Chemistry, Biology and Medicine* (Eds.: T. Yoshikawa, S. Toyokuni, Y. Yamamoto, Y. Naito), OICA International, London, **2000**, pp. 215-228.
- [149] D. I. Schuster, D. A. Dunn, G. E. Heibel, P. B. Brown, J. M. Rao, J. Woning, R. Bonneau, *J. Am. Chem. Soc.* **1991**, 113, 6245-6255.
- [150] R. P. Sinha, M. Klisch, A. Gröniger, D.-P. Häder, *Environ. Exp. Bot.* **2000**, 43, 33-43.
- [151] R. Sommaruga, D. Libkind, M. van Broock, K. Whitehead, *Yeast* **2004**, 21, 1077-1081.
- [152] M. Moliné, E. M. Arbeloa, M. R. Flores, D. Libkind, M. E. Farías, S. G. Bertolotti, M. S. Churio, M. R. Broock, *Rad. Res.* **2011**, 175, 44-50.
- [153] F. R. Conde, M. O. Carignan, M. Sandra Churio, J. I. Carreto, *Photochem. Photobiol.* **2003**, 77, 146-150.
- [154] K. Whitehead, J. I. Hedges, *J. Photochem. Photobiol. B* **2005**, 80, 115-121.
- [155] T. Misonou, J. Saitoh, S. Oshiba, Y. Tokitomo, M. Maegawa, Y. Inoue, H. Hori, T. Sakurai, *Mar. Biol.* **2003**, 5, 194-200.
- [156] S. E. Whitmore, C. S. Potten, C. A. Chadwick, P. T. Strickland, W. L. Morison, *Photodermatol. Photoimmunol. Photom.* **2001**, 17, 213-217.
- [157] F. Bosca, V. Lhiaubet-Vallet, M. C. Cuquerella, J. V. Castell, M. A. Miranda, *J. Am. Chem. Soc.* **2006**, 128, 6318-6319.
- [158] T. Kogel, C. Gostincar, M. Volkmann, A. A. Gorbushina, N. Gunde-Cimerman, *Environ. Chem.* **2006**, 3, 105-110.
- [159] A. Portwich, F. García-Pichel, *Arch. Microbiol.* **1999**, 172, 187-192.
- [160] J. M. Shick, W. C. Dunlap, *Ann. Rev. Phys.* **2002**, 64, 223-262.
- [161] J. H. Price, H. S. Forrest, *Comp. Biochem. Physiol.* **1969**, 30, 879-888.
- [162] T. A. Moisant, B. G. Mitchell, *Mar. Biol.* **2001**, 138, 217-227.

- [163] W. C. Dunlap, Y. Yamamoto, *Comp. Biochem. Physiol. B: Biochem. Mol. Biol.* **1995**, *112*, 105.
- [164] N. Wada, T. Sakamoto, S. Matsugo, *Antioxidants* **2015**, *4*, 603-646.
- [165] Y. M. A. Naguib, *Anal. Biochem.* **2000**, *284*, 93-98.
- [166] J. I. Carreto, M. O. Carignan, N. G. Montoya, *Mar. Biol.* **2005**, *146*, 237.
- [167] P. E. García, M. C. Diéguez, M. A. Ferraro, H. E. Zagarese, A. P. Pérez, *Photochem. Photobiol.* **2010**, *86*, 353-359.
- [168] D. F. Gleeson, G. M. Wellington, *Nature* **1993**, *365*, 286.
- [169] K. P. Lawrence, P. F. Long, A. R. Young, *Curr. Med. Chem.* **2018**, *25*, 5512-5527.
- [170] I. Tsujino, K. Yabe, I. Sekikawa, N. Hamanaka, *Tetrahedron Lett.* **1978**, *16*, 1401-1402.
- [171] E. Chrapusta, A. Kaminski, K. Duchnik, B. Bober, M. Adamski, J. Bialczyk, *Mar. Drugs* **2017**, *15*, 326-326.
- [172] F. De la Coba, J. Aguilera, F. Lopez Figueroa, WO2007026035, **8 March 2007**.
- [173] N. D. N. Rodrigues, V. G. Stavros, *Sci. Prog.* **2018**, *101*, 8-31.
- [174] R. P. Rastogi, A. Incharoensakdi, *Photochem. Photobiol. Sci.* **2014**, *13*, 1016-1024.
- [175] A. Hartmann, K. Becker, U. Karsten, D. Remias, M. Ganzera, *Mar. Drugs* **2015**, *13*, 6291-6305.
- [176] J. D. White, J. H. Cammack, K. Sakuma, *J. Am. Chem. Soc.* **1989**, *111*, 8970-8972.
- [177] J. D. White, J. H. Cammack, K. Sakuma, G. W. Rewcastle, R. K. Widener, *J. Org. Chem.* **1995**, *60*, 3600-3611.
- [178] R. Losantos, D. Sampedro, in *Photochemistry New Research* (Eds.: A. B. Smith, N. A. Johnson), Nova Science Publishers, New York, **2013**, pp. 1-20.
- [179] W.C.Dunlap, B.E.Chalker, ES8801184A1, **1986**.
- [180] B. E. Chalker, W. C. Dunlap, W. M. Bandaranayake, *AU 1529188 B* **1988**.
- [181] G. Bird, N. Fitzmaurize, W. C. Dunlap, B. E. Chalker, W. M. Bandaranayake, WO 88/02251, **1987**.
- [182] P. J. Chalmers, N. Fitzmaurice, D. J. Rigg, S. H. Thang, G. Bird, WO 90/09995, **1990**.
- [183] C. Llewellyn, E. Galley, WO2002039974 A1, **2002**.
- [184] W. C. Dunlap, B. E. Chalker, ES8801184A1, **1985**.
- [185] K. Dixon, J. V. Greenhill, *J. Chem. Soc. Perk. Trans. 2* **1974**, 164-168.
- [186] E. Napolitano, S. Basagni, S. Trasciatti, EP2371816A1, **2010**.
- [187] J. M. Kim, J. E. Na, C. G. Lee, J. N. Kim, *Bull. Korean Chem. Soc.* **2004**, *25*, 163-164.
- [188] D. L. Ostercamp, Y. Dinh, D. Graff, S. Wiles, *J. Org. Chem.* **2003**, *68*, 3099-3105.
- [189] K. H. M. Cardozo, R. Vessecchi, V. M. Carvalho, E. Pinto, P. J. Gates, P. Colepicolo, S. E. Galembeck, N. P. Lopes, *Int. J. Mass Spectrom.* **2008**, *273*, 11-19.
- [190] K. H. M. Cardozo, R. Vessecchi, S. E. Galembeck, T. Guaratini, P. J. Gates, E. Pinto, N. P. Lopes, P. Colepicolo, *J. Braz. Chem. Soc.* **2009**, *20*, 1625-1631.
- [191] D. Sampedro, *Phys. Chem. Chem. Phys.* **2011**, *13*, 5584-5586.
- [192] R. Losantos, M. S. Churio, D. Sampedro, *ChemistryOpen* **2015**, *4*, 155-160.

3. Objectives

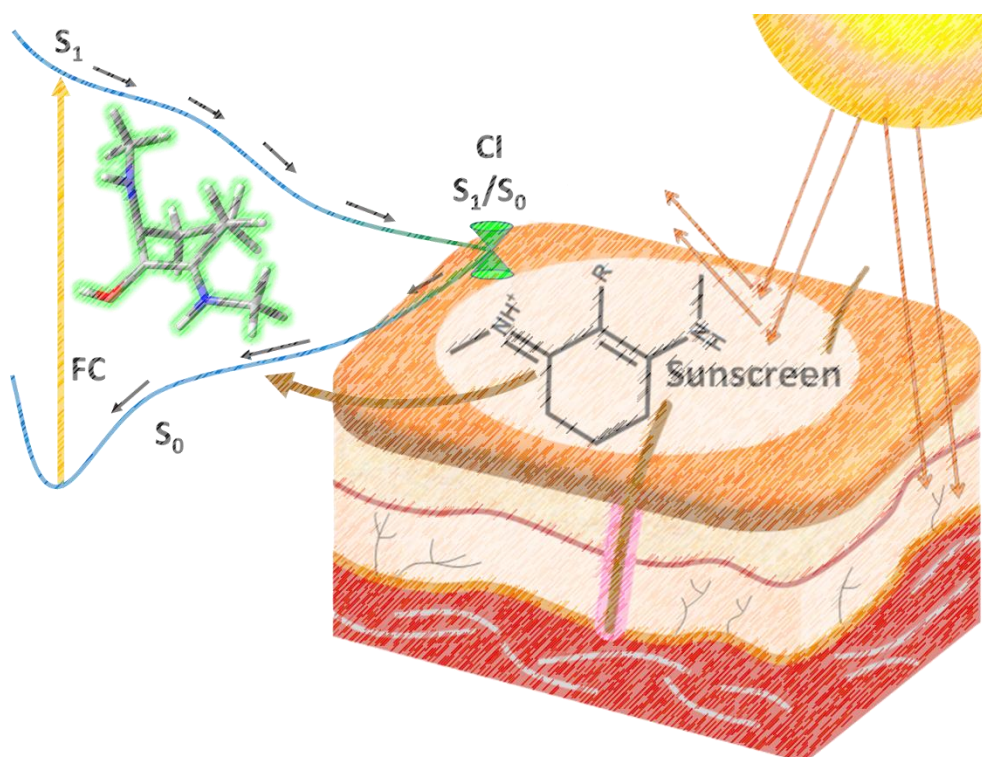


The objectives of this doctoral thesis could be briefly highlighted as follows:

- Firstly, a preliminary computational study will be performed to rationalize the key features in the considered sunscreen systems based on mycosporine-like aminoacids.
- Therefore, the development of novel synthetic procedures will be accomplished to obtain new derivatives, which should incorporate these suitable characteristics yielding on natural MAA mimics.
- Furthermore, the photophysical and photochemical properties will be studied for the prepared derivatives. With a main focus on the UV-Vis absorptivity, photostability, fluorescence emission and stability.
- In addition, computational calculations will be performed to support and complement the obtained experimental data.

However, the objectives marked for chapter 7 will be described laterly, after the introduction to the energy storage topic done in section 7.1.

4. Design and synthesis of new MAA analogues



As it was stated in the Background section, preliminary exploration of palythine^[1] throws promising perspectives of a new photoprotection mechanism that should be general in this type of compounds. For that reason, a further theoretical study to disclaim the core structure responsible for the photoprotective activity was performed. With this data in hand, the design of a new family of compounds that could be used as sunscreens was done.

The present chapter describes the *in-silico* design of this novel MAA-inspired family of UV filters and the posterior synthesis of a great number of compounds. The developed synthetic pathways offer a versatile synthesis, allowing the preparation of numerous species tuning different properties in function of the substituents incorporated into the general core structure.

4.1. Computational screening: finding the core structure responsible of photoprotection

As previously stated from the preliminary exploration of palythine^[1] and gadusol,^[2] a new photoprotection mechanism arises as an interesting alternative to the found in commercial sunscreens. This novel photoprotection mechanism,^[3] which seems to be general in this type of compounds, opens a challenging opportunity for the development of a new generation of sunscreen candidates.

Once this promising mechanism was discovered, a new computational approach based on this previous knowledge was performed in an attempt of identify the key features of these sunscreens. The first step in the computational screening was to clarify the core structure, which retains photoprotective capabilities of the preliminary studies on palythine or other natural MAAs. In order to study the contribution of each fragment of the natural MAAs to the photoprotection, the need to avoid the accessory "decorating substituents" from metabolic routes present in natural MAA molecules arises as the most desirable strategy. For that, from a photochemical point of view, it is essential to discern what parts of the molecule are absorbing light and what others are only a biosynthetic vestige. The most evident part to remove are the oxygenated groups in position 5 of both structures. Other points are the acidic part of the aminoacidic moieties together with the methoxy or methyl group in position 2. In

Figure 4.1, the basic core structure of cyclohexenone and neutral and protonated cyclohexenimine compounds could be found depicted in red, green and blue, respectively, alongside the grey groups representing the accessory moieties, which can be removed.

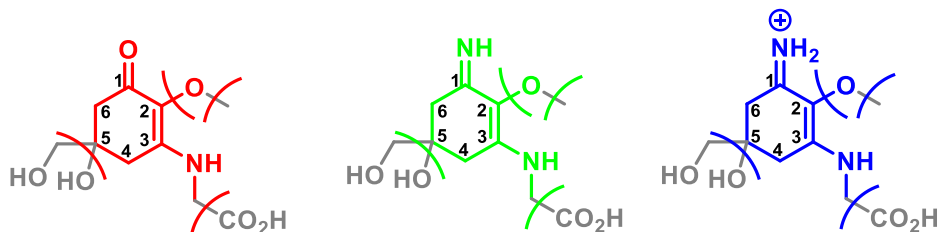


Figure 4.1. Natural MAAs and evaluation of accessory parts (in grey) and core (in red, green or blue).

Once the possible core structure was envisioned, some basic scaffolds as shown in Figure 4.2 were proposed for evaluation. Therefore, CASSCF//CASPT2 methodology was used to study the shape of the potential energy surface (PES) and all critical points along the PES. Also, minimum energy paths (MEPs) connecting the found critical points were computed. With that strategy, the simplest core structure responsible for photoprotection could be identified. More methodological details regarding this strategy can be found in section 9.2.1.

4.1.1. Static analysis to identify the best sunscreen core

A series of basic scaffolds was evaluated to understand how the different substitution affects the photochemical properties. For that reason, the core structures present in both types of mycosporines were considered. The studied models are based on cyclohexenone (**1** - **3**) and cyclohexenimine (**4** - **8**) derivatives. The substitution in position 2 seems to be relevant because it is a general feature observed in all mycosporines and MAAs. To study its influence, some unsubstituted derivatives (**2**, **5** and **7**) were chosen. Also, the addition of alkyl groups is considered (**8**), evaluating if the more electron donor oxygen is a crucial feature.

The importance of the keto-enaminone or imino-enaminone moieties seems to be crucial for the observed photoprotective capabilities. To prove that, core **3** was designed removing the enaminone nitrogen of **1** replacing it by a proton, yielding in the

α,β -unsaturated ketone. In addition, in cyclohexenimine derivatives, the influence of nitrogen protonation was explored between the pairs **4**, **5** and **6**, **7**. This protonation is known to be key into the enhanced photoprotective capabilities of these species, related to previous studies.^[1]

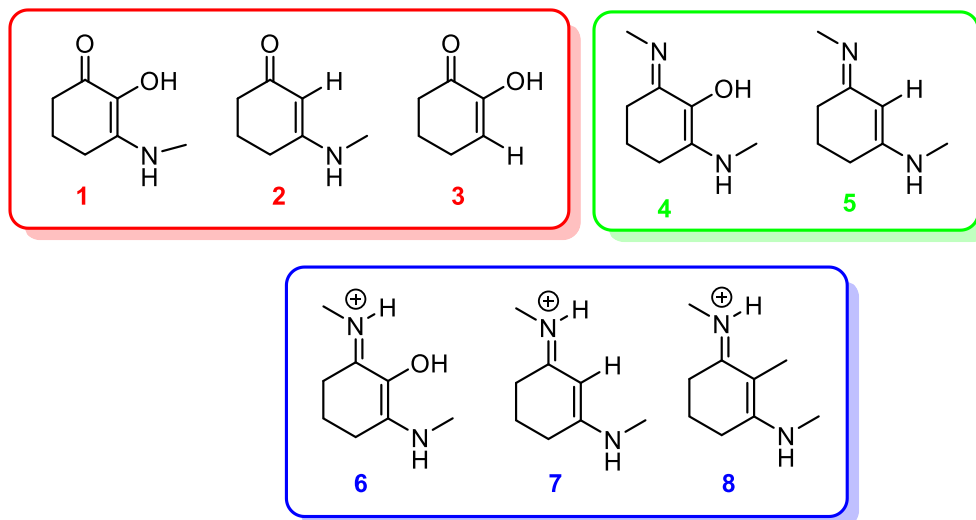


Figure 4.2. Model structures for the theoretical exploration of the active core, each type is colored.

In CASSCF//CASPT2 calculations, the selection of the active orbitals, which may vary their population depending on the possible excitations, is crucial. According to that, in every case, the selection of the active space must include the chromophore orbitals, being important for a precise modelling of the system. This selection is not evident in some cases and depends on the system. For that, some benchmarking on different active spaces or comparison with experimental data is needed to ensure a good representation of reality. If calculations use a wrong active space, the energies and critical points found there are not reliable and must be discarded.

Once a series of core structures have been proposed, different active spaces were checked for each core. A detailed description of the selected orbitals included in the different active spaces is presented below. As for any other system, the considered active space should include the chromophore orbitals. In an attempt to simplify the explanation, the molecular region where orbitals should be located are highlighted using different colors in Figure 4.3.

4. Design and synthesis of new MAAs analogues

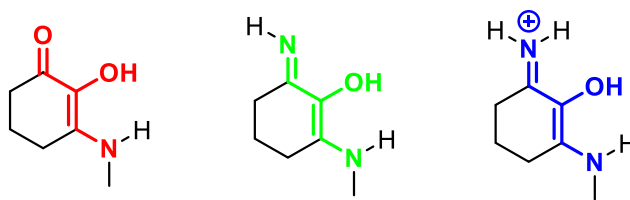


Figure 4.3. Chromophores for the three cores studied.

Looking into the chemical structures, the orbitals that should be present comprise the π system and the n orbitals of the heteroatoms, being the π and π^* orbitals ($C=C$, $C=N$, $C=O$) and the lone pairs of the nitrogen and oxygen atoms linked to the double bond. These orbitals seem to be the representative ones in the chromophores.

For cyclohexenone **1** (red core), an active space of 12 electrons in 8 orbitals (12,8) was used considering the π and π^* orbitals of carbonyl and alkene and the two n orbitals of N_{amine} and O_{hydroxy} . In this case, other smaller active spaces such as (10,7) and (8,6) were explored excluding one pair of the n orbitals, but convergence problems in the wavefunction were observed and the initial active space was kept.

In addition, the analogue orbitals are included giving active spaces of (8,6) for **2** and **3**. In these cases, both pairs of n O_{hydroxy} or N_{amine} were excluded respectively because these are not present in the structure.

For neutral cyclohexenimine **4** (green core), an active space of 8 electrons and 6 orbitals for neutral species was used. Here the (10,7) active space, which includes the π and π^* orbitals of imine and alkene and n orbitals of N_{imine} , N_{amine} and O_{hydroxy} was tested but any improvement with respect to (8,6) was obtained. This behavior was also observed in previous work on palythine, where the occupancy of both N_{amine} and O_{hydroxy} orbitals were 2.00 along all MEP, thus their contribution seems to be negligible.^[1] In this species, the π and π^* orbitals of imine and alkene and n orbitals of N_{imine} and O_{hydroxy} were included; the last one was include to avoid convergence problems in the wavefunction with respect to the (6,5). For compound **5**, without the oxygen atom, the active space was reduced to (6,5) without any further problem.

For protonated cyclohexenimines **6** - **8** (blue core), 6 electrons in 5 orbitals and (8,6) were used as active space, which comprises the π and π^* orbitals of imine and alkene and the N_{amine} lone pair. In the (8,6) the n O_{hydroxy} was included, as previously described, to solve convergence issues for compound **6**. As example of the included orbitals, active space of compound **8** is shown in Figure 4.4, but the orbitals in

compound **7** are almost the same. Here, the HOMO -2 is an orbital with major contribution from the π C=C bond, HOMO -1 from π C=N orbital and HOMO is from n_{amine} orbital, but in all cases these three are mixed in the resulting orbitals. LUMO corresponds to the π^* C=N orbital and LUMO +1 to the π^* C=C orbital. As happened in the bonding orbitals, mixing between orbitals continues, as it was expected, in the anti-bonding ones.

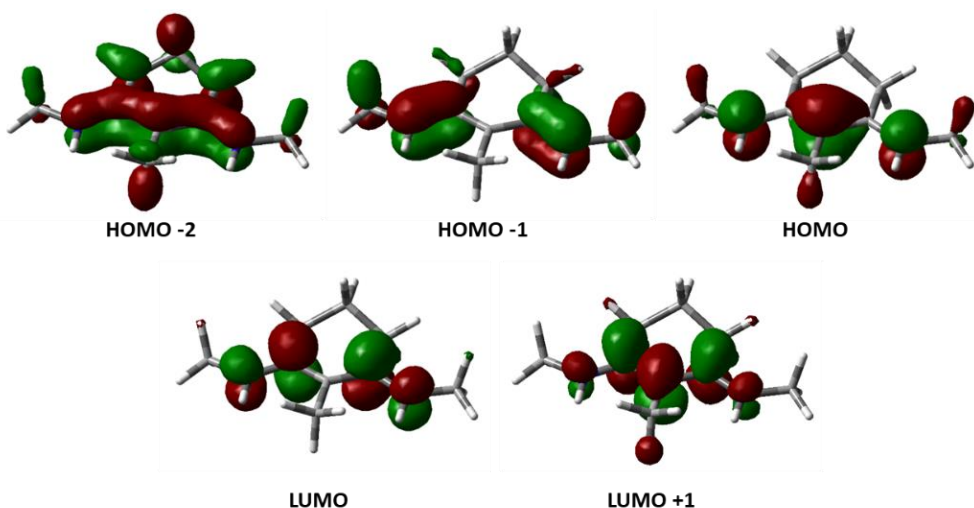


Figure 4.4. Orbitals in the active space of compound **8**.

Once clarified the active space selection importance, the described cores were computationally explored. Firstly, the UV-Vis absorption spectrum in water was calculated. The ground state minimum energy geometry is used, the so-called Franck-Condon point (FC), due to the principle that rules the electronic excitations. At this point, the obtained electronic transitions are described in function of the involved orbitals. In these cases, the nature of these transitions is n - π^* or π - π^* . In addition, the associated oscillator strength (f) is also shown, being the intensity of the absorption or the probability that it will occur. After determining the bright state (higher oscillator strength and marked in bold font in figures), relaxation on this root was performed. A detailed method description and how to proceed in this type of studies is explained in section 9.2.1.

Moving to the obtained computational data, analysis of critical points and shape of the PES for all compounds reveals two representative behaviors. A general behavior for cyclohexenones was observed. In compound **1** (see Figure 4.5), excitation leads to the second excited state (S_2) with an intense absorption with an oscillator strength of

$f = 0.56$ and centered at 271 nm. Regarding the nature of the orbitals involved in the absorption process, population of S_1 corresponds to a dark $n-\pi^*$ transition and a $\pi-\pi^*$ corresponds to S_2 bright transition. These results are in good agreement with the experimental band found at 310 nm in natural mycosporine analogues (mycosporine glycine),^[4] only with a blue-shift of ca. 40 nm. This character was also observed in the previous studies on palythine.^[1] After light absorption, a geometrical deformation begins the dissipation of the absorbed energy reaching a high-energy conical intersection (CI) between S_2/S_1 .

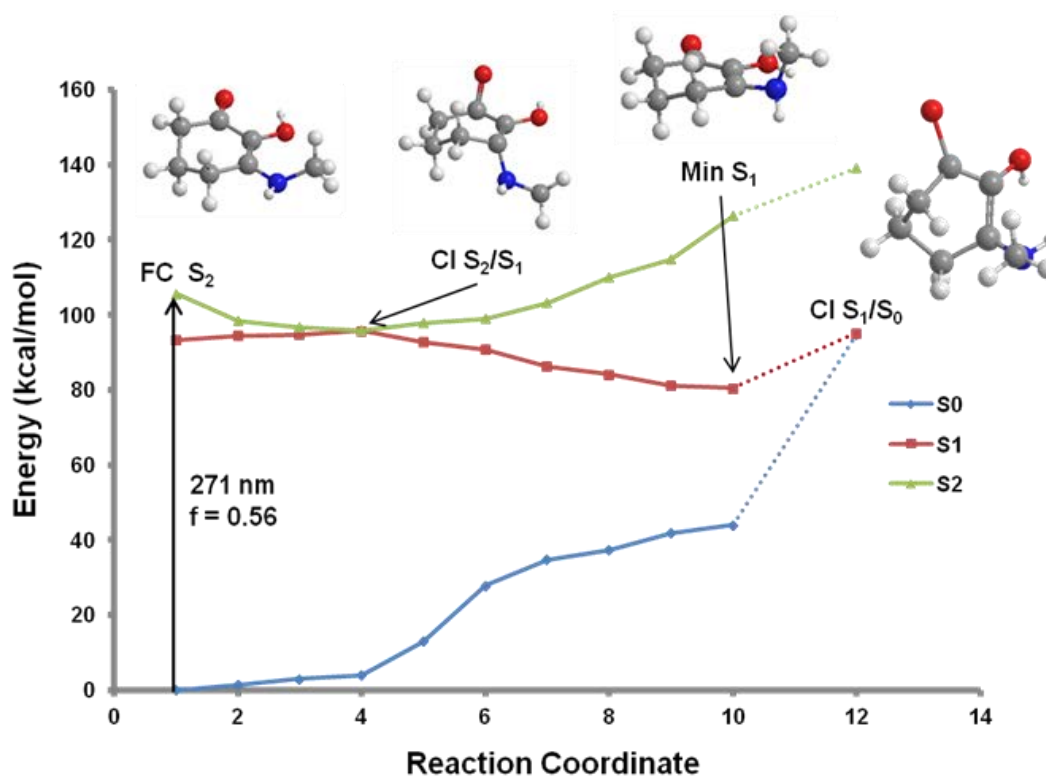


Figure 4.5. MEP connecting critical points of compound 1.

In this crossing point, the molecule suffers a non-planar deformation in the C=O group; this should be very fast due to the small energy gap between FC (Franck-Condon) region and CI S_2/S_1 , only 10 kcal/mol below FC. After this conical intersection (CI), relaxation in S_1 recovers a planar geometry in a minimum in the S_1 PES (Min S_1). This feature in the excited state usually yields in bigger excited state lifetimes and increases the possibility of radiative mechanism giving emission as a relaxation way to the ground state. In this system, a CI S_1/S_0 was found 15 kcal/mol above the minimum in S_1 . This conical intersection allows the non-radiative relaxation pathway but does not avoid the previously described radiative mechanism. When an excited state

minimum is present, the efficiency of the nonradiative mechanism depends on the energy difference with the CI S_1/S_0 . Consequently, a more suitable behavior is found with smaller gaps, which allow the nonradiative relaxation.

Looking at more detail into this CI, a strong deformation in the chromophore was found. This deformation implies an out-of-plane movement of the C-N moiety and the consequent nitrogen pyramidalization together with C=O elongation.

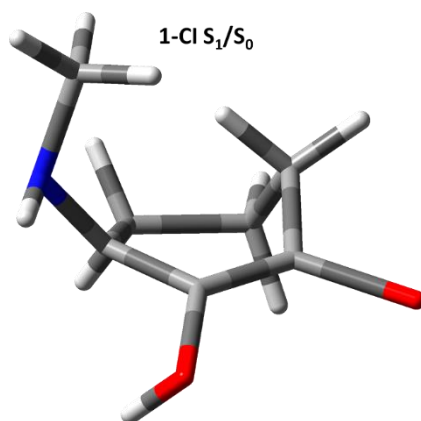


Figure 4.6. Conical intersection S_1/S_0 in **1**.

As can be seen in Figure 4.7, the same behavior is observed in **2** and **3**. In **2**, the relevant CI is only 4.5 kcal/mol above the minimum in a more suitable behavior compared with the 15 kcal/mol in **1**. By cons, in **3** the two obtained CIs are energetically disfavored being 7 and 20 kcal/mol above the FC and minimum S_1 point, respectively.

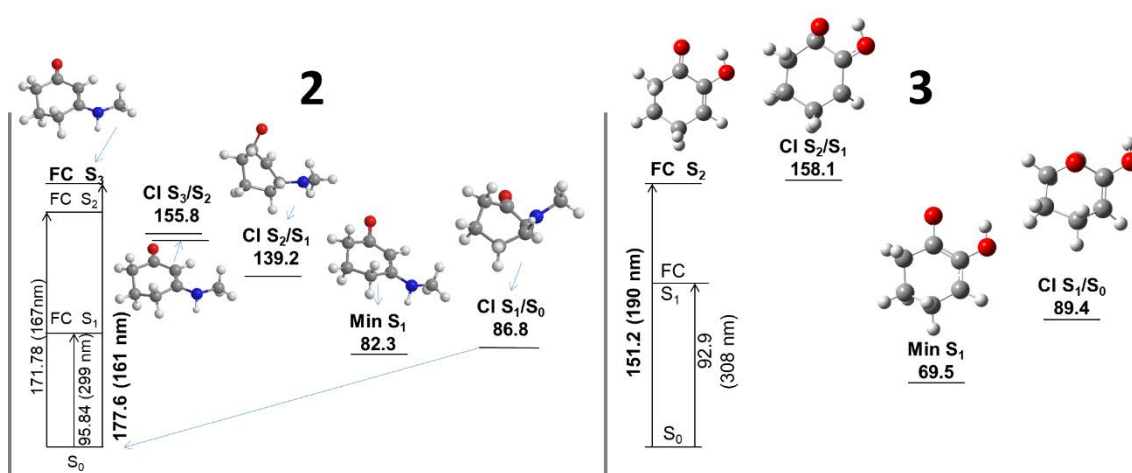


Figure 4.7. Critical points of **2** and **3**. Energy in kcal/mol referred to the ground state minimum.

Thus, **1-3** or in general cyclohexenones will not behave like an ideal UV-filter. Regarding the ideal features, this excited state minimum is not a suitable characteristic. This can induce fluorescent emission and increases the excited state lifetime, which can favor any type of photoreactivity. In addition, the absorption maximum is slightly blue shifted with respect to the ideal 290 nm, being the calculated values more in the UVC region.

In the other hand, cyclohexenimines (green and blue cores in Figure 4.2 and Figure 4.3) exhibit a similar behavior in all cases, but two series of compounds could be differentiated; compounds **4-5**, which have an imino group (neutral, in green) and compounds **6-8** that have it protonated as iminium salts (in blue).

In the first case, both neutral compounds **4** and **5** exhibit almost the same behavior. Looking into the nature of the orbitals involved in the absorption process, population of S_1 corresponds to an $n-\pi^*$ transition (dark transition) from N_{imine} orbital and a $\pi-\pi^*$ corresponds to S_2 bright transition. Excitation populates the second excited state (S_2) that rapidly reaches a CI with an out-of-plane deformation of both nitrogen atoms. This deformation allows the relaxation to S_1 . When reached S_1 , two different topologies are observed between **4** and **5**. In compound **4**, see Figure 4.8 left, relaxation yields in a planar structure which represents a minimum in the PES. Regarding the ideal features, excited state minima are not desirable. In contrast, this minimum is not relevant as a result of the low energy difference between it and the CI S_1/S_0 , as they are nearly isoenergetic (0.8 kcal/mol) and can be easily reached, almost in a barrierless pathway. This CI is achieved by an out-of-plane deformation in the iminic nitrogen and allows the recovery of the starting material and in some cases the *E/Z* isomerization product of the imine moiety.

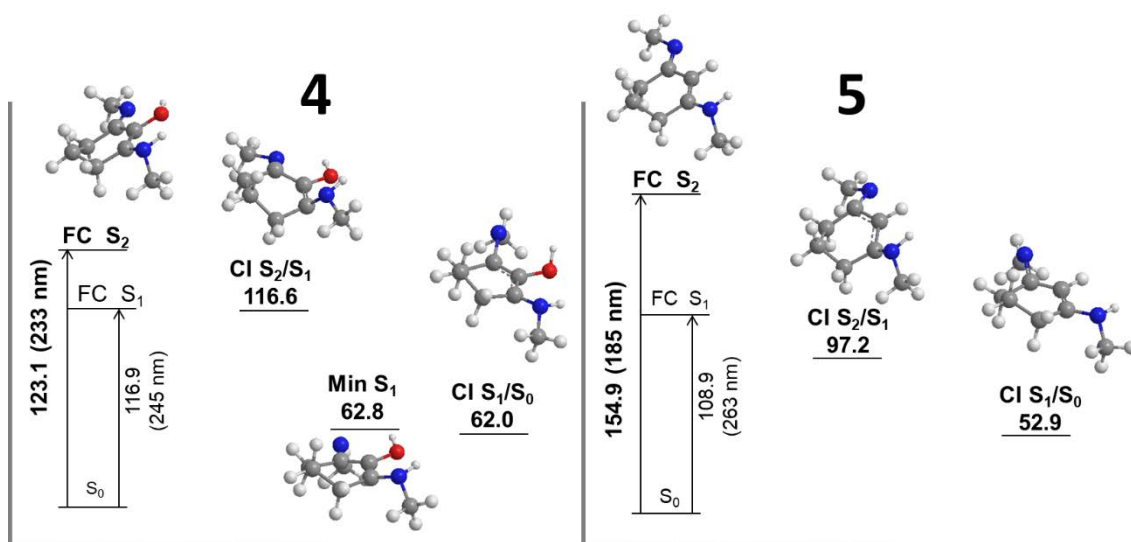


Figure 4.8. Critical points in compound **4** and **5**. Energy in kcal/mol referred to the ground state minimum

As counter point, in compound **5** (Figure 4.8, right), relaxation along the excited PES yields in a barrierless decay to a CI S_2/S_1 and subsequently to CI S_1/S_0 . These conical intersections are geometrically equivalent to the previously described for compound **4**, also presenting the same isomerization in the imine moiety in the ground state.

In the second set of molecules, compounds **6** to **8** show the same features in the potential energy surface. In all cases, when nitrogen is protonated, a strong absorption to the first excited state (S_1) is observed. These core structures present the higher oscillator strength values, more than $f > 1$ in the three compounds, with respect to $f = 0.56$ in **1**. This excitation matches with a π - π^* transition from the mixed C=C and $n_{\text{N}_{\text{amine}}}$ orbital to C=N π^* orbital, as mentioned above in Figure 4.4. In this case, the lone pair of the imine is compromised due to nitrogen protonation avoiding the n - π^* transition observed in neutral cyclohexenimines. Also remarkable is the absorption redshift of this chromophore related to **1**. This is very relevant, because it largely increases the spectral overlap with sun emission yielding in a more efficient sunlight absorption.

The detailed minimum energy path of compound **6** is shown in Figure 4.9. The MEP is almost the same for **7** and **8**, only changing the corresponding energies.

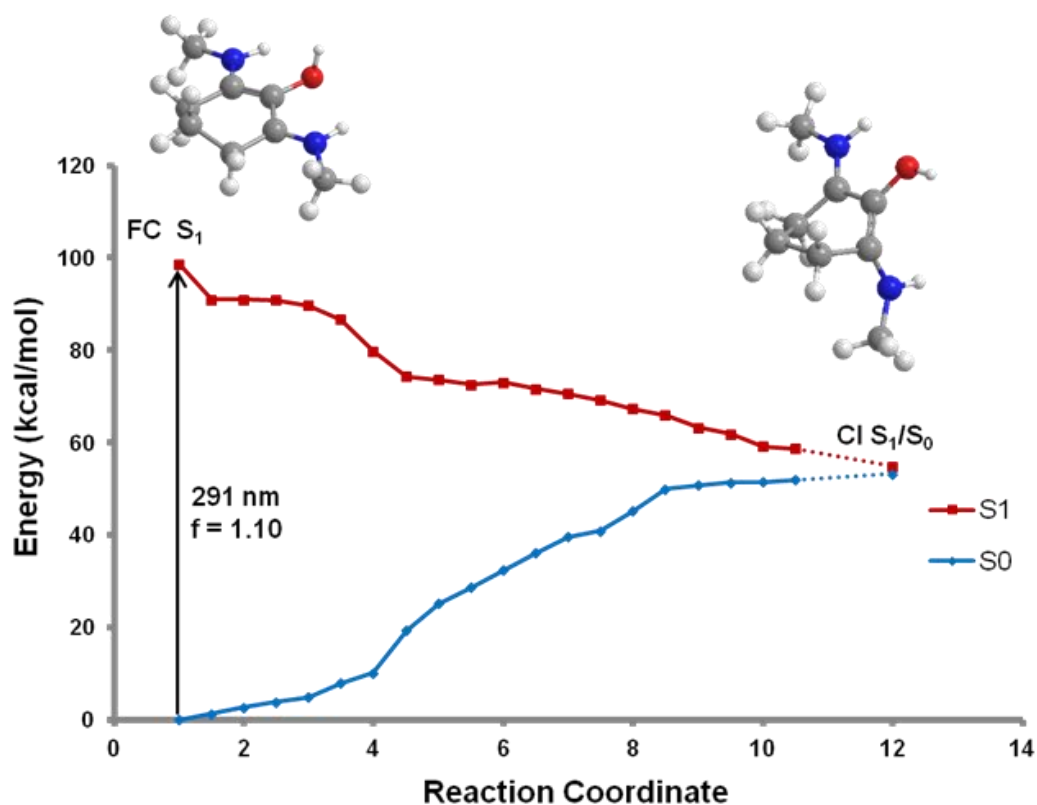


Figure 4.9. MEP connecting FC with a CI in compound 6.

After irradiation, S_1 relaxation yields to a conical intersection across a barrierless energy surface. This relaxation promotes a geometrical distortion. Nitrogen pyramidalization giving a CI structure analogue to the previously described for palythine.^[5] A further study of this type of CIs will be shown below for **8**. Relaxation in the ground state conduces in all cases to the starting material, not observing isomerization as in the neutral **4-5**.

As it is stated in the computational methods included in section 9.2.1, the characterization of a conical intersection comes from its characteristic vectors, gradient difference (GD) and derivative coupling (DC).^[6] The geometry of CI S_1/S_0 of **8** and the corresponding vectors can be seen with more detail in Figure 4.10.

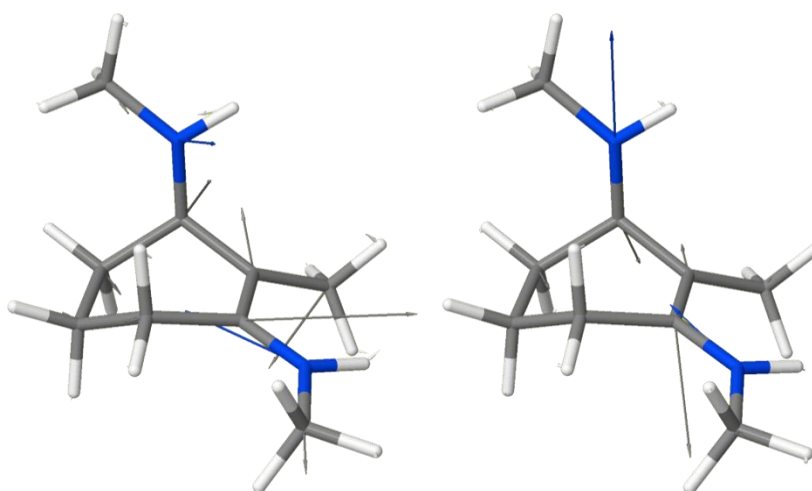


Figure 4.10. Gradient difference (left) and derivative coupling (right) vectors for **8-Cl**.

This conical intersection is practically identical to the observed in case of **6** and **7**, and the GD and DC vectors are in the same directions, so as expected these three compounds have almost the same behavior in the branching space. Molecule suffers a geometrical distortion that can be resumed as a pyramidalization on one of the iminic nitrogen atoms and the out-of-plane movement of the C=N bond that deforms the conformation of the N=C-C=C-N moiety, which is nearly planar in the Franck-Condon (FC) region. In the CI, the $N_{\text{imine}}\text{CCC}$ dihedral is 75° , which implies a great change from values close to 170° in FC. Also, elongation of the C=N and C-N bonds take place, changing from 1.32 Å to 1.42 and 1.29 Å, respectively.

As can be seen in the methods description in section 9.2, the other important feature to characterize a conical intersection is the topology around the CI. To explore it, a series of single point calculations of 20 geometries generated around the tip of the conical intersection for a loop defined on the branching plane with a 0.05 Å radius of the GD and DC vectors were performed.^[7]

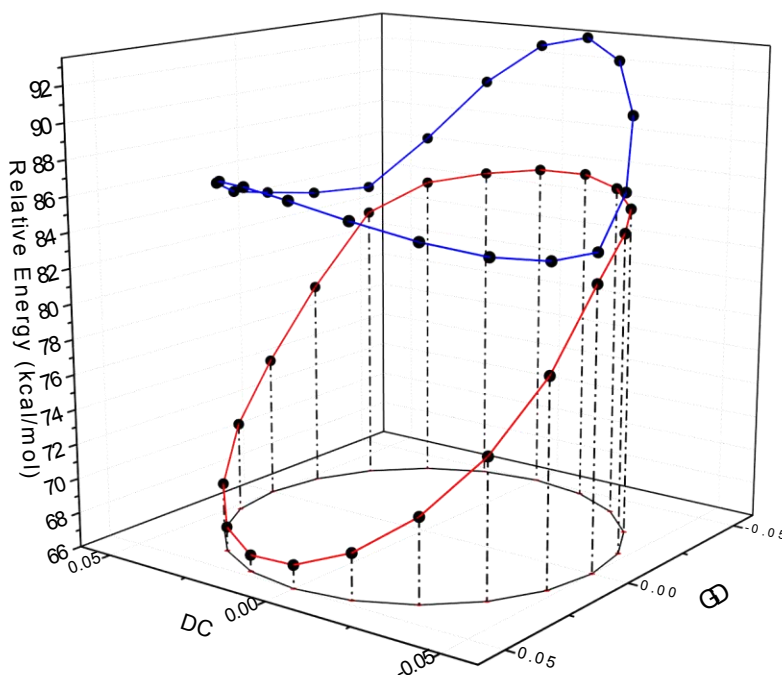


Figure 4.11. S_1 (blue) and S_0 (red) energy profiles around the tip of the conical intersection for a loop defined on the branching plane.

Looking into the topology around the CI, a sloped and single path conical intersection was found. This aborted geometrical distortion is a suitable behavior for this type of molecules, which should recover the starting material avoiding photoproduct formation or decomposition. This topology unambiguously offers an efficient crossing point between excited and ground state, which confers photostability to the molecule.

With all these data in hand, the most relevant features to consider during the design of these new molecules are described below to sum-up the theoretical screening on those compounds.

The main idea derived from this screening and our previously reported works^[1, 2] is the understanding and knowledge of a new photoprotection mechanism. This mechanism is unprecedented in bibliography and seems to be typical in this type of compounds and in similar ones like gadusol,^[2] involving an aborted geometrical deformation with an out-of-plane movement. This contrasts with other previously described photoprotection mechanisms typical in commercial sunscreens. In those cases, the most frequent is an *E/Z* isomerization of one of the double bonds present in

the molecule, as happens in cinnamates^[8] (although the low lying $n-\pi^*$ states are also relevant), or an excited state proton transfer, like occurs in oxybenzone.^[9]

Through the different studied core structures, two different behaviors are found depending on the studied system. This is depicted in Figure 4.12. In general, when high energy S_1/S_0 Cls (> 80 kcal/mol) are found usually a minimum in excited state (**1-3**) appears. This is not ideal because it increases the chances of photoreaction and radiative emission (red arrow from Min S_1). While with low energy S_1/S_0 Cls (< 70 kcal/mol, **4-8**, except for **8** where it is 77 kcal/mol due to a more planar PES, see section 5.2) a barrierless pathway to the ground state is observed. Regarding absorption, as mentioned in the previous discussion, cyclohexenimines exhibit a stronger and red-shifted absorption, related to a $\pi-\pi^*$ transition, than cyclohexenones where a more energetic transition to S_2 happens due to an $n-\pi^*$ transition to S_1 . This increases the spectral solar overlap enhancing the efficient absorption of UV light what is ideal for a sunscreen.

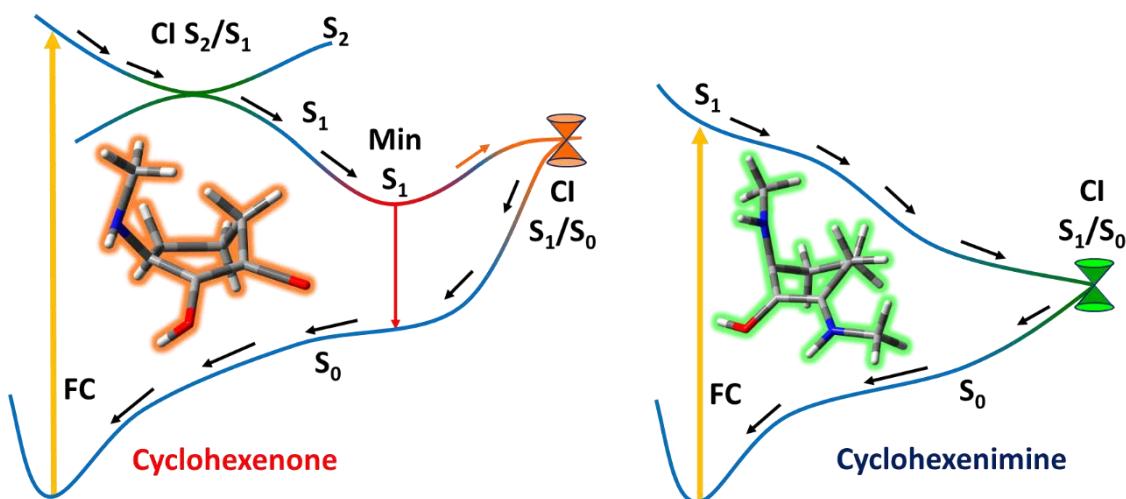


Figure 4.12. Summary with the schematic behavior of cyclohexenones (**1-3**) and cyclohexenimines (**4-8**).

In Figure 4.12, the suitable character of cyclohexenimine derivatives in green and the not ideal behavior of cyclohexenones in orange is depicted.

4.1.2. Dynamic analysis

To conclude the theoretical screening on these compounds and complement the static exploration into the reaction pathways of these molecules, a dynamical study is important to clarify if other pathways are also possible from a dynamical point of view. Therefore, this dynamic study was performed to throw some light into relaxation time scale for those molecules allowing comparison with commercial sunscreens. For an efficient sunscreen, a well-established and ultrafast deactivation mechanism is mandatory.^[10] A series of on-the-fly nonadiabatic molecular dynamics (NAMD) at the CASSCF(6,5)/6-31G* level for **8** and CASSCF(8,6)/6-31G* for **6** have been performed using the *dynamix* module in MOLCAS 8.0.^[11] In both cases, initial conditions were obtained by performing a Boltzmann distribution at 298 K with Gaussian 03.^[12] The dynamics were performed using a Nose–Hoover chain of thermostats with $T = 298$ K.^[13] ^{14]} For the full set of computational details and method description, see section 9.2.2.

For **8**, a total of 50 trajectories were computed up to the decay to the ground state with simulation times of ca. 700 fs. As can be seen in Figure 4.13, the variation of the excited and ground state energy versus time is represented only for one of the trajectories. The relaxation process along the PES reaches a hopping point (the used algorithm is similar to one employed to locate a conical intersection) relaxing to the ground state in a fast timescale. As expected from the relaxation process observed statically, a barrierless decay to a crossing point is obtained. After population of the ground state, a hot vibrational state is maintained to the end of simulation time. The electronic state of the molecule at each time is the so-called molecular dynamic state (MD state). Considering the energy variation for all trajectories, only one does not reach the ground state in this time scale. From the remaining 49 trajectories an averaged S_1 lifetime is calculated being $\tau_{S_1} = 239 \pm 65$ fs. This is an ultrafast process, being an ideal dynamical mechanism for a sunscreen, as it was stated before.

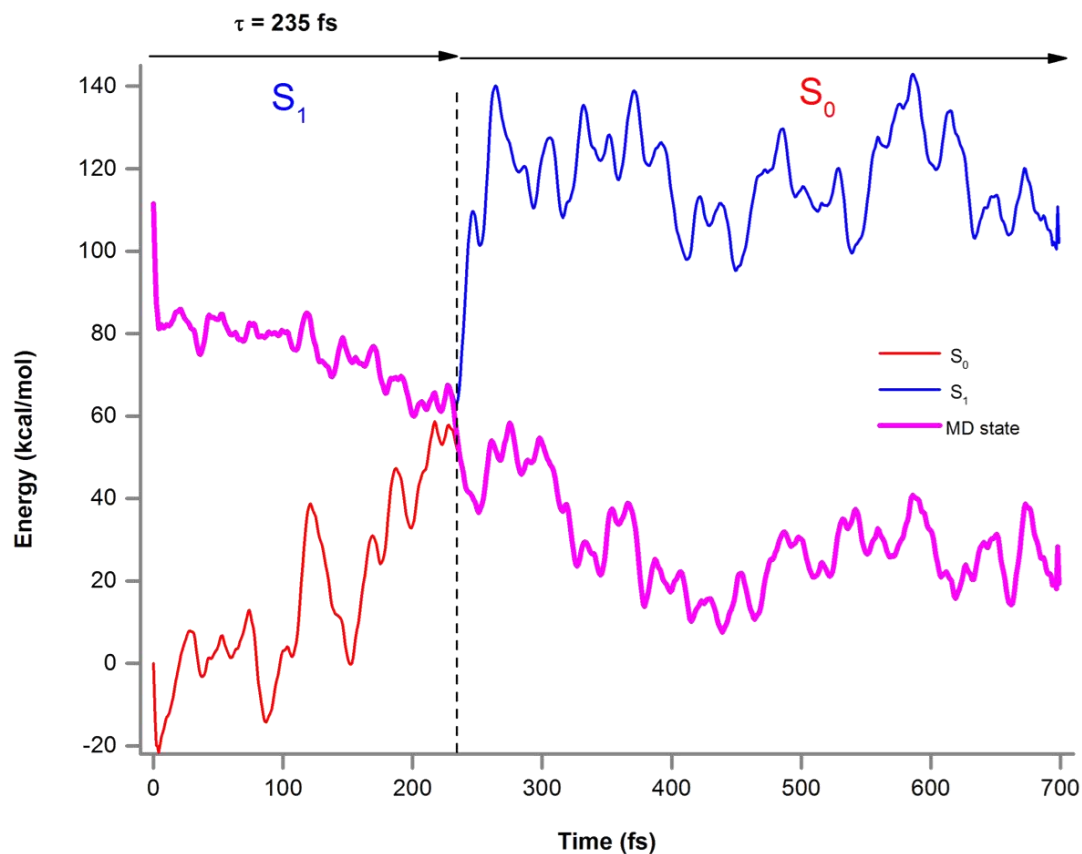


Figure 4.13. Non-adiabatic molecular dynamic simulation of **8**, S_1 and S_0 relative energies along one representative trajectory at 298 K.

Looking into the geometrical distortion along the computed trajectories, a great conformational change similar to the observed statically is obtained. In this case, 49 out of the total 50 trajectories showed a strong out-of-plane distortion of the imine moiety, similarly to the CI geometries, leading to ground state decay by an ultra-fast deactivation process. To probe this geometrical change, the variation of the dihedral N-C-C angle was monitored. The obtained positive and negative values are due to the out-of-plane bending that can occur to both sides of the molecular plane, but in all trajectories a dihedral bending (about 90 or -90 degrees) is observed, which confirms the excited state relaxation through a crossing point and not a different reactive pathway. The non-hopping trajectory exhibits a principle of isomerization in the imine substituent and no decay to S_0 was detected in this time scale, showing that the previously reported deactivation pathway^[15] can take place but it is not representative and non-competitive in this time-scale.

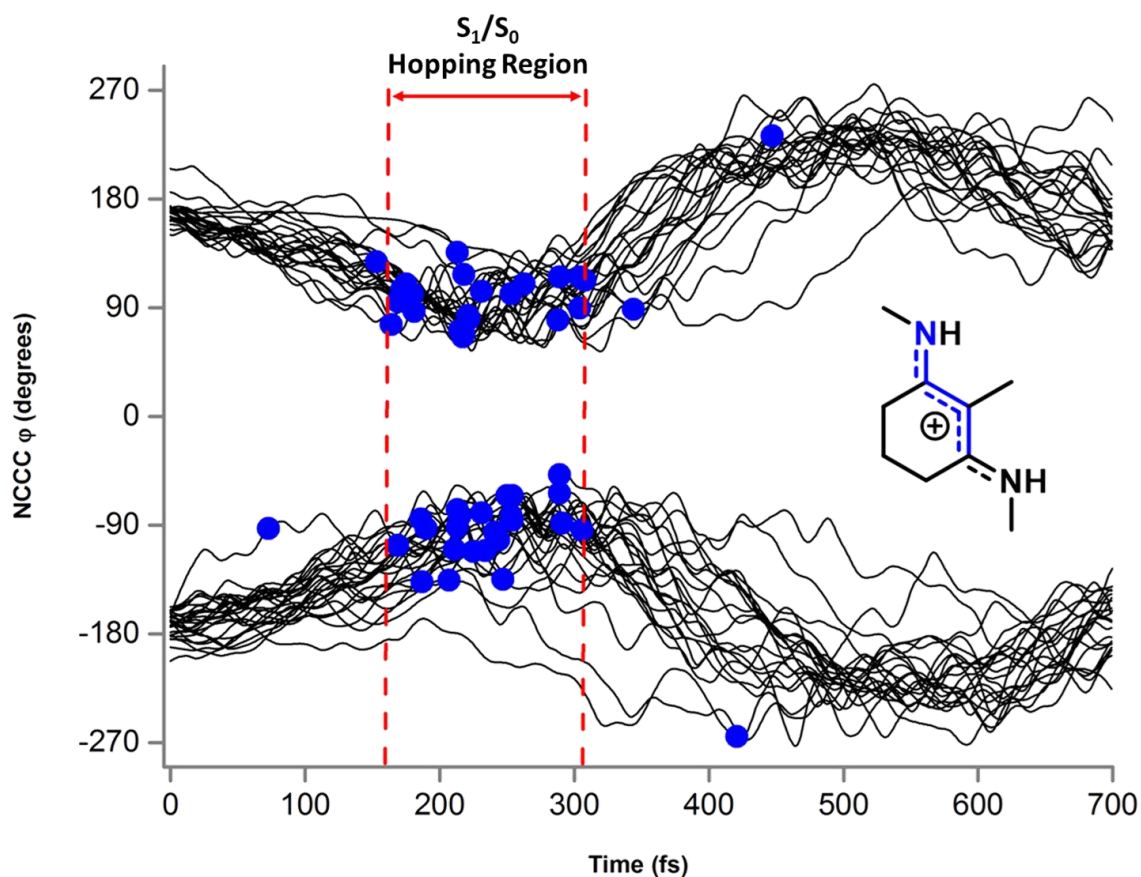


Figure 4.14. NCCC dihedral (see inset) monitoring across 49 MD trajectories. The blue dots mark the hopping points to S_0 .

In Figure 4.14, the relevant geometrical transformation is plotted along time, remarking the hopping points in blue. This data was extracted from the trajectory files using a set of self-made scripts interfacing a tool called *BondAngleDihedral*^[16] to extract automatically values of the desired geometrical property for a big number of trajectories and generating an easy-plot output with those results. The dihedral angles were corrected to allow their plot without a hop between 179° and -179° angles (which are only separated by 2 degrees) that would split each trajectory in the graph. As a consequence of that, dihedral values over 180° are represented.

As seen for **8**, a series of 25 trajectories for compound **6** were performed. As expected, the same behavior is observed, where only two of these trajectories remain in excited state due to long-time imine isomerization. The only difference between both systems is that this process is slightly faster than the previously described for **8**. This behavior could be explained according to the more planar PES observed in **8**. In this

case a relaxation lifetime of $\tau_{S_1} = 186 \pm 49$ fs was obtained from the theoretical data. The dynamic data is depicted in Figure 4.15.

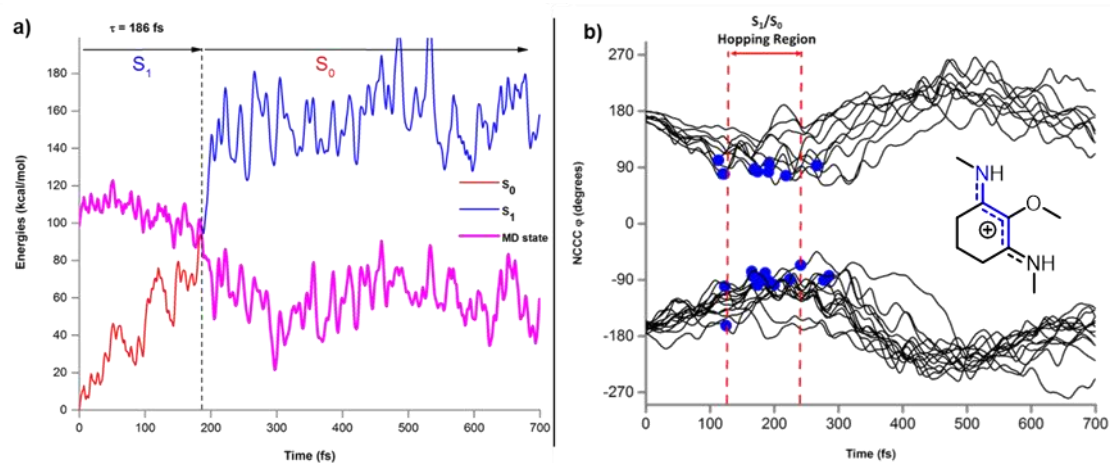


Figure 4.15. Non-adiabatic molecular dynamic simulations of **6**, a) S_1 and S_0 relative energies along one representative trajectory at 298 K. b) NCCC dihedral (see inset) monitoring across 23 MD trajectories. The blue dots mark the hopping points to S_0 .

Even being different, both values correspond to an ultra-fast deactivation process and no significant difference can be ensured because considering the standard deviation, both intervals match. It is important to note that these results are only theoretical calculations, not experimental data obtained for the prepared compounds.

Recently in Dr. Stavros group, an experimental comparison between cyclohexenimines and cyclohexenones were done.^[17] In this work, a compound similar to **2**, without the methyl moiety in the enamine nitrogen, and the previously described compound **11** (see Figure 4.16), were tested by time-resolved electronic absorption spectroscopy experiments to unravel the photochemical behavior in excited state and their lifetimes; these data will be commented deeper in the next chapter.

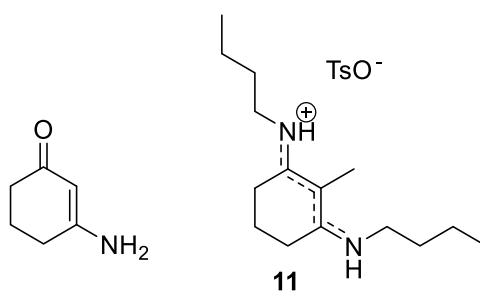


Figure 4.16. Compounds studied in Stavros group.^[17]

In these experiments, a clear confirmation of the static calculations presented in this section was obtained. In this case, the cyclohexenone compound presents a longer component in the excited state lifetime and it is suggested to be a minimum in S_1 . Electronically, the absence of the methyl group in the amine does not imply any effects on the PES shape, been almost the same. In the case of compound **11**, a shorter component from excited state absorption was obtained compared with the cyclohexenone derivative. In this case, a S_1 relaxation time of ca. 500 fs was measured. A graphical representation of this behavior is shown in Figure 4.17. Those values are in good agreement with the theoretical data. The gap observed is normal, because the calculations were carried out in vacuum and with methyl groups instead of butyl chains, which should move easier due to their smaller size. An extended study using some of the synthesized compounds described will be presented in the following chapter, looking at them from a spectroscopic point of view.

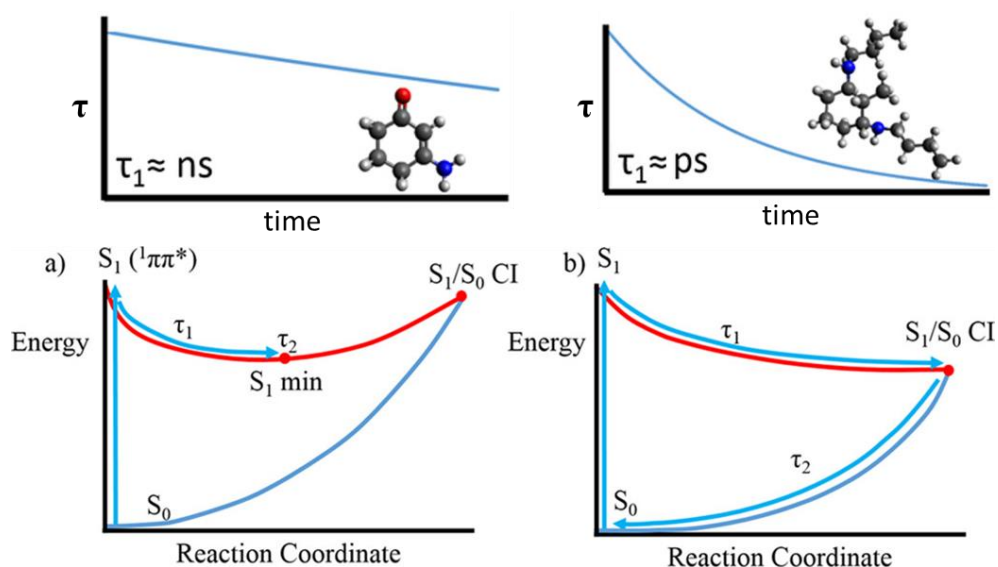


Figure 4.17. Schematic results from Stavros studies on MAAs. Adapted from *J. Phys. Chem. Lett.* **2018**, 9, 3043-3048.^[17]

As conclusion of both theoretical studies, static and dynamic, according to all the described properties, the most promising candidates are compounds **6** to **8**. For that reason, the development of synthetic routes to allow the preparation of some similar compounds was planned.

4.2. Synthesis and photochemical characterization of new MAA analogues

At this point, a good idea about the chromophore responsible for the photoprotective activity in natural MAAs has been acquired. From the computational screening data, a series of compounds were prepared with a main focus on the synthetic design. In addition, the new family of synthetic MAAs will be studied with an eye on the relation between structure and properties. Besides, the effectivity of this new mechanism could be tested in experimental conditions, validating in this way the previous theoretical design.

This section is divided in two subsections simultaneously developed, the synthetic procedure and the photochemical studies to test if the suitable behavior was obtained in the prepared MAA mimics, mainly in terms of UV absorbance and photostability.

4.2.1 A synthetic entryway to new efficient sunscreens

As it was noted in section 2.3.2 where different approaches to obtain MAA derivatives have been discussed, no practical solution for the preparation of this type of compounds has been proposed.^[4] Up to the start of this project, in 2013, the only evidence in literature was the synthesis of vinamidinium salts^[18] reported in 2004, which provided us with a keystone for the development of the synthetic work presented in this section. In this synthetic procedure, as remarked in the aims of this work, the goal was the obtention of cyclohexenimine derivatives in an affordable way focusing on the previously described as relevant core structures (see Figure 4.18).

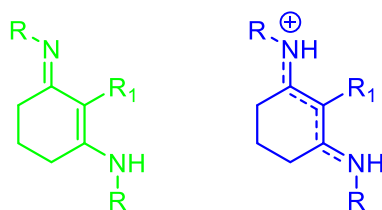
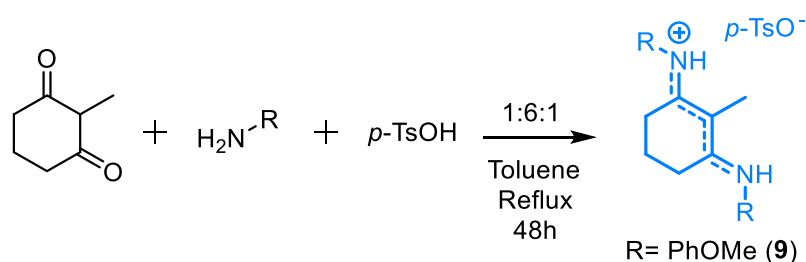


Figure 4.18. Target molecules to synthesize.

Owing to the ideal simplicity in the synthetic routes, the first attempts to obtain iminoderivatives were approached using the simplest raw materials possible. For that, the commercially available 2-methyl-1,3-cyclohexanedione was assayed in modified conditions as the ones described to obtain vinamidinium salts.^[18] Initially, reaction conditions using aniline were checked but only the corresponding aminocyclohexenone was obtained. After that, a series of experiments varying the amine and its amount, the *p*-toluenesulfonic acid presence and the reaction temperature and time were done as a fast way to check the viability of this synthetic approach with α -substituted cyclohexanediones. New conditions implied more than 2 equivalents of amine (*p*-anisidine was used in this case), increasing that value to 6 eq. to ensure reaction completion. Also, the reaction time was extended to 48 h or more, depending on the used amine from 22 h in the initial methodology.^[18] Together with these changes, a Dean-Stark condenser was incorporated to remove as much water as possible, avoiding possible hydrolysis of the imine moiety. The general reaction with the improved conditions is shown in Scheme 4.1. These conditions were selected in most of the compounds synthesized along this chapter, adapting the cyclic material, being the general reaction conditions.



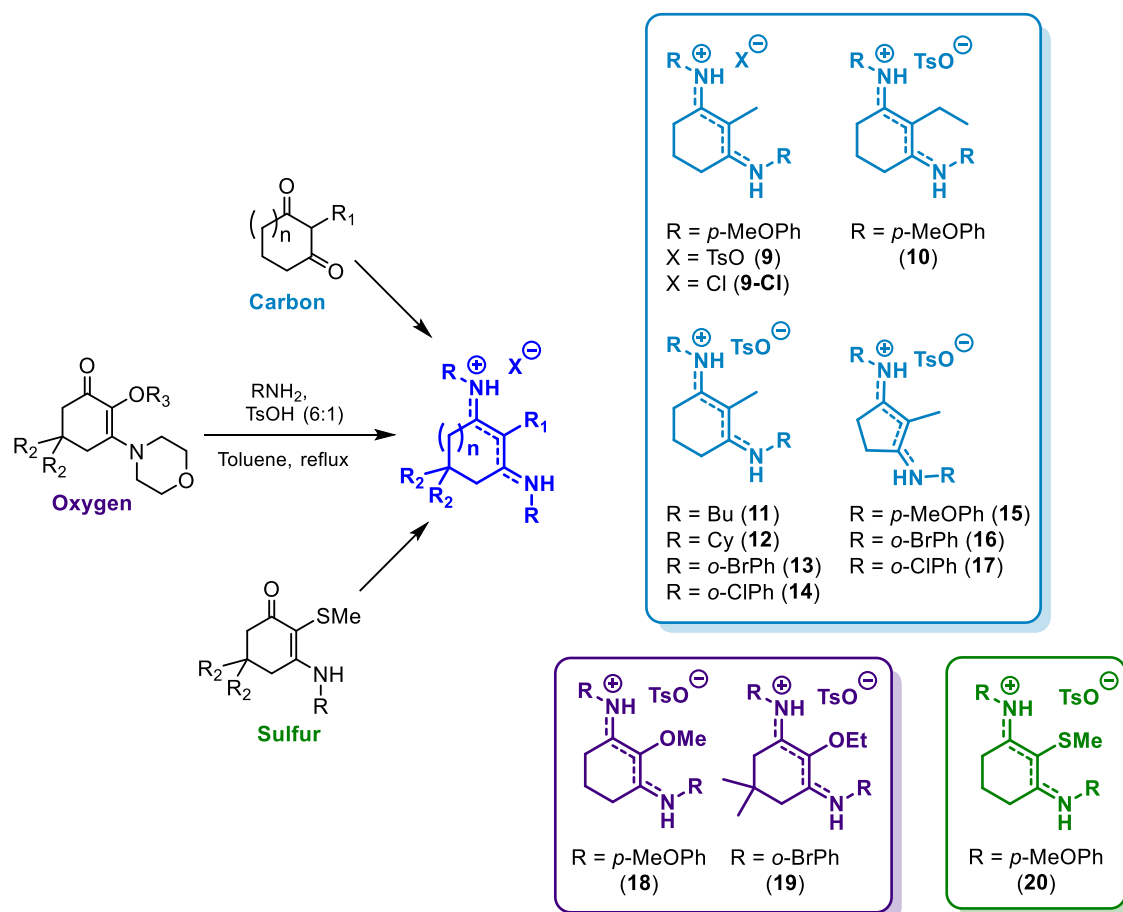
Scheme 4.1. General reaction to obtain cyclohexenimines substituted.

On paper, it seems to be a trivial synthetic pathway, but it demonstrated to be a tricky one due to the strong reactivity dependency on the nucleophilic character of the amine and the nature of the cyclic starting material. This reaction proceeds in two steps; in the first one, the corresponding cyclohexanedione (or similar) condensates with an amine to afford the aminocyclohexenone, which should further react forming the final cyclohexenimine salt. When some substituent in α of both carbonyl groups is included in the cyclohexanedione moiety (position 2), the electrophilicity of the intermediate aminocyclohexenone decreases drastically. This fact slows down the

reaction kinetics making this step the rate limiting one, increasing notably the reaction times.

With this problem in mind, to discern what type of amines should work properly was our next step. Regarding these limitations, amines with high nucleophilicity, such as *p*-anisidine, *o*-Br-aniline or butylamine are needed. The complete set of amines used in this work will be summarized after the description of the synthetic design.

A schematic representation of the diverse entryways to the obtained derivatives is depicted in Scheme 4.2 to sum up the different synthetic alternatives explored. Three different substitutions can be obtained in R₁ position according to the atom linked to the cyclic core. These residues are based on carbon (in blue), oxygen (in purple) and sulfur (in green).



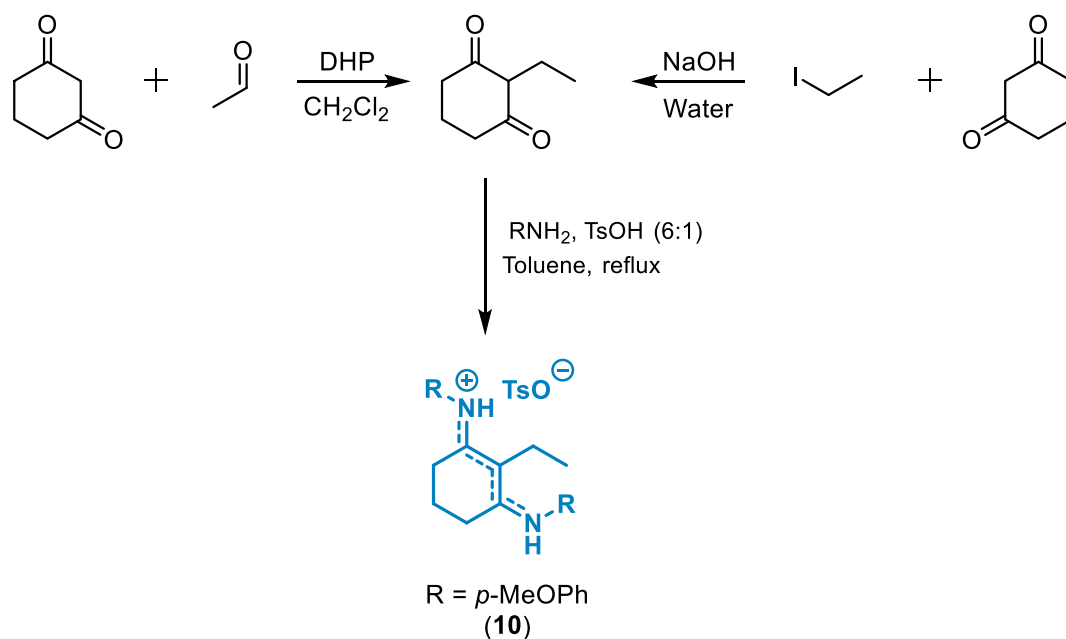
Scheme 4.2. Different synthetic approaches to MAAs.

In this scheme, only a general overview of the synthetic pathways is provided, with a summary of all the compounds obtained. As can be seen, the preparation of the

different substituted molecules is afforded from dissimilar starting materials sharing only a common last step. To explain the different alternatives in detail, the description will be split according to the three different substitutions placed in position 2.

4.2.1.1. Alkyl substituted derivatives

As it was described above, the first explored raw material was 2-methyl-1,3-cyclohexanedione, thanks to its simplicity and commercial availability. Looking to increase the scope of the prepared alkyl substituted compounds; other carbon chains were added in α -position, such as ethyl or butyl. For that matter, a condensation with the corresponding aldehyde followed by *in-situ* reduction with 1,4-dihydropyridine (DHP) was done to afford these compounds with quite good yields.^[19] Another option is the alkylation in α -position of the cyclohexanedione, but that reaction usually occurs with moderate yields around 60% and the dialkylated compound is also obtained as side-product.^[20]



Scheme 4.3. Different entries to compound **10** and possible similar derivatives.

Once the alkyl-*p*-anisidine substituted derivatives **9** and **10** were obtained, the reactivity with different amines was evaluated using the commercial 2-methyl-1,3-cyclohexanedione as raw material. The chosen complete set of amines is shown in the

final Scheme 4.9 together with all the synthetic possibilities. However, in this memory only the most relevant compounds will be explicitly mentioned. In Figure 4.19, the most representative compounds with this alkyl core structure can be seen.

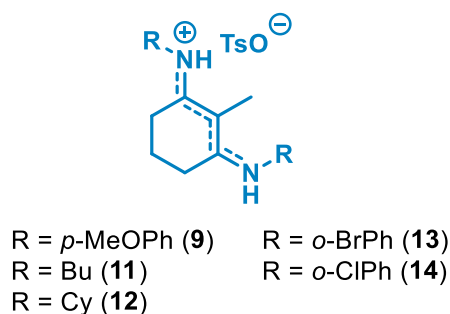


Figure 4.19. Derivatives synthesized from 2-methyl-1,3-cyclohexanedione.

In an attempt to increase the scope of the reaction and aiming to correlate the structure with the properties, other cyclic reactants were explored. In this case, the variation from the six-member ring to other cycles could be a critical modification even without modifying implicitly the chromophore. This change in the cycle size could increase the steric hindering along the relaxation process according to the more tensioned cycle, which could make more difficult the out-of-plane movement observed in the core derivatives and palythine.^[1] For that reason, the commercial 2-methyl-1,3-cyclopentanedione was used as starting material. No differences in the reactivity were observed with the same amines, independently of the cyclic moiety. Compounds in Figure 4.20 were synthesized as well.

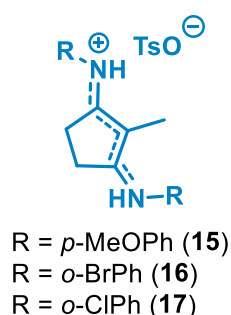


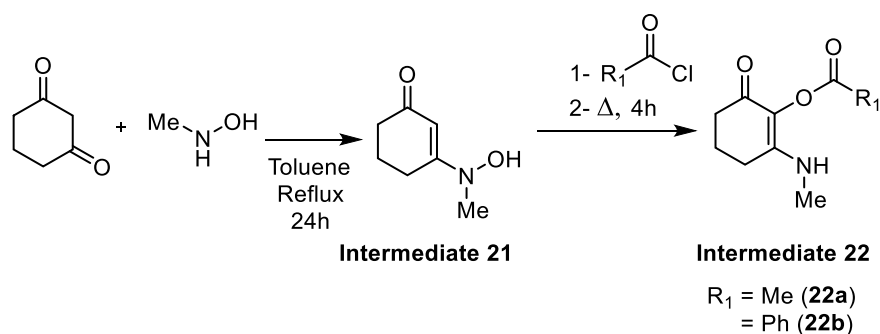
Figure 4.20. Five-member MAAs analogues.

In addition, other functionalized 1,3-cyclohexanedione derivatives were used; the 5,5-dimethyl-1,3-cyclohexanedione and other similar cyclohexanediones with one phenyl ring or methyl group in position 4. These raw materials work, but due to their

higher prices and worst solubility were dismissed looking into the potential applicability of these derivatives.

4.2.1.2. Oxygen substituted derivatives

Regarding the natural MAAs, the preparation of compounds with oxygenated residues in position 2 seemed to be imperative. Inspired in some previously described synthetic procedures, some α -oxygenated enaminones were obtained. One of this attempts^[21] uses an hydroxyaminocyclohexenone **21**, which when acylated rearranges upon heating yielding an oxygenated enaminone **22**. This step involves a thermally induced [3,3]-sigmatropic rearrangement. In that, the N-O bond is broken in the acylated intermediate **21** to yield the final compounds **22a** and **22b**, as can be seen in Scheme 4.4.

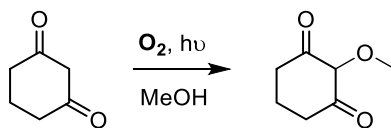


Scheme 4.4. Synthetic procedure to obtain derivatives substituted in position 2.

The obtained intermediates were assayed using the general conditions (see Scheme 4.1), but the only reaction observed was the exchange of methylamine by *p*-anisidine, obtaining the corresponding enaminone and not the expected iminoderivatives. In these cases, the use of stronger reaction conditions, such as xylene or dimethylformamide reflux, yields in decomposition and amine oxidation, even under inert atmosphere.

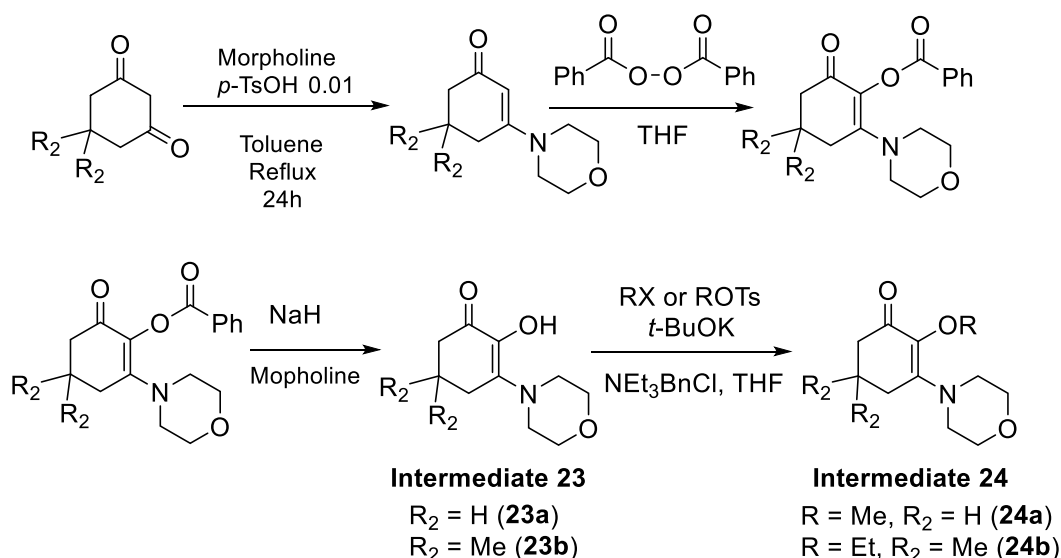
Other alternative paths were explored. The first one involves a photochemical addition of methanol to 1,3-cyclohexanedione.^[22] This is the simplest entryway to oxygen substitution, but unfortunately, only decomposition of cyclohexanedione was observed. Different reaction conditions were used changing the concentration, amount

of oxygen and irradiation time without further improvement. Therefore, this pathway was discontinued.



Scheme 4.5. Failed synthetic attempt to obtain oxygenated derivatives.^[22]

The second option implies a more complicated synthesis consisting on four steps to obtain the desired oxygenated intermediate, which can be used as starting material for the cyclohexenimine synthesis. This synthetic procedure was reported in 1979.^[23, 24] The global yield for the total synthesis is quite low (less than 10%) and it will not be an optimal starting material thinking of a big scale utilization.



Scheme 4.6. Synthetic procedure for the oxygenated cyclohexenimines.

As seen in Scheme 4.6, this synthesis begins with a condensation of 1,3-cyclohexanedione and morpholine, followed by a radical addition of an acylperoxide to the α -carbon of the cyclohexenone derivative. This reaction is the limiting step for the global yield of the synthesis, presenting a yield of 30%. After that, sodium hydride treatment releases the hydroxyl group in position 2, yielding the intermediate species **23a**. Different functionalization can be done in the oxygen by changing the alkylating reagent. Methylation affords the desired intermediate **24a**. This reaction can be done using the 5,5-dimethyl-1,3-cyclohexanedione instead of the cyclic carbonylic

compound shown in the previous scheme obtaining intermediates **23b**, which reacts with chloroethane to reach **24b**.

Looking into these last two steps to release the acyl group and functionalize the hydroxyl moiety, the same possibility surges as an opportunity for the previously obtained intermediates **22a** and **22b**. Treatment of intermediate **24a** with *p*-anisidine using general conditions affords the desired cyclohexenimine salt. The same treatment with *o*-Br-aniline of **24b** afforded it too.

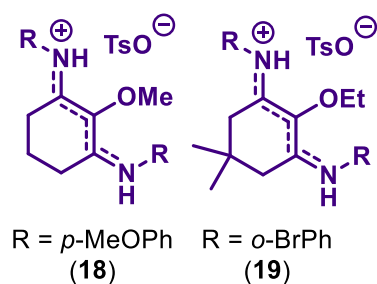
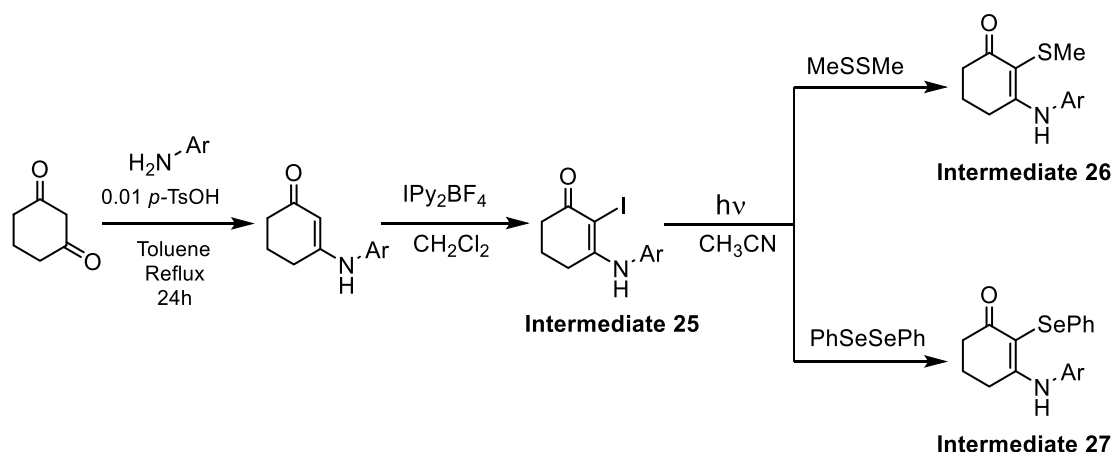


Figure 4.21. Oxygenated derivatives synthesized.

In this example (Figure 4.21) a new behavior was observed. Here, the used amine replaces the amine present in the enaminone. This fact limits the scope to obtain only symmetrically substituted compounds.

4.2.1.3. Sulfur and selenium substituted derivatives

Once oxygenated derivatives were obtained and aiming to expand the scope of the reaction, other synthetic possibilities were further explored. Focusing on other similar heteroatoms from the group 16, several attempts to attach sulfur and selenium moieties in α -position were done. For that, a photochemical reaction described in our research group^[25] was used. This methodology provides an accessible entryway for these sulfur and selenium derivatives.



Scheme 4.7. Obtention procedure for α -sulfur and selenium derivatives.

In Scheme 4.7, the irradiation with UV light, from a 400 W medium-pressure Hg lamp, of iodo-enaminone intermediate **25** produces the C-I homolytic bond cleavage generating the corresponding radical. This can be trapped by using, dimethyl disulfide or diphenyl diselenide, yielding the α -substituted enaminone (**26** and **27**).

Once obtained the different intermediates, reaction following the general synthetic procedure was performed. These compounds are clearly new in the literature and were attempted to evaluate the influence of high-weight atoms in the photochemical behavior of the system. Unfortunately, only the reaction with intermediate **26** was successful.

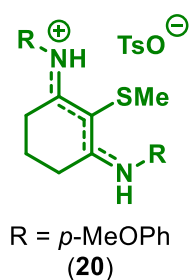


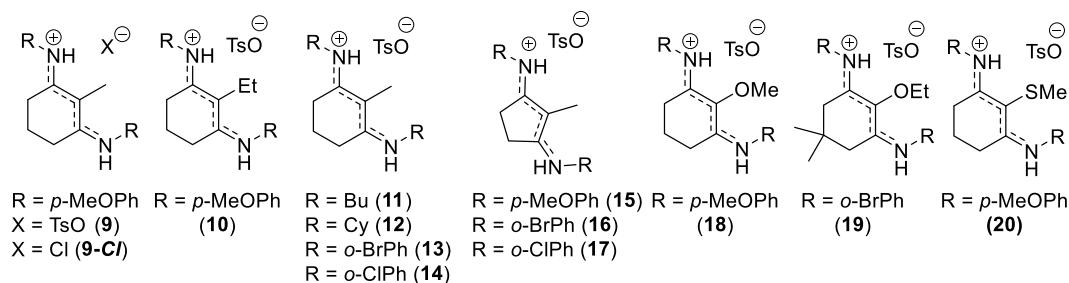
Figure 4.22. Sulfur derivative obtained.

In the case of intermediates **25** and **27**, decomposition was observed at reaction conditions. In **25**, also the thermal cleavage of iodine atom was significant as the starting unsubstituted enaminone was obtained. For **27**, no identifiable compound was found.

As it was stated, all the described derivatives present a tosylate as counterion. Another modification could be done changing this anion by other species. For that purpose, some compounds dissolved in methanol were treated in batch several times with anionic exchange resin in chlorine form obtaining, for example, **9-Cl**. In this case, the chlorine form of Amberlite IRA-402 was employed.

The synthetic alternatives with all the starting materials described across this section allow the preparation of a great number of compounds. The developed synthetic procedure permits the tuning of the synthesized molecules only changing the starting material. With this procedure, we can modify almost each position in the proposed core, the amine residue, cycle size, counterion and substitution in positions 5 and 2 as previously stated.

With this great number of combinations, only one or two examples of each cyclic moiety or amine fragment were performed as the synthesis with other substrates seems evident. These prepared set of molecules should provide enough information to understand the behavior of the system and to allow an approximate correlation between properties and structure. A summary with the most representative selected examples is described in Scheme 4.8.

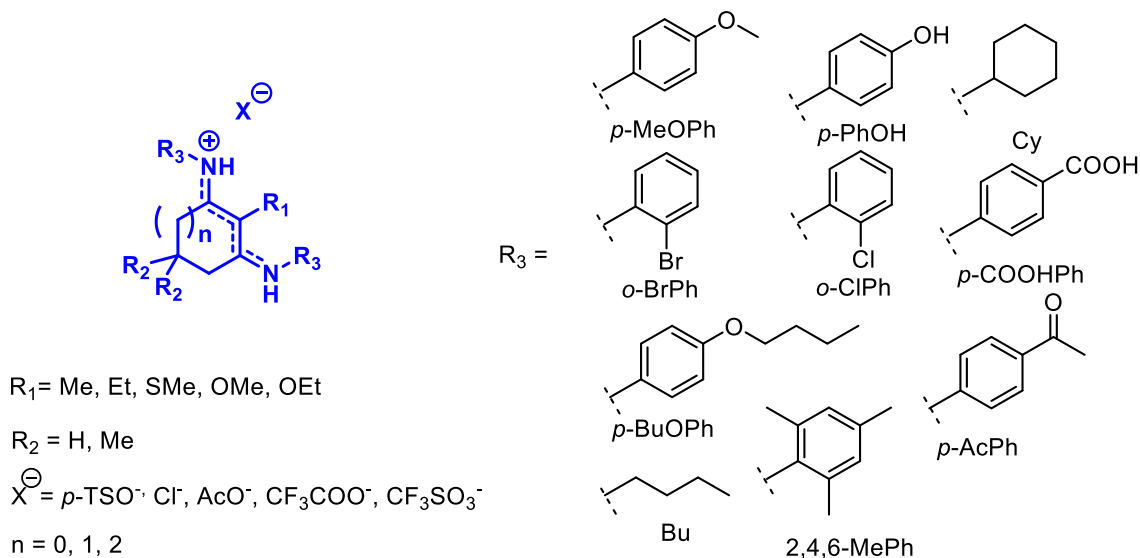


Scheme 4.8. MAA inspired compounds synthesized with our methodology.

Also relevant for any potential industrial application is the scale of this synthetic procedure. In all cases, reactions were carried out with 1 mmol of starting material obtaining around 200 - 500 mg of the desired product, depending on the molecular weight. If that scale could not be increased, the synthetic procedure would have a limited impact for an industrial use. This issue will be further discussed in the next section, but first tries allowed the preparation of *ca.* 10 g of compound **9** with the same yield without specific problems. Usually, this reaction proceeds in a good yield, 70 - 95% in most of cases. In others, using cyclohexylamine or mesidine (2,4,6-trimethylaniline),

the reaction yield decreases to around 50%. The current yield obtained for each compound is detailed in the experimental section at the end of this chapter.

To conclude with the description of the synthetic versatility of this procedure, a representation with the scope of the reaction with all the synthetic options grouped is shown in Scheme 4.9. Here, all possible synthetic combinations yield in more than a hundred compounds, which are summarized to provide a general look into the scope of the reaction.



Scheme 4.9. General structure with feasible target compounds.

Some new examples of these derivatives were synthesized and will be commented in the next section.

The described compounds included in the previous schemes, as a result of their high potential applications, were protected in a Spanish patent application, presented the 30/06/2015 with title "Compuestos fotoprotectores análogos de MAA, procedimiento de síntesis y composición que comprende los mismos" and publication code **ES 2 550 374 A1**. This patent includes the preparation and the use of those compounds in different formulation for skin protection.

4.2.2. Photophysical and photochemical properties

With all these derivatives synthesized, we focus on the correlation between the structure and the observed properties. For that purpose, enough data is needed to understand the system character, aiming to allow prediction of the molecular properties of new compounds in base of their structure and *vice versa*, permitting the design of compounds to fill a specific need.

As described in the Introduction, the aims for an efficient sunscreen should be met. As consequence, the study of these important features was performed, focusing on the UV-Vis absorptivity, thermal and photochemical stability and lack of fluorescence.

Looking into these properties, maybe the most important feature to asset is the shape and position of the UV-Vis absorbance band for each compound. For that, solutions around 5×10^{-5} M in acetonitrile and methanol were used to calculate the molar absorptivity (ϵ), which is the strength of the absorption. As mentioned before, to provide protection against sunlight, the absorption maximum λ_{\max} should be between 290 to 400 nm. In Figure 4.23, absorption spectra of some compounds from Scheme 4.8 are shown. Some compounds such as **14** and **17** are missing because their bands are quite similar to **13** and **16**.

A common feature observed in all cases is the presence of a single band in the UV region, which is in good agreement with the theoretical data that only predicts a π - π^* transition. The absorption maxima can be tuned to cover along the whole relevant UV range (from 290 to 400 nm) changing the cyclic structure and the amine. Also, with the obtained UV spectra, the mixture of two compounds should provide an extended broad UV protection as is needed in sunscreen formulations.

Here an important concept surges to quantify the strength of the absorption relating with molecular weight. It is an important fact in cosmetics due to incorporation in a formulation is calculated in weight/weight percentage. This specific extinction coefficient $E_{1,1}$ is referred to a 1% solution (or dispersion) of the absorber at a 1 cm optical path length. The relationship between ϵ and $E_{1,1}$ is the following, being M_w the molecular weight of the studied compound.

$$E_{1,1} = \epsilon (L \cdot mol^{-1} \cdot cm^{-1}) \cdot \frac{10(g/L)}{M_w(g/mol)} \cdot 1(cm)$$

The corresponding $E_{1,1}$ value for each compound is shown in Table 4.1, together with the values of some commercial filters. In all cases, the $E_{1,1}$ value is calculated at the absorption maximum (λ_{\max}) of each compound.

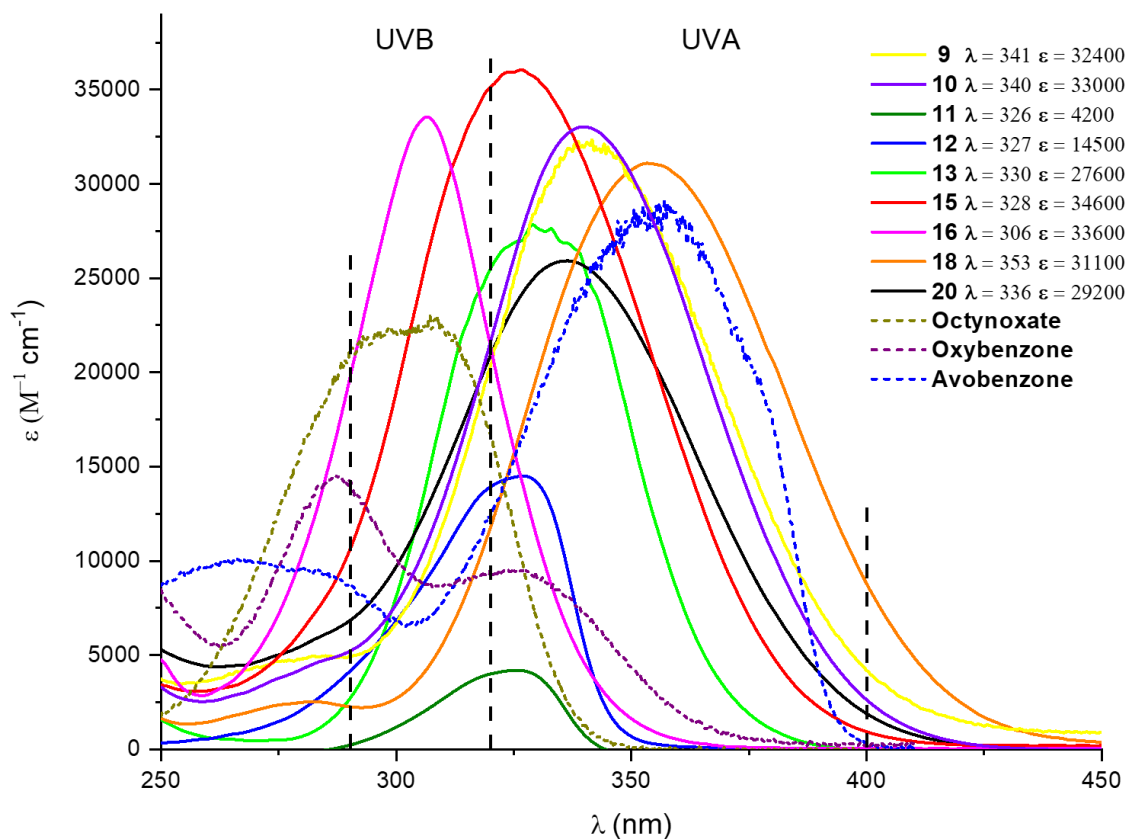


Figure 4.23. UV-Vis spectra of some of the UV absorbers developed.

The importance of the sunlight spectral overlapping with the compound used as sunscreen has been mentioned before. For that, it is better a UV filter with lower $E_{1,1}$ and better spectral overlap with respect to a molecule with the absorption maximum at 250 nm and a huge $E_{1,1}$ value. Looking to the UV region where absorption maximum is located, some prepared compounds could be classified as UVA filters as **9**, **10** and **18**, and UVB filters as **16**, **17**, **12** and **11**.

Once studied the UV-Vis absorption properties of these compounds, the luminescence on methanol was measured using 5×10^{-4} M solutions for most of the compounds **9** to **20**. In all cases, the behavior is almost the same. As previously stated, ideally, a sunscreen should relax to the ground state through non-radiative mechanisms, meaning that fluorescence or phosphorescence emission should be minimal.

All samples feature a very weak emission band, where due to the low intensity a reliable measurement of the quantum yield cannot be done. In addition, studies at lower temperature were performed to freeze the non-radiative mechanisms and favor the radiative ones. This is the normal behavior for this type of processes, which with lower temperatures a decrease in molecular vibrations is observed. This lower-energy vibrational state favors the relaxation following non-adiabatic processes, meaning an increase of the efficiency of radiative processes.

Normalized emission of compound **9** was measured using the same acquisition parameters, to obtain comparable measurements, at room temperature in an NMR tube containing a methanol solution around 5×10^{-4} M. The same tube was frozen with liquid nitrogen at 77 K and measured with liquid nitrogen covering to avoid condensation in the walls of the tube. The normalized emission spectra are shown in Figure 4.24.

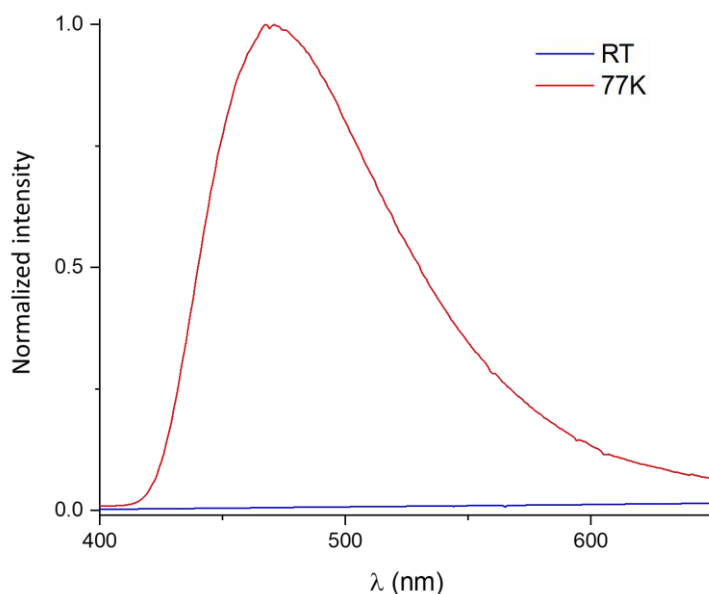


Figure 4.24. Fluorescence emission at 77K in red and room temperature in blue.

With this data at room temperature, the observed quantum yield is too low to be measured. Analogously, the quantum yield at 77 K could not be measured in spite of being stronger is below the detection limit of the instrument too. Consequently, for both samples the quantum yield can be estimated to be less than 1% in solution.

Other important feature is the thermal and chemical stability of the new derivatives. If they are to be applied in some formulation, they should be stable in the final products for months or even years. In those cases, a high chemical stability in

media conditions is needed. Some experiments to check their chemical stability were done. Firstly, by checking if decomposition takes place in after storage in common lab conditions. In this, no decomposition was observed during the storage of those compounds under air, ambient light and room temperature environments during almost 3 years. Other assays in solution were done at different pH media. Therefore, different buffer solutions were used with pH 4, 7 and 9. The hydrolysis of these derivatives was studied maintaining a solution of the corresponding sunscreen solubilized in methanol and mixed with the buffer stirring for one week. In compounds **9** to **20**, no hydrolysis is observed at pH 7, but in alkyl derivatives **11** and **12** some chemical instability is perceived at pH 4 and 9. It matches with hydrolysis obtaining the enaminone derivative in acidic media and with unknown products in basic conditions. As overview, most of these compounds are stable under air and light conditions and stable in neutral water solutions.

In terms of usability of these molecules as polymer additives, a high thermal stability to support extrusion or thermoforming processes is needed. Measured fusion or decomposition points for these salts are higher in all cases than 200°C. That temperature should be enough to allow the inclusion of those compounds as additives in different coating polymers adding some UV-protection to the material.

The second most important feature is the photostability under UV light exposure. None of the abovementioned described features has sense for a molecule without, at least, a moderate photostability. In these compounds, accordingly to all the previous rational design a high photochemical stability is expected. To prove this, direct irradiation of methanol solutions was performed using a Pyrex filtered (cutoff in 290 nm, removing more energetic light) 400 W medium-pressure Hg lamp. Those lamps present a non-homogenous (band structured) emission between 200 to 1000 nm. In addition, the low energy (infrared) radiation is removed with a water chamber that refrigerates also the lamp. The emission spectrum of this lamp is shown in the general experimental section in Figure 9.1.

Irradiation of 0.1 M solutions of all these compounds in *d*₄-methanol in Pyrex NMR tubes was performed. NMR tubes were capped to avoid evaporation or hydration of the samples. The irradiated samples were monitored by proton NMR. The irradiation was conducted up to 16 hours for all synthesized compounds; in all cases, no decomposition was observed. For the sake of comparison, three of the most used commercial UV filters; avobenzene, oxybenzone and octinoxate were irradiated under

4. Design and synthesis of new MAAs analogues

the same conditions. The obtained results for the irradiation experiments are summarized in Table 4.1, together with the absorption λ_{\max} of each compound.

Compound	λ_{nm} ($\epsilon \text{ M}^{-1}\text{cm}^{-1}$)	$E_{1,1}$	Photostability		
			1h	3h	6h
9	341 (37800)	743	>95%	>95%	>95%
9-Cl	341 (42200)	1132	>95%	>95%	>95%
10	340 (33000)	631	>95%	>95%	>95%
13	330 (56100)	925	>95%	>95%	>95%
14	330 (26400)	690	>95%	>95%	>95%
15	326 (36400)	736	>95%	>95%	>95%
16	306 (33600)	567	>95%	>95%	>95%
17	306 (32400)	884	>95%	>95%	>95%
18	354 (39600)	755	>95%	>95%	>95%
19	340 (35000)	526	>95%	>95%	>95%
20	336 (29400)	722	>95%	>95%	>95%
Oxybenzone	286 (14000)	630	82%	80%	78%
Octinoxate	308 (23000)	820	95%	89%	79%
Avobenzon	357 (29000)	1110	88%	84%	66%

Table 4.1. UV data and recovery under different irradiation times.

For all derivatives, no decomposition was measured but 95% is the maximum value that can be ensured attributable to the NMR detection error (5%). The same protocol with commercial filters yields in a decomposition starting from the beginning of UV exposure and a decay in the amount of the recovered compound was observed, reaching in 6 hours a decomposition higher than 20 - 30%.

In addition to these tests, some experiments in diluted solutions were performed, irradiating the samples with a solar simulator placing the cuvette at 5 cm of distance from the output. In these cases, the same behavior was obtained in a shorter time-scale due to the higher power of the solar simulator. Also, the same was measured using a Hg lamp with diluted solutions. Between the solar simulator and the mercury lamp a big difference in the spectral emission is observed. A further discussion on the emission both light sources could be found in the general comments of section 9. The

used solar simulator is composed by a 300 W xenon arc lamp, which emits a continuous spectrum along 200 to 800 nm, but with a special filter cuts off in 290 (similarly to Pyrex) yielding in a light quite similar to sunlight in the UV region, see Figure 2.1.

Another irradiation test was performed using real sunlight. For this, NMR capped tubes were irradiated under direct sunlight during all summer (from June to September) in the rooftop of Universidad de La Rioja (Logroño, Spain (42° 27' 56,6" N, 2° 26' 20,4" W, 384 m above the sea level). As expected, no decomposition was observed in any sample.

Other important feature for sunscreens is to know the behavior in cosmetic formulations to ensure compatibility with other components in a final preparation. For that, we explored it in collaboration with Dr. José Aguilera in the department of medicine and dermatology in Universidad de Málaga, where I did a short stay for one month. A series of base formulations (water in oil preparation) was performed including a set of compounds in several formulations to explore the individual contribution of each compound to the solar protection factor.

For the final testing with the best candidates, we prepared a formulation like those used in commercial products. For these formulations, the prepared compounds **15** and **16** at 10% and two of the most usual commercial filters (octinoxate and avobenzone) were included. These two compounds (**15** and **16**) were selected because of their better SPF values in individual tests. The desired formulation was prepared using three different phases as described in the *International Standard ISO-24443*^[26] Annex E. **M1** included (among other required ingredients) 10% of **15** and 10% of **16** as active species. **M2** included 10% of octinoxate and 5% of avobenzone. **M3** included a mixture of the four components in the same amount as above (10% of **15**, **16** and octinoxate and 5% of avobenzone). We used in these tests the maximum amount allowed to be used in commercial formulations (10% octinoxate and 5% avobenzone). A schematic representation with the composition of the prepared formulations is shown in Figure 4.25.

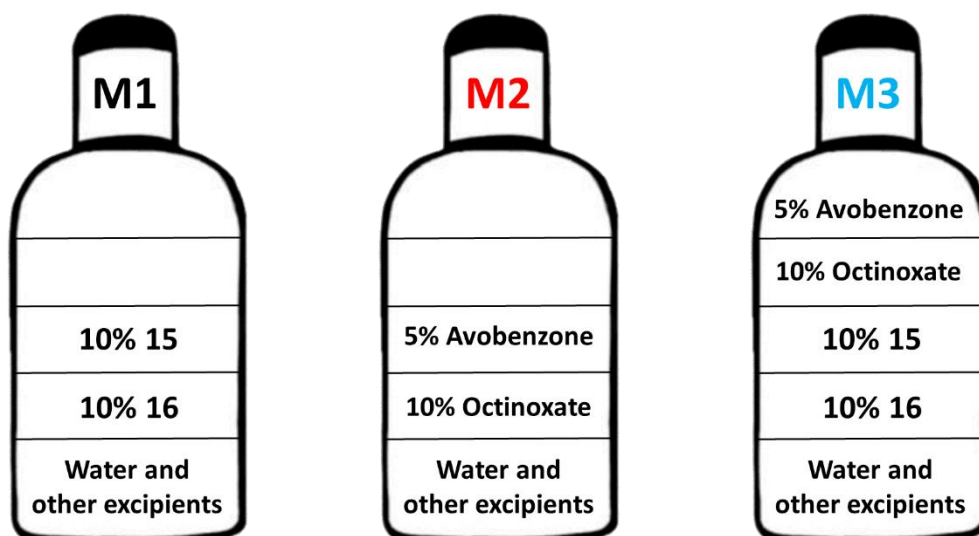


Figure 4.25. Scheme with the amount of sunscreen in the prepared samples M1, M2 and M3.

A brief introduction about how solar protection factor is measured is mandatory to clarify the methodology used in these experiments. All samples were measured at the same focus distance and detector position to ensure that all samples received the same UV dose. For these experiments, we used a solar simulator and a spectroradiometer with an integrating sphere that allows light quantification. During sample preparation for measurements, a PMMA standardized plate (5x5 cm) is used to get reliable and trusty data. In this plate, we put a known amount (1.3 mg/cm^2) of formulation, we extended manually and we waited for 5 minutes to stabilization. The setup is shown in Figure 4.26. A technical and more detailed description of the equipment used is included in the experimental section.



Figure 4.26. Experimental setup for SPF measurements.

According to the protocol described in the standard,^[26] solar protection factor (SPF) is the integral between 290 and 400 nm of the product of solar spectra ($S_s(\lambda)$) weighted by the relative erythemal potential of each wavelength according to the ICD erythema action spectrum.

$$SPF = \int_{290}^{400} \frac{S_s(\lambda) * s_{er}(\lambda)}{S_s(\lambda) * s_{er}(\lambda) * T(\lambda)} d\lambda \approx \frac{\sum_{290}^{400} S_s(\lambda) * s_{er}(\lambda)}{\sum_{290}^{400} S_s(\lambda) * s_{er}(\lambda) * T(\lambda)}$$

Moreover, UVA protection factor (UVA-PF) is the integral between 320 and 400 nm of the product of solar spectra ($S_s(\lambda)$) and weighted by the relative potential of skin persisting pigment darkening (PPD) according to the ICD action spectrum for PPD.

$$UVA - PF = \int_{320}^{400} \frac{S_s(\lambda) * S_{PPD}(\lambda)}{S_s(\lambda) * S_{PPD}(\lambda) * T(\lambda)} d\lambda \approx \frac{\sum_{320}^{400} S_s(\lambda) * S_{PPD}(\lambda)}{\sum_{320}^{400} S_s(\lambda) * S_{PPD}(\lambda) * T(\lambda)}$$

This information and the Erythema and Persistent Pigment darkening spectra are tabulated in the Annex C of the ISO.^[26]

The transmittance of the samples ($T(\lambda)$) is calculated using the irradiance of a blank plate with petroleum jelly, been the quotient of the sample irradiation $I_s(\lambda)$ and the blank irradiance $I_r(\lambda)$.

$$T(\lambda) = \frac{I_s(\lambda)}{I_r(\lambda)}$$

All measurements of **M1**, **M2**, and **M3** for SPF and UVAPF were performed in four samples and each one was measured four times (even though the ISO requires only three). In every case, the values reported are statistically significant. The variation coefficient of measurements was 11.9, 16.0 and 14.8%, in all cases below the required value in the ISO. Therefore, the methodology is adequate and the reported values are statistically significant. The noise in transmittance in the region between 290 to 300 nm is caused by the very low values of irradiance transmitted by the sample at those wavelengths.

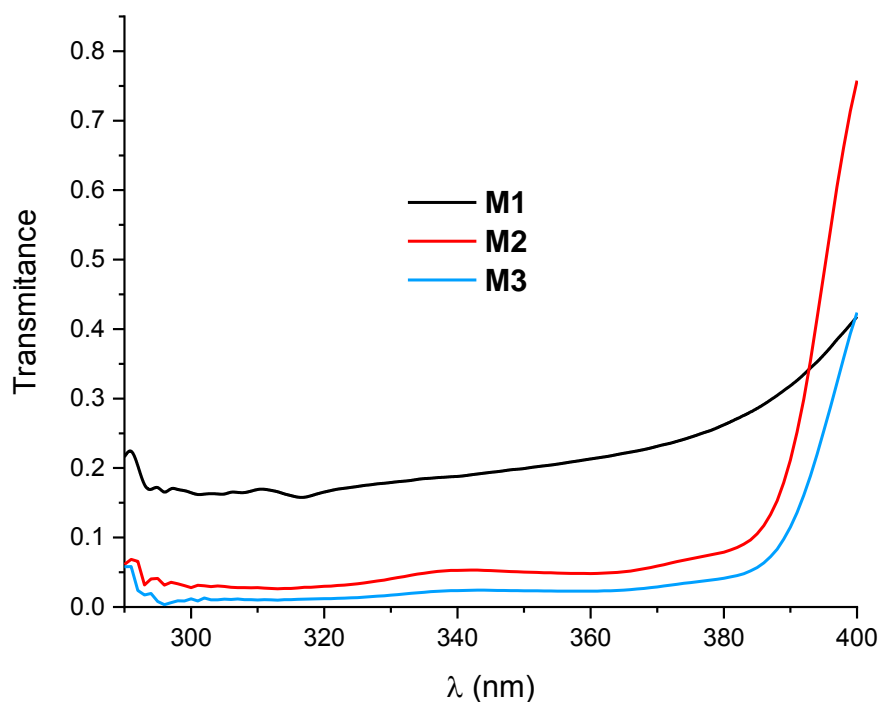


Figure 4.27. Transmittance in samples **M1-M3**.

With these transmittance values (Figure 4.27) treatment as described in the ISO standard procedure (Annex F) yields the SPF and UVA-PF values for each sample. As can be seen in Table 4.2, SPF associated uncertainties increase when higher SPF values are. This fact is due to the very low irradiance values, that are close to zero and cause a lower signal-to-noise ratio, especially in the 290-320 nm region when the erythema spectra gives more weight to the lower light intensities in the SPF calculation. This fact translates, as it can be observed in Table 4.2, to an increase of the standard deviation in the higher SPF measurements.

	SPF	UVA-PF
M1	5.9 ± 0.7	4.5 ± 0.4
M2	28.6 ± 4.5	11.7 ± 1.1
M3	72.8 ± 10.8	23.0 ± 1.3

Table 4.2. Solar protection factor and UVA-protection factor for three representative samples prepared.

Comparing three samples, **M1** by itself presents a low SPF and UVA-PF compared with **M2**, which includes the two commercial filters. Nevertheless, a clear

boost in these values was observed when adding our compounds together with commercials; here more than the expected additive effect was obtained. Both values, SPF and UVA-PF at least duplicates their values implying some boosting effect when mixing with our compounds.

For the sake of comparison, a mixture of four commercial sunscreens with a total amount of 35% (the same total amount as **M3**) was measured using a formulation with 10% titanium dioxide, 10% octocrylene, 10% octinoxate and 5% avobenzone, giving a SPF of 65.8 and UVA-PF of 14.0. Another example, with 10% titanium dioxide and 10% octocrylene, was measured giving a SPF of 31.2 and UVA-PF of 5.1. With that new formulation and the previous **M2**, the values from the formulation containing 35% of commercial sunscreens were obtained, so with that UV filters no boosting is measured, only the expected additive behavior.

Nowadays, some stabilization experiments are being done. For that matter, one of those compounds is mixed to commercial filters and degradation rate is monitored. This synergic effect is also observed between different commercial UV filters, for example, octocrylene stabilizes avobenzone delaying its photodecomposition. In this case, octocrylene avoids the triplet state population of avobenzone. But as counterpoint, titanium dioxide, if it is not properly coated,^[27] can favor avobenzone degradation. Therefore, this behavior is not trivial to foresee and it cannot be predicted in advance, without the proper experiments. Usually these experiments are conducted in formulation, but an extrapolation to solution could be done.

Regarding a cosmetic utilization, the solubility in the cosmetic formula is crucial to avoid aesthetic drawbacks. For this, some experiments to estimate the solubility in different solvents were performed. The chosen solvents were dichloromethane, methanol and water.

4. Design and synthesis of new MAAs analogues

	CH_2Cl_2 (g/L)	MeOH (g/L)	H_2O (g/L)
9	1.11	24	<0.0003
9-Cl	3	106	1.48
13	0.81	14.5	<0.001
15	2	34	0.001
Avobenzonone	240	6.3	0.0022
Octinoxate	-	-	0.00016
Oxybenzone	1080	22.3	0.069

Table 4.3. Solubility in different solvents.

These solvents were selected to cover a wide range of polarities. In the three compounds studied (**9**, **13** and **15**), solubility follows the same pattern, being these compounds slightly soluble in dichloromethane, moderate in methanol and almost insoluble in water. For the sake of comparison, the three studied commercial sunscreens were determined following the same method. This is described in the experimental section. Data for octinoxate is missed because is hard to quantify its dissolution being liquid, but water solubility corresponds to the tabulated value. These commercial filters are insoluble in water but extremely soluble in less polar solvents, as the ones used in cosmetic formulations.

During the formulation preparation with MAA analogues, some problems when including these compounds in formulation were observed due to the low solubility in the used phase. According to this, some attempts to modify the solubility without changing the MAA core were done using different ion exchange methods. For this, modification of the counterion was performed, treating the compound dissolved in methanol with some cycles of anionic exchange resin in chlorine form in batch. In this case, the chlorine form of Amberlite IRA-402 was employed. After ion exchange, reaction with water-soluble silver salts allows for the exchange of chlorine with trifluoroacetate, acetate or triflate, by precipitation of silver chloride. With that change, tuning the solubility in different solvents can be done; especially relevant is the change in water solubility, in case of compound **9** and **9-Cl** water solubility increases around a thousand times from 1 mg/L to around 1 g/L, but this value is far enough for the minimum desired in industry, 10% in weight.

Trying to improve water solubility, a new series of compounds are being developed and this data will be commented in the next section.

From the collected data on synthesis and characterization, some practical conclusions and knowledge arises. Based on our data, a prediction of the features and the design of new molecules can be achieved. We can predict with good precision the absorbance λ_{\max} of a new compound before synthesizing it. Some examples of this molecular engineering can be seen in Figure 4.28. On the left, the influence on absorption of the chosen core is shown. Here, each compound with *p*-anisidine is compared. From the first obtained derivative with a six-member ring (**9**), the change to the five-member ring (**15**) blue shifts the absorption around 15 nm (depending on the amine can increase to 25 nm). The presence of other alkyl chains does not shift the absorption significantly (**10**) from methyl substituted **9**. The inclusion of a heteroatom exhibits contrary effects, when an oxygenated moiety is added (**18**), absorption redshifts 10 - 15 nm (depending on the amine), but in sulfur derivative (**20**) a slight blueshift (5 nm respect to **9**) is observed.

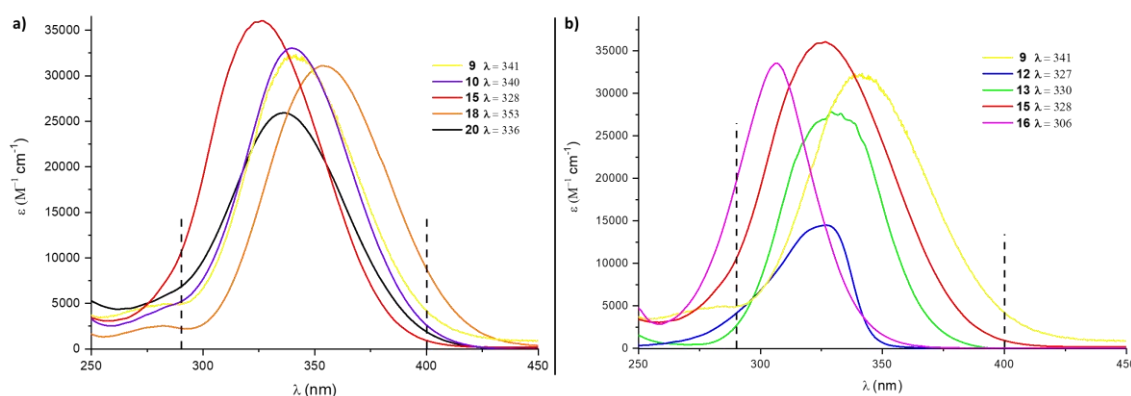


Figure 4.28. Comparative UV-Vis spectra of different core (left) and amines (right).

On the right, the amine residues can tune the absorption too, for sake of comparison the methyl-cyclohexane and methyl-cyclopentane cores were selected. Here, compounds with aliphatic substituents (**11**, **12**) are close to 320 nm. Aromatic substitution influence in five and six-member ring derivatives is shown. The *p*-anisidine derivatives **9** and **15** are the most redshifted respect to the *o*-bromo substituted **13** and **16**, this difference is attributable to the electronic density of the aromatic ring. This fact means in a redshift around 10 - 20 nm in the absorption.

4.3 Applications: further development and implementation attempts

With a new procedure that opens the possible utilization of this type of compounds obtained from a synthetic process and not from natural product extraction, some evident applications surge. The most evident and the main option for us it is their use as part of sunscreen lotions and other personal care products. For this purpose, a strict regulation is applied to allow the use of new compounds. Nevertheless, this need is becoming increasingly important due to the different problems observed in a great number of current UV-filters, which were commented in the Background section. This fact arouses an increasing interest of some companies in the development of new sunscreen molecules, trying to minimize the usage of certain present filters.

Other evident application for a UV-filter is the inclusion in polymeric matrixes as UV radiation blocker, which would improve the sun-exposed parts of the polymer increasing its lifespan. Not only the inclusion on polymers would be possible, but also it could be included in varnishes to protect all type of materials, like wood, ceramics or terrace materials. In general, it could be included in all type of coatings; depending on the material, the incorporation method and the desired properties of the molecules could be different. In this case, the coating material acts as a thin layer that protects the covered surface.

For these different requirements, a broad series of compounds and a versatile procedure have been developed, allowing the tuning of the chemical and photophysical properties.

Concerning the scale of the process, as mentioned in the previous section, the maximum amount obtained in the described synthetic process was less than one gram. Despite the great number of derivatives obtained up to date, the development of new molecules has not stopped.

Simultaneously, aiming to optimize the reaction, some modifications in the reagents ratio and purification process were done. With these modifications, the preparation of these derivatives with better yields and at a larger scale should be performed. Other significant parameter is the cost evaluation, with a view to a potential large-scale application. Looking that, a further reevaluation of the raw materials and the process should be done in more detail.

However, in a first step to improve the atomic economy of the synthesis, the excess of amine was reduced. Also, the reaction time was evaluated. In this case, the study was performed in compound **9**, because of the cheaper raw materials. Looking into the excess of amine different proportions were used. Ranging from 6 to 2 equivalents, the reaction maintains the yield up to 2.5 equivalents of amine. In addition, the reaction time is a critical factor in energy consumption terms and its reduction would permit the synthesis in a more efficient way regarding power and water consumption and minimizing the environmental impact. In this case, the reaction time could be reduced to 24 hours losing only a 5% in the global yield.

Taking all these factors into account, a progressive increase of the starting materials amount was made. This upscaling was done to obtain around 5, 10, 25 and 50 g in different experiments. Up to date, the largest scale used implied the preparation of ca. 50 g of **9**. Reaction occurs without any problem using 2.5 equivalents of amine and with a 93% of overall yield. Larger quantities were not synthesized, but the synthesis to obtain 500 g in one pot should be possible only using a mechanical stirrer in a 2 L flask to ensure an optimal mix during reaction.

With these synthetic improvements an initial cost evaluation was done. The estimated price for these derivatives is shown in Table 4.4.

Compound	Estimated cost (€/Kg)
9	810
13	1240
15	1150
16	1600

Table 4.4. Estimated cost for some compounds.

The initial cost evaluation is considering typical lab suppliers and some of the reagents surely can be obtained from lower cost sources. These are expensive materials because the corresponding cyclodiones are high-priced. To allow comparison, to become a competitive product in the market, the cost should be up to 150 €/Kg. As an example, most of the commercial sunscreens are below this limit.

To continue with the scale-up process, some regional financial support was obtained to develop and increase the synthesis of these derivatives. The aim of this

ADER project (**ADER217-I-IDD-00030**) is to improve the present synthetic procedure optimizing reaction conditions. The final goal is the production of 30 Kg. In addition, the optimization of the prepared cosmetic formulations derived from these compounds will be studied to maximize the solar protection factor.

Other important application in which we will be involved is the design of new molecules to use in combination with silica-based coating materials with agricultural purposes. In this Eurostars project (**E!12508 - NanoProtect**), the coating material acts as a thin layer that covers the plant or the fruit, preventing the attack of some fungi or insect. The novelty of this application is the incorporation of one or a mixture of sunscreen molecules to protect the plant against the harmful effects of UV radiation that can sunburn it, or especially the fruit, decreasing the market value due to defects produced during the maturation process, like fungal infections or high UV exposure.

At present, the latest development comprises the preparation of water-soluble MAA analogues. For this, some water-soluble amines were explored together with different acids replacing the *p*-toluenesulfonic acid. The reaction also works using tetrafluoroboric acid (HBF₄) and hydrochloric acid (HCl). This approach changing the counterion during the synthetic process presents two main problems. The obtained tetrafluoroborate salts are not soluble in water, but can be obtained with good yields, over 80%. The use of hydrochloric acid involves some problems by reason of its volatility. To improve conversion, an excess higher than 10 times should be added. These compounds are now under development and a patent will be filed in due time.

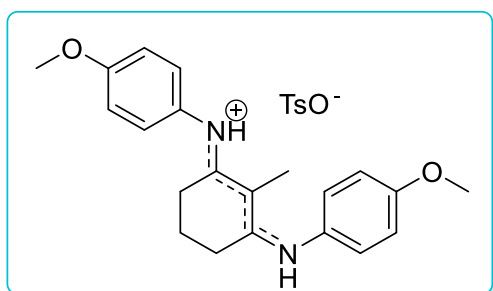
The research in this topic is still underway. Nowadays, collaborative work is especially focus on the prediction of UV absorption spectra and a quick analysis on the shape of the PES of the new possible sunscreen candidates.

4.4. Experimental section

The general synthetic protocol for the preparation of these compounds is the following. To a suspension of the corresponding enaminone (1 mmol) in dry toluene (50 ml), *p*-toluenesulfonic acid monohydrate (1 mmol) was added. The mixture was stirred for five minutes, the selected amine (6 mmol) was added and the mixture refluxed from 24 to 84 hours, depending on the compound. After cooling, the reaction mixture was concentrated under vacuum and purified by crystallization from *n*-hexane suspensions, and sequential washes with CH₂Cl₂ to obtain the final compound with yields ranging from 50 to 95%.

The characterization data for compounds **9-20** are reported below:

- (*E*)-4-methoxy-*N*-(3-((4-methoxyphenyl)amino)-2-methylcyclohex-2-en-1-ylidene)benzenaminium 4-methylbenzenesulfonate (**9**).



Empiric Formula: C₂₈H₃₂N₂O₅S

Molecular weight: 508.63

Yield: 95%

2-Methyl-1,3-cyclohexanedione and *p*-anisidine were used. After refluxing for 48 hours, the compound was obtained as a yellow solid.

¹H-NMR (400 MHz, MeOD) δ ppm 7.69 (d, *J* = 8.0 Hz, 2H), 7.21 (d, *J* = 8.8 Hz, 6H), 7.02 (d, *J* = 8.8 Hz, 4H), 3.83 (s, 6H), 2.52 (t, *J* = 5.8 Hz, 4H), 2.36 (s, 3H), 2.07 (s, 3H), 1.87 – 1.67 (m, 2H).

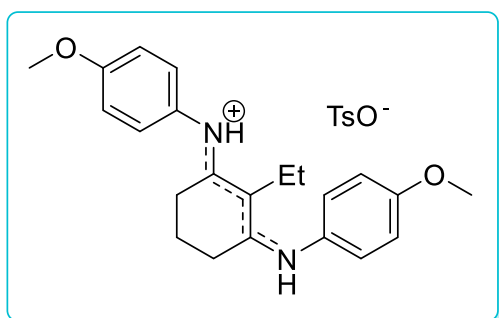
¹³C-NMR (100 MHz, MeOD) δ ppm 172.1, 160.9, 143.7, 141.6, 131.1, 129.8, 128.9, 127.0, 115.7, 100.4, 56.1, 28.7, 21.6, 21.3, 9.5.

UV-Vis (CH₃CN): λ (nm) = 341 (ε = 32410 M⁻¹cm⁻¹).

ES-MS (+) (C₂₁H₂₄N₂O₂ + H): calc. 337.1911, found 337.1917.

MP: 270°C (decomposition)

- (*E*)-*N*-(2-ethyl-3-((4-methoxyphenyl)amino)cyclohex-2-en-1-ylidene)-4-methoxybenzenaminium 4-methylbenzenesulfonate (**10**)



Empiric Formula: C₂₉H₃₄N₂O₅S

Molecular weight: 522.66

Yield: 90%

2-Ethyl-1,3-cyclohexanedione and *p*-anisidine were used. After refluxing for 48 hours, the compound was obtained as a yellow solid.

¹H-NMR (400 MHz, MeOD) δ ppm 7.70 (d, *J* = 8.1 Hz, 2H), 7.24 – 7.18 (m, 6H), 7.03 (d, *J* = 8.8 Hz, 4H), 3.84 (s, 6H), 2.62 (q, *J* = 7.4 Hz, 2H), 2.50 (t, *J* = 6.3 Hz, 4H), 2.36 (s, 3H), 1.81 – 1.71 (m, 2H), 1.18 (t, *J* = 7.5 Hz, 3H).

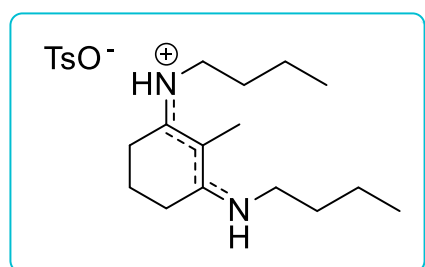
¹³C-NMR (100 MHz, MeOD) δ ppm 171.4, 161.0, 143.6, 141.6, 131.1, 129.8, 129.0, 127.0, 115.7, 106.9, 56.1, 28.7, 21.7, 21.3, 16.8, 12.2.

UV-Vis (CH₃CN): λ (nm) = 340 (ε = 33030 M⁻¹cm⁻¹).

ES-MS (+) (C₂₂H₂₆N₂O₂ + H): calc. 351.2067, found 351.2061.

MP: 245°C (decomposition)

- (*E*)-*N*-(3-(butylamino)-2-methylcyclohex-2-en-1-ylidene)butan-1-aminium 4-methylbenzenesulfonate (**11**)



Empiric Formula: C₂₂H₃₆N₂O₃S

Molecular weight: 408.60

Yield: 60%

2-Methyl-1,3-cyclohexanedione and *n*-butylamine (10 ml) were used as solvent instead of toluene. After refluxing for 48 hours, the reaction mixture was cooled and

concentrated under vacuum. Purification was carried out by crystallization from CH_2Cl_2 by *n*-hexane addition, and sequential washes with *n*-hexane to obtain the final compound as a brown solid. Partial hydrolysis during purification was observed.

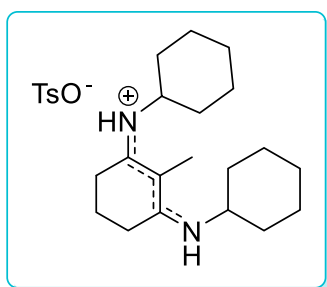
$^1\text{H-NMR}$ (300 MHz, MeOD) δ ppm 7.70 (bs, 2H), 7.24 (bs, 2H), 2.89 (bs, 4H), 2.60 (bs, 4H), 2.37 (bs, 6H), 1.94 – 1.62 (m, 2H), 1.61 (bs, 4H), 1.39 (bs, 4H), 0.96 (bs, 6H).

$^{13}\text{C-NMR}$ (75 MHz, MeOD) δ ppm 170.1, 143.5, 141.7, 129.8, 126.9, 79.4, 40.5, 33.1, 30.6, 26.2, 21.3, 20.6, 13.8, 8.9.

UV-Vis (CH_3CN): λ (nm) = 324 ($\epsilon = 4200 \text{ M}^{-1}\text{cm}^{-1}$).

ES-MS (+) ($\text{C}_{15}\text{H}_{28}\text{N}_2 + \text{H}$): calc. 237.2325, found 237.2327

- (*E*)-*N*-(3-(cyclohexylamino)-2-methylcyclohex-2-en-1-ylidene)cyclohexanaminium 4-methylbenzenesulfonate (**12**)



Empiric Formula: $\text{C}_{26}\text{H}_{40}\text{N}_2\text{O}_3\text{S}$

Molecular weight: 460.68

Yield: 52%

2-Methyl-1,3-cyclohexanedione and cyclohexylamine (10 ml) was used as solvent instead of toluene. After refluxing for 48 hours, the reaction mixture was cooled and concentrated under vacuum. Purification was carried out by crystallization from CH_2Cl_2 by *n*-hexane addition, and sequential washes with *n*-hexane to obtain the final compound as a brown solid. Partial hydrolysis during purification was observed.

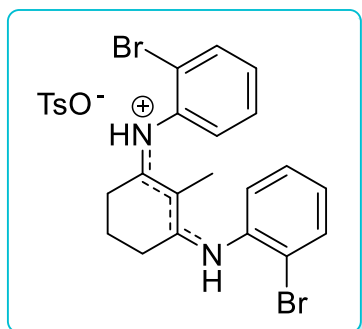
$^1\text{H-NMR}$ (300 MHz, MeOD) δ ppm 7.71 (d, $J = 8.1 \text{ Hz}$, 2H), 7.24 (d, $J = 7.9 \text{ Hz}$, 2H), 4.62 (s, 2H), 2.66 (t, $J = 6.3 \text{ Hz}$, 4H), 2.38 (s, 3H), 2.05 – 1.59 (m, 15H), 1.34 (m, 10H).

$^{13}\text{C-NMR}$ (75 MHz, MeOD) δ ppm 169.3, 143.5, 141.7, 129.8, 126.9, 97.9, 51.5, 34.0, 32.0, 26.3, 26.1, 25.9, 25.3, 21.3, 20.9, 9.1.

UV-Vis (CH_3CN): λ (nm) = 327 ($\epsilon = 14500 \text{ M}^{-1}\text{cm}^{-1}$).

ES-MS (+) ($\text{C}_{19}\text{H}_{32}\text{N}_2 + \text{H}$): calc. 289.2638, found 289.2640.

- (*E*)-2-bromo-*N*-(3-((2-bromophenyl)amino)-2-methylcyclohex-2-en-1-ylidene)benzenaminium 4-methylbenzenesulfonate (**13**)



Empiric Formula: $C_{26}H_{26}Br_2N_2O_3S$

Molecular weight: 606.37

Yield: 95%

2-Methyl-1,3-cyclohexanedione and *o*-bromoaniline were used. After refluxing for 48 hours, the reaction mixture was cooled and concentrated under vacuum. Purification was carried out by crystallization from CH_2Cl_2 by toluene addition, and sequential washes with toluene to obtain the final compound as a pale yellow-white solid.

1H -NMR (300 MHz, MeOD) δ ppm 7.82 (d, $J = 7.9$ Hz, 2H), 7.70 (d, $J = 8.1$ Hz, 2H), 7.57 – 7.37 (m, 8H), 7.23 (d, $J = 7.8$ Hz, 2H), 2.40 (t, $J = 6.6$ Hz, 4H), 2.37 (s, 3H), 2.15 (s, 3H), 1.88 – 1.75 (m, 2H).

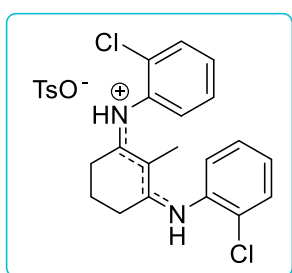
^{13}C -NMR (75 MHz, MeOD) δ ppm 173.5, 143.6, 141.6, 137.6, 134.8, 131.8, 130.8, 130.2, 129.8, 127.0, 123.4, 101.4, 28.5, 21.3, 21.1, 9.6.

UV-Vis (CH_3CN): λ (nm) = 330 ($\epsilon = 27610 M^{-1}cm^{-1}$).

ES-MS (+) ($C_{19}H_{18}Br_2N_2 + H$): calc. 432.9910, found 432.9918

MP: 210°C (decomposition)

- (*E*)-2-chloro-*N*-(3-((2-chlorophenyl)amino)-2-methylcyclohex-2-en-1-ylidene)benzenaminium 4-methylbenzenesulfonate (**14**)



Empiric Formula: $C_{26}H_{26}Cl_2N_2O_3S$

Molecular weight: 516.10

Yield: 80%

2-Methyl-1,3-cyclohexanedione and *o*-chloroaniline were used. After refluxing for 48 hours, the reaction mixture was cooled and concentrated under vacuum. Purification was carried out by crystallization from CH₂Cl₂ by toluene addition, and sequential washes with toluene to obtain the final compound as a white solid.

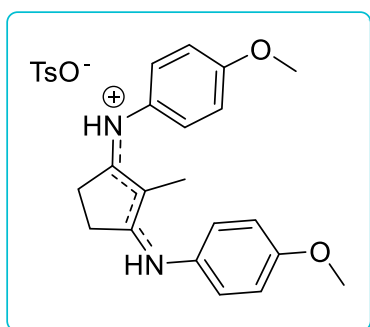
¹H-NMR (300 MHz, MeOD) δ ppm 7.70 (d, *J* = 8.2 Hz, 2H), 7.65 (m, *J* = 5.4, 3.4, 1.2 Hz, 2H), 7.55 – 7.41 (m, 6H), 7.27 – 7.19 (m, 2H), 2.42 (t, *J* = 6.3 Hz, 4H), 2.37 (s, 3H), 2.15 (s, 3H), 1.82 (q, *J* = 6.3 Hz, 2H).

¹³C-NMR (75 MHz, MeOD) δ = 173.5, 143.7, 141.5, 135.9, 133.0, 131.5, 131.4, 130.8, 129.7, 129.5, 126.9, 101.6, 28.3, 21.3, 21.1, 9.7.

UV-Vis (CH₃CN): λ (nm) = 330 (ε = 26400 M⁻¹cm⁻¹).

ES-MS (+) (C₁₉H₁₈Cl₂N₂+ H): calc. 345.0920, found 345.0927

- (*E*)-4-methoxy-*N*-(3-((4-methoxyphenyl)amino)-2-methylcyclopent-2-en-1-ylidene)benzenaminium 4-methylbenzenesulfonate (**15**)



Empiric Formula: C₂₇H₃₀N₂O₅S

Molecular weight: 494.61

Yield: 70%

2-Methyl-1,3-cyclopentanedione and *p*-anisidine were used. After refluxing for 48 hours, the final compound was obtained as a pale yellow solid.

¹H-NMR (400 MHz, MeOD) δ ppm 7.70 (d, *J* = 7.9 Hz, 2H), 7.26 (d, *J* = 8.6 Hz, 4H), 7.22 (d, *J* = 7.8 Hz, 2H), 7.01 (d, *J* = 8.6 Hz, 4H), 3.82 (s, 6H), 2.79 (s, 4H), 2.36 (s, 3H), 1.97 (s, 3H).

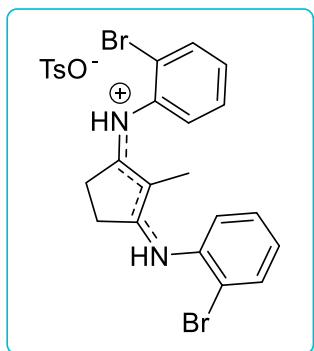
¹³C-NMR (100 MHz, MeOD) δ ppm 180.5, 160.5, 143.7, 141.6, 131.9, 129.8, 127.5, 126.9, 115.7, 106.9, 56.0, 29.1, 21.3, 7.3.

UV-Vis (CH₃CN): λ (nm) = 328 (ε = 34560 M⁻¹cm⁻¹).

ES-EM (+) (C₂₀H₂₂N₂O₂ + H): calc. 323.1754, found 323.1760.

MP: 217°C (decomposition)

- (*E*)-2-bromo-*N*-(3-((2-bromophenyl)amino)-2-methylcyclopent-2-en-1-ylidene)benzenaminium 4-methylbenzenesulfonate (**16**)



Empiric Formula: $C_{25}H_{24}Br_2N_2O_3S$

Molecular weight: 592.35

Yield: 70%

2-Methyl-1,3-cyclopentanedione and *o*-bromoaniline After refluxing for 48 hours, the final compound was obtained as a white solid.

¹H-NMR (300 MHz, MeOD) δ ppm 7.8 – 7.7 (m, 2H), 7.7 – 7.7 (m, 2H), 7.5 (s, 4H), 7.4 – 7.3 (m, 2H), 7.2 (d, $J = 7.8$ Hz, 2H), 2.6 (bs, 4H), 2.4 (s, 3H), 2.1 (bs, 3H).

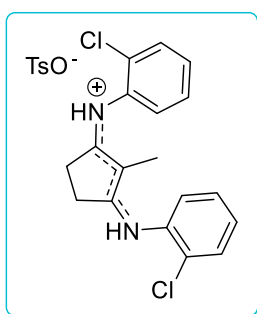
¹³C-NMR (75 MHz, MeOD) δ ppm 182.4, 143.4, 141.7, 137.7, 135.1, 134.7, 131.9, 131.7, 131.4, 130.4, 130.2, 129.8, 126.9, 125.7, 122.6, 117.9, 107.4, 29.1, 21.3, 7.3.

UV-Vis (CH₃CN): λ (nm) = 306 ($\epsilon = 33600$ M⁻¹cm⁻¹).

ES-EM (+) (C₁₈H₁₆Br₂N₂ + H): calc. 418.9753, found 418.9758.

MP: 205°C (decomposition).

- (*E*)-2-chloro-*N*-(3-((2-chlorophenyl)amino)-2-methylcyclopent-2-en-1-ylidene)benzenaminium 4-methylbenzenesulfonate (**17**)



Empiric Formula: $C_{25}H_{24}Cl_2N_2O_3S$

Molecular weight: 502.09

Yield: 75%

2-Methyl-1,3-cyclopentanedione and *o*-chloroaniline. After refluxing for 48 hours, the final compound was obtained as a white solid.

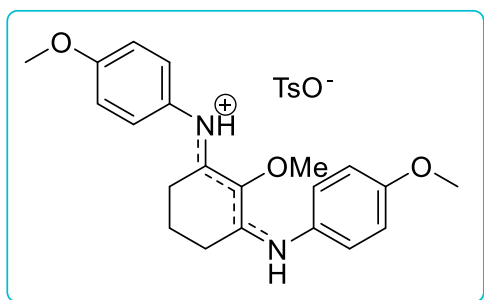
¹H-NMR (300 MHz, MeOD) δ 7.68 (d, J = 8.2 Hz, 2H), 7.64 – 7.57 (m, 2H), 7.55 – 7.39 (m, 6H), 7.24 – 7.17 (m, 2H), 2.80 – 2.51 (m, 4H), 2.35 (s, 3H), 2.09 (s, 3H).

¹³C-NMR (75 MHz, MeOD) δ = 142.3, 140.2, 134.8, 131.1, 130.2, 130.1, 128.8, 128.4, 128.2, 125.6, 27.7, 20.0, 5.8.

UV-Vis (CH₃CN): λ (nm) = 306 (ϵ = 32400 M⁻¹cm⁻¹).

ES-EM (+) (C₁₈H₁₆Cl₂N₂ + H): calc. 331.0763, found 331.0776.

- (*E*)-4-methoxy-*N*-(2-methoxy-3-((4-methoxyphenyl)amino)cyclohex-2-en-1-ylidene)benzenaminium 4-methylbenzenesulfonate (**18**)



Empiric Formula: C₂₈H₃₂N₂O₆S

Molecular weight: 524.46

Yield: 80%

2-Methoxy-3-morpholinocyclohex-2-en-1-one and *p*-anisidine were used. After refluxing for 48 hours, the reaction mixture was cooled and concentrated under vacuum. Purification was carried out by column chromatography (silica gel, gradient from CH₂Cl₂ to CH₂Cl₂/MeOH 1:1) to obtain the final compound as a yellow solid.

¹H-NMR (400 MHz, MeOD) δ ppm 7.70 (d, J = 8.0 Hz, 2H), 7.28 – 7.15 (m, 6H), 7.03 (d, J = 8.6 Hz, 4H), 3.83 (s, 6H), 3.78 (s, 3H), 2.62 (t, J = 5.8 Hz, 4H), 2.36 (s, 3H), 1.89 – 1.73 (m, 2H).

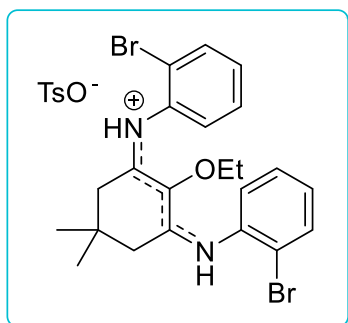
¹³C-NMR (100 MHz, MeOD) δ ppm 164.8, 160.8, 143.7, 141.6, 130.4, 129.8, 129.2, 128.4, 127.0, 115.7, 60.2, 56.1, 27.4, 21.5, 21.3.

UV-Vis (CH₃CN): λ (nm) = 353 (ϵ = 31120 M⁻¹cm⁻¹).

ES-MS (+) (C₂₁H₂₄N₂O₃ + H): calc. 353.1860, found 353.1858.

MP: 210°C (decomposition)

- (*E*)-2-bromo-*N*-(3-((2-bromophenyl)amino)-2-ethoxy-5,5-dimethylcyclohex-2-en-1-ylidene)benzenaminium 4-methylbenzenesulfonate (**19**)



Empiric Formula: C₂₉H₃₂Br₂N₂O₄S

Molecular weight: 664.45

Yield: 80%

2-Ethoxy-5,5-dimethyl-3-morpholinocyclohex-2-en-1-one and *o*-bromoaniline were used. After refluxing for 48 hours, the reaction mixture was cooled and concentrated under vacuum. Purification was carried out by crystallization from CH₂Cl₂ by *n*-hexane addition, and sequential washes with AcOEt to obtain the final compound as a yellow solid.

¹H-NMR (400 MHz, MeOD) δ ppm 7.82 (d, *J* = 7.8 Hz, 2H), 7.70 (d, *J* = 8.0 Hz, 2H), 7.57 – 7.48 (m, *J* = 7.4 Hz, 2H), 7.44 (d, *J* = 7.8 Hz, 2H), 7.42 – 7.38 (m, *J* = 7.3 Hz, 2H), 7.23 (d, *J* = 7.9 Hz, 2H), 4.17 (bs, 2H), 2.37 (s, 3H), 2.35 (bs, 4H), 1.57 (bs, 3H), 1.04 (s, 6H).

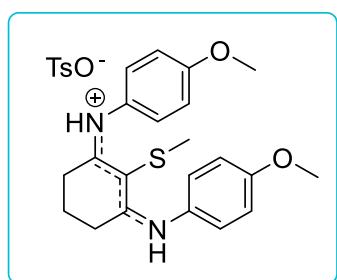
¹³C-NMR (100 MHz, MeOD) δ ppm 165.2, 143.6, 141.6, 136.8, 134.8, 131.9, 130.6, 130.2, 129.8, 127.2, 127.0, 123.2, 69.7, 40.6, 33.0, 28.0, 21.3, 15.3.

UV-Vis (CH₃CN): λ (nm) = 340 (ε = 35880 M⁻¹cm⁻¹).

ES-EM (+) (C₂₂H₂₄Br₂N₂O + H): calc. 491.0328, found 491.0328.

MP: 205°C (decomposition)

- (*E*)-4-methoxy-*N*-(3-((4-methoxyphenyl)amino)-2-(methylthio)cyclohex-2-en-1-ylidene)benzenaminium 4-methylbenzenesulfonate (**20**)



Empiric Formula: C₂₈H₃₂N₂O₅S₂

Molecular weight: 540.69

Yield: 70%

After 84 hours at reflux, reaction mixture was cooled and concentrated under vacuum. Purification was carried out by column chromatography (silica gel, gradient from CH₂Cl₂ to CH₂Cl₂/MeOH 1:1) to obtain the final compound as a yellow solid.

¹H-NMR (400 MHz, MeOD) δ ppm 7.70 (d, *J* = 8.1 Hz, 2H), 7.25 (d, *J* = 8.9 Hz, 4H), 7.22 (d, *J* = 8.0 Hz, 2H), 7.04 (d, *J* = 8.9 Hz, 4H), 3.84 (s, 6H), 2.64 (t, *J* = 6.2 Hz, 4H), 2.36 (s, 3H), 2.27 (s, 3H), 1.89 – 1.75 (m, 2H).

¹³C-NMR (100 MHz, MeOD) δ ppm 174.6, 161.1, 143.7, 141.6, 130.6, 129.8, 128.8, 127.0, 115.8, 98.3, 56.1, 29.1, 21.3, 21.1, 17.2.

UV-Vis (CH₃CN): λ (nm) = 336 (ε = 29240 M⁻¹cm⁻¹).

ES-MS (+) (C₂₁H₂₄N₂O₂S+ H): calc. 369.1631, found 369.1634

- Irradiation conditions

The irradiation of all samples was carried out in 0.1 M solutions in deuterated methanol in NMR tubes using a Pyrex filtered 400 W medium-pressure Hg lamp. The evolution was followed by ¹H-NMR. For all the irradiated compounds, no decomposition was observed after 16 h. This implies at least 5700 KJ/m², much higher than normal conditions for solar exposure. To quantify decomposition in commercial photoprotectors, 1,3,5-trimethoxybenzene was used as internal standard.

In addition, samples for all compounds were irradiated under direct solar light in the rooftop during all summer (June to September). Again, no decomposition was observed. The same behavior was found also for direct irradiation using a solar simulator, applying an erythemal UV dose of 294 DEMs.

- Solubility measurements

In these experiments, a known amount of compound was placed in a vial tube and increasing known volumes of the corresponding solvent are added. After each addition, at least 5 minutes of stirring were waited. Depending on the final application, water-soluble UV filters (for water paints, for instance) or hydrophobic compounds (for water-proof sunscreens) could be required. As can be seen, small structural

modifications are useful to tune the solubility of these compounds in some typical solvents, ranging from water to organic solvents.

- **Solar and UVA protection factor measurements**

All measurements of solar protection factor were made according to the international standard ISO-24443, using the standardized 5x5 cm² PMMA plates with 1.3 mg/cm². An Oriel 300 W solar simulator (Newport, Nebraska, USA) was used for sample irradiation. Spectral distribution of the light source and transmitted by control and samples probes in PMMA plates was measured by means of a double monochromator connected to an Ulbricht sphere (MACAM SR9910-v7, Irradian, Scotland, UK).

- **X-ray Data**

The data for the described structure has been deposited at the Cambridge Crystallographic Data Centre and assigned the deposition number CCDC 1495421. In an attempt to complete the structural characterization, the solid-state structure of **9** was determined by X-ray diffraction techniques. Presenting a symmetric disposition of the MAA core in a monoclinic punctual group.

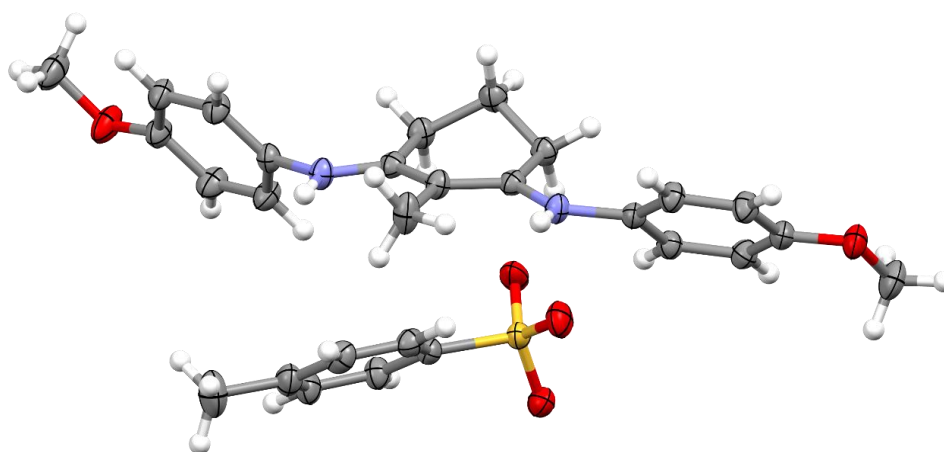


Figure 4.29. X-ray thermal ellipsoid plot of compound **9** (ellipsoid contour percent probability of 50%).

4.4.1. Computational details

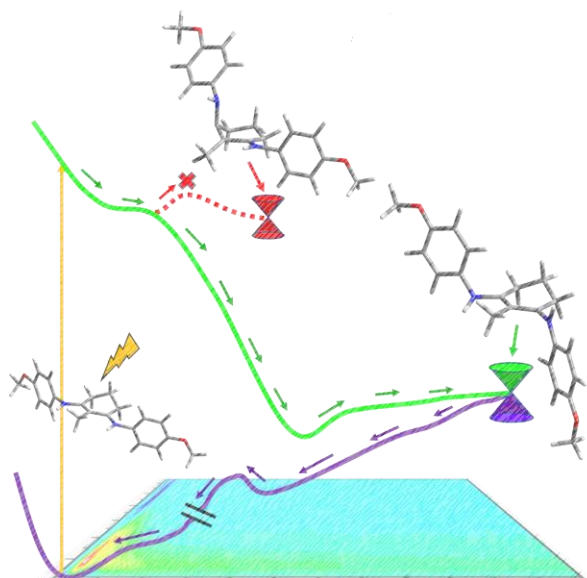
The geometries of the critical points were computed using fully unconstrained *ab initio* quantum chemical computations in the framework of a CASPT2//CASSCF strategy.^[28] The energy of the CASSCF geometries was recalculated using the CASPT2 method implemented in MOLCAS-6.4^[11] to take into account the effect of electron dynamic correlation. All CASPT2 results have been obtained with state average with equal weights for each state. Both CASSCF and CASPT2 calculations have been performed using the standard 6-31G* basis set. The indicated active spaces were checked comparing with available experimental data or between different active spaces. In all cases, the chromophore considered were explained below. Minimum energy paths (MEPs) were computed at the CASSCF level using the methodology present in MOLCAS-6.4. MEPs representing the steepest descendent minimum energy reaction path were built through a series of geometry optimizations, each requiring the minimization of the potential energy on a hyperspherical cross section of the potential energy surface centered on a given reference geometry and characterized by a predefined radius. The paths were computed using a value of 0.1 a.m.u. for the steps. Bulk solvent effects on the UV-spectra have been included using the polarizable continuum model (PCM)^[29] as implemented in MOLCAS-6.4. The molecule is considered as included in a cavity surrounded by an infinite medium with the dielectric constant corresponding to the specific solvent. The standard value of 78.39 for water was used in these calculations. The UV-spectra were computed under non-equilibrium conditions, that is, only solvent electronic polarization is in equilibrium with excited-state electron density. Thus, only fast solvent degrees of freedom are considered. This kind of calculations is more adequate to compute vertical excitation energies, as those needed for the UV-spectra. Conical intersections were optimized using Gaussian 03.^[12]

A series of on-the-fly nonadiabatic molecular dynamics (NAMD) at the CASSCF(6,5)/6-31G* level for **8** and CASSCF(8,6)/6-31G* for **6** have been performed using the dynamix module in MOLCAS 8.0.^[11] In both cases, initial conditions were obtained by performing a Boltzmann distribution at 298 K with Gaussian 03.^[12] The dynamics were performed using a Nose–Hoover chain of thermostats with $T = 298$ K.^{[13,}

4.5. Bibliography

- [1] D. Sampedro, *Phys. Chem. Chem. Phys.* **2011**, *13*, 5584-5586.
- [2] R. Losantos, M. S. Churio, D. Sampedro, *ChemistryOpen* **2015**, *4*, 155-160.
- [3] R. Losantos, D. Sampedro, M. S. Churio, *Pure Appl. Chem.* **2015**, *87*, 979-996.
- [4] K. H. Nguyen, M. Chellet-Krugler, N. Gouault, S. Tomasi, *Nat. Prod. Rep.* **2013**, *30*, 1490-1508.
- [5] D. Sampedro, in *Photochemistry: UV/VIS Spectroscopy, Photochemical Reactions and Photosynthesis* (Eds.: K. J. Maes, J. M. Willems), Nova Science Publishers **2011**.
- [6] I. F. Galván, M. G. Delcey, T. B. Pedersen, F. Aquilante, R. Lindh, *J. Chem. Theory Comput.* **2016**, *12*, 3636-3653.
- [7] L. M. Frutos, A. Markmann, A. L. Sobolewski, W. Domcke, *J. Phys. Chem. B* **2007**, *111*, 6110-6112.
- [8] E. M. M. Tan, M. Hilbers, W. J. Buma, *J. Phys. Chem. Lett.* **2014**, *5*, 2464-2468.
- [9] L. A. Baker, S. E. Greenough, V. G. Stavros, *J. Phys. Chem. Lett.* **2016**, *7*, 4655-4665.
- [10] N. D. N. Rodrigues, V. G. Stavros, *Sci. Prog.* **2018**, *101*, 8-31.
- [11] F. Aquilante, J. Autschbach, R. K. Carlson, L. F. Chibotaru, M. G. Delcey, L. D. Vico, I. F. Galván, N. Ferré, L. M. Frutos, et al., *J. Comput. Chem.* **2016**, *37*, 506-541.
- [12] Gaussian 03, Revision C.02, M. J. Frisch, G. W. Trucks, H. B. Schlegel, G. E. Scuseria, M. A. Robb, J. R. Cheeseman, et al. Gaussian, Inc., Wallingford CT, **2004**.
- [13] S. Nosé, *Mol. Phys.* **1984**, *52*, 255.
- [14] W. G. Hoover, *Phys. Rev. A* **1985**, *31*, 695.
- [15] F. R. Conde, M. S. Churio, C. M. Previtali, *J. Photochem. Photobiol. B* **2000**, *56*, 139-144.
- [16] A. Valentini, <https://github.com/acuzzio/BondAngleDihedral>.
- [17] J. M. Woolley, M. Staniforth, M. D. Horbury, G. W. Richings, M. Wills, V. G. Stavros, *J. Phys. Chem. Lett.* **2018**, *9*, 3043-3048.
- [18] J. M. Kim, J. E. Na, C. G. Lee, J. N. Kim, *Bull. Korean Chem. Soc.* **2004**, *25*, 163-164.
- [19] D. B. Ramachary, M. Kishor, *J. Org. Chem.* **2007**, *72*, 5056-5068.
- [20] K. Ma, C. Zhang, M. Liu, Y. Chu, L. Zhou, C. Hu, D. Ye, *Tetrahedron Lett.* **2010**, *51*, 1870-1872.
- [21] L. V. Reis, A. M. Lobo, S. Prabhakar, M.P.Duarte, *Eur. J. Org. Chem.* **2003**, 190-208.
- [22] S.-J. Ji, J. Lu, J.-P. Lang, C. A. Horiuchi, *Synth. Comm.* **2002**, *32*, 1659-1663.
- [23] M. Adler, K. S. V. Schmidt, M. Adler, V. Schmidt, *Chem. Ber.* **1979**, *112*, 2314-2323.
- [24] M. Adler, K. Schank, *Chem. Ber.* **1979**, *112*, 2324-2331.
- [25] H. F. González, Estudio del comportamiento fotoquímico y electroquímico de yodoalquenos, Doctoral dissertation, Universidad de La Rioja, **2013**.
- [26] International Standard ISO-24443. Determination of sunscreen UVA photoprotection in vitro, **2012**.
- [27] G. Wakefield, S. Lipscomb, E. Holland, J. Knowland, *Photochem. Photobiol. Sci.* **2004**, *3*, 648-648.
- [28] M. Olivucci, *Computational Photochemistry*, Elsevier, Amsterdam, **2005**.
- [29] J. Tomasi, B. Mennucci, R. Cammi, *Chem. Rev.* **2005**, *105*, 2999-3094.

5. Spectroscopic characterization of synthetic MAA analogues



As presented in the previous chapter, we were involved in a synthetic effort to obtain a series of mycosporine-based derivatives with tunable and, in some cases, improved capabilities regarding the natural MAAs. A large family of compounds with some relevant structural differences respect to the cyclohexenimine MAAs was developed. As the main difference with marine derivatives, the synthetic analogues present, in most of cases, aryl substituents as residues in the amino moieties. This modification could imply a significant change, which was not taken into account during the computational screening of the core structures previously described in Chapter 4 of this memory. In those cases, the change of an alkyl moiety to an aryl fragment could modify the electronic nature of the chromophore altering the shape of the PES altering the photochemical properties with respect to the ideal behavior.

In this chapter, a spectroscopic study on the excited state dynamics of the previously reported compounds **9**, **13**, **16** and **18** will be described. The four selected compounds were explored using time-resolved fluorescence and transient absorption spectroscopy techniques to determine the lifetime of the molecule in the excited state and the fate of the molecule during the relaxation process. Those experiments were conducted in collaboration with Dr. Asier Longarte in the University of País Vasco, in Leioa, Bilbao.

This experimental study was also combined with a complementary theoretical study to understand the effect of the inclusion of aryl residues in the system.

5.1. Spectroscopic study of MAA synthetic analogues

The aim of this chapter is to study the behavior in the excited state of the previously prepared compounds based on the structure of mycosporines like-aminoacids. For that, a series of spectroscopic techniques was used to understand the relaxation processes after light absorption on different representative compounds. To characterize the excited state population, two techniques were used, time-resolved fluorescence upconversion^[1, 2] and transient absorption spectroscopy,^[3, 4] which are described in detail below.

5.1.1. Spectroscopic techniques

The starting point in this chapter should be the introduction of the spectroscopic techniques used for the study of the sunscreen samples together with their theoretical background and experimental setup. In addition, the type of information that could be obtained from the different techniques will be presented.

As a common point, both techniques use a similar setup as described for each one, changing the property that is measured after the light pulse. In transient absorption spectroscopy, the variation of the optical density is detected. As counterpoint, in fluorescence upconversion the intensity of the fluorescent emission is observed. The two processes will be explained in more detail below. Both systems use as light source the high energy pulse from a laser to promote the population of the excited state. Light comes from an optical parametric amplifier (OPA), which allows to obtain a tunable radiation of different wavelengths covering the full range of the spectra between 190 to 2000 nm. The key feature in this light source is the temporal resolution, which allows the study of ultrafast processes due to the laser pulses with femtoseconds resolution. The full set of technical details about the setup used are summarize in the experimental section.

5.1.1.1. *Transient absorption spectroscopy*

Transient absorption spectroscopy (TAS), also called pump/probe spectroscopy, has been widely used in the investigation of ultrafast phenomena in different fields such as physics, chemistry, etc. The principle of this technique is that a pulse is used to excite the molecule under study, so-called pump, what triggers the photochemical process. At a variable delay time, another pulse of lower energy, so-called probe, is sent through the sample giving information on how the sample has been altered by the pump excitation (Figure 5.1).^[4] Accordingly, the probe records a snapshot of the molecule at each time delay, obtaining by combination of all these snapshots its time resolved spectrum.

This spectroscopic method^[5] allows an easy way to monitor the evolution of the excited state population by measuring the time-dependent change of the optical

density (OD) induced by the pump. By definition, the OD is calculated as the logarithmic ratio of the intensity of incident radiation to the intensity of transmitted radiation. This concept is very similar to the absorbance of the sample, but not exactly the same. Absorbance only concerns about the absorbed radiation by the sample accordingly to the Lambert-Beer law. As counterpoint, optical density cares about absorbed, reflected and scattered light in the sample.

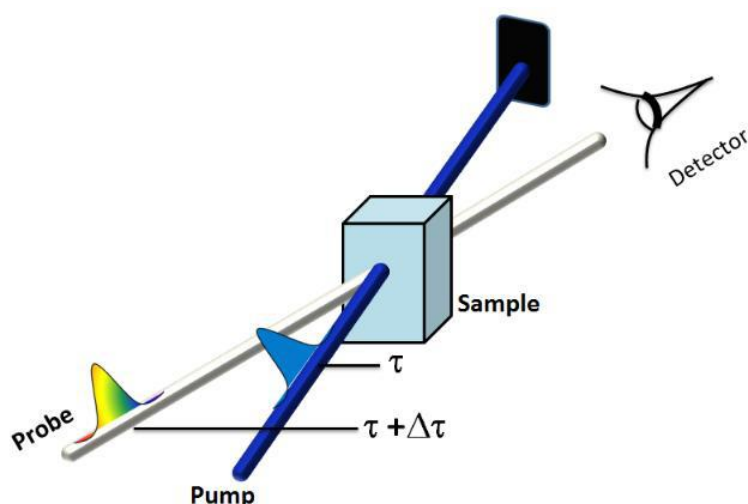


Figure 5.1. Schematic representation of the pump-probe spectroscopy setup.^[6]

The time-dependent change of the optical density (ΔOD) induced by the pump pulse can be described as the difference between optical densities with ($OD_w(\tau)$) and without ($OD_{w/o}(\tau)$) excitation, been I_0 the incident light intensity and $I(\tau)$ the light intensity transmitted through the sample.

$$\Delta OD(\tau) = OD_w(\tau) - OD_{w/o}(\tau) = \left(\log \frac{I_0}{I(\tau)} \right)_w - \left(\log \frac{I_0}{I(\tau)} \right)_{w/o}$$

Both sign optical density changes can be observed, corresponding to different photochemical processes, due to the intensity of the transmitted probe light can decrease or increase. The most common observed processes are represented schematically in Figure 5.2 and are the following:

- Ground State Bleaching (GSB): a negative response is detected because after excitation, molecules are promoted to the excited state, decreasing the population in the ground state, so reducing the OD.

- Excited State Absorption (ESA): a positive change of the optical density is observed when molecules are excited from an excited state (e.g. S_1) to upper in energy excited states (S_n).
- Stimulated Emission (SE): corresponding to a negative optical density change due to the radiation decay from the excited state to the ground state, that process corresponds with luminescence processes, generally fluorescence.
- Photoproduct Absorption (PA): being a positive response due to the absorption of photoproduct molecules formed during the photoreaction, in our case that contribution should not be relevant since no photoproduct is expected according to the previous photostability data for these compounds.

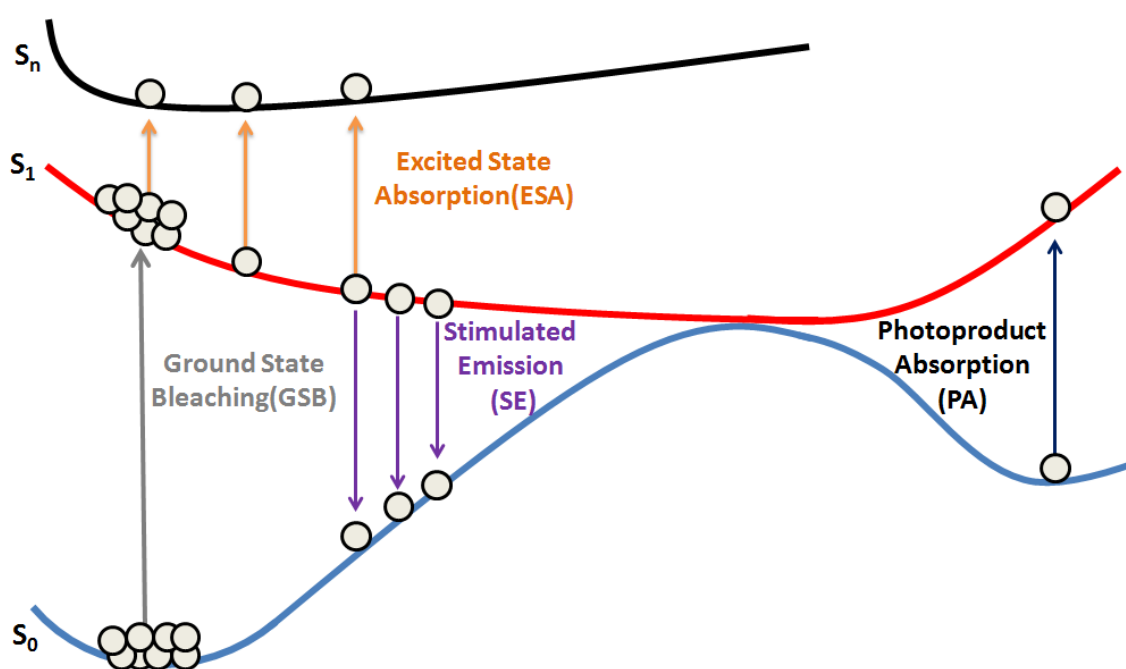


Figure 5.2. Photochemical processes responsible for the optical density changes in transient absorption (TA) spectra.^[6]

Experimentally, the recorded signals are a convolution of some of these contributions in most of the cases. It should be noted that the evolution of these processes with the delay time is related to the excited state lifetime under study. In an ideal scenario, where no photoproduct is formed, the main components in the difference absorption spectra (DAS) are the ESA, GSB and SE components, which should be a spectrum composed by the addition of the individual components, as shown in Figure 5.3.

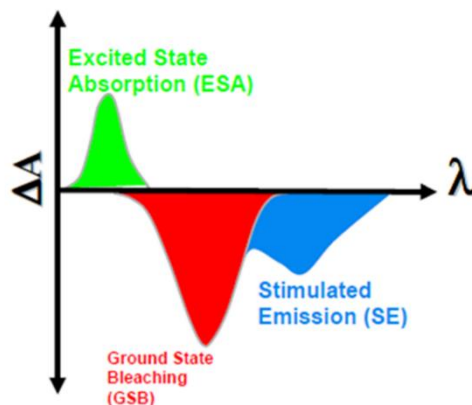


Figure 5.3. Ideal DAS spectrum, with the ESA, GSB and SE bands deconvoluted.^[7]

In a real scenario, however, the molecules' behavior is more complex than the ideal ESA, GSB and SE components: they jiggle around, interact with their environment (for example, the solvent). All these types of processes may occur after the excitation and they all influence the difference absorption spectrum. Typically, internal conversion (IC) yields in a redshift of the SE band when longer times are reached due to the decreasing energy gap between the PESs along the relaxation pathway. This example is meaningful in the studied compounds and this is why it is remarked explicitly.

Looking into the experimental setup, an OPA (Coherent Operasolo) was used to generate pulses in the femtosecond regime as an essential requirement for the study of ultrafast processes. Afterwards, the light beam is divided into two rays with a beam splitter in order to generate the pump and the probe pulses. Depending on the absorption spectrum of the sample and the spectral range to probe, the beam wavelength must be tuned in order to excite the molecule at the selected pump wavelength and to probe in the desired spectral range. For this purpose, non-linear wavelength-conversion processes are needed. These processes only occur when light is intense enough in comparison with the intensity of the electric field and takes place in the OPA system. This system provides the desired pump wavelength together with an 800 nm pulse. This pulse was used to generate the probe beam. Before this, a time delay was introduced in the probe allowing its use as a bookmark to monitor the changes in the OD of the sample. The 800 nm pulse passed through a CaF_2 crystal generates probe pulses of a continuum white light to better study the response after sample excitation. In our case, a probe beam with light from 340 to 750 nm was

obtained. The most usual crystals for this purpose are sapphire (Al_2O_3) and the used calcium fluoride (CaF_2). This phenomenon is a third-order non-linear optical process.

Once obtained the pump and the probe beam, with their corresponding time distribution, both beams were focused on the sample holder and the output of the probe beam was collected into an optical fiber connected to the detector. A schematic representation of the experimental setup used for these measurements can be seen in Figure 5.4.

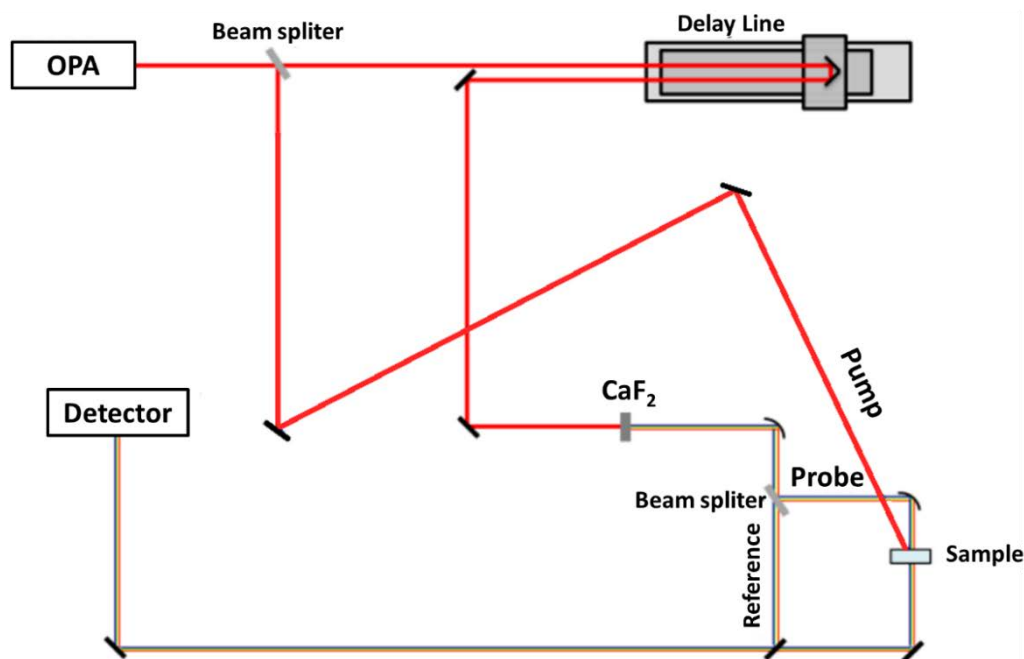


Figure 5.4. Schematic setup used in transient absorption spectroscopy measurements. Adapted from.^[6]

5.1.1.2. Time-resolved fluorescence upconversion

The other spectroscopic technique used is the time-resolved fluorescence upconversion; in this technique, the intensity of the fluorescent emission was measured in function of the time delay from excitation to obtain the time dependency of the fluorescent radiative process. In these experiments, the same light source, previously described in the TAS setup, was used as excitation source. Also, the 800 nm beam is used as probe but, in this case, without passing through the CaF_2 crystal. Instead of that, the light from the fluorescent emission (ω_f) was mixed with the probe (ω_p) by passing through a BBO (β -Barium borate) crystal, which mixes both beams by a

quadratic non-linear optics process, giving the upconversion signal (ω_s). The schematic representation of the setup is shown in Figure 5.5.

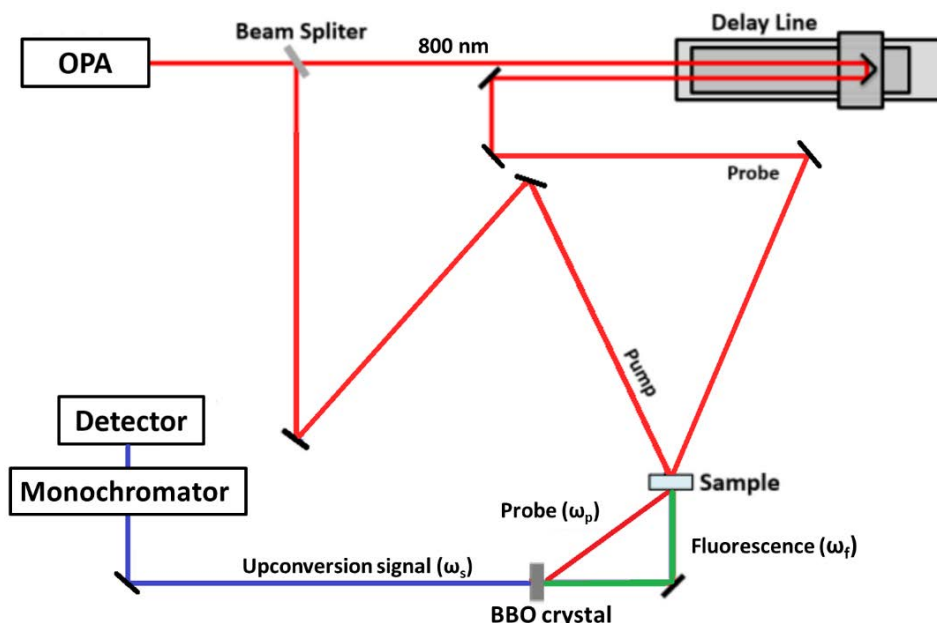


Figure 5.5. Schematic setup of Fluorescence upconversion experiments. Adapted from.^[6]

Also, a better explanation about how the probe signal and the fluorescent emission mixes to give the upconversion signal is necessary since that is the key step to provide the desired time resolution. For that, as can be seen in Figure 5.6,^[2] the variable delay introduced at different fluorescence times allows the temporal monitorization of the signal only recording fluorescence at a single time and spectral point. At these points, the resulting intensity (I_{ω_s}) is proportional to the product of both incident radiations in the BBO crystal, according to the following equation $I_{\omega_s} \sim I_{\omega_f} * I_{\omega_p}$. If the intensity of the probe pulse is maintained constant during all experiment, the resulting upconversion signal is proportional to the fluorescence signal intensity only when the fluorescent emission and the probe pulse are temporally overlapped.

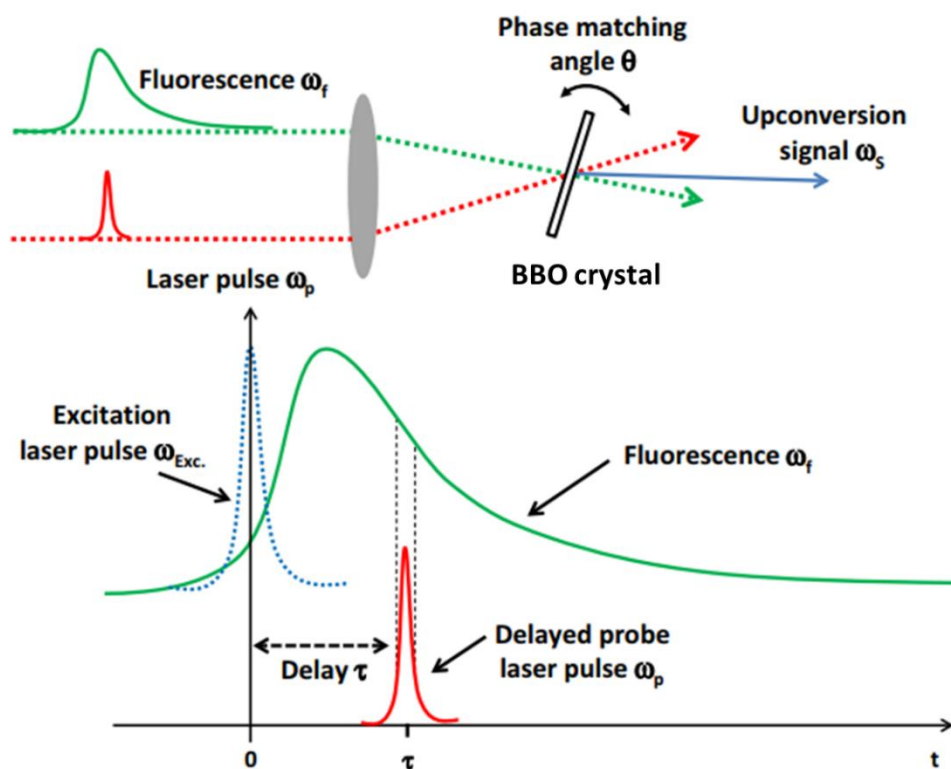


Figure 5.6. Time delayed probe and fluoresce mix in the collected signal.^[2]

Therefore, fluorescence upconversion is the method of choice when the investigated processes are extremely fast (faster than one ps). Other methods cannot compete for time resolution. However, there are also disadvantages. Frequency upconversion (sum frequency generation) is a nonlinear process, needing the use of intense excitation pulses, often damaging biological samples. Due to the uncertainties of non-linear optics conditions, different upconversion efficiencies at diverse wavelengths should be expected. As mentioned before, it is a single time and wavelength determination method, for that, to get spectro-temporal data, scanning of different wavelengths is needed, which takes long experiment times.

This technique allows the monitoring of the excited state population, but no information about the possible mechanism behind the depopulation can be obtain with this technique as a difference with respect to TAS. The time-resolved fluorescence measurements on this chapter were collected accumulating 5 to 10 delay scans containing 1500 laser shots at each delay position, obtaining temporal resolutions around 90 fs, reached at the studied excitation and emission wavelengths. Mathematical fitting was also used to adjust the fluorescence decay.

5.1.2. Time-resolved fluorescence upconversion and pump-probe experiments

Using the described spectroscopic techniques, the excited state of four representative examples of the previously synthesized MAA analogues was studied. The four selected derivatives were chosen to explore the influence of the size in the cyclic moiety, five-member ring **16** and six-member ring **13**, the substituents in phenyl rings, *o*-bromine in **13** and *p*-methoxy in **9**, and the substitution in position 2 of the cyclic core, changing from methyl in **9** to methoxy in **18**. Not only the chemical composition was taken into account, but also the associated transition energy could be relevant due to the different amount of energy to be dissipated in each case. These compounds are shown in order of the maximum absorption band observed in methanol solutions. They are sorted decreasingly the absorption energy, from shorter wavelengths in **16** to the longest in compound **18**.

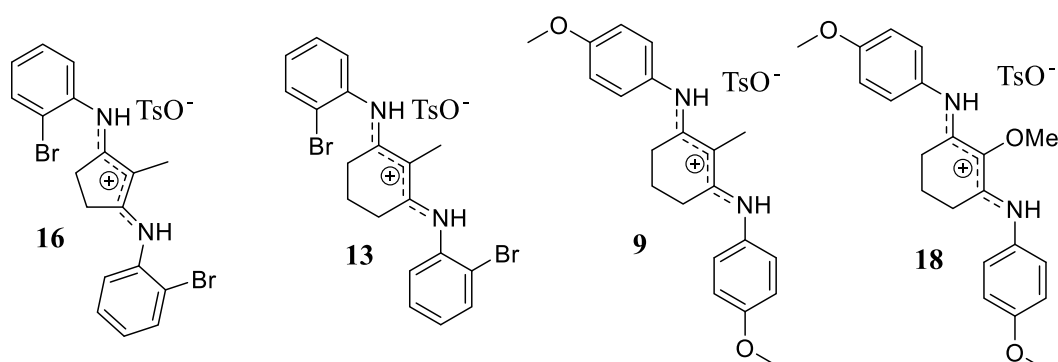


Figure 5.7. Molecules studied by pump-probe techniques.

As a brief reminder, the UV-Vis absorption spectra of the chosen compounds were measured in methanol, ranging in their maxima from 306 nm in **16** to 353 nm in **18**. These spectra can be seen in Figure 5.8. This broad distribution of the maxima, together with the amplitude of the absorption band, allows a large attenuation of the UV radiation emitted by the sun, absorbing by combination of two or three compounds a great amount of the total UV radiation between 260 to 400 nm.

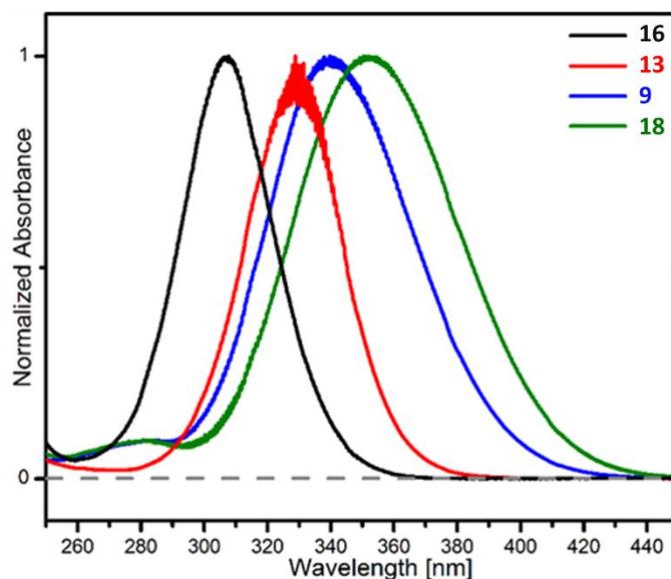


Figure 5.8. UV-Vis spectra of the studied compounds in methanol.

The corresponding λ_{\max} was used as excitation wavelength in the fluorescence upconversion measurements and depicted in blue for each measure in Figure 5.9.

At first stage, the fluorescent upconversion experiments were done. For these experiments, a $7\text{-}8 \times 10^{-4}$ M solution of the selected compound was used. As explained in the technical description, this technique only allows the observation of the remaining excited state population (S_1 in these cases) by measuring the decay of the fluorescence from this state to ground state, obtaining the fluorescence-associated lifetime of the excited state for each sample. Fluorescence upconversion decays of the four studied compounds in methanol solutions were collected, after excitation at 306 (**16**), 330 (**13**), 341 (**9**) and 353 nm (**18**), at different detection energies along the emission spectra, without finding any substantial differences in the transients. The measured decays, as shown in Figure 5.9, are fitted by single exponentials obtaining a τ_f that varies between 150 and 650 fs.

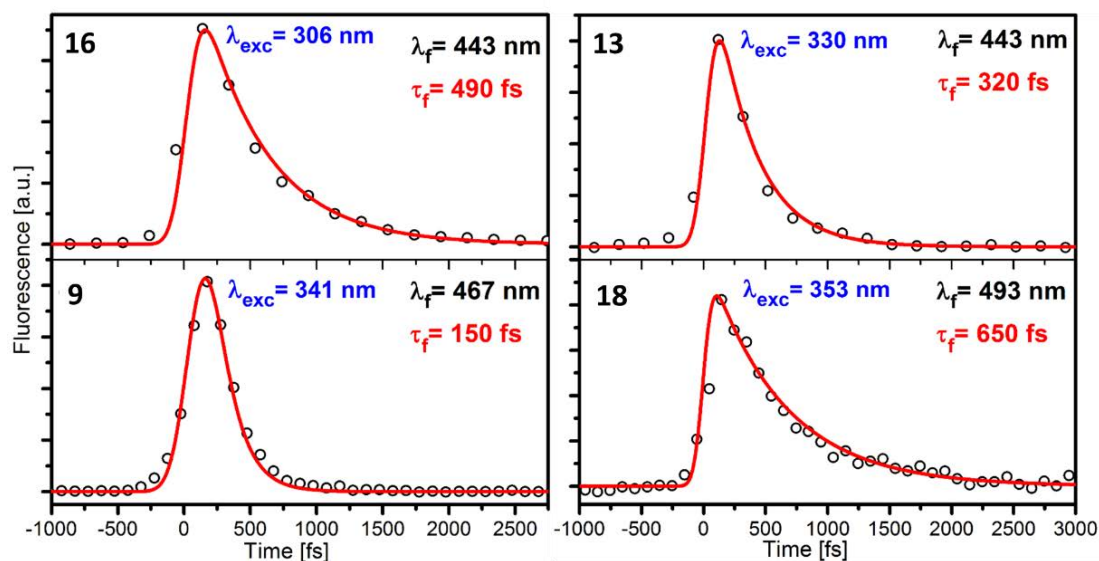


Figure 5.9. Time-resolved fluorescence upconversion spectra. Dots represent the experimental data and red lines the best exponential fitting obtained.

In all cases, according to the values obtained for the τ_f , in a few hundred femtoseconds the fluorescence signal has completely disappeared. This indicates that the formed excited state relaxes in few hundreds of femtoseconds toward a non-fluorescent location, which according to the theoretical predictions and the TA data exposed below, would lead to the formation of a hot ground state. For some of the samples, emission at wavelengths as long as 600 nm, which is about the detection limit of the experimental set-up, was observed. This bathochromic shift correlates with the stimulated emission (SE) contribution detected in the TA measurements at wavelengths longer than 675 nm (see below), revealing a large geometrical change along the excited state relaxation pathway. This is clearly in agreement with the computational predictions that will be seen in the next section.

More details about the photophysical behavior of the studied derivatives were gained by TA experiments, also using methanol solutions. The setup will be described in the experimental section including more technical details. The presented spectra of the samples were done exciting near the corresponding absorption maximum with the pump pulse and covering the 350 - 700 nm absorption (probe pulse) range for several picoseconds after the excitation. In all cases, the obtained spectra display a broad absorption in the 450 to 550 nm range. That extends further to the blue for **16** and **13**, whose red portion decays faster. It can also be noted, more clearly in **16** and **13**; that in this region the absorption is shifted from zero, indicating that it is not formed directly

from the excitation, it should be obtained after a relaxation process instead. This feature is remarked with a pink circle for compound **16** in Figure 5.10. In the case of compound **13** in Figure 5.10, it is not so evident due to the time resolution of the process, but a smaller shift is also observed.

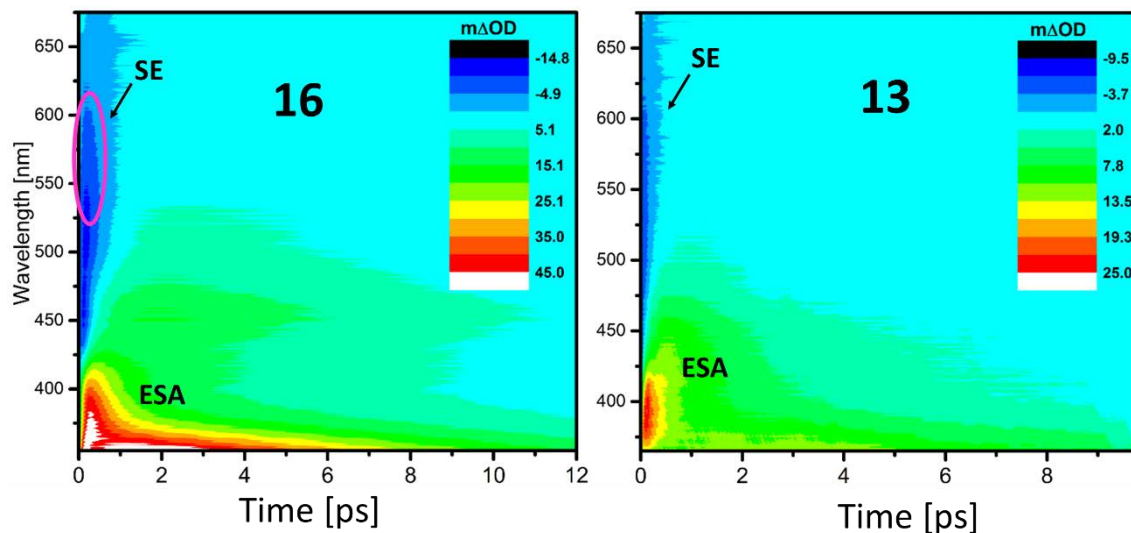


Figure 5.10. TA spectra for compounds **16** and **13**.

It should be noted as a key difference between the spectra of the pairs **16**, **13**; and **9**, **18** a missed region of the spectra. During the collecting of TA spectra, the probe beam used is in all cases 340 to 750 nm. That does not allow exploring the more energetic region from the absorption maxima of **16** and **13** (306 and 330 nm, respectively) to the starting wavelength of the probe (340 nm). As comparison between Figure 5.10 and Figure 5.11, the region corresponding to the GSB is missed in compounds **9**, **13** and more evident in **16**. As it is also explained in more detail below, this is due to the coupling between vibrational states.

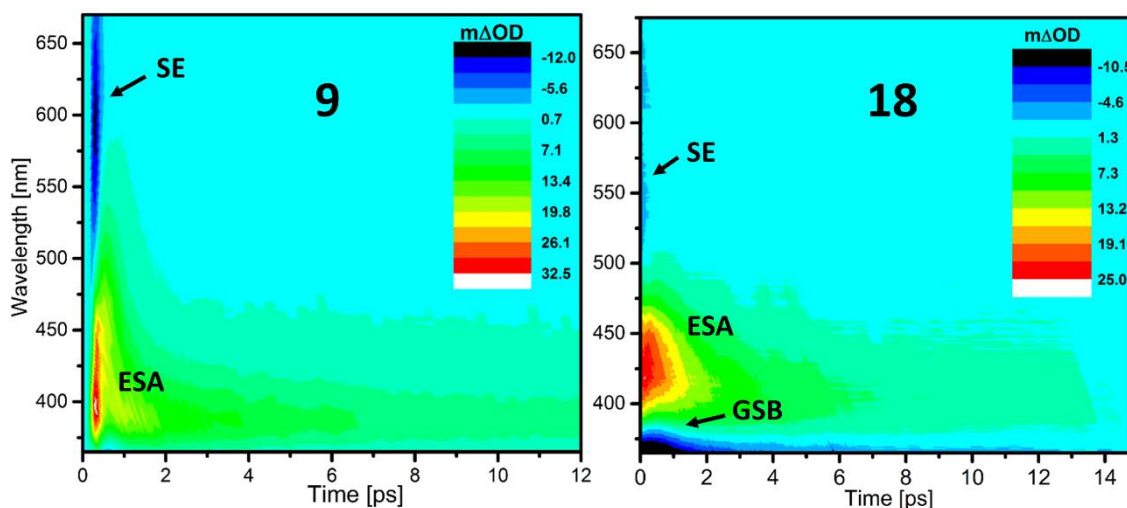


Figure 5.11. TA spectra for compounds **9** and **18**.

In all TA spectra seen in the previous figures, the spectral regions and their corresponding processes are also marked; these processes in some cases are mixed with some vibrational relaxation, which will be discussed below with the help of the decay-associated spectra.

In order to describe the temporal behavior of the four TAS samples, a global fit function resulting of the convolution of a Gaussian with three exponentials, τ_1 , τ_2 and τ_3 (τ_0 , τ_1 and τ_2 for **16**), was employed. The temporal evolutions of all absorption spectra are illustrated by the respective decay associated spectra (DAS) on Figure 5.12. In these plots, the spectral distribution of the pre-exponential factor (a_0 , a_1 , a_2 or a_3) associated to a particular temporal constant retrieved from the global fitting is shown in each trace. It should be remarked that the small spectral discrimination of the extracted time-constants notably complicates the analysis. However, the correlation with the computational and fluorescence data provides a reasonable interpretation of the involved dynamical processes as it is described below.

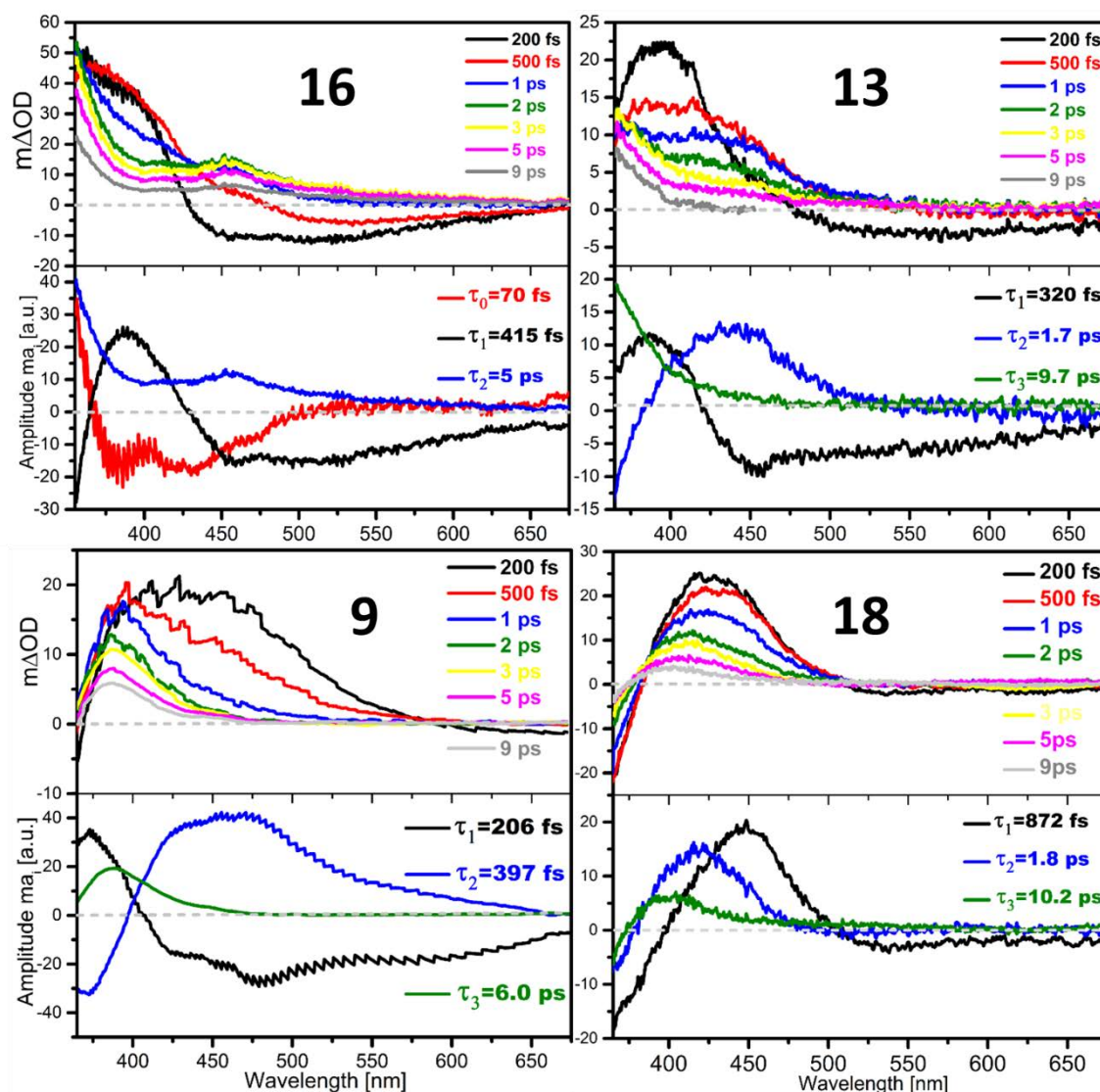


Figure 5.12. Spectra at different time delays and DAS for the lifetimes derived from the fitting of the TAS showed in Figure 5.10 and Figure 5.11.

Although the four studied samples exhibit singularities that should be discussed in more detail, a general relaxation scheme can be invoked to explain the observed dynamical behavior. Even supported with the theoretical data, the suggested mechanism indicates that the τ_1 constant, which correlates with the measured fluorescence lifetimes, reflects the relaxation of the initially prepared S_1 π - π^* state. In the case of **16**, an additional very short τ_0 component is required to model the early times of the relaxation. This τ_0 originated in the initially excited state seemed to account for the initial S_1 state population evolution out of the Franck-Condon (FC) region. The τ_0 DAS lifetime (Figure 5.12 compound **16**, red line) is positive only for the shortest wavelengths, acquiring negative values in the ~ 370 - 490 interval. This agrees with the

stretching found near the FC region and the population of a S_1 minimum according with computational data.

The τ_1 lifetime is present through the full studied range, where at least three distinctive spectral regions according to the signs of the τ_1 DAS and the TA signal, can be observed:

i) The lowest energy portion of the spectra that extends up to the detection limit at 650 nm, where τ_1 is the only temporal constant present. In this region, the τ_1 DAS and the TA signal, both have a negative character indicating the presence of an emission that owing to its τ_1 lifetime can be assigned to the prepared state SE. As already mentioned above, the SE presumably extends even to longer wavelengths beyond the detection limit. Also, it should be noted that in the case of **16** and **18** this longer wavelength contribution is considerably weaker.

ii) For **16**, **13** and **9** there is a region of positive TA signal in the $\sim 425 - 550$ nm range (the green part of the TA spectra at shorter times), where the τ_1 DAS stays negative while the τ_2 DAS shows a positive value. The signs indicate that this portion of the spectrum is formed with τ_1 and subsequently decays with τ_2 . Accordingly, we interpret it as the absorption of a vibrationally hot ground state formed from the S_1 internal conversion, which subsequently cools with the longer τ_2 lifetime. The fact that **18** does not exhibit this region, but a positive τ_1 instead, is explained in the next point.

iii) Peaking around 385 nm, the τ_1 DAS of **16**, **13** and **9** show a positive feature that is attributed to the S_1 excited state absorption (ESA). For **16**, this band overlaps with a negative τ_0 feature that accounts for the formation of this S_1 location. It should be noted that for **18** the τ_1 positive band is red shifted, with a maximum at ca. 450 nm. This causes an extensive overlap with the hot ground state absorption and it also permits to observe the GSB negative contribution at the highest energies of the spectra.

To assign the τ lifetimes retrieved from the fitting, the TA measurements can be correlated with the fluorescence and the computational results. The τ_1 component, which matches the fluorescence-up-conversion decays, is found in the red edge of the spectra and describes the disappearance of the SE signal. Accordingly, it can be assigned to the IC of the prepared S_1 state to form a hot ground state. The components

τ_2 and τ_3 can be associated to the vibrational cooling, which takes place in the ground state formed during the first hundreds femtoseconds. The absence of these components in the red portion of the spectra attributed to the SE, reinforces their assignment to ground state processes. For the four studied compounds, the DAS of τ_2 shows a positive value in the $\sim 385 - 500$ nm region that switches to negative (**13**, **9** and **18**) at the blue edge of the spectrum. This behavior accounts for the red to blue shift of the ground state spectrum cooling, corresponding to the relaxation across vibrational states. Accordingly, the longer τ_3 component, which appears at the blue portion of the TAS, characterizes the relaxation of colder sections of the ground state. During the modeling process, a considerable cross-talking between the values of the τ_2 and τ_3 constants was detected. That exchange between values can be justified by the nature of the cooling process. In the case of **16**, the longer τ_3 component is not required to model the ground state cooling. Probably this is related to the fact that the formed hot ground state is shifted to higher energies with respect to the other samples.

As a summary with all the experimental data, the relaxation times (fluorescence and TAS) are collected in the following Table 5.1.

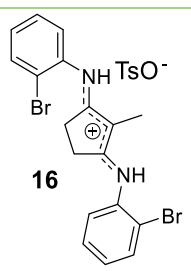
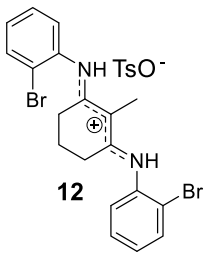
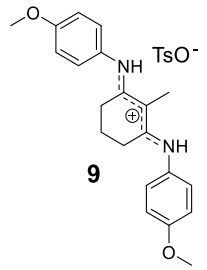
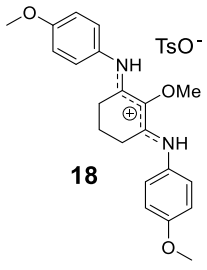
Compound	Fluorescence	TAS
 16	$\lambda_{\text{exc.}} = 306 \text{ nm}$ $\lambda_{\text{fl}} = 443 \text{ nm}; \tau_{\text{fl}} = 490 \pm 25 \text{ fs}$ $\lambda_{\text{fl}} = 493 \text{ nm}; \tau_{\text{fl}} = 490 \pm 25 \text{ fs}$	$\lambda_{\text{exc.}} = 306 \text{ nm}$ $\tau_0 = 70 \pm 21 \text{ fs}$ $\tau_1 = 415 \pm 43 \text{ fs}$ $\tau_2 = 5.0 \pm 0.22 \text{ ps}$
 12	$\lambda_{\text{exc.}} = 330 \text{ nm}$ $\lambda_{\text{fl}} = 443 \text{ nm}; \tau_{\text{fl}} = 320 \pm 16 \text{ fs}$ $\lambda_{\text{fl}} = 520 \text{ nm}; \tau_{\text{fl}} = 320 \pm 16 \text{ fs}$	$\lambda_{\text{exc.}} = 330 \text{ nm}$ $\tau_1 = 173 \pm 58 \text{ fs}$ $\tau_2 = 1.7 \pm 0.48 \text{ ps}$ $\tau_3 = 9.7 \pm 1.04 \text{ ps}$
 9	$\lambda_{\text{exc.}} = 341 \text{ nm}$ $\lambda_{\text{fl}} = 467 \text{ nm}; \tau_{\text{fl}} = 150 \pm 15 \text{ fs}$ $\lambda_{\text{fl}} = 520 \text{ nm}; \tau_{\text{fl}} = 200 \pm 15 \text{ fs}$	$\lambda_{\text{exc.}} = 341 \text{ nm}$ $\tau_1 = 100 \pm 33 \text{ fs}$ $\tau_2 = 570 \pm 226 \text{ fs}$ $\tau_3 = 8.1 \pm 0.51 \text{ ps}$
 18	$\lambda_{\text{exc.}} = 353 \text{ nm}$ $\lambda_{\text{fl}} = 493 \text{ nm}; \tau_{\text{fl}} = 650 \pm 32 \text{ fs}$ $\lambda_{\text{fl}} = 520 \text{ nm}; \tau_{\text{fl}} = 600 \pm 30 \text{ fs}$	$\lambda_{\text{exc.}} = 353 \text{ nm}$ $\tau_1 = 872 \pm 201 \text{ fs}$ $\tau_2 = 1.8 \pm 0.15 \text{ ps}$ $\tau_3 = 10.2 \pm 0.22 \text{ ps}$

Table 5.1. Summary with the TAS and fluorescence upconversion data.

In addition, the conclusions obtained from the spectroscopic data and the theoretical calculations (which are described below) are summarized at the end of the next section, allowing further discussion once experimental and theoretical data are exposed.

5.2. Theoretical study of MAA synthetic analogues

In order to justify the observed dynamical data and complement the knowledge about the obtained synthetic analogues, a computational study was done to analyze the effect of the aryl moieties in the non-radiative deactivation mechanism of the system. For this, a complete study following the CASSCF//CASPT2 strategy^[8] was performed. As mentioned during the methodology description in section 4.1, this strategy requires the reaction coordinate to be computed at the CASSCF level of theory and the corresponding energy profile should be re-evaluated through single point calculations at the CASPT2 level of theory.

To begin the computational study, the *E,E*-isomer in both C=N double bonds (see structure below) was selected as starting point. From the X-ray structure of this compound, presented in the previous section 4.4, this is the predominant disposition in solid state. To guarantee this configuration to be the most stable isomer also in solution, a conformational study at MP2/6-31G* was done, ensuring that the other isomers, *Z,E* and *Z,Z*, are less stable than the *E,E*-isomer. Once obtained the ground state minimum geometry, the definition of the active space is a keystone for the reliability of the obtained results. In this case, two different active spaces were checked to model compound **9**. The chromophore considered including the π density (orbitals π and π^* of bonds C=C, C=N and π N_{imine}) of the imine-enamine moiety and four of the π and π^* orbitals on the phenyl rings, as shown in Figure 5.13, being the selected active orbitals for the (14,13) active space. When using (6,5), the orbitals included in the active space are 1, 2, 5, 8 and 13, excluding all the phenyl orbitals (3, 4, 6, 7, 9-12). All CASSCF//CASPT2 calculations were performed using the MOLCAS 8.2^[9] package, due to convergence problems in the wavefunction when excluding the phenyl orbitals in the Gaussian 16^[10] software.

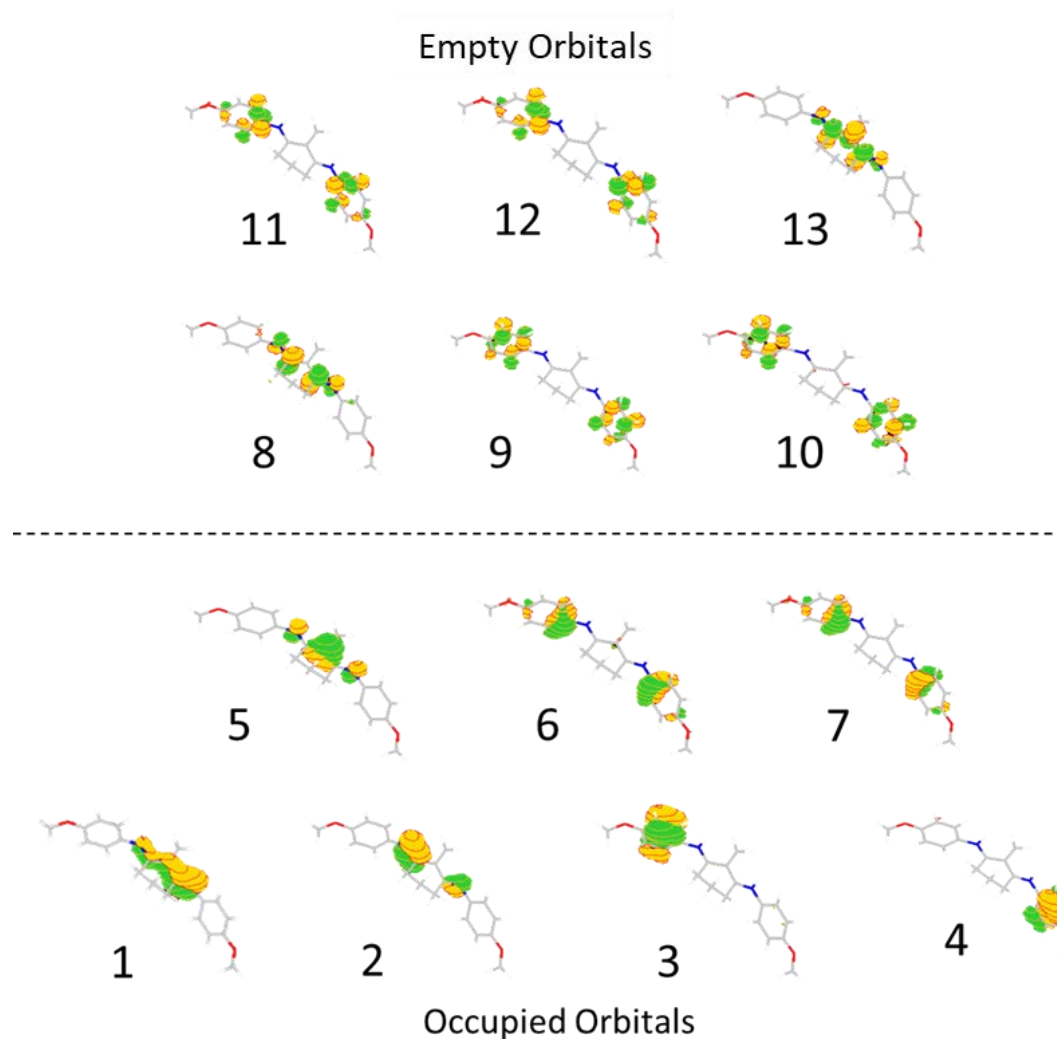


Figure 5.13. Orbitals included in (14,13) active space of 9.

The computed absorption spectra of **9-FC** (see Figure 5.14 for the structure) were obtained with both active spaces ((14,13) and (6,5)) to analyze possible differences between. In both cases, an excitation to S_1 was observed at 326 nm and 327 nm, respectively. The obtained wavelength is slightly blue shifted respect to the experimental absorption maximum located at 343 nm, as it has also been observed in previous studies.^[11] The only difference between both active spaces is an evident decrease in the oscillator strength from $f = 1.107$ to $f = 0.829$, which is due to the phenyl ring contribution but it is not relevant in energy terms. In both cases, the bright transition is a $\pi - \pi^*$, involving orbitals 5 and 8. Nevertheless, to ensure a good modelling of the behavior with the smaller active space, it is necessary to check the population of these orbitals along the minimum energy path and see how the population of the π and π^* orbitals centered in the phenyl rings changes. If their population changes

significantly, they could not be excluded from the active space without losing a good modelling of the system.

Despite this, the MEPs using both active spaces were computed. In all cases, the same energetic profile was obtained as expected if the inclusion of these orbitals was not relevant for this system. After an initial stretching, the geometric change along the S_1 PES reveals a new deactivation pathway. The previously discovered out-of-plane movement (as takes place in **8**)^[11] was not detected along these MEPs. Instead, the rotation of an imine moiety is observed. This new path presents a minimum (**9-Min S_1**) in the excited state PES, with a minimal energy gap between both states. Its geometry is shown in Figure 5.14, together with ground state minimum (**9-FC**).

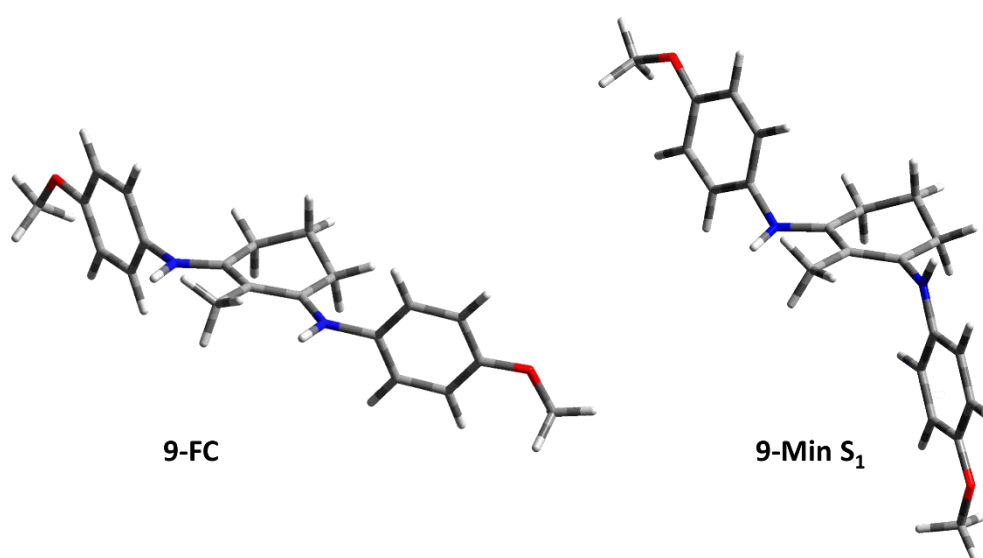


Figure 5.14. Structures of **9-FC** and **9-Min S_1** .

A comparison between both CASSCF active space calculations is shown in Figure 5.15, together with the preliminary TD-DFT minimum energy path computed at the TD-CAM-B3LYP/6-31G* level of theory, which presents the same behavior in qualitative terms.

Looking into the CASSCF MEPs, all seems to be favorable to use the (6,5) active space. In this case, the population of the phenyl orbitals along the (14,13) path doesn't change. They remain with occupations higher than 1.9 in bonding orbitals and lower than 0.1 in the antibonding orbitals, so the active space can be reduced to (6,5) decreasing considerably the computational cost, in terms of time and machine resources.

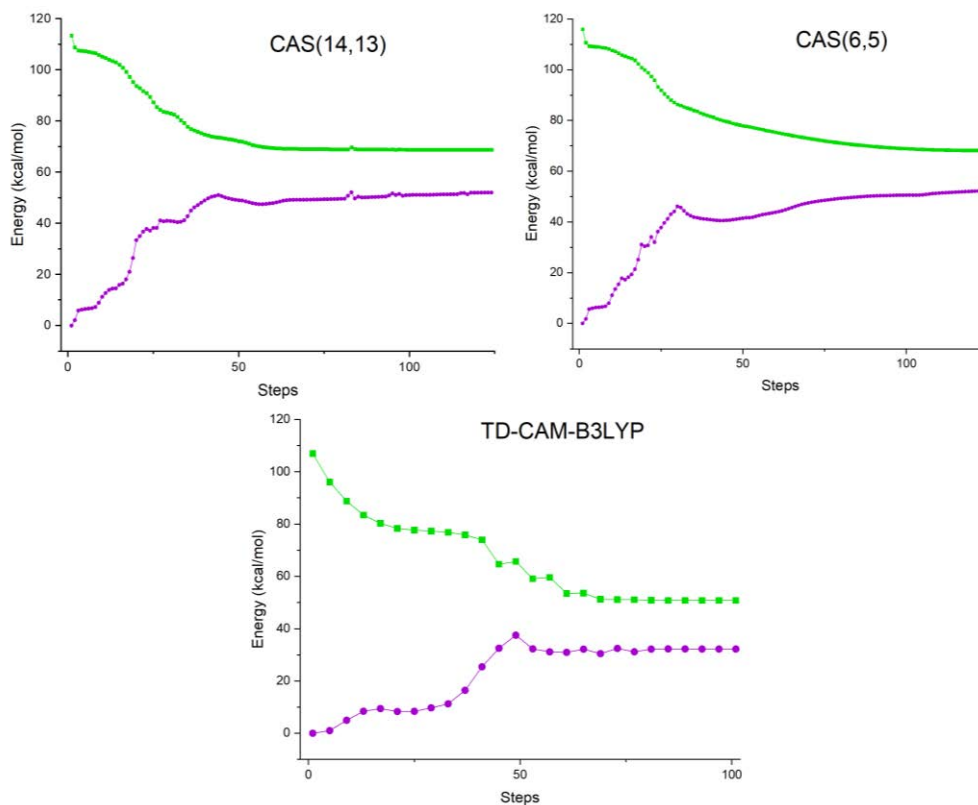


Figure 5.15. Comparison of MEP (CASSCF) with both active spaces and TD-DFT.

In all cases, the shape of the obtained potential energy surface is almost the same together with the geometrical deformation. Regarding this geometrical deformation along the minimum energy path, a new behavior surges with respect to the typical deactivation exhibited by the simplified compound **8**. In compound **9**, one of the phenyl rings is almost perpendicular regarding the planar cyclic core involving a C=N isomerization of the iminium moiety. This yields a minimum in the excited state not observed in compound **8**. To monitor this distortion, two dihedral angles were selected to quantify the strength of the geometrical deformation during the relaxation process. The dihedral angle φ_1 (in blue) represents the planarity of the nitrogen respect to the cyclic moiety involving the NCCC dihedral. The second dihedral angle φ_2 (in red) indicates the rotation with respect to the cyclic moiety of the plane represented by the phenyl ring. This dihedral comprises the angle between $C_{Ph}NCC$ atoms. A simplified representation of the PES can be seen in Figure 5.16 together with the described critical points.

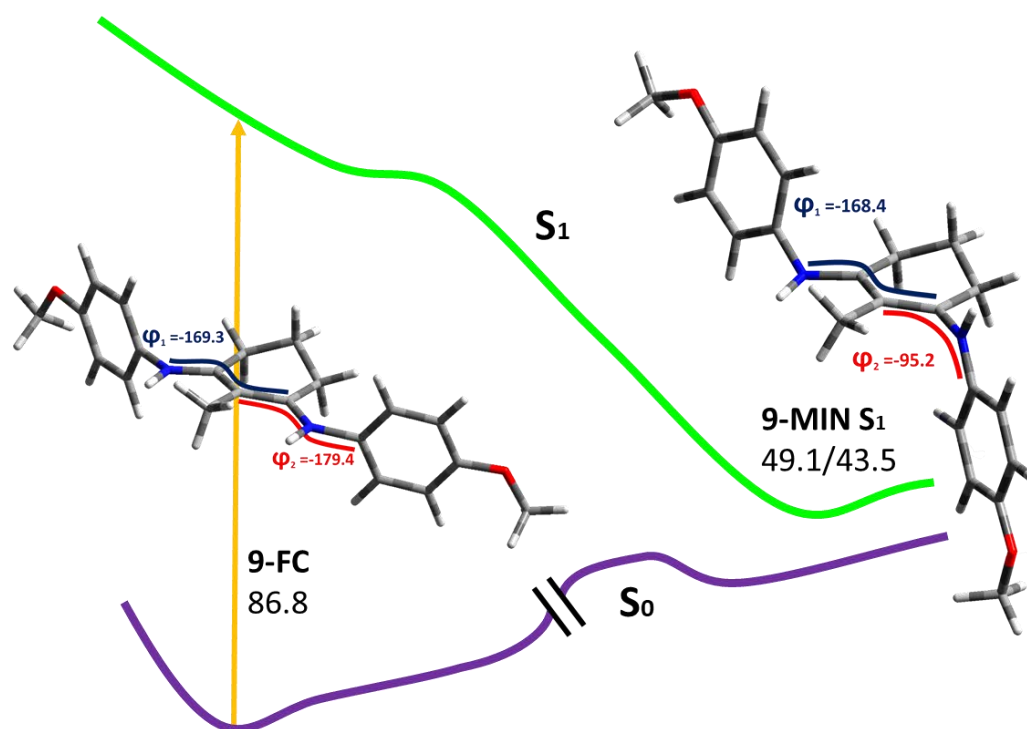


Figure 5.16. Schematic PES for the relaxation from 9-FC to 9-MIN S₁.

As previously mentioned, the energy difference between both PESs in the excited state minimum (**9-MIN S₁**) is only 6 kcal/mol. With this small energy gap, a conical intersection (**9-CI isomerization**) should be proximal and easily connected with this minimum, being only 8 kcal/mol above in energy. This energy barrier does not represent a problem in terms of fast deactivation to the ground state observed experimentally. This barrier could be easily surmounted only with the vibrational energy of the molecule. Both geometries can be seen in Figure 5.17, with a minimal geometric deformation from **9-MIN S₁** to **9-CI isomerization**.

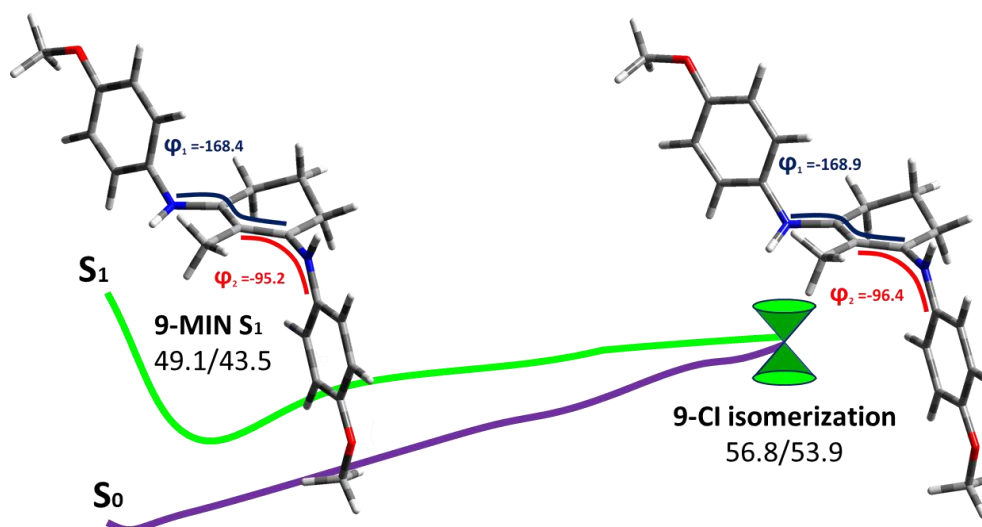


Figure 5.17. Schematic PES from **9-MIN S₁** to **9-CI isomerization**.

Before describing the branching space of **9-CI isomerization**, the out-of-plane conical intersection was computed in order to evaluate the observed relaxation path in alkyl derivatives, as compound **8**. This crossing point (**9-CI**) can be found at higher energies with respect to the novel isomerization pathway, 76 vs. 57 kcal/mol. The comparison between both conical intersections can be seen in Figure 5.18.

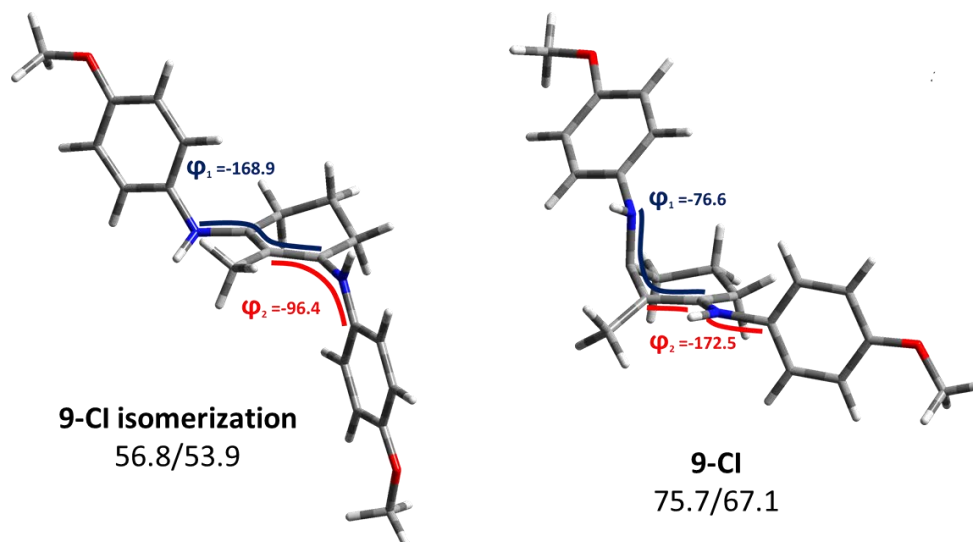


Figure 5.18. Comparison between **9-CI isomerization** and **9-CI**.

Regarding the conical intersection geometries, the previously mentioned dihedral angles were chosen to monitor the geometrical deformation. The dihedral angle φ_1 (in blue) represents the planarity of the nitrogen with respect to the cyclic

moiety involving the NCCC dihedral; this coordinate is the most relevant in the palythine-like deactivation path. In **9-CI**, where the out-of-plane distortion of the nitrogen is clearly relevant, it changes from -169.3° in **9-FC** to -76.6° in **9-CI**. In contrast, no significant change is found in **9-CI isomerization** (-168.9°). The second dihedral angle φ_2 (in red) quantifies the rotation with respect to the cyclic moiety of the plane represented by the imonium substituents, in this case, a proton and phenyl ring. This dihedral comprises the angle between $C_{Ph}NCC$ atoms, and its change is especially relevant during the isomerization path, changing from -179.4° in **9-FC** to -96.4° in the **9-CI isomerization** and remaining unaltered in **9-CI** (-172.5°).

As described for conical intersections in the previous chapter, the characteristic descriptors gradient difference (GD) and derivative coupling (DC) vectors should be analyzed to understand the topology of the conical intersection. In this case, only the **9-CI isomerization** was analyzed because it is the relevant crossing point along the excited state relaxation. Analyzing the movement related to the branching vectors (Figure 5.19), the DC vector promotes an aborted isomerization due to the force directions in the branching space. The component in the GD vector promotes the stretching specially of the C=N bonds. In this geometry, an elongation from 1.33 \AA in the distance of C=N in **9-FC** to 1.44 \AA in the **9-CI isomerization** was observed. This geometrical feature is usual in conical intersections mediating isomerization, due to the lower π - π orbital overlapping when the double bond is twisted and the π^* orbital populated.

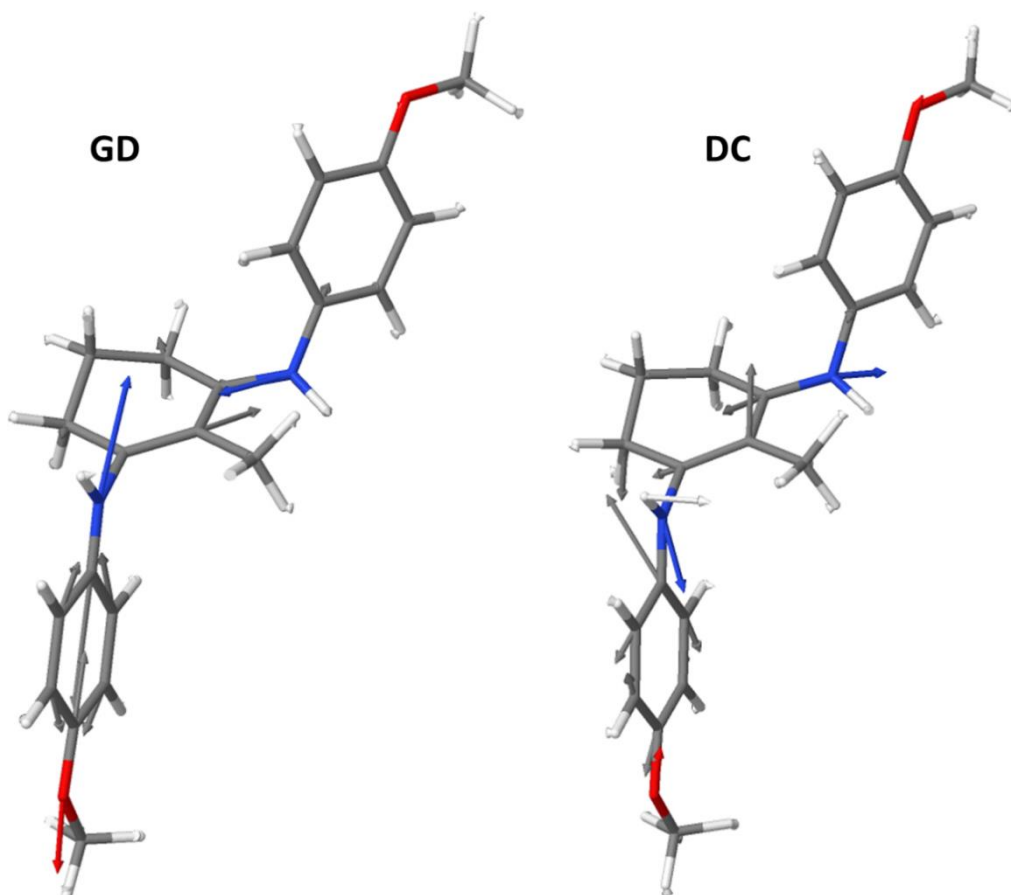


Figure 5.19. 9-CI isomerization GD (left) and DC (right) vectors.

Regarding this new isomerization pathway, the topology around the conical intersection is a key factor to understand the deactivation mechanism when the molecule decays to the ground state. In this case, we found, according to MOLCAS descriptors,^[12] a highly sloped ($P > 1$) and a single product ($B > 1$) formation funnel. This means a conical intersection, which promotes an aborted geometrical transformation where the appearance of new photoproducts seems to be not relevant. For that, we expected a low isomerization quantum yield for this process, as observed experimentally where no traces for any photoisomerization product were detected.

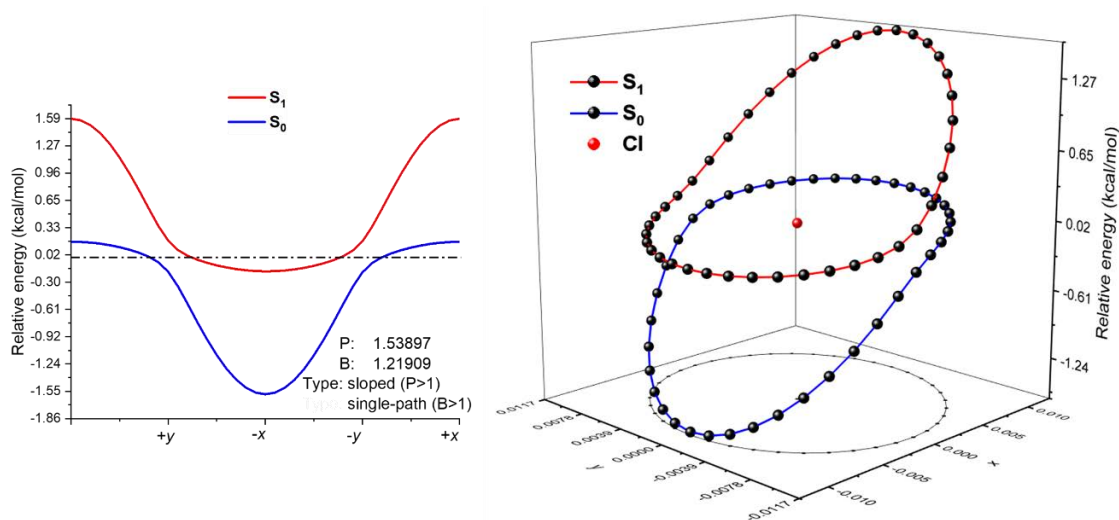


Figure 5.20. Energy distribution around the CI, energies of S₁ and S₀, dotted zero as energy difference (kcal/mol). *P* and *B* MOLCAS descriptors for CI (left). 3D plot of the PES around **9-Cl isomerization** (right).

The energy profile around the CI when geometrical distortions are applied along the *x* and *y* vectors is seen in Figure 5.20. Following both directions of the DC vector in the vicinity of the conical intersection, the forward direction promotes *E,E*-isomer recovery with a more sloped path compared with the backward direction which has slightly higher energies.

Even with this CI topology, a small population of the *Z,E*-isomer minimum could be possible. In this case, the sunscreen capabilities would not be compromised, as this feature was also observed in some natural MAAs as the complementary mechanism of photoprotection. However, the starting isomer and the photoisomer both could contribute to the UV attenuation as they absorb, according to computational data, in a similar region with a difference of *ca.* 30 nm.

In order to enlighten about the relative stability and the thermal conversion between isomers, we computed both isomers at the MP2^[13] level including methanol as implicit solvent (PCM),^[14] trying to reproduce as much as possible the experimental conditions described in the previous section. For these calculations the Gaussian 16^[10] software was used at the PCM-MP2/6-31G*^[15] level of theory.

A typical value for C=N isomerization barriers is *ca.* 20 kcal/mol,^[16] and these can be surmounted at room temperature. In this case, both isomers are almost isoenergetic with a difference of only 1.8 kcal/mol. The obtained transition state (**9-TS**) connects both isomers through a low energy barrier of 13.7 kcal/mol.

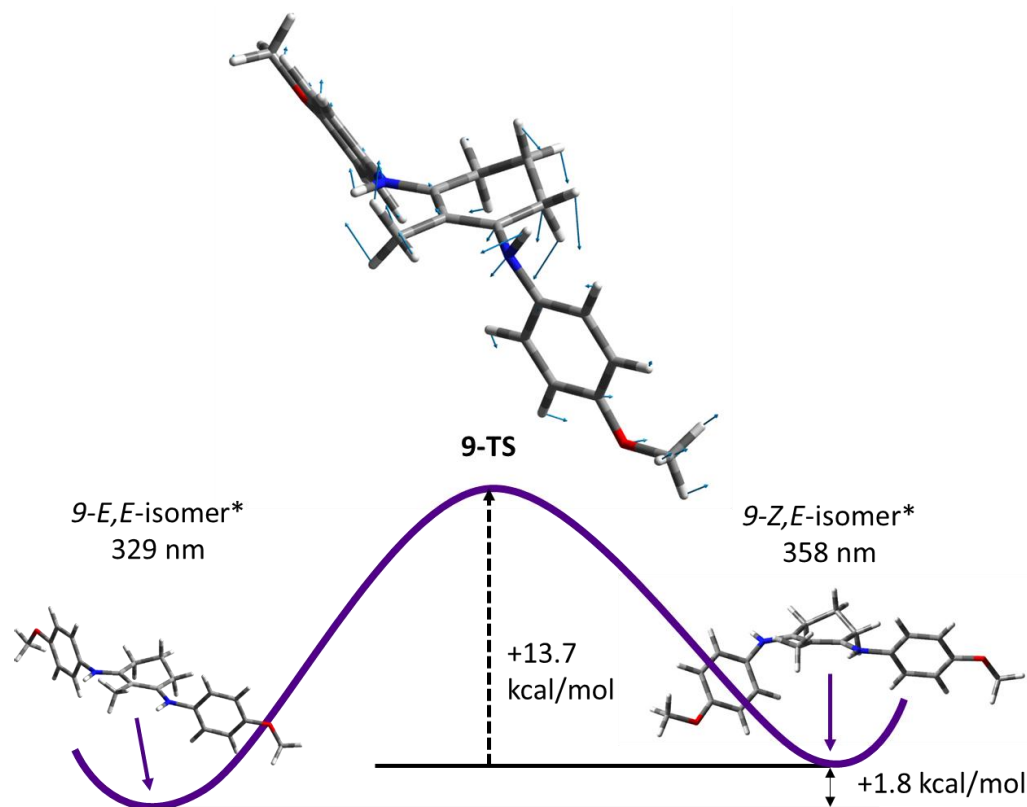


Figure 5.21. Schematic isomerization path and TS with displacement vectors. (Energies in kcal/mol and absorbance spectra in nm)

Even assuming the formation of this *Z,E*-isomer, this energy barrier implies that back conversion should be a fast process, being quick enough to avoid detection of the photoisomer at room temperature. The calculated lifetime according to the Eyring equation for a barrier of 13.7 kcal/mol is about 1.25 ms at room temperature, which justifies the impossibility to detect this isomer during the experiments. This transition state was also characterized with frequency calculation obtaining one imaginary frequency at $i42\text{ cm}^{-1}$ (see displacement vectors in Figure 5.21) and scanning the intrinsic reaction coordinate along the reactive frequency of the transition state to ensure the connection between both isomers.

To sum-up the features observed for **9**, the critical points found along the PES are depicted in Figure 5.22 together with their MS-CASPT2 energies.

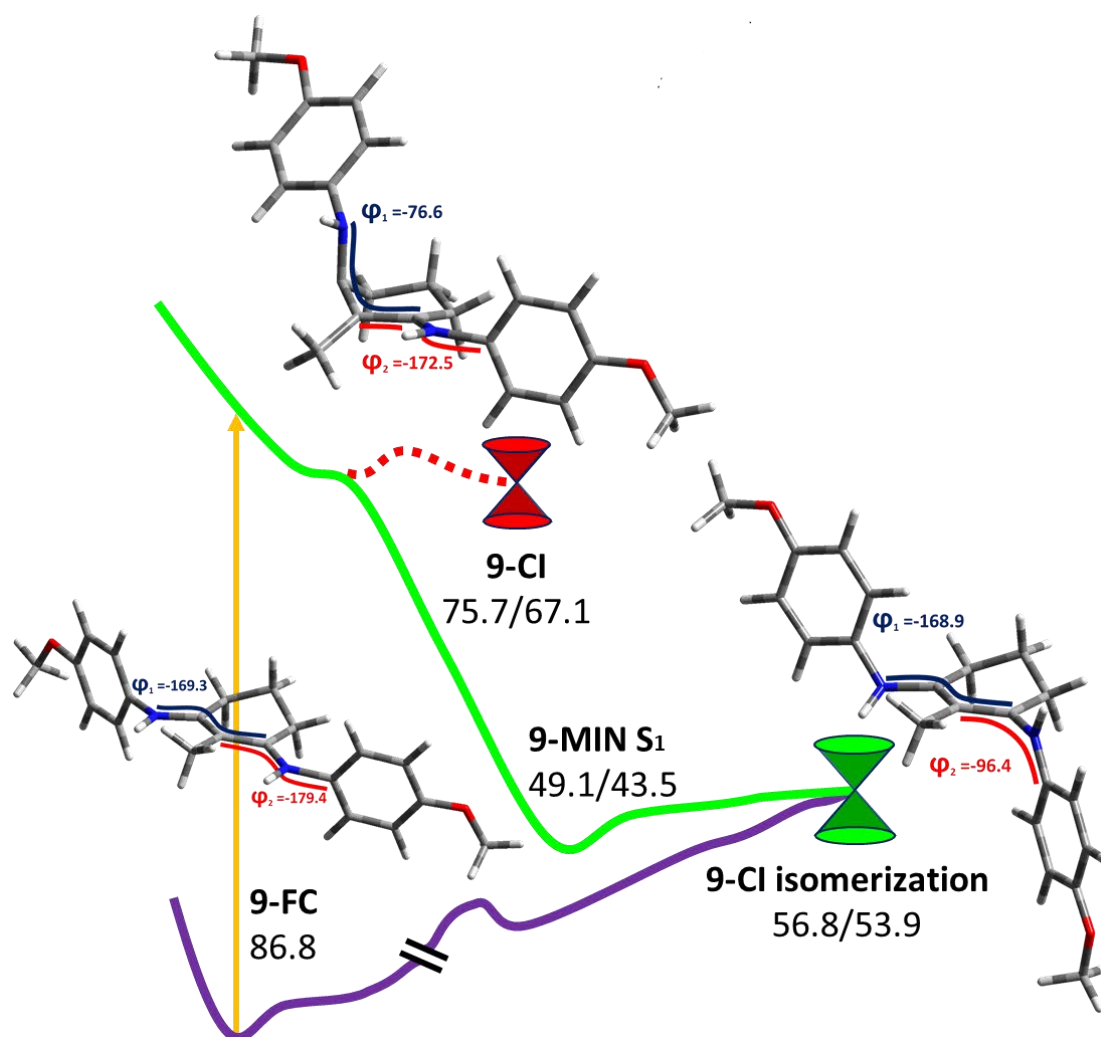


Figure 5.22. Schematic representation of the critical points along the PES for 9.

In order to evaluate the differential effect of aryl moieties on the shape of the PES, a comparison with the previously computed MEP for compound **8**, where methyl groups substitute the phenyl moieties, was done. As the more relevant feature, it should be noted that the shape of the PES clearly resembles of the one obtained for palythine and related compounds as shown in Figure 5.23 and the data from the previous chapter.

For compound **8**, a minimum in the excited state **8-MIN** can be located ca. 10 kcal/mol above the **8-CI**. This minimum is related to the photoisomerization of a C=N bond. Additionally, no conical intersection of isomerization was found even forcing the molecule to this geometrical disposition. For all attempts, the **8-CI** was obtained as the only and most stable conical intersection for this compound.

As comparison, the previously described deactivation pathway implying the pyramidalization CI seems to be the relevant deactivation path in presence of alkyl-substituted moieties. In contrast with aryl-substituted moieties where the relevant relaxation pathway appears to be the aborted isomerization process.

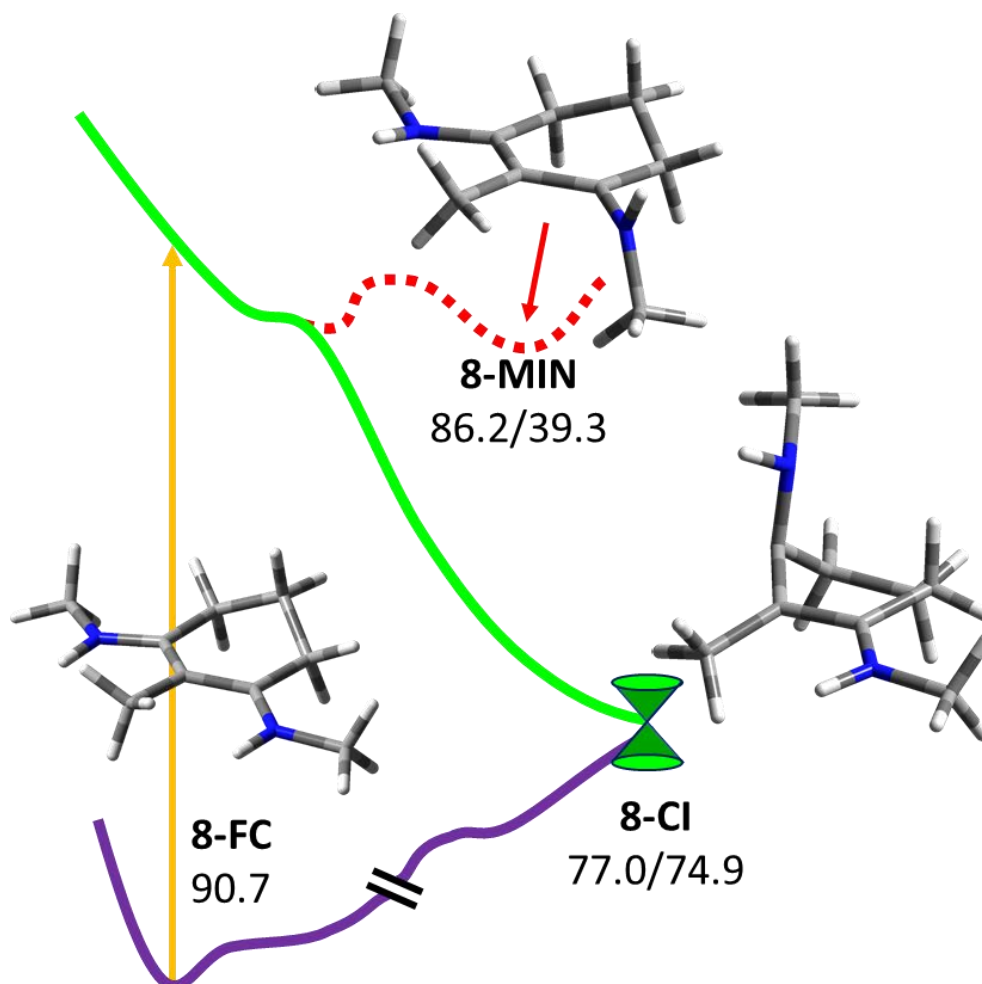


Figure 5.23. Schematic representation of the critical points along the PES for **8**.

On the light of the theoretical and experimental evidences, some conclusions regarding the relaxation mechanisms of these compounds can be drawn. The fluorescence up-conversion experiments establish that the prepared S₁ state relaxes in hundreds of femtoseconds. The detected emission spectra exhibit a notable Stokes shift, which unfortunately, due to the limited temporal resolution of the fluorescence set-up could not be time resolved. In all cases, the fluorescence lifetimes can be correlated with the τ_1 components extracted from the TA measurements. These evidences suggest that the prepared S₁ state relaxes by IC in hundreds of femtoseconds, forming a vibrationally hot ground state. The cooling of the formed hot

ground state in the ps timescale is described by the τ_2 and τ_3 constants retrieved from the TA data. The carried out computational research provides key insights regarding the paths that may promote the experimentally observed S_1/S_0 non-adiabatic coupling. According to it, the inclusion of the two phenyl substituents favors the C=N isomerization channel vs the out-of-plane ring deformation path, which is the calculated MEP for the simplified methyl-substituted model **8**. The former path should be accompanied, on the way to the corresponding CI, by a considerably larger S_1 stabilization (ca. 30 kcal/mol for **9**, see Figure 5.22), than the estimated for the out-of-plane coordinate (ca. 11 kcal/mol). The photoisomerization to yield the *E,Z*-isomer, while is possible from a purely geometric point of view, is prevented due to the shape of the PES around the **9-CI isomerization**. Fluorescence and TA data are fully compatible with the computed photoisomerization reaction path, although neither spectral features nor long-term dynamical constants that could be associated with the formation of the photoisomer were detected. In any case, the calculated low isomerization barrier (*Z-E*) on the ground state described in Figure 5.21 and the similar computed absorption spectrum for both isomers (329 vs. 359 nm) ensures the observed photoprotective capabilities of these species.

The current results should be compared with the recent work by Woolley et al.^[17] where on derivative **11** they found a similar S_1/S_0 IC channel, but in contrast with the results herein, a small population remain trapped in the S_1 for longer time-scales. However, according to our computational predictions, the presence of the aliphatic substituents in the molecule studied by Woolley et al. should favor the pyramidalization over the photoisomerization as the driving relaxation coordinate. In this scenario, although we cannot unambiguously identify from the experimental data the path leading to the observed S_1/S_0 , IC, we tentatively propose the photoisomerization coordinate as the motion behind the photophysical properties of the studied compounds **16**, **13**, **9** and **18**.

5.3. Comparison with commercial sunscreens

Once determined the complete relaxation pathways of MAA derivatives, a comparison between the mechanisms controlling the photoprotective capabilities of the commercial used sunscreens is needed. With this in mind, we can understand the novelty and possible advantages of these new derivatives with respect to the presently available compounds. As mentioned in the background section, a detailed analysis only from the dynamic point of view for the sunscreens in Figure 5.24 is committed herein, while the general mechanism was explained in section 2.2.

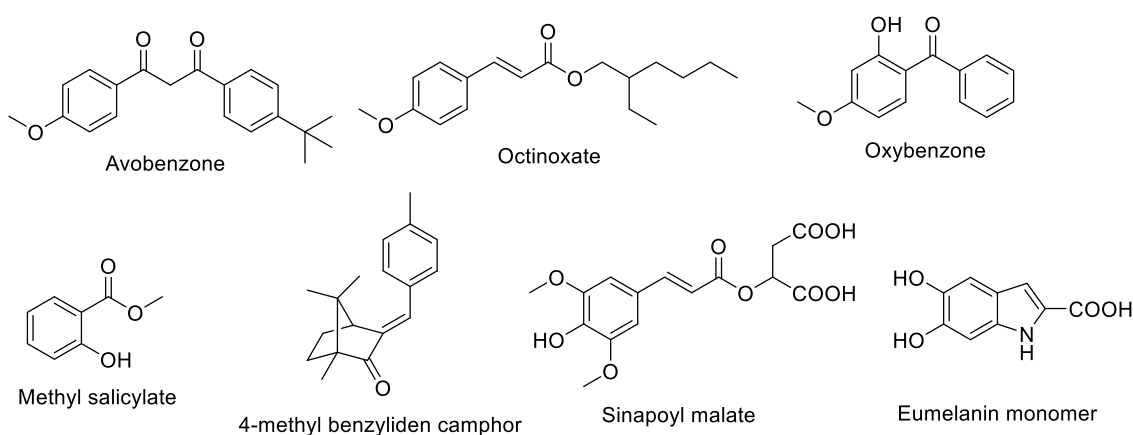


Figure 5.24. Diverse sunscreens explained in this section.

In the case of avobenzone, the photoprotection mechanism is due to a strong intramolecular hydrogen bond^[18, 19] and usually longer times comparing with MAA derivatives, in the range of $\sim 0.4 - 1.4$ ps, were obtained for the singlet state deactivation.^[20, 21]

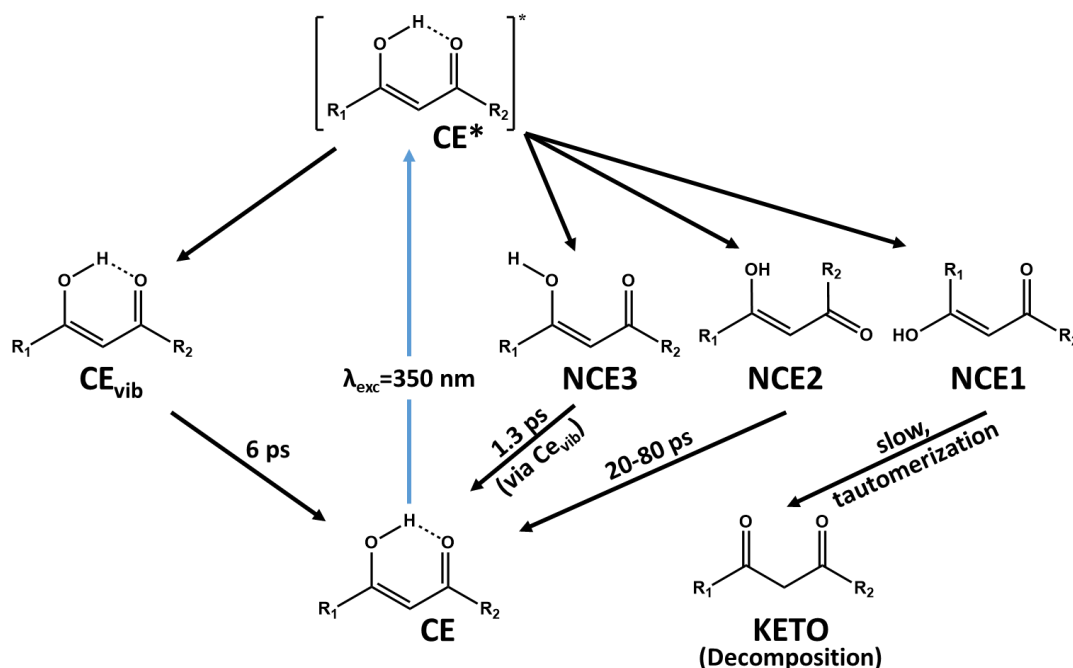


Figure 5.25. Different deactivation alternatives in avobenzone. Adapted from.^[20]

An *enol* to *keto* tautomerization also plays an important role in avobenzone photochemistry. The *keto* tautomer is the key intermediate in the photodegradation of avobenzone. Measurements in different solvents suggest that the *enol* to *keto* reaction is more favorable in the NCE1 (non-chelated *enol*) geometry than in CE (chelated *enol*) but that protic solvents stabilize NCE1, preventing the reaction to the *keto* isomer. Excitation of avobenzone in the CE form at 350 nm yields in a TA spectrum revealing relaxation from the electronically excited state in hundreds of femtoseconds followed by vibrational relaxation in several picoseconds.^[20] Long-lived offsets from zero in TA measurements arise from the slower dynamics of NCE1 and the *keto* isomer, without finding any evidence of reaction from NCE2 to the *keto* isomer.^[19, 20] This *keto* tautomer is mainly the responsible for the reactivity due to an intersystem crossing point, which promotes the population of the triplet state. In this way, the relaxation time increases to 665 ns.^[22] But also other reactivity, like singlet oxygen^[23] formation and Norris type fragmentation^[24] are able to occur.

A similar behavior to avobenzone is observed in oxybenzone,^[25] where the photoprotective activity is due to an excited state proton transfer (ESPT) between the hydroxyl group in the phenyl ring and the *keto*. In this case, the relaxation times for singlet and triplet states are around 400 fs and 2 – 3 ps,^[26] respectively.

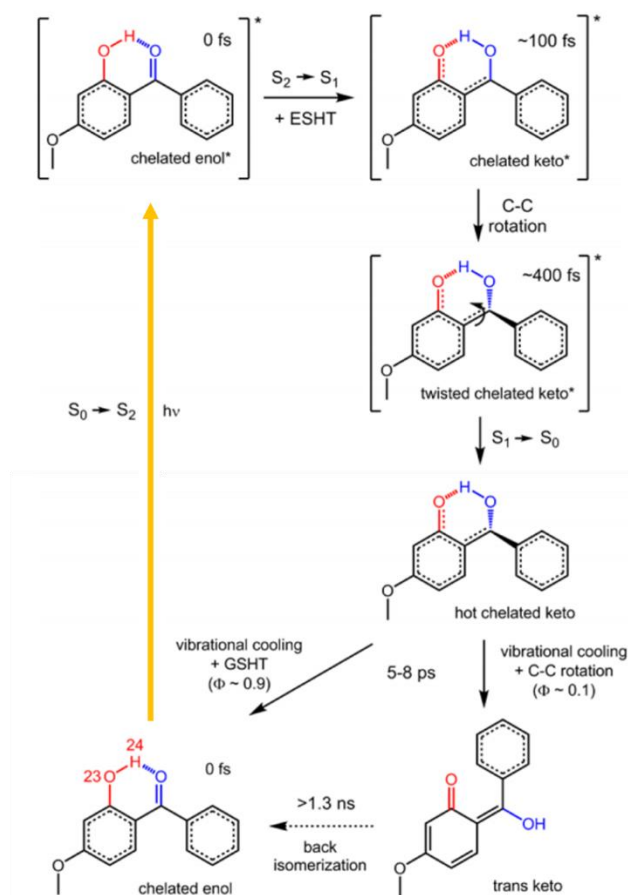


Figure 5.26. Oxybenzone deactivation mechanism in singlet state and timescale related to each process.^[25]

This compound usually exists in an energetically more stable chelated *enol* form, which after photoexcitation, predominately populates the S_2 π - π^* state. This species relaxes by internal conversion (IC) to the S_1 n - π^* state and then undergoes an excited-state hydrogen transfer to form a *keto* isomer, taking ~ 100 fs, as can be seen in Figure 5.26. A rotation around its aliphatic C-C bond occurs, which allows oxybenzone to couple to its S_0 state through a n - π^* S_1/S_0 conical intersection (CI) on a time scale of ~ 400 fs.^[21] A ground-state hydrogen transfer and vibrational energy transfer to the surrounding solvent re-forms the *enol* isomer, which takes place on a time scale of $\sim 5 - 8$ ps depending on the degree of hydrogen bonding to the solvent bath. An incomplete ground-state recovery suggests that a small portion of the molecules in the excited-state form a photoproduct, whose transient vibrational absorption studies attribute to a *trans keto* isomer from extended C-C rotation,^[25] although other studies have suggested that this could be attributed to the formation of a phenoxy radical.^[26]

In addition, an analogous mechanism is observed in salicylates and its derivatives, due to the same disposition on the hydroxyl group with respect to the carboxylic moiety as happens in oxybenzone. As the simplest example, methyl salicylate has been used in UV photoexcitation studies over the years, with attention on fluorescence properties.^[27] Previously reported ultrafast measurements in the gas-phase identified the ESHT occurring within 60 fs, as well as a longer decay channel of 120 ps.^[28] Octyl salicylate and homomenthyl salicylate are the most used salicylates in cosmetics, but not too much information on their mechanism is available.^[29]

In cinnamate derivatives, like natural sinapoyl malate^[30] or the widely used octyl methoxycinnamate^[21], the typical mechanism consists of an *E/Z* isomerization process. Surprisingly, octinoxate has not been studied from a dynamic point of view. In the case of sinapoyl malate,^[30] the ground-state *trans*-isomer populates an excited electronic state, which begins to relax with a short $\sim 50 - 600$ fs to ground state and a $\sim 1 - 5$ ps for the vibrational cooling, depending on the solvent. The study suggests two possibilities for the excited states involved. The first option is the excitation to a $\pi-\pi^*$ state, followed by IC mediated by a $\pi-\pi^*/2^1\pi-\pi^*$ CI to the $2^1\pi-\pi^*$ state, which have charge transfer nature. Next, IC along the *trans-cis* isomerization coordinate coupling to the ground state by a second CI, $2^1\pi-\pi^*/S_0$, and subsequent vibrational energy transfer to the surrounding environment. As second option, the excitation to the $\pi-\pi^*$ state, which couples to the ground state via a $\pi-\pi^*/S_0$ CI. For both mechanisms, it is suggested that the dynamics occur along a *trans-cis* isomerization coordinate.

This isomerization path is not unique in cinnamates, other sunscreens with exocyclic double bonds have the same relaxation mechanism, like 3-(4-methylbensylidene) camphor.^[31] Also this isomerization occurs together with the previously described mechanism^[11] in special cases of mycosporine-like aminoacids, like the pair usujirene (*Z*)/palythene (*E*) or *Z/E* palythenic acid.^[32]

Additionally, this type of pump-probe experiments were also done studying other natural sunscreens, like eumelanin monomer,^[33] which have an excited state deactivation lifetime in the range of few femtoseconds, being an ultrafast process.

In most of the commercial sunscreens commented in this section, independently from the mechanism, the excited state lifetime is in most cases larger than the measured values for the developed compounds inspired in MAAs. In this case, two different behaviors and relaxation mechanisms seem to be representative in this new prepared set of compounds. On one hand, when the imine moieties include

aromatic residues a measured excited state lifetime between 100 and 800 fs was obtained. On the other hand, the presence of alkyl residues yields in about 500 fs for the lifetime of excited state deactivation. Both mechanisms involve an ultrafast relaxation to the ground state and no intermediate was observed during the irradiation of the sample, exhibiting a great photostability even under irradiation with the high-energy laser pulses used. This study opens a new possibility to select between both mechanisms in function of the chosen substituents. In both cases, no long-live excited state population remains. This fact discards the population of triplet state, also avoiding the generation of reactive oxygen species. According to this ultrafast deactivation, it is expected that these compounds could act as stabilizers for commercial filters like avobenzene, but this feature is not already tested, being the natural step in a further study of possible applications involving these compounds, as it was noted in section 4.3.

As conclusions for this section, a further exploration on the excited state dynamics of the obtained compounds were done in collaboration with Dr. Asier Longarte in the University of País Vasco. Transient absorption spectroscopy and time-resolved fluorescent spectroscopy was used to characterize the evolution of the molecules when a photon is absorbed. In addition, a complementary computational study was performed obtaining a new relaxation pathway in this type of compounds depending on their substitution in the amine-imine moieties. The classical mechanism with an out-of-plane deformation is the reactive path in presence of alkyl residues. However, when aryl substituents are used, a new imine isomerization pathway surges as the reactive path, due to an orbital interaction between the π orbital in the phenyl with the orbital in the iminic nitrogen stabilizing the isomerization path. In addition, a brief overview of the mechanism dynamics of the most relevant commercial sunscreens was done for the sake of comparison.

5.4. Experimental section

5.4.1. Spectroscopic details

The experimental details and characterization for the measured compounds is described in the previous chapter experimental section 4.4.

The femtoseconds TA measurements were conducted in a homemade set-up, where methanol solutions of the problem samples were excited near the corresponding maxima, 306 (**16**), 330 (**13**), 341 (**9**) and 353 (**18**) nm, by the femtosecond laser pulses generated in an OPA (Coherent Operasolo). The evolution of the prepared species was probed by a broadband continuum, covering from 340 to 750 nm, obtained by focusing ($f = 100$ mm fused silica lens) an ~ 1 μ J 800 nm beam on a 2 mm CaF₂ plate. The excitation and probe beams are focused on the sample, after collimation of the latter, by two spherical mirrors with focal lengths of 500 and 250 mm, respectively. Typically, pump energies of 0.5 μ J and spot radii of 200 and 150 μ m at the interaction region were employed for the excitation and probe beams, in that order. The problem methanol solutions, at concentrations from 7 to 8×10^{-4} M were introduced in a 0.3 mm path rotatory cell to reach an absorbance around 0.7. The probe continuum transmitted through the sample, together with a portion of the excitation beam, is focused by a 100 mm lens onto an optical fiber coupled to an Avantes (Avaspec ULS2048XL). In order to extract the photo-induced absorbed signal, a synchronized chopper running at 100 Hz blocks alternatively bursts of ten excitation pulses. The excitation narrowband signal is also recorded to know the status of the excitation and to correct from intensity fluctuations. The data collection and processing are carried out by a Labview written software. Roughly, the average of 3×10^4 laser shots are required to reach sensitivities in the order of 10^{-4} OD.

The pump-probe delay is controlled by a linear translation stage (Thorlabs DDS220) that permits to adjust the probe beam pathway with 0.3 μ m precision. The cross-correlation and the zero-delay time at the different spectral wavelengths is derived from the coherent artifact signal (CAS).^[34] In order to analyze the TA data, first the spectra were aligned to correct from the broadband pulse chirp by using the CAS as a zero delay time reference. The baseline was also corrected by subtracting a spectrum collected at negative time delays.

The femtosecond fluorescence up-conversion experiments were carried out on the same solutions employed for TA by a commercial kit (CDP FOG 100), which has been modified to allow the introduction of an external pump beam from the OPA. This pump is focused by an $f = 60$ mm lens on a rotatory cuvette of 0.3 mm path that contains the same problem solutions described above. The sample emission is collected by a $f = 60$ mm lens and focused by a second one with $f = 150$ mm, on a 0.2 mm thick BBO crystal, where it interacts with an 800 nm beam to generate the up-converted signal. The latter is detected by a photomultiplier coupled to a monochromator (CDP 220D), whose signal is integrated by a BOXCAR (CDP 2021A). For a typical measurement, 5 to 10 delay scans containing 1500 laser shots at each delay position were accumulated. Temporal resolutions around 90 fs were reached at the studied excitation and emission wavelengths.

5.4.2. Computational details

The geometries of the critical points were computed using fully unconstrained *ab initio* quantum chemical computations in the framework of a CASPT2//CASSCF strategy.^[8] This requires the reaction coordinate to be computed at the complete active space self-consistent field (CASSCF) level of theory and the corresponding energy profile to be re-evaluated at the complete active space perturbation theory to the second order (CASPT2) level of theory. Conical intersections (CI) have been located at the CASSCF or CASPT2 level using the method implemented in MOLCAS-8.2.^[9] This method also provides the components of the branching space.^[12] The Gaussian16^[10] program package was used for MP2^[13] computations. The energy of the CASSCF geometries was recalculated using the CASPT2 method implemented in MOLCAS-8.2 to take into account the effect of electron dynamic correlation. All CASPT2 results have been obtained with state average with equal weights for each state. Both CASSCF and CASPT2 calculations have been performed using the standard 6-31G* basis set. Two different active spaces were checked against the experimental data (14,13) and (6,5). In all cases, the chromophore considered included the π density (orbitals π and π^* of bonds C=C, C=N and n N_{imine}). Minimum energy paths (MEPs) were computed at the CASSCF level using the methodology present in MOLCAS-8.2. MEPs representing the steepest descendent minimum energy reaction path were built through a series of geometry optimizations, each requiring the minimization of the potential energy on a

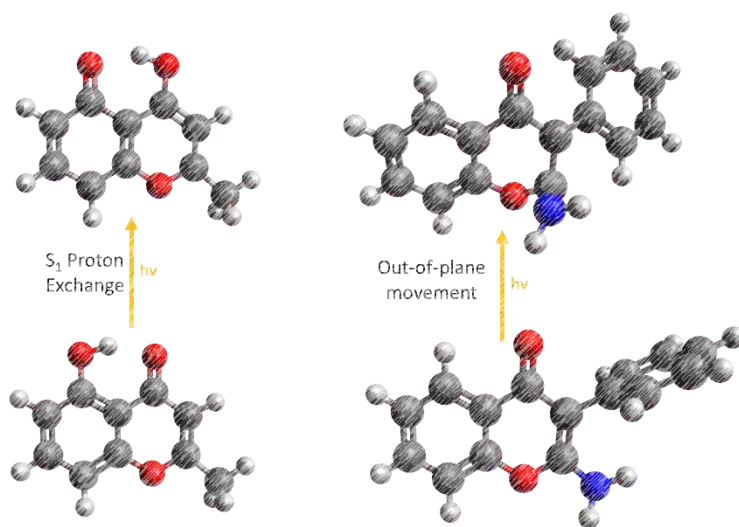
hyperspherical cross section of the potential energy surface centered on a given reference geometry and characterized by a predefined radius. The paths were computed using a value of 0.1 a.m.u. for the steps. Once the first lower energy optimized structure is converged, this is taken as the new hypersphere center, and the procedure is iterated until the bottom of the energy surface is reached. Bulk solvent effects on the UV-spectra have been included using the polarizable continuum model (PCM)^[14] as implemented in MOLCAS-8.2. The molecule is considered as included in a cavity surrounded by an infinite medium with the dielectric constant corresponding to the specific solvent. The standard value of 32.63 for methanol was used in these calculations. The UV-spectra were computed under non-equilibrium conditions, that is, only solvent electronic polarization is in equilibrium with excited-state electron density. Thus, only fast solvent degrees of freedom are considered. This kind of calculations is more adequate to compute vertical excitation energies, as those needed for the UV-spectra. For the computed structures **8** and **9**, the effect of the solvent in the photophysical properties seemed to be negligible. The same has been previously described for palythine^[11] and previously reported MAAs analogues in Chapter 4. Thus, the solvent was not included in the critical points calculations. Thermal conversion was studied using MP2/6-31G*^[15] together with the polarizable continuum model (PCM)^[14] as implemented in Gaussian16.^[10]

5.5. Bibliography

- [1] J. Xu, J. R. Knutson, in *Methods Enzymol.*, Vol. 450, Academic Press, **2008**, pp. 159-183.
- [2] H. Chosrowjan, S. Taniguchi, F. Tanaka, *FEBS J.* **2015**, *282*, 3003-3015.
- [3] F. E. Lytle, R. M. Parrish, W. T. Barnes, *Appl. Spectrosc.* **1985**, *39*, 444-451.
- [4] G. Cerullo, C. Manzoni, L. Lüer, D. Polli, *Photochem. Photobiol. Sci.* **2007**, *6*, 135-144.
- [5] R. Berera, R. van Grondelle, J. T. M. Kennis, *Photosynth. Res.* **2009**, *101*, 105-118.
- [6] C. García-Iriepa, Design, Synthesis and Computational Study of Photoactive Molecular Devices, Doctoral dissertation, University of Alcalá de Henares, **2016**.
- [7] Conference Proceedings, Introduction to time-resolved spectroscopy with applications in biophysics and physical chemistry, **2015**.
- [8] M. Olivucci, *Computational Photochemistry*, Elsevier, Amsterdam, **2005**.
- [9] F. Aquilante, J. Autschbach, R. K. Carlson, L. F. Chibotaru, M. G. Delcey, L. D. Vico, I. F. Galván, N. Ferré, L. M. Frutos, et al., *J. Comput. Chem.* **2016**, *37*, 506-541.
- [10] Gaussian 16, Revision A.03, M. J. Frisch, G. W. Trucks, H. B. Schlegel, G. E. Scuseria, M. A. Robb, J. R. Cheeseman, G. Scalmani, V. Barone, G. A. Petersson, H. Nakatsuji, X. Li, M. Caricato, A. V. Marenich, et al. Gaussian, Inc., Wallingford CT, **2016**.
- [11] D. Sampedro, *Phys. Chem. Chem. Phys.* **2011**, *13*, 5584-5586.
- [12] I. F. Galván, M. G. Delcey, T. B. Pedersen, F. Aquilante, R. Lindh, *J. Chem. Theory Comput.* **2016**, *12*, 3636-3653.
- [13] M. J. Frisch, M. Head-Gordon, J. A. Pople, *Chem. Phys. Lett.* **1990**, *166*, 281-289.
- [14] J. Tomasi, B. Mennucci, R. Cammi, *Chem. Rev.* **2005**, *105*, 2999-3094.
- [15] W. J. Hehre, R. Ditchfield, J. A. Pople, *J. Chem. Phys.* **1972**, *56*, 2257-2261.
- [16] F. Blanco, I. Alkorta, J. Elguero, *Croat. Chem. Acta* **2009**, *82*, 173-183.
- [17] J. M. Woolley, M. Staniforth, M. D. Horbury, G. W. Richings, M. Wills, V. G. Stavros, *J. Phys. Chem. Lett.* **2018**, *9*, 3043-3048.
- [18] M. Yamaji, M. Kida, *J. Phys. Chem. A* **2013**, *117*, 1946-1951.
- [19] A. Cantrell, D. J. McGarvey, *J. Photochem. Photobiol. B* **2001**, *64*, 117-122.
- [20] A. D. Dunkelberger, R. D. Kieda, B. M. Marsh, F. F. Crim, *J. Phys. Chem. A* **2015**, *119*, 6155-6161.
- [21] L. A. Baker, S. E. Greenough, V. G. Stavros, *J. Phys. Chem. Lett.* **2016**, *7*, 4655-4665.
- [22] C. Bonda, A. Pavlovic, *Cosmet. Toiletries* **2010**, *125*, 40-48.
- [23] V. Lhiaubet-Vallet, M. Marin, O. Jimenez, O. Gorchs, C. Trullas, M. A. Miranda, *Photochem. Photobiol. Sci.* **2010**, *9*, 552-558.
- [24] W. Schwack, T. Rudolph, *J. Photochem. Photobiol. B* **1995**, *28*, 229-234.
- [25] L. A. Baker, M. D. Horbury, S. E. Greenough, P. M. Coulter, T. N. V. Karsili, G. M. Roberts, A. J. Orr-Ewing, M. N. R. Ashfold, V. G. Stavros, *J. Phys. Chem. Lett.* **2015**, *6*, 1363-1368.
- [26] M. T. Ignasiak, C. Houée-Levin, G. Kciuk, B. Marciniak, T. Pedzinski, *ChemPhysChem* **2015**, *16*, 628-633.
- [27] P. Zhou, M. R. Hoffmann, K. Han, G. He, *J. Phys. Chem. B* **2015**, *119*, 2125-2131.
- [28] J. L. Herek, S. Pedersen, L. Bañares, A. H. Zewail, *J. Chem. Phys.* **1992**, *97*, 9046-9061.

- [29] K. Sugiyama, T. Tsuchiya, A. Kikuchi, M. Yagi, *Photochem. Photobiol. Sci.* **2015**, *14*, 1651-1659.
- [30] L. A. Baker, M. D. Horbury, S. E. Greenough, F. Allais, P. S. Walsh, S. Habershon, V. G. Stavros, *J. Phys. Chem. Lett.* **2016**, *7*, 56-61.
- [31] N. Tarras-Wahlberg, A. Rosén, G. Stenhagen, O. Larkö, A.-M. Wennberg, O. Wennerström, *J. Investig. Dermatol.* **1999**, *113*, 547-553.
- [32] F. R. Conde, M. O. Carignan, M. Sandra Churio, J. I. Carreto, *Photochem. Photobiol.* **2003**, *77*, 146-150.
- [33] M. F. Nazar, A. Badshah, A. Mahmood, M. N. Zafar, M. R. S. A. Janjua, M. A. Raza, R. Hussain, *J. Phys. Org. Chem.* **2016**, *29*, 152-160.
- [34] B. Dietzek, T. Pascher, V. Sundström, A. Yartsev, *Laser Phys. Lett.* **2007**, *4*, 38.

6. Synthesis and characterization of new sunscreen candidates



Together with the mycosporine-like analogues described in the previous chapters, other different families of sunscreens were synthesized to evaluate their usability as UV filters. In this case, some derivatives based on different promising core structures were obtained. Herein, two new families of compounds were studied mainly in terms of photostability and UV absorptivity. Some simplified chromone structures, and other structurally related set of molecules are presented in this chapter. A theoretical approach was also used to rationalize the different photoprotection mechanisms that rules these new candidates' behavior.

6.1. Chromone and chromenone derivatives

Chromones are an isomer of coumarins, where a 1,4-benzopyrone is the basic scaffold of these molecules.^[1] Usually, chromone derivatives are present in nature in a great number of living organisms, playing many roles ranging from antioxidant to thermoregulation or camouflage.^[2] In addition, these molecules are widely used due to their anti-inflammatory,^[3] antitumor or antioxidant capabilities.^[4] As mentioned before, chromone derivatives are present in a great number of vegetal species and in different families of insects and corals.^[5] They are active metabolites in numerous processes like growth regulation, stimulation of oxygen capture or protection against predators due to their coloration. However, their main role is to act as antioxidants, trapping free radicals,^[6] reducing the risk factor in certain diseases like some types of cancers and coronary affections. Other structurally related compounds are flavonoids,^[7] which are well-known natural molecules with promising UV absorber capabilities.^[8] They also present antioxidant properties, together with their structural isomers, *iso*-flavonoids. In humans, the most extended flavonoid is quercetin, which acts as a precursor in the further obtention of more complex derivatives.

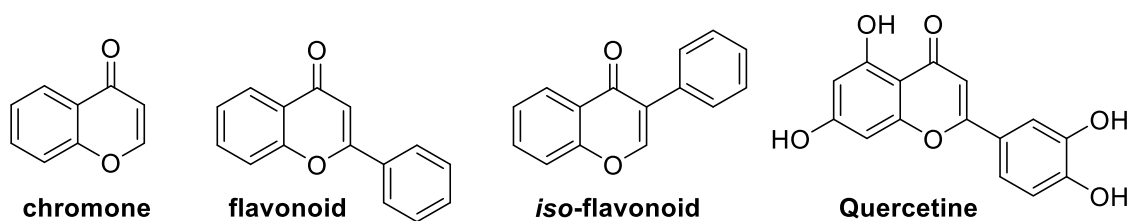


Figure 6.1. Basic scaffolds of chromone and flavonoid derivatives.

Based on these promising capabilities, a new set of molecules inspired on chromone and flavonoid was prepared using synthetic routes as simple as possible. Other more complex procedures were omitted for practical reasons.^[9]

6.1.1 Synthesis of new derivatives

The preparation of some new derivatives based on the basic core structure of 1,4-benzopyrone will be described in this section, aiming to explore the possible differences in the photostability of different chromones depending on their substitution. To achieve this, some derivatives with phenyl or methyl moieties were prepared. This synthesis consists on a single step process but with low reaction yields ranging from 10 to 20%. The following compounds in Figure 6.2 were obtained using the methodology described in the literature, as shown in the following schemes.

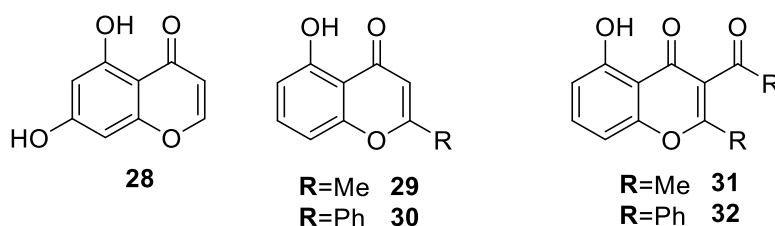
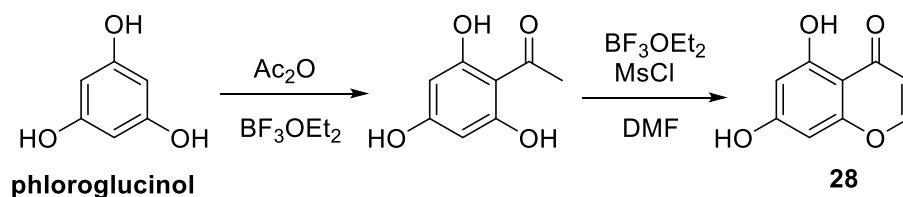


Figure 6.2. Prepared derivatives based on chromone core.

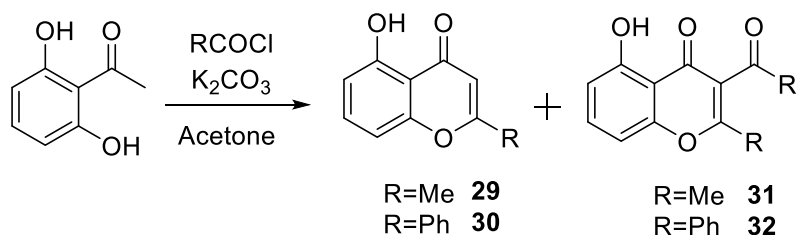
Another set of derivatives were obtained by reaction of salicylic esters with benzyl cyanides in hydride media to afford amino flavonoid derivatives with an amine moiety in the basic *iso*-flavonoid core. In addition, the same structures were obtained changing the pyranic oxygen to a nitrogen yielding in a quinolinone as main structure.

Firstly, the 5,7-dihydroxychromone (**28**) were obtained as shown in Scheme 6.1 with a moderate-low yield, 33%. This synthetic route starts with the Friedel-Crafts acylation of phloroglucinol to afford the acetyl phloroglucinol, which reacts with methane sulfonyl chloride in presence of a Lewis acid (BF_3) to yield the desired product.^[10]



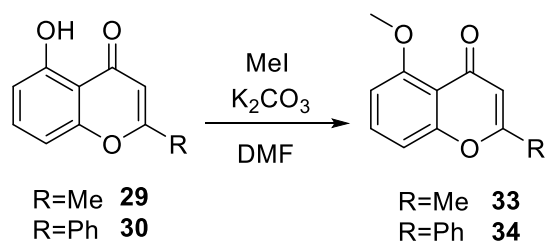
Scheme 6.1. Synthesis of chromone **28**.

Derivatives **29** and **30** were obtained in the same way by reaction of 2,6-dihydroxyacetophenone in presence of potassium carbonate in acetone with the corresponding acetyl chloride or benzoyl chloride, refluxing the mixture for 24 h. In addition, products **31** and **32** were obtained as side products from the double acylation process. These reaction yields are close to 10% and need further improvement, but they could be prepared^[11] in quantities large enough for the characterization and photochemical study.



Scheme 6.2. Obtention of compounds **29-32**.

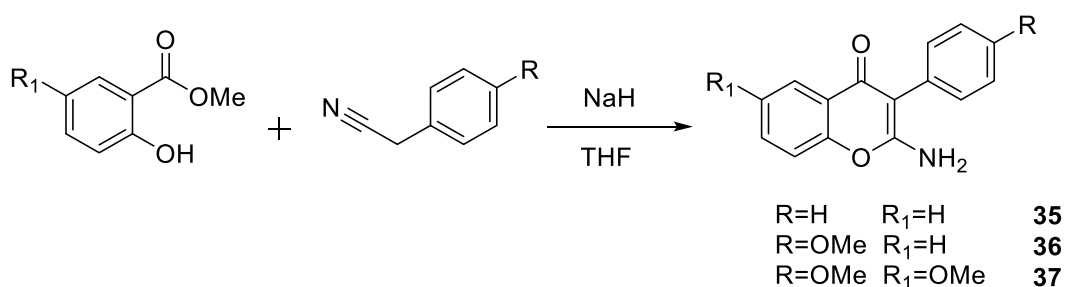
In this type of molecules, a photoprotection mechanism as occurring in benzophenone derivatives is expected. This mechanism was explained in detail in previous chapters. Considering the possible relevance of proton transfer in the photostability of these compounds, functionalization of the hydroxyl group of compounds **29** and **30** was done. Standard procedure involving methyl iodide in dimethylformamide and potassium carbonate as base was used as methylation reaction,^[12] obtaining compounds **33** and **34**, as shown in Scheme 6.3.



Scheme 6.3. Methylation of hydroxyl group to test influence of hydrogen bond.

With this new set of molecules, the relevant factors that could affect photostability were explored. In this type of molecules, as previously mentioned, the relaxation is expected to involve an excited state proton transfer. As a starting point, the influence of the excited-state proton transfer mechanism was studied between the pairs of compounds **29** - **33**, and **30** - **34**; in these cases, a decrease in the photostability of the methylated species is expected.

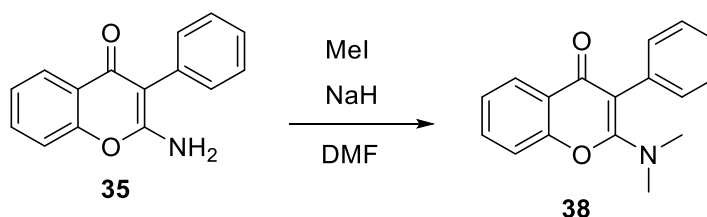
Together with this set of chromone derivatives, exploration of a new family of aminochromone derivatives were accomplished to test their photostability against UV exposure. These novel derivatives could be synthesized departing from methyl salicylate, and other functionalized methyl salicylates. In this, salicylates were treated with sodium hydride in THF solution, after some minutes of stirring, benzyl cyanide derivatives were added and the reaction was allowed to proceed obtaining the desired compounds **35** - **37**.^[13]



Scheme 6.4. Synthesis of new aminochromone derivatives.

These derivatives can be obtained with yields around 60% using cheap raw materials. As the main difference with the previously described compounds, these ones are obtained in a more efficient way, due to the better yield and less side product formation.

Aiming to increase the chemical stability of these molecules, the methylated derivative was prepared by adding methyl iodide and sodium hydride to a stirring solution of derivative **35** in dimethylformamide.



Scheme 6.5. Synthesis of compound **38**.

Following this procedure, different alkylating agents could be used also to increase the solubility in cosmetic oils or organic solvents.

The series of different compounds **28 - 30** and **35 - 37** were synthesized to check the influence of substitution in the pyranic ring and the effect of adding an amino group to the chromophore. Also, the effect of including electron-donating groups in compounds **35 - 37** were studied.

6.1.2. Photochemical and photophysical properties

Once this family of new derivatives is obtained, a further study into their photophysical and photochemical properties to evaluate their capabilities as possible sunscreen candidates was done. We focused specially on their UV absorption and their photostability. In addition, some computational calculations under the time-dependent density functional theory (TD-DFT) framework were performed to better understand the mechanism behind the light absorption and dissipation of energy processes.

Firstly, measurement of the UV-Vis spectra of all the obtained compounds was done. For these samples, solutions around 5×10^{-5} M with acetonitrile or methanol were used due to solubility issues. The UV-Vis spectra will be discussed differentiating between several families. At first place, the spectral properties of compounds **28 to 34** will be discussed. All of them present similar UV-Vis spectra. In all cases the absorption maxima were obtained between 286 and 336 nm, which indicates that all of them are UVB filters, and with moderated ϵ values ranging from 4000 to 8000 $\text{M}^{-1}\text{cm}^{-1}$.

As an example of this family UV spectra, the comparative spectra of compounds **28**, **29** and **33**, and **30** and **34** are shown in Figure 6.3.

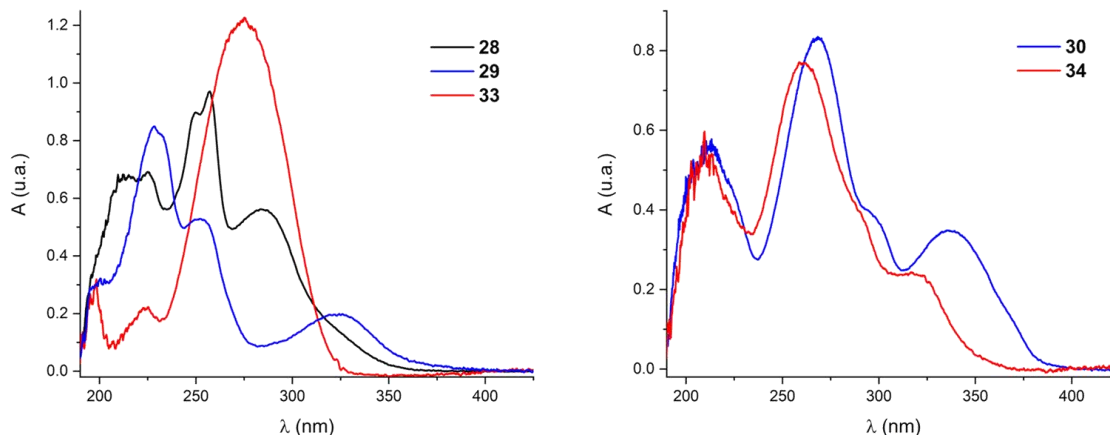


Figure 6.3. UV-Vis spectra of **28**, **29** and **33** (left), and **30** and **34** (right).

Comparing the UV-Vis spectra of these compounds, a redshift in the series between compounds **28**, **29** and **30** was observed, which is a normal behavior and was expected due to the increase in the electronic density of the chromophore with substitution (**28** to **29**) and changing from a methyl group (**29**) to a phenyl ring (**30**). In addition, a blueshift is observed when the methylated compounds **33** and **34** are analyzed. This fact can be better explained with theoretical support (see below), but the absence of the hydrogen bond seems to be responsible for this blue shift.

The spectra of the chromone derivatives **35** - **38**, which were also explored in methanol solutions due to solubility problems in acetonitrile, are plotted in Figure 6.4. Here, the expected behavior was observed when increasing the electronic density of the chromophore by addition of donating groups, as methoxy. In addition, the most remarkable effect appears in the substituted compound **38**, where a redshift of ca. 25 nm respect to the unsubstituted compound **35** is achieved.

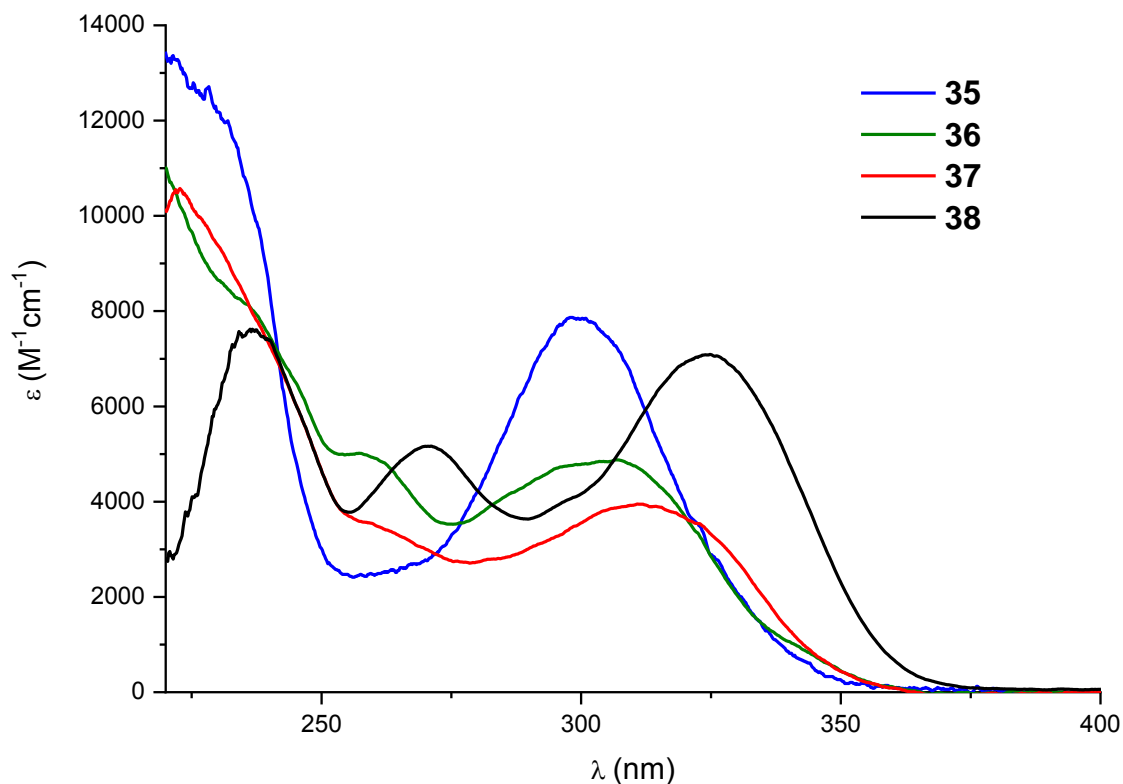


Figure 6.4. UV-Vis spectra of **35-38** in methanol.

These molecules present good properties as UVB absorbers but as mentioned throughout the memory, photostability is a key feature to act as UV filters. If these compounds are photostable, a further study to rationalize the photoprotective mechanism could be performed.

A set of 0.1 M *d*₄-methanol and *d*-chloroform solutions of the samples were irradiated under a 400 W medium-pressure Hg lamp, observing a remarkable photostability in most of the compounds. The percentage of decomposition was calculated by ¹H-NMR by total integration of signals using capped tubes to get reliable measurements without changes in the sample volume.

Solutions were irradiated through a Pyrex filter, which cuts off light more energetic than 280 nm. The measured decomposition for all described compounds is collected in the following tables, split in two because of the different timescale used for each family.

Compound	λ_{nm} (ϵ M ⁻¹ cm ⁻¹)	1h	2h	4h	8h
28	286 (8130)	>95	>95	95	91
29	322 (4480)	93	91	88	83
30	330 (4060)	93	92	90	87
31	336 (7740)	94	94	92	86
32	336 (6780)	93	91	90	89
33	273 (4340)	90	62	24	0
34	317 (5680)	77	59	56	54

Table 6.1. Recovery of the compounds from different irradiation times.

Compound	λ_{nm} (ϵ M ⁻¹ cm ⁻¹)	1h	3h	6h	17h
35	300 (8260)	>95	>95	>95	92
36	307 (4780)	80	78	74	
37	312 (3500)	93	81	73	

Table 6.2. Recovery of the compounds from different irradiation times.

As conclusion from the photostability tests, three different types of performance could be observed. Firstly, some molecules with a remarkable photostability were obtained, like **28** - **32** and **35**, as their recovery values ensure an efficient energy dissipation process. As a result of this, it would be interesting a further study of the mechanisms ruling in both families of derivatives. Compounds **36** and **37** present a moderate photostability with recoveries lower than 80% in 3 hours. In addition, **33** and **34** exhibit a large decomposition under UV irradiation and a decreased photoprotective capacity than the observed for non-methylated derivatives **29** and **30**, proving the importance of the hydrogen bond for the photostability in this system.

6.1.3. Computational study of the photoprotection mechanism

Due to the difference in properties found between the methylated and non-methylated compounds, a relaxation mechanism including an excited state proton transfer should be expected for this type of molecules. For that, a preliminary study on the shape of the PES was performed to evaluate this proposal. In this case, **29** was chosen due to its simple structure and the more adequate λ_{max} , which may favor its use as sunscreen due to its better overlapping with sunlight.

Comparatively, **29** and **33** were computed to evaluate the predicted effect based on the irradiation results. Firstly, an initial evaluation on the energetic distribution of the possible isomers was done at the CAM-B3LYP/6-31++G** level of theory and water as solvent. For **29**, there are two possible isomers depending on the disposition of the hydrogen of the hydroxyl moiety, being the configuration with the intramolecular hydrogen bond (**29** *endo*) favored with an energy difference of 9.7 kcal/mol with respect to the other conformer (**29** *exo*) of the phenolic hydrogen, geometries are depicted in Figure 6.5 for clarity. This feature would not be possible in the methylated compound **33**, which could not form the hydrogen bond and the opposite behavior was observed. In this case, the **33** *exo* disposition of the methyl group is favored, being 10.3 kcal/mol more stable than the **33** *endo* disposition.

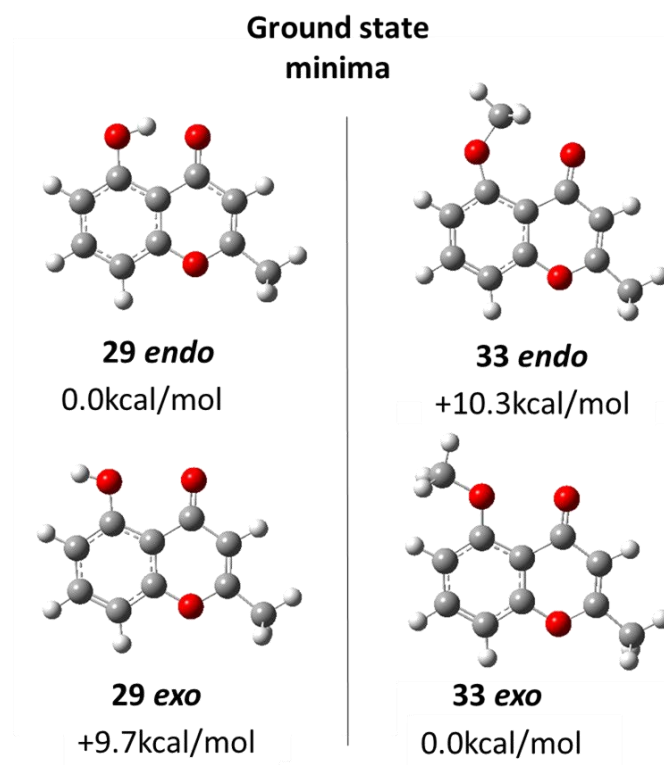


Figure 6.5. Isomers studied of compounds **29** (left) and **33** (right).

For the sake of comparison with experimental UV-Vis data, a series of TD-DFT calculations to get the absorption spectra of the four isomers were done. Looking into the spectral differences between each isomer, a good agreement with the most stable geometry was found in both cases. For **29**, the calculated spectra present a blueshift of ca. 30 nm from the experimental data but matches in shape with the *endo*-isomer. In case of **33**, the calculated spectrum better matches the *exo*-isomer, with only one band and blue shifted from the *endo*-isomer, whose calculated spectrum exhibits two bands and does not fit with the experimental data. With these computed spectra, we also prove that the major isomer in both compounds agrees with the more stable isomer in each case, as it is exposed in Figure 6.6.

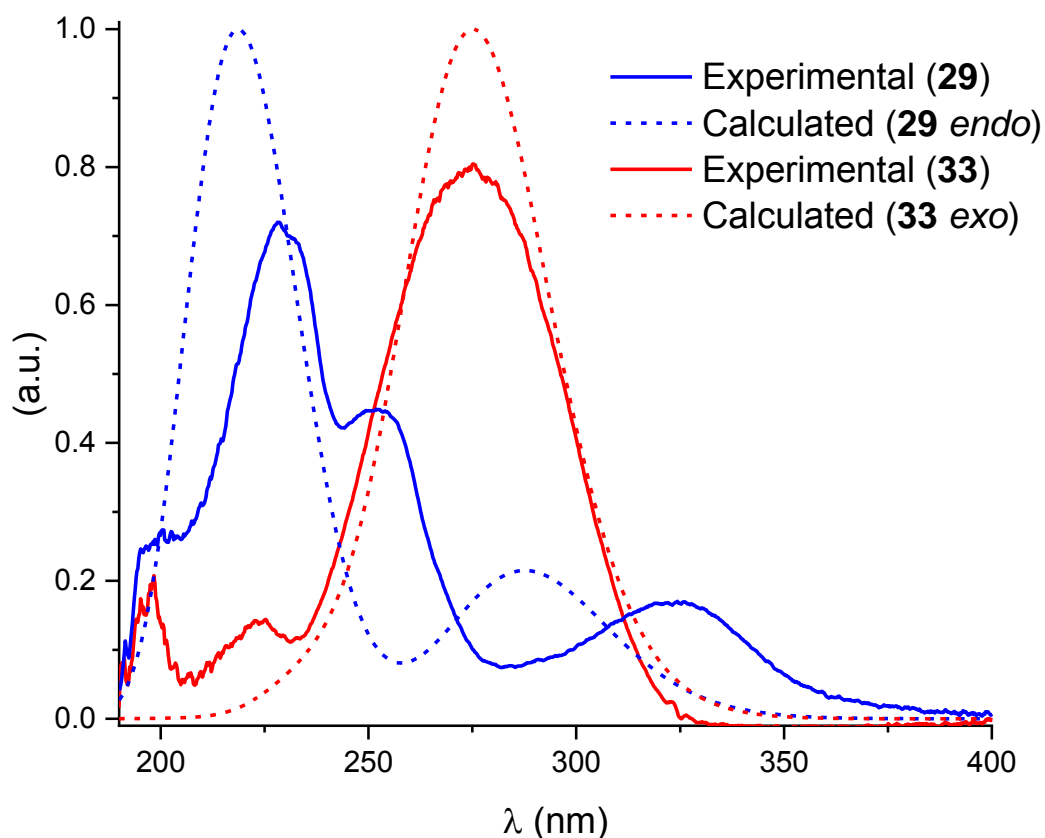


Figure 6.6. Comparative experimental and computed spectra of **29** and **33**.

Regarding the nature of the involved transitions, we also studied the orbitals that are relevant in the UV-Vis spectra. For **29**, the observed band is due to a transition between the HOMO and LUMO orbitals with an oscillator strength of $f = 0.1503$ but blue shifted 30 nm from the experimental value. The orbitals involved in this transition are shown in Figure 6.7.

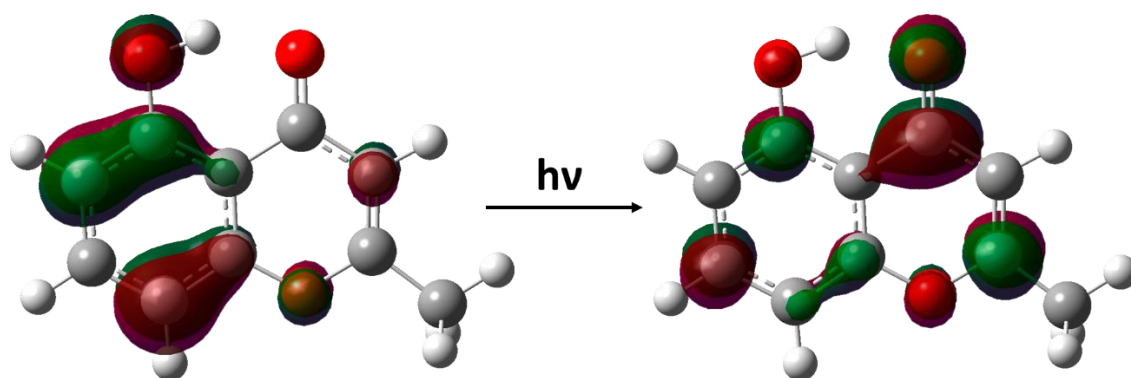


Figure 6.7. Orbitals involved in S_0 - S_1 transition for **29**.

The transition to populate S_1 is an excitation from a π orbital located in the phenyl ring and a small contribution of the n orbital from the oxygen atom to the π^* orbital centered in the *keto* moiety and the phenyl ring. In this system, the photoprotection mechanism clearly resembles the photoinduced proton transfer observed in oxybenzone.^[14] Firstly, optimization from FC relaxing in the excited state was performed to understand the first steps after light absorption. Two minima were reached in the excited state, the first one with a minimal distortion from the FC geometry (**29 keto**). Also, a more stable minimum was reached with the proton over the other oxygen (**29 enol**), see Figure 6.8. This more stable minimum clearly corresponds to the above-mentioned proton transfer mechanism. To prove that, a linear interpolation on internal coordinates (LIIC) calculation was performed to monitor the variation on the PES along the proton migration between both oxygen atoms. A series of ten geometries between both minima in S_1 were interpolated starting from the FC structure of the more stable isomer in ground state (**29 endo**) to the more stable minimum in excited state (**29 enol**). Both geometries and the energy profile along the scanned coordinate can be seen in Figure 6.8.

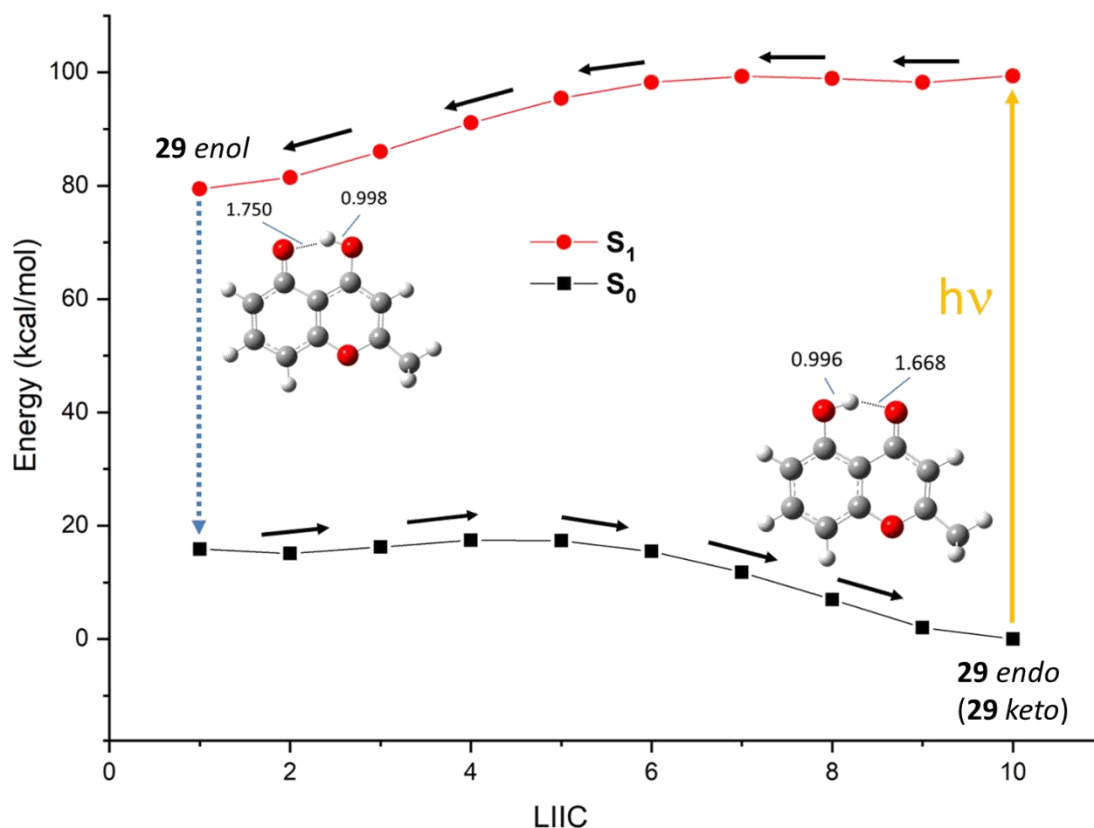


Figure 6.8. LIIC between excited state S_1 minima and FC for **29**. Yellow arrow depicted light absorption process. Blue dashed arrow represents the involved relaxation process to ground state.

The linear interpolation (LIIC) throws an affordable path between both isomers; practically a barrierless path on the excited state PES connects both minima. That is an unambiguous evidence of the viability of that mechanism. On the other hand, the relaxation to ground state was not studied in this preliminary exploration due to the reduced applicability of these derivatives, which present a complex and expensive synthesis. As expected, in the methylated derivative **33** this pathway is not available, drastically decreasing its photostability, as observed experimentally.

Comparatively to the previously described mechanism for **29**, the study of **35** yields, as expected, another type of deactivation channel, due to two main differences between both compounds. Firstly, the change of the methyl to an amino group, which affects the electronic properties of the chromophore, and the suppression of the hydroxyl moiety which prevents the proton intramolecular exchange. Taking into account these changes, the study of the relevant transitions involved in the absorption process was done at the TD-B3LYP/6-31+G** level of theory and including methanol as solvent.

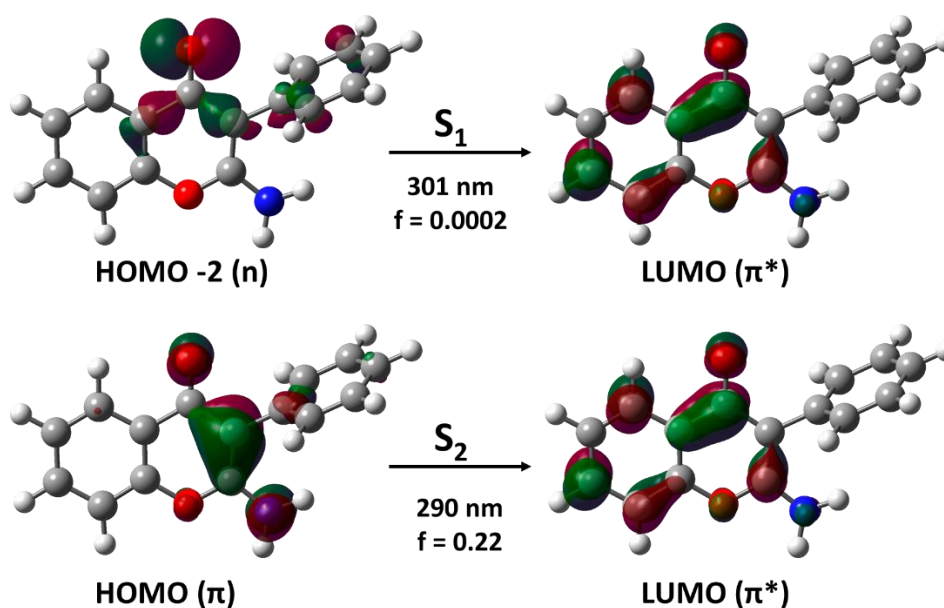


Figure 6.9. Transitions and orbitals involved in the population of excited states.

In this case, the bright state matches to the second excited state S_2 , corresponding to a π - π^* transition, the involved orbitals are shown in Figure 6.9. For the lower in energy S_1 , the population is due to an n - π^* transition from the n orbital of the keto oxygen.

Once light is absorbed and the molecule reached S_2 , a fast relaxation across a "CI" was observed to populate S_1 . Consequently, relaxation yields into a S_1 minimum with a geometrical distortion mainly in the phenyl ring. This minimum in S_1 presents a more coplanar disposition with respect to the FC geometry, see Figure 6.10. It should be noted that the term conical intersection is quoted in this section, which is due to the fact that the TD-DFT method is unable to locate crossing points between different potential energy surfaces. That points can be identified as a consequence of a hop in the order of the states of interest, but not a real crossing point can be computed.

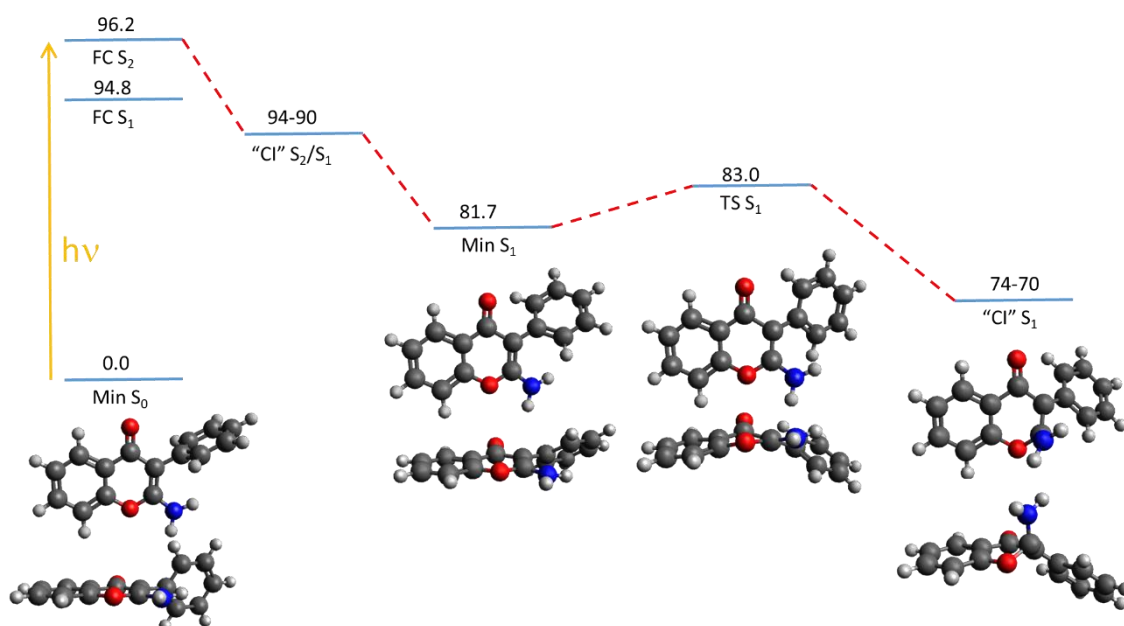


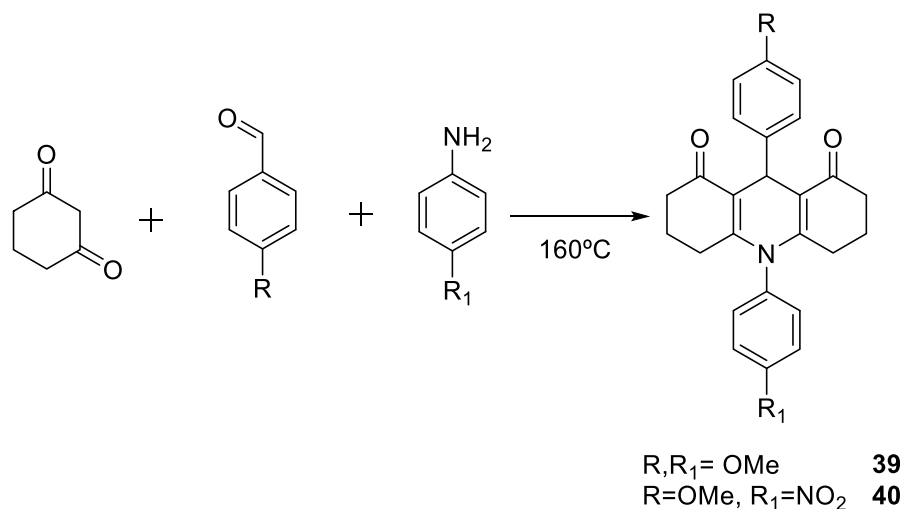
Figure 6.10. Critical points along the PES for **35**.

After the population of this S₁ minimum, a transition state in S₁ surges when an out-of-plane movement of the phenyl and amino moieties is observed. This movement favors the break of the planarity and allow the possibility to reach a new "Cl" where the nitrogen is completely pyramidalized and S₁ and S₀ are basically isoenergetic, permitting the relaxation to the ground state. The proposed mechanism for **35** seems to be interesting, due to the good results in photostability obtained experimentally. For that, some further studies to improve the solar overlap will be done in a near future.

6.2. Other cyclohexanedione derivatives

Other compounds based on the aminocyclohexenone moiety were also prepared. As it was previously rationalized, they are less stable than cyclohexenimine derivatives, but some examples of this system were also studied in order to complement the work described in chapter 4.

Together with these compounds, a different approach from another interesting family of cyclic enaminone derivatives surges as a new alternative. These new molecules can be obtained from the condensation of an aminocyclohexenone in a polycyclic structure, generating a double enaminone-like moiety with a shared nitrogen between two enaminone scaffolds. This is a three cyclic structure, yielding in a less flexible system. With this system, a different deactivation mechanism with respect to the observed for aminocyclohexenones should be obtained due to a geometry more constrained, playing an important role regarding the photostability.



Scheme 6.6. Synthesis of **39** and **40**.

Two derivatives were prepared according to this methodology using a neat and high temperature version of the previously reported methodology.^[15] Also, an improvement in the purification from the previously reported method allowed better results. In this case, a mixture of the reagents with the ratio 2:1:1 was poured into a capped flask. It was heated to 160°C and when the reagents melt, the reaction was allowed to proceed for 5 - 10 minutes. After this time, the desired compound is afforded as a yellowish solid.

Looking to the UV-Vis absorption, these spectra were recorded using 5×10^{-5} M solutions in methanol. In this case, the most remarkable feature observed is a redshift of ca. 50 nm with respect to the previously reported non-cyclic aminocyclohexenone derivatives. In these compounds, the absorption maximum in the interest region is centered between 360 - 370 nm for the two obtained derivatives being UVA filters, as can be seen in Figure 6.11.

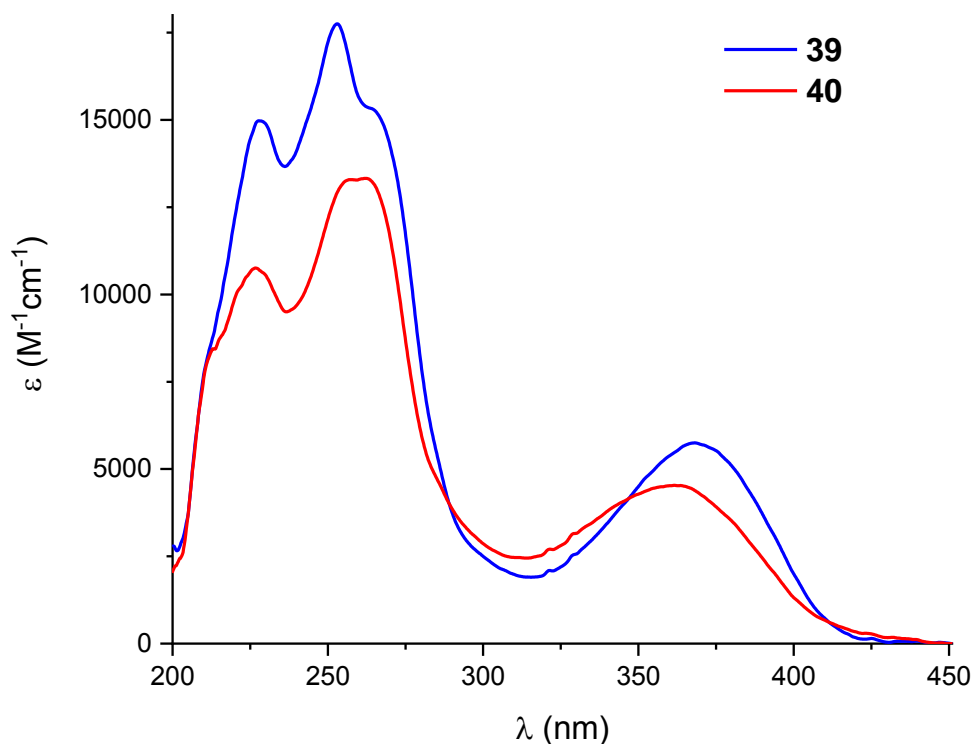


Figure 6.11. UV spectra of **39** and **40**.

This redshifted UV absorption could be an appreciated feature to expand the range of application of all presented compounds added in combination together with this new family of derivatives. These are the compounds with absorption bands at longer wavelength presented in this memory.

Looking into the photostability, some irradiation experiments were conducted as described in the previous section but using chloroform instead of methanol, due to a better solubility of the samples. The measured recovery for both samples is shown in Table 6.3.

6. Synthesis and characterization of new sunscreen candidates

Compound	λ_{nm} (ϵ M⁻¹cm⁻¹)	1h	3h	6h
39	369 (6000)	92%	90%	85%
40	359 (5500)	63%	20%	-

Table 6.3. Photostability (recovery) at different irradiation times.

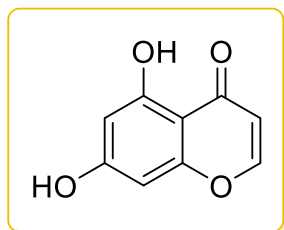
For compound **39** a small decomposition was observed, being about 15% in 6 hours of irradiation in 400 W medium pressure Hg lamp. In contrast, a very fast decomposition was observed in **40**, which decomposes completely in 4 hours.

The generated push-pull like system in **40** was expected to redshift the absorption maxima, but the effect was the opposite, so together with the lower photostability of that compound this result discards its use as sunscreen.

In addition, a further study under the density functional theory framework in conjunction with transient absorption spectroscopy and time-resolved fluorescence experiments will be performed in an attempt to understand the mechanism behind the relaxation of compounds **35** to **40**. This work is being performed in collaboration with Dr. Vasilios Stavros at Warwick University.

6.3. Experimental section and theoretical methods

- 5,7-dihydroxy-4*H*-chromen-4-one (**28**)



Empiric Formula: C₉H₆O₄

Molecular weight: 178.14 g/mol

Yield: 33%

A solution of phloroglucinol and acetic anhydride and BF₃·OEt₂ was stirred for 34 hours at room temperature. After that, a solution of sodium acetate at 10% was added and stirred overnight. Once the yellow solid was filtered out, it was washed with cold water.

To a solution of this compound in dry-dimethylformamide under nitrogen atmosphere, 4.5 equivalents of BF₃·OEt₂ were added allowing to proceed for one hour at room temperature. After that, 3.3 equivalents of mesityl chloride in dry-DMF were added. The resulting solution was heated at 50°C for 4 hours. Once reaction completes, the mixture was poured onto crushed ice and the black precipitate is removed by filtration. The resulting solution is extracted three times with ethyl acetate. The combined organic layers were dried over Na₂SO₄ and the solvent removed under reduced pressure. The obtained residue was purified by silica gel column chromatography using as eluent a mixture of CH₂Cl₂/MeOH in proportion 20:1 to afford the desired product as an orange solid.

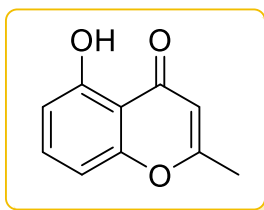
¹H NMR (400 MHz, DMSO-*d*₆) δ ppm 12.69 (s, 1H), 10.85 (s, 1H), 8.17 (d, *J* = 6.0 Hz, 1H), 6.36 (d, *J* = 2.0 Hz, 1H), 6.27 (d, *J* = 6.0 Hz, 1H), 6.20 (d, *J* = 2.0 Hz, 1H).

¹³C NMR (100 MHz, DMSO-*d*₆) δ ppm 181.2, 164.2, 157.7, 157.3, 149.8, 110.4, 104.8, 98.9, 93.9.^[16]

UV-Vis (CH₃CN): λ (nm) = 224 (ε = 11047 M⁻¹cm⁻¹), 257 (ε = 14251 M⁻¹cm⁻¹), 286 (ε = 8128 M⁻¹cm⁻¹).

ES-MS (+) (C₉H₆O₄ + H): calc.179.0339, found 179.0346.

- 5-hydroxy-2-methyl-4*H*-chromen-4-one (**29**)



Empiric Formula: C₁₀H₈O₃

Molecular weight: 176.17 g/mol

Yield: 8%.

5 equivalents of potassium carbonate were added to a solution of 2,6-dihydroxyacetophenone. The mixture was stirred for 15 minutes. After that, one equivalent of acetyl chloride was added heating the mixture for 24 hours at 75°C. Once reaction completes, solvent is removed under vacuum and the residue is dissolved in water, adjusting the pH to 4 by addition of hydrochloric acid 1M. This solution was extracted three times with ethyl acetate. The combined organic layers were dried over Na₂SO₄ and solvent removed under reduced pressure. The obtained residue was purified by silica gel column chromatography using as eluent a mixture of AcOEt/n-hexane in proportion 1:4 to afford the desired product as a yellow solid.

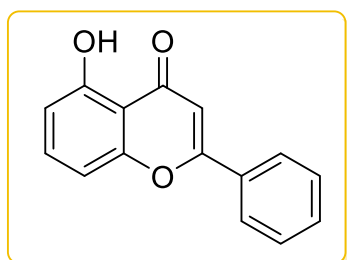
¹H NMR (400 MHz, CDCl₃): δ ppm 12.53 (s, 1H), 7.46 (t, 1H, J = 8.4 Hz), 6.83 (d, 1H, J = 8.0 Hz, 0.8 Hz), 6.74 (dd, 1H, J = 8.0 Hz, 0.8 Hz), 6.08 (s, 1H), 2.37 (s, 3H).

¹³C NMR (100 MHz, CDCl₃): δ ppm 183.4, 167.6, 160.7, 156.7, 135.0, 111.1, 110.3, 109.0, 106.7, 20.5.^[17]

UV-Vis (CH₃CN): λ (nm) = 227 (ε = 17580 M⁻¹cm⁻¹), 252 (ε = 11100 M⁻¹cm⁻¹), 322 (ε = 4480 M⁻¹cm⁻¹).

ES-MS (+) (C₁₀H₈O₃ +H): calc. 177.0546, found 177.0572.

- 5-hydroxy-2-phenyl-4*H*-chromen-4-one (**30**)



Empiric Formula: C₁₅H₁₀O₃

Molecular weight: 238.24 g/mol

Yield: 11%

5 equivalents of potassium carbonate were added to a solution of 2,6-dihydroxyacetophenone. The mixture was stirred for 15 minutes. After that, one equivalent of benzoyl chloride was added heating the mixture for 24 hours at 75°C. Once reaction completes, solvent is removed under vacuum and the residue is dissolved in water, adjusting the pH to 4 by addition of hydrochloric acid 1M. This solution was extracted three times with ethyl acetate. The combined organic layers were dried over Na₂SO₄ and solvent removed under reduced pressure. The obtained residue was purified by silica gel column chromatography using as eluent a mixture of AcOEt/n-hexane in proportion 3:7 to afford the desired product as a yellowish solid.

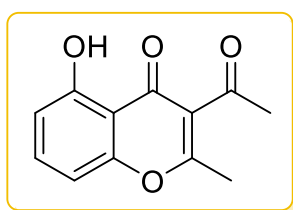
¹H NMR (400 MHz, CDCl₃) δ ppm 12.65 (s, 1H), 8.11 (d, J = 1.6, 2H), 7.68 (d, J = 8.3, 1H), 7.61 (m, 1H), 7.59 (m, 2H), 7.19 (d, J = 8.3, 1H), 7.10 (s, 1H), 6.81 (d, J = 8.3, 1H).

¹³C NMR (100 MHz, CDCl₃) δ ppm 183.2, 164.1, 159.8, 155.9, 135.9, 132.3, 130.5, 129.2, 126.6, 111.0, 110.1, 107.5, 105.7.^[18]

UV-Vis (CH₃CN) λ (nm) = 213 (ε = 12020 M⁻¹cm⁻¹), 267 (ε = 17420 M⁻¹cm⁻¹), 336 (ε = 7740 M⁻¹cm⁻¹).

ES-MS (+) (C₁₅H₁₀O₃ + H): calc. 239.0703, found 239.0712

- 3-acetyl-5-hydroxy-2-methyl-4H-chromen-4-one (**31**)



Empiric Formula: C₁₂H₁₀O₄

Molecular weight: 218.21 g/mol

Yield: 11%

Isolated as side product on the obtention of compound **29** as a yellow solid.

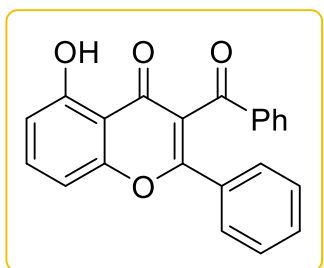
¹H NMR (400 MHz, CDCl₃): δ ppm 12.50 (s, 1H), 7.52 (t, 1H), 6.85 (d, 1H, J = 8.8 Hz), 6.80 (d, 1H, J = 8.8 Hz), 2.60 (s, 3H), 2.50 (s, 3H).^[19]

¹³C NMR (75 MHz, CDCl₃): δ ppm 213.9, 199.1, 181.3, 170.2, 161.0, 155.5, 135.7, 122.1, 112.0, 106.8, 32.3, 20.0.

UV-Vis (CH₃CN): λ (nm) = 262 (ε = 23020 M⁻¹cm⁻¹), 330 (ε = 4060 M⁻¹cm⁻¹).

ES-MS (+) (C₁₂H₁₀O₄ + H): calc. 219.0652, found 219.0656.

- 3-benzoyl-5-hydroxy-2-phenyl-4*H*-chromen-4-one (**32**)



Empiric Formula: C₂₂H₁₄O₄

Molecular weight: 342.35 g/mol

Yield: 10%

Isolated as side product on the obtention of compound **30** as a yellow solid.

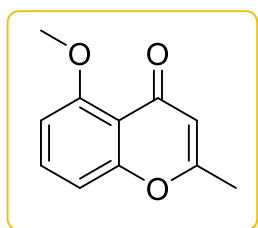
¹H NMR (400 MHz, CDCl₃): δ ppm 12.17 (s, 1H), 7.93 (d, J=7.9 Hz, 2H), 7.59 (m, 4H), 7.48–7.32 (m, 5H), 7.02 (t, J=10.6 Hz, 1H), 6.86 (t, J=8.2 Hz, 1H).^[20]

¹³C NMR (75 MHz, CDCl₃): δ ppm 213.9, 192.5, 181.6, 163.7, 160.8, 156.2, 136.7, 136.1, 135.1, 131.8, 131.1, 129.3, 128.8, 128.8, 128.5, 126.4, 121.0, 111.9, 110.1, 107.5, 77.2, 33.4.

UV-Vis (CH₃CN): λ (nm) = 218 (ε = 17000 M⁻¹cm⁻¹), 262 (ε = 29200 M⁻¹cm⁻¹), 336 (ε = 6780 M⁻¹cm⁻¹).

ES-MS (+) (C₂₂H₁₄O₄ + H) calc. 343.0965, found 343.0970.

- 5-methoxy-2-methyl-4*H*-chromen-4-one (**33**)



Empiric Formula: C₁₁H₁₀O₃

Molecular weight: 190.20 g/mol

Yield: 94%

3 equivalents of methyl iodide and potassium carbonate were added to a solution of **29** in dimethylformamide. After stirring for 24 hours, the solvent was removed under vacuum and the residue dissolved in water and extracted three times with ethyl acetate. The combined organic layers were dried over Na₂SO₄ and the solvent removed under reduced pressure affording the compound as a yellow orangish solid.

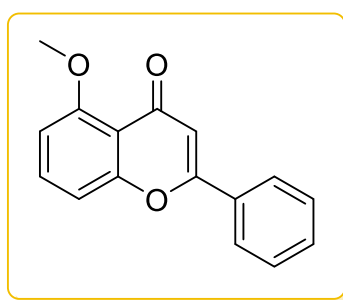
$^1\text{H NMR}$ (300 MHz, CDCl_3) δ ppm 2.27 (s, 3H), 3.93 (s, 3H), 6.04 (s, 1H), 6.75 (d, $J = 8.2$ Hz, 1H), 6.94 (d, $J = 8.5$ Hz, 1H), 7.27 (dd, $J = 8.5, 8.2$ Hz, 1H).

$^{13}\text{C NMR}$ (75 MHz, CDCl_3): δ ppm 19.9, 56.4, 106.3, 109.9, 112.1, 114.2, 133.5, 158.6, 159.7, 163.8, 178.3, 196.1.^[21]

UV-Vis (CH_3CN) λ (nm) = 223 ($\epsilon = 4120 \text{ M}^{-1}\text{cm}^{-1}$), 273 ($\epsilon = 24340 \text{ M}^{-1}\text{cm}^{-1}$).

ES-MS (+) ($\text{C}_{11}\text{H}_{10}\text{O}_3 + \text{H}$): calc. 191.0709, found 191.0713.

- 5-methoxy-2-phenyl-4*H*-chromen-4-one (**34**)



Empiric Formula: $\text{C}_{16}\text{H}_{12}\text{O}_3$

Molecular weight: 252.27 g/mol

Yield: 96%

3 equivalents of methyl iodide and potassium carbonate were added to a solution of **30** in dimethylformamide. After stirring for 24 hours, the solvent was removed under vacuum and the residue dissolved in water and extracted three times with ethyl acetate. The combined organic layers were dried over Na_2SO_4 and the solvent removed under reduced pressure affording the compound as a yellow solid.

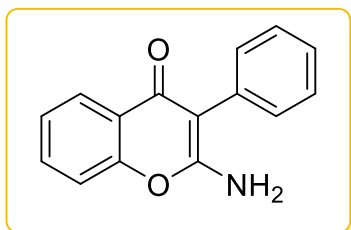
$^1\text{H NMR}$ (400 MHz, $\text{DMSO}-d_6$) δ ppm 8.03 (dd, $J = 2.0, J = 7.6, 2\text{H}$), 7.68 (dd, $J = 8.4, J = 8.4, 1\text{H}$), 7.56 (m, 1H), 7.54 (m, 2H), 7.25 (m, 1H), 6.97 (d, 8.4, 1H), 6.83 (s, 1H), 3.86 (s, 3H).

$^{13}\text{C NMR}$ (400 MHz, $\text{DMSO}-d_6$) δ ppm 176.4, 160.0, 159.1, 157.6, 134.2, 131.5, 130.8, 129.0, 126.0, 113.8, 110.0, 108.4, 107.2, 56.1.^[22]

UV-Vis (CH_3CN) λ (nm) = 208 ($\epsilon = 12620 \text{ M}^{-1}\text{cm}^{-1}$), 260 ($\epsilon = 16340 \text{ M}^{-1}\text{cm}^{-1}$), 317 ($\epsilon = 5680 \text{ M}^{-1}\text{cm}^{-1}$).

ES-MS (+) ($\text{C}_{16}\text{H}_{12}\text{O}_3 + \text{H}$): calc.253.0859, found 253.0867.

- 2-amino-3-phenyl-4*H*-chromen-4-one (**35**)



Empiric Formula: C₁₅H₁₁O₂N

Molecular weight: 237.26 g/mol

Yield: 70%

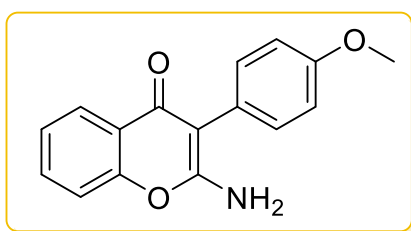
To a suspension of 60% sodium hydride (40 mmol, 4.0 equivalents) in THF (30 mL) were added methyl salicylate (11 mmol, 1.1 equivalents) and benzyl cyanide (10 mmol, 1.0 equivalent). The mixture was stirred at 60 °C until TLC indicated the total consumption of the benzyl cyanide. After cooling, hydrochloric acid (2 N, 20 mL) was added, and the formed precipitate was filtered, washed with AcOEt (3 × 30 mL), and air-dried.^[13]

¹H NMR (300 MHz, MeOD) δ ppm 8.08 (dd, *J* = 7.9, 1.7 Hz, 1H), 7.65 (ddd, *J* = 8.7, 7.2, 1.7 Hz, 1H), 7.54 – 7.28 (m, 7H).

UV-Vis (CH₃CN): λ (nm) = 300 (ε = 8260 M⁻¹cm⁻¹).

ES-MS (+) (C₁₅H₁₁O₂N + H): calc. 238.0863, found 238.0868.

- 2-amino-3-(4-methoxyphenyl)-4*H*-chromen-4-one (**36**)



Empiric Formula: C₁₆H₁₃O₃N

Molecular weight: 267.28 g/mol

Yield: 60%

To a suspension of 60% sodium hydride (40 mmol) in THF (30 mL) were added methyl salicylate (11 mmol) and *p*-methoxybenzyl cyanide (10 mmol). The mixture was stirred at 60 °C until TLC indicated the total consumption of the benzyl cyanide. After cooling, hydrochloric acid (2 N, 20 mL) was added, and the formed precipitate was filtered, washed with AcOEt (3 × 30 mL), and air-dried.

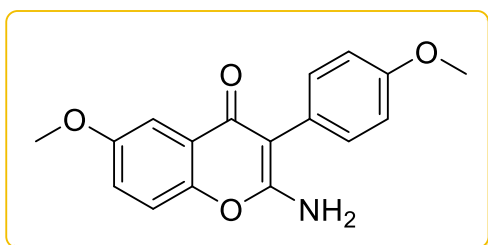
$^1\text{H NMR}$ (300 MHz, MeOD) δ ppm 8.08 (dd, $J = 7.9, 1.6$ Hz, 1H), 7.69 – 7.58 (m, 1H), 7.46 – 7.33 (m, 2H), 7.28 (d, $J = 8.8$ Hz, 2H), 7.03 (d, $J = 8.8$ Hz, 2H), 3.84 (s, 3H).

$^{13}\text{C NMR}$ (75 MHz, MeOD) δ ppm 174.9, 164.2, 159.3, 153.0, 132.1, 132.0, 125.0, 124.4, 124.4, 122.5, 116.2, 114.1, 100.0, 54.3.

UV-Vis (CH_3CN): λ (nm) = 307 ($\epsilon = 4780 \text{ M}^{-1}\text{cm}^{-1}$).

ES-MS (+) ($\text{C}_{16}\text{H}_{13}\text{O}_3\text{N} + \text{H}$): calc. 268.0968, found 268.0970.

- 2-amino-6-methoxy-3-(4-methoxyphenyl)-4*H*-chromen-4-one (**37**)



Empiric Formula: $\text{C}_{17}\text{H}_{15}\text{O}_4\text{N}$

Molecular weight: 297.31 g/mol

Yield: 55%

To a suspension of 60% sodium hydride (40 mmol) in THF (30 mL) were added 4-methoxy methyl salicylate (11 mmol) and *p*-methoxybenzyl cyanide (10 mmol). The mixture was stirred at 60 °C until TLC indicated the total consumption of the benzyl cyanide. After cooling, hydrochloric acid (2 N, 20 mL) was added, and the formed precipitate was filtered, washed with AcOEt (3 × 30 mL), and air-dried.

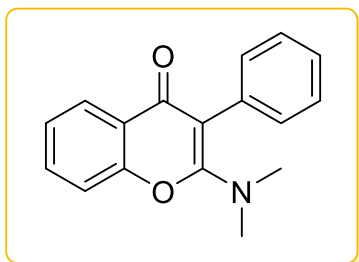
$^1\text{H NMR}$ (300 MHz, CDCl_3) δ ppm 7.63 (d, $J = 3.0$ Hz, 1H), 7.32 (dd, $J = 8.8, 0.7$ Hz, 2H), 7.19 – 7.08 (m, 1H), 6.98 (d, $J = 8.9$ Hz, 1H), 3.88 (s, 3H), 3.82 (s, 3H).

$^{13}\text{C NMR}$ (75 MHz, CDCl_3) δ ppm 161.4, 159.3, 156.8, 147.7, 132.1, 124.4, 121.6, 117.8, 114.8, 106.6, 100.9, 56.1, 55.4.

UV-Vis (CH_3CN): λ (nm) = 312 ($\epsilon = 3500 \text{ M}^{-1}\text{cm}^{-1}$).

ES-MS (+) ($\text{C}_{17}\text{H}_{15}\text{O}_4\text{N} + \text{H}$): calc. 298.1074, found 298.1068.

- 2-(dimethylamino)-3-phenyl-4*H*-chromen-4-one (**38**)



Empiric Formula: C₁₇H₁₅O₂N

Molecular weight: 265.31 g/mol

Yield: 95%

To a suspension of 60% sodium hydride (3.0 mmol) in DMF were added 1 mmol of compound **35** and methyl iodide (3 mmol). The mixture was stirred overnight at room temperature. After cooling, diluted hydrochloric acid was added to neutralize the mixture and the aqueous solution extracted three times with AcOEt. The combined organic layers were dried over Na₂SO₄ and solvent removed under reduced pressure affording the compound as a yellowish solid.

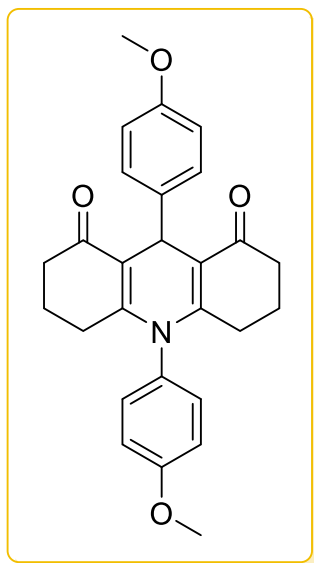
¹H NMR (300 MHz, MeOD) δ ppm 8.06 (dd, *J* = 7.9, 1.3 Hz, 1H), 7.66 (ddd, *J* = 8.8, 7.2, 1.7 Hz, 1H), 7.57 – 7.08 (m, 7H), 2.85 (s, 6H).

¹³C NMR (75 MHz, MeOD) δ ppm 177.7, 163.8, 154.5, 135.8, 133.8, 132.6, 129.2, 128.0, 126.4, 125.9, 123.6, 117.6, 104.0, 40.7.

UV-Vis (CH₃CN): λ (nm) = 320 (ε = 7600 M⁻¹cm⁻¹).

ES-MS (+) (C₁₅H₁₁O₂N + H): calc. 266.1176, found 266.1180.

- 9,10-bis(4-methoxyphenyl)-3,4,6,7,9,10-hexahydroacridine-1,8(2*H*,5*H*)-dione
(39)



Empiric Formula: C₂₇H₂₇O₄

Molecular weight: 429.52 g/mol

Yield: 90%

A mixture of 1 mmol of 1,3-cyclohexanedione, 0.5 mmol of *p*-anisidine and 0.5 mmol of *p*-anisaldehyde, with a ratio 2:1:1, was poured into a capped flask with a magnetic stirrer. It was heated to 160°C and when the reagents melt, the reaction was allowed to proceed for 5 minutes. After this time, the flask was cooled to room temperature and the inner solid was triturated with AcOEt to afford the desired compound as a yellowish solid.

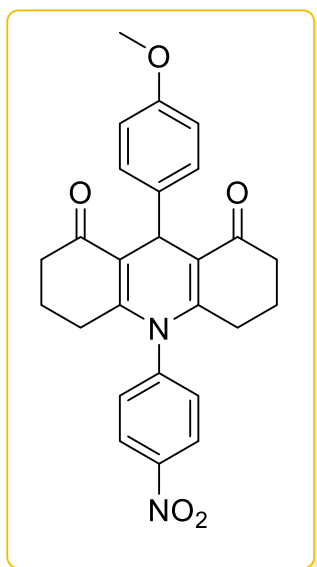
¹H NMR (400 MHz, CDCl₃) δ ppm 7.33 (d, *J* = 8.6 Hz, 2H), 7.16 (d, *J* = 9.1 Hz, 2H), 7.00 (d, *J* = 8.9 Hz, 2H), 6.80 (d, *J* = 8.7 Hz, 2H), 5.32 (s, 1H), 3.88 (s, 3H), 3.76 (s, 3H), 2.59 – 1.98 (m, 8H), 1.97 – 1.65 (m, 4H).

¹³C NMR (75 MHz, CDCl₃) δ ppm 196.2, 159.8, 157.7, 152.0, 139.1, 131.5, 130.8, 130.1, 128.6, 115.5, 115.1, 114.7, 113.5, 55.6, 55.1, 36.8, 31.1, 28.2, 21.1.

UV-Vis (CH₃CN): λ (nm) = 369 (ε = 6000 M⁻¹cm⁻¹).

ES-MS (+) (C₂₇H₂₇O₄ + H): calc. 430.2013, found 430.2013.

- 9-(4-methoxyphenyl)-10-(4-nitrophenyl)-3,4,6,7,9,10-hexahydroacridine-1,8(2*H*,5*H*)-dione (**40**)



Empiric Formula: C₂₆H₂₄O₅N₂

Molecular weight: 444.49 g/mol

Yield: 80%

A mixture of 1 mmol of 1,3-cyclohexanedione, 0.5 mmol of *p*-nitroaniline and 0.5 mmol of *p*-anisaldehyde, with a ratio 2:1:1, was poured into a capped flask with a magnetic stirrer. It was heated to 160°C and when the reagents melt, the reaction was allowed to proceed for 5 minutes. After this time, the flask was cooled to room temperature and the inner solid was triturated with AcOEt to afford the desired compound as a yellowish solid.

¹H NMR (400 MHz, CDCl₃) δ ppm 8.42 (d, *J* = 8.8 Hz, 2H), 7.50 (d, *J* = 8.8 Hz, 2H), 7.31 (d, *J* = 8.7 Hz, 2H), 6.81 (d, *J* = 8.7 Hz, 1H), 5.32 (s, 1H), 3.76 (s, 3H), 2.57 – 2.04 (m, 8H), 2.08 – 1.68 (m, 4H).

¹³C NMR (75 MHz, CDCl₃) δ ppm 196.0, 158.1, 150.0, 148.1, 145.0, 138.5, 131.3, 128.7, 125.3, 116.5, 113.8, 55.3, 36.8, 31.3, 28.5, 21.2.

UV-Vis (CH₃CN): λ (nm) = 359 (ε = 5500 M⁻¹cm⁻¹).

ES-MS (+) (C₂₆H₂₄O₅N₂ + H): calc. 445.1758, found 445.1751.

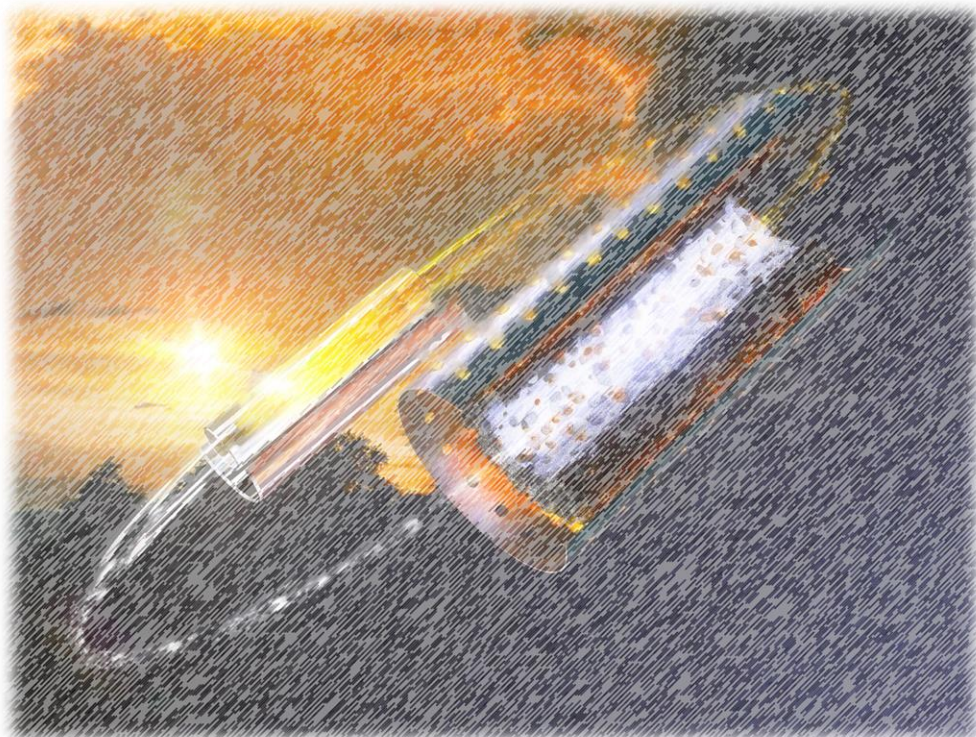
6.3.1 Computational details

Time dependent density functional theory (TD-DFT)^[23] calculations were performed using the Gaussian16^[24] software. In this chapter, the TD-CAM-B3LYP^[25]/6-31++G**^[26] level of theory was used for chromone derivatives **29** and **33** and the TD-B3LYP/6-31+G**^[26] for aminochromone derivative **35**. The computed UV-Vis spectra were done using 5 states and including solvent effects by the polarizable continuum model (PCM)^[27] using water and methanol, respectively. In both cases the standard ϵ_r value of 78.355 and 32.613 were used. The crossing points founds are detected by the change of the involved states order, yielding in an energy gap and not a specific value. Relative energies of the different isomers are calculated using the free energy term. All critical points in the PES were characterized with frequency calculations to include ZPE and free energy corrections and verified the stationary points as transition states (one imaginary frequency) or minima (zero imaginary frequencies).

6.4. Bibliography

- [1] C. Wiart, in *Lead Compounds from Medicinal Plants for the Treatment of Cancer* (Ed.: C. Wiart), Academic Press, **2013**, pp. 1-95.
- [2] S. Khadem, R. J. Marles, *Molecules* **2011**, *17*, 191–206.
- [3] R. G. Naik, S. L. Kattige, S. V. Bhat, B. Alreja, N. J. de Souza, R. H. Rupp, *Tetrahedron* **1988**, *44*, 2081-2086.
- [4] G. Kaur, M. S. Alam, Z. Jabbar, K. Javed, M. Athar, *J. Ethnopharmacol.* **2006**, *108*, 340-348.
- [5] G. P. Ellis, in *The Chemistry of Heterocyclic Compounds, Vol. 31*, Wiley, New York, **1977**, pp. 11–139.
- [6] Y. Hanasaki, S. Ogawa, S. Fukui, *Free Radical Biol. Med.* **1994**, *16*, 845-850.
- [7] A. N. Panche, A. D. Diwan, S. R. Chandra, *J. Nutr. Sci.* **2016**, *5*, e47.
- [8] A. Takahashi, T. Ohnishi, *Biol. Sci. Space* **2004**, *18*, 255-260.
- [9] M. A. Brimble, J. S. Gibson, J. Sperry, in *Comprehensive Heterocyclic Chemistry III* (Eds.: A. R. Katritzky, C. A. Ramsden, E. F. V. Scriven, R. J. K. Taylor), Elsevier, Oxford, **2008**, pp. 419-699.
- [10] G. Wei, B. Yu, *Eur. J. Org. Chem.* **2008**, *2008*, 3156-3163.
- [11] S. Okombi, J. Schmidt, A. M. Mariotte, E. Perrier, A. Boumendjel, *Chem. Pharm. Bull.* **2005**, *53*, 1460-1462.
- [12] L. Cai, R. Xu, X. Guo, V. W. Pike, *Eur. J. Org. Chem.* **2012**, *7*, 1303-1310.
- [13] J. Sun, D. Zhang-Negrerie, Y. Du, K. Zhao, *J. Org. Chem.* **2015**, *80*, 1200-1206.
- [14] T. N. V. Karsili, B. Marchetti, M. N. R. Ashfold, W. Domcke, *J. Phys. Chem. A* **2014**, *118*, 11999-12010.
- [15] P. Sarkar, C. Mukhopadhyay, *Green Chemistry* **2016**, *18*, 6556-6563.
- [16] S. K. Yadav, *Int. J. Org. Chem.* **2014**, *4*, 236-246.
- [17] J. Liu, Z. Li, P. Tong, Z. Xie, Y. Zhang, Y. Li, *J. Org. Chem.* **2015**, *80*, 1632-1643.
- [18] Y. Park, B.-H. Moon, E. Lee, Y. Lee, Y. Yoon, J.-H. Ahn, Y. Lim, *Magn. Reson. Chem.* **2007**, *45*, 674-679.
- [19] T. Javed, S. S. Kahlon, *J. Heterocycl. Chem.* **2002**, *39*, 627-630.
- [20] C. F. Chee, M. J. C. Buckle, N. A. Rahman, *Tetrahedron Lett.* **2011**, *52*, 3120-3123.
- [21] A. Y. Shaw, C.-Y. Chang, H.-H. Liao, P.-J. Lu, H.-L. Chen, C.-N. Yang, H.-Y. Li, *Eur. J. Med. Chem.* **2009**, *44*, 2552-2562.
- [22] S. Lee, B.-H. Moon, Y. Park, E. Lee, S. Hong, Y. Lim, *Bull. Korean Chem. Soc.* **2008**, *29*, 1793-1796.
- [23] G. Scalmani, M. J. Frisch, B. Mennucci, J. Tomasi, R. Cammi, V. Barone, **2006**, *124*, 094107.
- [24] Gaussian 16, Revision A.03, M. J. Frisch, G. W. Trucks, H. B. Schlegel, G. E. Scuseria, M. A. Robb, J. R. Cheeseman, G. Scalmani, V. Barone, G. A. Petersson, H. Nakatsuji, X. Li, M. Caricato, A. V. Marenich, et al. Gaussian, Inc., Wallingford CT, **2016**.
- [25] T. Yanai, D. P. Tew, N. C. Handy, *Chem. Phys. Lett.* **2004**, *393*, 51-57.
- [26] W. J. Hehre, R. Ditchfield, J. A. Pople, *J. Chem. Phys.* **1972**, *56*, 2257-2261.
- [27] J. Tomasi, B. Mennucci, R. Cammi, *Chem. Rev.* **2005**, *105*, 2999-3094.

7. Molecular Energy Storage Systems



7.1. MOST concept and relevant systems

Nowadays, availability of energy sources, like fossil fuels, is becoming a problem due to the high energy demand from industries and transports.^[1] According to the described in different energy reports,^[2] renewable energies contributed in 18.1% to humankind global energy consumption, also representing a 24.5% of electricity generation in 2016. This energetic consumption can be divided according to the source. A 7.5% comes from traditional biomass, 4.2% as heat energy (modern biomass, geothermal and solar heat), 3.6% from hydroelectricity and the remaining 2% is electricity from wind, solar and other forms of biomass. However, with less than a 20% of the total energy consumption, a real sustainable alternative to fossil fuels or nuclear energy is not yet provided.

For that, scientists have largely endeavored the challenge of getting a new energy source environmentally friendly, durable and economic. As mentioned during the Background section 2.1, the sun is a practically unlimited energetic alternative. In Earth, a huge amount of energy is coming from the sun yearly.^[3] Apart from all the processes where sunlight is involved, as photosynthesis, plant growth or some other metabolic transformations, a great part of these radiant energy is lost as heat, increasing oceanic water and earth surface temperature, or simply reflected as albedo radiation. Solar exploitation represents only around 2% of the global energy consumption. The most typical way to use solar energy at present is obtaining electricity from it. For that purpose, the photovoltaic (PV) input,^[4] followed by concentrating solar power, are the most used strategies. The concentrating solar power (CSP) consists of a series of reflective mirrors focused on a unique point, which concentrates all the solar power to yield in electricity by thermal procedure.^[5] In 2017, Spain had almost half of the world's capacity, being the world leader in CSP.^[6] The other alternative and the most common is photovoltaics. The used devices, so-called solar panels or solar cells consist of a semiconductor material. This technology is based on the photoelectric principle generating electricity due to the interaction of light and a semiconductor material.

In contrast, photovoltaic systems present evident problems to get a continuous energy flow.^[7] To solve this issue, arises the idea of solar energy storage.^[8] The most usual procedure is to store the electrical energy produced by PV or CSP, but by now the needed technology has not been widely implemented for a large-scale utilization. This

7. Molecular energy storage systems

is a consequence of its high cost and the limited energy storage time. Regarding other renewable energy sources, similar problems arise as their geographical, seasonal and storage limitations, making it a non-efficient alternative to provide a time-constant energy flux, limiting their practical use by the need of an alternative energy source to supply during the non-effective periods of these sources.^[9]

There are a great number of approaches to store the solar energy; the simplest is probably hot water or the use of molten salts, which albeit scientifically simple, suffer from the fact that the storage medium must be kept extremely well insulated to avoid thermal losses.^[10] A further development of this energy storage technology surges with the involution of solar driven thermally activated reactions, such as cracking of dicyclopentadiene^[11] or store it in high energy molecular bonds. This issue is currently being studied using several approaches, such as photoinduced water splitting^[1, 10] or CO and CO₂ reduction.^[1, 10] But other systems are usable, like photoswitches,^[12, 13] that can be classified in two main types: those based on an *E/Z* isomerization and those based on cyclization. These systems present some practical advantages, like temporal and spatial resolution and lack of wastage products.^[14] Mainly, photoswitches have been used to control and modify some molecular properties like a peptide conformation^[15] or the structure of liquid crystals.^[16] As the general behavior, these applications rely on light absorption to interconvert the system between two different states and typically, a thermal back reversion occurs at different temperatures. In this novel approach to store solar energy, the difference between both isomers is crucial to get a reliable energy storage capacity^[17] together with the ability to release the energy with a controlled trigger. This concept is known as MOST,^[7] molecular solar thermal, that consists of the storage of sun energy as a high-energy compound for a long time, being able to obtain that energy according to required demands. Nowadays, this research field has become relevant due to the important energy problem that we will face in the near future.^[1] In a MOST energy storage, a chemical compound undergoes a light-induced chemical reaction to form a metastable product. In contrast to a solar fuel, the storage medium is recycled by passage over a catalyst to regenerate the solar harvesting medium with the evolution of heat.

As can be seen in Figure 7.1, a MOST implemented system is used to heat a house, converting the parent molecule (A) in the solar collectors to the photoisomer (B), which is collected and stored in a reservoir. This solution of B is pumped through a catalyst bed to release as heat the stored energy and warm the water to heat the house. After one cycle of usage, the parent molecule is recovered and can initiate the working flow again.

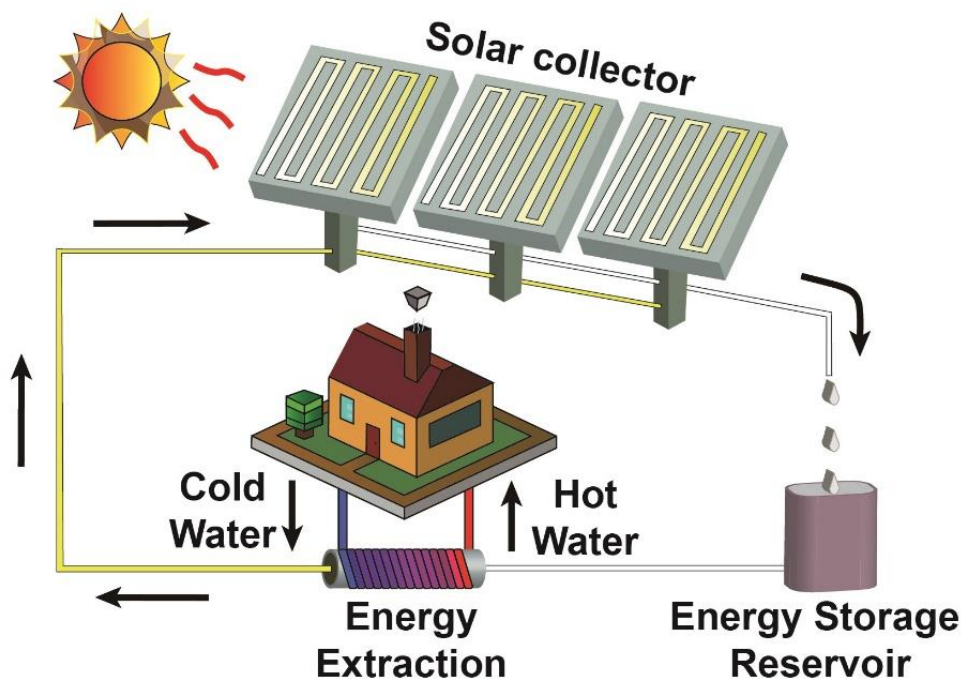


Figure 7.1. Schematic implementation of a MOST system. Adapted from *Energy Environ. Sci.*, 2019,12, 187-193.^[18]

Once explained the MOST concept, the definition of the critical features that a suitable system should exhibit is mandatory before developing working candidates. The desirable features can be divided according to four main criteria and should be fulfilled for a successful MOST system. Each criterion represents an engineering challenge almost by itself, so a combination of all the requirements is very grueling to reach for a single molecule. A summary of these desired criteria can be seen in Figure 7.2.

7. Molecular energy storage systems

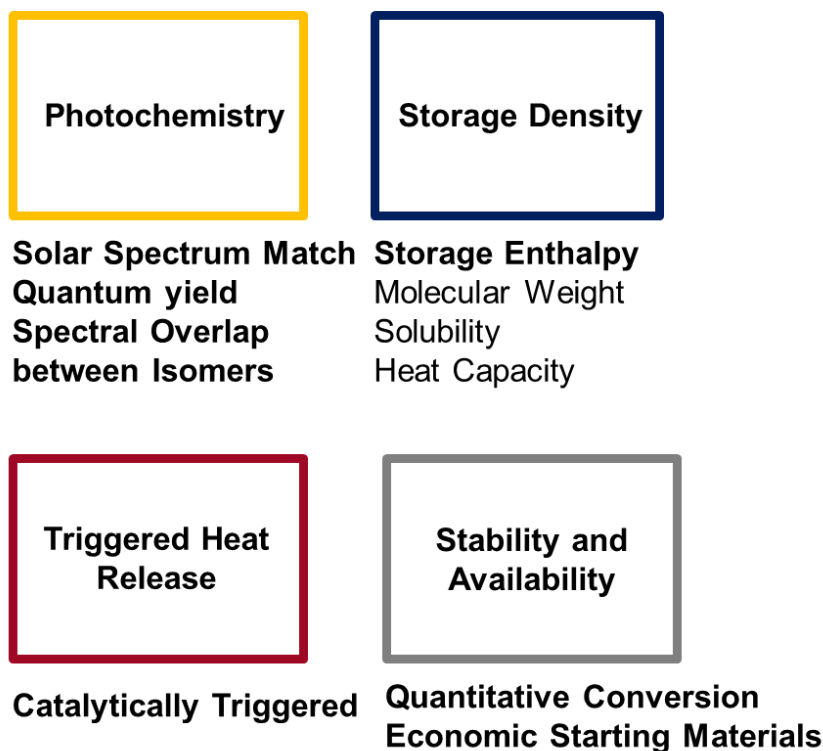


Figure 7.2. Design criteria for a MOST system.^[8]

The first criterion regarding the photochemistry is related to three parameters: the solar spectrum match, isomers overlap and isomerization quantum yield. The solar spectrum match is one of the main challenges in all types of solar exploitation technologies. As shown in the solar spectrum in Figure 2.1, half of the energy is centered in the UV and Visible wavelengths (300 - 700 nm). From the point of view of efficiency, obtaining a broad absorption along all this range is almost impossible, so maximizing the absorption capacity in this region is the most desirable behavior. For that, an increase of the π density or the use of a donor-acceptor (push-pull) system are the usual ways to improve the solar match.^[19] The spectral overlap between isomers should be minimum to avoid a simultaneous absorption and allow the use of high optical density solutions. Also, thinking on the efficiency, a high isomerization or photoreaction yield is needed instead of the presence of other radiative or non-radiative deactivation processes, as fluorescence or internal conversion.

The second criterion is about the energy storage capacity, where several factors are important for a MOST system. The obtainable change in the temperature depends on the enthalpy difference ($\Delta H_{\text{storage}}$) in J/g and the specific heat capacities of the involved molecules or solvents. To obtain the greatest ΔT , minimization of the amount

of solvent and the molecular weight of the compounds, and the maximization of the $\Delta H_{\text{storage}}$ should be achieved. Ideally, $\Delta H_{\text{storage}} > 300 \text{ J/g}$ is desirable to obtain a greater capacity than the obtained for water (209 J/g) or salt hydrates with 250 J/g.^[20]

The third criterion is heat release, or how to trigger the liberation of the stored energy. For that, the photoisomer needs to be stable for extended periods of time. Therefore, a high-energy barrier for the back-conversion is needed to avoid the recovery of the parent molecule. To trigger this process, an external stimulus is the optimal way due to the greater control over the process that offers. For that reason, a catalyzed reaction in heterogeneous phase is the most desirable for a simplified device design and implementation.^[7]

The fourth criterion concerns the molecular stability and availability. Considering the previously described challenges and looking for an ideal implementation, a strong stability and also photostability are indispensable for a MOST system. It should be stable along a great number of interconversion experiments between both isomers (**A** and **B**). Also, the availability of the molecule should facilitate a feasible implementation due to lower costs and easier synthesis from inexpensive materials.

To sum-up the key characteristics for a MOST system, Figure 7.3 represents the schematic work of a parent molecule **A** photoisomerized to **B**. This **B** isomer could be reverted to **A** through the non-catalyzed path (ΔH_{therm}) or through the catalyzed one (ΔH_{cat}) releasing in both ways the stored energy.

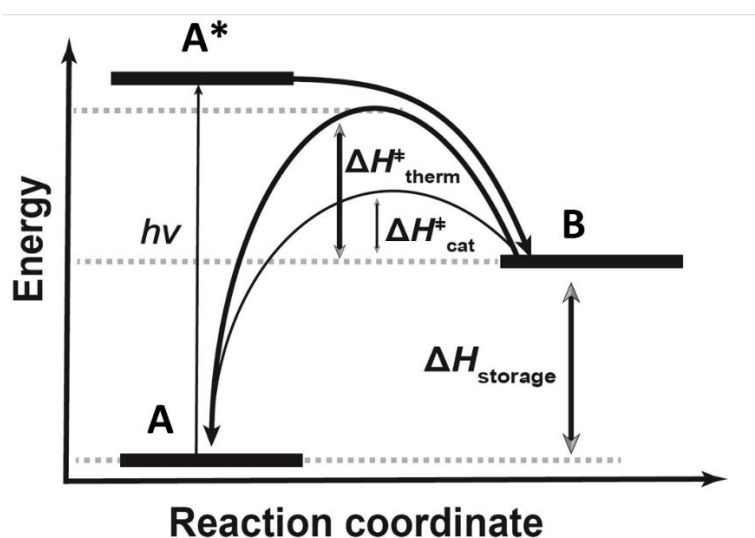


Figure 7.3. Reaction mechanism of a MOST system interconverting between **A** to **B**.^[18]

Considering the most typically explored molecular systems to be used as MOST, the main part of it as previously described are photoswitches. Mainly they can be divided in two categories depending on the interconversion mechanism: isomerization or cycloaddition. In addition, the intramolecular rearrangements in organometallic diruthenium fulvalenes were also studied.^[21]

In the first category stilbenes, azobenzenes and other families of *cis-trans* photoswitches could be included, as it will be described below. Stilbenes or stilbene-like compounds have been considered as potential MOST candidates.^[22] The double bond isomerization of the basic stilbene yields in an energy difference of only 5 kJ/mol, but two strategies arose to increase it. Stabilization of *E*-isomer happens when increasing the electronic delocalization, together with a destabilization of the *Z*-isomer due to steric interactions between vicinal groups. As can be seen in Figure 7.4, an increment near to a hundred kJ/mol can be reached following these strategies.^[23]

The secondly most used *cis-trans* photoswitch is azobenzene, being the most studied photoswitch from its discovery in 1937. The most recent attempt for the design of new azobenzene derivatives as MOST was developed by Grossman mainly from a theoretical point of view.^[24, 25] In that contribution, azobenzene derivatives were supported in carbon nanotubes reaching an energy storage increased around a 30% and global energy densities comparable to the presently available with lithium ion batteries.^[24] The challenging synthetic attempts revealed that the obtained substitution rate on nanotubes is much lower than the theoretically predicted azobenzene densities, obtaining almost the same results as free azobenzene.^[26] Also, a thin film material with azobenzene unities bounded to a polymeric backbone was obtained.^[27] From a computational perspective, some macrocyclic polyazobenzene were studied exhibiting energy densities of *ca.* 600 kJ/kg.^[28] The effect of substitution in bisdiazobenzenes (Figure 7.4) was also studied, finding lower isomerization quantum yields. In addition, a novel liquid azobenzene derivative was obtained in Japan a few years ago.^[29] In this case, the inclusion of large chains turns the compound into a liquid. Used as a neat liquid, the maximum energy density increases in these solvent free conditions. Similar behavior is postulated with azobenzene based ionic liquids.

Other examples have been described but have been explored less thoroughly. Some indigo derivatives with lower quantum yields than azobenzene and stilbene were reported.^[30] In our research group some of the studied families of photoswitches were

7. Molecular energy storage systems

proved as MOST prototypes but a low storage enthalpy was achieved in all cases.^[31] In this case, a series of retinal-based switches were studied, mainly focusing on the back-conversion reaction. These barriers can be tuned in function of the pH of the medium; neutral compounds easily revert at room temperature and in contrast protonated forms are stable for 6 days. In addition, absorption maxima can be adjusted in function of the substituents.

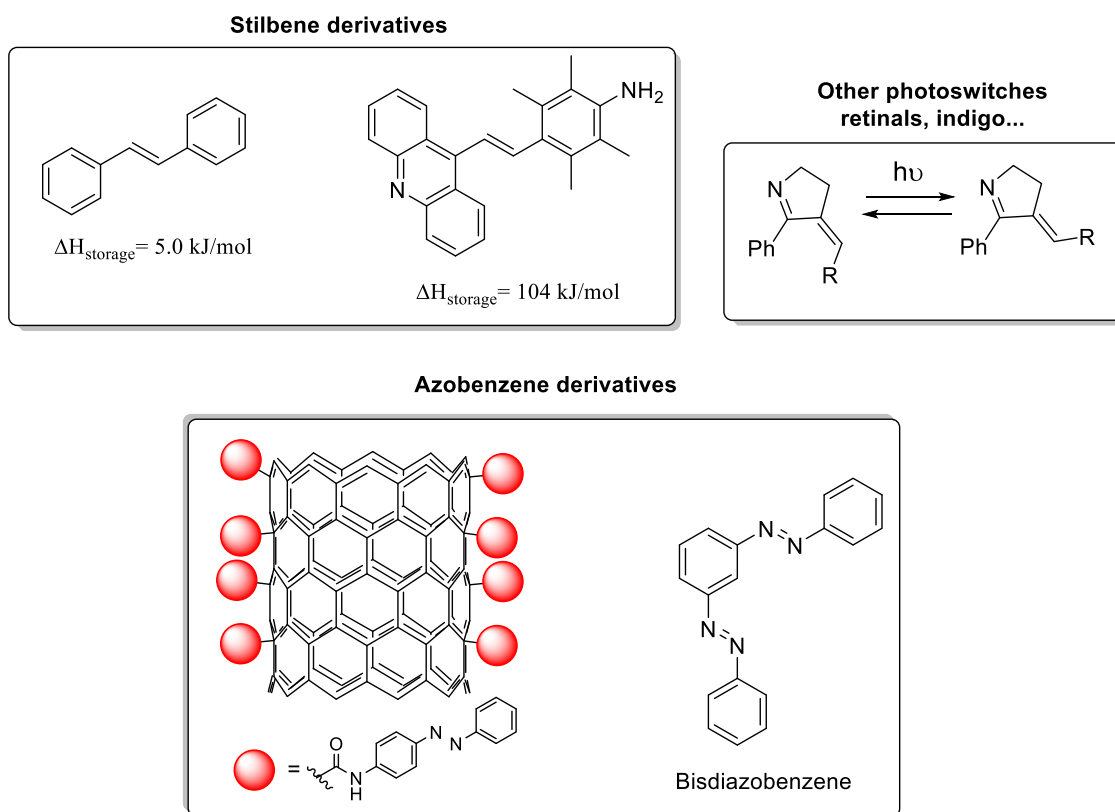


Figure 7.4. Cis-trans derivatives used in energy storage.

Regarding the classification in function of the interconversion mechanism, the second category concerns derivatives based on a cycloaddition reaction. One of the first proposed systems were anthracene derivatives due to their intermolecular [4+4] cycloaddition reaction. To favor that reaction, the synthesis of linked anthracene derivatives was achieved, Figure 7.5. This cycloaddition is a reversible process that can take place thermally induced or upon irradiation below 300 nm. This system presents several problems; when increasing the energy difference between isomers the reaction quantum yield drastically decreases. Other system used is the pair based on the dihydroazulene (DHA) and the vinylheptafulvene (VHF) system.^[32] Additionally, this couple presents a small energy difference between isomers.

7. Molecular energy storage systems

However, the most studied system for store solar energy is norbornadiene (NBD) and its derivatives. From its photochemical properties discovered around 1960, a great number of derivatives have been synthesized adjusting the absorption and relative stability between both adducts.^[33] The reaction responsible for the energy storage is an intramolecular [2+2] cycloaddition yielding in the other isomer, so-called quadricyclane (QC). The NBD derivatives are typically synthesized by a Diels-Alder reaction. Norbornadiene exhibits attractive properties; especially interesting is the energy difference between both isomers ($\Delta H_{\text{storage}} = 89 \text{ kJ/mol}$ in the base system).^[34] As a counterpoint, the solar spectral match in the simplest NBD is practically null and in presence of air, explosive peroxides could be formed.

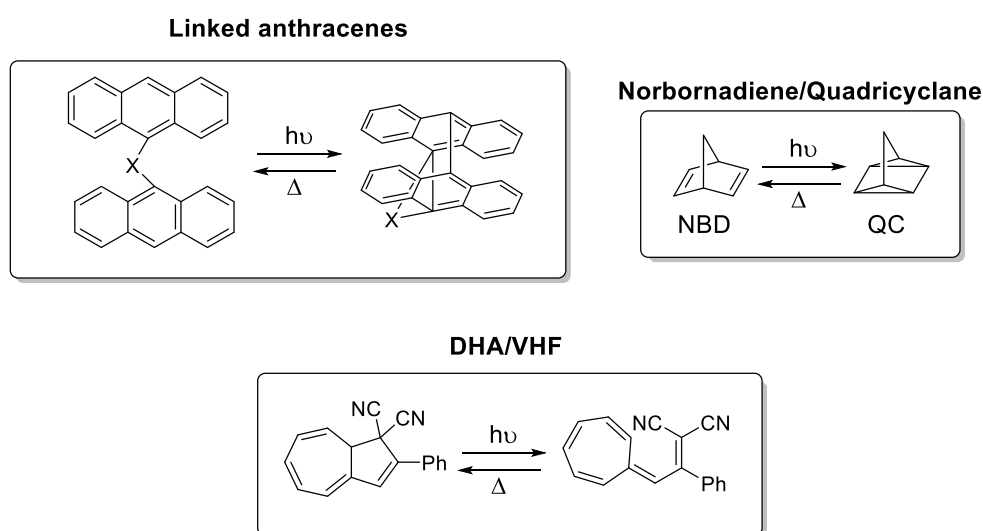


Figure 7.5. Cycloaddition-based MOST systems.

Due to these problems, some molecular engineering strategies have been used to redshift the absorption maximum, but usually this redshift in NBD derivatives means lower back-conversion energy barriers for the isomer QC.^[35] The introduction of methyl substituents on the bridgehead and trifluoromethyl groups on one of the double bonds has been described as an improvement on the lifetime of the QC. From the 1980's a great effort has been putted into designing NBD derivatives with improved capabilities.^[36] The most widely employed strategy consist of the introduction of electron withdrawing groups, or a combination of an electron withdrawing and an electron-donating group at the vinylic positions. In addition, the introduction of aromatic substituents at the vinylic positions give rise to an extended conjugated system. This larger conjugation is loosed in the photoisomerization product QC, helping

to decrease the NBD/QC spectral overlap, improving efficiency.^[37] Besides, an increase on the reaction quantum yield is achieved with substitution. Other computational studies were done evaluating the effect of a push-pull system in the NBD substitution.^[19]

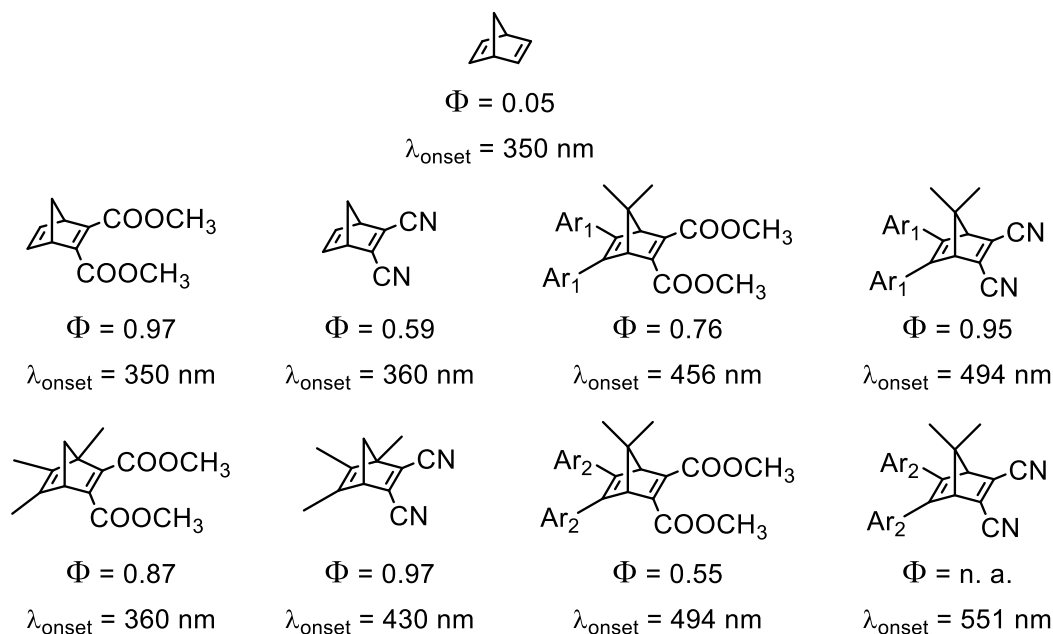


Figure 7.6. Engineering the NBD/QC system by introducing donor–acceptor groups. Ar₁ denotes a phenyl group and Ar₂ a *p*-methoxyphenyl group.^[8]

Another series of NBDs displaying large cationic heterocyclic substituents presented excellent spectroscopic properties, with absorption onsets up to 580 nm, causing a fast isomerization even in diffuse light. This is indeed very close to the calculated optimal absorption for a MOST system of ca. 600 nm,^[17] but unfortunately, irradiation leads into an unstable photoisomer, which rapidly decomposes.

In this chapter, some attempts to modify hydantoin-based photoswitches trying to increase their energy storage capacity and trigger the back-conversion reaction will be described. Together with that, some studies made in collaboration with Prof. Kasper Moth-Poulsen at Chalmers University of Technology will be reported too.

7.2. Objectives in this section

In this section, the specific objectives are included inside the chapter, and not in the background section since they differ from the rest of the thesis. In this chapter, the objectives can be summarized as follows:

- Firstly, the reported hydantoin based photoswitches will be approached to increase its energy storage capabilities. Furthermore, some analysis of the catalytic back-conversion reaction will be done.
- In addition, macroscopic temperature gradient experiments will be assayed using systems based on NBD/QC and azobenzene. The utilization of different heterogeneous catalysts will be explored.
- Complementarily, the catalytic mechanism for both systems will be rationalized by DFT calculations.

7.3. Evaluation of MOST capabilities in different photoswitches

In our research group, we have been involved for a long time in a continuous effort to design,^[38, 39] synthesize^[40] and characterize^[41] diverse families of photoswitches. Based on this background, in the next section we will try to clarify and give some keys on how to convert a well-known photoswitch^[40] into a MOST system. Here we focus on the hydantoin-based photoswitches^[40] which present some practical advantages with respect to other molecular devices. For instance, they can be prepared through an easy synthesis, they have a large scope of possible structural modifications and they feature a low global cost due to inexpensive raw materials.

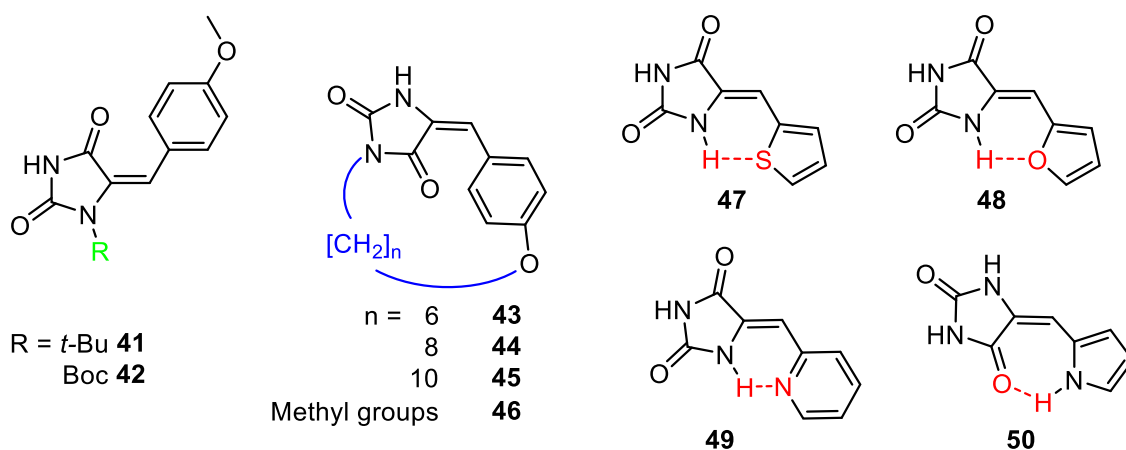
7.3.1. Computational screening of $\Delta H_{\text{storage}}$

Firstly, an *in-silico* study was performed under the framework of the density functional theory to evaluate and trying to clarify some key molecular characteristics, which could lead to an improvement of MOST capabilities of the photoswitches focused on different aspects.

The improvement on energy storage is approached from three different points; the studied compounds can be shown in Scheme 7.1:

1. Steric hindering with large protective groups like *tert*-butyl (**41**) or Boc (**42**) moieties in R position,
2. Mechanical hindering from a carbon chain linking both parts of the photoswitch (**43** - **45**) using as model the non-cyclic (**46**).
3. Formation of hydrogen bonds between the NH of the hydantoin moiety and the added heterocycle (**47** - **50**).

7. Molecular energy storage systems



Scheme 7.1. Computational models to study the described chemical features.

In the case of Boc protection (**42**), the steric hindering is not effective due to the high degrees of freedom that allow a twisted conformation that decreases energy difference due to a minimal distortion of 4 degrees in the dihedral angle yielding in only 6.0 kJ/mol differentiation. The less flexible *t*-butyl group (**41**) gives a slightly less planar conformation (7 degrees) due to the fact that the twisted conformation is not allowed. In this case, the stored energy raised to 14.5 kJ/mol instead of 3.2 kJ/mol obtained for the free system. In both cases, a pyramidalization of the nitrogen is obtained for the *Z*-isomer, as can be seen in Figure 7.7. The presence of voluminous groups like Boc (**42**) or *tert*-butyl (**41**) in R_1 position does not lead to the desired differentiation between isomers.

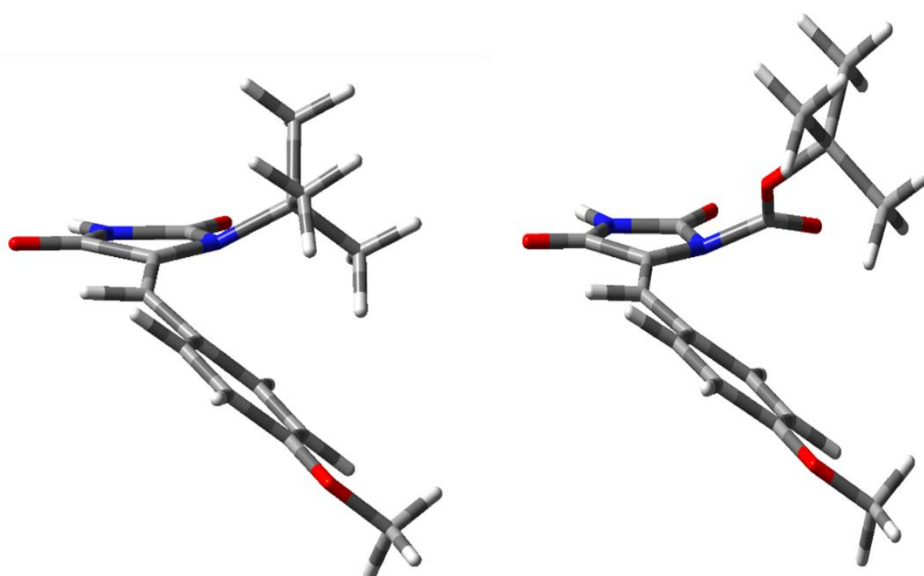


Figure 7.7. Structures of *Z*-isomer of compounds **41** and **42**.

Another option to alter the amount of stored energy is the linkage of both moieties that composes the photoswitch through a carbon chain. In this case, a practical problem to discriminate between both isomers arises due to the small difference in the distance between both ends, which differs only by 0.04 Å from one isomer to the other. To monitor this geometrical change, the distance between hydantoin nitrogen and *p*-hydroxyphenyl oxygen, as depicted in Figure 7.8, is chosen. From this minimal spatial variation, the *E*-isomer stabilization and *Z* destabilization do not represent a differential effect in energetic terms. The difference in free energy between each cyclic derivative is less than 4 kJ/mol. The geometrical disposition of both isomers of compound **44** were computed using the B3LYP functional and 6-31G* as standard basis set.

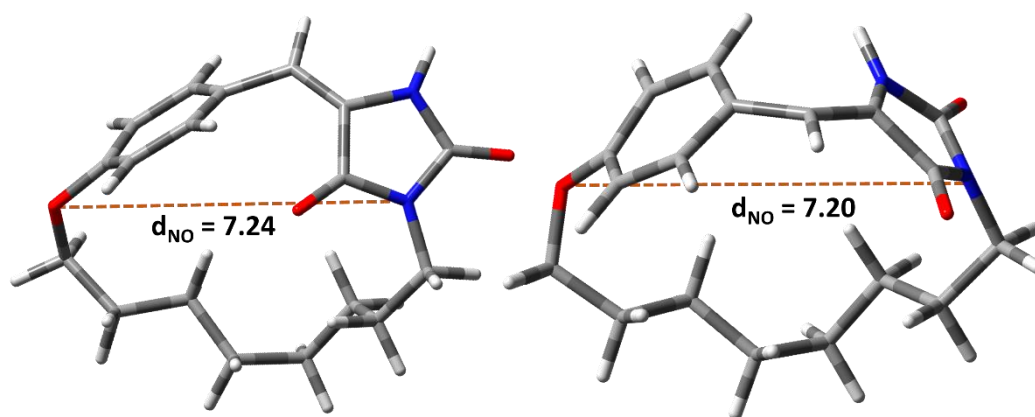


Figure 7.8. *E* (left) and *Z*-isomer (right) of compound **44**.

All the studied compounds present a restrained conformation, which yields in a large deformation of the photoswitch moiety. The 10- and 6-members ring (**45** and **43**) are closer to an optimal and strained, respectively, conformation of the central double bond, arising in a similar energy difference. In contrast, in the 8-members ring (**44**) the trend changes. The *Z*-isomer presents a shorter d_{NO} being more strained than the other isomer. The distance and ΔG between both isomers are summarized in Table 7.1.

7. Molecular energy storage systems

	$d_{NO} E (\text{Å})$	$d_{NO} Z (\text{Å})$	$\Delta G (\text{kJ/mol})$
43	6.37	6.48	31.6
44	7.24	7.20	36.8
45	7.64	8.13	32.6
46	8.51	8.94	3.8

Table 7.1. Distance and ΔG between both isomers.

For that, compound **44** with the octyl carbon chain yields in the maximum energy difference with $\Delta G = 36.8$ kJ/mol, which is a significant improvement in the energy storage capacity from the free system.

The effect of different hydrogen bonds was evaluated considering the most common heterocycles: thiophene, furan, pyridine and pyrrole. The tendency to give hydrogen bonds in the sequence of $N > O > S$ was clearly observed with the distance between X-H and with the stabilization due to the hydrogen bond strength. In this case the desired system as MOST is **49**; presenting the highest energy differentiation between isomers, as can be seen in Table 7.2

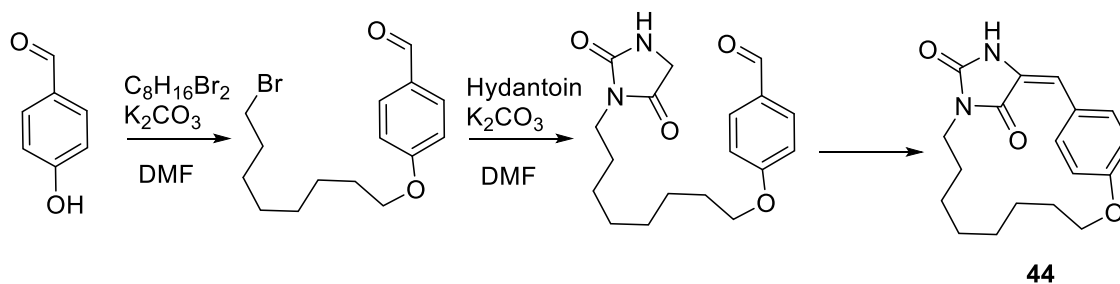
	$d_{X-HN} (\text{Å})$	$\Delta G(\text{kJ/mol})$
47	2.67	15.4
48	2.29	31.0
49	2.16	53.9
50^a	1.82	25.3

Table 7.2. Distance between amide H and X. ^a distance between NH of pyrrole and C=O.

7.3.2. Synthesis of promising derivatives

With those computational hints in hand, we focused our synthesis on a series of compounds with similar structures to test experimentally their availability to act as a MOST system.

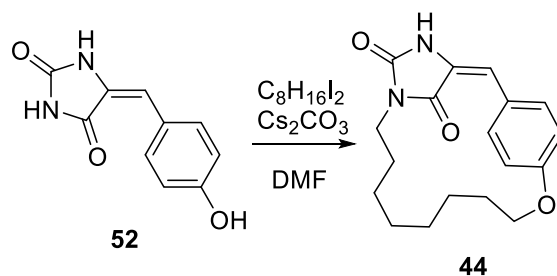
Multiple attempts were done trying to obtain chain derivatives, following two different strategies. Firstly, the multi-step synthetic pathway described in Scheme 7.2, was proposed. Synthesis was successful until the last step, the formation of the final derivative **44**, which is the most challenging step. This step involves the formation of a sterically disfavored double bond. Different reactivities were tried, the typical refluxing acetic acid as solvent and NH_4AcO as catalyst and many different conditions including microwave assisted methodology. All the conducted attempts only yield in decomposition of the substrate when forcing the experimental conditions. In that synthetic path, sequential alkylation was carried out in DMF and using K_2CO_3 as base at room temperature for 24 hours.



Scheme 7.2. Synthetic proposal for the cyclic compound.

Based on these previous unsuccessful results, a novel approach was assayed. In this case, the photoswitch is obtained prior to the cyclizing reaction. For this reaction, 1,8-diiodooctane and Cs_2CO_3 in DMF were used. These conditions are the most favored for ring formation with entropy disfavored systems. Unfortunately, derivative **44** was not obtained experimentally and could only be studied by computational means.

7. Molecular energy storage systems

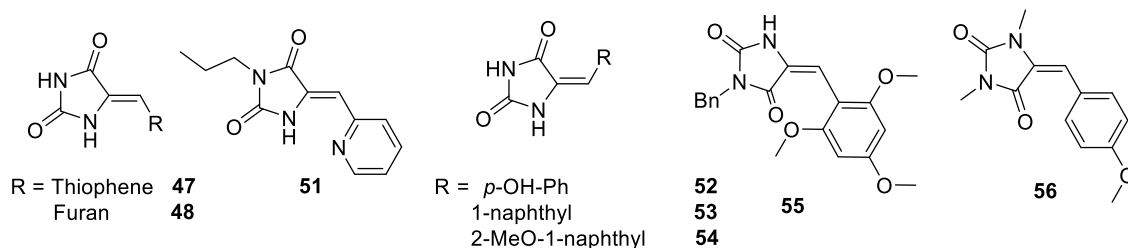


Scheme 7.3. Alternative synthetic proposal for the cyclic compound.

As proposed in the previous section, a series of compounds based on the hydrogen bond behavior were made following the previously reported method.^[40] That procedure yields mainly the *E*-isomer in compounds **52** - **56**, but as expected, the *Z*-isomer in case of **47**, **48** and **51** was obtained because that is the thermodynamically stable isomer due to the hydrogen bond. Compound **51** was provided by Dr. Sucunza's group in Alcalá de Henares, because of the impossibility of obtain derivative **49**.

In addition, a complementary series of derivatives was made, exploring the influence of the use of donating electron aryl fragments trying to modulate the absorption maximum of the UV-Vis spectra or improve the water solubility. Also, some derivatives that includes naphthyl substituents were obtained. This group was previously used in other proposed MOST systems.^[31]

Here, a new family of hydantoin derivatives were synthesized, as can be seen in Scheme 7.4.



Scheme 7.4. Hydantoin derivatives prepared experimentally.

7.3.3. Photochemical study of the new hydantoin derivatives

All compounds were photochemically characterized, specially focusing on their absorption capabilities. UV-Vis spectra of each compound can be seen in Figure 7.9 and they were collected over 5×10^{-5} M solutions in acetonitrile.

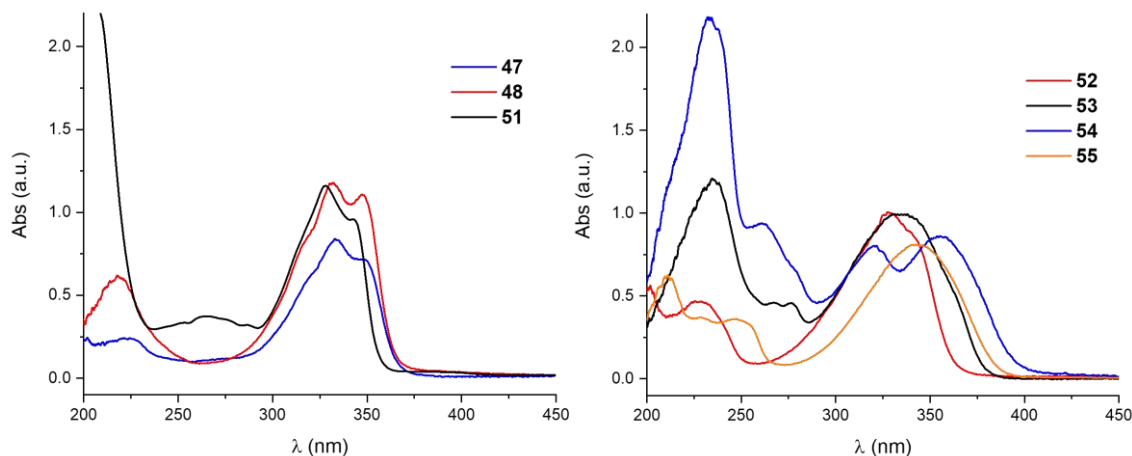


Figure 7.9. UV-Vis spectra of **47**, **48** and **51** (left) and **52-55** (right).

A similar behavior was observed for all derivatives with an intramolecular hydrogen bond (**47**, **48** and **51**) presenting a spectral band with two maxima. As mentioned, a red shift of 20 nm was achieved with inclusion of methoxy substitution in the pair **53** - **54**.

Irradiation experiments were conducted using different light sources to find the photostationary state (PSS) for each derivative. The PSSs were calculated by NMR integration with the corresponding vinylic proton signal for both isomers in $\text{DMSO-}d_6$. Irradiations were done using a 400 W Pyrex-filtered medium-pressure Hg lamp and in a LUZCHEM photoreactor with UVA lamps with an emission wavelength centered at 350 nm (14 lamps x 8 W/lamp).

7. Molecular energy storage systems

Compound	λ_{max}^a	PSS (Z/E) ^b	PSS (Z/E) ^c	PSS (Z/E) ^d
47	333, 348	55/45	27/73	27/73
48	335, 350	63/37	43/57	43/57
51	328, 343	100/0	100/0	95/5
52	328	7/93	47/53	
53	335	10/90	66/34	
54	322, 355	40/60	69/31	
55	345	5/95	66/34	

Table 7.3. Absorption spectra and photostationary state (PSS) in different irradiation conditions. ^{a)} Value in nm for the *E* isomer, except for **47,48** and **51** that refer to the *Z*-isomer. ^{b)} Using a 400 W Pyrex-filtered medium-pressure Hg lamp. ^{c)} Using a photoreactor at 350 nm. ^{d)} Using a photoreactor at 350 nm with *d*₄-methanol solutions.

All compounds shown a similar spectrum in the UV-Vis region, with a maximum in all cases located between 330 and 350 nm. Irradiation with 350 nm light improves isomerization efficiency between 20 - 40%. In the case of **47** and **48** the presence of methanol does not improve the isomerization weakening the hydrogen bond; this effect is partially observed in **51**, which can switch 5% in methanol and no isomerization was observed in DMSO. With those compounds, no thermal back reversion was observed during 4 weeks at RT.

7.3.4. Catalyzed back-conversion reaction

As previously mentioned, another important feature in MOST systems is the possibility of controlling the back-conversion reaction with some catalyst to trigger the process. As it was described before^[40] these photoswitches exhibit a high back-reaction barrier and that process does not take place even with high temperatures in a reasonable time scale, needing more than a week at 100°C to observe some change in the isomers ratio. Here, a methylated form of **52** (**56**, represented in Scheme 7.4) were used to avoid any possible reaction between the mobile hydrogens and metallic salts.

For demonstrating their possibilities as MOST devices, some compound to accelerate the back-conversion reaction is needed.

To gather some information on the process, a large screening of around one hundred of inorganic salts and organometallic catalysts was performed. To speed up the screening, harsh conditions such as 90°C and 12 hours of reaction time were employed. These assays were done in parallel using a homemade setup to allow stirring for 20 vial tubes simultaneously and without magnetic stirring, improving by this way the reproducibility on the experiments. The reaction ratio was monitored by TLC for a qualitative interpretation. For a more accurate description, proton NMR experiments were done to quantify the back-conversion. In Table 7.4 the preliminary results are summarized, starting from an 82/18 (Z/E) solution of **56** in DMSO-*d*₆. The best conversion ratios were observed for Ce(IV) salts, MoO₃, AlCl₃ and TiCl₄.

Catalyst	Conversion (E/Z)
AlCl₃	55/45
TiCl₄	42/58
SnCl₂	32/68
Ce(NO₃)₃	55/45
MoO₃	62/38
Mo(CO)₆	55/45
CAN^a	63/37
SnCl₄	36/64

Table 7.4. Conversion with different catalyst. ^a Cerium ammonium nitrate, (NH₄)₂[Ce(NO₃)₆]

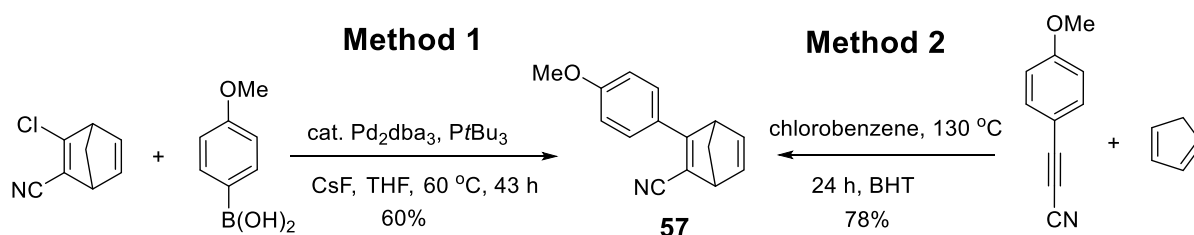
CAN was selected due to the very low solubility observed for MoO₃, which gives practical problems when monitoring the isomerization.

For that, a further study testing solvent influence was done at 40°C and 12 h with the following solvents: toluene, THF, diethyl ether, acetone, chloroform, dichloromethane, methanol, DMSO, acetonitrile, DMF and ethyl acetate. For most of these solvents, slow isomerization takes place with a 10% molar catalyst and the best results are from DMSO. Additionally, a catalyst charge test was done finding the lower activity limit in 5% molar.

7.4. NBD/QC derivatives as MOST devices

This part of the Ph.D. thesis was developed during an internship in the group of Prof. Kasper Moth-Poulsen at Chalmers University of Technology in Goteborg, Sweden. Not all the presented work in this section was done by me, a contribution report is presented in section 7.4.4.

As previously stated, this group is generating the main part of the present improvements on the NBD/QC system. Based on the previous knowledge,^[19] a new NBD derivative was prepared.^[18] The synthesis was accomplished by two different methods; Method 1 uses the previously prepared chlorocyano-norbornadiene by a Suzuki cross-coupling reaction to afford compound **57**. In addition, **57** can be prepared by a Diels-Alder reaction of cyclopentadiene with the corresponding alkyne.



Scheme 7.5. Synthesis of compound **57**, by two different methods.

This new prepared derivative **57** presents very promising properties, making it a suitable species to be assayed in a device implementation. **57** features a stored energy density of 400 kJ/mol, which is much higher than the previously reported in section 7.1. The moderate photoreaction quantum yield of 61% together with the maximum absorption at 326 nm and an onset value of 346 nm, allows a fast and efficient conversion into **58** under sunlight conditions. In addition, the robustness of the system to interconvert between both species was tested obtaining a decomposition rate of 0.14% per cycle, as shown in Figure 7.10

7. Molecular energy storage systems

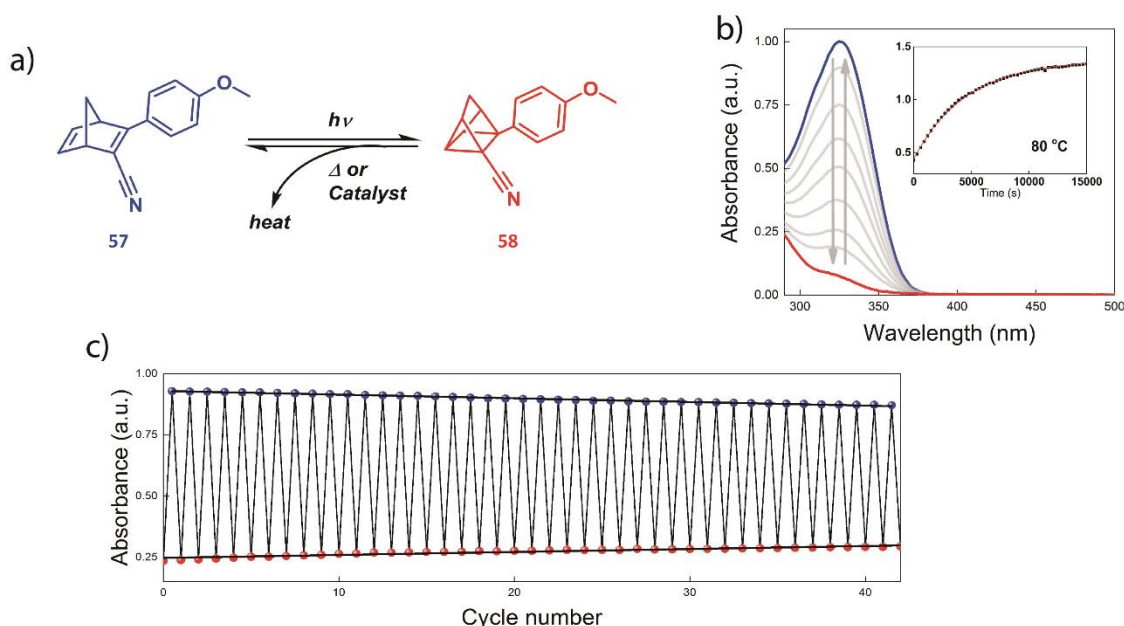


Figure 7.10. a) Structure of **57** and **58**; b) Absorption spectra of **57** (in blue) and its photoisomer **58** (in red). The sample was irradiated with a $\lambda = 310$ nm LED light. Inset figure shows the kinetic back conversion of **58** under 80 °C; c) Cyclability experiment for a solution of 7×10^{-5} M in toluene showing an absorbance of **57** in blue dots and **58** in red dots at $\lambda = 325$ nm.

7.4.1. Catalyst screening and preparation of supported materials

An efficient catalytic conversion from **58** to **57**, in which all the accumulated energy is quickly released is mandatory for a MOST system.^[7] Furthermore, the ideal energy release process should include a heterogeneous catalyst, or supported catalyst in a solid material. In this case, an easier device design could be accomplished together with a simpler workflow avoiding an additional purification step after each energy release cycle. Firstly, a fast scan using UV-Vis spectroscopy as probe with different transition metal catalysts was performed. The possible candidates were selected from the previously reported to convert substituted QC to NBD.^[42] Here, 14 different candidates regarding metallic salts and complexes, focusing in Cu, Co and Pd species, were screened looking for their catalytic activity by evaluating the outcome product using UV-Vis spectroscopy. This analysis was used to measure the qualitative rate of the back reaction in the active catalysts.

In this case, cobalt phthalocyanine (**CoPc**) exhibits the most promising results, being the most attractive candidate due to a clean conversion (checked by NMR) and high conversion rate $\approx 172 \text{ s}^{-1} \text{ M}^{-1}$, as can be seen in Table 7.5. Although, a very low

7. Molecular energy storage systems

solubility in toluene is observed for **CoPc** ($7.2 \times 10^{-5} \text{M}$). The task remained to immobilize **CoPc** in some way to prevent leaching when the toluene solution flows through a catalyst bed. For that, some solid supports were developed, obtaining the best reaction rate in the carbon-supported material, entry 2 in Table 7.5.

Entry	Catalyst	CDCl_3 Activity	Toluene Activity	Reaction rate in toluene ($\text{s}^{-1} \text{M}^{-1}$)
Co(II)				
1	CoPc	✓	✓	172.05
2 ^a	CoPc@C	✓	✓	11788.22
3	$\text{Co}(\text{NO}_3)_2 \cdot 6\text{H}_2\text{O}$	✗	✓	3.88
Cu(I)				
4	CuBr	Degradation	✓	2.41
5	CuI	✗	✓	8.73
6	CuCN	✓	✓	4.09
7	$[\text{Cu}(\text{CH}_3\text{CN})_4]\text{PF}_6$	Degradation	/	/
7 [*]	$[\text{Cu}(\text{CH}_3\text{CN})_4]\text{PF}_6$ + BHT	Low degradation	/	/
Cu(II)				
8	CuCl_2	Degradation	✓	2.52
9	$\text{CuCl}_2 \cdot 2\text{H}_2\text{O}$	Degradation	✗	0.03
10	CuSO_4	✓	✓	6.07
11	$(\text{CH}_3\text{COO})_2\text{Cu}$	✓	✓	0.02
12	$(\text{CH}_3\text{COO})_2\text{Cu} \cdot \text{H}_2\text{O}$	✓	✓	32.39
Pd(II)				
13	PdCl_2	✓	✓	3.62
14	$(\text{CH}_3\text{COO})_2\text{Pd}$	✓	✓	Hard to follow by UV-Vis.

Table 7.5. Catalysts activity and reaction rates. ^a) Supported material, afterwards development.

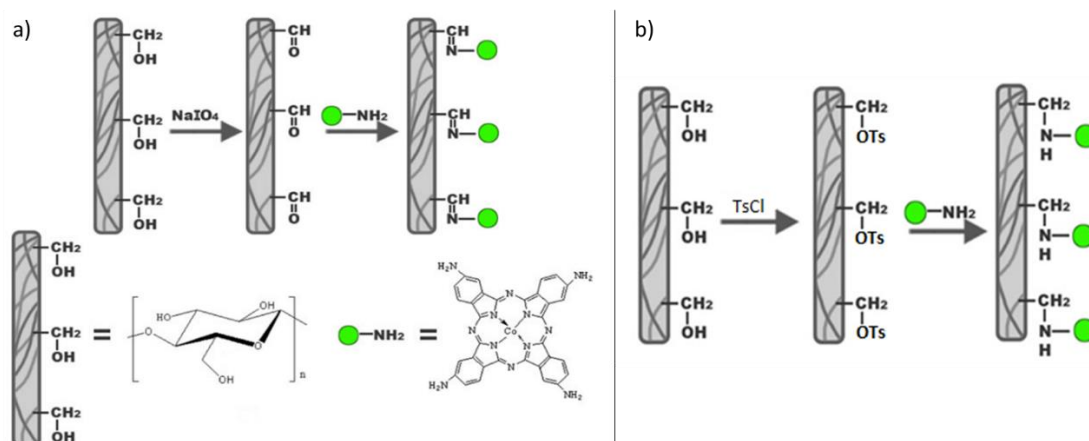
Some materials like activated carbon, silica and cotton were chosen for the incorporation of the **CoPc** catalyst. In order to generate a high reaction surface in a heterogeneous catalyst, **CoPc** was physisorbed onto activated carbon. The amount of catalyst adsorbed was measured by X-ray photoelectron spectrometry showing a load of 13% of **CoPc** with this preparation method. The reaction rate in toluene was

7. Molecular energy storage systems

measured, being about seventy times higher than the one found for the **CoPc** in solution ($\approx 11788 \text{ s}^{-1} \text{ M}^{-1}$). This can be rationally explained by the strong intermolecular π stacking that could undergo in solutions of pure **CoPc**. However, the higher spatial dispersion of **CoPc** onto charcoal gives a larger contact surface area. This was the material (**CoPc@C**) used in the flow experiments to study the heat release capabilities of the system.

Even being physisorbed onto charcoal, no covalent interactions between the carbon and the **CoPc** were reached. For that and trying to prevent a possible leaching, some attempts to covalently immobilize the catalyst were done. The other materials chosen as support were silica and cotton, being both cases an inexpensive material with a great abundance.

Several attempts with cotton were done, trying to functionalize the terminal hydroxyl groups of the cellulose matrix. For that, an exhaustive oxidation to obtain the aldehyde was done using NaIO_4 . After that, the reaction with an **amino-CoPc** was done using a ratio of 5 mmol/g of cotton, as described in Scheme 7.6.a.

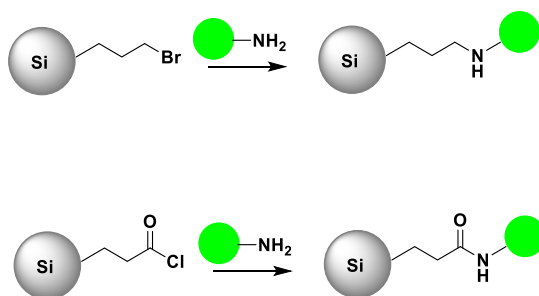


Scheme 7.6. **Amino-CoPc** immobilization attempts in cellulose.

Some functionalization is achieved in the range of $10\text{--}20 \mu\text{mol g}^{-1}$ of sample, which is really lower (four magnitude orders) than a 13% achieved by physisorption. An alternative synthetic strategy was assayed changing the oxidation step to an exhaustive tosylation with tosylchloride, as can be seen in Scheme 7.6.b. This prepared sample was treated with a DMF solution of the **amino-CoPc** and base. The resulting material presented a slightly higher functionalization rate, ca. $45 \mu\text{mol g}^{-1}$ of sample.

7. Molecular energy storage systems

In addition, other functionalization strategy was assayed; in this case, two different functionalized silica matrixes were suggested, as can be shown in Scheme 7.7.



Scheme 7.7. **Amino-CoPc** immobilization attempts in functionalized silica.

The reaction of bromo propyl-silica was performed using a suspension of **amino-CoPc** in DMF. The obtained material also presents a low functionalization rate, but close to ten times higher than the obtained with cotton samples. These promising results turns unsuccessful when flow experiments were assayed with it, as it will be mentioned below. Due to this reason, the other derivative was not synthesized.

7.4.2 Heat release experiments

To evaluate the heat release capabilities of the system **57/58**, a flow setup was used. For initial testing, a syringe pump with **58** stock solutions at different concentrations is pumped through a Teflon tube containing a catalyst bed inside. The back-conversion rate is probed using UV-Vis spectroscopy before and after catalyst contact. This procedure was used for initial testing of all the prepared catalysts with diluted **58** samples. The setup used is shown in Figure 7.11.

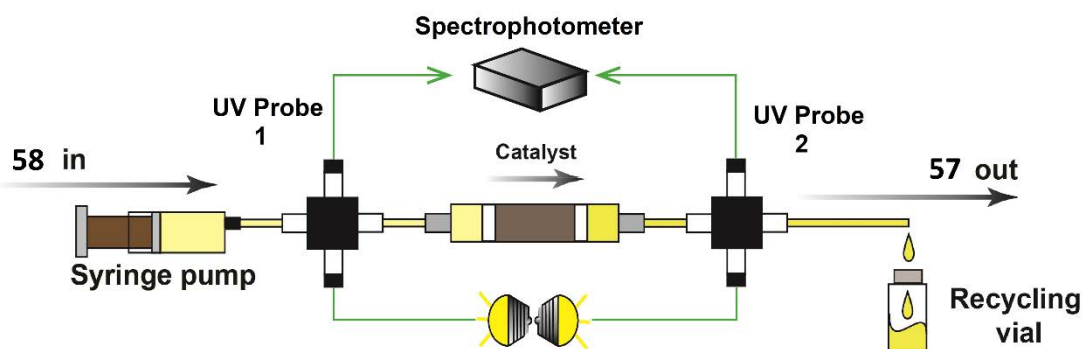


Figure 7.11. Preliminary setup to test the catalyzed back-conversion reaction by UV-Vis. Adapted from *Energy Environ. Sci.* **2019**, *12*, 187-193.^[18]

As could be expected, the better conversion rates were obtained with the **CoPc@C** catalyst due to the hundred times higher **CoPc** load. With the functionalized cotton fibers, a full back-conversion is only obtained with diluted samples (10^{-3} M) but when increasing concentration, only partial reaction is observed. This conclusion clearly hampers the use of this device to obtain an efficient heat release in a large-scale implementation. In the case of the silica-supported catalyst, no assay could be done due to the high pressure needed to pump the solution through the smaller particle size of the silica matrix. In this case, the smaller particle size yields in a more stacked catalyst bed, which seems to be impenetrable under the used flow rates and working pressures (more technical data will be reported below).

After these preliminary tests, increasing concentrations of **58** were used. For testing the behavior against concentration, thermocouples before and after the catalyst were introduced in the setup. To demonstrate the possible operation of **58** in conjunction with **CoPc@C**, a heat release device was constructed as can be seen in Figure 7.12. In that, a PTFE tubing containing approximately 5 mg of **CoPc@C** was placed in the center of a high vacuum chamber (up to 10^{-5} mbar), which provides thermal insulation for the catalyst bed. Two thermocouples were placed before (T_1) and after (T_2) the catalytic bed monitoring the temperature rise resulting from the back conversion of **58** ($\Delta T = T_2 - T_1$). With this configuration, it is possible to pass a solution of **58** through the **CoPc@C** site under flow conditions.

7. Molecular energy storage systems

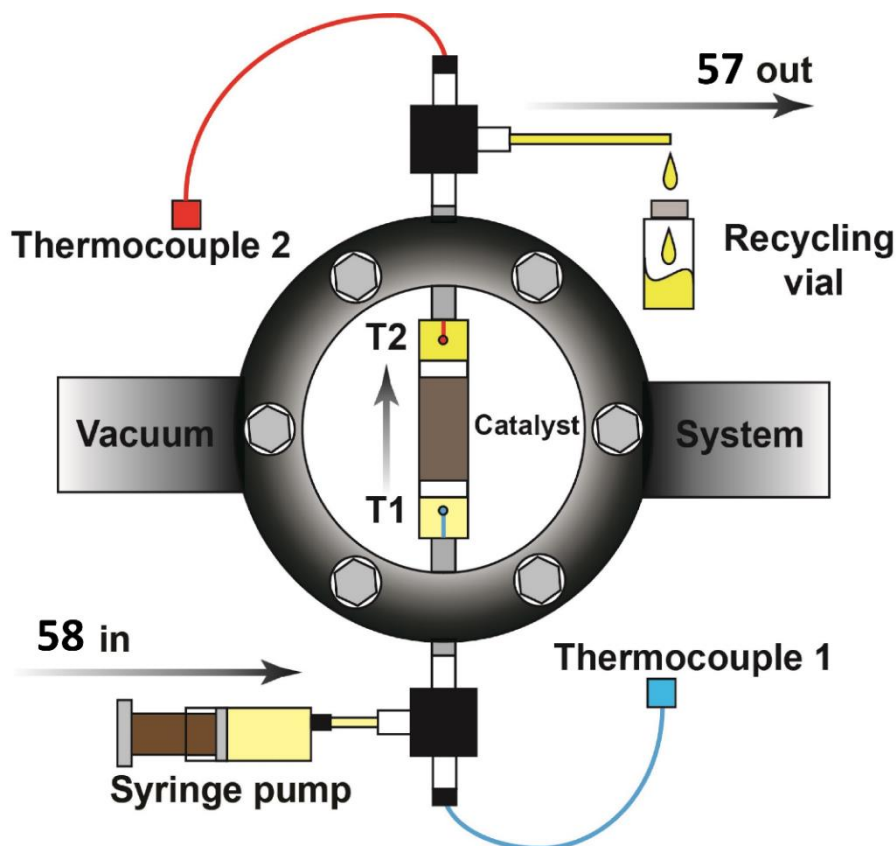


Figure 7.12. Illustration depicting the design of the vacuum chamber.^[18]

Once developed the setup, five different solutions of **58** in toluene with concentrations varying from 0.1 to 1.5 M (corresponding to 22.3 – 334.9 g L⁻¹) were prepared by photolysis using a high-pressure mercury lamp. After that, the corresponding dark stored solution was pumped through the catalytic bed with a constant flow rate of 5 mL h⁻¹. These experiments were repeated at each concentration twice. As expected, a progressive increase in the heat release (ΔT) was observed as the concentration of **58** was increased when the solution was passed through the bed reactor. The maximum adiabatic heat release from a solution of **58** can be calculated from the following equation.¹⁴

$$\Delta T = \frac{C \cdot M_w \cdot \Delta H_{storage}}{C \cdot M_w \cdot C_{p,58} + \rho_{solvent} \cdot C_{p,solvent}}$$

Where C and M_w represent the concentration of **57** and molecular weight, respectively; $\Delta H_{storage}$ is the DSC measured energy storage capacity of **57/58** couple in J g⁻¹; $C_{p,58}$ is the specific heat capacity of **58** in J g⁻¹ K⁻¹; $\rho_{solvent}$ and $C_{p,solvent}$ correspond

to the volumetric mass density in g L^{-1} and the specific heat capacity in $\text{J g}^{-1} \text{K}^{-1}$ of the solvent (867 g L^{-1} and $1.7 \text{ J g}^{-1} \text{K}^{-1}$).

The results for the heat release experiments are summarized in Figure 7.13.a. In that, the previous equation was used to simulate the expected temperature gradient at each concentration. As can be seen, the simulated temperature increases predicted by the previous equation, fits very well with the measured data, demonstrating that the heat losses in the device were negligible and that the energy storage from DSC in neat samples are very close to the energy storage in the prepared solutions.

When using a 1.5 M solution of **58**, the temperature increases to a maximal $\Delta T = 63.4^\circ\text{C}$ (absolute temperature of 83.2°C) only after 2.5 minutes, being a super-fast reaction. Thus, demonstrating that a high temperature increase can be reached over a short duration of time as observed in Figure 7.13.b. An absolute temperature above 70°C was sustained for $\sim 340 \text{ s}$ after which the catalyst was depleted.

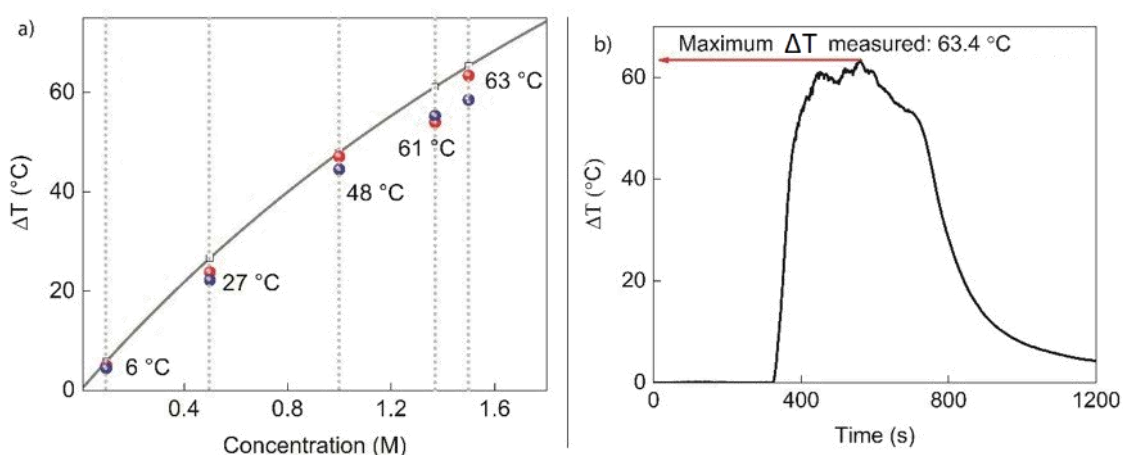


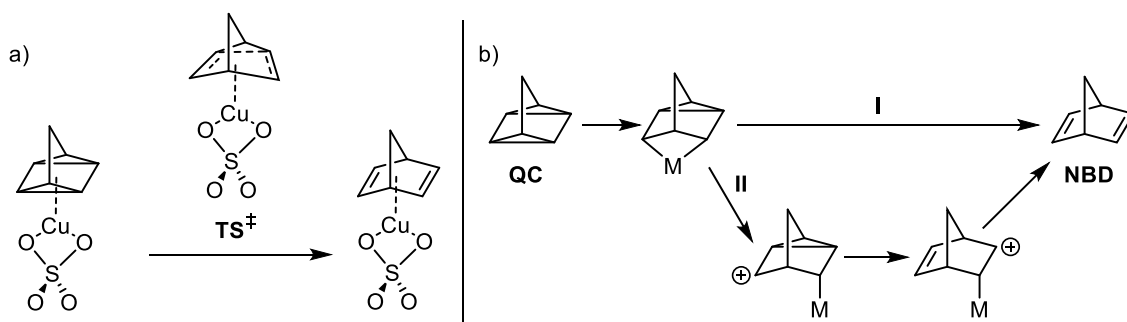
Figure 7.13. a) Theoretical simulation (grey line) and experimental data (colored dots for separate measurements) of heat release vs. concentration b) Thermogram for heat release from a 1.5 M toluene solution of **58**, where the highest temperature difference of 63.4°C was measured.^[18]

To further evaluate the capabilities of **CoPc@C**, the turnover number (TON) and frequency (TOF) were calculated as the converted **58** concentration in moles per amount of catalyst loaded in moles per time unit. This result equated to a minimum TON in excess of 482 and a TOF of 2.0 s^{-1} . Being not brilliant results from a catalytic perspective, but considering the operating conditions, these are quite good regarding the huge amount of **58** that should be converted.

To the best of our knowledge, a 63.4°C temperature gradient (registering 83.2°C as the absolute temperature) measured in the solution flowing through the device is the new record within the field, showing that e.g. steam production using MOST systems is potentially within reach.

7.4.3 Computational exploration of the back-reaction mechanism

The use of several salts allows for the catalyzed back-reaction from **QC** to **NBD** but the working mechanism remained only hypothesized.^[37, 42-44] In addition, limited computational information about the photochemical behavior of the parent **NBD**^[45] and the evaluation of the substituents effect on the energy storage in **NBD/QC** systems is available.^[19, 46] In addition, the mechanism for the energy release has not been explored in detail. An initial mechanistic proposal for the reaction using cobalt was reported.^[42] The suggested mechanism involved an oxidative addition of **QC** to **CoPC** followed by (I) a concerted step or (II) a multi-step pathway with cationic species. More recently,^[47] the catalytic activity of CuSO_4 and SnCl_2 was tested and two different mechanisms were proposed. In the case of the copper catalyst, a concerted rearrangement was observed due to the electronically available d orbitals in the metallic atom. In the tin species, as the d orbitals are not available the rearrangement is not possible. Both proposals are depicted in Scheme 7.8.



Scheme 7.8. a) Concerted mechanism observed with CuSO_4 . b) Multistep mechanism, involving an oxidative addition.

A systematic mechanistic picture of the back-reaction could be helpful in the design of new and more efficient catalysts. Thus, as the energy release is affected by the mechanism of the back-reaction,^[36] the study of this back-conversion reaction was

approached by computational means. Particularly, the role of **CoPc** as catalyst in the back-conversion from **QC** to **NBD** was explored within the framework of the density-functional theory (DFT). For that, a set of different functionals, chemical structures and conditions were used to ensure a comprehensive view of the reaction together with a good modelling of the experimental conditions.

Based on these preliminary mechanistic proposals, we envisioned a multi-step pathway, where the d orbitals in **CoPc** are involved. Trying to reduce the computational model, the **QC/NBD** parent system was used, notably decreasing the computational cost. At the highest chosen level of theory (PCM-M06/6-31+G*), the full **57/58** and **CoPc** structures were used considering the four possible orientations between **58** and **CoPc**.

A preliminary study on the parent **QC/NBD** system in gas phase was performed to find the key steps in the reaction pathway using BP86 as the functional and 6-31+G* as the basis set. In addition, an initial step involving an oxidative addition to C-C in **QC** bond was evaluated for the parent **QC**. The first step of the mechanism seems to be clearly the rate-limiting step. The two possible alternatives for the first step present energy barriers around 86 kJ/mol, differing less than 8 kJ/mol.

The first path, which is depicted with a black line in Figure 7.14, consists of an oxidative addition of the C-C **QC** bond to the cobalt atom to yield intermediate **60**. A small energy barrier then leads to the formation of the carbocation **61**.

The second path is plotted with a red line in Figure 7.14 and implies the direct formation of intermediate **61** through a single transition state **TS (59-61)**. It consists of a combination of the two steps described in first path, oxidative addition and radical formation.

A second mechanistic alternative^[47] was also computed, optimizing the geometries of **TS (59-60)** and **TS (59-61)** as minima in quadruplet state multiplicity. The high energy values obtained dismiss this alternative as not competitive with the main path. The formation of **NBD** is completed through **TS (61-62)**, implying the elongation of the remaining C-C **QC** bond to yield the final **NBD** coordinated to **CoPc** in complex **62**.

In addition, the solvent effect was subsequently evaluated using PCM with toluene as solvent, energies in orange in Figure 7.14. In this case, only the second reaction path could be found. The energy barrier of **TS (59-61)** is slightly higher than in

7. Molecular energy storage systems

the gas phase, that could be explained due to the higher dipolar moment found for **TS (59-61)** in solvent.

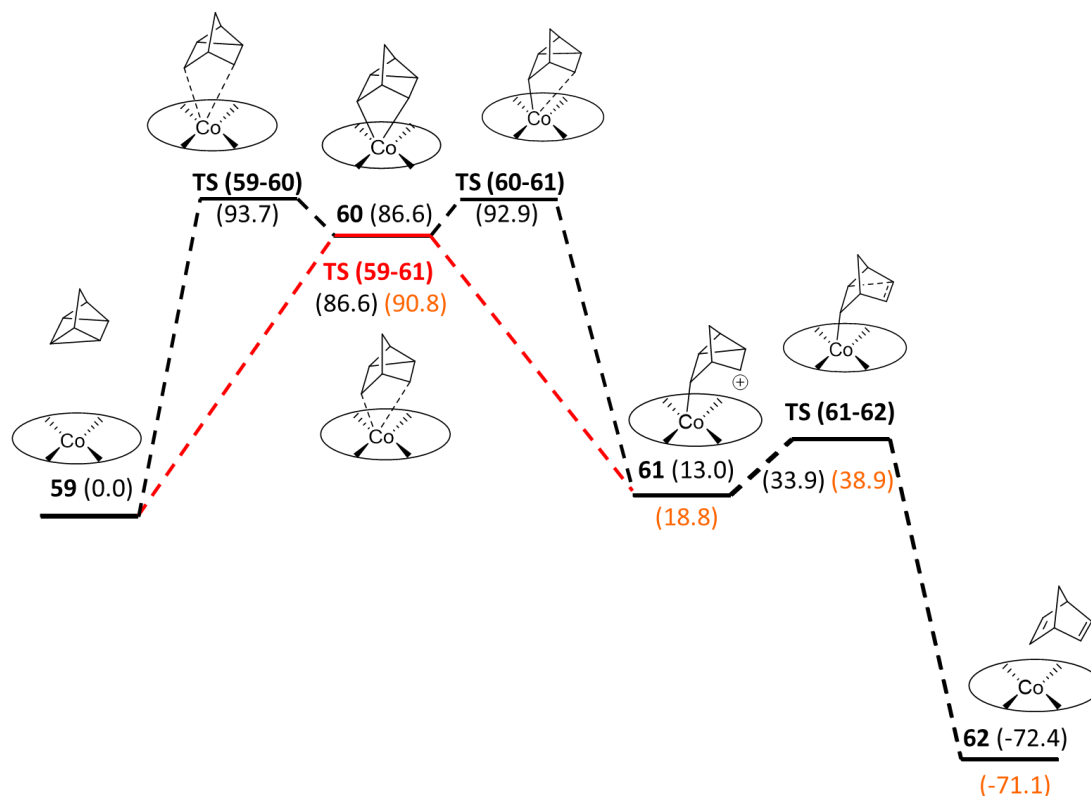


Figure 7.14. QC to NBD conversion in gas phase (black) and toluene (orange). Energies in kJ/mol related to the starting reagent.

In order to benchmark the functional used, a re-evaluation of the whole path at the M06/6-31G++ level of theory was done. As can be seen in Figure 7.15, both functionals exhibit a similar shape of the PES, being more energetic the intermediate **61** and **TS (61-62)** due to an over estimation of the charge in the carbocation center. This feature could be due to the differences between gradient corrected (BP86) and hybrid (M06) functionals. M06 has been shown to give reliable results with previously reported cobalt systems,^[48] and for non-covalent interactions, which are relevant to this system and for this reason it is chosen instead of BP86.

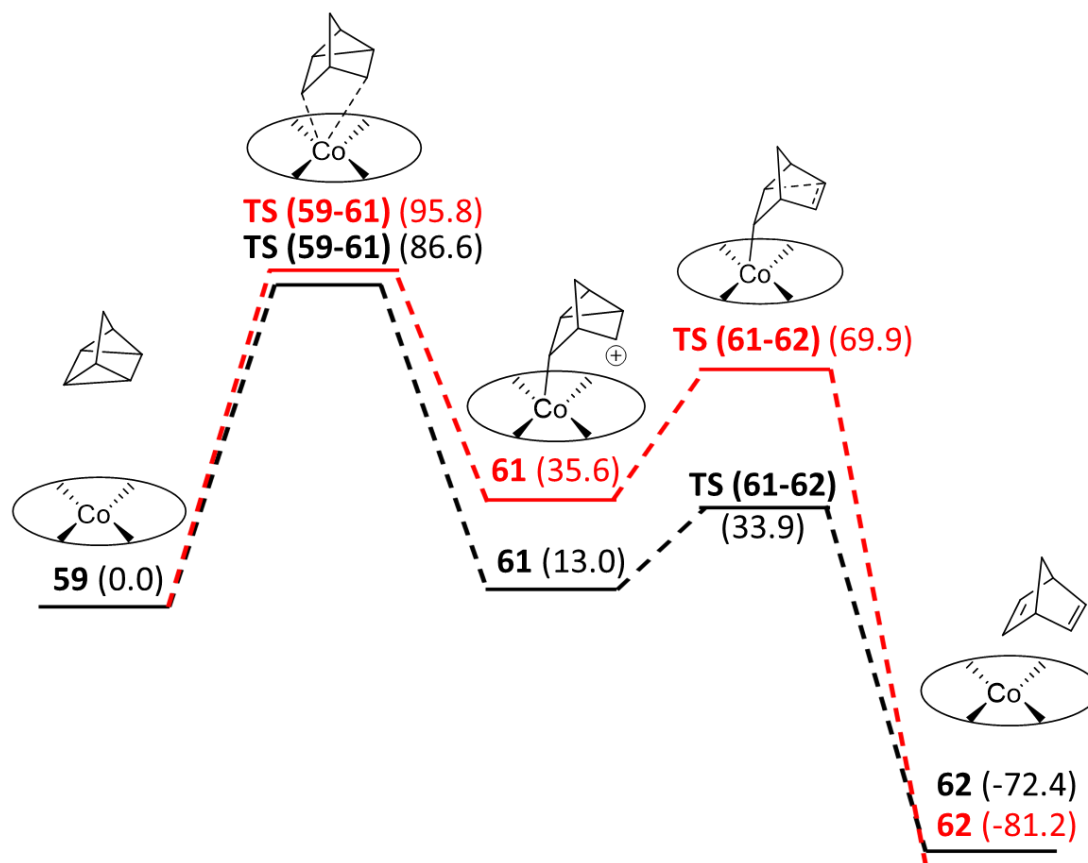


Figure 7.15. QC to NBD conversion in gas phase for two different functionals (black line BP86/6-31G++, red line, M06/6-31G++). Energies in kJ/mol related to **59**.

Once identified the main features of the mechanism with the simplified parent system, we performed a complete study of the reaction at our best level of theory. As previously mentioned, it should be noted that the parent **NBD/QC** system is highly symmetric, but up to four different orientations between the **QC** and the catalyst are possible for the **57/58** system, as can be seen in Figure 7.16.

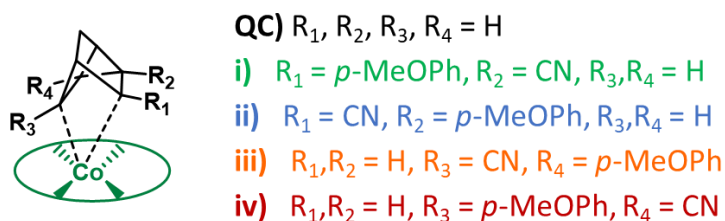


Figure 7.16. Different orientations between **QC** and the catalyst. In all cases, **QC** bonds the metal atom through the carbon substituted by R_3 .

7. Molecular energy storage systems

The computed mechanism implies an initial step comprising an oxidative addition of the metal center in **CoPc** to one of the labile C-C bonds in **QC**. The different possible orientations imply the appearance of numerous alternative transition structures and energy minima. As can be observed, these four minima (**64_i** to **64_iv**, see Figure 7.17) have very different energies, a detailed explanation about that can be found below. Only two of the four possible TSs, could be located (**TS (63-64)_i** and **TS (63-64)_ii**) presenting similar free energies of 45.1 kJ/mol and 58.6 kJ/mol respectively. These are relative free energies computed in toluene referred to an initial situation (**63**) with a 10 Å separation between **CoPc** and **58**. Nevertheless, with the high-energy difference obtained for **64_iii**, **64_iv** respect to **64_i** and **64_ii**, which are more than 54 kJ/mol; these TSs could be further discarded, as they will not represent competitive reaction pathways for the global reaction.

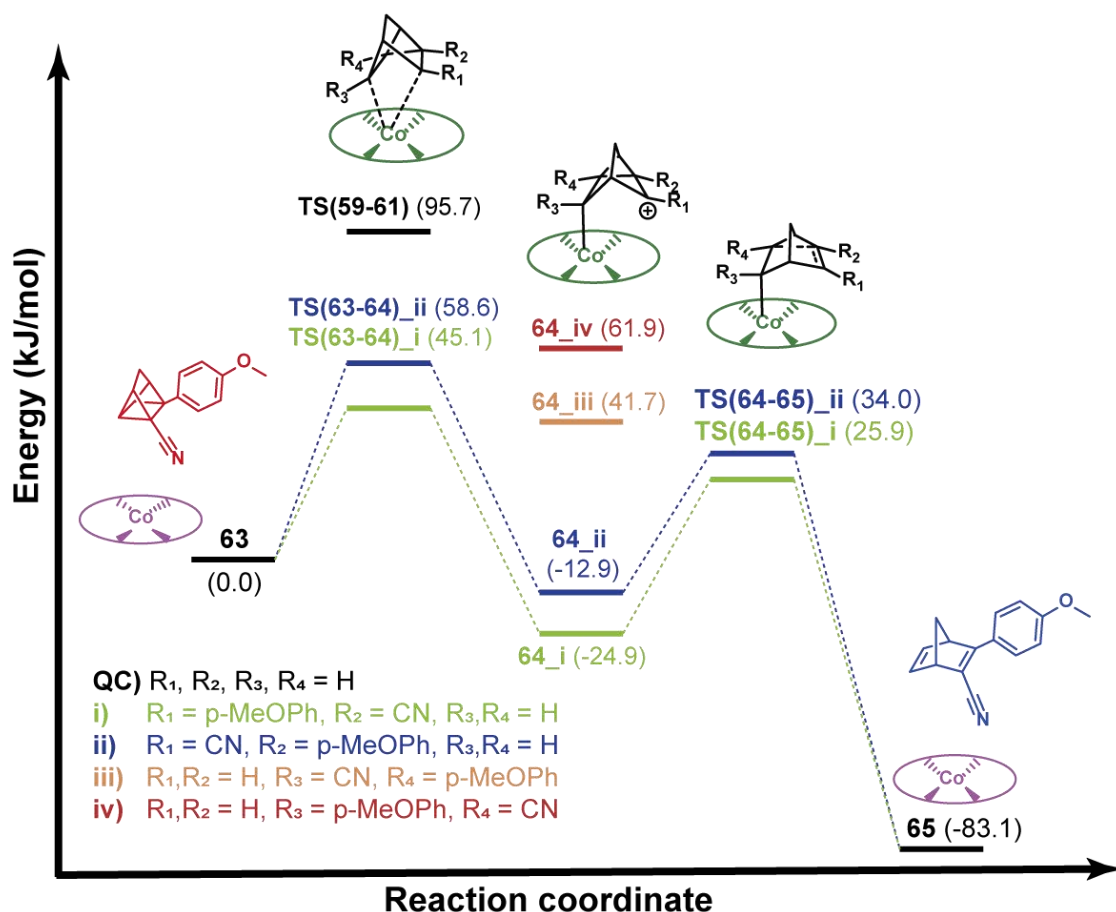


Figure 7.17. Critical points along the potential energy surface for the catalytic back-conversion of **58** to **57** using **CoPc**. The color-coding represents molecular structures or orientations.

Therefore, the relative energy of the four minima coming from the different orientations are clearly different. Two of the possible intermediates (**64_iii** and **64_iv**) are too high in energy compared to the other two (**64_i** and **64_ii**). The development of a positive charge and the different stabilizing effects of the substituents R_1 - R_4 , meaning the combined effect of electronic stabilization and steric hindrance, could explain the energy ordering from **64_i** to **64_iv**. Detailed structures of these can be seen in Figure 7.18.

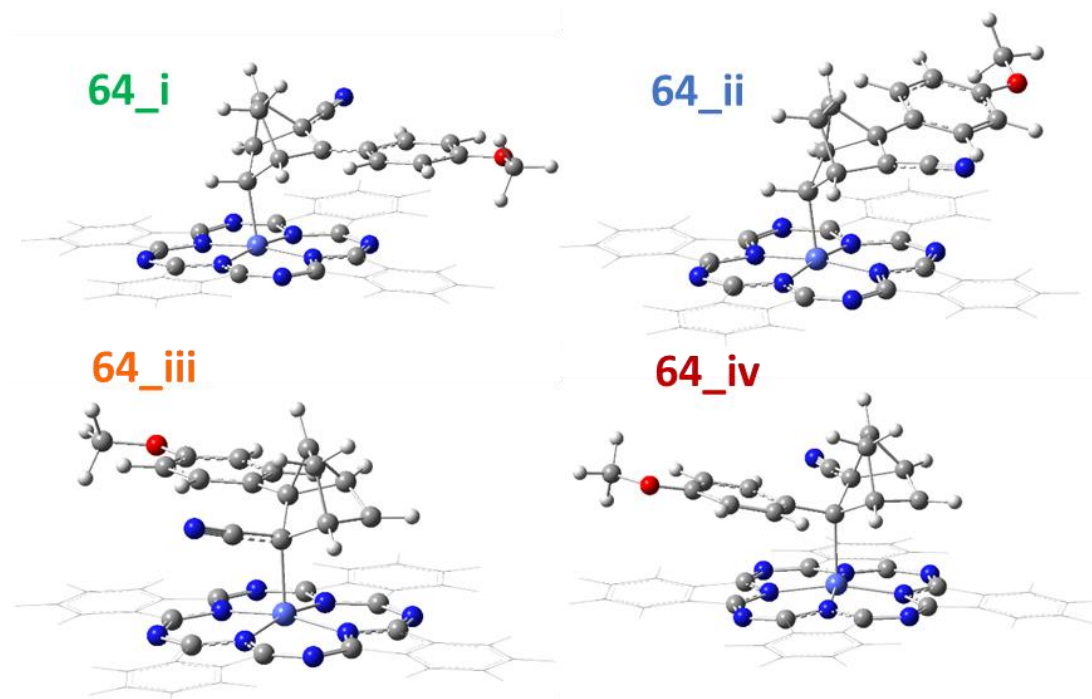


Figure 7.18. Structures of the intermediates **64_i** – **64_iv**.

From these intermediates (**64_i** and **64_ii**) a new barrier with a similar energy, 50.8 kJ/mol for **TS (64-65)_i** and 46.9 kJ/mol for **TS (64-65)_ii**, has to be surmounted to finally afford **65** and the recovery of the **CoPc**. As it was expected, the final product is clearly more stable than the starting **63** implying a neat energy release. From the presented computational data, both energy barriers (**TS (63-64)** and **TS (64-65)**) from both orientations (**i** and **ii**) seem to be ruling the reaction outcome for the back-reaction. Considering the very similar maximum energy barriers (50.8 kJ/mol for **TS (64-65)_i** and 58.6 kJ/mol for **TS (63-64)_ii**), the two pathways could be acting at the same time, while the path **i** would be slightly preferred. These lower energy barriers are caused by the substituents included in the **57/58** system, as in the unsubstituted **QC** features an energy barrier of 95.8 kJ/mol, see Figure 7.15.

7. Molecular energy storage systems

These low energy barriers cause the efficient heat release as experimentally measured for **57** and they are due to the charge stabilization in the oxidative addition adduct when cyano (ii) or *p*-methoxyphenyl (i) substituents are placed in R₁. Considering the computed relative energy between **63** and **65**, a neat heat release value of 61.7°C could be obtained, in excellent agreement with the experimental data (63.4°C) as well as with the theoretical maximum limit achieved from DSC data, corresponding to 65.4°C.

To sum-up the overall behavior observed for the **NBD/QC** system (**57/58**) studied in this section, a unified scheme comprising the catalytic and photochemical mechanism is depicted in Figure 7.19.

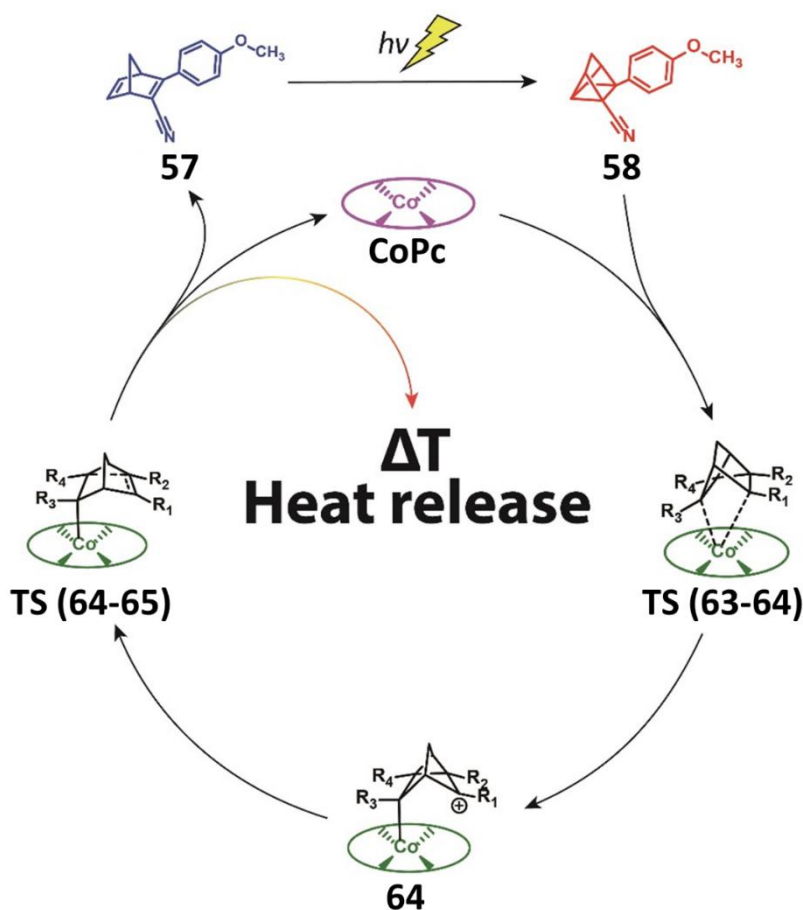


Figure 7.19. Catalytic cycle for the back-reaction.

Any subsequent improvement in the catalytic energy release would imply the design of new norbornadiene/catalyst pairs to further reduce the ruling energy barrier. From the results shown here, a new generation of MOST systems could be envisioned in which the charge generated in the rate-determining step of the back-reaction could

be further stabilized to provide an improved heat release. For the design of these new structures, the whole system must be considered as the substituents present in the quadricyclane, the metal and ligands of the catalyst and the solvent could have an impact in the energy barrier.

7.4.4. Contribution report

As can be seen in the contribution report of this published work,^[18] the following people contributed to the development of this section.

I synthesized the cotton and silica catalyst and did the flow and heat release experiments with those samples. Together with some experiments in the vacuum chamber with concentrate solutions. In addition, Diego Sampedro and I mainly performed the computational study.

Zhihang Wang measured the quantum yields, did the catalyst screening and the cycling test. Also, the catalyst physisorption, outdoor test and the main part of the heat release assays (together with Ana Roffey).

Anders Lennartson, Martyn Jevric and Anne U. Petersen designed and contributed to the syntheses of the studied NBD derivative. Ambra Dreos measured absorptivity and DSC. Also, Maria Quant performed kinetic studies and measured quantum yield.

Zhihang Wang, Ana Roffey, Karl Börjesson and Kasper Moth-Poulsen designed some of the experiments presented here. Some of the presented work, not included on the referred paper, was also designed together with me.

7.5. Azobenzene as MOST

The research reported in this section was also performed in collaboration with Kasper Moth-Poulsen's group. My contribution was to provide computational support to unveil and further investigate the thermal mechanism of the azobenzene back-conversion catalyzed with copper(I) salts. As mentioned before, a novel liquid azobenzene was developed in Japan in 2014.^[29] This molecule was also reinvestigated looking into a device application in Sweden and computationally investigated in La Rioja.

At first place, a re-evaluation of the critical features for a MOST system were performed. An initial study in terms of its absorptivity, half-life of energy storage and quantum yields of photoisomerization reaction was done to obtain the relevant values in the desired solvent. As previously stated for **NBD/QC** experiments, toluene was chosen.

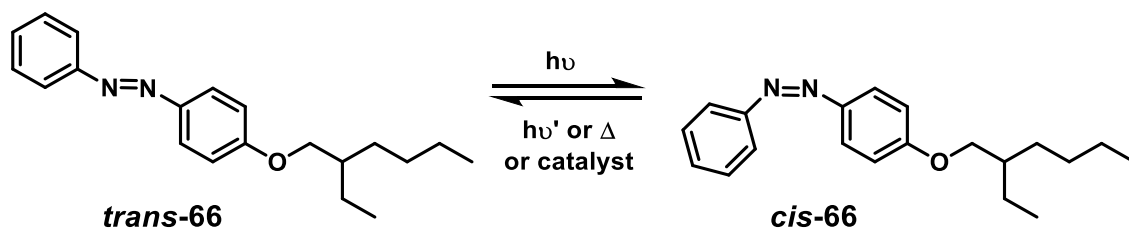


Figure 7.20. Structure and reactivity of the studied compound **66**.

Comparing these results with the previously reported data of **66** in methanol,^[29] the absorption maximum is slightly red shifted, indicating a low solvent polarity effect. In this case, a red shifting of 5 nm is observed with a maximum absorptivity of $\epsilon_{\text{Max}@350\text{nm}} = 2.6 \times 10^4 \text{ M}^{-1} \text{ cm}^{-1}$, as can be seen in Figure 7.21.a). Concerning the storage lifetime, a half-life from *cis* to *trans* isomerization of 36.3 h in toluene can be obtained from the data of the Eyring model. For that, the activation enthalpy was calculated as $\Delta H_{\text{therm}}^{\ddagger} = 22.39 \text{ kcal/mol}$, with an associated free energy $\Delta G = 24.7 \text{ kcal/mol}$ for the heat release reaction. In addition, the quantum yield of the *trans* to *cis* photoisomerization reaction was determined to be 21% at 340 nm. Additionally, it was observed that the *cis*-**66** state can photoisomerize back to the *trans* form. The corresponding quantum yield of the *cis* to *trans* photoisomerization was determined to be 23% at 455 nm, slightly higher than the reverse process.

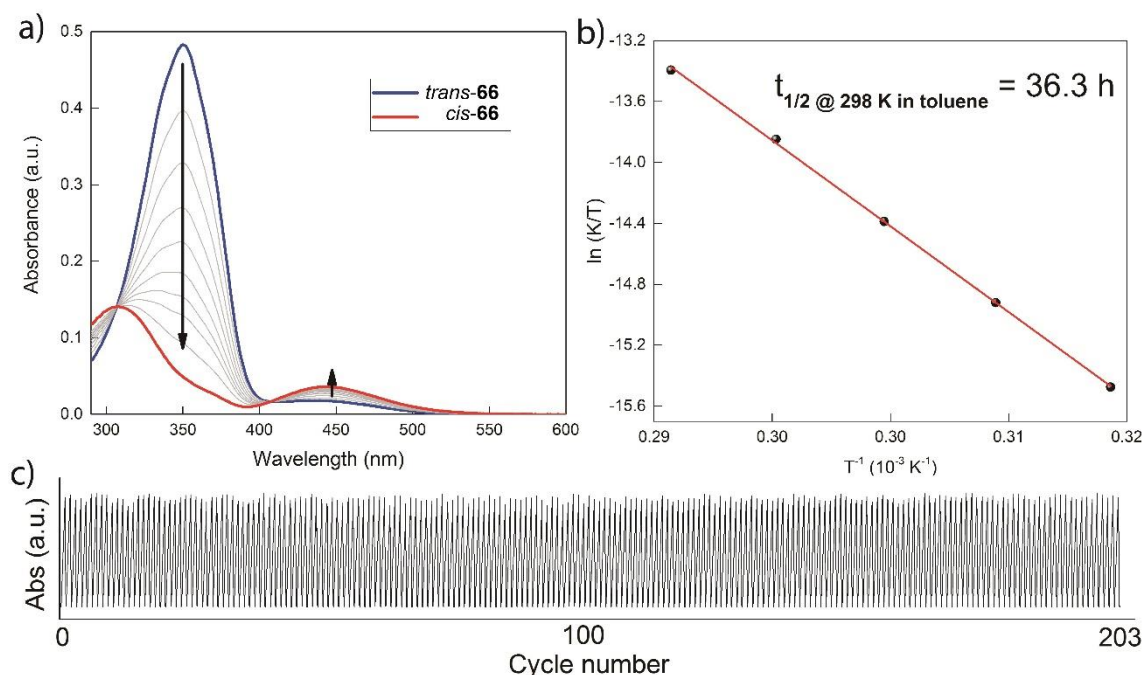


Figure 7.21. a) Absorption spectra of *trans*-**66** (in blue) and its corresponding photoisomer *cis*-**66** (in red). b) Eyring plot of *cis*-**66** in toluene solution. c) Optical cycling test of **66** in toluene.

To investigate the robustness of **66**, two controllable LED light sources (340 and 455 nm) were turned on and off alternatively to charge and discharge the molecules back and forth. After 203 complete cycles, during a total operation time of 22.6 h, no significant signs of degradation were observed, thus demonstrating a high robustness of **66**, even in the presence of oxygen (see Figure 7.21.c).

7.5.1. Exploration of azobenzene on device tests

To further demonstrate the functionality of **66** in a real device, a continuous flow system was built. For this lab-scale implementation, an AM1.5 solar simulator was used as irradiation source and diluted solutions of **66** were irradiated, probing conversion by UV-Vis spectroscopy (gray boxes 1 and 2 in Figure 7.22.a). For that, two concentrations of compound **66** solutions, $2 \times 10^{-4} \text{ M}$ in green, and $5 \times 10^{-4} \text{ M}$ in red, were pumped individually through a microfluidic chip,^[32] with varying residence time (33.9 mm^3 inner volume with a channel depth of $100 \mu\text{m}$, item 3 in Figure 7.22.a). Since *cis*-**66** can be back-converted by visible light, an optical UV transmitting band pass filter ($< 400 \text{ nm}$) was inserted in between the solar simulator and the microfluidic chip. The UV-

7. Molecular energy storage systems

Vis spectra of the **66** solution before and after the microfluidic chip were measured, obtaining the *cis*-to-*trans* conversion percentage with the following equation:

$$\text{Conversion \%} = \frac{\frac{A_{@350 \text{ nm}}}{A_{iso@306 \text{ nm}}} \epsilon_{iso@306 \text{ nm}} - \epsilon_{isomer@350 \text{ nm}}}{\epsilon_{parent@350 \text{ nm}} - \epsilon_{isomer@350 \text{ nm}}},$$

where $A_{@350 \text{ nm}}$ is the current absorbance at 350 nm. $A_{iso@306 \text{ nm}}$ and $\epsilon_{iso@306 \text{ nm}}$ correspond to the absorbance and absorptivity of the solution at its isosbestic point at 306 nm, respectively; and $\epsilon_{parent@350 \text{ nm}}$ and $\epsilon_{isomer@350 \text{ nm}}$ are the absorptivity of the **trans-66** and **cis-66** isomers at 350 nm, respectively.

A maximum conversion of around 80% from **trans-66** to the *cis* state was obtained, mainly reaching a photo-stationary state, which maintains this isomers ratio.

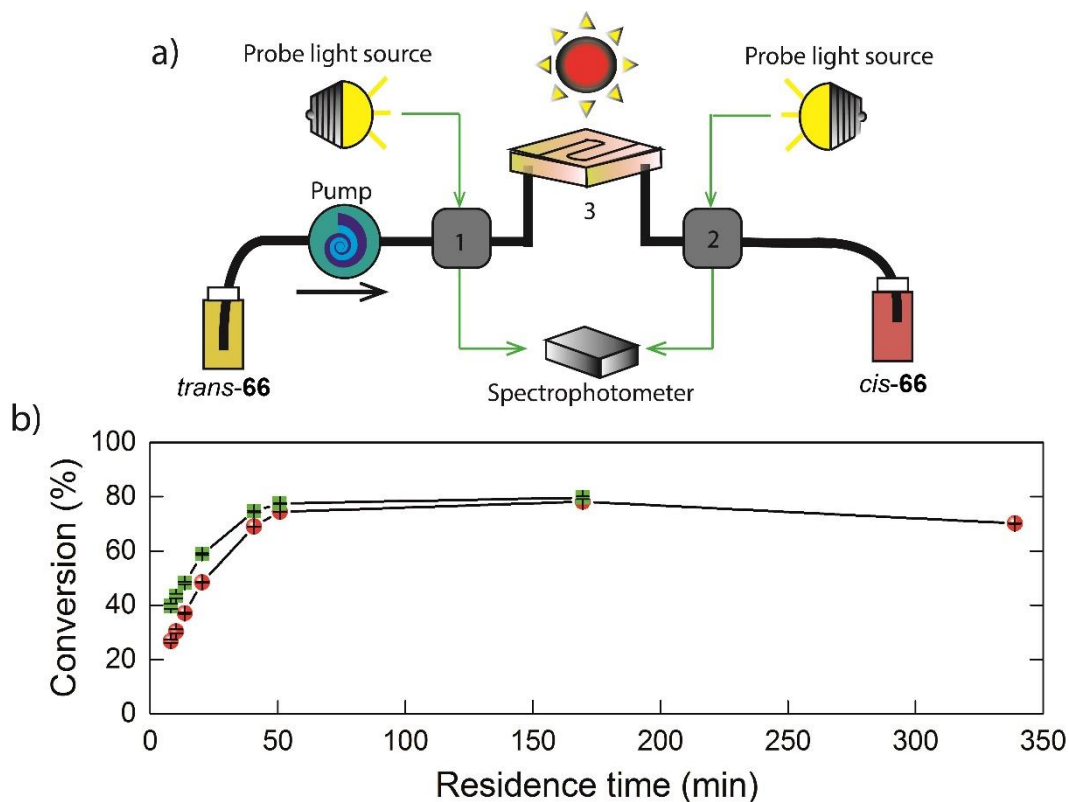


Figure 7.22. a) Experimental setup of **66** in a fluidic chip device. b) Conversion percentage of *trans-66* with different residence times in the microfluidic chip.

After the solar light capture, energy release is the second fundamental process for the MOST concept. To estimate the adiabatic heat release as a function of concentration, a modified equation from previous work^[18] needs to be used when considering a neat sample. In this case, the solvent term can be dismissed and the equation simplified as follows.

$$\Delta T = \frac{\Delta H_{storage}}{C_{p,66}}$$

where $\Delta H_{storage}$ corresponds to the DSC measured energy storage capacity of **cis-66** which equals to 167.5 J g^{-1} ; $C_{p,66}$ is the specific heat capacity of **66** in $\text{J g}^{-1} \text{ K}^{-1}$, assuming similar as unsubstituted azobenzene.^[49]

In the case of **66**, the theoretical maximum temperature difference was calculated as ca. 226°C for a fully charged neat sample.

7.5.2. Catalyst screening for the back-conversion reaction

Regarding the election of the catalyst, several candidates including mineral acids like perchloric acid, Cu(II) salts ($\text{CuCl}_2, \text{Cu}(\text{OAc})_2$), gold nanoparticles which involve a redox mechanism,^[50] as well as electrocatalytic methods^[51] have been reported to be able to induce the back conversion of azobenzene derivatives. However, for a closed cycle system, which could be operated in devices, a heterogeneous catalyst that can be fixed in a reaction center is required. Based on this fact, a heterogeneous catalyst or a supported catalyst needs to be developed.

For **66**, two potential catalysts, cobalt(II) phthalocyanine physisorbed on the surface of activated carbon (**CoPc@C**) and $[\text{Cu}(\text{CH}_3\text{CN})_4]\text{PF}_6$ fulfill the described physical properties and thus, they were tested individually. Both showed a positive effect on reducing the back-conversion half-life at room temperature. $[\text{Cu}(\text{CH}_3\text{CN})_4]\text{PF}_6$ has a very low solubility in toluene, being active for various MOST systems, including norbornadiene/quadricyclane derivatives^[18] as well as the dihydroazulene/vinylheptafulvene couple.^[32] For **cis-66** compound, a back conversion reaction rate at room temperature was calculated to be 30 s^{-1} (up to 6×10^6 time higher compared to a reaction rate of $5 \times 10^{-6} \text{ s}^{-1}$ without catalyst at 25°C , see Figure 7.23.a).

7. Molecular energy storage systems

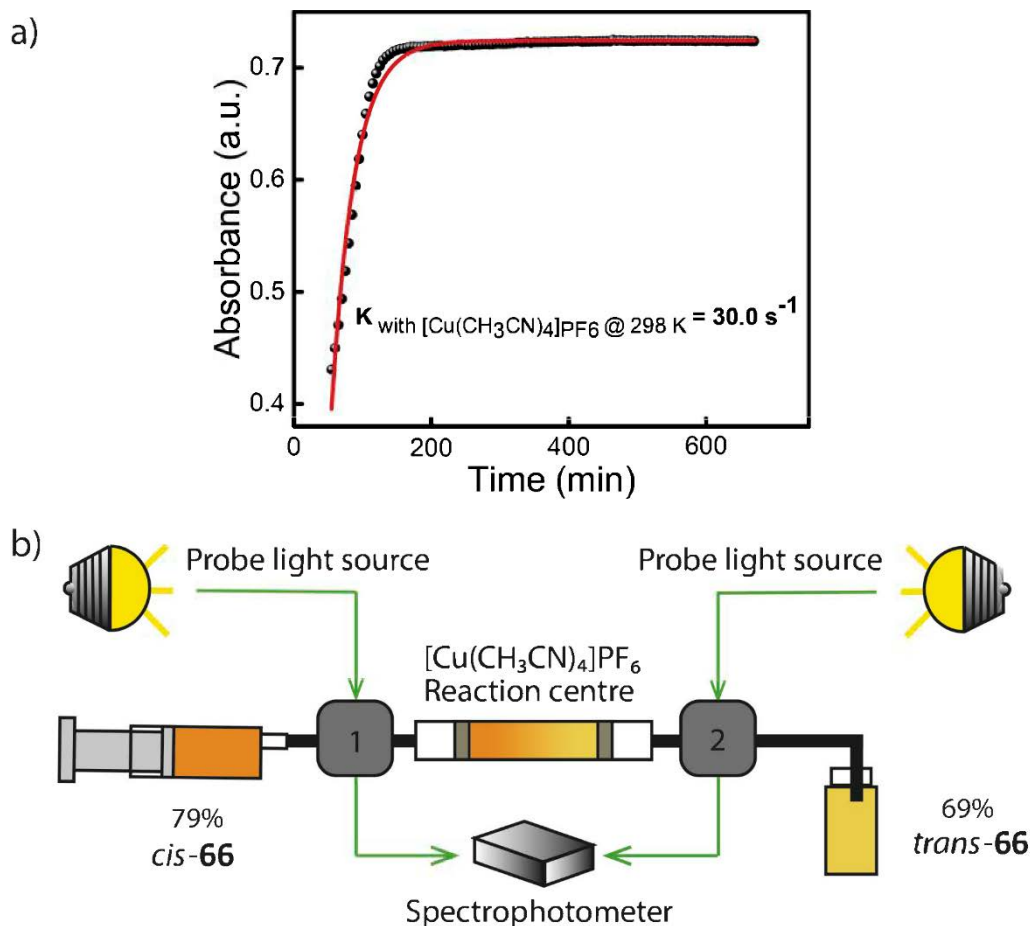


Figure 7.23. **a)** Kinetics study of *cis*-**66** in presence of $[\text{Cu}(\text{CH}_3\text{CN})_4]\text{PF}_6$ in toluene at 25 °C. **b)** Conceptual device demonstration of catalytic back conversion of *cis*-**66**.

With this result in mind, a small-sized reaction center was built. 5 mg of the Cu(I) salt was inserted into a Teflon tube which has a 1 mm inner diameter (see Figure 7.23.b). A 5×10^{-4} M of 79% *cis*-**66** solution from microfluidic chip experiments was then flowed through the catalytic bed with a speed of 1 mL h^{-1} . As result, 48% of the *cis*-**66** was successfully back converted to the corresponding *trans* state. Thus, the described continuous fluidic chip experiments can achieve the requirements for a complete application of the MOST concept including photon capture/storage and energy release process.

7.5.3. Computational exploration of the catalytic mechanism

Regarding the back-conversion of azobenzene, several possible mechanisms have been proposed. As previously reported,^[52] the mechanism of the thermal reversion of azobenzene could proceed by two main pathways (see Figure 7.24), inversion and rotation. Also, other mechanistic alternatives can rule it, such as concerted inversion and inversion-assisted rotation. The dominant mechanism seems to be very influenced by the substituents of the azo moiety and the reaction conditions.

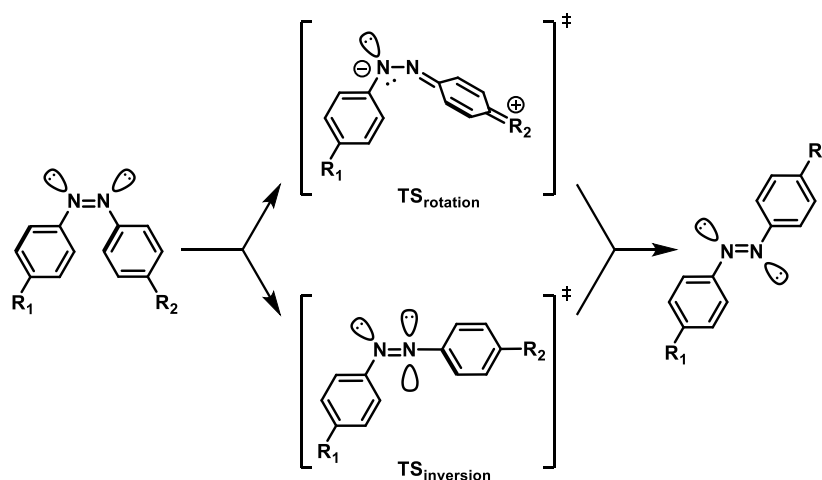


Figure 7.24. Main mechanisms that can rule the azobenzene back-reversion.^[52]

In compounds similar to **66**, the inversion mechanism is usually the relevant one in the thermal back-conversion. This fact was also verified through this computational study. For this study a simplified **66** system was used replacing the ethylhexyl moiety with a methyl group (**67**). From a preliminary exploration, the isomerization of **67** was evaluated considering both possible mechanisms. The scan along the torsion coordinate does not yield in the desired rotation transition state. Instead, the two possible inversion TSs were obtained (**TS 67a** and **TS 67b**). The scan along torsion coordinate and the critical points are represented in Figure 7.25. The energy barrier for the back-conversion was found to be of 25.4 kcal/mol.

7. Molecular energy storage systems

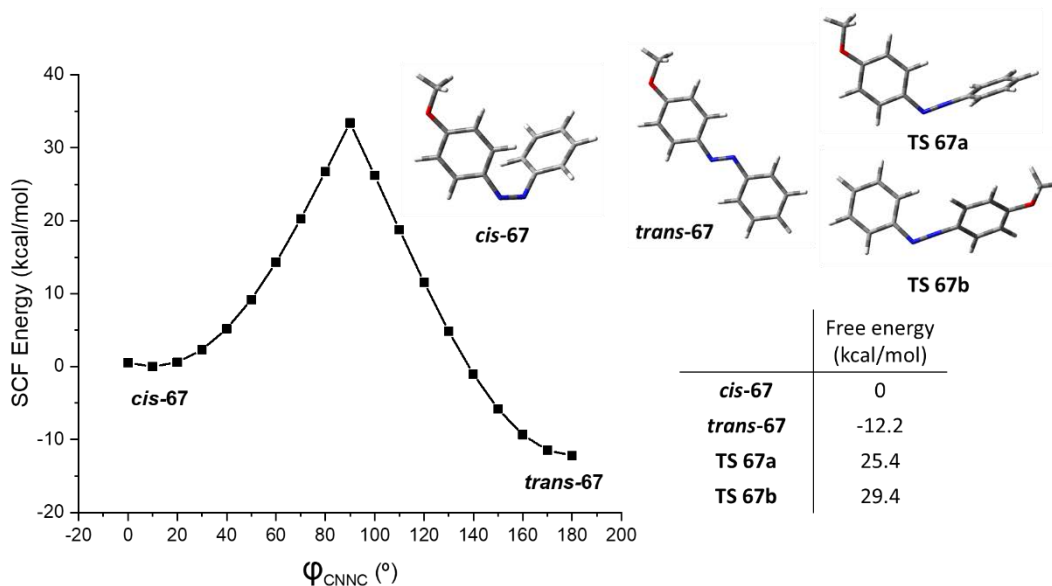


Figure 7.25. Scan along the CNNC dihedral torsion, without find a TS. Free energies for **67** critical points.

To further study the mechanism of back-conversion with $[\text{Cu}(\text{CH}_3\text{CN})_4]\text{PF}_6$, a simplified system **67** was used at the PCM-B3LYP-D3BJ/6-31G(d)+SDD(Cu) level of theory. Among the different coordination options, the CH_3CN ligands could be displaced by the new ligand (the *cis* isomer of the azobenzene moiety, in this case). As the azobenzene derivative is not symmetric, two sets of coordination alternatives arise, with that, the four different coordination possibilities were considered to ensure a good modelling of the experimental conditions. Additionally, a π coordination of the azobenzene to the copper atom was explored. In all cases, this structure collapses to either **68_i** or **68_ii** minima. Also, alternative mechanisms such as cyclometallation,^[53] loss of two CH_3CN molecules and electron transfer mechanisms were computed. In all cases, these pathways feature more energetic species that allowed to rule out different reaction mechanisms. After this preliminary consideration, a complete mechanistic evaluation was performed considering the relevant options shown in Figure 7.26.

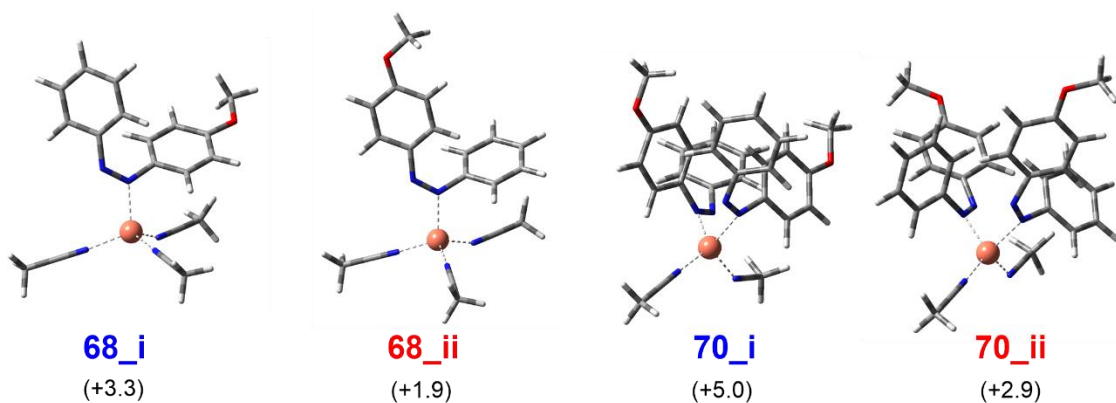


Figure 7.26. Different coordination types and relative energies in kcal/mol. Cu ion is the central atom in the figure.

However, it was impossible to reach a converged structure for the corresponding transition states of **70_i**-**70_{ii}** due to methyl rotation in acetonitrile molecules. Thus, only one molecule of **67** could be bonded to the metal center giving compound **68**.

In all cases, the formation of the new complex **68** is slightly endergonic (1-5 kcal/mol). Coordination through the nitrogen atom directly linked to the unsubstituted phenyl ring (path **ii**, in red) is favored (by *ca.* 2.3 kcal/mol) as compared to the methoxyphenyl linked nitrogen atom (path **i**, in blue). Rotation and inversion mechanisms of the isomerization were considered. As in the not catalyzed thermal reaction,^[54] the inversion transition states (TS (**68-69**)_{**i**} and TS (**68-69**)_{**ii**}) were found to be preferred, as can be seen in Figure 7.27.

7. Molecular energy storage systems

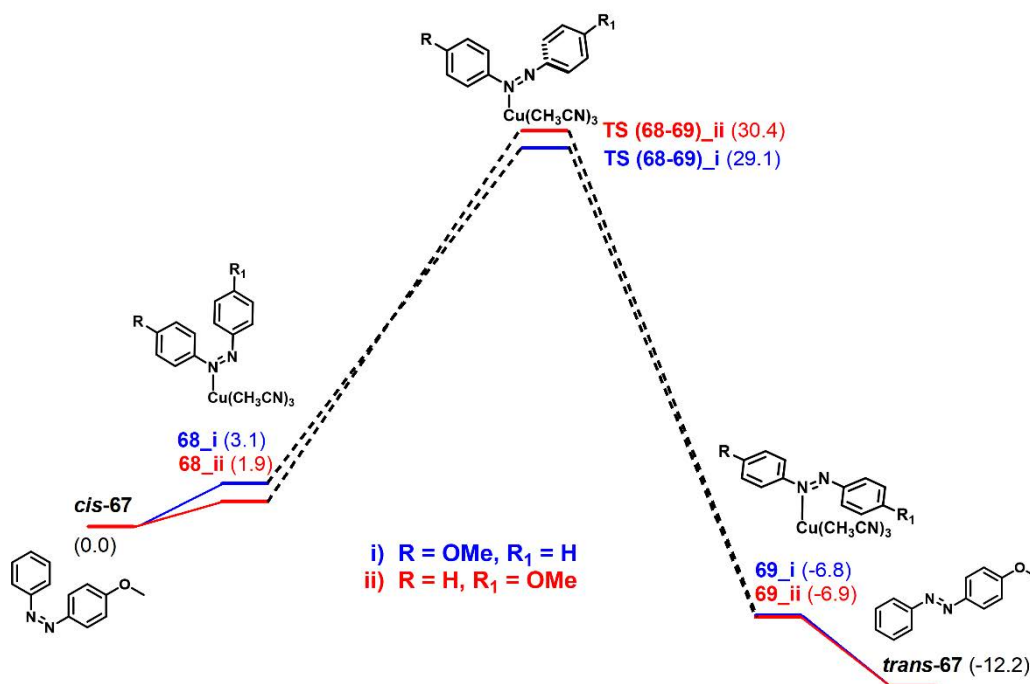


Figure 7.27. Reaction paths for *cis-trans* isomerization. Free energies referred to *cis-67*+Cu(CH₃CN)₄⁺.

As it was discussed in previous papers,^[54, 55] the minimum in the T₁ PES is found at the twisted geometry, well below the S₀ energy. The S₀ and T₁ PESs cross along the torsion of the central N=N bond, but not along the inversion coordinate. For that, a relaxed scan along the rotation coordinate (CNNC dihedral) in compound **68** reveals a possible S₀-T₁-S₀ mechanism accessible by coordination of the nitrogen atom of *cis-67* to copper (see Figure 7.28), which reveals a MLCT (metal-to-ligand charge transfer) transition. In turn, this implies the participation of a π* orbital of the azobenzene allowing rotation along the N=N with participation of the T₁ state. At relative high torsion angles, the triplet state becomes less energetic and this path yields a barrier of around 20 kcal/mol. This alternative mechanism allows for the bypassing of the more energetic inversion TS (**68-69**) in the ground state (ca. 30 kcal/mol), as can be seen in Figure 7.29,

and it should be available at room temperature. The minimum energy crossing points (MECP) were also located to clearly define the topology of the surface crossing.

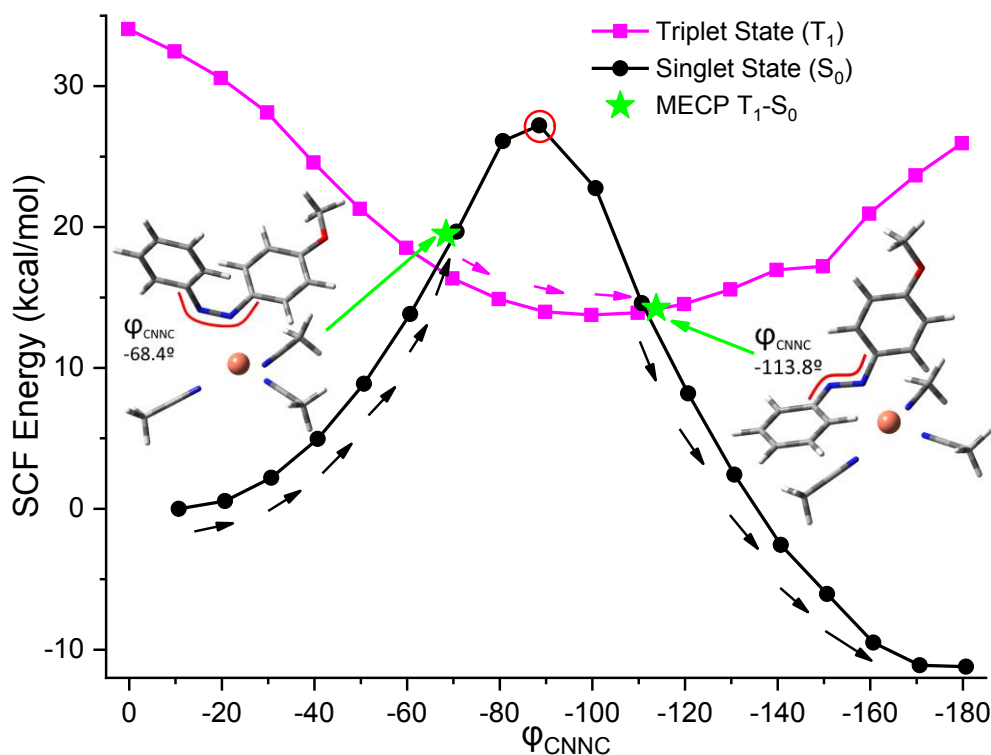


Figure 7.28. Relaxed scan along CNNC rotation and MECPs. Red circle depicts TS (68-69).

To better understand the nature of the triplet state, some TD-DFT calculations considering singlets and triplets were performed. The lowest excited triplet state matches with a HOMO-LUMO transition (with a weight of 73%), which presents a clear MLCT nature (ca. 30% of contribution from copper to HOMO). Also, the same behavior is observed in S_1 . Thus, the metal center plays a major role in the population possibility of excited state (singlet or triplet).

The reaction rate then depends on the energy barrier connecting the S_0 minimum and the MECP to the T_1 state and the relevant SO (spin-orbit) couplings. Without catalyst, the computed MECP for **67** (MECP **67**) is located at 16.1 kcal/mol above *cis*-**67** isomer. This energy barrier should be compared with the experimental values (23.5 kcal/mol from the Arrhenius equation, 24.7 kcal/mol from Eyring equation, see Figure 7.21.b). However, in this case the SO coupling will be low enough to avoid triplet state population in the *cis-trans* isomerization of **67** without metal complex. The transition state barrier (TS **67**, 25.4 kcal/mol) is closer to the experimental values. In contrast, for the Cu mediated back-conversion, a computed barrier of 19.4 kcal/mol was found. This

7. Molecular energy storage systems

is consistent with the experimental barrier of 15.5 kcal/mol, calculated from the kinetic constant measured of 30 s^{-1} , by means of the Eyring equation with a transmission coefficient of $\kappa = 1$ for all cases.

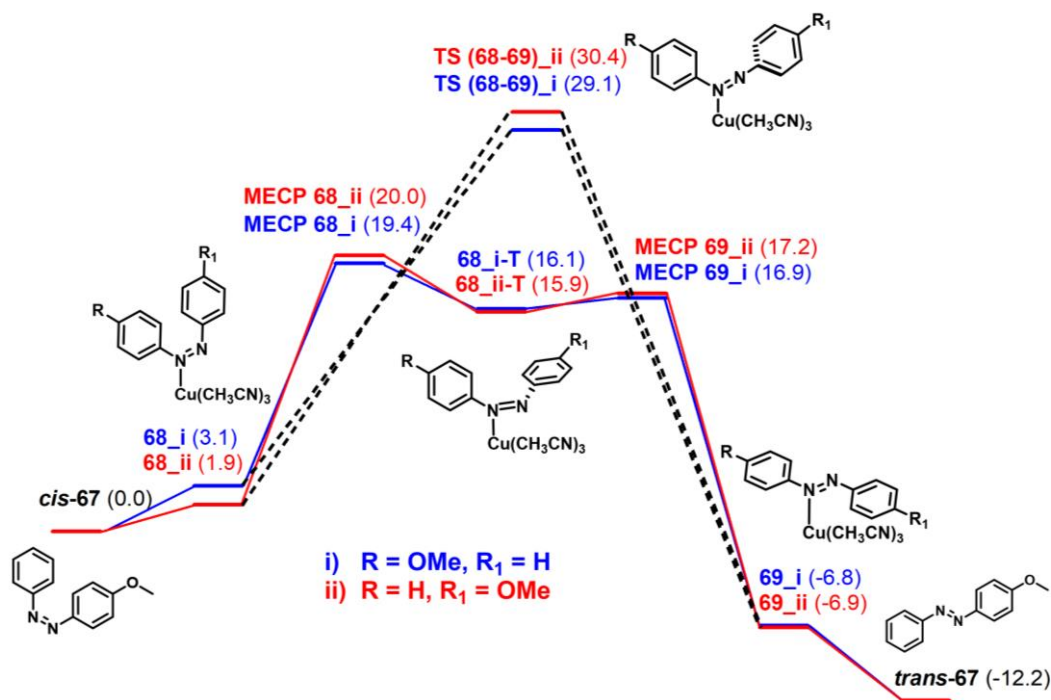


Figure 7.29. Complete mechanism, bypassing of the more energetic inversion TS by a MECP between singlet and triplet states.

Thus, copper coordination yields in a decrease in the isomerization barrier of ca. 6 kcal/mol (computed barrier decreases from 25.4 kcal/mol for **67** to 19.4 kcal/mol). Even being this small decrease in the energy barrier, it is enough to allow the isomerization process to occur in a few minutes instead of some days. Thus, accelerating the isomerization by 4 orders of magnitude, allowing a good agreement with experiments (energy difference of 8 kcal/mol, from 23.5 kcal/mol for the free **66** to 15.6 kcal/mol for the copper activated reaction). Overall, while $[\text{Cu}(\text{CH}_3\text{CN})_4]\text{PF}_6$ is useful to increase notably the reaction rate, there is still great potential for improvement in the design of the energy release step. This could be done, for instance, favoring the MLCT or stabilizing the MECP between singlet and triplet states to increase the efficiency of the crossing. In both cases, this could lead to a decrease in the energy barrier and a subsequent acceleration of the back-conversion.

7.5.4. Contribution report

I performed the computational study regarding the catalyzed back-conversion of azobenzene.

Zhihang Wang did the re-evaluation of the photochemical and photophysical properties in toluene. Also did the catalyst screening and the device tests explained before. Together with the design of experiments with Kasper Moth-Poulsen.

Masa-aki Morikawa and Nobuo Kimizuka provided the compound.

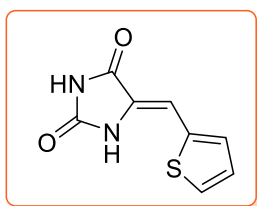
7.6. Experimental section

7.6.1. Experimental details

- General procedure

A solution of imidazolidine-2,4-dione (20 mmol) and ammonium acetate (3.6 mmol) in acetic acid (5 mL) was added to aldehyde (20 mmol), and the resulting mixture was stirred at 120°C for 16 h. After cooling, the reaction mixture was poured in water. The resulting precipitate was filtered and dried affording the 5-arylideneimidazolidine-2,4-diones as pale color solids (with yields ranging from 75 to 90%).

- (Z)-5-(thiophen-2-ylmethylene)imidazolidine-2,4-dione (**47**)



Empiric Formula: C₈H₆N₂O₂S

Molecular weight: 194.21

Yield: 80%

The compound was obtained as a brownish solid.

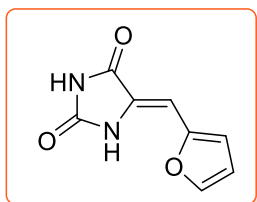
¹H NMR (300 MHz, DMSO-*d*₆) δ ppm 11.25 (s, 1H), 10.34 (s, 1H), 7.70 (dd, *J* = 5.0, 1.0 Hz, 1H), 7.60 (dt, *J* = 3.7, 0.9 Hz, 1H), 7.17 (ddd, *J* = 5.1, 3.7, 0.5 Hz, 1H), 6.57 (s, 1H).

¹³C NMR (75 MHz, DMSO-*d*₆) δ ppm 165.2, 155.4, 136.0, 129.0, 128.8, 128.6, 126.2, 101.5.

UV-Vis (CH₃CN): λ (nm) = 333, 348 (ε = 5200 M⁻¹cm⁻¹).

ES-MS (+) (C₈H₆N₂O₂S + H): calc. 195.0223 found 195.0224.

- (Z)-5-(furan-2-ylmethylene)imidazolidine-2,4-dione (**48**)



Empiric Formula: C₈H₆N₂O₃

Molecular weight: 178.15

Yield: 80%

The compound was obtained as a brownish solid.

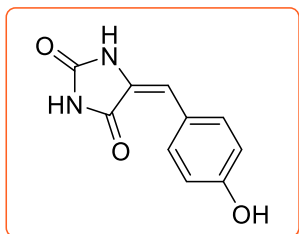
¹H NMR (300 MHz, MeOD) δ ppm 7.69 (d, *J* = 1.4 Hz, 1H), 6.72 (dd, *J* = 3.5, 0.6 Hz, 1H), 6.56 (dd, *J* = 3.5, 1.8 Hz, 1H), 6.43 (s, 1H).

¹³C NMR (75 MHz, MeOD) δ ppm 167.0, 156.8, 151.3, 146.0, 127.2, 114.9, 113.4, 99.0.

UV-Vis (CH₃CN): λ (nm) = 335, 350 (ε = 4800 M⁻¹cm⁻¹).

ES-MS (+) (C₈H₆N₂O₃ + H): calc. 179.0451.0223 found 179.0449.

- (E)-5-(4-hydroxybenzylidene)imidazolidine-2,4-dione (**52**)



Empiric Formula: C₁₀H₈N₂O₃

Molecular weight: 204.19

Yield: 90%

The compound was obtained as a yellowish solid.

¹H NMR (300 MHz, DMSO-*d*₆) δ ppm 10.42 (bs, 3H), 7.47 (d, *J* = 8.7 Hz, 2H), 6.79 (d, *J* = 8.6 Hz, 2H), 6.35 (s, 1H).

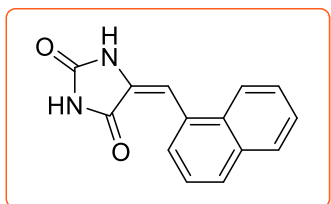
¹³C NMR (75 MHz, DMSO-*d*₆) δ ppm 165.7, 158.0, 155.6, 131.3, 125.4, 123.9, 115.7, 109.3.

UV-Vis (CH₃CN): λ (nm) = 328 (ε = 15400 M⁻¹cm⁻¹).

ES-MS (+) (C₁₀H₈N₂O₃ + H): calc. 205.0608 found 205.0603.

7. Molecular energy storage systems

- (*E*)-5-(naphthalen-1-ylmethylene)imidazolidine-2,4-dione (**53**)



Empiric Formula: C₁₄H₁₀N₂O₂

Molecular weight: 238.25

Yield: 85%

The compound was obtained as a yellowish solid.

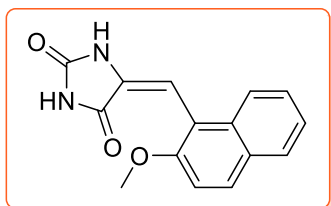
¹H NMR (400 MHz, DMSO-*d*₆) δ ppm 10.63 (s, 1H), 8.11 – 8.04 (m, 1H), 8.01 – 7.93 (m, 1H), 7.93 (d, *J* = 8.2 Hz, 1H), 7.73 (dt, *J* = 7.2, 1.0 Hz, 1H), 7.70 (bs, 1H), 7.66 – 7.50 (m, 3H), 7.00 (s, 1H).

¹³C NMR (101 MHz, DMSO-*d*₆) δ ppm 174.3, 165.7, 158.8, 156.1, 133.7, 131.5, 130.7, 129.8, 129.1, 127.7, 127.3, 126.7, 126.2, 124.0, 104.8.

UV-Vis (CH₃CN): λ (nm) = 335 (ε = 14300 M⁻¹cm⁻¹).

ES-MS (+) (C₁₄H₁₀N₂O₂ + H): calc. 239.0815 found 239.0818.

- (*E*)-5-((2-methoxynaphthalen-1-yl)methylene)imidazolidine-2,4-dione (**54**)



Empiric Formula: C₁₅H₁₂N₂O₃

Molecular weight: 268.27

Yield: 85%

The compound was obtained as a green-yellow solid.

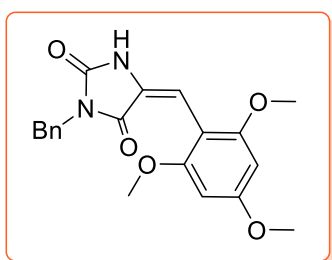
¹H NMR (400 MHz, DMSO-*d*₆) δ ppm 8.31 (bs, 1H), 7.98 (d, *J* = 9.1 Hz, 1H), 7.94 – 7.86 (m, 1H), 7.75 (dd, *J* = 8.6, 1.1 Hz, 1H), 7.53 (ddd, *J* = 8.4, 6.8, 1.4 Hz, 1H), 7.47 (d, *J* = 9.1 Hz, 1H), 7.39 (ddd, *J* = 8.0, 6.8, 1.1 Hz, 1H), 6.70 (s, 1H), 3.94 (s, 3H).

¹³C NMR (101 MHz, DMSO-*d*₆) δ ppm 164.9, 154.9, 154.7, 131.8, 131.2, 130.4, 128.4, 128.3, 127.1, 123.6, 114.1, 113.4, 102.2, 79.2, 56.0.

UV-Vis (CH₃CN): λ (nm) = 322, 355 (ϵ = 15800 M⁻¹cm⁻¹).

ES-MS (+) (C₁₅H₁₂N₂O₃ + H): calc. 269.0921 found 269.0925.

- (*E*)-3-benzyl-5-(2,4,6-trimethoxybenzylidene)imidazolidine-2,4-dione (**55**)



Empiric Formula: C₂₀H₂₀N₂O₅

Molecular weight: 368.39

Yield: 75%

The compound was obtained as a yellowish solid.

¹H NMR (400 MHz, CDCl₃) δ ppm 7.76 (bs, 1H), 7.41 (d, J = 6.6 Hz, 2H), 7.34 – 7.19 (m, 3H), 6.96 (s, 1H), 6.13 (s, 2H), 4.73 (s, 2H), 3.83 (s, 6H), 3.81 (s, 3H).

¹³C NMR (101 MHz, CDCl₃) δ ppm 164.1, 162.8, 159.2, 153.6, 136.3, 128.6, 128.5, 127.7, 124.8, 104.4, 104.4, 91.2, 56.2, 55.4, 42.1.

UV-Vis (CH₃CN): λ (nm) = 345 (ϵ = 17900 M⁻¹cm⁻¹).

ES-MS (+) (C₂₀H₂₀N₂O₅ + H): calc. 369.1445 found 369.1446.

- **Norbornadiene and azobenzene derivatives**

Norbornadiene **57** and the parent quadricyclane **58** were prepared according to the literature,^[18] as happened with the azobenzene derivative **66**.^[29]

7.6.2. Computational details

All calculations were carried out using the B3LYP-D3BJ,^[56] M06^[57] or BP86^[58] functionals included in the Gaussian09^[59] and Gaussian16^[60] program packages. Also, the standard basis sets 6-31G+(d)^[61] for **QC** and 6-31G(d)^[61] for C, N, H and O atoms and the SDD^[62] effective core potential for Cu. This base was selected for copper atom to reduce the computational cost. In this, the core electrons are represented by a potential instead of their corresponding wavefunctions. All critical points in the PES were characterized with frequency calculations to include the ZPE and free energy corrections and verify the stationary points as transition states (one imaginary frequency) or minima (zero imaginary frequencies). Minimum energy crossing points (MECP) were computed using the *easymecp* software,^[63] which is a simplified Python wrapper around the original MECP Fortran code from J. Harvey (2003) developed by J. Rodríguez-Guerra and I. Funes-Ardóiz. All geometry optimizations were computed in solution with implicit solvent applying the PCM solvation model^[64] with toluene as solvent ($\epsilon = 2.3741$). We also checked the transition states by relaxing them towards reactants and products or with IRC calculations. Relaxed scan was done in triplet and singlet states along the CNNC dihedral from *cis* to *trans*-isomer. TD-DFT spectra were calculated using CAM-B3LYP^[65]/6-31G(d) + SDD(Cu) considering 10 singlets and 10 triplets. *Gausssum*^[66] was used to calculate contribution percentage of the different fragments to molecular orbitals and contributions to different transitions from orbitals involved.

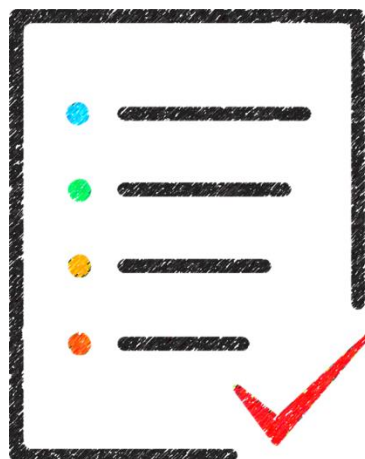
7.7. Bibliography

- [1] N. S. Lewis, D. G. Nocera, *Proc. Natl. Acad. Sci. U.S.A.* **2006**, *103*, 15729–15735.
- [2] REN21 COMMUNITY; in *Renewables 2018, Global Status Report*, **2018**.
- [3] United Nations Development Programme and World Energy Council, in *Energy and the challenge of sustainability*, **September 2000**. Retrieved 17 January 2017.
- [4] O. Inganäs, V. Sundström, *Ambio* **2016**, *45 Suppl 1*, S15-23.
- [5] E. W. Law, A. A. Prasad, M. Kay, R. A. Taylor, *Solar Energy* **2014**, *108*, 287-307.
- [6] www.ree.es (in Spanish). Retrieved 2017-07-04, **2017**.
- [7] Z.-I. Yoshida, *J. Photochem.* **1985**, *29*, 27-40.
- [8] K. Moth-Poulsen, in *Organic Synthesis and Molecular Engineering* (Ed.: M. B. Nielsen), John Wiley & Sons, Inc., **2014**, pp. 179-196.
- [9] M. Armand, J. M. Tarascon, *Nature* **2008**, *451*, 652-657.
- [10] R. E. Blankenship, D. M. Tiede, J. Barber, G. W. Brudvig, G. Fleming, M. Ghirardi, M. R. Gunner, W. Junge, D. M. Kramer, A. Melis, T. A. Moore, C. C. Moser, D. G. Nocera, A. J. Nozik, D. R. Ort, W. W. Parson, R. C. Prince, R. T. Sayre, *Science* **2011**, *332*, 805-809.
- [11] M. Dinda, S. Chakraborty, M. Kanti Si, S. Samanta, B. Ganguly, S. Maiti, P. K. Ghosh, *RSC Adv.* **2014**, *4*, 54558-54564.
- [12] A. Lennartson, A. Roffey, K. Moth-Poulsen, *Tetrahedron Lett.* **2015**, *56*, 1457-1465.
- [13] C.-L. Sun, C. Wang, R. Boulatov, *ChemPhotoChem* **2019**, *0*.
- [14] C. García-Iriepa, M. Marazzi, L. M. Frutos, D. Sampedro, *RSC Adv.* **2013**, *3*, 6241-6266.
- [15] M. Blanco-Lomas, S. Samanta, P. J. Campos, G. A. Woolley, D. Sampedro, *J. Am. Chem. Soc.* **2012**, *134*, 6960-6963.
- [16] J. Ma, Y. Li, T. White, A. Urbas, Q. Li, *Chem. Commun.* **2010**, *46*, 3463-3465.
- [17] K. Börjesson, A. Lennartson, K. Moth-Poulsen, *ACS Sustain. Chem. Eng.* **2013**, *1*, 585-590.
- [18] Z. Wang, A. Roffey, R. Losantos, A. Lennartson, M. Jevric, A. U. Petersen, M. Quant, A. Dreos, X. Wen, D. Sampedro, K. Börjesson, K. Moth-Poulsen, *Energy Environ. Sci.* **2019**, *12*, 187-193.
- [19] M. Kuisma, A. Lundin, K. Moth-Poulsen, P. Hyldgaard, P. Erhart, *ChemSusChem* **2016**, *9*, 1745-1745.
- [20] V. A. Bren, A. D. Dubonosov, V. I. Minkin, V. A. Chernov, *Usp. Khim.* **1991**, *60*, 913-948.
- [21] K. Börjesson, D. Ósoso, V. Gray, J. C. Grossman, J. Guan, C. B. Harris, N. Hertkorn, Z. Hou, Y. Kanai, D. Lee, J. P. Lomont, A. Majumdar, S. K. Meier, K. Moth-Poulsen, R. L. Myrabo, S. C. Nguyen, R. A. Segalman, V. Srinivasan, W. B. Tolman, N. Vinokurov, K. P. C. Vollhardt, T. W. Weidman, *Chem. Eur. J.* **2014**, *20*, 15587-15604.
- [22] R. E. Schwerzel, N. E. Klosterman, J. R. Kelly, L. J. Hillenbrand, U.S. Patent 4105014/1978, **1978**.
- [23] C. Bastianelli, V. Caia, G. Cum, R. Gallo, V. Mancini, *J. Chem. Soc. Perk. Trans. 2* **1991**, 679-683.
- [24] A. M. Kolpak, J. C. Grossman, *Nano Lett.* **2011**, *11*, 3156-3162.
- [25] A. M. Kolpak, J. C. Grossman, *J. Chem. Phys.* **2013**, *138*, 1-6.
- [26] T. J. Kucharski, N. Ferralis, A. M. Kolpak, J. O. Zheng, D. G. Nocera, J. C. Grossman, *Nat. Chem.* **2014**, *6*, 441-447.

- [27] S. P. Jeong, L. A. Renna, C. J. Boyle, H. S. Kwak, E. Harder, W. Damm, D. Venkataraman, *Sci. Rep.* **2017**, *7*, 17773.
- [28] E. Durgun, J. C. Grossman, *J. Phys. Chem. Lett.* **2013**, *4*, 854-860.
- [29] K. Masutani, M.-a. Morikawa, N. Kimizuka, *Chem. Commun.* **2014**, *50*, 15803-15806.
- [30] A. Lennartson, K. Moth-Poulsen, in *Molecular Devices for Solar Energy Conversion and Storage* (Eds.: H. Tian, G. Boschloo, A. Hagfeldt), Springer Singapore, Singapore, **2018**, pp. 327-352.
- [31] M. Blanco-Lomas, D. Martínez-López, P. J. Campos, D. Sampedro, *Tetrahedron Lett.* **2014**, *55*, 3361-3364.
- [32] Z. Wang, J. Udmark, K. Börjesson, R. Rodrigues, A. Roffey, M. Abrahamsson, M. B. Nielsen, K. Moth-Poulsen, *ChemSusChem* **2017**, *10*, 3049-3055.
- [33] W. G. Dauben, R. L. Cargill, *Tetrahedron* **1961**, *15*, 197-201.
- [34] X.-W. An, Y.-D. Xie, *Thermochim. Acta* **1993**, *220*, 17-25.
- [35] M. J. Kuisma, A. M. Lundin, K. Moth-Poulsen, P. Hyldgaard, P. Erhart, *J. Phys. Chem. C* **2016**, *120*, 3635-3645.
- [36] A. D. Dubonosov, V. A. Bren, V. A. Chernoiyanov, *Russ. Chem. Rev.* **2002**, *71*, 917-927.
- [37] V. Gray, A. Lennartson, P. Ratanalert, K. Börjesson, K. Moth-Poulsen, *Chem. Commun.* **2014**, *50*, 5330-5330.
- [38] D. Sampedro, A. Migani, A. Pepi, E. Busi, R. Basosi, L. Latterini, F. Elisei, S. Fusi, F. Ponticelli, V. Zanirato, M. Olivucci, *J. Am. Chem. Soc.* **2004**, *126*, 9349-9359.
- [39] C. García-Iriepa, M. Marazzi, F. Zapata, A. Valentini, D. Sampedro, L. M. Frutos, *J. Phys. Chem. Lett.* **2013**, *4*, 1389-1396.
- [40] D. Martinez-Lopez, M. L. Yu, C. Garcia-Iriepa, P. J. Campos, L. M. Frutos, J. A. Golen, S. Rasapalli, D. Sampedro, *J. Org. Chem.* **2015**, *80*, 3929-3939.
- [41] L. Rivado-Casas, M. Blanco-Lomas, P. J. Campos, D. Sampedro, *Tetrahedron* **2011**, *67*, 7570-7574.
- [42] V. A. Bren', A. D. Dubonosov, V. I. Minkin, V. A. Chernoiyanov, *Russ. Chem. Rev.* **1991**, 451-469.
- [43] A. L. Tchougréeff, A. M. Tokmachev, R. Dronskowski, *Int. J. Quantum Chem* **2013**, *113*, 1833-1846.
- [44] F. Ghani, J. Kristen, H. Riegler, *J. Chem. Eng. Data* **2012**, *57*, 439-449.
- [45] I. Antol, *J. Comput. Chem.* **2013**, *34*, 1439-1445.
- [46] K. Jorner, A. Dreos, R. Emanuelsson, O. El Bakouri, I. Fdez. Galván, K. Börjesson, F. Feixas, R. Lindh, B. Zietz, K. Moth-Poulsen, H. Ottosson, *J. Mater. Chem. A* **2017**, *5*, 12369-12378.
- [47] T. E. Shubina, T. Clark, *Z. Naturforsch.* **2010**, *65b*, 347 - 356.
- [48] H. Ge, X. Chen, X. Yang, *Chem. Commun.* **2016**, *52*, 12422-12425.
- [49] J. A. Bouwstra, V. V. D. Leeuw, J. C. V. Miltenburg, *J. Chem. Thermodynam.* **1985**, *17*, 685-695.
- [50] E. Titov, L. Lysyakova, N. Lomadze, A. V. Kabashin, P. Saalfrank, S. Santer, *J. Phys. Chem. C* **2015**, *119*, 17369-17377.
- [51] A. Goulet-Hanssens, M. Utecht, D. Mutruc, E. Titov, J. Schwarz, L. Grubert, D. Bléger, P. Saalfrank, S. Hecht, *J. Am. Chem. Soc.* **2017**, *139*, 335-341.
- [52] J. García-Amorós, D. Velasco, *Beilstein J. Org. Chem.* **2012**, *8*, 1003-1017.
- [53] E. Léonard, F. Mangin, C. Villette, M. Billamboz, C. Len, *Catal. Sci. Technol.* **2016**, *6*, 379-398.
- [54] A. Cembran, F. Bernardi, M. Garavelli, L. Gagliardi, G. Orlandi, *J. Am. Chem. Soc.* **2004**, *126*, 3234-3243.
- [55] E. R. Talaty, J. C. Fargo, *Chem. Commun.* **1967**, 65-66.
- [56] S. Grimme, S. Ehrlich, L. Goerigk, *J. Comput. Chem.* **2011**, *32*, 1456.
- [57] Y. Zhao, D. G. Truhlar, *Theor. Chem. Acc.* **2008**, *120*, 215-241.

- [58] J. P. Perdew, *Phys. Rev. B* **1986**, 33, 8822-8824.
- [59] Gaussian 09, Revision D.01, M. J. Frisch, G. W. Trucks, H. B. Schlegel, G. E. Scuseria, M. A. Robb, J. R. Cheeseman, G. Scalmani, V. Barone, B. Mennucci, et al. Gaussian, Inc., Wallingford CT, **2009**.
- [60] Gaussian 16, Revision A.03, M. J. Frisch, G. W. Trucks, H. B. Schlegel, G. E. Scuseria, M. A. Robb, J. R. Cheeseman, G. Scalmani, V. Barone, G. A. Petersson, H. Nakatsuji, X. Li, M. Caricato, A. V. Marenich, et al. Gaussian, Inc., Wallingford CT, **2016**.
- [61] W. J. Hehre, R. Ditchfield, J. A. Pople, *J. Chem. Phys.* **1972**, 56, 2257-2261.
- [62] T. H. D. Jr., P. J. Hay, H. F. Schaefer III, Vol. 3, Plenum, New York,, **1977**, pp. 1-28.
- [63] <https://github.com/jaimergp/easymecp> repository, publication in preparation. ,
- [64] J. Tomasi, B. Mennucci, R. Cammi, *Chem. Rev.* **2005**, 105, 2999-3094.
- [65] T. Yanai, D. Tew, N. Handy, *Chem. Phys. Lett.* **2004**, 393, 51-57.
- [66] N. M. O'Boyle, A. L. Tenderholt, K. M. Langner, *J. Comput. Chem.* **2008**, 29, 839-845.

8. Conclusions / Conclusiones



8.1. Conclusions

In this doctoral thesis, four families of promising sunscreen molecules and three types of systems for solar energy storage were studied. Moreover, a computational approach was successfully applied for the design of new UV filters. In addition, a complete study in photophysical and photochemical terms was performed for all derivatives.

At first place, concerning mycosporine-like sunscreens, some conclusions can be outlined:

- A rational design to unveil the key features on natural MAAs was performed. For that, a static and dynamic computational study was done. As result, a new and promising photoprotection mechanism surges for these MAAs.
- Based on these hints, different synthetic approaches were developed allowing a novel and versatile synthesis of aminocyclohexenimine derivatives.
- The prepared derivatives were characterized in terms of UV-Vis absorption, photostability, fluorescence and thermal and chemical stability. These compounds feature excellent properties to be used as sunscreens.
- A great tunability of the photophysical and physicochemical properties was achieved in these synthetic analogues. In addition, solubility, chemical stability and UV absorption region can be modified according to the requirements for different applications.
- For some of the prepared compounds (chapter 5), a spectroscopic study using time-resolved fluorescence upconversion and TAS was performed. An ultra-fast relaxation to ground state was observed in all derivatives, proving their efficient deactivation.
- The computational exploration of the synthetic analogues revealed a new imine isomerization mechanism as deactivation pathway. According to that, the ruling

mechanism seems to be dependent on the imine substituents, being the isomerization favored in aryl moieties and the out-of-plane in case of alkyl residues.

Secondly, new families of sunscreens such as chromone, aminochromone and aminocyclohexenone were obtained and studied. Photochemical and photophysical properties demonstrate a promising behavior as sunscreens and were studied computationally to understand their photoprotection mechanisms.

To conclude, three different approaches were followed with the aim of demonstrating diverse energy storage systems:

- A computational study to adapt the previously obtained hydantoin-based photoswitches, together with catalytic back-conversion experiments.
- A complete study of the photophysical properties and heat release experiments with a norbornadiene/quadracyclane system. Within the use of a heterogeneous catalyst, a record macroscopic heat release was measured, together with a rationalization of the back-conversion mechanism by DFT methods.
- Lastly, a liquid azobenzene derivative was studied in conjunction with a catalyst to understand the back-conversion process. From a computational perspective, the reaction pathway was explored featuring an interesting S_0 - T_1 - S_0 mechanism along the rotation coordinate, increasing thousands of times the reaction rate.

8.2. Conclusiones

En esta tesis doctoral se han estudiado cuatro familias de fotoprotectores y tres tipos de sistemas para almacenamiento de energía solar. Además, el diseño de nuevos filtros UV se realizó en base al estudio computacional realizado. Junto a éste se realizó un estudio completo de las propiedades fotofísicas y fotoquímicas para todos los derivados obtenidos.

En primer lugar, sobre los fotoprotectores basados en MAAs se pueden sacar las siguientes conclusiones:

- Se realizó un diseño racional para explorar las características clave en los compuestos naturales. Para ello, se llevó a cabo un estudio computacional estático y dinámico. Como resultado surge un nuevo y prometedor mecanismo de fotoprotección.
- En base a estas premisas se han desarrollado una serie de rutas sintéticas que permiten una versátil obtención de derivados de ciclohexenimina.
- Estos derivados han sido caracterizados en términos de absorción UV-Vis, fotoestabilidad, fluorescencia y estabilidad, tanto térmica como química. En todos los casos presentan excelentes propiedades como fotoprotectores.
- Estos análogos sintéticos pueden ser fácilmente modificados en términos de solubilidad, estabilidad química y rango de absorción UV-Vis. Es decir, sus propiedades fotofísicas y fisicoquímicas pueden modularse mediante la síntesis de acuerdo con las necesidades concretas.
- Para varios de los compuestos obtenidos (capítulo 5), se ha llevado a cabo un estudio espectroscópico usando técnicas de fluorescencia resuelta en el tiempo y TAS. Para todos los derivados se observa una ultrarrápida desactivación al estado fundamental, probando su eficiencia en la relajación.

- El estudio computacional de los análogos sintéticos revela un nuevo camino de desactivación a través de la isomerización de la imina. De acuerdo a esto, el mecanismo dominante parece dependiente de los sustituyentes de la imina, estando favorecida la isomerización con residuos arilo y la deformación fuera del plano con grupos alquilo.

Además, se han obtenido y estudiado nuevas familias de filtros UV, como cromonas, aminocromonas y aminociclohexenonas. Sus propiedades fotofísicas y fotoquímicas presentan un comportamiento prometedor. También han sido estudiados computacionalmente para entender sus mecanismos de fotoprotección.

Para concluir, tres aproximaciones diferentes se han seguido con el objetivo de probar diversos sistemas para almacenamiento de energía solar:

- Un estudio computacional para adaptar los interruptores basados en la hidantoína, junto con experimentos de reversión térmica catalizada.
- Un estudio completo de las propiedades fotofísicas y experimentos de liberación de calor para un sistema norbornadieno/cuadriciclano. Considerando el uso de un catalizador heterogéneo, se ha medido el récord de liberación de calor. Además del estudio del mecanismo usando métodos DFT.
- Finalmente, se ha estudiado un derivado de azobenceno líquido junto a un catalizador para entender el proceso de reversión. El camino de reacción se ha explorado desde una perspectiva computacional, mostrando un interesante mecanismo $S_0-T_1-S_0$ a lo largo de la coordenada de rotación, aumentando notablemente la velocidad de reacción.

From the research reported in this Ph.D Thesis, a series of papers has been published in different journals or presented in conferences.

Scientific Publications

- "Photoprotective Role of Mycosporine-Like Aminoacids" chapter in the book Photochemistry: New Research, pp 1-20. Nova Science Publishers. **ISBN:** 978-1-62808-615-7
- R. Losantos, M.S. Churio, D. Sampedro, Computational Exploration of the Photoprotective Potential of Gadusol, *ChemistryOpen* **2015**, 4, 155 – 160
- I. Funes-Ardoiz, R. Losantos, D. Sampedro, On the mechanism of the Shapiro reaction: understanding the regioselectivity, *RSC Adv.* **2015**, 5, 37292
- R. Losantos, D. Sampedro, M.S. Churio, Photochemistry and photophysics of mycosporine-like amino acids and gadusols, nature's ultraviolet screens, *Pure Appl. Chem.* **2015**, 87(9-10), 979-996.
- Spanish patent application, "Compuestos fotoprotectores análogos de MAA, procedimiento de síntesis y composición que comprende los mismos". Publication code ES 2 550 374 A1, **2015**.
- R. Losantos, I. Funes-Ardoiz, J. Aguilera, E. Herrera-Ceballos, C. García-Iriepa, P. J. Campos, D. Sampedro, Rational Design and Synthesis of Efficient Sunscreens To Boost the Solar Protection Factor, *Angew. Chem. Int. Ed.* **2017**, 56, 2632-2635.

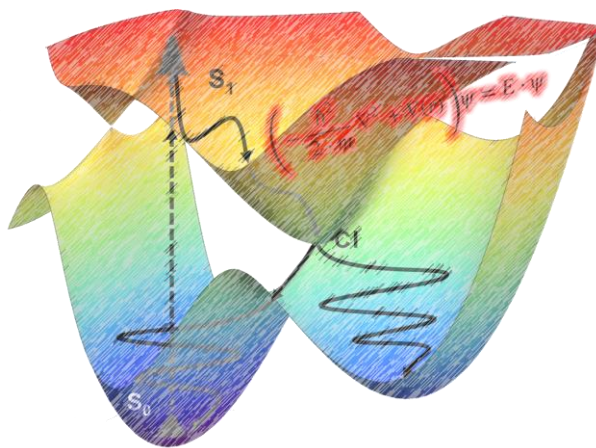
- Z. Wang, A. Roffey, R. Losantos, A. Lennartson, M. Jevric, A. U. Petersen, M. Quant, A. Dreos, X. Wen, D. Sampedro, K. Börjesson, K. Moth-Poulsen, Macroscopic heat release in a molecular solar thermal energy storage system, *Energy Environ. Sci.* **2019**, *12*, 187-193.
- R. Losantos, I. Lamas, R. Montero, A. Longarte, D. Sampedro, Photophysical characterization of new and efficient synthetic sunscreens, *Phys. Chem. Chem. Phys.* **2019**, *21*, 11376-11384.
- Z. Wang, R. Losantos, D. Sampedro, M.-a. Morikawa, K. Börjesson, N. Kimizuka, K. Moth-Poulsen, Demonstration of an azobenzene derivative based solar thermal energy storage system, *J. Mater. Chem. A* **2019**, *7*, 15042-15047.

Conference communications

- "Design and synthesis of photoactive systems with improved performance" Oral communication. XXV Reunión Bienal de Química Orgánica. Alicante. 2014
- "Chemical sensors based on new hydrazone derivatives" Poster communication. XXIV Reunión Nacional de Espectroscopia-VIII Congreso Ibérico Espectroscopia. Logroño. 2014
- "Photoprotective role of natural sunscreens" Poster communication. XXV IUPAC Symposium on Photochemistry. Bordeaux. 2014
- "Learning from nature: unveiling the mechanisms of photoprotection" Invited oral communication. 16th International Congress on Photobiology. Buenos Aires. 2014
- "Síntesis de Compuestos con Actividad Fotoprotectora" Oral communication. XI Simposio de Jóvenes Investigadores RSEQ-Sigma Aldrich. Bilbao. 2014

- "Diseño, síntesis y propiedades de nuevos compuestos fotoprotectores" Invited oral communication. VI Jornada Química CISQ. 2015
- "Síntesis de compuestos fotoprotectores" Poster communication. XII Simposio de Jóvenes Investigadores RSEQ-Sigma Aldrich. Barcelona. 2015
- "Molecular photoswitches as solar energy storage devices" Poster communication. NanoSpain 2016 conference. Logroño. 2016
- "Análogos sintéticos del gadusol: fotoestabilidad y reactividad frente a oxígeno singlete" Oral communication. III Reunión de Fotobiólogos Moleculares Argentinos GRAFOB del Bicentenario. Tucumán. 2016
- "Rational Design and Synthesis of Efficient Sunscreens To Boost the Solar Protection Factor" Poster communication. 28th International Conference on Photochemistry ICP2017. Strasbourg. 2017
- "Rational Design and Synthesis of Efficient Sunscreens To Boost the Solar Protection Factor" Poster communication. 27th International Symposium on Photochemistry PhotoIUPAC2018. Dublin. 2018
- "Molecules as Solar Energy Store: feasible implementation and new perspectives" Oral communication. XXXVII Bienal de Química RSEQ. San Sebastián. 2019
- "Almacenando energía en moléculas" Invited Oral communication. X Jornada Química CISQ. Logroño 2019

9. General comments and theoretical methods



9.1. General comments

- **Reagents**

All solvents and reagents were used as received without further purification.

- **Chromatography**

Thin Layer Chromatography (TLC) was performed using Polygram Sil G/UV254 F254 plates (0.2 mm silica gel layer with fluorescence indicator on pre-coated plastic sheets). Column chromatography was carried out with silica gel (230-240 mesh) as stationary phase.

9.1.1. Characterization techniques

- **Nuclear Magnetic Resonance**

^1H and ^{13}C NMR spectra were recorded on a Bruker ARX-300 and/or a BrukerAvance 400 spectrometers. Methanol- d_4 has been used as usual deuterated solvent, using its signal as standard. Nevertheless, other solvents have been also used to measure the NMR spectra such as dimethyl sulfoxide, acetonitrile and chloroform. Chemical shifts are given in ppm and coupling constants in hertz.

- **UV-Vis spectrometry**

Absorption molecular spectra were recorded on an Ocean Optics USB4000 UV-Vis diode array spectrophotometer (200-850 nm). All the experiments were carried out in quartz cuvettes (1 cm path length).

- **Electrospray-Mass Spectrometry**

Electrospray mass spectra were recorded on an Ultra Performance Liquid Chromatography Acquity Waters with an interface to High Resolution Mass

Spectrometry was performed in a Bruker Microtof-Q electrospray source in positive-ion mode.

- **Luminescence**

All luminescence measures were recorded at room temperature with a Jobin-Yvon Horiba Fluorolog 3-22 Tau-3 spectrofluorimeter. Further data analysis was performed with different versions of Origin Pro suite.

- **X-ray diffraction**

The crystals were mounted in inert oil on glass fibers and transferred to a Nonius Kappa CCD diffractometer equipped with an Oxford Instruments low-temperature attachment. Data were collected by monochromatic Mo-K α radiation ($\lambda = 0.71073 \text{ \AA}$). Absorption corrections: numerical (based on multiple scans). Images were processed using the DENZO and SCALEPACK suite of programs.

9.1.2. Lamps and photochemical techniques

- **Irradiation in a medium pressure Hg lamp**

Some of the irradiations were carried out in photochemical reactors with a 400 W medium pressure Hg lamp (Photochemical Reactors LTD (UK)). Furthermore, a Pyrex or quartz filter was used to perform the irradiation (Figure 9.1). The sample solution was placed in an immersion well reactor or a Pyrex/quartz NMR tube.

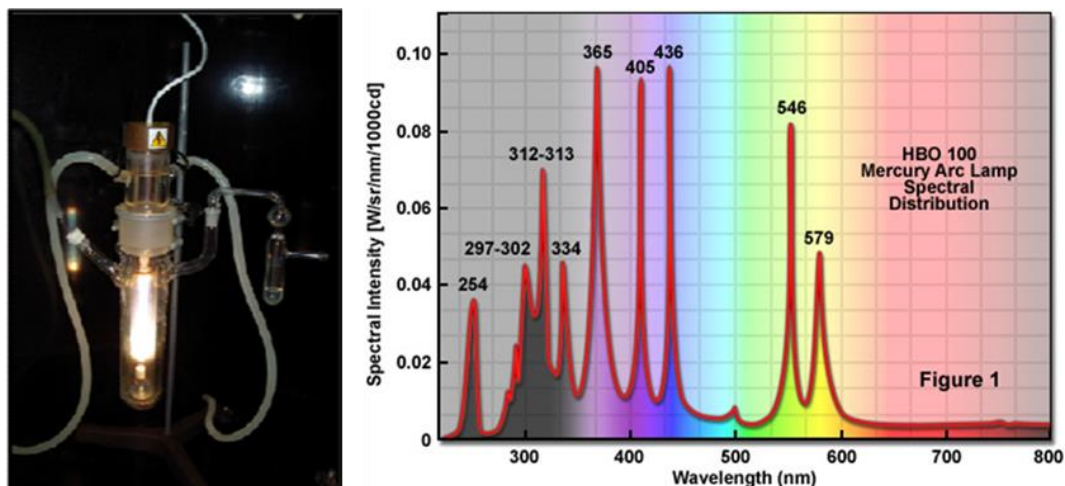


Figure 9.1. Lamp, photochemical reactor scheme and emission of a medium-pressure Hg lamp.

- Photoreactor

To produce the isomerization of hydantoin-based molecular switches, it was also used a Luzchem UV-Vis photoreactor (LZC-4), provided with LZC-UVA lamps with emission wavelength centered at 350 nm (14 lamps x 8 W/lamp) (Figure 9.2).

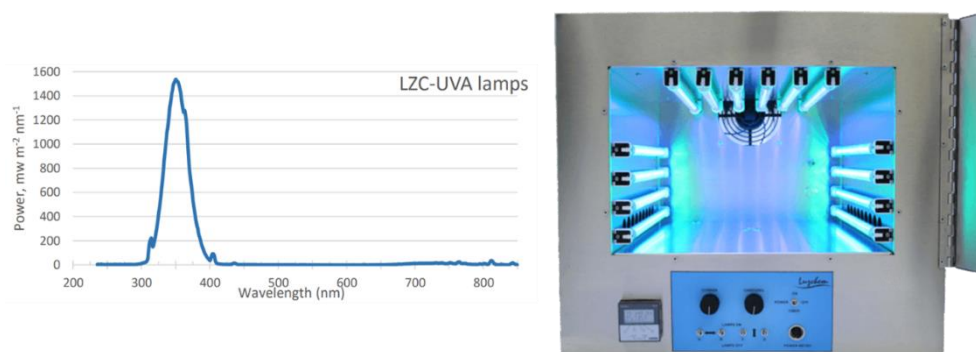


Figure 9.2. Irradiance of the lamps used and photoreactor LZC-4.

- Solar simulator (Equipment Universidad de Málaga, Dr. J. Aguilera)

All measurements of solar protection factor were made according to the international standard ISO-24443, using the standardized 5x5 cm² PMMA plates with 1.3 mg/cm². An Oriel 300 W solar simulator (Newport, Nebraska, USA) was used for sample irradiation. Spectral distribution of the light source and transmitted by control and samples probes in PMMA plates was measured by means of a double monochromator connected to an Ulbrich sphere (MACAM SR9910-v7, Irradian, Scotland, UK). Experimental setup can be seen below in Figure 9.3.



Figure 9.3. Solar simulator and experimental setup for SPF measurements.

- **Temperature controlled monochromatic irradiation.**

A homemade-assemble setup composed by an Oriel Cornerstone 130 1/8m monochromator coupled with a Quantum Northwest qpod-2e thermostatic sample holder were used. In this, a 500 W Hg arc lamp in a proper lamp housing (Oriel, USA) with an Oriel water filter was used as light source. Also, the sample holder is a Peltier temperature-controlled system. This sample holder is attached to an Ocean Optics USB4000 UV-Vis spectrometer to allow simultaneous UV-Vis monitoring. Standard 1 cm quartz cuvettes were used.

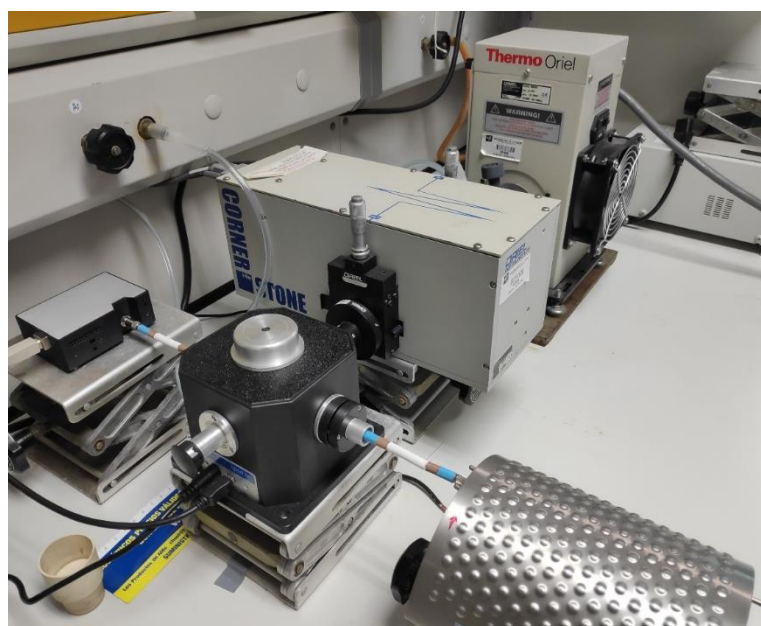


Figure 9.4. Oriel Cornerstone 130 monochromator attached to a qpod-2e holder and UV-Vis spectrometer.

9.2 Computational methods

9.2.1 CASSCF//CASPT2 strategy

Complete **Active Space-Self Consistent Field** is a multiconfigurational method that arose as a solution to model some characteristic molecular processes, like bond rupture forming radical species^[1] or processes that happens in the excited state.^[2] In those cases, a single configurational wavefunction is not enough to describe the system. For that, multiconfigurational methods (MCSCF) are needed. In these methods, the wavefunction is described by a linear combination of Slater determinants leading to an expansion of the Hartree-Fock wavefunction, which is monoconfigurational. Along MCSCF methods, CASSCF^[3] is the most widely used and extended nowadays. In that, wavefunction is a combination of diverse configurations, which corresponds to a different occupation of the molecular orbitals. This is the characteristic factor of CASSCF, the orbitals to consider in optimization must be selected by the user. Molecular orbitals can be divided in three groups as can be seen in Figure 9.5. These are, i) inactive or core orbitals, that doesn't change occupation and are fully occupied, ii) virtual orbitals, that remain unoccupied and iii) active orbitals, which occupations can range from 0 to 2 as all possible electronic excitations are allowed. These orbitals are the so-called active space,^[3] as briefly explained in Chapter 4.

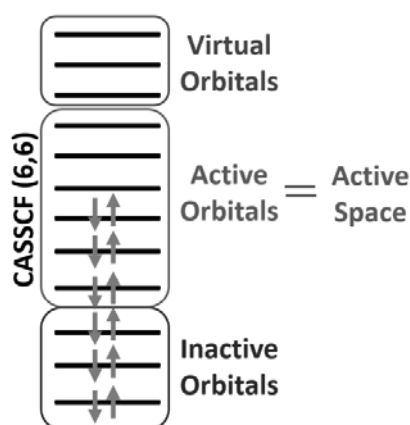


Figure 9.5. Orbital types in CASSCF method.

Orbital selection depends on the system and the process of interest; in case of a homolytic bond rupture σ and σ^* orbitals should be included. In our case, we consider the π density, which is the responsible of the relevant electronic excitations in our

molecules. Choosing the right active space is a complex process and should be done carefully to ensure a good reproduction of the real system properties. Notation used to mention this method is CASSCF (m,n), where m is the number of electrons selected and n the number of orbitals included in the active space.

Usually this method works well to describe the shape and critical points along the potential energy surface (PES) but can fail in some cases where there are dynamic correlation effects,^[4] which means that some interactions between different states that cannot be considered by CASSCF exist. For that, CASSCF is considered as a qualitative method and to obtain accurate transition energies, inclusion of the dynamic correlation is mandatory.

For that, the CASPT2 method is needed, where the inclusion of a second order perturbation to CASSCF wavefunction considers the dynamic correlation in the system. There are other methods to include it, the so-called post-Hartree-Fock, as *CI* (configuration interaction), MP2 or some MCSCF methods. In this memory, I have focused on the last ones. CASPT2 method gives a quantitative description of the system, but it is not used as the starting point to our studies due to the high time and resources that consumes. Other problem to perform molecular optimizations with this level of theory is that analytical energy gradients are not feasible, so numerical gradient should be done in each step, which increases the calculation time in $6N-12+1$ times (where N is the number of atoms). Accordingly, CASSCF//CASPT2 strategy is the most extended method in the study of photochemical organic systems.^[5] Firstly, a qualitative description of the PES is obtained with CASSCF, and the obtained critical points are recalculated as single point calculations with CASPT2 method. Normal way to proceed for a photochemical study of the PES of a molecule is to firstly optimize the molecular geometry in the ground state at the CASSCF (m,n) level. With this geometry, the absorption spectrum is computed, including the solvent to compare with experimental values. Also, it provides information about the nature of the transitions involved in the absorption process. For more accurate results, instead of the geometry optimized with CASSCF the optimized at MP2 level is a better starting point because CASSCF overestimate bond distances. The relevant state in the UV absorption usually presents the largest oscillator strength (*f*) and it is called "bright state", the *f* value indicates the intensity of the absorption. If the system is well reproduced with this level of theory, the energy difference between ground state and the relevant excited state should correspond to the experimental λ_{\max} . Once identified the bright state, the relaxation

along the PES is carried out. For this, a minimum energy path (MEP) calculation is needed. In this special type of optimization, a hypersphere with a defined radius is used and the local minima is found in the inner part of the sphere. With that method, the minimum energy path can be ensured due to energy minimum in each point. Other critical points can be found tuning the geometry with conical intersection (CI) or transition state (TS)^[6] optimization algorithms.

Conical intersections^[7] are a characteristic point in the PES; these points represent a branching space between two different PESs. Usually they are described as efficient funnels for non-radiative decay between PESs of the same multiplicity. There are two main types of CIs depending on the shape of the PES; an example of those topologies is in Figure 9.6.

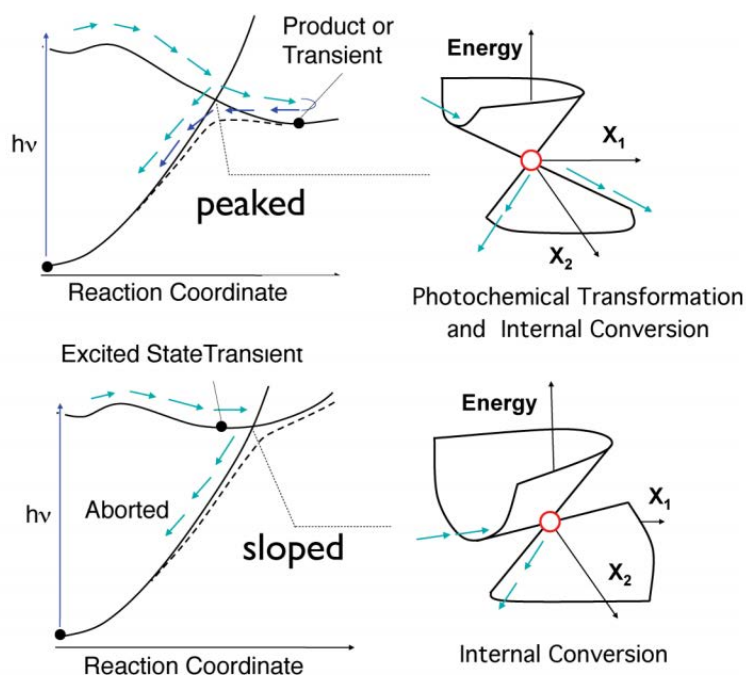


Figure 9.6. Types of conical intersections. Left, PES plot along reaction MEP. Right, 3D scheme of CI topology with vectors in branching space.^[8]

To characterize a conical intersection, definition of the characteristic vectors is needed. This is the equivalent to the imaginary frequency in a transition state geometry. In right part of Figure 9.6, X_1 and X_2 represent those vectors. X_1 is the gradient difference vector (GD) which describes the geometry distortion that causes the largest energy difference variation between the two states involved. Whereas X_2 is parallel to the

direction of the derivative coupling vector (DC) and measures the geometry change that maximizes the coupling between these two states. Each crossing should be characterized by the analysis of the branching plane,^[9] that is, of the GD and DC vectors, which give us information about the possible and accessible reaction pathways after the surface hop. Apart from the characteristic vectors, the topology of the CI is also important to extract information about the reactive options after surface hop. This throws information about the efficiency of the crossing.

According to the topology, two different types of CI can be observed. Peaked CIs are the most typical shape when some reactivity is found. As an example, this shape is typical in *cis-trans* isomerization of molecular switches. This allows the molecule to yield a photoproduct or recover the starting material through internal conversion. In those cases, isomerization efficiency depends drastically on the topology of the conical intersection. Slopped CIs are the other type of topology that can be found. Usually this CIs yield in an aborted reaction, which means molecule is recovered in the ground state without photoreactivity.

9.2.2. Dynamic study

Dynamical studies are crucial in order to study time-dependent properties such as conformational changes, thermodynamics of biological molecules, reaction rates or lifetimes.^[10] Moreover, although the computation of minimum energy paths (*i.e.* static study) gives insight into the reaction pathways of a given molecule, it is important to clarify if other pathways are also possible from a dynamical point of view. In addition, the possibility of computing a large number of trajectories let us evaluate some statistical properties such as the quantum yield of a given photoreaction, the rate between different products or the number of relevant conformations in biomolecules.

Therefore, the time-dependent behavior of a molecule can be investigated in terms of molecular dynamic simulations.^[10] Trajectories can be generated assuming that nuclei behave like classical particles and hence, by solving iteratively Newton's equations of motion. These equations must be solved numerically and diverse numerical algorithms have been developed for integrating them. In this case, the Velocity Verlet algorithm^[11] is used as implemented in MOLCAS 8.0. In this algorithm, the positions and velocities are calculated at the same time. In order to simulate

realistic conditions, constant temperature and pressure are achieved via thermostat and barostat algorithms. In this Ph.D. Thesis, the presented dynamics were performed using a Nose–Hoover chain of thermostats with $T = 298 \text{ K}$.^[12, 13]

As previously noted, the calculation of the force on each atom is needed in order to propagate the coordinates. In this case, the potential energy calculation is performed using electronic structure QM methods. The electronic Hamiltonian is built and the electronic wavefunction solved, assuming the Born–Oppenheimer approximation. In this case, the electronic structure of the system is explicitly described, leading to the so-called semiclassical dynamics. Within this approximation, regions of the PES where the nuclei and electrons coupling is considerable can be explored from a dynamical point of view. These regions are ubiquitous in photochemical reactions. The Born–Oppenheimer approximation is no more valid in these regions of the PES and hence, a methodology that treats the degeneracy is necessary, leading to the so-called non-adiabatic molecular dynamics (NAMD). In this Ph.D. Thesis, NAMDs have been performed by application of the algorithm developed by I. Schapiro^[14] (implemented in Molcas7.7 and 8.0). This algorithm is similar to a MEP calculation, because a minimization on a series of hyperspheres is performed. The hop criterion is defined in two different ways. Firstly, a small energy difference between both states. Secondly, a change on the CI coefficients from the previous iteration, meaning a change in the electronic nature of the states. A better option to calculate it, is the use of the Tully's fewest switches algorithm^[15] with decoherence correction for the surface hop^[16, 17] as implemented in Molcas 8.2.^[18] However, this method was not yet available when this study was performed.

9.2.3. DFT

Density functional theory (DFT) methods allow to achieve a relatively high level of accuracy of medium-large systems with a low computational cost. The idea behind DFT is simpler than the one of previously described for multiconfigurational methods: the electronic energy is expressed as a function of the electron density, which depends just on three spatial and one spin coordinates. It was in 1964 when Hohenberg and Kohn demonstrated that the energy of a molecule depends on the ground state electron density.^[19] Thanks to the Hohenberg–Kohn theorem, the electronic energy can be

described as a functional of the electron density. The other key in its development was the Kohn–Sham approach that appeared in 1965 as a way to calculate the energy directly without the need of the wavefunction.^[20] In this approach, an auxiliary system of non-interacting electrons has been introduced. This term does not present an exact solution and different approximations have been included for calculations, giving rise to diverse types of density functionals, like the local density approximation (LDA), generalized gradient approximation (GGA) and hybrid functionals. In these last ones, a fraction of the exchange term is computed and combined with GGA functionals.

In this Ph.D. Thesis, hybrid functionals have been mainly used, particularly the B3LYP^[21] and M06^[22] functionals. The choice of the functional has to be done carefully as the final energy value depends on the selected functional. In this thesis, the choice of the functional has been done after comparison with experimental data and/or calibration with multiconfigurational *ab initio* methods.

9.2.4. TD-DFT

Time-dependent DFT is an extension of the density functional theory (DFT). That extension allows considering excited states, the time-dependent density functional theory (TD-DFT) is required. Runge and Gross showed in 1984 that all observable properties, beginning from a given initial state, could be extracted from the time-dependent electron density.^[23] This theorem is the analogue of the Hohenberg–Kohn theorem extended to time-dependent systems, which is the so-called time-dependent Kohn–Sham theorem.^[24] Thanks to the TD-DFT development, it has been possible to do quantum mechanical studies in the excited state of relatively large systems, which are larger for other multiconfigurational methods, like CASSCF. This fact has great importance in diverse fields like chemistry, biology and material science.^[25]

9.3. Bibliography

- [1] G. Herzberg, A. Monfils, *J. Mol. Spectrosc.* **1961**, *5*, 482-498.
- [2] S. Larsson, *Int. J. Quantum Chem* **2011**, *111*, 3424-3430.
- [3] B. O. Roos, in *Advanced Chemistry and Physics: Ab Initio Methods in Quantum Chemistry II.*, Lawley KP (Wiley, Chicester, UK), **1987**, pp. 399-445.
- [4] P.-O. Löwdin, *Phys. Rev.* **1955**, *97*, 1509-1520.
- [5] M. Olivucci, *Computational Photochemistry*, Elsevier, Amsterdam, **2005**.
- [6] X. Li, M. J. Frisch, *J. Chem. Theory Comput.* **2006**, *2*, 835-839.
- [7] M. A. Robb, M. Olivucci, *J. Photochem. Photobiol. A* **2001**, *144*, 237-243.
- [8] I. Schapiro, F. Melaccio, E. N. Laricheva, M. Olivucci, *Photochem. Photobiol. Sci.* **2011**, *10*, 867-886.
- [9] I. Fdez. Galván, M. G. Delcey, T. B. Pedersen, F. Aquilante, R. Lindh, *J. Chem. Theory Comput.* **2016**, *12*, 3636-3653.
- [10] B. F. E. Curchod, T. J. Martínez, *Chem. Rev.* **2018**, *118*, 3305-3336.
- [11] W. C. Swope, H. C. Andersen, P. H. Berens, K. R. Wilson, *J. Chem. Phys.* **1982**, *76*, 637-649.
- [12] S. Nosé, *Mol. Phys.* **1984**, *52*, 255.
- [13] W. G. Hoover, *Phys. Rev. A* **1985**, *31*, 695.
- [14] I. Schapiro, D. Roca-Sanjuán, R. Lindh, M. Olivucci, *J. Comput. Chem.* **2015**, *36*, 312-320.
- [15] J. C. Tully, *J. Chem. Phys.* **1990**, *93*, 1061-1071.
- [16] G. Granucci, M. Persico, *J. Chem. Phys.* **2007**, *126*, 134114.
- [17] H. M. Jaeger, S. Fischer, O. V. Prezhdo, *J. Chem. Phys.* **2012**, *137*, 22A545.
- [18] F. Aquilante, J. Autschbach, R. K. Carlson, L. F. Chibotaru, M. G. Delcey, L. D. Vico, I. F. Galván, N. Ferré, L. M. Frutos, et al., *J. Comput. Chem.* **2016**, *37*, 506-541.
- [19] P. Hohenberg, W. Kohn, *Phys. Rev.* **1964**, *136*, B864-871.
- [20] W. Kohn, L. J. Sham, *Phys. Rev.* **1965**, *140*, A1133-A1138.
- [21] A. D. Becke, *J. Chem. Phys.* **1993**, *98*, 5648-5652.
- [22] Y. Zhao, D. G. Truhlar, *Theor. Chem. Acc.* **2008**, *120*, 215-241.
- [23] E. Runge, E. K. U. Gross, *Phys. Rev. Lett.* **1984**, *52*, 997-1000.
- [24] M. A. L. Marques, E. K. U. Gross, *Annu. Rev. Phys. Chem.* **2004**, *55*, 427-455.
- [25] C. A. Ullrich, Z.-h. Yang, *Braz. J. Phys.* **2014**, *44*, 154-188.

Appendix A: Annex VI European Regulation

Appendix A: Annex VI European Regulation

Annex VI European Regulation

Last update: 01/03/2019

LIST OF UV FILTERS ALLOWED IN COSMETIC PRODUCTS

Ref. number	Substance identification		Conditions	Type of filter
	Chemical name / INN / XAN	Name of Common Ingredients Glossary	Maximum concentration	
2	N,N,N-Trimethyl-4-(2-oxoborn-3-ylidenemethyl) anilinium methyl sulphate	CAMPHOR BENZALKONIUM METHOSULFATE	6%	UVB
3	Benzoic acid, 2-hydroxy-, 3,3,5-trimethylcyclohexyl ester / Homosalate	HOMOSALATE	10%	UVB
4	2-Hydroxy-4-methoxybenzophenone / Oxybenzone	BENZOPHENONE-3	6%. Not more than 0,5 % to protect product formulation	UVA/B
6	2-Phenylbenzimidazole-5-sulphonic acid and its potassium, sodium and triethanolamine salts / Ensulizole	PHENYLBENZIMIDAZOLE SULFONIC ACID	8%(as acid)	UVB
7	3,3'-(1,4-Phenylenedimethylene) bis (7,7-dimethyl-2-oxobicyclo-[2.2.1] hept-1-ylmethanesulfonic acid) and its salts / Ecamsule	TEREPHTHALYLIDENE DICAMPHOR SULFONIC ACID	10%(as acid)	UVA
8	1-(4-tert-Butylphenyl)-3-(4-methoxyphenyl) propane-1,3-dione / Butyl methoxydibenzoylmethane / avobenzone	BUTYL METHOXYDIBENZOYLMETHANE, AVOBENZONE	5%	UVA
9	alpha-(2-Oxoborn-3-ylidene)toluene-4-sulphonic acid and its salts	BENZYLIDENE CAMPHOR SULFONIC ACID	6%(as acid)	UVB

Appendix A: Annex VI European Regulation

10	2-Cyano-3,3-diphenyl acrylic acid, 2-ethylhexyl ester / Octocrilene	OCTOCRYLENE	10%(as acid)	UVB
11	Polymer of N-(2 and 4)-[(2-oxoborn-3-ylidene)methyl]benzylacrylamide	POLYACRYLAMIDOMETHYL BENZYLIDENE CAMPHOR	6%	UVB
12	2-Ethylhexyl 4-methoxycinnamate / Octinoxate	ETHYLHEXYL METHOXYCINNAMATE	10%	UVB
13	Ethoxylated Ethyl-4-Aminobenzoate	PEG-25 PABA	10%	UVB
14	Isopentyl-4-methoxycinnamate / Amiloxate	ISOAMYL P-METHOXYCINNAMATE	10%	UVB
15	2,4,6-Trianiilino-(p-carbo-2'-ethylhexyl-1'-oxy)-1,3,5-triazine	ETHYLHEXYL TRIAZONE	5%	UVB
16	Phenol, 2-(2H-Benzotriazol-2-yl)-4-Methyl-6-(2-Methyl-3-(1,3,3,3-Tetramethyl-1-(Trimethylsilyl)Oxy)-Disiloxanyl)Propyl	DROMETRIZOLE TRISILOXANE	15%	UVA/B
17	Benzoic acid, 4,4-[6-[[[(1,1-dimethylethyl)amino]carbonyl]phenyl]amino]-1,3,5-triazine-2,4-diyl]diiminobis-, bis(2-ethylhexyl)ester / Iscotrizinol	DIETHYLHEXYL BUTAMIDO TRIAZONE	10%	UVB
18	3-(4'-Methylbenzylidene)-dl-camphor / Enzacamene	4-METHYLBENZYLIDENE CAMPHOR	4%	UVB
20	2-Ethylhexyl salicylate / Octisalate)	ETHYLHEXYL SALICYLATE	5%	UVB

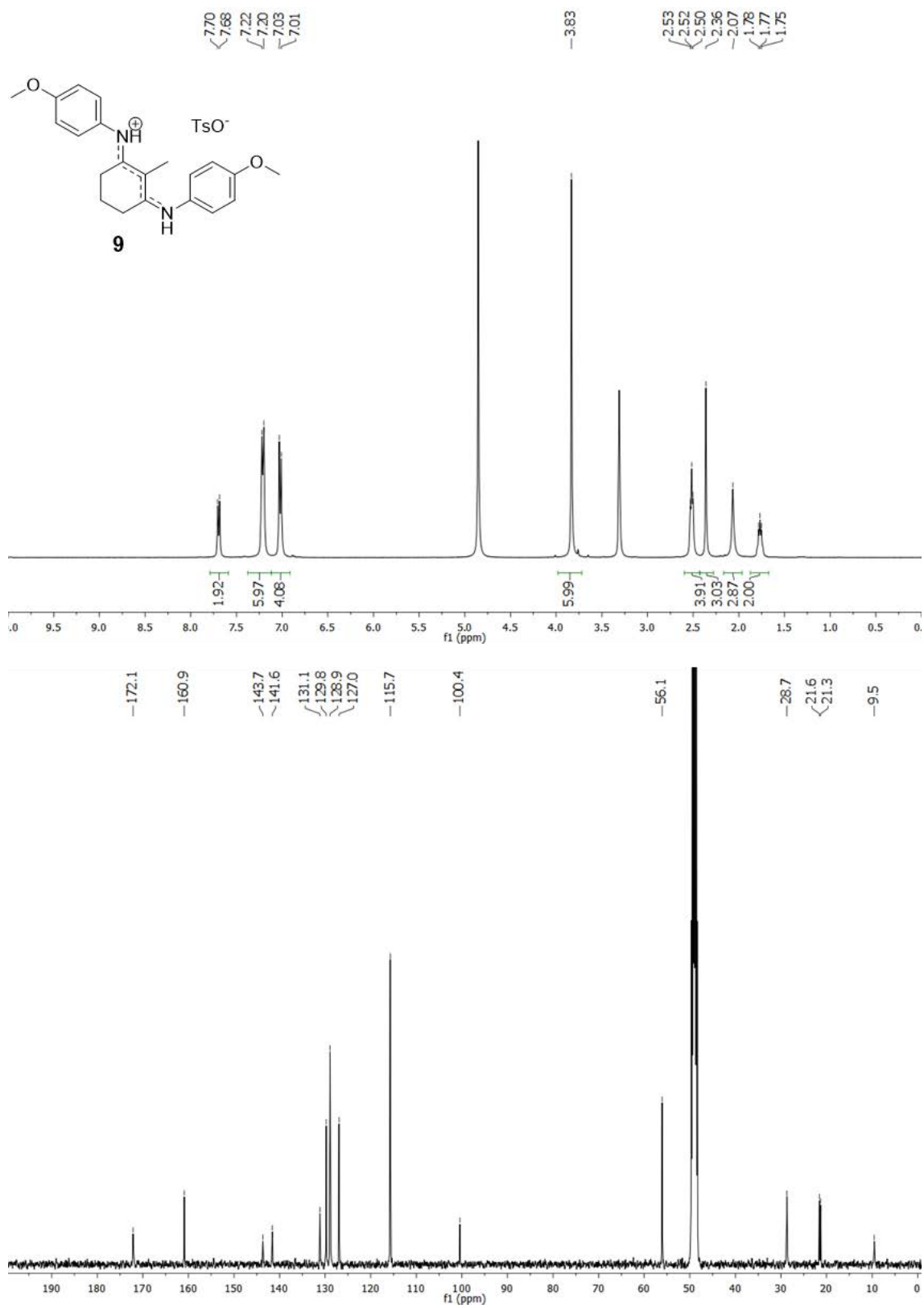
Appendix A: Annex VI European Regulation

21	2-Ethylhexyl 4-(dimethylamino)benzoate / Padimate O (USAN:BAN)	ETHYLHEXYL DIMETHYL PABA	8%	UVB
22	2-Hydroxy-4-methoxybenzophenone-5-sulfonic acid (Benzophenone-5) and its sodium salt / Sulisobenzone	BENZOPHENONE-4; BENZOPHENONE-5	5%(as acid)	UVA/B
23a	Methylene Bis-Benzotriazolyl Tetramethylbutylphenol (nano)	METHYLENE BIS-BENZOTRIAZOLYL TETRAMETHYLBUTYLPHENOL (NANO)	10%	UVA/B
23	2,2'-Methylene bis(6-(2H-benzotriazol-2-yl)-4-(1,1,3,3-tetramethylbutyl)phenol) / Bisotrizole	METHYLENE BIS-BENZOTRIAZOLYL TETRAMETHYLBUTYLPHENOL	10%	UVA/B
24	Sodium salt of 2,2'-bis(1,4-phenylene)-1H-benzimidazole-4,6-disulfonic acid / Bisdisulizole disodium (USAN)	DISODIUM PHENYL DIBENZIMIDAZOLE TETRASULFONATE	10%(as acid)	UVA
25	2,2'-(6-(4-Methoxyphenyl)-1,3,5-triazine-2,4-diyl)bis(5-((2-ethylhexyl)oxy)phenol) / Bemotrizinol	BIS-ETHYLHEXYLOXYPHENOL METHOXYPHENYL TRIAZINE	10%	UVA/B
26	Dimethicodiethylbenzalmalonate	POLYSILICONE-15	10%	UVB
27a	Titanium dioxide (nano)	TITANIUM DIOXIDE (NANO)	25%	UVA/B
28	Benzoic acid, 2-[4-(diethylamino)-2-hydroxybenzoyl]-, hexylester	DIETHYLAMINO HYDROXYBENZOYL HEXYL BENZOATE	10%	UVA
29	1,3,5-Triazine, 2,4,6-tris(1,1'-biphenyl)-4-yl-, including as nanomaterial	TRIS-BIPHENYL TRIAZINE / TRIS-BIPHENYL TRIAZINE (NANO)	10%	UVB
30a	Zinc oxide (nano)	ZINC OXIDE (NANO)	25%	UVA/B
30	Zinc oxide	ZINC OXIDE		

Appendix B: Selected NMR Spectra

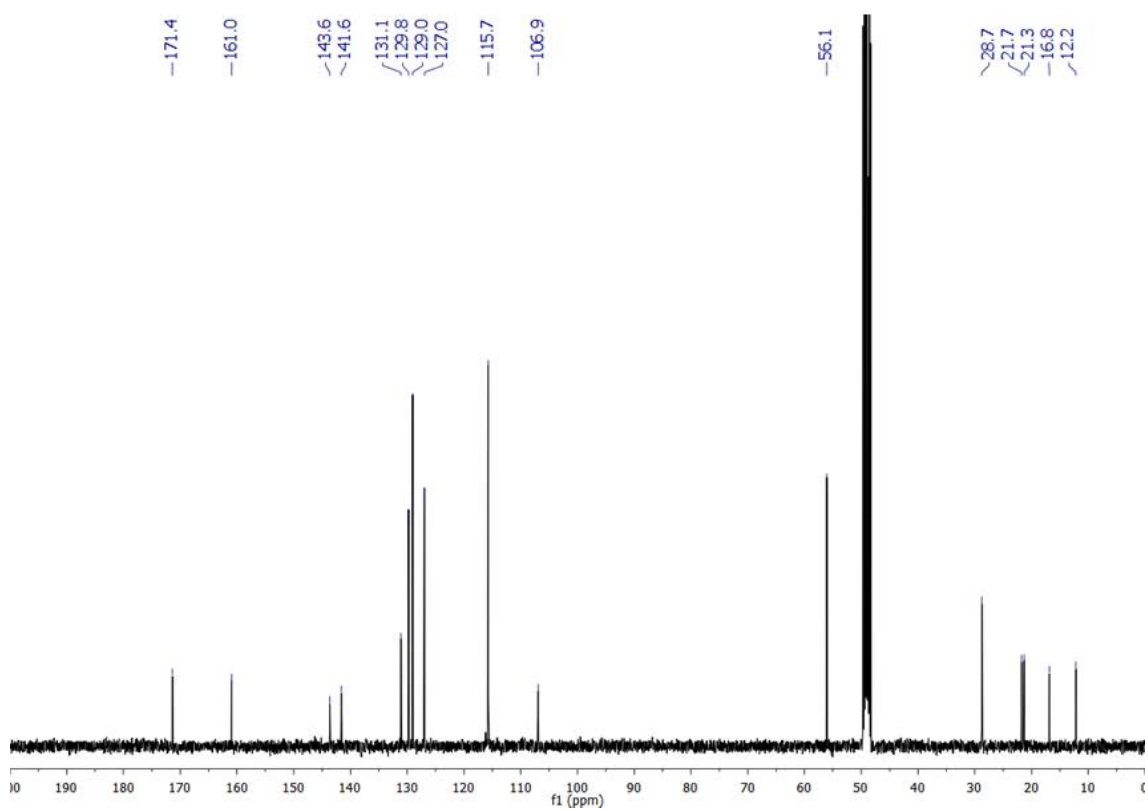
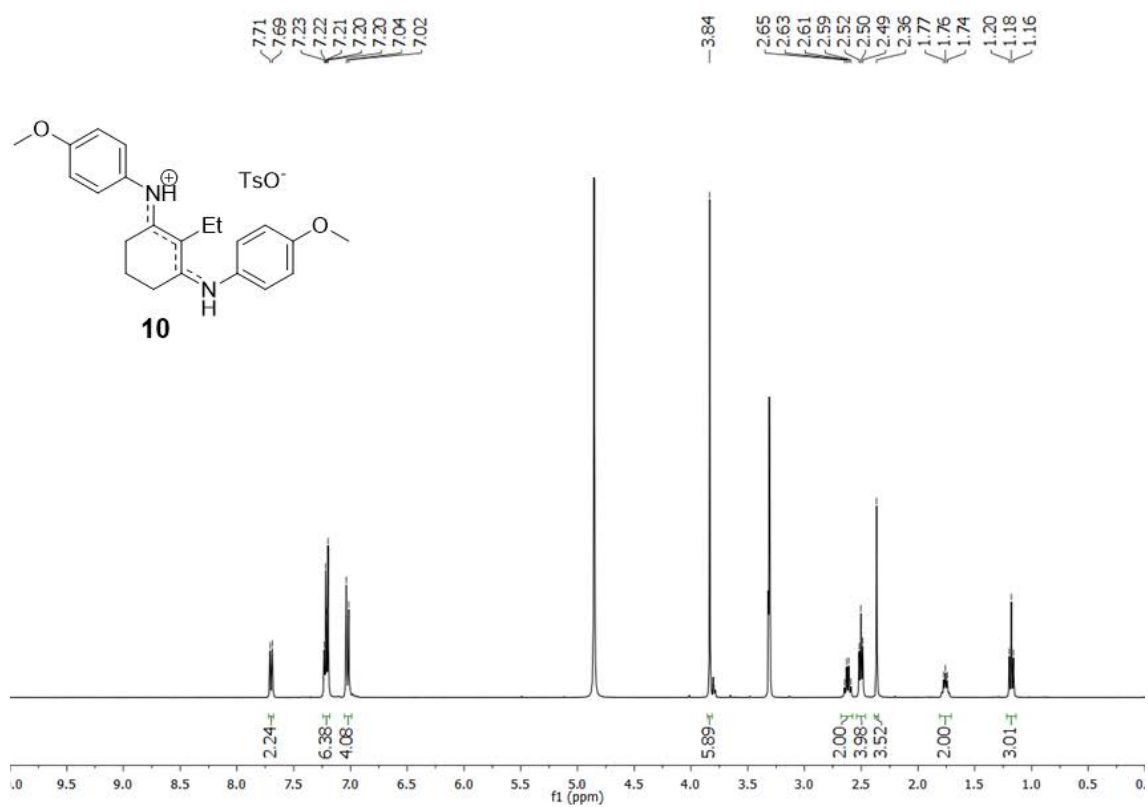
Appendix B: Selected NMR Spectra

Chapter 4

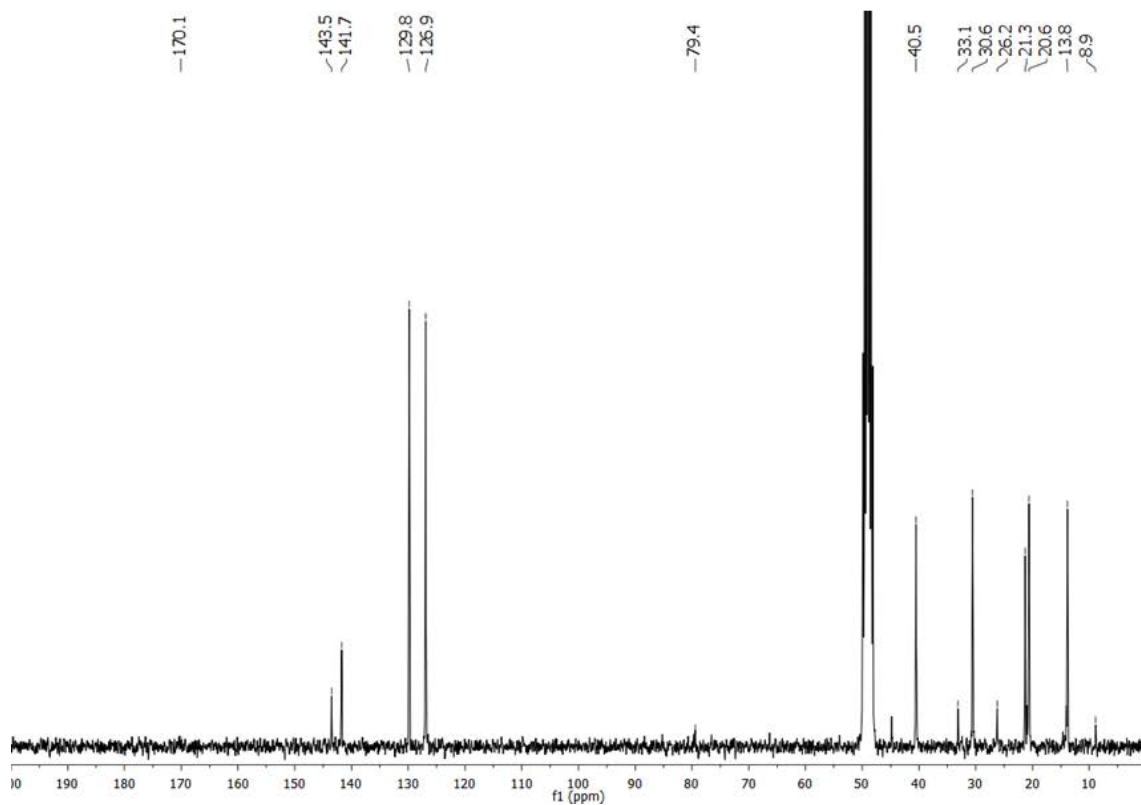
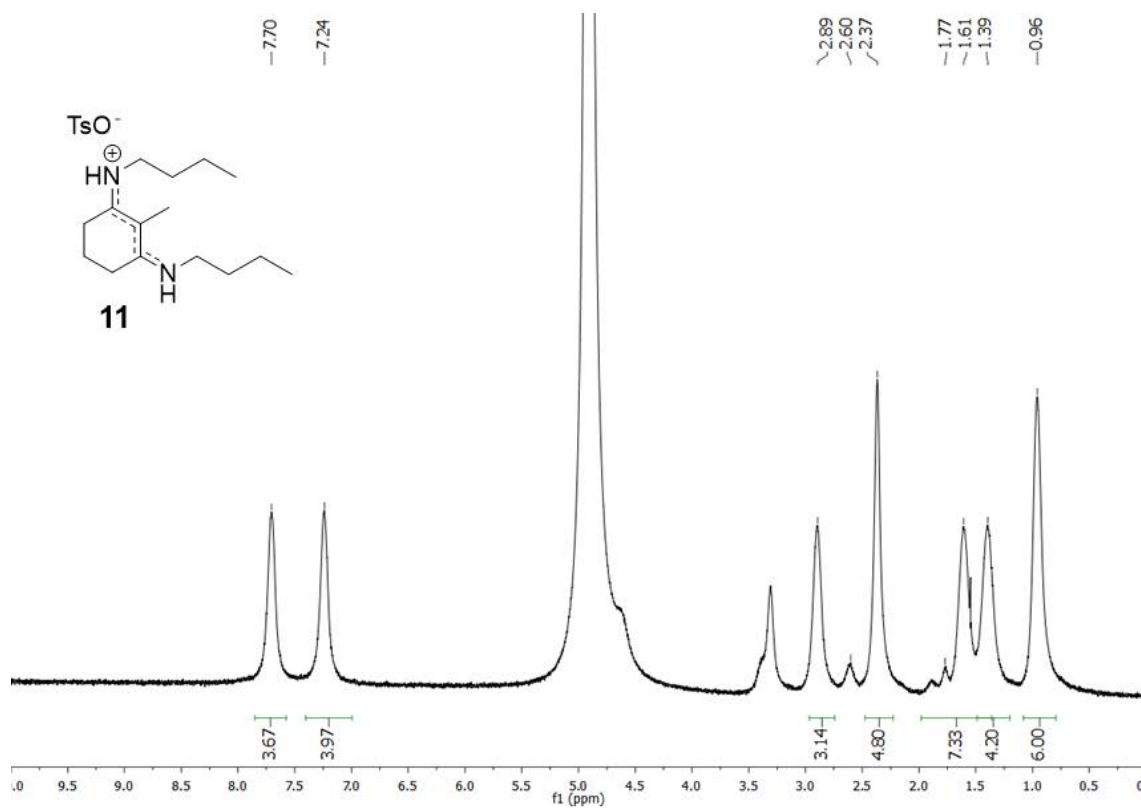


X

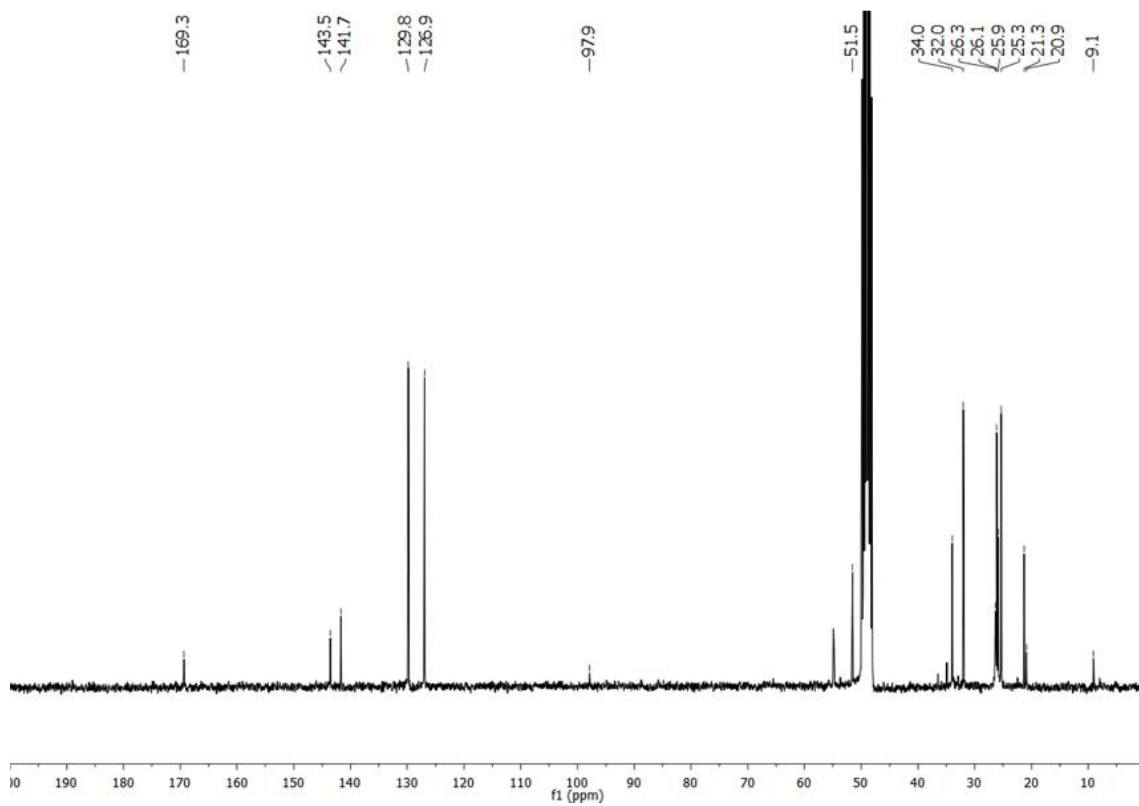
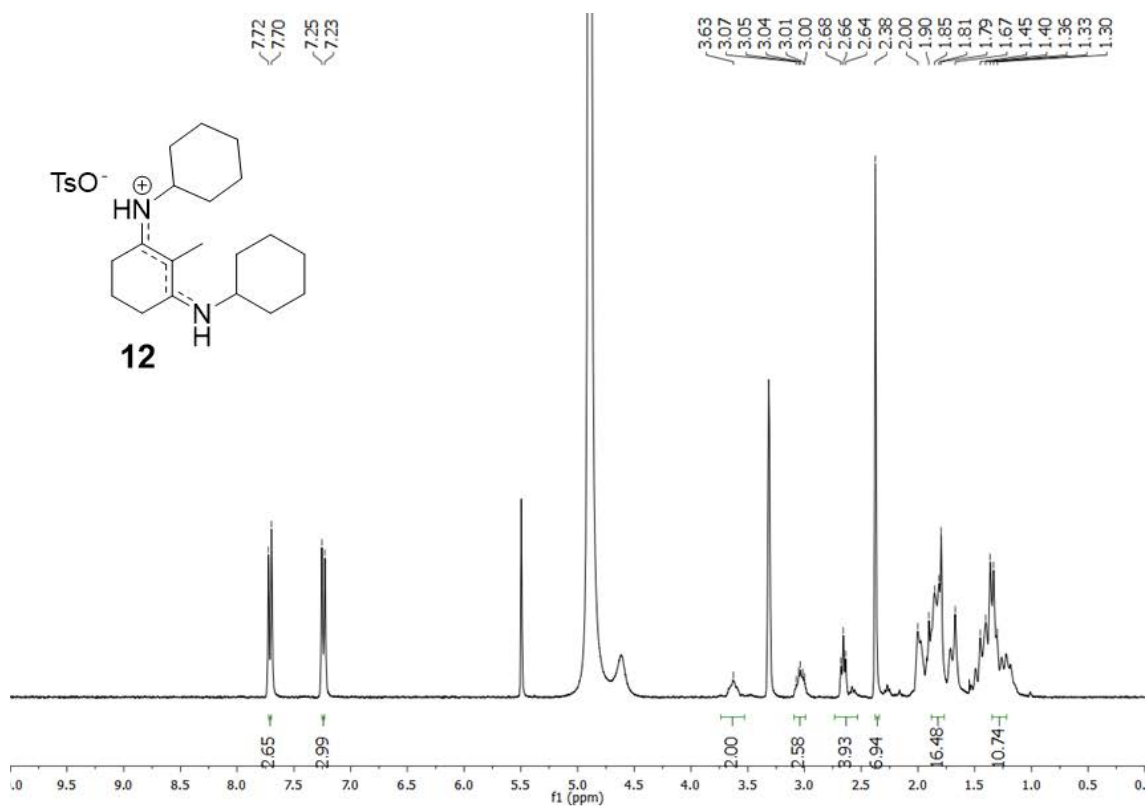
Appendix B: Selected NMR Spectra



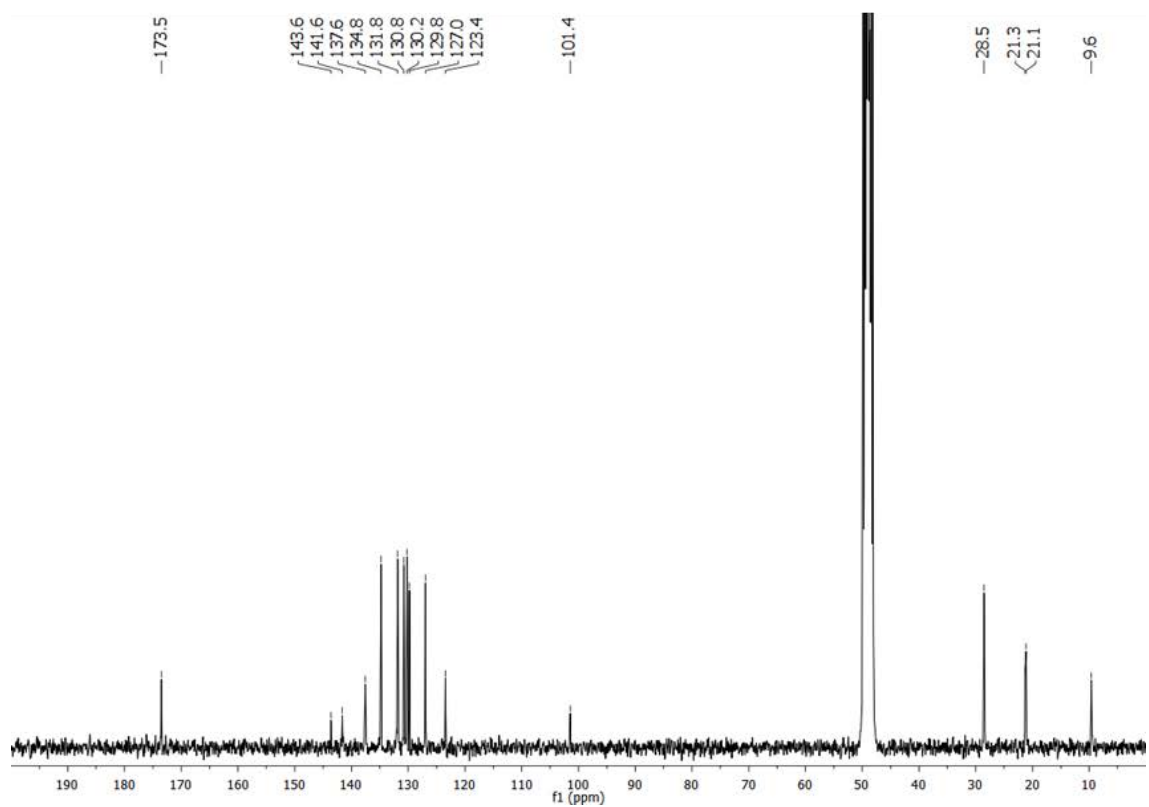
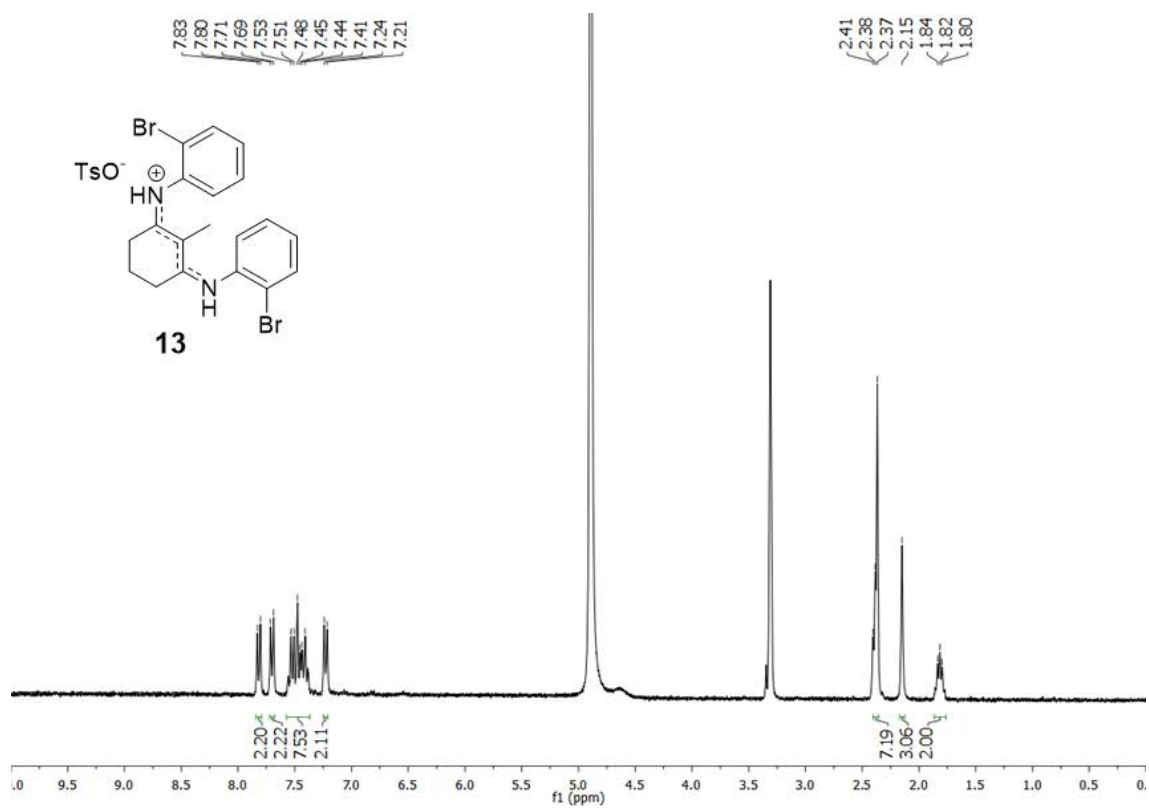
Appendix B: Selected NMR Spectra



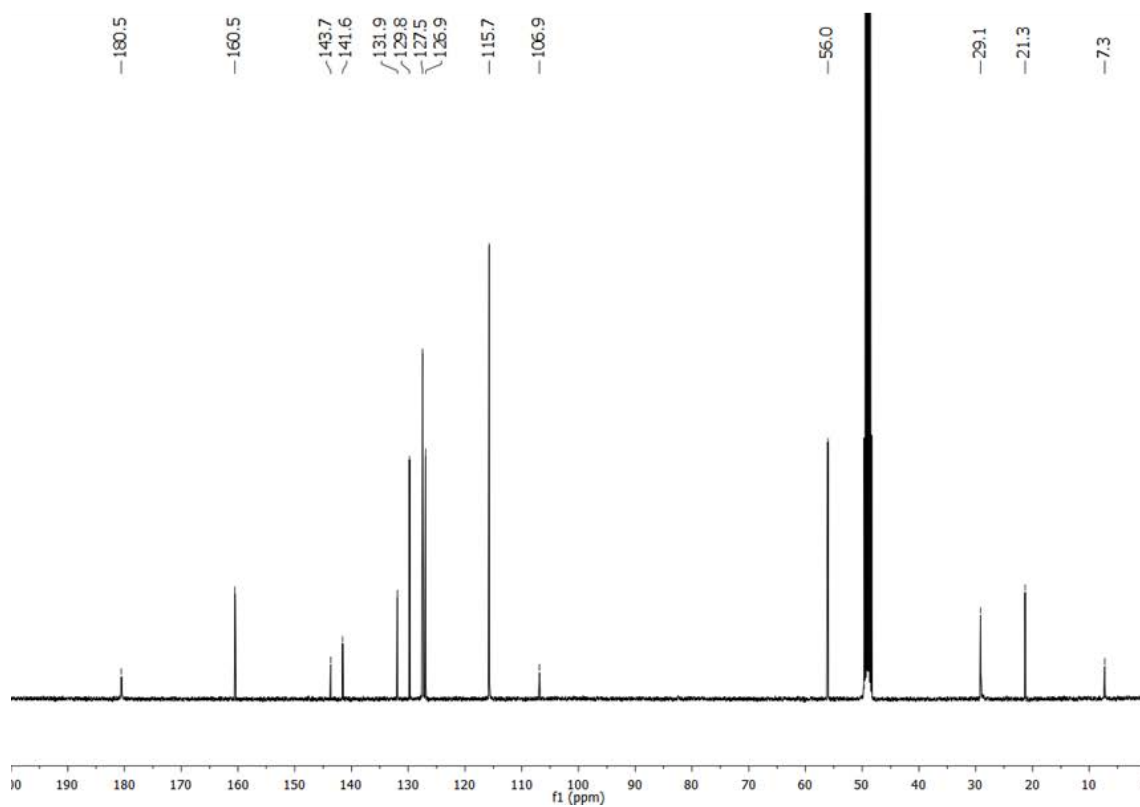
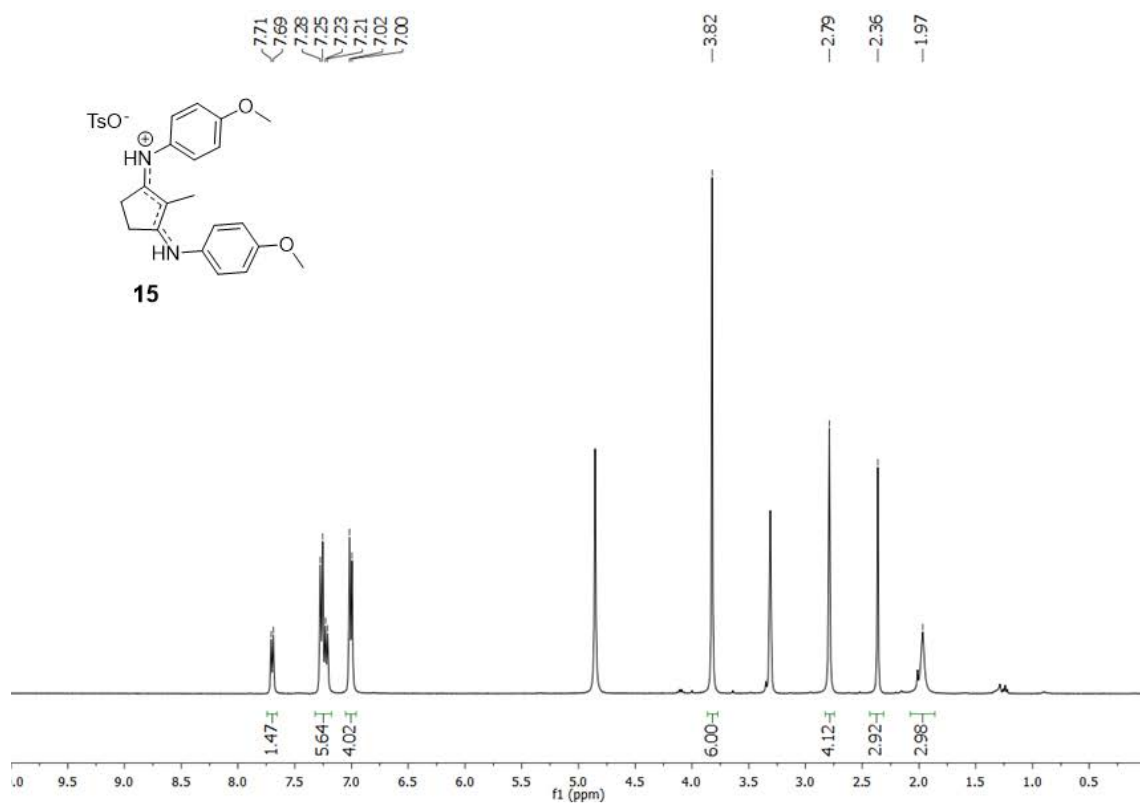
Appendix B: Selected NMR Spectra



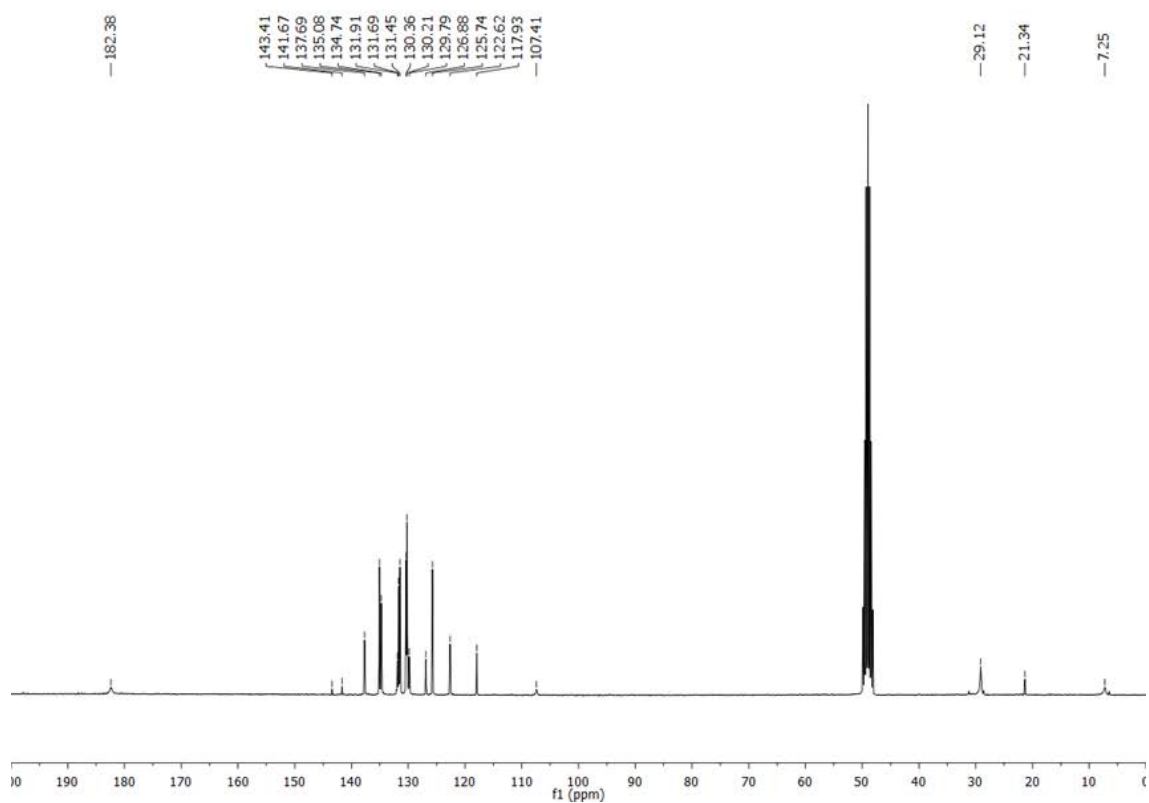
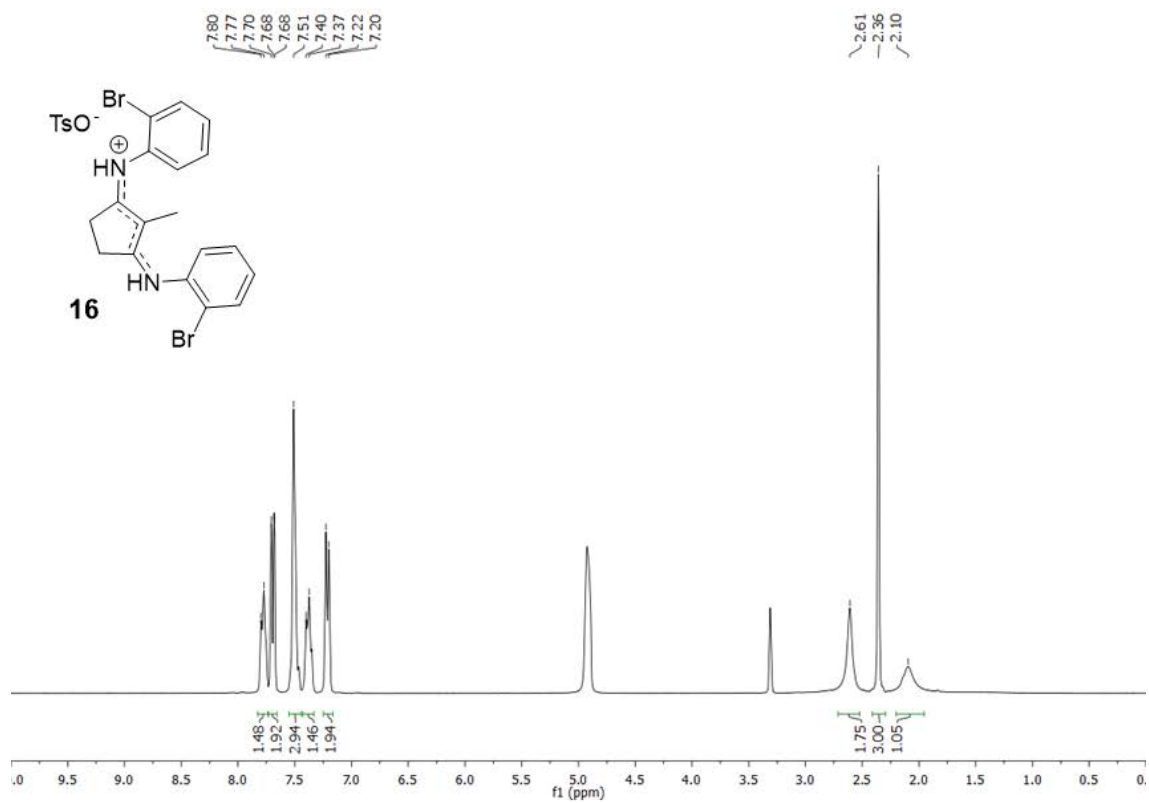
Appendix B: Selected NMR Spectra



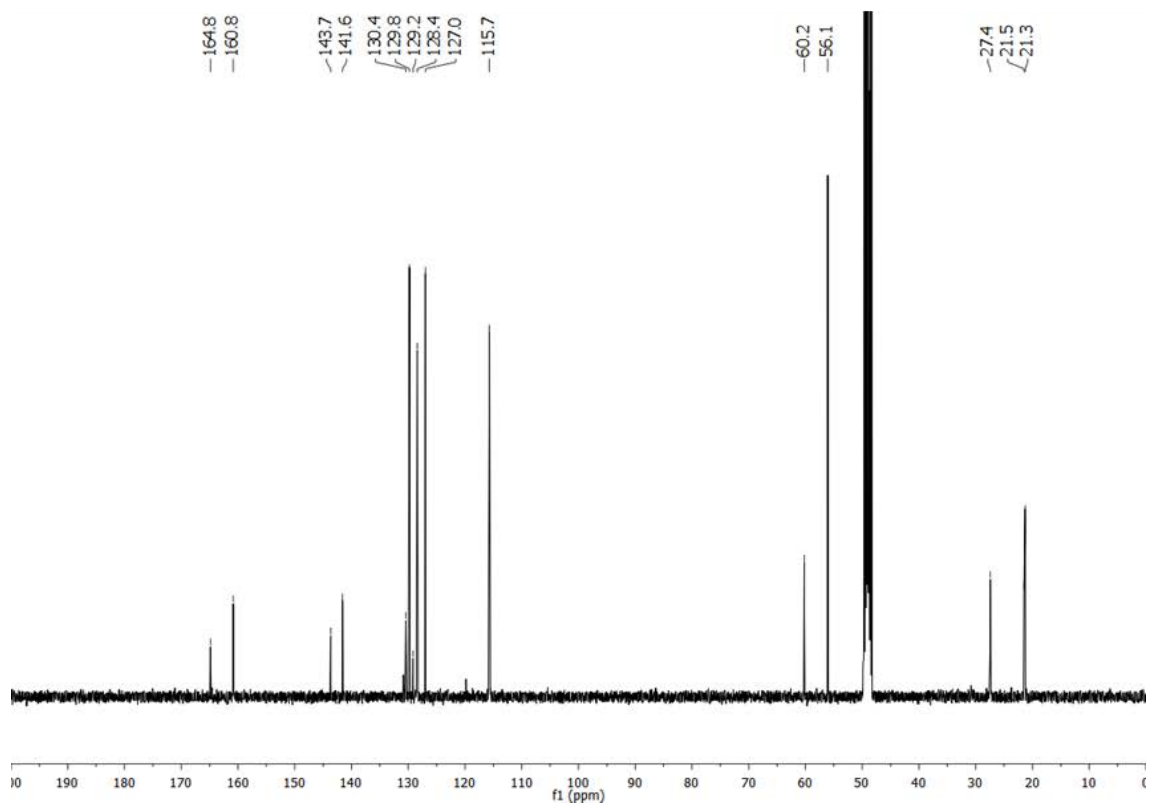
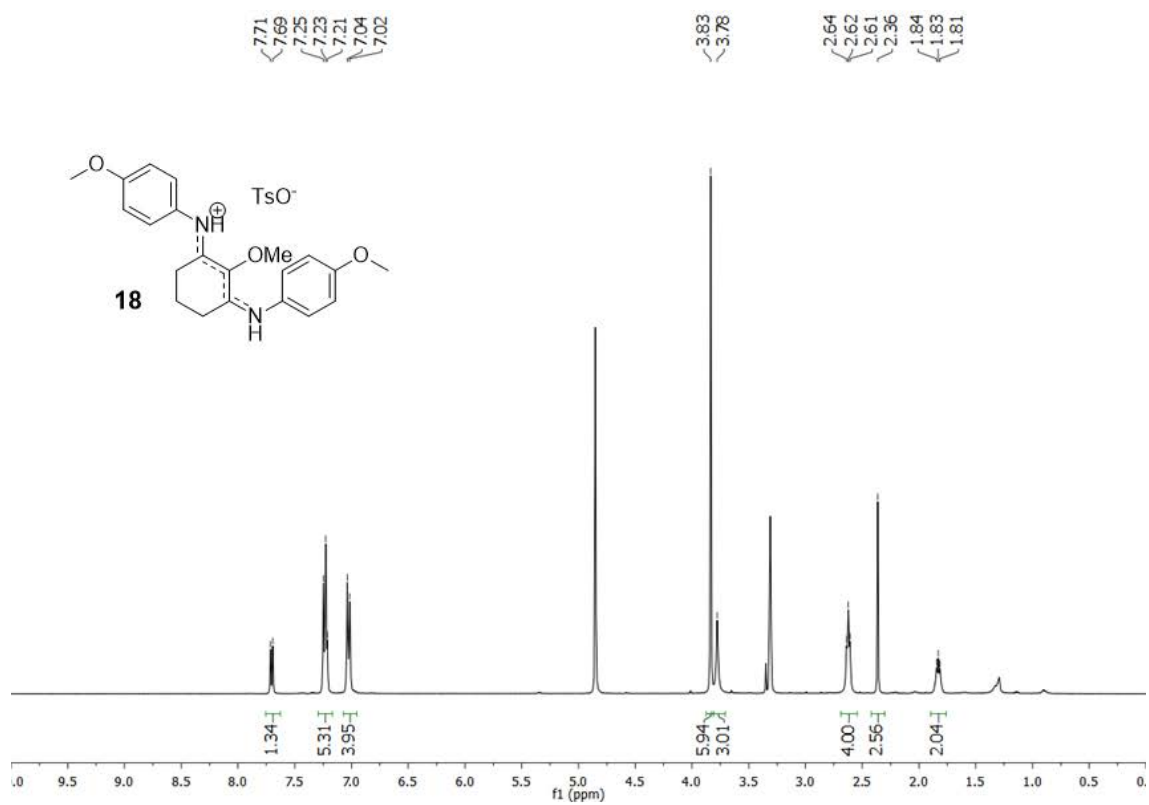
Appendix B: Selected NMR Spectra



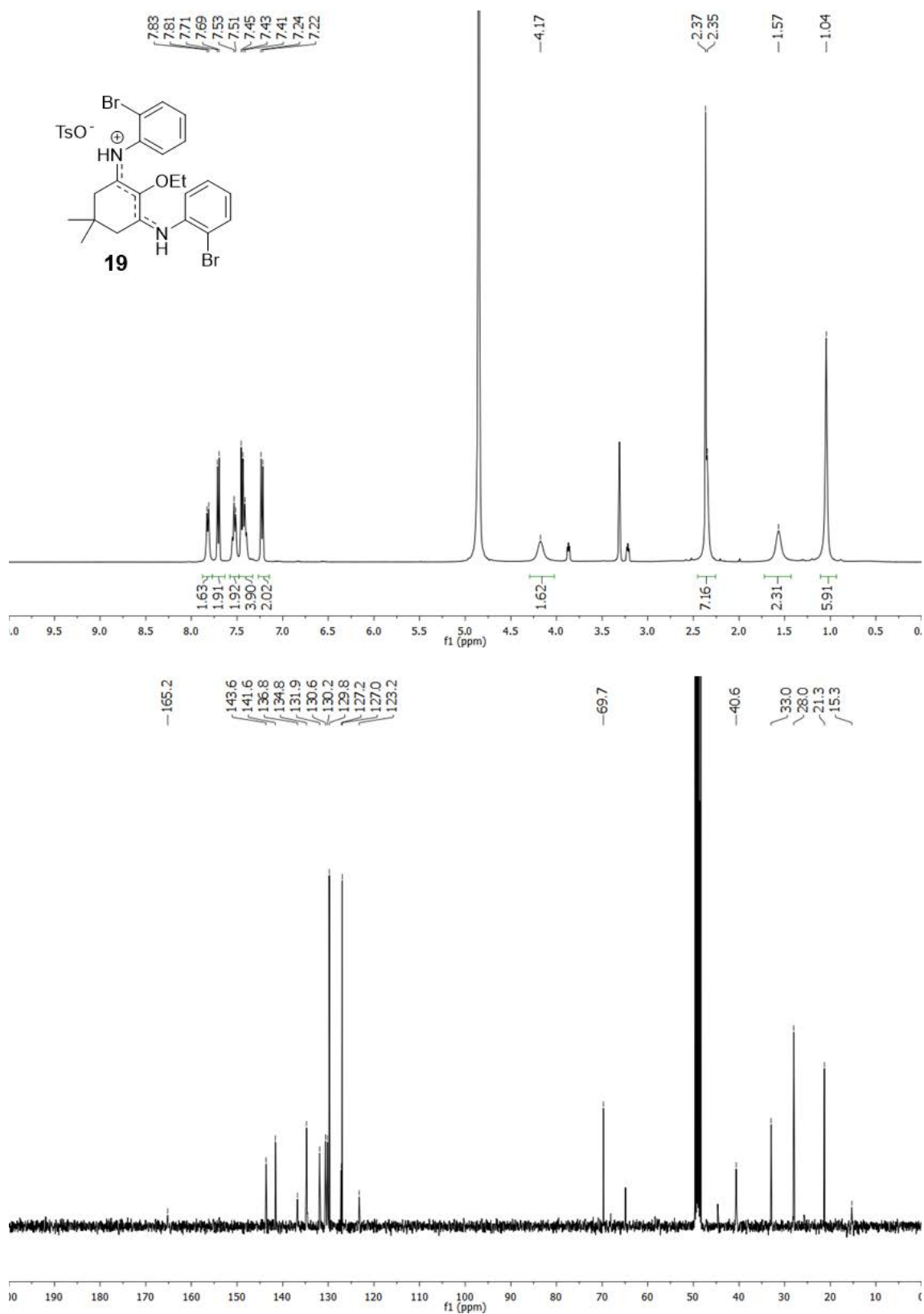
Appendix B: Selected NMR Spectra



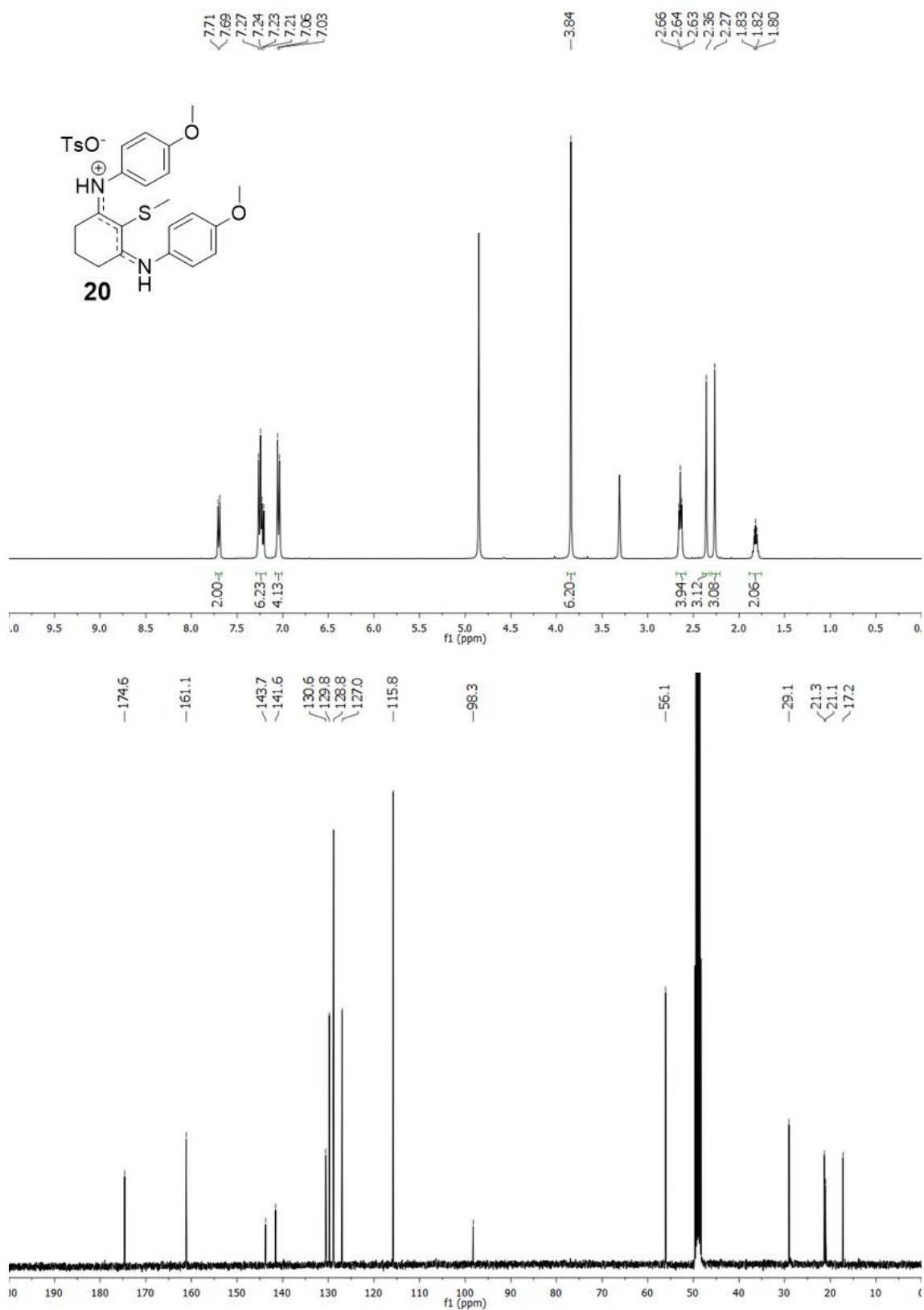
Appendix B: Selected NMR Spectra



Appendix B: Selected NMR Spectra

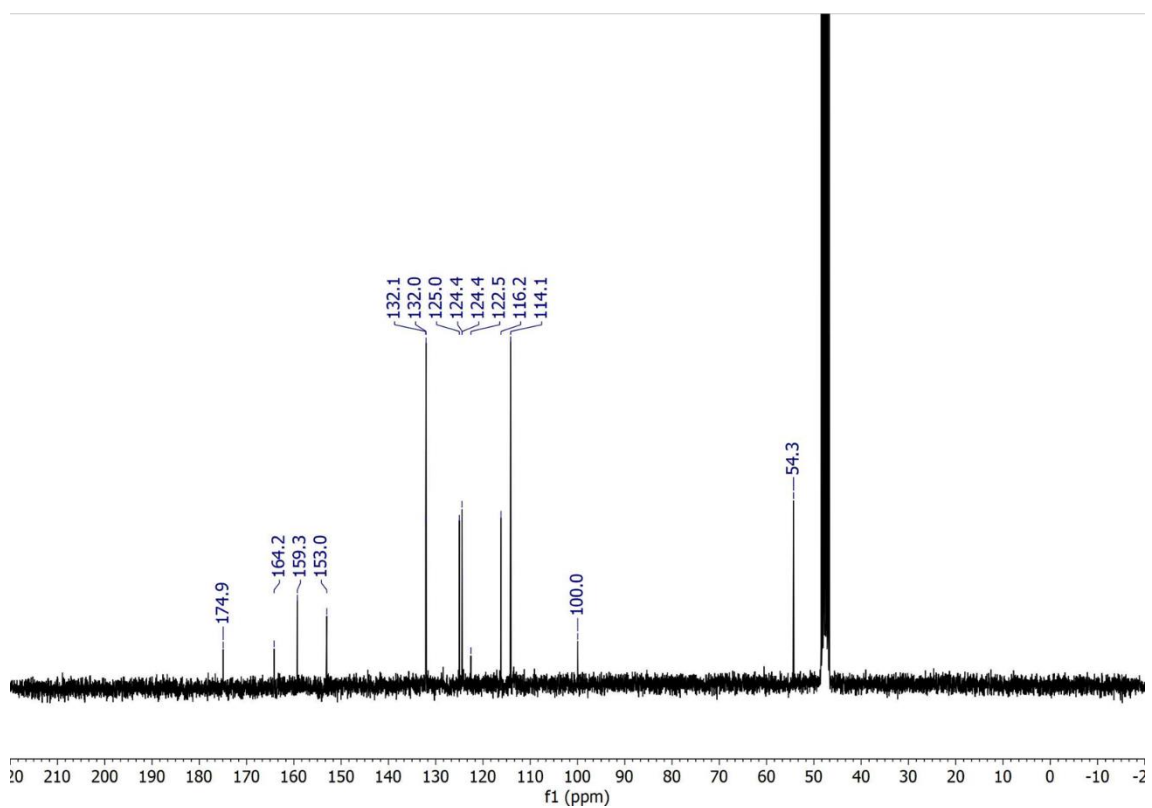
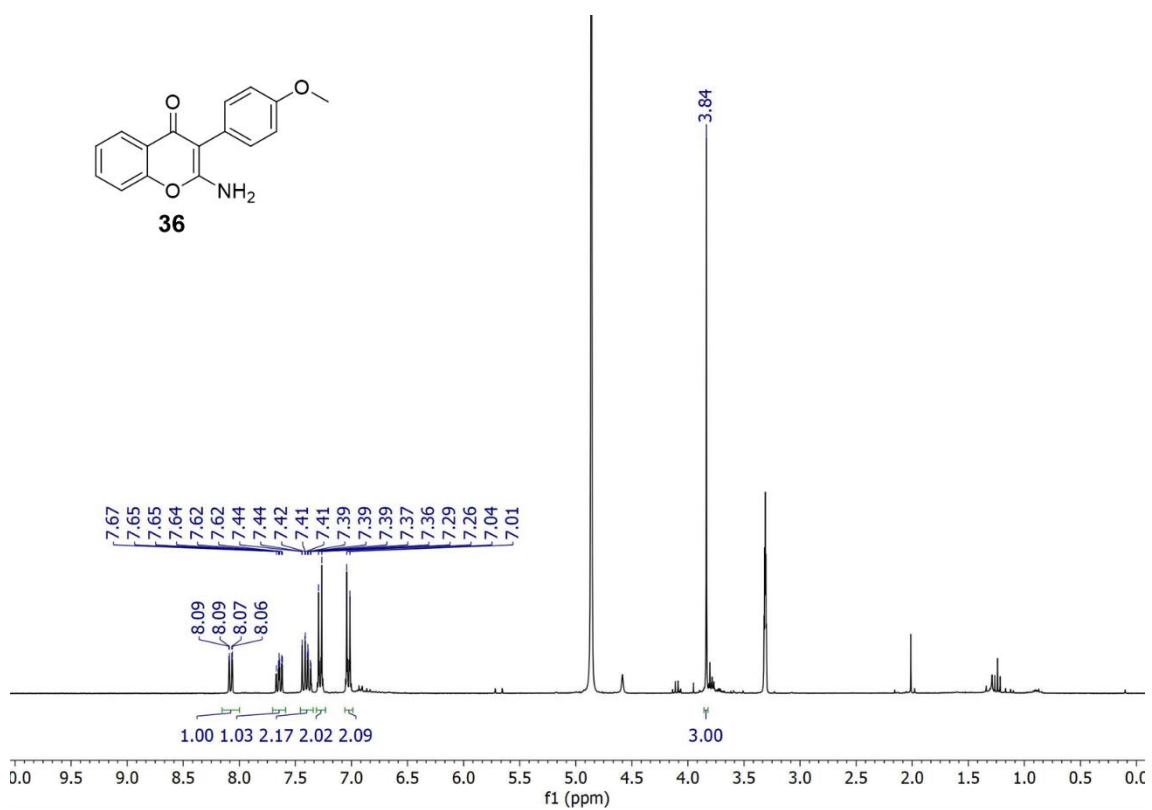


Appendix B: Selected NMR Spectra

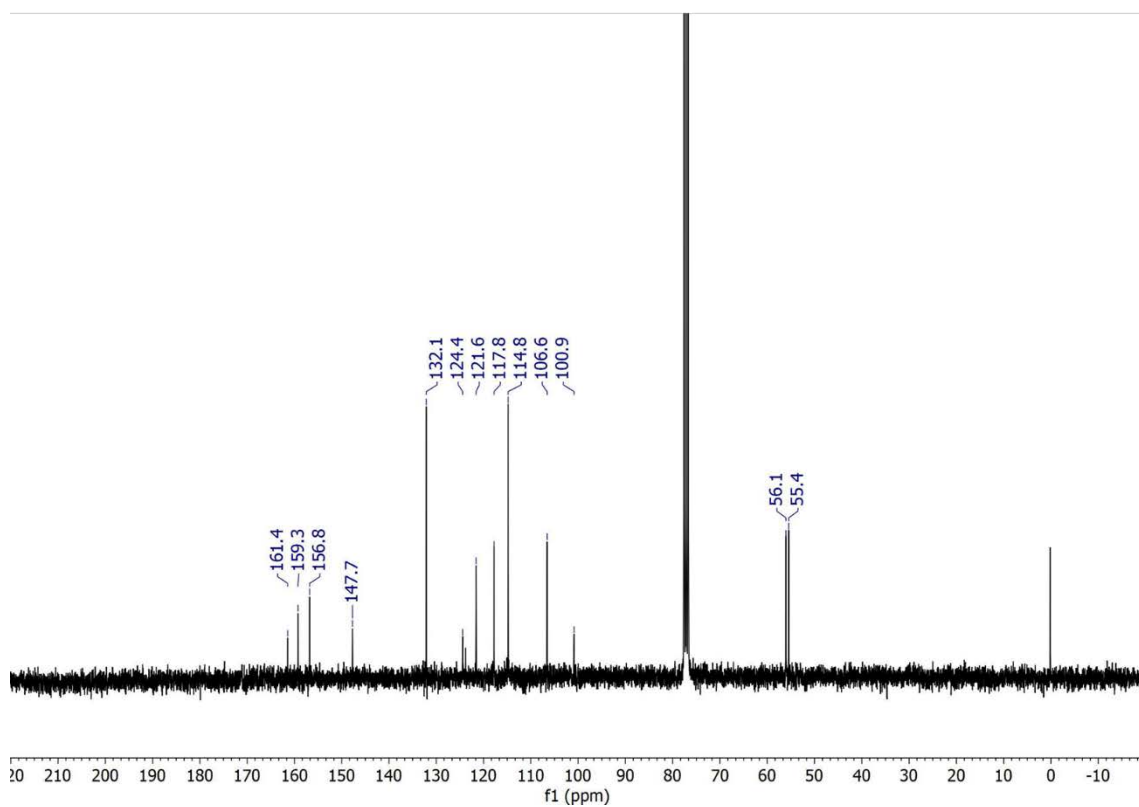
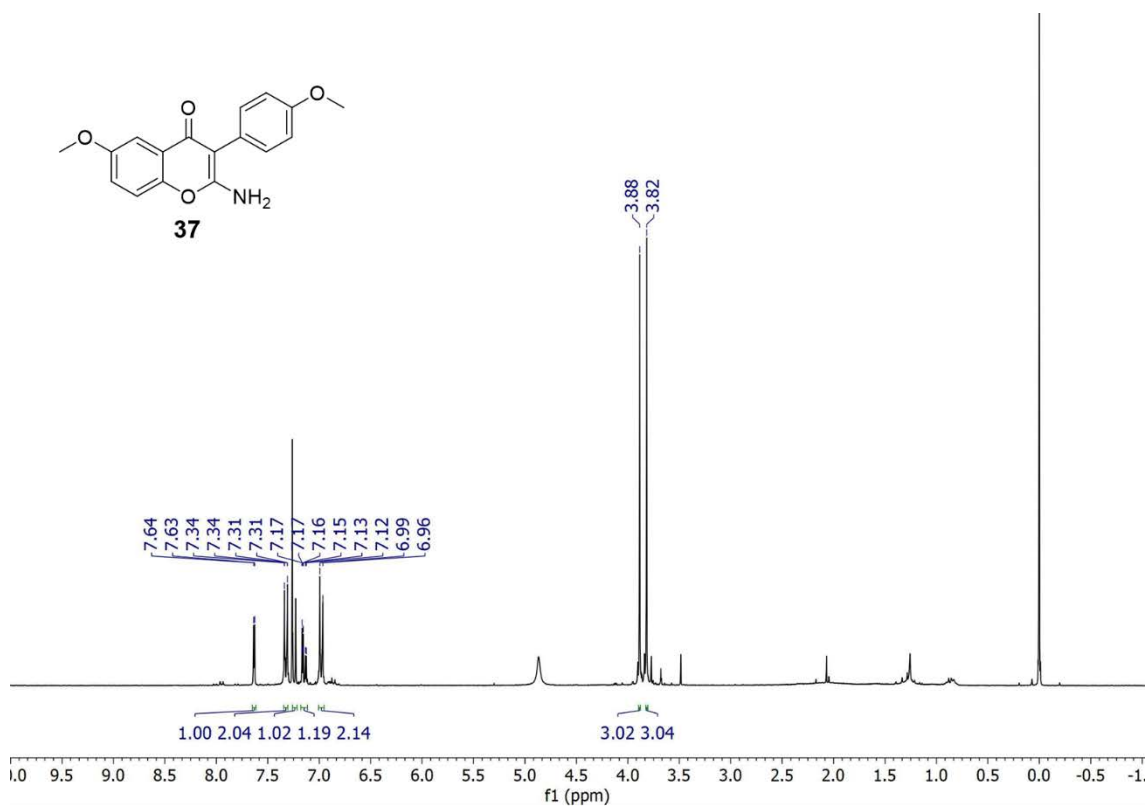


Appendix B: Selected NMR Spectra

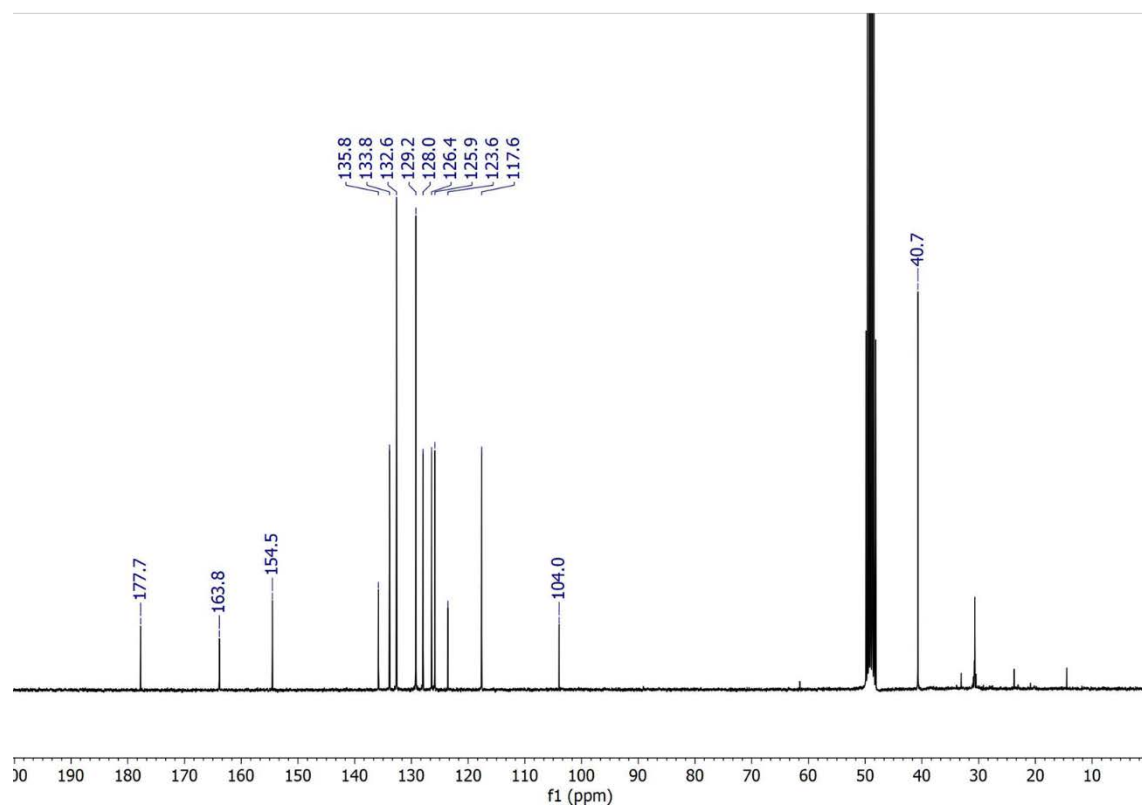
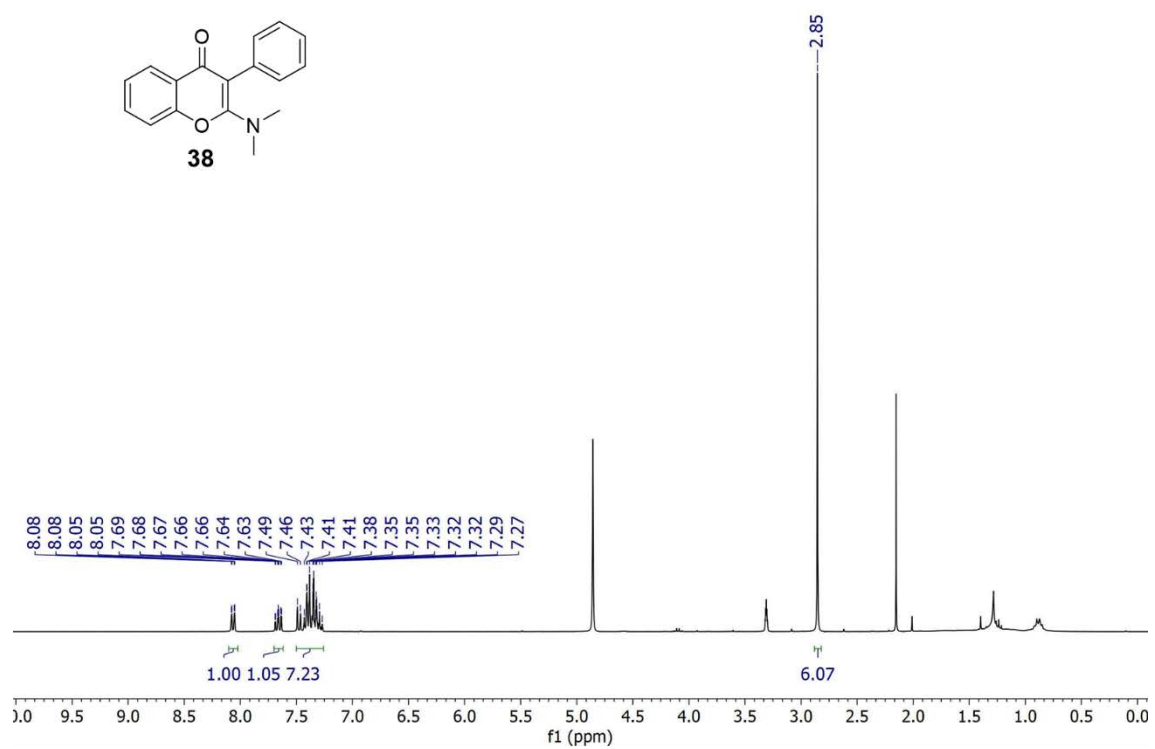
Chapter 6



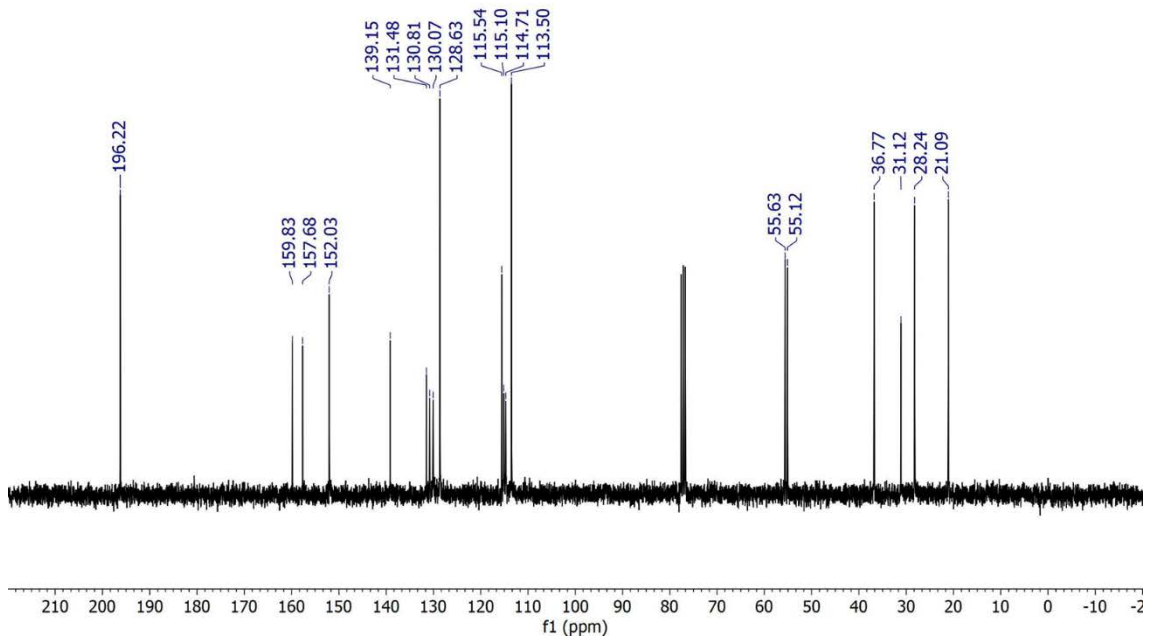
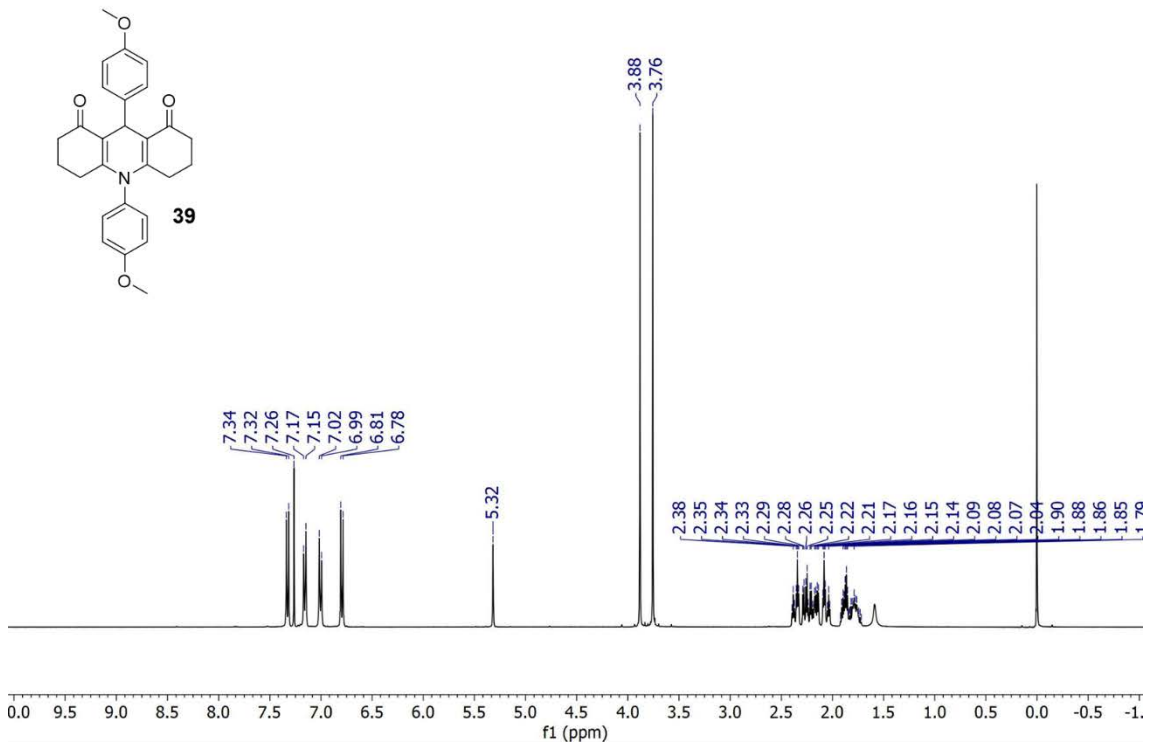
Appendix B: Selected NMR Spectra



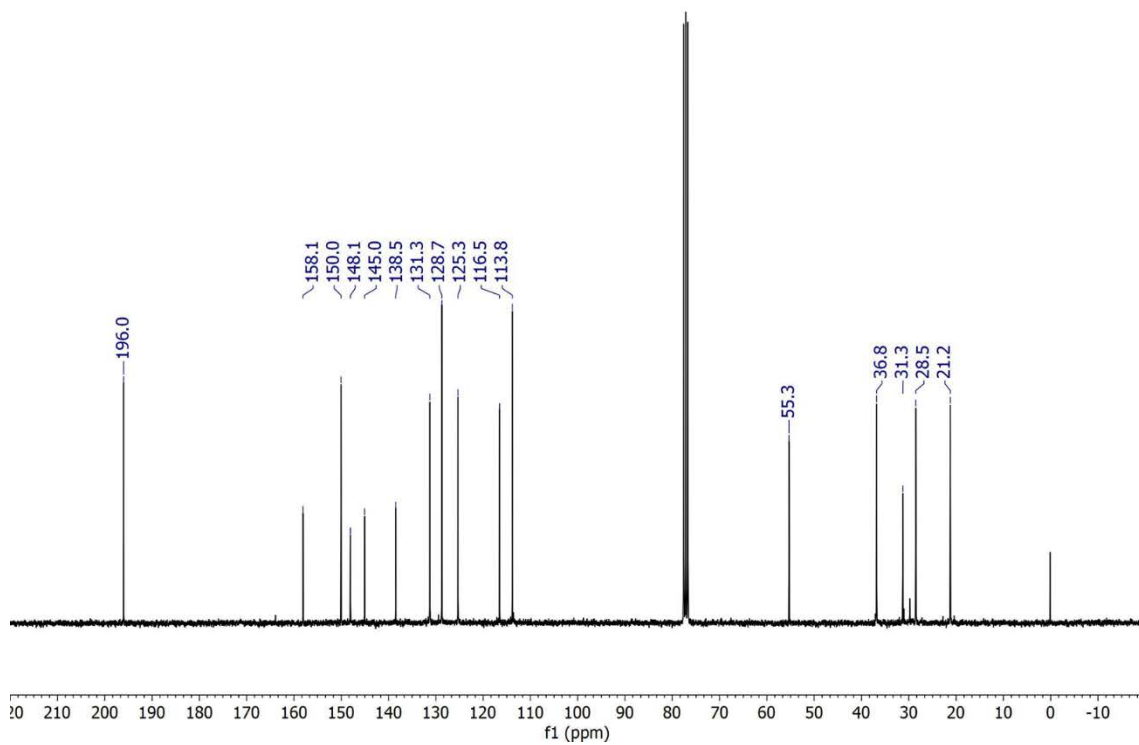
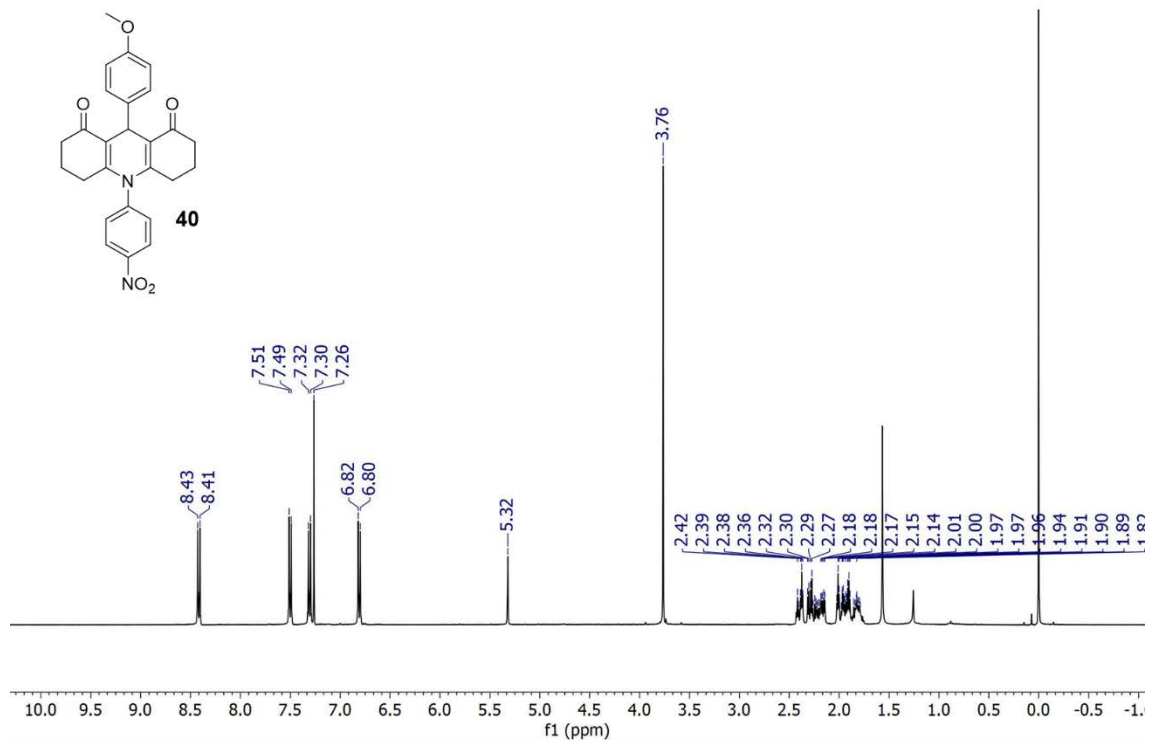
Appendix B: Selected NMR Spectra



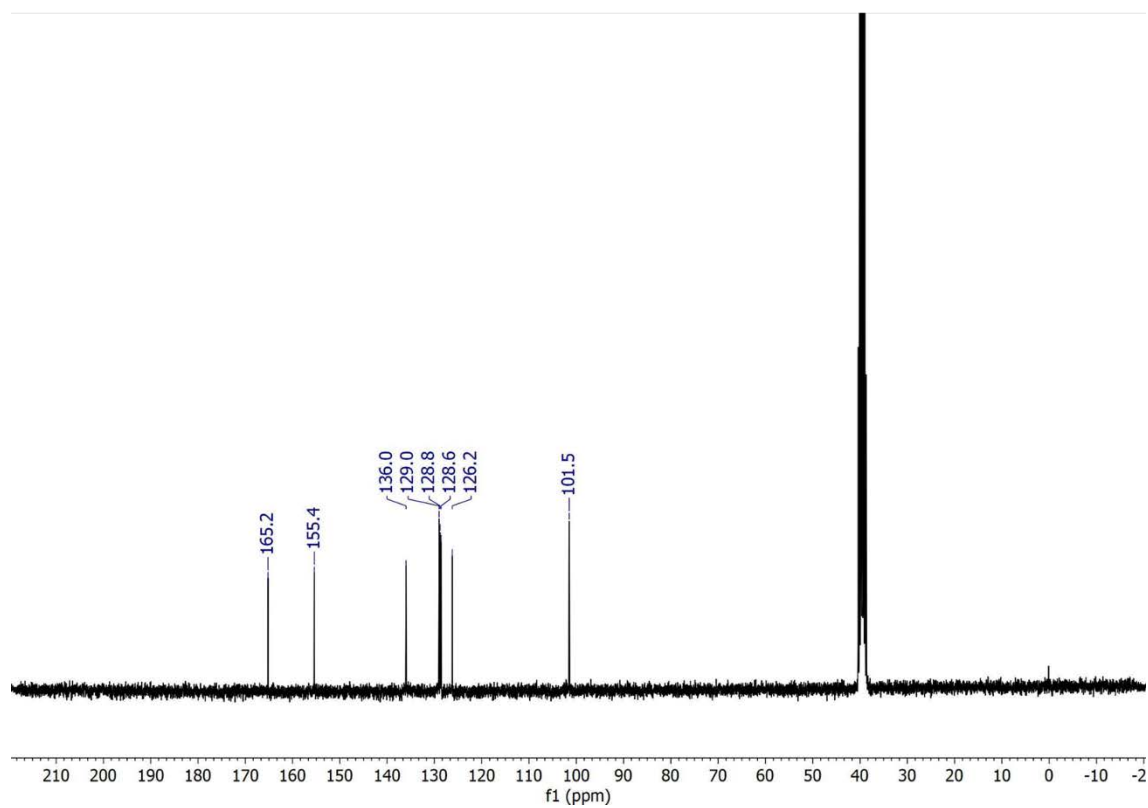
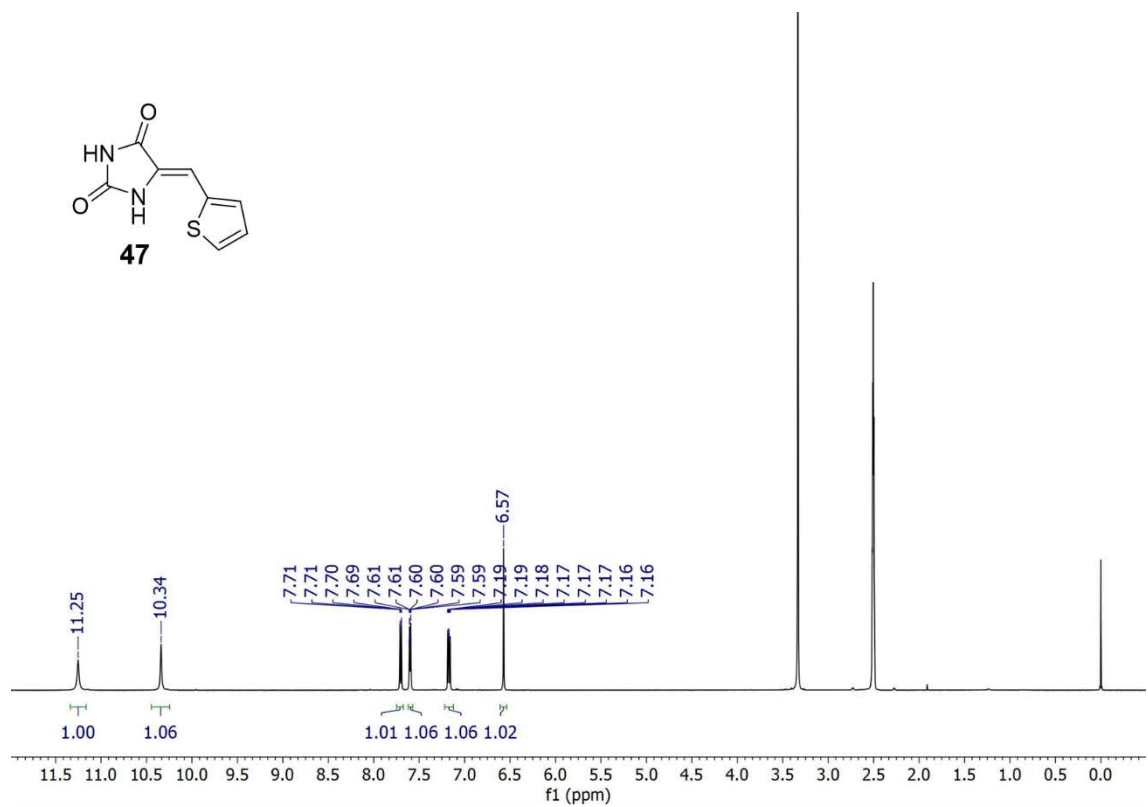
Appendix B: Selected NMR Spectra



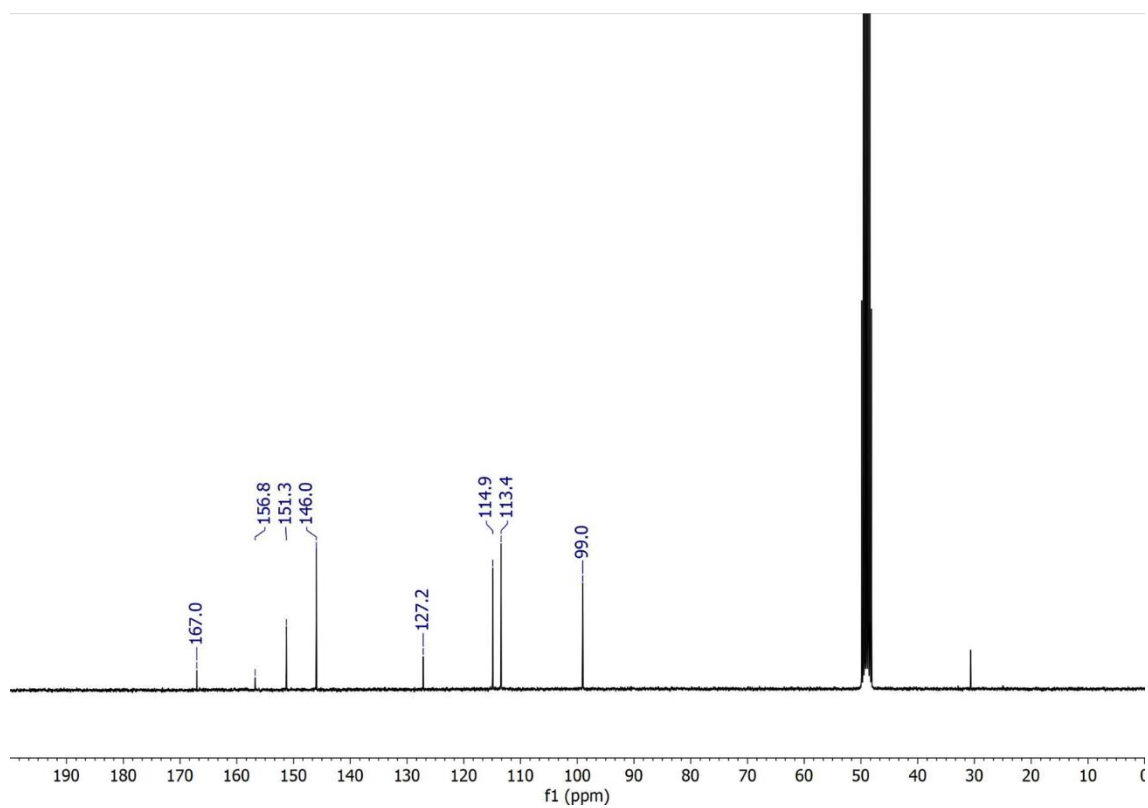
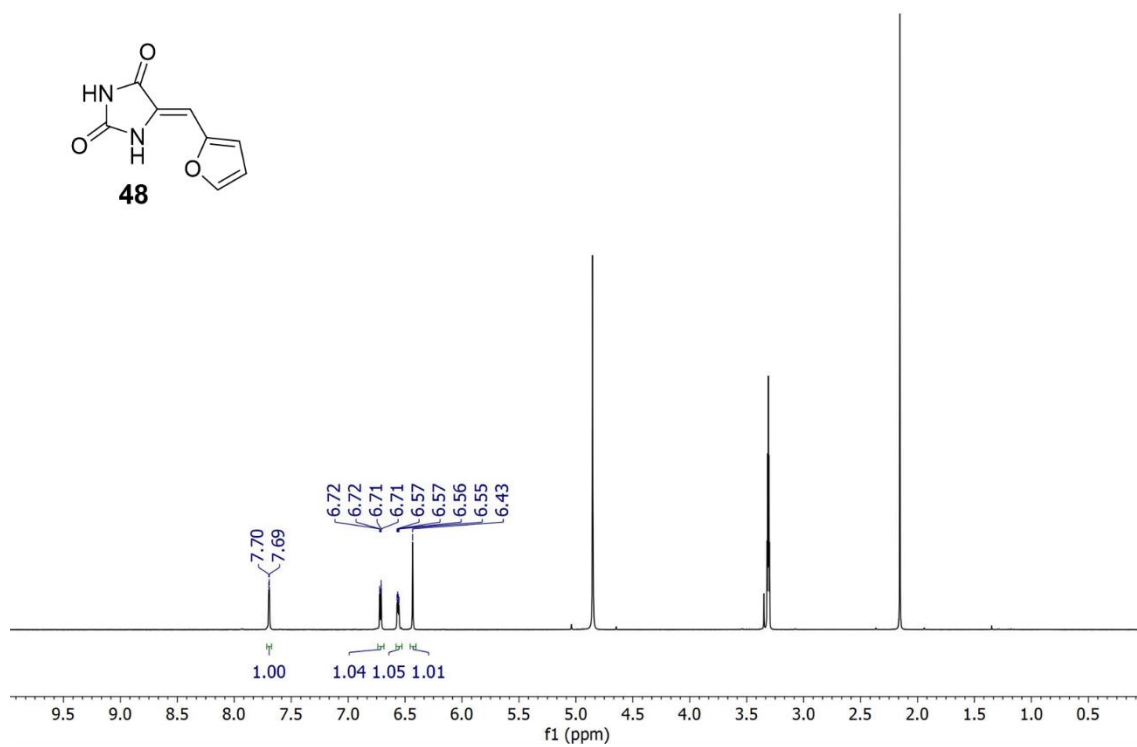
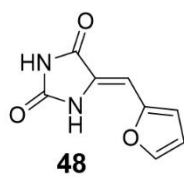
Appendix B: Selected NMR Spectra



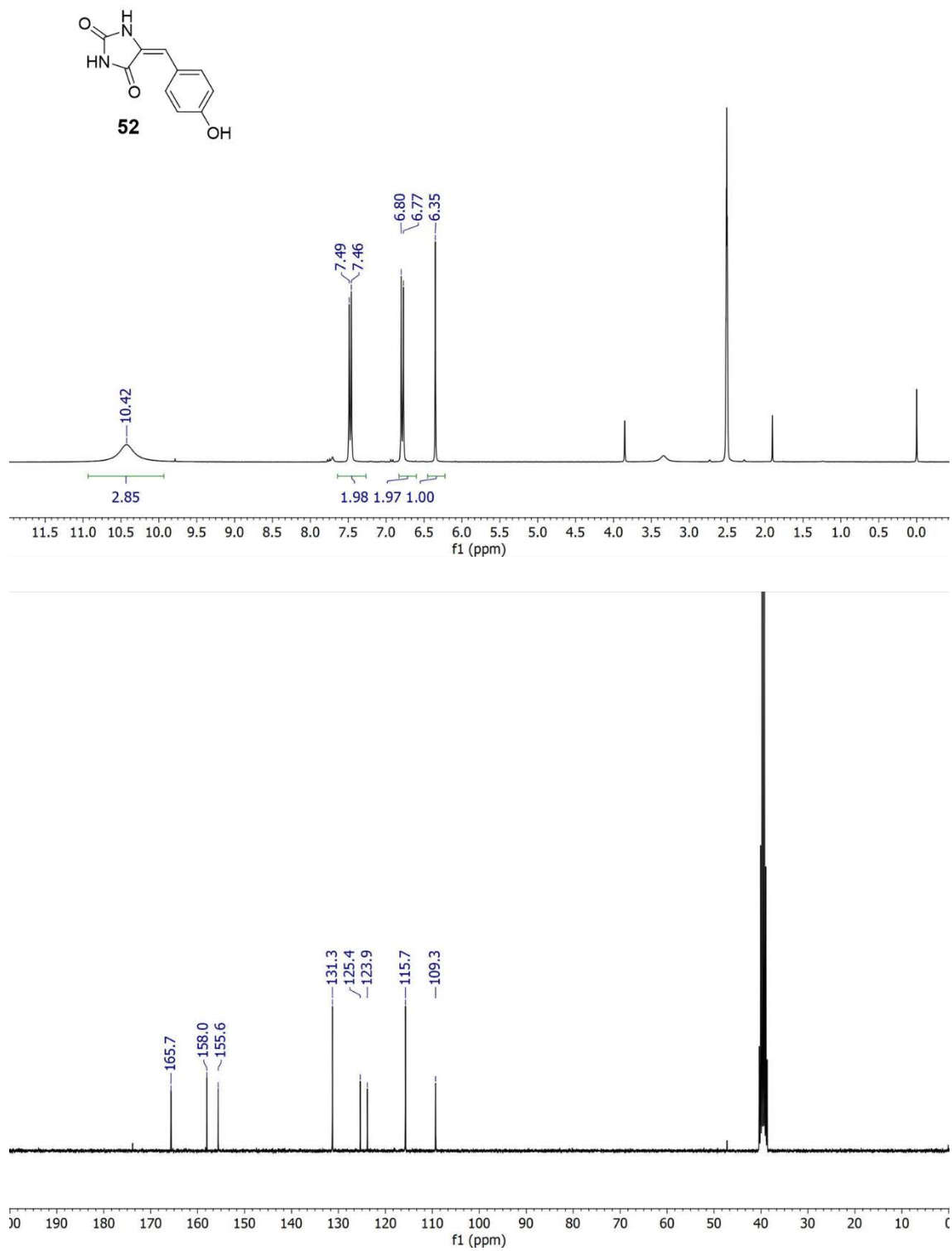
Chapter 7



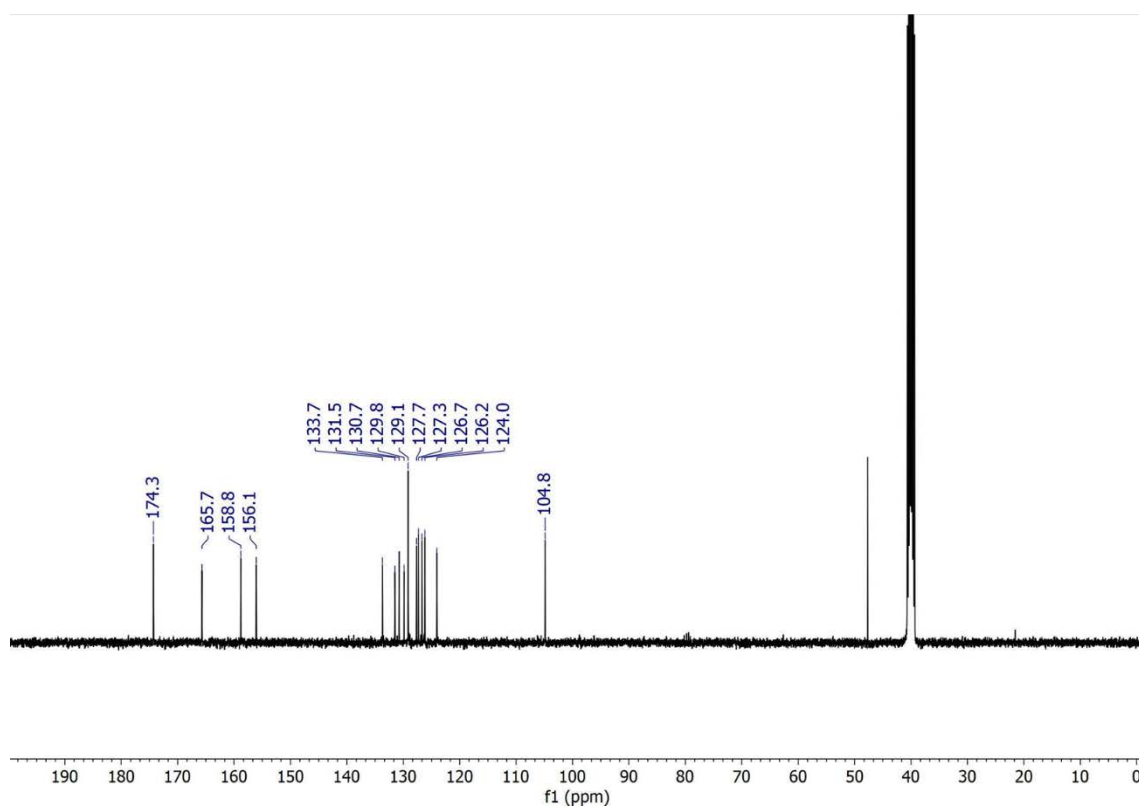
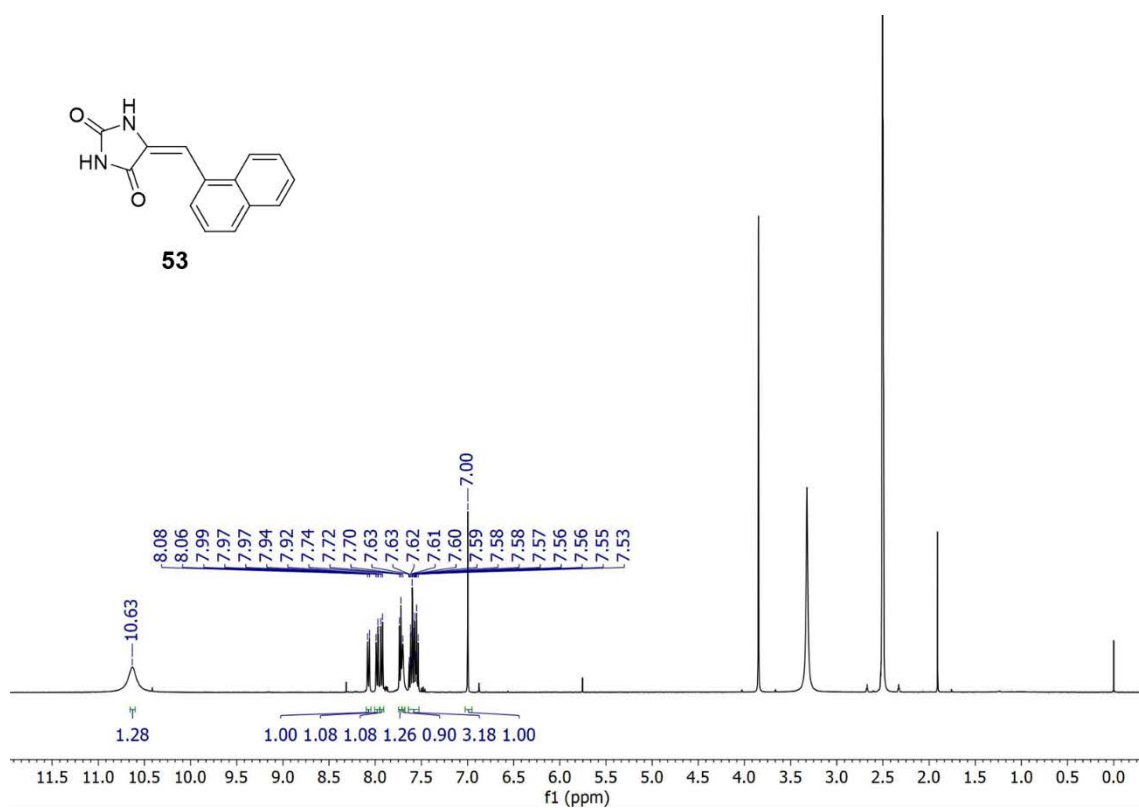
Appendix B: Selected NMR Spectra



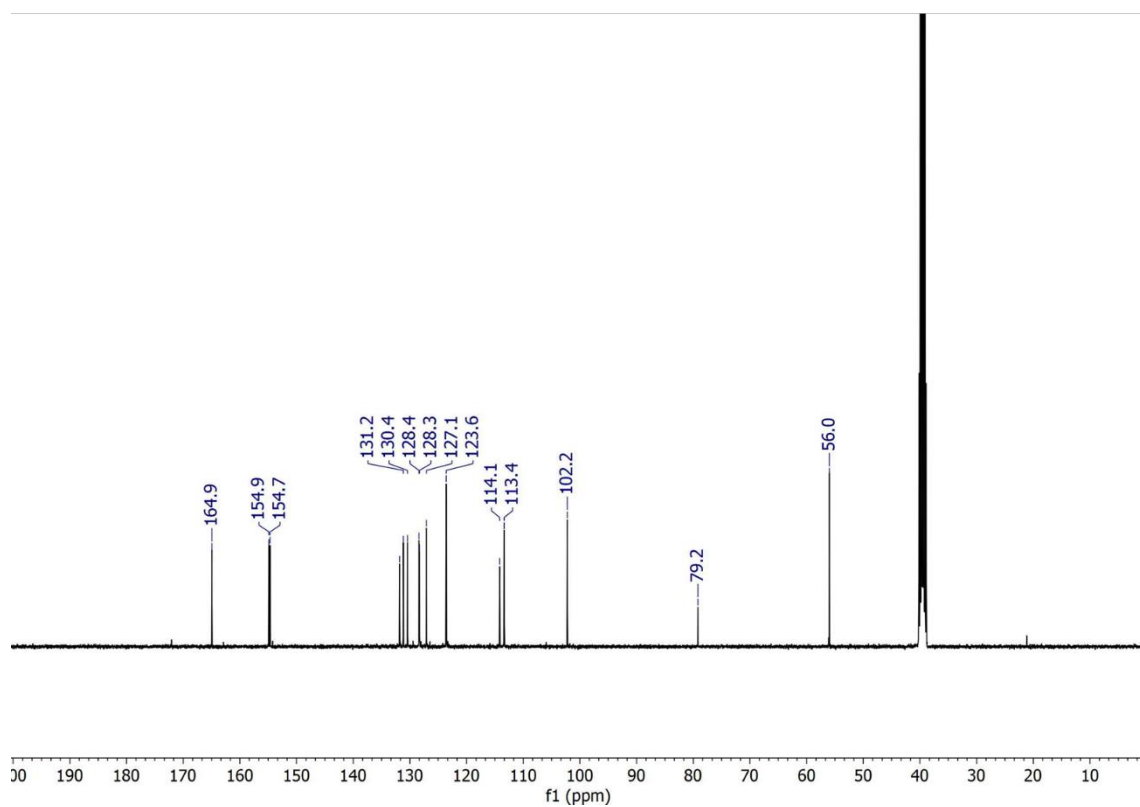
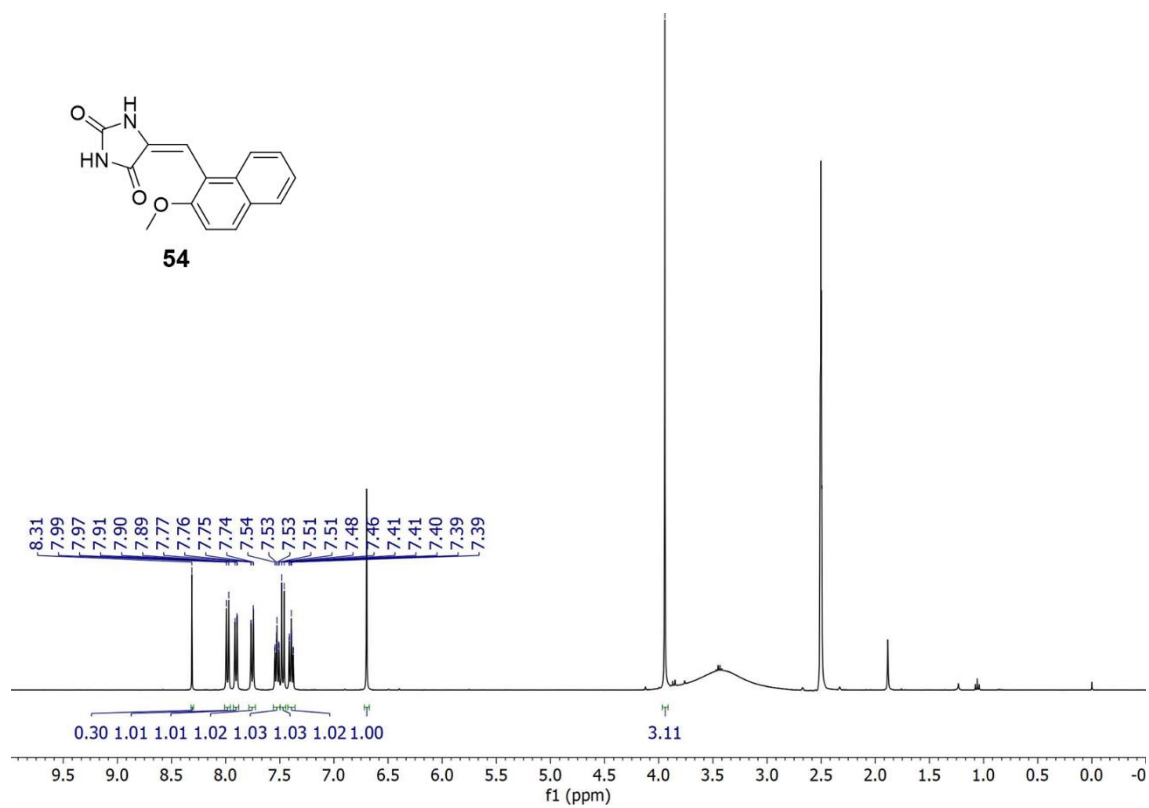
Appendix B: Selected NMR Spectra



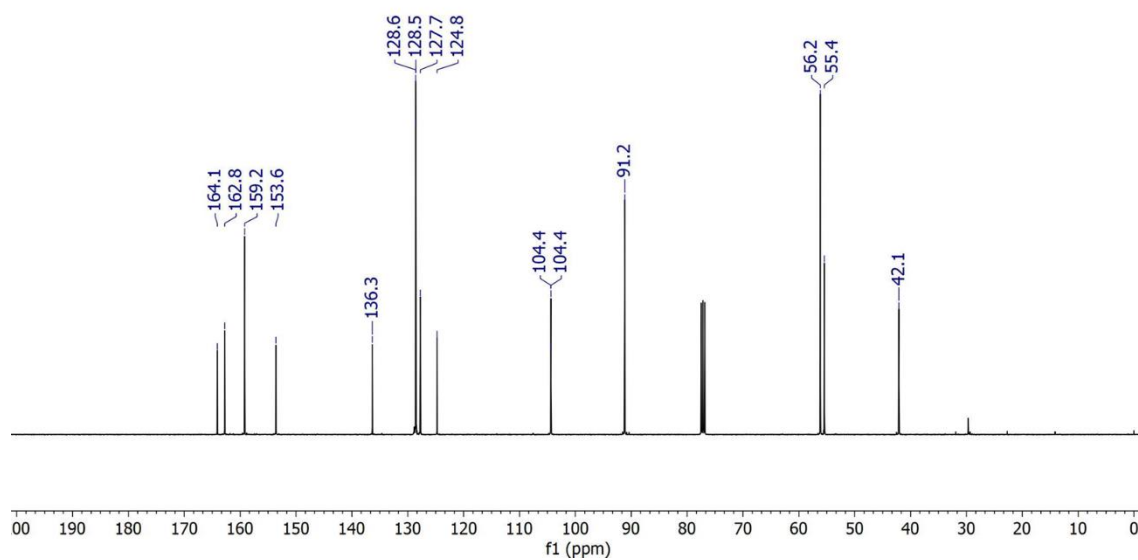
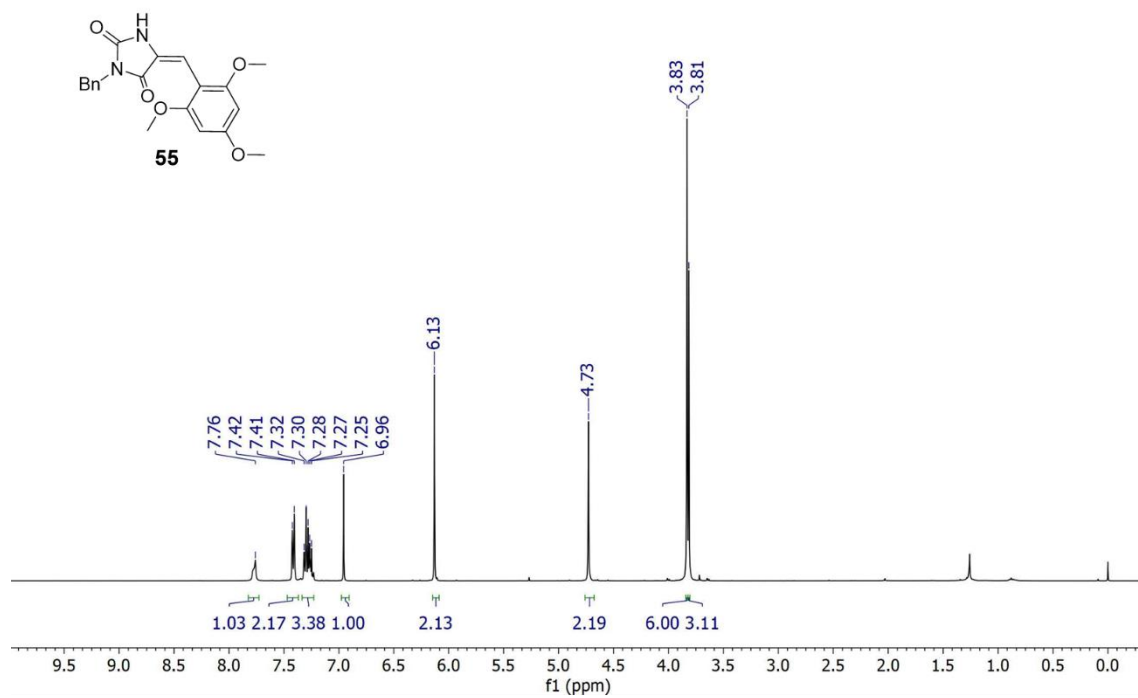
Appendix B: Selected NMR Spectra



Appendix B: Selected NMR Spectra

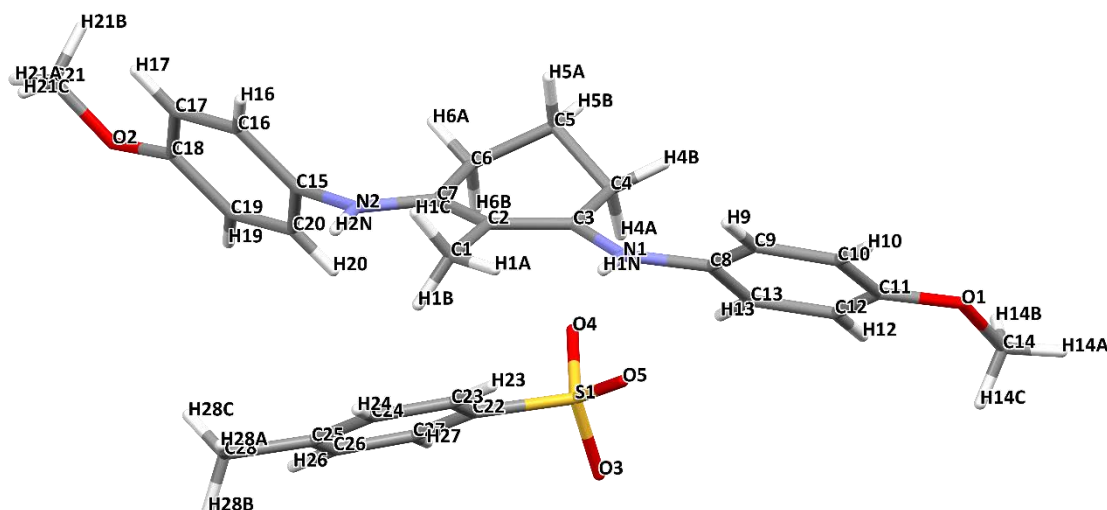


Appendix B: Selected NMR Spectra



Appendix C: X ray diffraction

Appendix C: X ray diffraction



Empirical formula	C ₂₈ H ₃₂ N ₂ O ₅ S	
Formula weight	508.62	
Temperature	173(2) K	
Wavelength	0.71073 Å	
Crystal system	MONOCLINIC	
Space group	P 21/c	
Unit cell dimensions	a = 15.5807(4) Å	a = 90°.
	b = 10.7860(5) Å	b = 108.501(3)°.
	c = 16.2551(8) Å	g = 90°.
Volume	2590.54(19) Å ³	
Z	4	
Density (calculated)	1.304 Mg/m ³	
Absorption coefficient	0.166 mm ⁻¹	
F(000)	1080	
Crystal size	0.6 x 0.25 x 0.2 mm ³	
Theta range for data collection	2.30 to 27.52°.	
Index ranges	0 ≤ h ≤ 20, 0 ≤ k ≤ 14, -21 ≤ l ≤ 20	
Reflections collected	5871	
Independent reflections	5871 [R(int) = 0.0000]	
Completeness to theta = 27.52°	98.4 %	
Absorption correction	Semi-empirical from equivalents	
Max. and min. transmission	1.022 and 0.808	
Refinement method	Full-matrix least-squares on F ²	
Data / restraints / parameters	5871 / 0 / 333	
Goodness-of-fit on F ²	1.038	
Final R indices [I > 2σ(I)]	R1 = 0.0502, wR2 = 0.1167	

Appendix C: X ray diffraction

R indices (all data) R1 = 0.0745, wR2 = 0.1332
 Largest diff. peak and hole 0.453 and -0.436 e.Å⁻³

Atomic coordinates (x 10⁴) and equivalent isotropic displacement parameters (Å²x 10³) for **9**.

U(eq) is defined as one third of the trace of the orthogonalized U_{ij} tensor.

	x	y	z	U(eq)
C(22)	7338(1)	6730(2)	7648(1)	26(1)
C(23)	6955(1)	7580(2)	8074(1)	30(1)
C(24)	7502(2)	8248(2)	8772(1)	35(1)
C(25)	8435(2)	8088(2)	9058(1)	35(1)
C(26)	8811(1)	7229(2)	8629(1)	35(1)
C(27)	8273(1)	6551(2)	7935(1)	32(1)
C(28)	9021(2)	8797(3)	9828(2)	57(1)
O(3)	7025(1)	6168(1)	6034(1)	33(1)
O(4)	6761(1)	4605(1)	6982(1)	41(1)
O(5)	5743(1)	6364(2)	6561(1)	40(1)
S(1)	6655(1)	5902(1)	6732(1)	27(1)
C(1)	5112(2)	8221(2)	9287(2)	39(1)
C(2)	5173(1)	6939(2)	8946(1)	27(1)
C(3)	4561(1)	6535(2)	8153(1)	25(1)
C(4)	4599(1)	5241(2)	7827(1)	28(1)
C(5)	5040(1)	4360(2)	8573(1)	31(1)
C(6)	5965(1)	4855(2)	9086(1)	30(1)
C(7)	5895(1)	6158(2)	9380(1)	26(1)
C(8)	3281(1)	7106(2)	6833(1)	25(1)
C(9)	2401(1)	7522(2)	6697(1)	30(1)
C(10)	1761(1)	7433(2)	5887(1)	32(1)
C(11)	1989(1)	6908(2)	5197(1)	29(1)
C(12)	2867(1)	6497(2)	5328(1)	30(1)
C(13)	3512(1)	6609(2)	6143(1)	28(1)
C(14)	1539(2)	6495(3)	3685(1)	44(1)
C(15)	7335(1)	5889(2)	10575(1)	26(1)
C(16)	7459(1)	5672(2)	11440(1)	31(1)
C(17)	8239(1)	5104(2)	11967(1)	33(1)

Appendix C: X ray diffraction

C(18)	8903(1)	4764(2)	11612(1)	32(1)
C(19)	8780(2)	4976(2)	10738(1)	35(1)
C(20)	7999(1)	5539(2)	10221(1)	32(1)
C(21)	9843(2)	3918(3)	12954(2)	50(1)
N(1)	3926(1)	7309(2)	7674(1)	27(1)
N(2)	6544(1)	6567(2)	10078(1)	28(1)
O(1)	1298(1)	6848(2)	4428(1)	36(1)
O(2)	9707(1)	4210(2)	12068(1)	44(1)

Bond lengths [Å] and angles [°] for import.

C(22)-C(23)	1.392(3)
C(22)-C(27)	1.395(3)
C(22)-S(1)	1.772(2)
C(23)-C(24)	1.385(3)
C(23)-H(23)	0.9500
C(24)-C(25)	1.389(3)
C(24)-H(24)	0.9500
C(25)-C(26)	1.396(3)
C(25)-C(28)	1.503(3)
C(26)-C(27)	1.382(3)
C(26)-H(26)	0.9500
C(27)-H(27)	0.9500
C(28)-H(28A)	0.9800
C(28)-H(28B)	0.9800
C(28)-H(28C)	0.9800
O(3)-S(1)	1.4549(15)
O(4)-S(1)	1.4516(16)
O(5)-S(1)	1.4467(16)
C(1)-C(2)	1.505(3)
C(1)-H(1A)	0.9800
C(1)-H(1B)	0.9800
C(1)-H(1C)	0.9800
C(2)-C(7)	1.403(3)
C(2)-C(3)	1.407(3)
C(3)-N(1)	1.339(3)
C(3)-C(4)	1.500(3)

Appendix C: X ray diffraction

C(4)-C(5)	1.523(3)
C(4)-H(4A)	0.9900
C(4)-H(4B)	0.9900
C(5)-C(6)	1.514(3)
C(5)-H(5A)	0.9900
C(5)-H(5B)	0.9900
C(6)-C(7)	1.499(3)
C(6)-H(6A)	0.9900
C(6)-H(6B)	0.9900
C(7)-N(2)	1.334(3)
C(8)-C(13)	1.389(3)
C(8)-C(9)	1.392(3)
C(8)-N(1)	1.434(2)
C(9)-C(10)	1.380(3)
C(9)-H(9)	0.9500
C(10)-C(11)	1.398(3)
C(10)-H(10)	0.9500
C(11)-O(1)	1.368(2)
C(11)-C(12)	1.389(3)
C(12)-C(13)	1.391(3)
C(12)-H(12)	0.9500
C(13)-H(13)	0.9500
C(14)-O(1)	1.427(3)
C(14)-H(14A)	0.9800
C(14)-H(14B)	0.9800
C(14)-H(14C)	0.9800
C(15)-C(16)	1.377(3)
C(15)-C(20)	1.386(3)
C(15)-N(2)	1.440(2)
C(16)-C(17)	1.388(3)
C(16)-H(16)	0.9500
C(17)-C(18)	1.384(3)
C(17)-H(17)	0.9500
C(18)-O(2)	1.373(2)
C(18)-C(19)	1.392(3)
C(19)-C(20)	1.382(3)
C(19)-H(19)	0.9500
C(20)-H(20)	0.9500

Appendix C: X ray diffraction

C(21)-O(2)	1.422(3)
C(21)-H(21A)	0.9800
C(21)-H(21B)	0.9800
C(21)-H(21C)	0.9800
N(1)-H(1N)	0.85(2)
N(2)-H(2N)	0.91(3)
C(23)-C(22)-C(27)	119.48(19)
C(23)-C(22)-S(1)	120.82(15)
C(27)-C(22)-S(1)	119.69(16)
C(24)-C(23)-C(22)	120.00(19)
C(24)-C(23)-H(23)	120.0
C(22)-C(23)-H(23)	120.0
C(23)-C(24)-C(25)	121.1(2)
C(23)-C(24)-H(24)	119.4
C(25)-C(24)-H(24)	119.4
C(24)-C(25)-C(26)	118.4(2)
C(24)-C(25)-C(28)	120.7(2)
C(26)-C(25)-C(28)	120.9(2)
C(27)-C(26)-C(25)	121.2(2)
C(27)-C(26)-H(26)	119.4
C(25)-C(26)-H(26)	119.4
C(26)-C(27)-C(22)	119.8(2)
C(26)-C(27)-H(27)	120.1
C(22)-C(27)-H(27)	120.1
C(25)-C(28)-H(28A)	109.5
C(25)-C(28)-H(28B)	109.5
H(28A)-C(28)-H(28B)	109.5
C(25)-C(28)-H(28C)	109.5
H(28A)-C(28)-H(28C)	109.5
H(28B)-C(28)-H(28C)	109.5
O(5)-S(1)-O(4)	113.77(10)
O(5)-S(1)-O(3)	112.99(9)
O(4)-S(1)-O(3)	111.73(10)
O(5)-S(1)-C(22)	106.18(10)
O(4)-S(1)-C(22)	105.44(9)
O(3)-S(1)-C(22)	105.95(9)
C(2)-C(1)-H(1A)	109.5

Appendix C: X ray diffraction

C(2)-C(1)-H(1B)	109.5
H(1A)-C(1)-H(1B)	109.5
C(2)-C(1)-H(1C)	109.5
H(1A)-C(1)-H(1C)	109.5
H(1B)-C(1)-H(1C)	109.5
C(7)-C(2)-C(3)	118.48(18)
C(7)-C(2)-C(1)	120.09(17)
C(3)-C(2)-C(1)	121.20(17)
N(1)-C(3)-C(2)	120.08(18)
N(1)-C(3)-C(4)	118.59(17)
C(2)-C(3)-C(4)	121.33(17)
C(3)-C(4)-C(5)	110.98(16)
C(3)-C(4)-H(4A)	109.4
C(5)-C(4)-H(4A)	109.4
C(3)-C(4)-H(4B)	109.4
C(5)-C(4)-H(4B)	109.4
H(4A)-C(4)-H(4B)	108.0
C(6)-C(5)-C(4)	109.17(17)
C(6)-C(5)-H(5A)	109.8
C(4)-C(5)-H(5A)	109.8
C(6)-C(5)-H(5B)	109.8
C(4)-C(5)-H(5B)	109.8
H(5A)-C(5)-H(5B)	108.3
C(7)-C(6)-C(5)	110.68(17)
C(7)-C(6)-H(6A)	109.5
C(5)-C(6)-H(6A)	109.5
C(7)-C(6)-H(6B)	109.5
C(5)-C(6)-H(6B)	109.5
H(6A)-C(6)-H(6B)	108.1
N(2)-C(7)-C(2)	119.98(18)
N(2)-C(7)-C(6)	117.99(17)
C(2)-C(7)-C(6)	122.03(18)
C(13)-C(8)-C(9)	119.38(18)
C(13)-C(8)-N(1)	123.11(18)
C(9)-C(8)-N(1)	117.31(17)
C(10)-C(9)-C(8)	120.45(19)
C(10)-C(9)-H(9)	119.8
C(8)-C(9)-H(9)	119.8

Appendix C: X ray diffraction

C(9)-C(10)-C(11)	120.14(19)
C(9)-C(10)-H(10)	119.9
C(11)-C(10)-H(10)	119.9
O(1)-C(11)-C(12)	125.19(18)
O(1)-C(11)-C(10)	115.15(18)
C(12)-C(11)-C(10)	119.67(18)
C(11)-C(12)-C(13)	119.82(19)
C(11)-C(12)-H(12)	120.1
C(13)-C(12)-H(12)	120.1
C(8)-C(13)-C(12)	120.52(18)
C(8)-C(13)-H(13)	119.7
C(12)-C(13)-H(13)	119.7
O(1)-C(14)-H(14A)	109.5
O(1)-C(14)-H(14B)	109.5
H(14A)-C(14)-H(14B)	109.5
O(1)-C(14)-H(14C)	109.5
H(14A)-C(14)-H(14C)	109.5
H(14B)-C(14)-H(14C)	109.5
C(16)-C(15)-C(20)	119.79(18)
C(16)-C(15)-N(2)	118.46(18)
C(20)-C(15)-N(2)	121.56(18)
C(15)-C(16)-C(17)	121.07(19)
C(15)-C(16)-H(16)	119.5
C(17)-C(16)-H(16)	119.5
C(18)-C(17)-C(16)	119.00(19)
C(18)-C(17)-H(17)	120.5
C(16)-C(17)-H(17)	120.5
O(2)-C(18)-C(17)	124.41(19)
O(2)-C(18)-C(19)	115.39(18)
C(17)-C(18)-C(19)	120.20(19)
C(20)-C(19)-C(18)	120.2(2)
C(20)-C(19)-H(19)	119.9
C(18)-C(19)-H(19)	119.9
C(19)-C(20)-C(15)	119.78(19)
C(19)-C(20)-H(20)	120.1
C(15)-C(20)-H(20)	120.1
O(2)-C(21)-H(21A)	109.5
O(2)-C(21)-H(21B)	109.5

Appendix C: X ray diffraction

H(21A)-C(21)-H(21B)	109.5
O(2)-C(21)-H(21C)	109.5
H(21A)-C(21)-H(21C)	109.5
H(21B)-C(21)-H(21C)	109.5
C(3)-N(1)-C(8)	128.64(18)
C(3)-N(1)-H(1N)	119.6(15)
C(8)-N(1)-H(1N)	111.8(15)
C(7)-N(2)-C(15)	126.31(18)
C(7)-N(2)-H(2N)	118.2(15)
C(15)-N(2)-H(2N)	115.4(15)
C(11)-O(1)-C(14)	116.34(17)
C(18)-O(2)-C(21)	117.42(18)

Anisotropic displacement parameters ($\text{\AA}^2 \times 10^3$) for **9**.

The anisotropic displacement factor exponent takes the form: $-2p^2 [h^2 a^* 2U^{11} + \dots + 2h k a^* b^* U^{12}]$

	U ¹¹	U ²²	U ³³	U ²³	U ¹³	U ¹²
C(22)	26(1)	29(1)	23(1)	2(1)	6(1)	-1(1)
C(23)	28(1)	33(1)	30(1)	5(1)	10(1)	4(1)
C(24)	41(1)	33(1)	31(1)	0(1)	12(1)	5(1)
C(25)	38(1)	35(1)	28(1)	-2(1)	4(1)	-2(1)
C(26)	26(1)	42(1)	33(1)	-2(1)	3(1)	-1(1)
C(27)	26(1)	37(1)	30(1)	-3(1)	7(1)	1(1)
C(28)	53(2)	60(2)	46(2)	-18(1)	-2(1)	-4(1)
O(3)	37(1)	36(1)	26(1)	-1(1)	9(1)	-2(1)
O(4)	42(1)	29(1)	41(1)	7(1)	-2(1)	-9(1)
O(5)	24(1)	53(1)	37(1)	-2(1)	2(1)	1(1)
S(1)	24(1)	28(1)	26(1)	2(1)	3(1)	-2(1)
C(1)	40(1)	35(1)	32(1)	-9(1)	-3(1)	12(1)
C(2)	28(1)	27(1)	23(1)	-2(1)	6(1)	3(1)
C(3)	24(1)	27(1)	24(1)	1(1)	9(1)	1(1)
C(4)	29(1)	25(1)	29(1)	-2(1)	7(1)	0(1)
C(5)	32(1)	24(1)	34(1)	1(1)	6(1)	0(1)
C(6)	29(1)	27(1)	32(1)	0(1)	6(1)	4(1)

Appendix C: X ray diffraction

C(7)	26(1)	29(1)	24(1)	1(1)	10(1)	1(1)
C(8)	26(1)	26(1)	23(1)	0(1)	5(1)	-1(1)
C(9)	29(1)	37(1)	25(1)	-2(1)	9(1)	2(1)
C(10)	24(1)	44(1)	28(1)	0(1)	7(1)	3(1)
C(11)	29(1)	33(1)	23(1)	0(1)	4(1)	-3(1)
C(12)	33(1)	32(1)	25(1)	-2(1)	9(1)	0(1)
C(13)	25(1)	29(1)	28(1)	0(1)	7(1)	1(1)
C(14)	48(1)	57(2)	22(1)	-3(1)	5(1)	5(1)
C(15)	24(1)	28(1)	25(1)	-1(1)	4(1)	1(1)
C(16)	27(1)	39(1)	26(1)	-2(1)	9(1)	4(1)
C(17)	31(1)	45(1)	22(1)	1(1)	6(1)	3(1)
C(18)	25(1)	40(1)	28(1)	3(1)	5(1)	4(1)
C(19)	30(1)	46(1)	31(1)	4(1)	13(1)	7(1)
C(20)	33(1)	40(1)	24(1)	4(1)	9(1)	5(1)
C(21)	36(1)	81(2)	29(1)	16(1)	5(1)	12(1)
N(1)	29(1)	25(1)	23(1)	-3(1)	4(1)	2(1)
N(2)	27(1)	28(1)	26(1)	-2(1)	4(1)	5(1)
O(1)	32(1)	49(1)	23(1)	-2(1)	2(1)	2(1)
O(2)	29(1)	70(1)	30(1)	13(1)	7(1)	17(1)

Appendix D: Cartesian Coordinates

Appendix D: Cartesian Coordinates

Chapter 4

1

MIN S₀: -477.049061

C	-2.675048	0.534640	0.284344
C	-2.571481	-0.863546	-0.317147
C	-1.252706	-1.525270	0.075053
C	-0.045578	-0.647496	-0.181487
C	-0.185569	0.692767	-0.296314
C	-1.475290	1.370164	-0.091970
O	-1.533647	2.578209	-0.198207
O	0.854036	1.518901	-0.594769
N	1.144277	-1.351393	-0.323707
C	2.439152	-0.782463	0.009910
H	-3.568475	1.055192	-0.038108
H	-2.711680	0.472469	1.370554
H	-2.628423	-0.795145	-1.399886
H	-3.405741	-1.476667	0.007254
H	-1.129087	-2.446270	-0.487725
H	-1.274819	-1.805905	1.127756
H	0.516323	2.408139	-0.594594
H	1.054997	-2.289048	-0.000248
H	3.173947	-1.575341	-0.058632
H	2.705753	-0.005805	-0.687480
H	2.471539	-0.365435	1.014332

CI S₂/S₁: -476.894960

C	-2.561517	0.321708	-0.597832
C	-2.159367	-1.155597	-0.431421
C	-1.259996	-1.323820	0.798464
C	0.026100	-0.549528	0.588632
C	-0.198023	0.857829	0.261295
C	-1.483264	1.312907	-0.197392
O	-1.851996	2.174475	0.771380
O	0.781612	1.732862	0.523916
N	0.948293	-1.263420	-0.202857
C	2.214697	-0.675454	-0.591006
H	-2.883097	0.505663	-1.616926
H	-3.414559	0.535113	0.037111
H	-1.615988	-1.498342	-1.303973
H	-3.054627	-1.765471	-0.350621
H	-1.033925	-2.373456	0.967077
H	-1.771336	-0.961351	1.685703
H	0.504960	2.608380	0.264250
H	1.070571	-2.187791	0.156064
H	2.054600	0.138095	-1.285369
H	2.795521	-0.295860	0.245102
H	2.793820	-1.436244	-1.102667

Min S₁: -476.920936

C	-2.615633	0.337036	-0.5120346
C	-2.213058	-1.147757	-0.4053278

Appendix D: Cartesian Coordinates

C -1.243586 -1.373054 0.7548566
 C 0.022796 -0.595484 0.4629824
 C -0.229127 0.807156 0.2482352
 C -1.505689 1.272900 -0.0694747
 O -1.923223 2.427790 0.5454008
 O 0.781851 1.691302 0.4941483
 N 1.010216 -1.308942 -0.2338967
 C 2.272293 -0.675956 -0.5693450
 H -2.874665 0.538708 -1.5473641
 H -3.500592 0.558294 0.0769452
 H -1.706470 -1.449487 -1.3157104
 H -3.108752 -1.753825 -0.3165531
 H -1.030237 -2.427711 0.8999701
 H -1.689230 -1.003212 1.6736756
 H 0.500021 2.573963 0.3002001
 H 1.149270 -2.215981 0.1613846
 H 2.108859 0.109088 -1.2952088
 H 2.781778 -0.242240 0.2863999
 H 2.915658 -1.421888 -1.0203534

CI S₁/S₀: -476.897510

C -1.714542 -1.281445 -0.226455
 C -2.027987 -0.464210 -1.391497
 C -0.611852 0.256461 -1.571535
 C 0.049998 0.632091 -0.205578
 C -0.816201 0.600240 1.110088
 C -1.859879 -0.275968 0.917081
 O -3.209924 -0.501451 1.900149
 O -0.863853 1.682948 1.912850
 N 1.377824 0.249697 0.096135
 C 1.686281 -1.143403 0.405343
 H -2.184638 -2.226762 0.013182
 H -0.611355 -1.505498 -0.253509
 H -2.788068 0.302893 -1.235102
 H -2.245122 -1.007181 -2.302747
 H -0.668946 1.130620 -2.207339
 H 0.071923 -0.440354 -2.055254
 H -0.661489 2.402588 1.324780
 H 1.624284 0.783862 0.903573
 H 1.556228 -1.778903 -0.456369
 H 2.720637 -1.188107 0.716233
 H 1.079160 -1.527417 1.224896

2**MIN S₀: -328.022194**

C -2.502816 0.587582 0.244024
 C -2.374032 -0.752080 -0.478429
 C -1.100524 -1.480633 -0.052308
 C 0.121432 -0.592484 -0.136131
 C 0.020002 0.755637 -0.113421
 C -1.270167 1.447308 0.040946
 O -1.340556 2.656876 0.033899

Appendix D: Cartesian Coordinates

N 1.321775 -1.280247 -0.134492
 C 2.578970 -0.595683 -0.324627
 H -3.369737 1.145485 -0.088545
 H -2.618618 0.418887 1.313602
 H -3.240316 -1.374297 -0.278510
 H -2.347813 -0.582122 -1.551692
 H -0.951474 -2.358939 -0.675877
 H -1.194909 -1.843963 0.968764
 H 0.882589 1.392246 -0.167809
 H 1.275083 -2.171399 -0.576336
 H 3.375294 -1.328695 -0.319901
 H 2.626530 -0.036824 -1.257861
 H 2.755644 0.092307 0.493039

Cl S₃/S₂: -327.773863

C -2.5215 0.4190 0.3400
 C -2.3895 -0.9470 -0.3440
 C -1.1145 -1.6800 0.0810
 C 0.1075 -0.7920 0.0500
 C -0.0045 0.5880 0.0520
 C -1.2855 1.2820 0.1890
 O -1.3665 2.5340 0.0870
 N 1.3065 -1.4810 -0.0140
 C 2.5505 -0.7750 -0.2070
 H -3.3525 1.0140 -0.0070
 H -2.6005 0.2900 1.4150
 H -3.2515 -1.5690 -0.1500
 H -2.3345 -0.7890 -1.4150
 H -0.9255 -2.5340 -0.5590
 H -1.1895 -2.0420 1.1020
 H 0.8525 1.2260 -0.0110
 H 1.2485 -2.3440 -0.5030
 H 3.3525 -1.4910 -0.2820
 H 2.5375 -0.1490 -1.0920
 H 2.7365 -0.1410 0.6470

Cl S₂/S₁: -327.800444

C -2.4835 0.6810 0.4195
 C -2.3555 -0.5980 -0.4135
 C -1.0575 -1.3290 -0.0635
 C 0.1595 -0.4740 -0.3285
 C -0.0725 1.0060 -0.4095
 C -1.2605 1.5430 0.2315
 O -0.8295 2.2610 1.2815
 N 1.3265 -0.9240 0.3025
 C 2.6215 -0.4290 -0.1205
 H -3.3835 1.2280 0.1525
 H -2.5715 0.4230 1.4725
 H -3.2105 -1.2410 -0.2335
 H -2.3605 -0.3550 -1.4725
 H -0.9835 -2.2610 -0.6215
 H -1.0785 -1.6040 0.9935
 H 0.7335 1.6790 -0.6255

Appendix D: Cartesian Coordinates

H 1.3305 -1.9180 0.3985
H 3.3835 -0.8850 0.4995
H 2.8485 -0.6450 -1.1635
H 2.6815 0.6400 0.0285

Min S₁: -327.891073

C -2.5545 0.4575 0.3215
C -2.3985 -0.9355 -0.2985
C -1.1225 -1.6365 0.1765
C 0.0975 -0.7615 0.0245
C -0.0335 0.6175 0.0965
C -1.2755 1.2215 0.1595
O -1.3615 2.5615 0.4455
N 1.3225 -1.4355 0.0275
C 2.5485 -0.7015 -0.1765
H -3.3725 0.9885 -0.1575
H -2.8045 0.3795 1.3795
H -3.2635 -1.5475 -0.0615
H -2.3665 -0.8345 -1.3795
H -0.9895 -2.5615 -0.3795
H -1.2225 -1.9255 1.2215
H 0.8365 1.2485 0.1215
H 1.2835 -2.2765 -0.5055
H 3.3725 -1.4035 -0.1975
H 2.5645 -0.1245 -1.1015
H 2.7165 -0.0205 0.6495

CI S₁/S₀: -327.883949

C -1.702160 0.230503 1.085910
C -2.208890 -0.880873 0.136344
C -1.104400 -1.465010 -0.808325
C 0.133367 -0.615632 -0.649518
C -0.092085 0.813319 -0.729890
C -0.973890 1.326740 0.297489
O -1.253420 2.506620 0.441499
N 1.036940 -1.103670 0.237216
C 2.260930 -0.438216 0.623090
H -2.537940 0.684794 1.602920
H -1.045000 -0.195724 1.838040
H -2.641420 -1.684970 0.721839
H -3.008430 -0.472182 -0.471024
H -1.438690 -1.428390 -1.838040
H -0.900077 -2.506620 -0.572184
H 0.104344 1.394790 -1.611740
H 1.027040 -2.089500 0.371359
H 2.059850 0.591537 0.871650
H 2.657680 -0.935512 1.498970
H 3.008430 -0.467853 -0.164247

3**Min S₀: -381.619033**

Appendix D: Cartesian Coordinates

C -1.293008 0.599240 0.319430
 C -1.336111 -0.716818 -0.459731
 C -0.095618 -1.568274 -0.177187
 C 1.177778 -0.772084 -0.329270
 C 1.202778 0.567870 -0.241045
 C -0.017776 1.361410 0.046322
 O 0.055322 2.570027 0.091847
 O 2.340832 1.277688 -0.392512
 H -2.133982 1.240971 0.085930
 H 1.328684 0.397295 1.388731
 H -2.236916 -1.266331 -0.207288
 H -1.384188 -0.500982 -1.523889
 H -0.072479 -2.417655 -0.852803
 H -0.151671 -1.983670 0.828182
 H 2.102005 -1.295624 -0.497468
 H 2.131101 2.200587 -0.299974

Cl S₂/S₁: -381.367084

C -1.201075 0.690190 -0.093206
 C -1.354604 -0.780294 -0.247928
 C -0.059618 -1.621056 -0.200533
 C 1.224605 -0.843111 -0.360356
 C 1.272863 0.699548 -0.238612
 C 0.033355 1.547191 -0.511387
 O 0.223602 2.216232 0.551849
 O 2.300508 1.323532 0.171616
 H -2.064736 1.189334 -0.525773
 H -1.267979 0.933883 0.945077
 H -2.034062 -1.110731 0.532715
 H -1.878739 -0.963302 -1.179164
 H -0.129392 -2.353725 -1.010674
 H -0.011074 -2.211484 0.716491
 H 1.974215 -1.295477 -1.008472
 H 1.931512 2.272920 0.237634

Min S₁: -381.508278

C -1.308604 0.617189 0.258309
 C -1.341472 -0.733877 -0.462659
 C -0.099241 -1.573276 -0.144046
 C 1.168197 -0.791340 -0.367218
 C 1.170947 0.607633 -0.250560
 C 0.012720 1.289866 0.018882
 O 0.021785 2.648918 0.199156
 O 2.363133 1.246280 -0.420775
 H -2.108450 1.255824 -0.102015
 H -1.465231 0.482031 1.326978
 H -2.241838 -1.275260 -0.191149
 H -1.382024 -0.557080 -1.533429
 H -0.095075 -2.468504 -0.757644
 H -0.144750 -1.914087 0.890074
 H 2.100548 -1.295399 -0.521375
 H 2.308735 2.154731 -0.163253

L

Appendix D: Cartesian Coordinates

CI S_1/S_0 : -381.476565

C	-1.113508	0.947852	-0.483431
C	-1.516005	-0.468151	-0.164821
C	-0.217363	-1.332739	0.046743
C	1.030138	-0.808399	-0.708460
C	1.279812	0.477060	-0.404895
C	0.156856	1.233095	0.185315
O	-0.147009	0.715369	2.175665
O	2.524860	0.953320	-0.218545
H	-0.891838	1.028297	-1.553458
H	-1.864390	1.671261	-0.232457
H	-1.996344	-0.605816	0.792759
H	-2.161214	-0.884097	-0.921662
H	-0.422356	-2.363406	-0.078205
H	-0.053343	-1.213410	1.091151
H	1.737240	-1.481142	-1.153647
H	2.613847	1.824553	-0.592778

4

Min S_0 : -495.659496

C	-2.124139	0.051477	-0.310858
C	-2.115964	-1.310896	0.383998
C	-0.873356	-2.124202	0.023707
C	0.390561	-1.322056	0.217801
C	0.371172	0.025169	0.194593
C	-0.848687	0.821068	-0.033525
N	-0.702383	2.089841	-0.029199
O	1.518108	0.725487	0.406095
N	1.572056	-2.031549	0.502209
C	1.974589	-3.049809	-0.450954
C	-1.830844	2.963035	-0.286644
H	-2.215785	-0.084664	-1.387581
H	-2.986470	0.625536	0.006359
H	-3.013359	-1.861433	0.118965
H	-2.140659	-1.160764	1.459733
H	-0.949254	-2.475352	-1.004561
H	-0.820207	-3.008011	0.650893
H	1.294948	1.649944	0.354527
H	2.318944	-1.391224	0.673914
H	1.234198	-3.839332	-0.494440
H	2.123565	-2.668479	-1.461911
H	2.903031	-3.493895	-0.113232
H	-1.467549	3.976126	-0.395731
H	-2.365343	2.694937	-1.192831
H	-2.533605	2.947897	0.541148

CI S_2/S_1 : -495.473682

C	-2.103639	0.084001	0.140217
C	-1.904136	-1.425460	0.300350
C	-0.841941	-1.964007	-0.665867
C	0.494156	-1.311174	-0.399809

Appendix D: Cartesian Coordinates

C	0.401218	0.127830	-0.210427
C	-0.798408	0.829381	0.166940
N	-0.727139	2.218442	-0.122102
O	1.565031	0.802834	-0.221079
N	1.351877	-1.970364	0.513076
C	1.952767	-3.220487	0.082019
C	-1.932863	2.976847	-0.275743
H	-2.627219	0.266279	-0.796461
H	-2.760994	0.441675	0.927958
H	-2.854336	-1.925445	0.134874
H	-1.597780	-1.648710	1.316751
H	-1.148140	-1.761660	-1.689612
H	-0.764609	-3.040311	-0.568886
H	1.373473	1.731127	-0.093707
H	2.060347	-1.345963	0.837826
H	1.187348	-3.957099	-0.125969
H	2.570988	-3.114160	-0.808560
H	2.566941	-3.608883	0.885883
H	-1.677846	4.023110	-0.382447
H	-2.486942	2.670744	-1.159221
H	-2.584588	2.870307	0.586467

Min S₁: -495.559418

C	-2.432246	-0.143949	0.230583
C	-2.153129	-1.586151	0.656041
C	-0.945406	-2.144951	-0.097235
C	0.261777	-1.265968	0.117949
C	0.081417	0.086425	0.317829
C	-1.168163	0.694620	0.226117
N	-1.287925	2.071261	0.476721
O	1.201409	0.851923	0.529895
N	1.511338	-1.864798	0.352422
C	2.031965	-2.737481	-0.685932
C	-1.281793	2.894133	-0.722646
H	-2.876693	-0.136337	-0.765569
H	-3.150575	0.322742	0.895771
H	-3.027575	-2.207512	0.489933
H	-1.939218	-1.604607	1.720037
H	-1.191654	-2.213881	-1.156345
H	-0.719024	-3.149236	0.241964
H	0.948071	1.680432	0.904509
H	2.178842	-1.167940	0.609367
H	1.361097	-3.574110	-0.839878
H	2.173297	-2.237987	-1.644635
H	2.985039	-3.138966	-0.363763
H	-1.357765	3.942254	-0.460935
H	-0.369301	2.734392	-1.292481
H	-2.120217	2.644542	-1.367243

CI S₁/S₀: -495.560693

C	-2.334244	-0.195348	-0.235955
C	-2.108091	-1.464695	0.585813
C	-0.843527	-2.172856	0.097964

Appendix D: Cartesian Coordinates

C	0.312312	-1.209031	-0.028401
C	0.109937	0.164446	-0.019917
C	-1.174870	0.745096	-0.037164
N	-1.392339	1.968099	0.646578
O	1.218795	0.965001	0.116010
N	1.595194	-1.734254	0.111375
C	1.928537	-2.968749	-0.566810
C	-1.459912	3.086950	-0.274860
H	-2.397874	-0.465708	-1.289808
H	-3.264835	0.282833	0.032458
H	-2.958557	-2.132911	0.514346
H	-1.991582	-1.199727	1.632139
H	-1.038385	-2.670478	-0.848454
H	-0.556686	-2.942942	0.803767
H	1.135144	1.481306	0.906532
H	2.285864	-1.028390	-0.008394
H	1.341380	-3.786603	-0.170352
H	1.776925	-2.930727	-1.644444
H	2.968465	-3.194952	-0.374674
H	-1.601084	4.017216	0.266469
H	-0.546512	3.163458	-0.866333
H	-2.290488	2.971815	-0.975409

5**Min S₀: -420.708834**

C	-2.106421	0.068752	-0.313381
C	-2.092036	-1.301052	0.366935
C	-0.848103	-2.108612	-0.002064
C	0.410231	-1.296772	0.203588
C	0.384878	0.050812	0.197644
C	-0.832467	0.846320	-0.028086
N	-0.712667	2.119446	-0.016391
N	1.582300	-2.021276	0.481606
C	1.949489	-3.096715	-0.422747
C	-1.867029	2.957918	-0.270566
H	-2.198839	-0.058885	-1.391593
H	-2.976101	0.628375	0.009214
H	-2.987255	-1.854380	0.099835
H	-2.114653	-1.163005	1.444602
H	-0.915396	-2.439035	-1.037560
H	-0.795339	-3.003200	0.609453
H	2.353829	-1.403310	0.626813
H	1.193534	-3.871127	-0.414183
H	2.091123	-2.770612	-1.453552
H	2.873620	-3.540936	-0.074295
H	-1.533696	3.981724	-0.381296
H	-2.402312	2.678874	-1.174220
H	-2.568016	2.926604	0.559543
H	1.285126	0.619512	0.353502

CI S₂/S₁: -420.553936

C	-2.126651	0.155633	-0.013592
---	-----------	----------	-----------

Appendix D: Cartesian Coordinates

C -2.041328 -1.317912 0.385717
 C -0.871114 -2.064318 -0.264756
 C 0.424021 -1.333524 -0.094133
 C 0.365182 0.153966 0.174546
 C -0.876121 0.890914 0.342129
 N -0.632537 2.289370 -0.007962
 N 1.512373 -2.044923 0.439302
 C 2.013228 -3.174503 -0.331830
 C -1.865773 2.920307 -0.394529
 H -2.319449 0.208795 -1.082639
 H -2.992285 0.592165 0.469518
 H -2.971938 -1.805781 0.110990
 H -1.956403 -1.383175 1.464352
 H -1.099330 -2.220937 -1.320349
 H -0.792040 -3.052005 0.179036
 H 2.260889 -1.432597 0.687161
 H 1.238971 -3.922885 -0.430973
 H 2.352371 -2.899544 -1.328771
 H 2.837593 -3.626876 0.203974
 H -1.648097 3.917407 -0.750847
 H -2.373705 2.380718 -1.183352
 H -2.544196 3.000645 0.447033
 H 1.280140 0.718479 0.272778

Cl S₁/S₀: -420.624533

C -2.333785 -0.170839 -0.138075
 C -2.137786 -1.501044 0.595179
 C -0.867292 -2.190647 0.097456
 C 0.295066 -1.229957 0.075169
 C 0.112890 0.149190 0.189073
 C -1.155062 0.738622 0.126461
 N -1.396613 2.019788 0.651181
 N 1.572125 -1.790652 0.203811
 C 1.920901 -2.932844 -0.616406
 C -1.441633 3.058617 -0.355495
 H -2.406798 -0.366411 -1.208422
 H -3.256648 0.303196 0.165542
 H -2.992785 -2.152314 0.452358
 H -2.048610 -1.313013 1.660744
 H -1.035112 -2.610593 -0.891255
 H -0.611226 -3.017276 0.750047
 H 2.282743 -1.093374 0.177113
 H 1.296020 -3.778458 -0.363227
 H 1.828904 -2.746524 -1.685461
 H 2.944300 -3.210029 -0.402149
 H -1.629644 4.022258 0.106297
 H -0.502693 3.120353 -0.908596
 H -2.233769 2.871957 -1.084780
 H 0.970308 0.769413 0.376238

6**Min S₀: -496.085038**

Appendix D: Cartesian Coordinates

C	-2.137247	0.094413	-0.134769
C	-1.994239	-1.307805	0.451585
C	-0.790319	-2.041548	-0.133782
C	0.460812	-1.204014	-0.043376
C	0.365272	0.180273	0.093242
C	-0.842358	0.862814	-0.044417
N	-0.844899	2.174012	-0.126995
O	1.533783	0.916035	0.123388
N	1.643196	-1.770515	-0.124954
C	1.924766	-3.193106	-0.300715
C	-2.008007	3.040272	-0.302297
H	-2.423998	0.044600	-1.182835
H	-2.922158	0.633489	0.380255
H	-2.895073	-1.875941	0.257006
H	-1.885879	-1.238913	1.528687
H	-0.958303	-2.278915	-1.181938
H	-0.642410	-2.982143	0.381290
H	0.055505	2.606697	-0.146309
H	1.796779	1.085203	1.021637
H	2.420725	-1.143212	-0.145694
H	1.405685	-3.586666	-1.163319
H	2.986606	-3.302408	-0.456515
H	1.644197	-3.752610	0.581222
H	-1.649616	4.044191	-0.467960
H	-2.591850	2.735270	-1.159254
H	-2.628785	3.035060	0.583318

CI S₁/S₀: -496.000258

C	-1.715130	0.727455	0.872954
C	-1.812930	-0.545582	-0.012314
C	-0.549201	-0.778322	-0.913624
C	0.762973	-0.473620	-0.133521
C	0.722505	0.846490	0.426234
C	-0.569085	1.554070	0.386469
N	-0.857339	2.171160	-0.788594
O	1.642940	1.341590	1.250020
N	1.755260	-1.309530	0.051566
C	1.858150	-2.703900	-0.453277
C	-2.147110	2.754240	-1.034670
H	-2.612110	1.322700	0.793414
H	-1.581110	0.507535	1.912000
H	-2.653010	-0.407382	-0.686746
H	-2.045990	-1.397050	0.599376
H	-0.628325	-0.063183	-1.733720
H	-0.594833	-1.758460	-1.355250
H	-0.140427	2.700700	-1.168350
H	1.356180	2.217750	1.542880
H	2.554040	-0.977111	0.593785
H	1.666770	-2.750270	-1.523740
H	2.867780	-3.059300	-0.273039
H	1.164290	-3.363710	0.066730
H	-2.055920	3.357780	-1.912000
H	-2.867780	1.986560	-1.223040

Appendix D: Cartesian Coordinates

H -2.458750 3.363710 -0.207677

7

Min S_0 : -421.144364

C -2.047391 0.103035 -0.308932
 C -1.970158 -1.331997 0.203785
 C -0.714756 -2.040748 -0.295611
 C 0.523190 -1.221949 -0.021335
 C 0.437924 0.163977 0.112736
 C -0.765186 0.853184 -0.039707
 N -0.798048 2.168302 0.016493
 N 1.686201 -1.834137 0.051008
 C 1.944500 -3.264858 -0.106919
 C -1.969351 3.032259 -0.122174
 H -2.219774 0.116413 -1.383037
 H -2.883542 0.613310 0.150301
 H -2.847616 -1.879835 -0.116200
 H -1.973634 -1.327817 1.288624
 H -0.770925 -2.207761 -1.369249
 H -0.630514 -3.013532 0.170246
 H 1.338966 0.724587 0.294986
 H 0.070147 2.632605 0.182194
 H 2.489330 -1.257737 0.190602
 H 1.553088 -3.823867 0.732097
 H 1.515187 -3.635039 -1.026768
 H 3.013767 -3.402774 -0.146088
 H -1.620375 4.050845 -0.191106
 H -2.516195 2.794529 -1.022950
 H -2.620765 2.944973 0.736962

CI S_1/S_0 : -421.002056

C -1.840064 -0.010986 -0.156225
 C -1.610761 -1.529372 -0.071124
 C -0.592793 -2.121774 -1.052510
 C 0.659759 -1.318383 -0.882768
 C 0.544680 0.139488 -1.158380
 C -0.572615 0.827708 -0.452480
 N -0.611477 2.116117 -0.251174
 N 1.070030 -1.510302 0.422276
 C 1.310193 -2.884100 0.814282
 C -1.734970 2.907877 0.351902
 H -2.570313 0.180046 -0.937510
 H -2.297364 0.278798 0.789378
 H -2.546331 -2.049973 -0.153875
 H -1.215856 -1.778404 0.907034
 H -0.912058 -2.147235 -2.069566
 H -0.366476 -3.133183 -0.762172
 H 1.326499 0.607283 -1.783355
 H 0.211129 2.677588 -0.489940
 H 1.858544 -1.003002 0.646945
 H 0.402407 -3.333498 1.154516
 H 1.718281 -3.438622 -0.007665

Appendix D: Cartesian Coordinates

H	2.007500	-2.869517	1.621299
H	-1.536313	3.961445	0.182973
H	-2.685800	2.656067	-0.108420
H	-1.791759	2.731903	1.426519

8**Min S₀: -459.452555**

C	0.000068	2.066073	0.499135
C	1.247987	1.436588	-0.098666
C	1.208916	-0.071141	-0.005659
C	0.000006	-0.770419	0.139247
C	-1.208850	-0.071036	-0.005642
C	-1.247806	1.436673	-0.098845
N	2.360702	-0.708180	-0.100081
N	-2.360643	-0.708074	-0.099966
C	-0.000243	-2.275713	0.324018
C	3.689679	-0.114899	-0.243670
C	-3.689580	-0.114818	-0.244039
H	0.000121	3.132844	0.313187
H	-0.000013	1.926196	1.574841
H	2.129164	1.810246	0.405668
H	1.347258	1.707613	-1.147769
H	-2.129053	1.810478	0.405258
H	-1.346817	1.707588	-1.147999
H	-2.336819	-1.703328	-0.096535
H	0.855576	-2.605749	0.901711
H	-0.855681	-2.605202	0.902612
H	-0.000878	-2.824876	-0.615060
H	4.386609	-0.916015	-0.435273
H	3.718488	0.572897	-1.076289
H	3.988104	0.394480	0.662535
H	-4.386468	-0.915973	-0.435627
H	-3.988222	0.394767	0.661979
H	-3.718184	0.572789	-1.076821
H	2.336898	-1.703430	-0.096592

CI S₁/S₀: -459.320339

C	0.191395	1.805495	-0.716309
C	1.479286	0.931073	-0.819324
C	1.351771	-0.313335	0.031069
C	0.106825	-1.045527	-0.272362
C	-1.091946	-0.269549	-0.064798
C	-0.903527	1.205434	0.194917
N	1.566121	-0.183021	1.425511
N	-2.260897	-0.815511	-0.134447
C	0.098986	-2.438192	-0.829850
C	2.694399	0.617163	1.888771
C	-3.575847	-0.158297	0.005719
H	0.429228	2.786834	-0.326672
H	-0.222861	1.961590	-1.705856
H	2.352287	1.506233	-0.546311
H	1.622753	0.625536	-1.849192

Appendix D: Cartesian Coordinates

H	-0.607944	1.289955	1.233599
H	-1.829067	1.748624	0.065535
H	-2.286334	-1.804280	-0.300555
H	-0.029057	-3.183203	-0.043814
H	-0.679079	-2.600183	-1.571507
H	1.050062	-2.642845	-1.303166
H	2.797663	0.464355	2.954302
H	3.635878	0.357761	1.410893
H	2.505618	1.671112	1.731388
H	-4.327970	-0.930279	0.007878
H	-3.610290	0.384898	0.936041
H	-3.737328	0.504991	-0.829874
H	1.602793	-1.087546	1.848562

Chapter 5

9-FC (Minimum S_0): $S_0 = -1068.33004984$ $S_1 = -1068.14914901$

C	-0.000183	-0.876515	1.575765
C	-1.246992	-0.672208	0.731242
C	-1.207930	0.649164	-0.001976
C	0.000169	1.315775	-0.262872
C	1.207923	0.648574	-0.001735
C	1.246452	-0.673151	0.730760
N	-2.363798	1.142925	-0.421808
H	-2.341397	1.982321	-0.958646
C	-3.672257	0.582314	-0.220072
C	-4.456375	1.018934	0.857241
C	-5.727981	0.510337	1.026743
C	-6.242111	-0.438291	0.120717
C	-5.469710	-0.857560	-0.939724
C	-4.180589	-0.342705	-1.112763
O	-7.482624	-0.859043	0.385260
C	-8.110463	-1.788898	-0.461906
N	2.363849	1.142692	-0.420938
H	2.341510	1.982787	-0.956724
C	3.672266	0.581857	-0.219598
C	4.179433	-0.344808	-1.111248
C	5.468463	-0.859958	-0.938466
C	6.241997	-0.439240	0.120580
C	5.729077	0.511108	1.025483
C	4.457498	1.019893	0.856319
O	7.482569	-0.860073	0.384704
C	8.109268	-1.791583	-0.461489
H	-0.000513	-1.874203	1.997141
H	0.000264	-0.177550	2.405998
H	-2.136799	-0.716034	1.343062
H	-1.340464	-1.463492	-0.008444
H	2.136553	-0.718013	1.342084
H	1.338749	-1.464223	-0.009296

Appendix D: Cartesian Coordinates

H	-4.068087	1.747362	1.545908
H	-6.349405	0.826633	1.842491
H	-5.838550	-1.573804	-1.646883
H	-3.588706	-0.666735	-1.949564
H	-9.090481	-1.956713	-0.044968
H	-8.209499	-1.396036	-1.467235
H	-7.565024	-2.725390	-0.486335
H	3.586709	-0.669916	-1.947033
H	5.836367	-1.577540	-1.644755
H	6.351350	0.828480	1.840165
H	4.070085	1.749533	1.544195
H	8.207534	-1.400432	-1.467560
H	9.089603	-1.959087	-0.045171
H	7.563443	-2.727901	-0.483859
C	0.001659	2.679985	-0.927717
H	-0.857541	3.268370	-0.629108
H	0.855575	3.270695	-0.618352
H	0.008301	2.623263	-2.013232

9-Min S₁ (14,13):S₀ = -1068.24710157S₁ = -1068.22038198

C	-0.443386	-0.998368	2.464876
C	-1.178578	-1.198214	1.143038
C	-0.941877	-0.052326	0.189034
C	0.240889	0.696024	0.241987
C	1.209170	0.358315	1.190153
C	1.041138	-0.720156	2.231180
N	-1.839728	0.086101	-0.857886
H	-1.569609	0.703322	-1.588848
C	-3.253405	-0.009709	-0.682736
C	-3.923962	0.717583	0.314202
C	-5.296293	0.625132	0.444649
C	-6.039258	-0.181608	-0.434522
C	-5.389097	-0.885954	-1.421748
C	-3.996616	-0.806414	-1.537657
O	-7.365942	-0.189717	-0.220976
C	-8.200978	-0.957057	-1.045915
N	2.440226	1.088552	1.253713
H	2.461683	1.892934	1.853585
C	3.578372	0.770291	0.666649
C	3.692145	-0.344588	-0.214398
C	4.885578	-0.645688	-0.807877
C	6.023327	0.137609	-0.564845
C	5.929503	1.262698	0.312276
C	4.748677	1.574571	0.911207
O	7.208131	-0.066380	-1.083594
C	7.458150	-1.143022	-1.973602
H	-0.557475	-1.873570	3.093942
H	-0.882679	-0.160932	2.998804
H	-2.237681	-1.316454	1.328258
H	-0.851019	-2.120864	0.664335

Appendix D: Cartesian Coordinates

H	1.518917	-0.414824	3.158065
H	1.547149	-1.630968	1.912311
H	-3.365827	1.351985	0.980029
H	-5.822133	1.172837	1.203728
H	-5.929537	-1.509900	-2.106329
H	-3.493939	-1.372668	-2.300150
H	-9.205554	-0.800247	-0.685188
H	-8.137277	-0.634437	-2.079386
H	-7.957646	-2.011927	-0.979961
H	2.826753	-0.943991	-0.414154
H	4.939468	-1.489546	-1.466278
H	6.814687	1.845002	0.479391
H	4.678498	2.419505	1.571719
H	6.849592	-1.048122	-2.862824
H	8.499684	-1.065212	-2.234195
H	7.272109	-2.089675	-1.484481
C	0.464010	1.825436	-0.746093
H	-0.419422	2.448211	-0.820396
H	1.281869	2.470839	-0.457049
H	0.688380	1.447490	-1.739661

9-Cl Isomerization S_1/S_0 (14,13): $S_0 = -1068.21609300$ $S_1 = -1068.21603983$

C	-0.346060	-1.275977	2.478879
C	-1.039935	-1.666659	1.176477
C	-0.910374	-0.596146	0.120760
C	0.158513	0.301059	0.124853
C	1.153172	0.152600	1.103558
C	1.102659	-0.852957	2.225599
N	-1.838601	-0.669540	-0.937273
H	-1.511471	-0.324395	-1.811261
C	-3.220069	-0.397413	-0.714038
C	-3.668389	0.465285	0.296066
C	-5.021657	0.699239	0.473466
C	-5.963184	0.097227	-0.372241
C	-5.529897	-0.742069	-1.375035
C	-4.165566	-0.999321	-1.533336
O	-7.250252	0.405044	-0.117363
C	-8.266726	-0.154292	-0.901927
N	2.282296	1.047736	1.120817
H	2.176488	1.900131	1.641788
C	3.455908	0.844566	0.585787
C	3.747313	-0.327413	-0.185865
C	4.980759	-0.512147	-0.726417
C	5.997530	0.445345	-0.541921
C	5.726633	1.629288	0.220927
C	4.501957	1.829373	0.767857
O	7.207344	0.358382	-1.015983
C	7.642503	-0.753154	-1.791077
H	-0.366081	-2.099523	3.183106
H	-0.879492	-0.449483	2.939066

LX

Appendix D: Cartesian Coordinates

H	-2.089038	-1.861577	1.363943
H	-0.626734	-2.598503	0.792075
H	1.534168	-0.428043	3.127771
H	1.706960	-1.725449	1.979650
H	-2.959533	0.951116	0.942783
H	-5.374290	1.353188	1.248856
H	-6.224939	-1.222516	-2.035725
H	-3.840035	-1.679001	-2.300145
H	-9.195770	0.232321	-0.512159
H	-8.168530	0.136487	-1.942423
H	-8.272347	-1.236582	-0.828805
H	2.976376	-1.054872	-0.335666
H	5.171197	-1.397654	-1.299029
H	6.520694	2.340320	0.341305
H	4.295503	2.714039	1.341614
H	7.059043	-0.829968	-2.697882
H	8.670642	-0.546892	-2.032618
H	7.575225	-1.663741	-1.212364
C	0.256826	1.380951	-0.936112
H	-0.726987	1.752480	-1.189296
H	0.840230	2.231614	-0.605985
H	0.715207	1.009397	-1.848677

9-CI S₁/S₀(14,13):

S₀ = -1068.19275993

S₁ = -1068.19275245

C	-0.447722	-1.390969	-0.179482
C	-1.455283	-0.671545	-1.097470
C	-1.328980	0.806567	-0.812446
C	0.002923	1.325819	-1.164762
C	1.117979	0.634185	-0.558777
C	0.990617	-0.857949	-0.306377
N	-1.705768	1.211158	0.485409
H	-1.592215	2.195535	0.609720
C	-2.949358	0.763821	1.051757
C	-2.951131	0.219381	2.343046
C	-4.134076	-0.184278	2.932945
C	-5.349569	-0.059207	2.239489
C	-5.355375	0.476764	0.971135
C	-4.157469	0.895497	0.382971
O	-6.434064	-0.490299	2.902658
C	-7.703475	-0.386291	2.314380
N	2.251026	1.230005	-0.384945
H	2.284798	2.207774	-0.612202
C	3.497874	0.644402	0.068418
C	4.358975	0.079960	-0.849102
C	5.578701	-0.449146	-0.416016
C	5.916671	-0.399970	0.919195
C	5.029734	0.187912	1.847044
C	3.825888	0.713289	1.427778
O	7.045255	-0.871360	1.443861
C	8.020555	-1.472539	0.623569

Appendix D: Cartesian Coordinates

H	-0.426965	-2.451186	-0.402900
H	-0.776660	-1.289818	0.845359
H	-2.452977	-1.040925	-0.903932
H	-1.230352	-0.861636	-2.142263
H	1.583804	-1.144626	0.551213
H	1.467325	-1.309648	-1.174027
H	-2.023011	0.127699	2.877312
H	-4.151045	-0.598653	3.922992
H	-6.268741	0.590642	0.420733
H	-4.180679	1.325578	-0.602697
H	-8.401344	-0.781322	3.035744
H	-7.954809	0.646865	2.101794
H	-7.763343	-0.969676	1.402219
H	4.104771	0.045506	-1.892938
H	6.235830	-0.885791	-1.141054
H	5.317767	0.216958	2.880150
H	3.152438	1.164530	2.133659
H	8.391972	-0.771890	-0.114544
H	8.823748	-1.759868	1.282106
H	7.624571	-2.353160	0.131997
C	0.180529	2.421666	-2.173941
H	-0.005755	3.404577	-1.740194
H	1.167457	2.436932	-2.625555
H	-0.547871	2.299012	-2.968995

9-Min S₁ (6,5):**S₀** = -1068.15857300**S₁** = -1068.13623018

C	-0.413995	-0.997229	2.487036
C	-1.146627	-1.247732	1.172829
C	-0.933593	-0.122685	0.190885
C	0.230427	0.657694	0.223439
C	1.214845	0.367883	1.175231
C	1.062487	-0.690240	2.239882
N	-1.832278	-0.041345	-0.868897
H	-1.552252	0.533639	-1.630410
C	-3.246837	-0.084347	-0.683064
C	-3.883418	0.650385	0.316054
C	-5.251263	0.606650	0.459680
C	-6.026655	-0.157989	-0.411712
C	-5.403864	-0.882151	-1.416598
C	-4.019788	-0.847747	-1.534850
O	-7.352077	-0.126522	-0.195980
C	-8.215118	-0.855852	-1.026054
N	2.425572	1.131432	1.222710
H	2.433062	1.941006	1.811672
C	3.572309	0.810400	0.643538
C	3.688597	-0.321696	-0.215991
C	4.876186	-0.635325	-0.805159
C	6.010954	0.166837	-0.569810
C	5.909489	1.305180	0.282816
C	4.736149	1.617245	0.867788

Appendix D: Cartesian Coordinates

O	7.187993	-0.041957	-1.079830
C	7.459965	-1.135399	-1.950791
H	-0.506031	-1.857478	3.139756
H	-0.871491	-0.156587	3.000296
H	-2.203638	-1.382529	1.359435
H	-0.800743	-2.176272	0.718229
H	1.538250	-0.355721	3.157067
H	1.585201	-1.599473	1.941745
H	-3.298937	1.261158	0.981467
H	-5.746813	1.167354	1.229866
H	-5.970037	-1.481950	-2.101774
H	-3.537837	-1.426561	-2.301885
H	-9.212477	-0.667764	-0.660421
H	-8.143791	-0.525035	-2.056348
H	-8.009200	-1.919207	-0.971596
H	2.822237	-0.924465	-0.399897
H	4.937181	-1.490775	-1.447307
H	6.793134	1.893543	0.438307
H	4.660995	2.474144	1.512011
H	6.856787	-1.061074	-2.844855
H	8.502666	-1.046240	-2.201706
H	7.280644	-2.072649	-1.442762
C	0.416040	1.771083	-0.790293
H	-0.488129	2.361818	-0.877059
H	1.213462	2.446128	-0.513585
H	0.651440	1.380315	-1.776721

9-Cl isomerization S_1/S_0 (6,5): $S_0 = -1068.13304316$ $S_1 = -1068.13304286$

C	-0.339966	-1.221785	2.516047
C	-1.036906	-1.631313	1.221613
C	-0.910077	-0.571249	0.156050
C	0.160591	0.327499	0.144220
C	1.167387	0.193415	1.113666
C	1.105824	-0.797858	2.250715
N	-1.833824	-0.655375	-0.903891
H	-1.502115	-0.330465	-1.784515
C	-3.216050	-0.398681	-0.696658
C	-3.686602	0.405507	0.338619
C	-5.037903	0.625043	0.505658
C	-5.959258	0.066007	-0.374467
C	-5.499853	-0.725518	-1.417244
C	-4.139774	-0.963664	-1.558538
O	-7.253842	0.350876	-0.135022
C	-8.250332	-0.183660	-0.961931
N	2.288860	1.093112	1.118890
H	2.190078	1.945517	1.634871
C	3.467498	0.868156	0.579174
C	3.734498	-0.315499	-0.183489
C	4.957339	-0.532812	-0.731423
C	5.987824	0.420140	-0.555671

Appendix D: Cartesian Coordinates

C	5.737308	1.609764	0.197412
C	4.527805	1.828150	0.742578
O	7.184782	0.310711	-1.033982
C	7.610908	-0.811096	-1.807951
H	-0.355983	-2.036484	3.231133
H	-0.874504	-0.390965	2.967300
H	-2.084986	-1.828266	1.411872
H	-0.620468	-2.565229	0.845162
H	1.541929	-0.361509	3.144836
H	1.709637	-1.675277	2.015683
H	-2.991332	0.865326	1.018149
H	-5.401749	1.241144	1.306999
H	-6.180006	-1.176736	-2.113560
H	-3.795048	-1.604920	-2.350298
H	-9.189717	0.175724	-0.571153
H	-8.138597	0.155401	-1.986477
H	-8.245689	-1.268173	-0.937454
H	2.946850	-1.028127	-0.321001
H	5.133754	-1.424571	-1.297844
H	6.544831	2.307774	0.306962
H	4.339296	2.720756	1.309853
H	7.022498	-0.883248	-2.711520
H	8.639624	-0.611168	-2.050848
H	7.535787	-1.716234	-1.222635
C	0.241273	1.393934	-0.932099
H	-0.745100	1.777340	-1.157232
H	0.850558	2.235103	-0.628156
H	0.662131	1.005382	-1.856019

9-Cl S₁/S₀ (6,5):**S₀** = -1068.10960675**S₁** = -1068.10960332

C	-0.451846	-1.390474	-0.185942
C	-1.455487	-0.670733	-1.108962
C	-1.328332	0.805085	-0.817935
C	0.003657	1.328183	-1.165815
C	1.115781	0.636989	-0.556482
C	0.985856	-0.853763	-0.301080
N	-1.712295	1.210240	0.476508
H	-1.588141	2.192192	0.609228
C	-2.952217	0.761221	1.047010
C	-2.949959	0.215340	2.326550
C	-4.122717	-0.189468	2.923761
C	-5.335212	-0.064622	2.247114
C	-5.348920	0.477923	0.969567
C	-4.159877	0.893038	0.385303
O	-6.420066	-0.492772	2.907618
C	-7.691420	-0.388400	2.321889
N	2.252756	1.232635	-0.383191
H	2.286479	2.209625	-0.612241
C	3.498999	0.644962	0.069715
C	4.356603	0.071508	-0.842221

Appendix D: Cartesian Coordinates

C	5.565766	-0.455390	-0.414854
C	5.906991	-0.395700	0.931961
C	5.027120	0.198313	1.843794
C	3.831185	0.720393	1.416607
O	7.035973	-0.868255	1.449205
C	8.008000	-1.476619	0.629014
H	-0.427861	-2.450096	-0.411815
H	-0.789380	-1.291949	0.836096
H	-2.454202	-1.038552	-0.919125
H	-1.225327	-0.859019	-2.152833
H	1.571854	-1.135394	0.563020
H	1.473165	-1.308807	-1.160894
H	-2.018436	0.119881	2.854647
H	-4.128061	-0.606809	3.912963
H	-6.265177	0.592497	0.424786
H	-4.184650	1.325331	-0.599730
H	-8.386638	-0.785102	3.044903
H	-7.944094	0.644899	2.112096
H	-7.753406	-0.971120	1.409512
H	4.099905	0.030900	-1.885581
H	6.222743	-0.899698	-1.135208
H	5.310776	0.237941	2.877796
H	3.160656	1.180114	2.119988
H	8.379269	-0.781091	-0.113838
H	8.811900	-1.761065	1.287760
H	7.609369	-2.359686	0.144381
C	0.181845	2.427405	-2.171879
H	-0.002733	3.407775	-1.731866
H	1.169719	2.442551	-2.620557
H	-0.546744	2.307924	-2.966711

9-TS (MP2-MeOH): $S_0 = -1068.24764811$ Freq = $i42.8402 \text{ cm}^{-1}$

C	-0.485488	-1.141712	2.229964
C	-1.323939	-1.038664	0.960144
C	-1.118375	0.297174	0.322248
C	0.159620	0.979893	0.396099
C	1.157936	0.384579	1.114722
C	0.977010	-0.884716	1.900068
N	-2.092998	0.869706	-0.345319
H	-1.918131	1.803488	-0.722844
N	2.457921	0.986453	1.114174
H	2.692756	1.300994	2.059295
H	-0.614869	-2.134390	2.671163
H	-0.836461	-0.406767	2.962901
H	-2.387572	-1.195854	1.159150
H	-1.009024	-1.814322	0.247911
H	1.579842	-0.811848	2.813316
H	1.395344	-1.722605	1.323684
C	0.347144	2.278049	-0.338485
H	-0.316012	3.056213	0.056091

Appendix D: Cartesian Coordinates

H	1.376131	2.609857	-0.208635
H	0.150202	2.162441	-1.410005
C	3.482372	0.125850	0.615637
C	3.307900	-0.510802	-0.624436
C	4.694143	-0.026586	1.293505
C	4.317155	-1.309688	-1.147764
H	2.378180	-0.383547	-1.175509
C	5.723575	-0.809100	0.758756
H	4.842930	0.462463	2.254894
C	5.534572	-1.458008	-0.466326
H	4.189689	-1.812714	-2.102975
H	6.650981	-0.902524	1.313462
C	-3.395251	0.330994	-0.604456
C	-4.509129	1.087639	-0.244596
C	-3.533210	-0.887700	-1.279073
C	-5.789719	0.606112	-0.518035
H	-4.384182	2.037107	0.270214
C	-4.807761	-1.365558	-1.549644
H	-2.658740	-1.444035	-1.604794
C	-5.940743	-0.624875	-1.173324
H	-6.646813	1.200436	-0.223407
H	-4.949963	-2.306516	-2.073074
O	6.461149	-2.258908	-1.084708
O	-7.135691	-1.191859	-1.493864
C	-8.321240	-0.466335	-1.136054
H	-9.148396	-1.085132	-1.478584
H	-8.384013	-0.329682	-0.052880
H	-8.351704	0.504718	-1.637979
C	7.710159	-2.433000	-0.408924
H	7.568047	-2.902525	0.569415
H	8.296816	-3.089996	-1.049362
H	8.229913	-1.477728	-0.286231

9-*E,E*-isomer (MP2-MeOH): $S_0 = -1068.27254679$

C	-3.295090	-0.629501	1.829206
C	-3.499235	0.873406	1.729336
C	-2.231854	1.547059	1.285379
C	-1.224004	0.857493	0.592540
C	-1.529450	-0.419995	0.096568
C	-2.774367	-1.156797	0.502103
N	-2.087438	2.845557	1.576186
H	-1.236597	3.312657	1.272086
C	-3.040322	3.659896	2.265826
C	-2.708433	4.183567	3.521308
C	-3.612553	5.006628	4.180303
C	-4.849270	5.316525	3.591318
C	-5.174482	4.798252	2.330669
C	-4.257792	3.980361	1.665500
O	-5.658413	6.128827	4.332341
C	-6.931927	6.467609	3.768120
N	-0.704142	-1.027655	-0.764328

Appendix D: Cartesian Coordinates

H	0.137120	-0.533180	-1.051327
C	-0.905030	-2.318600	-1.347256
C	-1.934857	-2.524003	-2.265190
C	-2.111058	-3.779043	-2.853021
C	-1.228584	-4.820130	-2.535256
C	-0.181000	-4.599911	-1.626147
C	-0.015918	-3.354141	-1.034595
O	-1.296339	-6.083214	-3.048760
C	-2.353483	-6.350892	-3.979215
H	-4.239771	-1.119850	2.082403
H	-2.579167	-0.855879	2.626555
H	-3.811152	1.299156	2.688325
H	-4.300563	1.095970	1.011730
H	-2.552247	-2.227263	0.556622
H	-3.539820	-1.034376	-0.276171
H	-1.754452	3.932983	3.978746
H	-3.381728	5.422286	5.157191
H	-6.116198	5.032273	1.847119
H	-4.491045	3.601214	0.673677
H	-7.412986	7.104782	4.508133
H	-6.812363	7.016361	2.829500
H	-7.537764	5.572354	3.600658
H	-2.596679	-1.703804	-2.531902
H	-2.919818	-3.917667	-3.561617
H	0.492004	-5.421561	-1.397412
H	0.787542	-3.182881	-0.322384
H	-2.263571	-5.719976	-4.868199
H	-2.233332	-7.396683	-4.256548
H	-3.332485	-6.201267	-3.514748
C	0.084575	1.526657	0.258307
H	0.387893	2.215746	1.051619
H	0.895095	0.795171	0.193535
H	0.048555	2.083481	-0.684832

9-Z,E-isomer (MP2-MeOH): $S_0 = -1068.26639260$

C	-0.077213	-0.917354	1.467639
C	-1.282702	-0.672484	0.571581
C	-1.341901	0.778714	0.191536
C	-0.185994	1.583703	0.114314
C	1.051753	0.938903	0.225556
C	1.175146	-0.473533	0.735670
N	-2.538876	1.316363	-0.060220
H	-2.574871	2.306444	-0.295865
C	-3.793867	0.631892	-0.049987
C	-4.788819	1.053894	0.840424
C	-6.026147	0.423679	0.831459
C	-6.281713	-0.625224	-0.067048
C	-5.286889	-1.037565	-0.963740
C	-4.047555	-0.393145	-0.961251
O	-7.528874	-1.172627	0.018668
C	-7.830382	-2.248190	-0.880049

Appendix D: Cartesian Coordinates

N	2.223933	1.504970	-0.108682
H	3.058525	0.998058	0.182059
C	2.449934	2.577556	-1.018747
C	3.396545	3.553050	-0.706579
C	3.678582	4.576588	-1.614608
C	3.007481	4.613534	-2.844295
C	2.065287	3.620419	-3.157711
C	1.797628	2.596132	-2.259446
O	3.192636	5.564875	-3.806894
C	4.149804	6.594005	-3.526204
H	-0.010212	-1.978580	1.724564
H	-0.188530	-0.355174	2.401005
H	-2.215222	-0.951313	1.070874
H	-1.208850	-1.292204	-0.332313
H	2.058699	-0.537817	1.382694
H	1.365927	-1.132865	-0.122912
H	-4.584165	1.858023	1.543086
H	-6.813595	0.728017	1.515261
H	-5.462230	-1.833999	-1.678088
H	-3.284459	-0.685734	-1.677910
H	-8.852907	-2.539045	-0.645939
H	-7.768714	-1.918843	-1.921219
H	-7.158028	-3.095562	-0.717481
H	3.903286	3.527098	0.255448
H	4.415695	5.325658	-1.348094
H	1.571141	3.657764	-4.124761
H	1.089769	1.811414	-2.515408
H	5.148800	6.172620	-3.380852
H	4.145888	7.237016	-4.404642
H	3.858577	7.171399	-2.643890
C	-0.328392	3.073397	-0.069088
H	-1.127745	3.446091	0.581488
H	0.584035	3.588353	0.231114
H	-0.553455	3.368023	-1.100156

8-FC (Min S₀):**S₀** = -459.45255680**S₁** = -459.27059318

C	0.000068	2.066073	0.499135
C	1.247987	1.436588	-0.098666
C	1.208916	-0.071141	-0.005659
C	0.000006	-0.770419	0.139247
C	-1.208850	-0.071036	-0.005642
C	-1.247806	1.436673	-0.098845
N	2.360702	-0.708180	-0.100081
N	-2.360643	-0.708074	-0.099966
C	-0.000243	-2.275713	0.324018
C	3.689679	-0.114899	-0.243670
C	-3.689580	-0.114818	-0.244039
H	0.000121	3.132844	0.313187
H	-0.000013	1.926196	1.574841
H	2.129164	1.810246	0.405668

Appendix D: Cartesian Coordinates

H	1.347258	1.707613	-1.147769
H	-2.129053	1.810478	0.405258
H	-1.346817	1.707588	-1.147999
H	-2.336819	-1.703328	-0.096535
H	0.855576	-2.605749	0.901711
H	-0.855681	-2.605202	0.902612
H	-0.000878	-2.824876	-0.615060
H	4.386609	-0.916015	-0.435273
H	3.718488	0.572897	-1.076289
H	3.988104	0.394480	0.662535
H	-4.386468	-0.915973	-0.435627
H	-3.988222	0.394767	0.661979
H	-3.718184	0.572789	-1.076821
H	2.336898	-1.703430	-0.096592

8-Cl S₁/S₀:**S₀** = -459.31917383**S₁** = -459.31917134

C	0.191395	1.805495	-0.716309
C	1.479286	0.931073	-0.819324
C	1.351771	-0.313335	0.031069
C	0.106825	-1.045527	-0.272362
C	-1.091946	-0.269549	-0.064798
C	-0.903527	1.205434	0.194917
N	1.566121	-0.183021	1.425511
N	-2.260897	-0.815511	-0.134447
C	0.098986	-2.438192	-0.829850
C	2.694399	0.617163	1.888771
C	-3.575847	-0.158297	0.005719
H	0.429228	2.786834	-0.326672
H	-0.222861	1.961590	-1.705856
H	2.352287	1.506233	-0.546311
H	1.622753	0.625536	-1.849192
H	-0.607944	1.289955	1.233599
H	-1.829067	1.748624	0.065535
H	-2.286334	-1.804280	-0.300555
H	-0.029057	-3.183203	-0.043814
H	-0.679079	-2.600183	-1.571507
H	1.050062	-2.642845	-1.303166
H	2.797663	0.464355	2.954302
H	3.635878	0.357761	1.410893
H	2.505618	1.671112	1.731388
H	-4.327970	-0.930279	0.007878
H	-3.610290	0.384898	0.936041
H	-3.737328	0.504991	-0.829874
H	1.602793	-1.087546	1.848562

8-MIN (S₁):**S₀** = -459.38297013**S₁** = -459.29521969

C	-0.419956	-0.912681	2.509802
---	-----------	-----------	----------

Appendix D: Cartesian Coordinates

C	-1.190387	-1.117667	1.206601
C	-0.961529	0.005408	0.222975
C	0.216892	0.752654	0.249121
C	1.181236	0.453961	1.213298
C	1.061852	-0.639362	2.253014
N	-1.875165	0.170600	-0.795903
H	-1.796636	1.011964	-1.316873
N	2.412617	1.145917	1.221520
H	2.504487	1.966851	1.801517
H	-0.519082	-1.787459	3.141429
H	-0.844533	-0.074194	3.052343
H	-2.243785	-1.196230	1.441336
H	-0.908568	-2.063160	0.745229
H	1.555807	-0.345339	3.175031
H	1.560908	-1.539887	1.899186
C	0.442401	1.846019	-0.777263
H	-0.332520	2.602599	-0.717136
H	1.386597	2.360513	-0.646697
H	0.435827	1.439151	-1.782611
C	-3.225245	-0.358689	-0.758547
H	-3.709533	-0.095632	-1.688408
H	-3.215397	-1.438222	-0.692205
H	-3.821365	0.037827	0.059902
C	3.624088	0.674800	0.573809
H	4.263495	1.516835	0.355236
H	4.130344	0.008931	1.267629
H	3.354983	0.132544	-0.318289

Chapter 6

35-FC:

C	6.71214100	-1.19686200	0.09982000
C	5.98322100	-1.78966300	1.13500700
C	4.58512200	-1.75073900	1.11974200
C	3.89563500	-1.12463300	0.06774800
C	4.63960600	-0.53357900	-0.96723200
C	6.03648400	-0.56724200	-0.95110800
C	2.40271500	-1.07934500	0.05222200
C	1.70300200	0.12606100	0.42747300
C	0.22215600	0.05128900	0.37190800
C	-0.40262700	-1.13741200	-0.01842400
O	0.33499900	-2.24899200	-0.36146600
C	1.68633000	-2.20029500	-0.32802800
C	-0.59359100	1.14639200	0.70778500
C	-1.97859900	1.04294700	0.65038600
C	-2.57652900	-0.16602700	0.25463600
C	-1.79182500	-1.26525100	-0.08228800
O	2.27824600	1.17545700	0.78567000
N	2.22124600	-3.36850200	-0.75278000
H	-2.23110800	-2.20795500	-0.39061700
H	-0.10968700	2.06856000	1.01135200
H	-2.59942600	1.89420400	0.91092600

LXX

Appendix D: Cartesian Coordinates

H	-3.65792400	-0.24868700	0.20940800
H	4.02248000	-2.20409400	1.93159000
H	4.11813100	-0.04566000	-1.78582300
H	6.49987400	-2.27779200	1.95640200
H	6.59622400	-0.10431200	-1.75879100
H	7.79786400	-1.22431300	0.11159000
H	3.20868300	-3.52814900	-0.61982800
H	1.62296900	-4.18006900	-0.81577400

35_ "Cl" S₂/S₁:

C	6.71139500	-1.13064300	0.00369300
C	6.04299000	-2.16996300	0.67801400
C	4.65948400	-2.19699600	0.73113900
C	3.87742200	-1.16768000	0.11689200
C	4.58303400	-0.11182200	-0.54768500
C	5.96972500	-0.10731700	-0.60319200
C	2.44099600	-1.15808700	0.16466800
C	1.68515300	0.16158400	0.28991500
C	0.26719700	0.10076100	0.21877900
C	-0.40298000	-1.15055700	0.12719300
O	0.34026700	-2.34479400	0.04076100
C	1.67813100	-2.33731800	0.01528800
C	-0.58212600	1.26044900	0.31921800
C	-1.96411900	1.13161000	0.31134100
C	-2.58334700	-0.12796600	0.21009700
C	-1.77070800	-1.29049800	0.11692400
O	2.34586400	1.21882400	0.49239100
N	2.16201700	-3.56265000	-0.22546900
H	-2.20683400	-2.28153400	0.04364400
H	-0.11224300	2.23423800	0.39849400
H	-2.57977100	2.02455000	0.38673300
H	-3.66359300	-0.22109000	0.20985800
H	4.16974500	-2.96166000	1.32492700
H	4.01456400	0.65987000	-1.04765200
H	6.61389800	-2.94399500	1.18117200
H	6.48081500	0.68955200	-1.13454700
H	7.79566800	-1.12211800	-0.04296000
H	3.13788300	-3.71298900	-0.43495700
H	1.51528300	-4.32642400	-0.37317200

35_Min S₁:

C	6.71171900	-1.12936500	0.01726000
C	6.04160400	-2.17167000	0.68520000
C	4.65793700	-2.19912300	0.73426300
C	3.87750900	-1.16729700	0.12220900
C	4.58477800	-0.10841300	-0.53565400
C	5.97163600	-0.10349500	-0.58726800
C	2.44091800	-1.15823300	0.16588400
C	1.68427500	0.16069800	0.29426100
C	0.26655800	0.09986600	0.21760500
C	-0.40297900	-1.15124500	0.11877400
O	0.34087800	-2.34505800	0.03144700

Appendix D: Cartesian Coordinates

C	1.67880500	-2.33706800	0.00916500
C	-0.58345700	1.25898200	0.31904700
C	-1.96536700	1.12985800	0.30542100
C	-2.58390700	-0.12947500	0.19709900
C	-1.77063900	-1.29146600	0.10269400
O	2.34389100	1.21726800	0.50366800
N	2.16374400	-3.56110200	-0.23596100
H	-2.20623900	-2.28232400	0.02407900
H	-0.11409700	2.23258400	0.40361500
H	-2.58154000	2.02235500	0.38178700
H	-3.66412200	-0.22283500	0.19255800
H	4.16665800	-2.96647000	1.32328700
H	4.01765100	0.66554100	-1.03363400
H	6.61118600	-2.94778200	1.18664600
H	6.48414700	0.69570500	-1.11372100
H	7.79612400	-1.12043700	-0.02628700
H	3.14038400	-3.71025700	-0.44265800
H	1.51775600	-4.32440400	-0.38928000

35_TS S₁:

C	3.22895200	-0.93510000	-3.01518100
C	3.23638100	-0.52071100	-1.63928600
C	4.37256100	0.23426300	-1.19997900
C	5.43990100	0.47932400	-2.04926300
C	5.42344200	0.02289500	-3.37760500
C	4.30038500	-0.67478500	-3.85251600
C	2.13825100	-0.80337600	-0.75588600
C	1.24486100	-1.87070500	-1.00098000
O	0.00594700	-1.90700200	-0.49677100
C	-0.51190900	-0.77940100	0.18097600
C	0.39080100	0.16582500	0.74609700
C	1.78137900	0.09150700	0.45194700
C	-0.18962300	1.12973700	1.64324700
C	-1.56001800	1.16402900	1.85346500
C	-2.42371500	0.24668000	1.22062900
C	-1.87060500	-0.76287800	0.39178300
N	1.52182000	-2.97790300	-1.69944800
O	2.67918300	0.70448700	1.08826300
H	-2.49115700	-1.54065000	-0.04228500
H	0.46974500	1.83764400	2.13358100
H	-1.97623700	1.91699500	2.51797900
H	-3.49521000	0.28849300	1.38189300
H	4.38569100	0.58567800	-0.17770800
H	2.35022100	-1.41536200	-3.42859500
H	6.29872100	1.03103600	-1.67919000
H	4.25696800	-0.99175800	-4.88985500
H	6.26043000	0.22617400	-4.03798000
H	2.46918900	-3.21209400	-1.95809200
H	0.79990100	-3.67316400	-1.83888400

35_"Cl" S₁/S₀:

C	-1.93902400	-0.97848900	-0.47747900
---	-------------	-------------	-------------

Appendix D: Cartesian Coordinates

C	-0.54540700	-0.99281600	-0.44120500
C	0.17684400	-0.20065200	0.47892300
C	-0.55329200	0.58640000	1.38485300
C	-1.94503500	0.59123000	1.37739900
C	-2.63565600	-0.18366900	0.43364000
O	0.11100400	-1.81763900	-1.35487600
C	1.40555600	-2.12782000	-0.93316200
C	2.23706800	-0.92702500	-0.65584500
C	1.67180200	-0.06364100	0.38136100
C	3.27783500	-0.55793800	-1.55369000
C	3.92057500	0.71836300	-1.51574300
C	4.90455700	1.03963000	-2.43611600
C	5.28617800	0.12137400	-3.43045300
C	4.67218600	-1.13657700	-3.48857500
C	3.69730600	-1.48120500	-2.56139500
O	2.26573600	0.83460300	1.00706300
N	1.43252500	-3.14169800	-0.00515000
H	-2.45816500	-1.59153800	-1.20715400
H	0.00227000	1.20223300	2.08544400
H	-2.49266500	1.20015500	2.08955600
H	-3.72106700	-0.17208100	0.40943600
H	3.61661100	1.43529100	-0.76340800
H	3.25296900	-2.46995900	-2.57783600
H	5.37651400	2.01676200	-2.39519300
H	4.97807800	-1.85649900	-4.24165700
H	6.06113700	0.38358900	-4.14380600
H	2.30467100	-3.41283400	0.41930500
H	0.65437700	-3.77720700	0.07879900

Chapter 7**BP86****59**

C	-1.48223800	-5.40179200	-0.65112200
C	-0.73835500	-6.58960600	-0.73386700
C	0.67628200	-6.56570000	-0.81614500
C	1.38399200	-5.35319100	-0.81765000
C	0.63786900	-4.16647700	-0.73451100
C	-0.77214400	-4.19030700	-0.65247200
C	1.02815100	-2.76035700	-0.71081900
N	-0.10034000	-1.94911400	-0.62249000
C	-1.20398700	-2.79798000	-0.58145500
N	-2.48532900	-2.45868400	-0.49055900
N	2.29946900	-2.37852100	-0.76548800
C	-2.86479400	-1.18628500	-0.44326200
C	2.63879400	-1.09393300	-0.75641100
N	-2.05380100	-0.05464000	-0.47738500
C	-2.90125000	1.04911100	-0.42327900
C	-4.29206700	0.61407600	-0.34366000
C	-4.26901600	-0.79815800	-0.35666900
C	4.03056100	-0.65925500	-0.82736500
C	4.00745400	0.75286000	-0.81427400

Appendix D: Cartesian Coordinates

C	2.60232100	1.14055600	-0.73616200
N	1.79239500	0.00947200	-0.69732900
N	-2.56298800	2.33386400	-0.44907500
N	2.22162600	2.41337800	-0.72440300
C	-1.29329800	2.71584000	-0.53508900
N	-0.16278700	1.90423700	-0.59021700
C	0.93848000	2.75290800	-0.66461800
C	0.50277300	4.14590700	-0.66551800
C	-0.90715400	4.12253800	-0.58285200
C	-5.50196800	1.32312500	-0.27102600
C	-6.68896100	0.57583100	-0.20941700
C	-6.66582700	-0.84111800	-0.22268600
C	-5.45497200	-1.54775500	-0.29780500
C	1.20934800	5.35765800	-0.73051100
C	0.46217800	6.54616200	-0.70957500
C	-0.95235700	6.52258200	-0.62628300
C	-1.65670500	5.30975600	-0.56222600
C	5.24012500	-1.36826900	-0.90439400
C	6.42730900	-0.62097900	-0.96596300
C	6.40407200	0.79584900	-0.95321600
C	5.19298900	1.50241600	-0.87829000
H	-2.57535800	-5.41129100	-0.58805400
H	-1.25863200	-7.55432800	-0.73562100
H	1.22515900	-7.51227400	-0.88011500
H	2.47677600	-5.32541200	-0.88116300
H	-5.51093500	2.41804700	-0.26338300
H	-7.65238600	1.09517800	-0.15050400
H	-7.61171400	-1.39276000	-0.17397200
H	-5.42798200	-2.64233200	-0.31057100
H	2.30237900	5.36689600	-0.79559000
H	0.97969600	7.51109800	-0.75909500
H	-1.50398200	7.46962500	-0.61254700
H	-2.74950600	5.28227200	-0.49897400
H	5.24882900	-2.46318800	-0.91683200
H	7.39058700	-1.14035600	-1.02714000
H	7.34973900	1.34763200	-1.00469500
H	5.16580700	2.59706600	-0.87090100
Co	-0.12857800	-0.02260000	-0.56650600
C	0.02063500	0.73187900	2.77267800
C	0.33386100	-0.77847700	2.74873600
C	1.81986500	-0.46741300	3.07885700
C	1.50966300	1.02796800	3.10166500
C	-0.44699100	-0.17086100	3.91038700
C	1.76648200	0.28098100	4.41022000
C	0.45315700	-0.00311400	5.12971700
H	-0.65050500	1.32771600	2.14999300
H	-0.04896700	-1.57251200	2.10352300
H	2.69956300	-0.98503500	2.68801300
H	2.10842200	1.86373800	2.73063800
H	-1.51557500	-0.39392400	4.00042000
H	2.69944300	0.46601800	4.95353800
H	0.13430400	0.84017600	5.77161700
H	0.50065700	-0.92250800	5.74396100

Appendix D: Cartesian Coordinates

TS (59-60)

C	-1.30425900	-5.35123300	-0.56211700
C	-0.54665300	-6.52261800	-0.72430500
C	0.86735200	-6.47740100	-0.80343200
C	1.56097600	-5.25891200	-0.72255400
C	0.80197500	-4.08988000	-0.55345800
C	-0.60836400	-4.13482000	-0.47502800
C	1.17387600	-2.68141100	-0.44226700
N	0.03939600	-1.89442200	-0.30303900
C	-1.05332400	-2.75312600	-0.31218100
N	-2.33976700	-2.43483100	-0.19073200
N	2.44087500	-2.27899200	-0.48938800
C	-2.74740400	-1.17198700	-0.09619200
C	2.75014000	-0.98522100	-0.48481200
N	-1.96352600	-0.02171300	-0.07442500
C	-2.83699700	1.05874900	-0.04248300
C	-4.21999400	0.59099000	0.01054600
C	-4.16333000	-0.81988200	-0.02986400
C	4.12456100	-0.51827800	-0.65452600
C	4.06111100	0.89244200	-0.69869500
C	2.65120900	1.24460700	-0.54802900
N	1.88343700	0.09564100	-0.39190800
N	-2.53326200	2.35162700	-0.11242800
N	2.23171400	2.50535200	-0.60461400
C	-1.27599900	2.75154700	-0.28386000
N	-0.13361400	1.96312600	-0.32574500
C	0.94131600	2.82169100	-0.53273900
C	0.47294000	4.20030000	-0.64609500
C	-0.92993200	4.15668200	-0.48216700
C	-5.44746200	1.27064300	0.05948200
C	-6.61824500	0.49525000	0.08156600
C	-6.56154700	-0.91995600	0.04174700
C	-5.33271400	-1.59699200	-0.02073700
C	1.14290900	5.41365200	-0.87105400
C	0.36747400	6.58326900	-0.92316400
C	-1.03954400	6.53914400	-0.76024800
C	-1.70804600	5.32390000	-0.54067800
C	5.34487800	-1.19797800	-0.79582700
C	6.50365500	-0.42319800	-0.96865400
C	6.44013700	0.99153200	-1.01170300
C	5.21642500	1.66869100	-0.88324900
H	-2.39749000	-5.37743000	-0.50496200
H	-1.05622300	-7.49063400	-0.79352800
H	1.42703100	-7.41101300	-0.93217100
H	2.65317800	-5.21398300	-0.78776800
H	-5.48234300	2.36491800	0.08088700
H	-7.59462100	0.99125600	0.12764100
H	-7.49507400	-1.49422000	0.05731200
H	-5.28014100	-2.69004300	-0.06000900
H	2.23005800	5.43843800	-0.99983900
H	0.85662400	7.54907600	-1.09472800

Appendix D: Cartesian Coordinates

H	-1.61398200	7.47142500	-0.80856600
H	-2.79530200	5.28001000	-0.41815500
H	5.38339900	-2.29211700	-0.77149600
H	7.47504000	-0.91952800	-1.07604600
H	7.36355400	1.56534400	-1.15144600
H	5.15731100	2.76134400	-0.92447100
Co	-0.01606200	0.03564300	0.01779500
C	0.74153100	0.85413300	2.12060800
C	-0.40634600	-0.74383000	2.18633100
C	0.87217600	-1.35163400	2.75396100
C	1.75000200	-0.12761100	2.70201600
C	-0.48409800	0.55771200	2.96280000
C	1.17944800	-0.58950500	4.05999000
C	-0.02020000	0.28595200	4.40962800
H	1.00141900	1.85974200	1.77380300
H	-1.29573000	-1.33459400	1.94024500
H	1.22033300	-2.36655100	2.55162100
H	2.81378000	-0.14266700	2.45694400
H	-1.36868400	1.18437000	2.79037600
H	1.83758600	-1.02845800	4.81767500
H	0.26552900	1.21266100	4.94206100
H	-0.78431800	-0.25027400	5.00330100

TS (59-61)

C	-1.34715800	-5.39290300	-0.52944200
C	-0.58738300	-6.56661900	-0.66232700
C	0.82558700	-6.51921600	-0.75660900
C	1.51550500	-5.29647700	-0.72000900
C	0.75398400	-4.12479500	-0.58255000
C	-0.65479200	-4.17208600	-0.48846200
C	1.12287500	-2.71333200	-0.51226200
N	-0.01523700	-1.92200200	-0.39024200
C	-1.10408800	-2.78793000	-0.36487200
N	-2.39034000	-2.47215900	-0.24566000
N	2.38860400	-2.31090800	-0.56073900
C	-2.79779300	-1.20748400	-0.18798300
C	2.70131700	-1.01789900	-0.54956600
N	-2.01071500	-0.05938600	-0.21152600
C	-2.88334100	1.02387400	-0.15944600
C	-4.26587300	0.55897400	-0.08540800
C	-4.21176300	-0.85243700	-0.10458300
C	4.08082600	-0.55437300	-0.67486000
C	4.02413600	0.85722700	-0.69624400
C	2.61225700	1.21222000	-0.57923200
N	1.83253000	0.06416400	-0.46863300
N	-2.57396100	2.31554900	-0.20224300
N	2.19905700	2.47578200	-0.61282600
C	-1.31305200	2.71763100	-0.33195300
N	-0.16869600	1.92619100	-0.36684600
C	0.90906800	2.79231300	-0.54222500
C	0.44344700	4.17397300	-0.62031100
C	-0.96192300	4.12685300	-0.48201500

Appendix D: Cartesian Coordinates

C	-5.49182600	1.24040900	-0.02032400
C	-6.66293900	0.46709800	0.03283100
C	-6.60857200	-0.94868100	0.01354600
C	-5.38153900	-1.62781800	-0.05945600
C	1.11785800	5.39307500	-0.79715000
C	0.34456900	6.56486200	-0.82788100
C	-1.06503400	6.51743800	-0.68994500
C	-1.73765600	5.29683800	-0.51809900
C	5.30336800	-1.23601500	-0.78739600
C	6.46969100	-0.46337000	-0.91174400
C	6.41280800	0.95225300	-0.93215700
C	5.18799500	1.63170200	-0.82897700
H	-2.43964900	-5.42057800	-0.45968200
H	-1.09431100	-7.53792100	-0.69620400
H	1.38749400	-7.45447600	-0.86188800
H	2.60697600	-5.25020200	-0.79632700
H	-5.52527300	2.33495800	-0.01190300
H	-7.63784000	0.96513800	0.08828600
H	-7.54223800	-1.52152600	0.05436000
H	-5.33050700	-2.72149500	-0.08026000
H	2.20701600	5.42032100	-0.90786000
H	0.83731300	7.53459000	-0.96340900
H	-1.63825800	7.45124500	-0.72096300
H	-2.82698200	5.25048500	-0.41615000
H	5.33763500	-2.33059500	-0.77928600
H	7.44203400	-0.96193200	-0.99862400
H	7.34201800	1.52470100	-1.03428300
H	5.13418400	2.72526500	-0.85186500
Co	-0.07696400	-0.00128000	-0.19274200
C	0.96779700	1.13203800	2.39278100
C	-0.18870000	-0.44508500	2.08095900
C	1.07150400	-1.12869700	2.63970300
C	1.94670000	0.09456000	2.84406400
C	-0.31390200	0.73049000	3.05325200
C	1.27596600	-0.60531800	4.05958800
C	0.04897200	0.21001500	4.46278000
H	1.16446800	2.03788300	1.81891700
H	-1.10255600	-1.00340000	1.84517800
H	1.46436700	-2.08537400	2.28896200
H	3.02165100	0.12473400	2.65976000
H	-1.18556000	1.38320500	2.92095700
H	1.89051800	-1.15433400	4.78049200
H	0.28770500	1.03002800	5.16581700
H	-0.75361600	-0.41606300	4.89416700

60

C	-1.33966500	-5.31591400	-1.08275500
C	-0.58360400	-6.47999300	-1.29396900
C	0.83340900	-6.44542600	-1.29488000
C	1.53166500	-5.24576800	-1.08415600
C	0.77456300	-4.08121900	-0.87695100
C	-0.64024600	-4.11559900	-0.87678000

Appendix D: Cartesian Coordinates

C	1.14872600	-2.69154200	-0.62618500
N	0.01473900	-1.89780000	-0.54799400
C	-1.08024700	-2.74622000	-0.62166800
N	-2.36067100	-2.43562000	-0.42097900
N	2.41581900	-2.31521000	-0.45541600
C	-2.75311300	-1.18227800	-0.20618100
C	2.74055100	-1.03860000	-0.26746300
N	-1.95940600	-0.04193700	-0.12863200
C	-2.81522600	1.05235700	-0.19682300
C	-4.20593900	0.60264700	-0.15335400
C	-4.16671200	-0.81053700	-0.15988600
C	4.13296100	-0.59053900	-0.26199000
C	4.09373400	0.82200400	-0.27004100
C	2.67856100	1.19253100	-0.27859100
N	1.88693300	0.05383100	-0.17862400
N	-2.49165100	2.32750400	-0.39555900
N	2.28395600	2.44791100	-0.47282600
C	-1.22914400	2.70338000	-0.59994200
N	-0.09342500	1.90970300	-0.54832100
C	0.99860900	2.75955700	-0.63600500
C	0.55336000	4.13014800	-0.87545100
C	-0.86112500	4.09487900	-0.85119700
C	-5.42558100	1.29777900	-0.16378000
C	-6.60667100	0.53784200	-0.15251900
C	-6.56752300	-0.87828800	-0.15869500
C	-5.34621900	-1.57170300	-0.17634900
C	1.24854600	5.33155500	-1.08899800
C	0.48837100	6.49598400	-1.28289100
C	-0.92839500	6.46051900	-1.25907400
C	-1.62240300	5.25967000	-1.04066600
C	5.35153700	-1.28600100	-0.30243200
C	6.53285600	-0.52605800	-0.32154800
C	6.49371200	0.88990600	-0.32869600
C	5.27207600	1.58340900	-0.31727700
H	-2.43451600	-5.33505300	-1.07737900
H	-1.09581900	-7.43462600	-1.46072000
H	1.39137600	-7.37395100	-1.46212600
H	2.62614400	-5.21120300	-1.08000600
H	-5.44690300	2.39250900	-0.17786800
H	-7.57726100	1.04708800	-0.14480500
H	-7.50850400	-1.44039900	-0.15568700
H	-5.30712500	-2.66577100	-0.19961700
H	2.34332700	5.35097200	-1.10293000
H	0.99704700	7.45150300	-1.45528500
H	-1.48971300	7.38926000	-1.41344000
H	-2.71662200	5.22458100	-1.01767200
H	5.37256800	-2.38078500	-0.31611200
H	7.50328000	-1.03544500	-0.33786800
H	7.43450200	1.45194300	-0.35034100
H	5.23231900	2.67746200	-0.34189300
Co	-0.03547200	0.00504800	0.10320100
C	0.02928400	1.06325900	1.99455800
C	-0.16780400	-1.05541200	1.97253200

Appendix D: Cartesian Coordinates

C	1.17058400	-0.88365300	2.66692400
C	1.31093200	0.62958500	2.68498500
C	-0.94742900	0.07886200	2.64658800
C	0.91465900	-0.11024900	3.97802700
C	-0.59322100	0.02858400	4.15549700
H	-0.21430000	2.12965800	1.88940900
H	-0.60962200	-2.05447000	1.84986100
H	2.02147400	-1.55648700	2.53857200
H	2.27289400	1.13419200	2.57128900
H	-2.00674300	0.17986500	2.38319900
H	1.61630400	-0.18499800	4.81631800
H	-0.88338800	0.95428200	4.68806400
H	-1.05171900	-0.83932100	4.66657900

TS (60-61)

C	-1.28800000	-5.45959100	-1.22060500
C	-0.52438700	-6.61829300	-1.43709900
C	0.89183000	-6.57938200	-1.41271000
C	1.58199900	-5.38032400	-1.17120900
C	0.81703500	-4.22354700	-0.95218000
C	-0.59651400	-4.26185300	-0.97810300
C	1.18222000	-2.83429400	-0.68399900
N	0.04552100	-2.05186300	-0.56969700
C	-1.04551800	-2.89675500	-0.71372700
N	-2.33285200	-2.58185300	-0.59095600
N	2.44893700	-2.44126400	-0.56459500
C	-2.73495600	-1.33101800	-0.38083900
C	2.75790700	-1.15585300	-0.41868500
N	-1.95211800	-0.18623000	-0.24578900
C	-2.82471500	0.89599800	-0.23143700
C	-4.20962500	0.43134300	-0.24499200
C	-4.15248600	-0.97649300	-0.34652600
C	4.14444700	-0.69258600	-0.42389400
C	4.09309200	0.71912600	-0.40587800
C	2.67718600	1.07767000	-0.38407700
N	1.89238100	-0.07086100	-0.33762100
N	-2.51388900	2.18750600	-0.29160600
N	2.26907800	2.33957400	-0.47019200
C	-1.25121800	2.58416100	-0.43255900
N	-0.10928300	1.79450400	-0.44519900
C	0.97806600	2.65542200	-0.53476100
C	0.51883800	4.03521500	-0.66280500
C	-0.89239800	3.99076100	-0.59263600
C	-5.43724900	1.11208700	-0.22184400
C	-6.60882900	0.33980900	-0.28145900
C	-6.55184800	-1.07227000	-0.38252600
C	-5.32203600	-1.74918700	-0.42609200
C	1.20250500	5.25162800	-0.82039900
C	0.43218500	6.42258400	-0.90658800
C	-0.98254700	6.37768900	-0.83768300
C	-1.66444100	5.16021300	-0.68043000
C	5.36912700	-1.37676300	-0.47998700

Appendix D: Cartesian Coordinates

C	6.54330100	-0.60615700	-0.49632500
C	6.49185900	0.80961500	-0.47668700
C	5.26485500	1.49198600	-0.44050200
H	-2.38268100	-5.48138200	-1.23924900
H	-1.03061300	-7.57129400	-1.62954800
H	1.45616200	-7.50285800	-1.58649600
H	2.67620600	-5.34117100	-1.15210500
H	-5.47184400	2.20472300	-0.15799400
H	-7.58573600	0.83614400	-0.25423000
H	-7.48575500	-1.64396300	-0.43213900
H	-5.26875200	-2.83910100	-0.51724200
H	2.29593600	5.27773900	-0.87318100
H	0.93178500	7.39036200	-1.03023600
H	-1.55226800	7.31135100	-0.90920200
H	-2.75724100	5.11619700	-0.62695000
H	5.39925400	-2.47103100	-0.50830200
H	7.51800500	-1.10650100	-0.52917100
H	7.42759000	1.38016600	-0.49480200
H	5.21540900	2.58588200	-0.43818100
Co	-0.01706700	-0.11918200	-0.05567000
C	0.37894500	0.60231800	1.91591700
C	-0.56964400	-1.32967800	2.04563700
C	0.77021900	-1.62139000	2.63918200
C	1.44577000	-0.26570500	2.57553800
C	-0.85787800	0.04628100	2.62804300
C	0.87744400	-0.73685300	3.92170600
C	-0.47361900	-0.05525500	4.13303100
H	0.54307300	1.68800100	1.86549000
H	-1.32979200	-2.08612800	1.82199300
H	1.31134900	-2.56347500	2.52924200
H	2.51954000	-0.15669900	2.40687600
H	-1.82342800	0.50447800	2.38013200
H	1.54023000	-1.02731500	4.74451600
H	-0.38389400	0.93707500	4.61410600
H	-1.18668800	-0.67381400	4.71027100

61

C	0.20440300	-0.34591200	0.00000000
C	0.97564100	-1.51890300	-0.01329800
C	2.39206300	-1.46640400	-0.00812800
C	3.07373700	-0.23928400	0.00999400
C	2.30004100	0.93279900	0.01744900
C	0.88860500	0.88054700	0.01270400
C	2.65859400	2.34689500	0.03801600
N	1.51242500	3.13749500	0.05359500
C	0.42683400	2.26433100	0.03024800
N	-0.86421600	2.57799200	0.03248500
N	3.92303900	2.75439200	0.05739900
C	-1.27250000	3.84085300	0.08265800
C	4.23111500	4.04513500	0.11008500
N	-0.48333800	4.98946400	0.10795500
C	-1.35812400	6.07128200	0.15807500

Appendix D: Cartesian Coordinates

C	-2.74117000	5.60614900	0.18149000
C	-2.68688100	4.19576700	0.13263700
C	5.61389800	4.50466800	0.18858000
C	5.55966000	5.91385200	0.25107000
C	4.14589600	6.27306000	0.20193500
N	3.35620300	5.12993400	0.11479700
N	-1.04539100	7.36161700	0.19776200
N	3.74238000	7.53629800	0.25650300
C	0.22074900	7.76317200	0.21242900
N	1.36658100	6.97273500	0.15890800
C	2.45189000	7.84471300	0.23280600
C	1.98908100	9.22567400	0.32600700
C	0.57859500	9.17441400	0.31038700
C	-3.96780900	6.28682200	0.24631100
C	-5.13932700	5.51307500	0.25591100
C	-5.08477500	4.09767900	0.20633700
C	-3.85702400	3.41939100	0.14682000
C	2.67349000	10.44758800	0.42837300
C	1.90230500	11.61828100	0.50771200
C	0.48604300	11.56669700	0.49129200
C	-0.19557500	10.34299100	0.39556800
C	6.83952700	3.81965200	0.21889300
C	8.01054900	4.58933600	0.30697800
C	7.95603600	6.00421500	0.36938100
C	6.72877400	6.68593800	0.34510500
H	-0.89014900	-0.37771400	-0.00068900
H	0.47604400	-2.49443000	-0.02670400
H	2.96290700	-2.40208600	-0.01752800
H	4.16760500	-0.18950400	0.01744000
H	-4.00104400	7.38056000	0.28775400
H	-6.11513200	6.00998400	0.30404600
H	-6.01918300	3.52479100	0.21682100
H	-3.80540100	2.32615000	0.11221800
H	3.76798900	10.47752500	0.44517200
H	2.40187700	12.59077100	0.58616600
H	-0.08487200	12.50009500	0.55678600
H	-1.28943100	10.29333600	0.38739700
H	6.87253800	2.72598200	0.17490100
H	8.98578500	4.08946800	0.32984000
H	8.88992600	6.57376800	0.43959800
H	6.67681100	7.77853100	0.39632200
Co	1.43523400	5.06002900	-0.02833900
C	2.19370000	7.01803300	-2.84854000
C	1.29417700	4.94882600	-2.03283600
C	2.57314200	4.64021100	-2.78652000
C	3.13332600	5.97905800	-3.31184800
C	0.89571600	6.24301500	-2.80494000
C	2.28991600	5.04816400	-4.23382000
C	0.87297000	5.64114200	-4.26863300
H	2.31057000	8.09970600	-2.94293900
H	0.53893800	4.15026200	-2.12993800
H	3.22503300	3.79260100	-2.56228600
H	4.20211900	6.12842400	-3.48246700

Appendix D: Cartesian Coordinates

H	-0.01860400	6.76062300	-2.48666900
H	2.74558900	4.51521300	-5.07451000
H	0.74988500	6.42809700	-5.03526200
H	0.08407200	4.87778700	-4.40414900

TS (61-62)

C	0.20097000	-0.36373700	0.07863100
C	0.96979500	-1.53866800	0.07961200
C	2.38607500	-1.48900800	0.07293300
C	3.07018700	-0.26284700	0.06477500
C	2.29897800	0.91064600	0.05820800
C	0.88747400	0.86121800	0.06552900
C	2.66003000	2.32487700	0.05413100
N	1.51591800	3.11777700	0.06579200
C	0.42857300	2.24668200	0.06251700
N	-0.86204700	2.56273900	0.05957400
N	3.92544600	2.73066500	0.05781200
C	-1.27016200	3.82692700	0.08761000
C	4.23543400	4.02202000	0.10385900
N	-0.48082600	4.97474500	0.10044700
C	-1.35448300	6.05733400	0.12527800
C	-2.73883100	5.59437200	0.13995900
C	-2.68531900	4.18317000	0.11732300
C	5.61962800	4.48015100	0.17051900
C	5.56673400	5.88945200	0.23748700
C	4.15239700	6.24864900	0.20307800
N	3.36203200	5.10700200	0.11553600
N	-1.03967500	7.34777000	0.15923000
N	3.74871900	7.51194900	0.27683800
C	0.22663000	7.74691000	0.19471100
N	1.37298800	6.95439900	0.14696300
C	2.45799900	7.82237000	0.26320200
C	1.99616100	9.20223800	0.37595900
C	0.58575300	9.15502600	0.32565600
C	-3.96537800	6.27686100	0.17954100
C	-5.13793800	5.50429500	0.19025400
C	-5.08421300	4.08841400	0.16683000
C	-3.85624100	3.40825100	0.13282300
C	2.68057700	10.42080200	0.51693400
C	1.91036000	11.59155500	0.60114500
C	0.49459000	11.54384300	0.55135100
C	-0.18725200	10.32418900	0.41628800
C	6.84504300	3.79438600	0.18968400
C	8.01749700	4.56295900	0.27033400
C	7.96440600	5.97758100	0.33747100
C	6.73729300	6.66017900	0.32534300
H	-0.89363400	-0.39324700	0.08724000
H	0.46809700	-2.51319500	0.08745800
H	2.95515200	-2.42582700	0.07569000
H	4.16419800	-0.21523300	0.06342000
H	-3.99811200	7.37120800	0.20133200
H	-6.11369000	6.00286000	0.21878400

Appendix D: Cartesian Coordinates

H	-6.01917300	3.51640200	0.17764500
H	-3.80535800	2.31449500	0.11869800
H	3.77448000	10.44764400	0.55940700
H	2.41006600	12.56107100	0.70965300
H	-0.07562800	12.47731000	0.62169200
H	-1.28073100	10.27754400	0.38211200
H	6.87688900	2.70073500	0.14363500
H	8.99249900	4.06228400	0.28427100
H	8.89916100	6.54637900	0.40238100
H	6.68673300	7.75262300	0.38178400
Co	1.43999800	5.04151100	-0.03577500
C	2.09325100	7.04326400	-2.91457500
C	1.28907500	4.90000300	-2.08069800
C	2.51458500	4.54164300	-2.83660100
C	3.08725600	6.21684000	-3.47628600
C	0.84956700	6.17327700	-2.90333100
C	2.39569400	5.09715200	-4.22941800
C	0.92877600	5.56113900	-4.34843000
H	2.24456200	7.96606300	-2.35317800
H	0.53698300	4.09170000	-2.09479000
H	3.26671700	3.80327100	-2.55009300
H	4.16567000	6.38594200	-3.50233600
H	-0.10474800	6.63405600	-2.61510300
H	2.91734100	4.60153200	-5.05714300
H	0.78228500	6.32197600	-5.13653700
H	0.22625300	4.72249600	-4.50343300

62

C	4.67928500	2.75422100	-0.21265000
C	5.02520400	4.11509200	-0.21646400
C	4.03102100	5.12482200	-0.22895100
C	2.66491400	4.80019100	-0.23756400
C	2.32156400	3.43869100	-0.23067500
C	3.31246800	2.43213100	-0.21901300
C	1.03504100	2.74861500	-0.24090600
N	1.22793100	1.37052400	-0.22965800
C	2.60287000	1.15620800	-0.21725900
N	3.24447200	-0.00677200	-0.20755000
N	-0.11861600	3.40754400	-0.26980300
C	2.58564200	-1.16039100	-0.20191400
C	-1.28228500	2.76712500	-0.30809100
N	1.20760000	-1.35401400	-0.21038900
C	0.99362800	-2.72934800	-0.20418200
C	2.26947900	-3.43856100	-0.18489100
C	3.27557400	-2.44694000	-0.18699100
C	-2.55695100	3.47560100	-0.37002800
C	-3.56249600	2.48400800	-0.40662300
C	-2.87415100	1.19764500	-0.36385200
N	-1.49620800	1.39108700	-0.30352800
N	-0.17006400	-3.37070000	-0.22585000
N	-3.53187000	0.04331300	-0.38258900
C	-1.32404300	-2.71334200	-0.27385900

Appendix D: Cartesian Coordinates

N	-1.51714000	-1.33404200	-0.28688000
C	-2.89200900	-1.12071400	-0.34986600
C	-3.59970000	-2.39687400	-0.37691700
C	-2.60925600	-3.40302400	-0.32754900
C	2.59242700	-4.80508500	-0.17342200
C	3.95345500	-5.15003700	-0.16064700
C	4.96276300	-4.15533200	-0.16216800
C	4.63736300	-2.78949000	-0.17663100
C	-4.96503200	-2.71988300	-0.43691600
C	-5.30992300	-4.08077100	-0.44411700
C	-4.31627400	-5.09011300	-0.39497000
C	-2.95173000	-4.76487300	-0.33756300
C	-2.87899400	4.84224800	-0.39735500
C	-4.23852100	5.18718600	-0.45895700
C	-5.24725400	4.19237300	-0.49517100
C	-4.92278000	2.82663100	-0.47077300
H	5.44082600	1.96737700	-0.20552900
H	6.08243400	4.40434800	-0.21117300
H	4.33675900	6.17740900	-0.23306500
H	1.89032100	5.57408200	-0.24965400
H	1.80631100	-5.56737400	-0.17463100
H	4.24328300	-6.20707500	-0.15041700
H	6.01550100	-4.46042700	-0.15328700
H	5.41074100	-2.01425700	-0.18076500
H	-5.72614000	-1.93365200	-0.47609000
H	-6.36600700	-4.37070900	-0.48913600
H	-4.62141000	-6.14284400	-0.40297600
H	-2.17745300	-5.53830100	-0.30128700
H	-2.09316600	5.60438000	-0.37131200
H	-4.52774100	6.24421300	-0.48060800
H	-6.29885700	4.49756000	-0.54402600
H	-5.69556900	2.05146100	-0.50022500
Co	-0.14463200	0.01894100	-0.21183500
C	-0.51661300	0.71420700	3.03687200
C	-0.40952800	-0.63519600	2.99782600
C	0.74906100	-1.02625100	3.94744900
C	0.49881900	0.05639600	5.05496900
C	0.57039700	1.22710300	4.01304300
C	1.95195900	0.89657000	3.39948100
C	2.05875300	-0.44754500	3.36094300
H	-1.22013900	1.35240700	2.49650300
H	-1.01043000	-1.34480700	2.42383100
H	0.77964300	-2.08230100	4.25579900
H	1.30392200	0.09803500	5.81027100
H	-0.48909600	-0.03615400	5.54164700
H	0.43616000	2.25540900	4.38171900
H	2.87164900	-1.04956800	2.94618600
H	2.65683900	1.64221700	3.02175700

M06**59**

C	4.76789900	2.74541400	0.00036500
---	------------	------------	------------

Appendix D: Cartesian Coordinates

C	5.09997000	4.09513600	0.00042300
C	4.10736700	5.09014100	0.00041600
C	2.75684500	4.76133100	0.00035300
C	2.42764300	3.40892900	0.00028600
C	3.41471800	2.41947200	0.00029200
C	1.15571800	2.71551600	0.00019000
N	1.36090000	1.35763500	0.00019200
C	2.71829200	1.14922000	0.00020100
N	3.35582200	-0.00401400	0.00018000
N	0.00401500	3.35579700	0.00016400
C	2.71552600	-1.15571500	0.00013800
C	-1.14922400	2.71827900	0.00013400
N	1.35765200	-1.36088400	0.00017700
C	1.14922400	-2.71828200	0.00012400
C	2.41947100	-3.41471300	0.00012100
C	3.40893400	-2.42764300	0.00012800
C	-2.41947000	3.41471300	0.00013400
C	-3.40893400	2.42764400	0.00014200
C	-2.71552800	1.15571500	0.00015000
N	-1.35765100	1.36088500	0.00018300
N	-0.00401400	-3.35579600	0.00015800
N	-3.35582100	0.00401500	0.00019100
C	-1.15571900	-2.71551500	0.00018900
N	-1.36090000	-1.35763600	0.00019300
C	-2.71829200	-1.14922100	0.00020800
C	-3.41471800	-2.41947200	0.00029800
C	-2.42764200	-3.40892900	0.00028900
C	2.74540600	-4.76789600	0.00011200
C	4.09512600	-5.09997400	0.00009700
C	5.09013700	-4.10737700	0.00010400
C	4.76133500	-2.75685200	0.00012500
C	-4.76789900	-2.74541500	0.00037400
C	-5.09996900	-4.09513600	0.00043100
C	-4.10736600	-5.09014200	0.00042100
C	-2.75684400	-4.76133200	0.00035500
C	-2.74540300	4.76789600	0.00012700
C	-4.09512300	5.09997600	0.00011500
C	-5.09013500	4.10738000	0.00012200
C	-4.76133400	2.75685500	0.00014100
H	5.52884100	1.96715500	0.00036900
H	6.14785300	4.39110400	0.00047500
H	4.40586500	6.13730700	0.00046300
H	1.98040400	5.52413100	0.00034600
H	1.96714400	-5.52883400	0.00010700
H	4.39108900	-6.14785900	0.00008100
H	6.13730100	-4.40588000	0.00009400
H	5.52413800	-1.98041600	0.00013200
H	-5.52884100	-1.96715600	0.00038000
H	-6.14785300	-4.39110500	0.00048500
H	-4.40586400	-6.13730700	0.00046800
H	-1.98040300	-5.52413100	0.00034500
H	-1.96714000	5.52883300	0.00012100
H	-4.39108400	6.14786100	0.00010100

Appendix D: Cartesian Coordinates

H	-6.13729900	4.40588400	0.00011500
H	-5.52413800	1.98041900	0.00014900
Co	0.00000000	0.00000000	0.00019100
C	-0.15221100	0.25733100	10.87672200
C	-1.56412400	0.78559200	10.89728100
C	-2.10316500	-0.65639100	10.93066300
C	-0.69133800	-1.18470000	10.91004700
C	-0.70109200	0.89265300	12.13081300
C	-1.50316700	-1.25286100	12.18048400
C	-1.08218000	-0.16482300	13.13786500
H	0.71204800	0.62205700	10.32955600
H	-1.99033100	1.63325300	10.36890500
H	-2.98884200	-1.03725300	10.43078200
H	-0.28644200	-2.04854100	10.39121000
H	-0.33062900	1.87095200	12.43068200
H	-1.86056200	-2.22112800	12.52535000
H	-0.23221100	-0.46807900	13.76566200
H	-1.90628500	0.15830000	13.78981900

TS (59-61)

C	-1.34450800	-5.38475100	-0.48836200
C	-0.58618300	-6.54746600	-0.57050200
C	0.81617100	-6.49903000	-0.64442900
C	1.49643400	-5.28648300	-0.63789000
C	0.73477300	-4.12496900	-0.55248000
C	-0.66052300	-4.17290000	-0.47919800
C	1.09550500	-2.71962900	-0.52678300
N	-0.03344700	-1.94784700	-0.44130500
C	-1.11023600	-2.79478300	-0.40805000
N	-2.38678600	-2.47393800	-0.31886100
N	2.34870300	-2.31260700	-0.57937800
C	-2.79689100	-1.22060700	-0.27172200
C	2.66398200	-1.03133000	-0.59771400
N	-2.02779600	-0.08602500	-0.28491300
C	-2.87657100	0.98762200	-0.20798300
C	-4.25200300	0.52928000	-0.14240700
C	-4.20140000	-0.86715700	-0.18598300
C	4.03678700	-0.57367200	-0.70879800
C	3.98079200	0.82295900	-0.74530000
C	2.57652500	1.17531800	-0.64717500
N	1.81439800	0.04087000	-0.54538200
N	-2.55841400	2.26699200	-0.20932800
N	2.16265400	2.42767900	-0.66506900
C	-1.30912200	2.67373300	-0.33283400
N	-0.18184000	1.90083800	-0.42543100
C	0.88627700	2.74774200	-0.57398800
C	0.43176100	4.12556600	-0.57259800
C	-0.95651000	4.07869900	-0.41177100
C	-5.46462800	1.20742400	-0.06284000
C	-6.62489900	0.44211300	-0.02348600
C	-6.57366500	-0.96148900	-0.06651700
C	-5.36085600	-1.63595600	-0.15019100

Appendix D: Cartesian Coordinates

C	1.10602300	5.33753000	-0.69252000
C	0.34590400	6.50070300	-0.64467500
C	-1.04945500	6.45317200	-0.48417700
C	-1.72049000	5.24125600	-0.36781800
C	5.24939600	-1.25182600	-0.78923300
C	6.40520100	-0.48667000	-0.90128000
C	6.34869400	0.91685400	-0.93820200
C	5.13511800	1.59137100	-0.86318500
H	-2.43146000	-5.41126100	-0.43321200
H	-1.08503800	-7.51546600	-0.57943800
H	1.37666200	-7.43048200	-0.70922100
H	2.58231200	-5.23700100	-0.69824100
H	-5.49350900	2.29533800	-0.03345700
H	-7.59333000	0.93612000	0.04032000
H	-7.50343700	-1.52758300	-0.03523900
H	-5.30970200	-2.72275400	-0.18736100
H	2.18694900	5.36315200	-0.82012400
H	0.83711000	7.46850400	-0.73441900
H	-1.61189500	7.38514800	-0.45247400
H	-2.80127300	5.19285900	-0.24642500
H	5.28146200	-2.33982300	-0.76521700
H	7.37363900	-0.98077900	-0.96429700
H	7.27447500	1.48305400	-1.02948400
H	5.07962500	2.67816500	-0.89570300
Co	-0.09621100	-0.02377800	-0.28736800
C	1.00459400	1.23587100	2.35715800
C	-0.17476200	-0.38581200	2.08567500
C	1.09461500	-1.03493200	2.59530600
C	1.96122000	0.17132400	2.77600600
C	-0.26925300	0.80471400	2.99956800
C	1.32239100	-0.49946200	3.99503600
C	0.10897600	0.31110300	4.40052800
H	1.21581700	2.18234700	1.86826500
H	-1.07457300	-0.94152000	1.82186000
H	1.47699200	-1.99327500	2.25425500
H	3.02936000	0.18499400	2.58159000
H	-1.14147300	1.45047800	2.87475600
H	1.93608500	-1.04325300	4.71000100
H	0.35510400	1.13599200	5.08369300
H	-0.68058600	-0.30665000	4.85017200

61

C	0.20834900	-0.30857100	0.00002900
C	0.97870100	-1.46515700	-0.02771200
C	2.38322000	-1.40596200	-0.03654200
C	3.05311900	-0.18850200	-0.01807000
C	2.27868700	0.96810500	0.00635800
C	0.88218200	0.90954100	0.01504600
C	2.62683700	2.37448100	0.03300600
N	1.48997400	3.14074700	0.06308500
C	0.41886100	2.28237600	0.04629500
N	-0.86145700	2.59374000	0.06031400

Appendix D: Cartesian Coordinates

N	3.87788000	2.79098300	0.02974500
C	-1.27735700	3.84268000	0.11474700
C	4.18401300	4.07078300	0.08230600
N	-0.51084100	4.98164000	0.14673900
C	-1.37000500	6.04901900	0.18621200
C	-2.74318500	5.58453000	0.19547500
C	-2.68414800	4.18892500	0.15122100
C	5.55785200	4.53335400	0.11269600
C	5.49818500	5.92638000	0.19747600
C	4.09027600	6.27338900	0.20667300
N	3.32358800	5.13925700	0.12950100
N	-1.05962000	7.32988700	0.22028400
N	3.67980800	7.52209400	0.28686400
C	0.19228100	7.73837100	0.24503800
N	1.32876800	6.96948600	0.21959900
C	2.39886200	7.82644700	0.28157700
C	1.93666200	9.19937800	0.33785200
C	0.54118600	9.14406400	0.30959600
C	-3.96108800	6.25709900	0.24212700
C	-5.11765400	5.48607300	0.23958900
C	-5.05803500	4.08233600	0.19484700
C	-3.84038600	3.41375300	0.15170300
C	2.61286800	10.41406200	0.40670500
C	1.84424900	11.57189200	0.44443900
C	0.43999900	11.51587000	0.41792600
C	-0.23187100	10.30080700	0.35236700
C	6.77602500	3.86048100	0.08656800
C	7.93258000	4.63007100	0.14249300
C	7.87217800	6.03169100	0.22713200
C	6.65347500	6.69987800	0.25784800
H	-0.87966800	-0.34355900	0.00914900
H	0.48867000	-2.43754800	-0.04194900
H	2.95302100	-2.33371000	-0.05731100
H	4.14019600	-0.13096300	-0.02199800
H	-3.99607400	7.34455000	0.27865000
H	-6.09014100	5.97492700	0.27360600
H	-5.98561700	3.51188600	0.19514100
H	-3.78264100	2.32720300	0.11878900
H	3.70081400	10.44518100	0.42991500
H	2.33550100	12.54236600	0.49671500
H	-0.12843600	12.44414600	0.44993900
H	-1.31889200	10.24563800	0.33365200
H	6.81158600	2.77417800	0.02473400
H	8.90546100	4.14121300	0.12185700
H	8.79951200	6.60091900	0.27056300
H	6.59434100	7.78468800	0.32636600
Co	1.40615600	5.05946200	0.00226000
C	2.46494400	6.90875300	-2.66723100
C	1.27864600	4.98222600	-1.96719800
C	2.51335900	4.52453500	-2.69859200
C	3.26287900	5.76578400	-3.14593300
C	1.08261300	6.31574700	-2.71088600
C	2.35080900	5.01410500	-4.11877400

Appendix D: Cartesian Coordinates

C	1.04486700	5.79001200	-4.17535700
H	2.70531300	7.95820800	-2.82491900
H	0.43053800	4.29668100	-2.10786600
H	3.02961100	3.59062800	-2.48987600
H	4.34315400	5.77003300	-3.26512300
H	0.23942400	6.94259800	-2.40789500
H	2.75513200	4.45491400	-4.95924600
H	1.06287200	6.60952600	-4.90758800
H	0.17107100	5.15302100	-4.37367500

TS (61-62)

C	0.20987700	-0.32140600	0.07280300
C	0.98028400	-1.47821700	0.03857700
C	2.38381900	-1.41827600	-0.00168400
C	3.05286400	-0.19980700	-0.00881700
C	2.27866000	0.95643700	0.02178100
C	0.88245400	0.89710000	0.06221200
C	2.62584800	2.36442900	0.03160800
N	1.48908800	3.12879100	0.07563400
C	0.41872700	2.27107800	0.08895100
N	-0.86216500	2.58281700	0.11610200
N	3.87637300	2.78368000	0.00755600
C	-1.28099100	3.83257400	0.14890500
C	4.18337100	4.06429700	0.06944200
N	-0.51774800	4.97241900	0.15027500
C	-1.37611100	6.03921100	0.15484900
C	-2.75028300	5.57419300	0.17244800
C	-2.68957800	4.17759600	0.17385800
C	5.55778400	4.52708600	0.10295400
C	5.49718600	5.91869600	0.21605400
C	4.08822100	6.26334400	0.23304200
N	3.32435600	5.13116900	0.13367100
N	-1.06446700	7.32094400	0.16262700
N	3.67388400	7.51096100	0.33508000
C	0.18703100	7.73108400	0.20428900
N	1.32524300	6.96375500	0.19127100
C	2.39239100	7.81696800	0.31517100
C	1.92808700	9.18896900	0.38919500
C	0.53405400	9.13533400	0.30701600
C	-3.96896200	6.24588000	0.19484500
C	-5.12510100	5.47371100	0.21502900
C	-5.06381000	4.06979600	0.21579200
C	-3.84474900	3.40180800	0.19624200
C	2.60063000	10.40154700	0.51298100
C	1.83109200	11.55874000	0.55002900
C	0.42889000	11.50433300	0.46993900
C	-0.23973600	10.29159700	0.35061000
C	6.77670800	3.85628200	0.06242200
C	7.93307800	4.62535000	0.13139900
C	7.87176000	6.02480200	0.24410500
C	6.65237600	6.69117900	0.29036800
H	-0.87766900	-0.35705700	0.10671700

Appendix D: Cartesian Coordinates

H	0.49063500	-2.45092000	0.04455600
H	2.95401300	-2.34573400	-0.02616000
H	4.13963700	-0.14181300	-0.03628100
H	-4.00556200	7.33394100	0.19649700
H	-6.09814000	5.96245400	0.23167600
H	-5.99060300	3.49827000	0.23317800
H	-3.78573300	2.31477600	0.19877000
H	3.68690900	10.43170500	0.57888200
H	2.31996300	12.52723900	0.64451400
H	-0.14063600	12.43190800	0.50354700
H	-1.32541100	10.23767900	0.29179600
H	6.81314800	2.77127800	-0.01960100
H	8.90625700	4.13760500	0.09984600
H	8.79866600	6.59390100	0.29798800
H	6.59300700	7.77435400	0.38196900
Co	1.40394000	5.05090100	-0.00056500
C	2.44253000	6.90020300	-2.78676100
C	1.25794400	4.92723200	-2.07772300
C	2.40947200	4.37706700	-2.78202500
C	3.30108500	5.93879800	-3.32022800
C	1.08181200	6.25860900	-2.86960800
C	2.48265900	4.98764000	-4.13843700
C	1.14007000	5.69256200	-4.31379700
H	2.71412600	7.77284200	-2.20140700
H	0.38572000	4.26089200	-2.07125200
H	2.98662300	3.50041300	-2.49602700
H	4.38657300	5.91697000	-3.27913000
H	0.20966200	6.86560800	-2.61169200
H	2.95783000	4.43557600	-4.94856900
H	1.16885100	6.48359700	-5.07534900
H	0.32172600	4.99431700	-4.53531100

M06/6-31+G*, toluene**63**

Co	9.23050000	1.98849000	-5.93270200
N	9.21157900	3.16199400	-4.40793800
N	9.97366700	0.58645400	-4.84441300
N	8.48731800	3.39052300	-7.02098600
N	9.24938500	0.81497400	-7.45745700
C	8.77639600	4.46376400	-4.38916500
C	9.63074000	2.85197400	-3.13808000
C	10.27684800	0.66852900	-3.50812300
C	10.29858600	-0.68053200	-5.26099100
C	8.16243100	4.65751700	-6.60441600
C	8.18414900	3.30845100	-8.35728100
C	9.68452800	-0.48680800	-7.47622100
C	8.83016600	1.12497500	-8.72730100
C	8.91992600	5.01573000	-3.05643400
N	8.29076700	5.16442300	-5.39446900
C	9.45985800	3.99708500	-2.26577900
N	10.12358400	1.70667800	-2.71052500
C	10.81828800	-0.59347600	-3.04376500

Appendix D: Cartesian Coordinates

C	10.83202100	-1.44604800	-4.15156900
N	10.17021500	-1.18744900	-6.47093000
C	7.62912300	5.42307700	-7.71387000
C	7.64283900	4.57049900	-8.82167100
N	8.33736500	2.27028700	-9.15486500
C	9.54098400	-1.03877900	-8.80894800
C	9.00103400	-0.02014000	-9.59959800
C	8.62827900	6.26899600	-2.52430500
C	9.72816900	4.19390900	-0.91369600
C	11.27040600	-1.01765800	-1.79694800
C	11.29837000	-2.75440200	-4.05365900
C	7.16289100	6.73147100	-7.81180800
C	7.19081800	4.99471700	-10.06851100
C	9.83263800	-2.29204300	-9.34107700
C	8.73271300	-0.21696800	-10.95167800
C	8.89508500	6.46855200	-1.17453100
H	8.20793400	7.05684000	-3.14690900
C	9.43801500	5.44424300	-0.37949700
H	10.14868400	3.39536800	-0.30499300
C	11.73665300	-2.32354100	-1.69604800
H	11.25632800	-0.34739900	-0.93928800
C	11.75045700	-3.18083900	-2.81000900
H	11.30567100	-3.41188100	-4.92123500
C	6.71088900	7.15793700	-9.05547800
H	7.15560000	7.38895200	-6.94423400
C	6.72467500	6.30063500	-10.16943600
H	7.20488000	4.32445300	-10.92616700
C	9.56580500	-2.49160800	-10.69084400
H	10.25299500	-3.07988400	-8.71847700
C	9.02285800	-1.46730600	-11.48587500
H	8.31218400	0.58156800	-11.56037900
H	8.68091200	7.43493500	-0.72091700
H	9.63350900	5.63774300	0.67400900
H	12.09876600	-2.69300600	-0.73797400
H	12.12298600	-4.19717500	-2.69246800
H	6.33844200	8.17430200	-9.17303900
H	6.36263100	6.67012400	-11.12752600
H	9.77997200	-3.45799500	-11.14445800
H	8.82734600	-1.66081200	-12.53937600
C	-0.34619900	-0.64530200	-1.37711100
C	-1.19703000	0.42375400	-2.05625600
C	-1.31028600	-0.48132500	-3.31044600
C	-0.47587700	-1.53580700	-2.61912000
C	-1.74664600	-0.41684700	-0.90959500
C	-1.95837800	-1.74224300	-2.76578900
C	-2.67271100	-1.46855100	-1.46609700
H	0.54424500	-0.46995800	-0.78232900
H	0.29371500	-2.17681300	-3.03963700
H	-1.91830900	0.07757200	0.04383200
H	-2.32339700	-2.46492100	-3.49345100
H	-2.71788400	-2.35371400	-0.81674200
H	-3.69156700	-1.08905300	-1.61867400
C	-1.02337500	1.82843600	-1.99893100

Appendix D: Cartesian Coordinates

N	-0.87640200	2.98365500	-1.94752900
C	-1.33368500	-0.04899100	-4.71706800
C	-0.80471700	-0.86624000	-5.72634300
C	-1.90973700	1.16415600	-5.09157500
C	-0.86083200	-0.48837200	-7.05693300
H	-0.33547700	-1.81529300	-5.46283300
C	-1.96359500	1.56400100	-6.42700100
H	-2.32885300	1.82443900	-4.33215600
C	-1.43990100	0.73346800	-7.41700300
H	-0.44938800	-1.12115300	-7.84159400
H	-2.41416600	2.52208500	-6.67420400
O	-1.43912100	1.02239500	-8.74449800
C	-1.99987200	2.25087600	-9.15415200
H	-1.89489600	2.28773000	-10.24097900
H	-3.06592700	2.31135500	-8.89075100
H	-1.46500200	3.10233100	-8.70894700

TS (63-64)_i

C	-1.52889171	-5.53046445	0.86785290
C	-0.75816980	-6.68324528	0.97221496
C	0.64604369	-6.62234534	0.98820194
C	1.31550130	-5.40692717	0.89998267
C	0.54126448	-4.25444801	0.79410761
C	-0.85618287	-4.31470349	0.77856460
C	0.88906386	-2.85020403	0.68751072
N	-0.24775991	-2.09022081	0.61185571
C	-1.31987559	-2.94533786	0.65925594
N	-2.60027425	-2.63606723	0.59052529
N	2.14214664	-2.43415807	0.65957531
C	-3.02134286	-1.38992562	0.47690656
C	2.45171445	-1.15394641	0.59454755
N	-2.25906853	-0.25115767	0.41681258
C	-3.11372807	0.81046903	0.27775268
C	-4.48573948	0.34162586	0.24369904
C	-4.42723303	-1.04996045	0.37680018
C	3.82450580	-0.68266868	0.61701108
C	3.75724350	0.71278858	0.59345059
C	2.34736810	1.05240528	0.56248600
N	1.58953538	-0.08956689	0.53113452
N	-2.80164301	2.09205917	0.21887534
N	1.92355868	2.29951954	0.58200016
C	-1.55512450	2.51176154	0.31467184
N	-0.41824023	1.74983166	0.39370025
C	0.64366524	2.60678545	0.50862865
C	0.17579563	3.97993042	0.52092704
C	-1.21401275	3.92050563	0.38403392
C	-5.70384027	1.00633504	0.12589497
C	-6.86004060	0.23422088	0.14101429
C	-6.80080312	-1.16405263	0.27407274
C	-5.58395766	-1.82518734	0.39514759
C	0.84327651	5.19629055	0.62639961
C	0.07263063	6.35380535	0.59679269

Appendix D: Cartesian Coordinates

C	-1.32497222	6.29518400	0.45768921
C	-1.98806158	5.07681194	0.34881033
C	5.04558045	-1.34780360	0.64484715
C	6.19800091	-0.56904991	0.63291093
C	6.13020717	0.83342278	0.59545388
C	4.90705248	1.49563346	0.57888648
H	-2.61683696	-5.56988413	0.85608357
H	-1.24816955	-7.65300011	1.04391123
H	1.21655395	-7.54596777	1.07191231
H	2.40266149	-5.35115131	0.91316668
H	-5.74234887	2.08995681	0.02726536
H	-7.83133380	0.71802613	0.05040741
H	-7.72735327	-1.73589827	0.28404370
H	-5.53014583	-2.90721622	0.50239237
H	1.92763761	5.23411578	0.72282386
H	0.55919600	7.32513353	0.68020189
H	-1.89638708	7.22241742	0.44038228
H	-3.07059524	5.02323994	0.24514815
H	5.09180696	-2.43531601	0.66149000
H	7.17339476	-1.05271390	0.64325016
H	7.05429193	1.40901180	0.57833209
H	4.84355385	2.58270808	0.55071534
Co	-0.32900297	-0.17269639	0.39502231
C	0.63560934	0.71749810	-2.93072105
C	-0.50045826	-0.77582914	-2.18905031
C	0.71950177	-1.57761160	-2.55414772
C	1.58976411	-0.45695232	-3.07347032
C	-0.64073197	0.09675379	-3.39609965
C	0.90627629	-1.44935765	-4.04135210
C	-0.29871898	-0.75162618	-4.62414719
H	-1.37092238	-1.15971822	-1.66367747
H	1.13880084	-2.39280117	-1.97024774
H	-1.52478022	0.73507532	-3.43116138
H	1.52664696	-2.14969214	-4.59644435
H	-0.05547458	-0.14219185	-5.50451762
H	-1.09975902	-1.45847702	-4.87888075
C	0.93140036	2.10805584	-2.78531852
C	-0.07521123	3.08340183	-2.95165612
C	2.24329498	2.57545873	-2.52806009
C	0.19893443	4.43991388	-2.88750324
H	-1.10371352	2.77387565	-3.13281113
C	2.52771170	3.92361947	-2.47878826
H	3.05572570	1.86817669	-2.37033494
C	1.51022606	4.87078253	-2.65500416
H	-0.61408749	5.15131569	-3.01192073
H	3.54014674	4.27483623	-2.28536569
C	3.00057649	-0.47030326	-2.89605155
N	4.15632485	-0.52136350	-2.75821575
O	1.88677178	6.16620059	-2.57924534
C	0.91170795	7.16341130	-2.81376586
H	0.10819133	7.11660081	-2.06403561
H	1.43111926	8.12073512	-2.72942305
H	0.48410778	7.06837234	-3.82196988

Appendix D: Cartesian Coordinates

TS (63-64)_ii

C	-1.82098700	-5.43112600	0.71328900
C	-1.18875700	-6.66463200	0.81293900
C	0.21193500	-6.76166300	0.89538900
C	1.01472900	-5.62746200	0.88008800
C	0.37933700	-4.39163900	0.77911700
C	-1.01449600	-4.29514700	0.69783800
C	0.88393200	-3.03467400	0.73977800
N	-0.15882600	-2.14935000	0.64185200
C	-1.31896200	-2.88233800	0.60582900
N	-2.55312900	-2.42884800	0.48102600
N	2.17395100	-2.75612900	0.79966600
C	-2.82623700	-1.14351800	0.38535300
C	2.62425500	-1.51825100	0.79596600
N	-1.93765400	-0.09451000	0.39894300
C	-2.66251900	1.06062600	0.27657300
C	-4.07505400	0.75048600	0.16703900
C	-4.17864500	-0.64240700	0.23954100
C	4.03319600	-1.20285300	0.93819100
C	4.12296400	0.19193000	0.93913800
C	2.77030000	0.68747500	0.77877700
N	1.89175200	-0.35980700	0.69583400
N	-2.21163300	2.30166300	0.28056100
N	2.49480300	1.97679100	0.74409000
C	-0.93065700	2.57790700	0.40757600
N	0.10979000	1.68958300	0.51377000
C	1.26367600	2.42402200	0.61520000
C	0.95870100	3.84069300	0.55909000
C	-0.42848100	3.93889600	0.43705000
C	-5.20289200	1.55453400	0.02519600
C	-6.43767300	0.91899500	-0.04382800
C	-6.54180700	-0.48093700	0.02957000
C	-5.41406600	-1.28129600	0.17312700
C	1.77076800	4.96915100	0.55994900
C	1.14325900	6.20561800	0.44295300
C	-0.25324600	6.30481600	0.33039700
C	-1.06028000	5.17170500	0.32550600
C	5.16520700	-2.00032000	1.08291000
C	6.38778900	-1.35404200	1.23657200
C	6.47480600	0.04875300	1.24684400
C	5.34347300	0.84204600	1.09170600
H	-2.90471200	-5.34813600	0.65104800
H	-1.78545600	-7.57527800	0.82917200
H	0.67182700	-7.74549100	0.97401200
H	2.09936700	-5.69443800	0.94619300
H	-5.11351800	2.63806100	-0.03006600
H	-7.34296100	1.51344800	-0.15605100
H	-7.52596100	-0.94343200	-0.02650500
H	-5.48691500	-2.36587800	0.23310900
H	2.85323400	4.87956300	0.64068400
H	1.74234300	7.11479700	0.43417000

Appendix D: Cartesian Coordinates

H	-0.70868500	7.28936400	0.23666600
H	-2.14144500	5.24072000	0.22043400
H	5.08935400	-3.08648500	1.08524100
H	7.29524000	-1.94352100	1.36094700
H	7.44745400	0.52143400	1.38020300
H	5.40295700	1.92950500	1.08799700
Co	-0.02084400	-0.22915500	0.51238900
C	0.53460300	0.87995200	-2.97823800
C	-0.12509200	-0.97646400	-2.34878600
C	1.32248100	-1.26354100	-2.55947400
C	1.83329400	0.09535500	-2.99724300
C	-0.45631900	-0.11778000	-3.52237200
C	1.58549000	-1.00426300	-4.03188700
C	0.25999100	-0.75474200	-4.71652000
H	-0.83479200	-1.48452400	-1.70549900
H	1.91968700	-1.93088400	-1.94243100
H	-1.48670800	0.22329900	-3.63077900
H	2.43760100	-1.45451500	-4.53744600
H	0.34187800	-0.06457600	-5.56621200
H	-0.22815500	-1.68199700	-5.04522000
C	0.25434800	2.21555700	-2.73696400
N	-0.01721000	3.34619300	-2.56657600
C	3.18132400	0.60886700	-2.67358700
C	3.42709100	1.96524700	-2.42511200
C	4.27218000	-0.26491200	-2.63108200
C	4.70809800	2.42519700	-2.15797500
H	2.61137700	2.68707600	-2.43411100
C	5.56326100	0.18255900	-2.37165700
H	4.12451100	-1.33311900	-2.79854900
C	5.78602500	1.53939000	-2.13179800
H	4.88987400	3.47987900	-1.95598100
H	6.37667300	-0.53843800	-2.33956800
O	7.00260000	2.08010100	-1.85473000
C	8.12866800	1.23184100	-1.91447200
H	8.24362400	0.79397100	-2.91706500
H	8.99617900	1.85790800	-1.69195400
H	8.06361000	0.42327400	-1.17062600

64_i

C	0.25713300	-5.52753500	0.62805000
C	1.30485800	-6.43752600	0.71727100
C	2.63440800	-6.00903600	0.86928900
C	2.95242200	-4.65739700	0.93804100
C	1.90223400	-3.75059700	0.83981000
C	0.58051300	-4.17519100	0.68465900
C	1.86702300	-2.30181700	0.84487300
N	0.58065900	-1.85864700	0.66739600
C	-0.22315900	-2.97093200	0.59988700
N	-1.53531800	-3.00465200	0.49261600
N	2.94928600	-1.57667500	1.03513700
C	-2.25795800	-1.90207200	0.42729600
C	2.91419400	-0.26142400	1.00581600

Appendix D: Cartesian Coordinates

N	-1.80904100	-0.60671000	0.41281100
C	-2.91022100	0.20678000	0.29469900
C	-4.11705100	-0.59465000	0.26001500
C	-3.70397800	-1.92803700	0.34280800
C	4.09777100	0.54345400	1.23350100
C	3.70020600	1.87448400	1.08799100
C	2.28061700	1.84355000	0.79055100
N	1.83364200	0.54467500	0.74833000
N	-2.93173000	1.52139000	0.20924000
N	1.57749700	2.94191100	0.60824400
C	-1.83347200	2.24841000	0.26629400
N	-0.54281800	1.80497900	0.42223400
C	0.26881000	2.90937300	0.43829500
C	-0.52369100	4.11247700	0.28329500
C	-1.85403100	3.69392900	0.17763600
C	-5.46570200	-0.25948400	0.16718500
C	-6.38480600	-1.30234200	0.15722900
C	-5.96867800	-2.64289400	0.23955700
C	-4.62230600	-2.97475400	0.33429400
C	-0.18419000	5.46282600	0.24399600
C	-1.21845000	6.37859000	0.09021600
C	-2.55591200	5.95731300	-0.01609400
C	-2.89272500	4.60969900	0.02860900
C	5.41543200	0.20550500	1.52526600
C	6.32515400	1.24794400	1.66510600
C	5.92676500	2.58756200	1.51698100
C	4.60711800	2.92077300	1.22748400
H	-0.77398300	-5.85418300	0.50586100
H	1.09511800	-7.50448900	0.66368800
H	3.42741100	-6.75249000	0.92920200
H	3.97941100	-4.31319900	1.05080100
H	-5.78153900	0.78042300	0.10475800
H	-7.44836300	-1.08076900	0.08478000
H	-6.71809800	-3.43258700	0.22889000
H	-4.29125800	-4.00972100	0.39936000
H	0.85300000	5.78196300	0.33099100
H	-0.99312900	7.44316200	0.05267100
H	-3.33944600	6.70408800	-0.13390400
H	-3.92600100	4.27595400	-0.04903100
H	5.71750300	-0.83546100	1.62899800
H	7.36687000	1.02426100	1.89232700
H	6.66697400	3.37782700	1.63565800
H	4.29065900	3.95643200	1.11487100
Co	0.02431500	-0.03371400	0.42334600
C	0.00386600	-0.03938500	-1.54174700
C	-0.07411700	-1.38310600	-2.21850400
C	1.36458900	-1.76943400	-2.58271300
C	1.23789600	0.49037200	-2.29089200
C	0.38838500	-1.17243000	-3.62557800
C	0.77462100	0.28867100	-3.75973500
H	1.56746600	1.49869600	-2.02969300
H	0.03416500	-1.79211100	-4.44559400
H	1.58990900	0.45563300	-4.47667300

Appendix D: Cartesian Coordinates

H	-0.08067600	0.92379700	-4.02768000
C	1.71841100	-3.14867400	-2.66475700
N	1.97459200	-4.28233600	-2.73582600
H	-0.79827900	-2.15807400	-1.97859900
C	2.23503800	-0.63514700	-2.16864700
C	3.64387500	-0.54627800	-2.09365500
C	4.29391300	0.71344800	-2.08787500
C	4.47947700	-1.69299200	-1.98153100
C	5.67096300	0.83376200	-1.97028700
H	3.70279200	1.62442000	-2.17984900
C	5.84583100	-1.57615200	-1.85368900
H	4.03683800	-2.68797100	-1.97135100
C	6.45813700	-0.31281700	-1.83851400
H	6.11535800	1.82661700	-1.96222600
H	6.47543600	-2.45905600	-1.75358200
O	7.80664300	-0.30819500	-1.68281200
C	8.47238000	0.93637600	-1.70824600
H	8.13282900	1.58921100	-0.89044900
H	9.53488700	0.71737000	-1.57852100
H	8.32177000	1.44847900	-2.66975100
H	-0.88696300	0.56474400	-1.76600700

64_ii

C	-2.59603200	-5.58538400	1.14352800
C	-1.94375900	-6.79551300	1.34776800
C	-0.54858500	-6.85313400	1.51388100
C	0.22967900	-5.70196000	1.47987800
C	-0.42619400	-4.49077300	1.27272200
C	-1.81353000	-4.43374500	1.10735200
C	0.04944400	-3.12525200	1.18383300
N	-1.00455100	-2.27041100	0.98813800
C	-2.14320000	-3.03567000	0.92166200
N	-3.37877300	-2.62318400	0.71827300
N	1.32850700	-2.81602000	1.28313800
C	-3.68004000	-1.34847400	0.57853600
C	1.74861600	-1.56923500	1.23199000
N	-2.82017200	-0.27694200	0.60338100
C	-3.57486800	0.85545800	0.43965500
C	-4.97418400	0.50571400	0.30107900
C	-5.04087600	-0.88820200	0.38920400
C	3.15115200	-1.22033200	1.34996100
C	3.21499500	0.17321600	1.26901000
C	1.85055900	0.63184300	1.09780900
N	0.99009800	-0.43500000	1.06912300
N	-3.15520800	2.10620800	0.41900300
N	1.54680500	1.91049000	1.00762000
C	-1.88418500	2.41496800	0.56988300
N	-0.82590800	1.55116800	0.72392200
C	0.30569600	2.32039100	0.85027400
C	-0.03360300	3.72597100	0.77178100
C	-1.41715400	3.78744600	0.59217000
C	-6.11990500	1.27720800	0.12351600

Appendix D: Cartesian Coordinates

C	-7.33426400	0.60680700	0.03421600
C	-7.40177300	-0.79471800	0.12424500
C	-6.25675200	-1.56194900	0.30521500
C	0.74750900	4.87631200	0.81697900
C	0.09430800	6.09487400	0.67274000
C	-1.29798700	6.15790500	0.49339100
C	-2.07518200	5.00551700	0.45296800
C	4.29942100	-1.99066700	1.51084300
C	5.51453600	-1.31763400	1.58531900
C	5.57803700	0.08403800	1.50640000
C	4.42823100	0.85019500	1.34887200
H	-3.67593000	-5.53260600	1.01669000
H	-2.52037500	-7.71844000	1.38182100
H	-0.07289100	-7.81948800	1.67312400
H	1.30990500	-5.73821900	1.61017900
H	-6.05968300	2.36210800	0.05780900
H	-8.25271900	1.17417800	-0.10689800
H	-8.37138000	-1.28469300	0.05167700
H	-6.30175600	-2.64712300	0.37914100
H	1.82658100	4.81562600	0.94944100
H	0.66871200	7.01943100	0.69242300
H	-1.77365300	7.13043000	0.37846800
H	-3.15306100	5.04812300	0.30721500
H	4.24228900	-3.07588500	1.57611300
H	6.43620600	-1.88461700	1.70959400
H	6.54725600	0.57786400	1.56465800
H	4.46941600	1.93604300	1.28273700
Co	-0.90431200	-0.36821700	0.70724000
C	0.04213500	1.35950400	-2.15676100
C	-0.81167100	-0.66462900	-1.23407200
C	0.56292700	-0.93765200	-1.78385400
C	1.13579300	0.37849600	-2.32159900
C	-1.18061000	0.47347300	-2.19702900
C	0.49953700	-0.67957900	-3.25665200
C	-0.91658100	-0.22058900	-3.56326200
H	-1.49028600	-1.51913700	-1.36775700
H	1.24471600	-1.67924500	-1.37330200
H	-2.15261800	0.95918600	-2.08046100
H	1.12955600	-1.20939400	-3.96830000
H	-0.97339500	0.48563700	-4.40206200
H	-1.60561700	-1.05585000	-3.74921100
C	0.02183600	2.71534100	-2.44737700
N	-0.03753000	3.86907100	-2.66677100
C	2.58709700	0.66937300	-2.26563700
C	3.06742700	1.94732000	-1.94929000
C	3.52775800	-0.34369500	-2.46396400
C	4.42547400	2.19483200	-1.83003900
H	2.37482200	2.76844200	-1.76890600
C	4.89583100	-0.11288100	-2.33886900
H	3.19983100	-1.35530200	-2.70751600
C	5.35006300	1.16437900	-2.01014900
H	4.79164300	3.18763900	-1.57251800
H	5.58738700	-0.93923200	-2.48508300

Appendix D: Cartesian Coordinates

O	6.65653100	1.49495500	-1.83157900
C	7.62190100	0.47867700	-1.98929500
H	7.61037600	0.07031500	-3.01052100
H	8.59174300	0.94520900	-1.80022400
H	7.46517200	-0.33865100	-1.26891600

64_iii

C	-0.46811000	0.24953500	0.43340400
C	0.26858500	-0.87635300	0.78492500
C	1.64594400	-0.79167000	1.05679500
C	2.32433700	0.41902400	0.97508200
C	1.58437000	1.54065200	0.61293900
C	0.21512000	1.46003200	0.35182400
C	1.95569600	2.92652400	0.41653100
N	0.85756000	3.66174900	0.03715300
C	-0.21657300	2.80485400	0.02466300
N	-1.47958700	3.10209100	-0.19517600
N	3.17835900	3.35775200	0.62841400
C	-1.87068900	4.33635900	-0.43282400
C	3.50327600	4.62509200	0.48324900
N	-1.09444200	5.46780300	-0.48719100
C	-1.93013700	6.51794000	-0.78355300
C	-3.29181900	6.04547700	-0.92889700
C	-3.25455500	4.66830700	-0.69769900
C	4.84523300	5.10534300	0.73693300
C	4.80389800	6.49181700	0.56933100
C	3.43553800	6.81762000	0.22109100
N	2.68414100	5.66972100	0.13370800
N	-1.61174500	7.79074500	-0.88994800
N	3.02816100	8.06009100	0.07176300
C	-0.38377800	8.21985600	-0.67208500
N	0.72776100	7.46971000	-0.38232300
C	1.77444500	8.34464000	-0.21358200
C	1.32174700	9.70516100	-0.41196500
C	-0.04161700	9.62617800	-0.71125600
C	-4.48666100	6.70126100	-1.21345500
C	-5.64082200	5.92841600	-1.26806300
C	-5.60222000	4.54177400	-1.03936300
C	-4.40854300	3.89171100	-0.74883700
C	1.98209400	10.93059400	-0.35536100
C	1.23241800	12.07259100	-0.61039100
C	-0.13991200	11.99319100	-0.90898800
C	-0.79707500	10.76994700	-0.96070600
C	6.02369100	4.44851100	1.08244200
C	7.16172800	5.22838100	1.25331900
C	7.11948300	6.62490400	1.09154400
C	5.93993000	7.27704500	0.75125400
H	-1.53521600	0.19347700	0.22591200
H	-0.22794500	-1.84278500	0.85662600
H	2.18855900	-1.69449000	1.33465600
H	3.39284600	0.49286700	1.17325700
H	-4.50863000	7.77535400	-1.38894200

Appendix D: Cartesian Coordinates

H	-6.59487800	6.40225300	-1.49333300
H	-6.52699800	3.96971800	-1.09318700
H	-4.36910100	2.81860200	-0.57157300
H	3.04363100	10.98366900	-0.11974700
H	1.71236900	13.04936800	-0.57816000
H	-0.69425700	12.91009700	-1.10232900
H	-1.85922400	10.70078000	-1.18881600
H	6.04370300	3.36689000	1.20841400
H	8.10489500	4.75365000	1.51902500
H	8.03071200	7.20294200	1.23657900
H	5.89954700	8.35782800	0.62730200
Co	0.82826500	5.54285900	-0.37438100
C	2.51451800	7.14118700	-2.84350400
C	1.07913300	5.31193600	-2.38469500
C	2.41759800	4.74478100	-2.89817600
C	3.30507100	5.94468700	-3.17499200
C	1.13339100	6.66053000	-3.17763100
C	2.54904500	5.28162900	-4.32331000
C	1.35592700	6.16223500	-4.62846800
H	0.28935400	7.33922200	-3.03292100
H	3.06113600	4.66876700	-5.06208900
H	1.60357500	6.99562400	-5.30032600
H	0.49818700	5.61740400	-5.04319500
C	-0.04084900	4.51728500	-2.84224500
N	-0.92974500	3.89970800	-3.27399300
H	4.38723300	5.89166200	-3.09278300
C	2.96753900	3.38755400	-2.62730300
C	4.30496000	3.19624000	-2.26017900
C	2.17939400	2.24662700	-2.80081700
C	4.82464400	1.92838200	-2.04803700
H	4.95664400	4.05711300	-2.10953000
C	2.67963300	0.96587100	-2.57949200
H	1.14068200	2.34572200	-3.11374500
C	4.01050800	0.80290900	-2.19348500
H	5.86248100	1.78973200	-1.74788000
H	2.01668100	0.11197900	-2.70373200
O	4.59445100	-0.39726400	-1.93674500
C	3.81566500	-1.56148000	-2.11431700
H	3.47366400	-1.65719700	-3.15519200
H	4.46638200	-2.40454900	-1.86956800
H	2.94380000	-1.56664600	-1.44235500
H	2.85589300	8.16679900	-2.96489000

64_iv

C	-0.44653400	-5.81271600	1.42704300
C	0.48852100	-6.80271200	1.70781400
C	1.86447900	-6.51850800	1.73664200
C	2.34188100	-5.23700200	1.48388000
C	1.40275600	-4.25125300	1.19496500
C	0.03605000	-4.53383200	1.17088600
C	1.52937300	-2.83871500	0.89436800
N	0.29220900	-2.28765900	0.66541800

C

Appendix D: Cartesian Coordinates

C	-0.63142400	-3.28954900	0.84552400
N	-1.94175800	-3.20052900	0.76673000
N	2.69285300	-2.22175000	0.90906400
C	-2.54651500	-2.04495400	0.57077600
C	2.79088400	-0.91815200	0.74193500
N	-1.96697800	-0.81630600	0.41244000
C	-2.98554700	0.09956200	0.30391700
C	-4.26917000	-0.57142400	0.36084700
C	-3.99198000	-1.93066300	0.52239500
C	4.06151000	-0.22779400	0.82170600
C	3.78654400	1.12537000	0.60501200
C	2.35576800	1.22022000	0.40022900
N	1.78036300	-0.02348300	0.49174400
N	-2.88393000	1.40070300	0.15028200
N	1.75652000	2.36916600	0.16109800
C	-1.71519700	2.00436500	0.06482600
N	-0.46861200	1.43604800	0.12438900
C	0.44613300	2.45734600	0.04937800
C	-0.23394700	3.72459100	-0.12478600
C	-1.60255800	3.43745200	-0.10983000
C	-5.57438800	-0.10444200	0.24100300
C	-6.59596000	-1.04753600	0.28516100
C	-6.31800900	-2.41603800	0.44863600
C	-5.01128200	-2.87719500	0.57327400
C	0.23051400	5.03016000	-0.26840800
C	-0.71931600	6.03476600	-0.41152200
C	-2.09545800	5.74469300	-0.40413900
C	-2.55680800	4.44244200	-0.24950400
C	5.35845200	-0.67608200	1.05936800
C	6.37225500	0.27494800	1.06770900
C	6.09598100	1.63643400	0.84967300
C	4.79941700	2.08139600	0.61819700
H	-1.51379800	-6.02421200	1.39845100
H	0.15262200	-7.81900900	1.90723200
H	2.56710700	-7.31965000	1.96044900
H	3.40603800	-5.00865700	1.50635800
H	-5.77890400	0.95634900	0.10360400
H	-7.63158700	-0.72400600	0.18993200
H	-7.14359000	-3.12549900	0.47761200
H	-4.78777200	-3.93563500	0.69556600
H	1.29720300	5.24792400	-0.27021600
H	-0.39575500	7.06742200	-0.53185200
H	-2.80957100	6.55840500	-0.52023700
H	-3.62016500	4.20864000	-0.23777600
H	5.56247300	-1.73160900	1.23088000
H	7.40021100	-0.03567200	1.24745700
H	6.91576000	2.35290600	0.86481800
H	4.57778000	3.13434300	0.45267700
Co	-0.07270100	-0.44948900	0.20343500
C	2.41043700	-0.41456400	-2.17693900
C	0.01642700	-0.64860500	-1.88640800
C	0.62017200	-1.97677700	-2.36327500
C	2.13437000	-1.80570900	-2.55733800

Appendix D: Cartesian Coordinates

C	1.11418600	0.24109100	-2.55243000
C	1.21195400	-1.71306500	-3.75224000
C	1.02062000	-0.23569800	-4.03315300
H	3.38654600	0.06049700	-2.23112100
H	2.80351300	-2.64806600	-2.40218000
H	1.04109200	1.31925600	-2.39373100
H	1.16750700	-2.49265900	-4.50868900
H	1.84209000	0.17358600	-4.63699300
H	0.06633800	-0.00224900	-4.51873000
C	-1.36158100	-0.38431400	-2.40512000
C	-2.30770700	-1.40399700	-2.56271500
C	-1.76686800	0.91154600	-2.77429300
C	-3.59991400	-1.15745900	-3.01401500
H	-2.06111600	-2.43015100	-2.29327400
C	-3.04202100	1.17621800	-3.24108400
H	-1.06929500	1.74499400	-2.69247800
C	-3.98056000	0.14496900	-3.34282800
H	-4.29944900	-1.98760500	-3.08367200
H	-3.34312800	2.18945900	-3.50396200
O	-5.22071900	0.49948400	-3.75781000
C	-6.21844800	-0.50113800	-3.79084300
H	-6.36978800	-0.94246200	-2.79366800
H	-7.13696000	-0.00455400	-4.11220300
H	-5.96527900	-1.29429900	-4.50875000
C	0.13062300	-3.29759700	-2.14187400
N	-0.22734000	-4.40016100	-2.02646600

TS (64-65)_i

C	0.34196300	-5.50877700	0.57415400
C	1.38795200	-6.41845700	0.68951200
C	2.71573500	-5.98783200	0.84663200
C	3.03293800	-4.63441200	0.89420600
C	1.98429300	-3.72883600	0.77417200
C	0.66379000	-4.15603400	0.61383700
C	1.94493300	-2.27898700	0.77477500
N	0.66074100	-1.84007900	0.59287600
C	-0.14185300	-2.95133400	0.52796300
N	-1.45667900	-2.98570100	0.43886900
N	3.02358500	-1.54891400	0.97520500
C	-2.18569000	-1.88448200	0.40763300
C	2.98516400	-0.23268700	0.94572300
N	-1.74235400	-0.58831200	0.40272400
C	-2.84689000	0.22344200	0.32867000
C	-4.05339300	-0.58114800	0.30772700
C	-3.63438000	-1.91493800	0.35473900
C	4.15761000	0.57596000	1.21686900
C	3.75973900	1.90626500	1.06413700
C	2.34839700	1.87147500	0.72810900
N	1.91142200	0.57063900	0.65931500
N	-2.87285600	1.54058300	0.26562600
N	1.64116200	2.96980500	0.55788800
C	-1.77573500	2.27240900	0.30317700

Appendix D: Cartesian Coordinates

N	-0.48012500	1.83314000	0.41279300
C	0.32825700	2.93690300	0.41253200
C	-0.47106200	4.14097100	0.28997500
C	-1.80375500	3.71984300	0.22660400
C	-5.40488100	-0.24963500	0.25473400
C	-6.32146400	-1.29521600	0.24716600
C	-5.89961400	-2.63536700	0.29322100
C	-4.54982400	-2.96388800	0.34844500
C	-0.13703400	5.49236300	0.24988700
C	-1.17802300	6.40728400	0.13823800
C	-2.51694600	5.98358100	0.07369700
C	-2.84840500	4.63422200	0.11933600
C	5.46288100	0.24260400	1.56468700
C	6.36048500	1.28773200	1.75328400
C	5.96278200	2.62702400	1.59573300
C	4.65552700	2.95553300	1.25067700
H	-0.68844400	-5.83744600	0.45042500
H	1.17760800	-7.48609400	0.65327800
H	3.50808200	-6.73000800	0.92894900
H	4.05878900	-4.28874400	1.01534300
H	-5.72549100	0.79022100	0.22102400
H	-7.38715100	-1.07556000	0.20595600
H	-6.64656000	-3.42753100	0.28624000
H	-4.21406600	-3.99877500	0.38637700
H	0.90169500	5.81391000	0.30499100
H	-0.95622700	7.47272200	0.10195900
H	-3.30606100	6.72904100	-0.01117800
H	-3.88304500	4.29836500	0.07488500
H	5.76451000	-0.79795300	1.67644800
H	7.39135000	1.06724300	2.02899200
H	6.69262300	3.41993600	1.75478100
H	4.33833100	3.99074600	1.13552400
Co	0.09625800	-0.01061100	0.36994100
C	-0.03057100	-0.00178800	-1.75489200
C	-0.35453800	-1.27576600	-2.35635300
C	1.41603000	-1.83107400	-2.88532700
C	1.17865400	0.42314900	-2.63250200
C	0.24075200	-1.34260300	-3.70762200
C	0.60752800	0.09806100	-4.03894900
H	1.53579800	1.44393700	-2.47924100
H	-0.17430300	-2.02644800	-4.44708700
H	1.36135500	0.18174400	-4.83271500
H	-0.27098700	0.70421500	-4.29473100
C	1.71381000	-3.21019500	-2.79610000
N	1.92518100	-4.35645400	-2.74608500
H	-1.04065300	-2.02925400	-1.97537900
C	2.18233800	-0.70227600	-2.49798500
C	3.56820300	-0.59401700	-2.16983400
C	4.19763200	0.66781400	-2.12256000
C	4.39084500	-1.72911900	-1.95306900
C	5.55901500	0.80492900	-1.89307500
H	3.61210900	1.57190200	-2.28387800
C	5.73840400	-1.59974200	-1.70021900

Appendix D: Cartesian Coordinates

H	3.95632800	-2.72765300	-1.96393600
C	6.33903200	-0.33159500	-1.66888600
H	5.99256200	1.80180100	-1.86575000
H	6.36049600	-2.47443100	-1.51726200
O	7.66634500	-0.31193800	-1.40770700
C	8.32370100	0.93972800	-1.38957200
H	7.90944800	1.59460000	-0.60817200
H	9.37262700	0.72888900	-1.16913600
H	8.25040600	1.43941200	-2.36604100
H	-0.86201900	0.71125100	-1.74311500

TS (64-65)_ii

C	-2.58216000	-5.52729800	1.26586500
C	-1.93346800	-6.73526300	1.49301300
C	-0.53543300	-6.79723100	1.63170200
C	0.24866600	-5.65267700	1.54675500
C	-0.40334900	-4.44324300	1.31726400
C	-1.79421500	-4.38189000	1.17929600
C	0.07821500	-3.08396300	1.17654300
N	-0.97539100	-2.22945800	0.97905300
C	-2.11877100	-2.98783300	0.95652000
N	-3.35511100	-2.57419800	0.74761400
N	1.36196700	-2.77835800	1.23052900
C	-3.65466800	-1.30351000	0.57191300
C	1.78726100	-1.53449300	1.14430200
N	-2.79405300	-0.23231900	0.57434200
C	-3.54419900	0.89650200	0.38979700
C	-4.94389100	0.54663400	0.24330600
C	-5.01421300	-0.84528000	0.36091700
C	3.19303200	-1.18800200	1.23415300
C	3.25662600	0.20664400	1.15846400
C	1.88869100	0.66654100	1.01191800
N	1.03036000	-0.39911100	0.98463000
N	-3.12447700	2.14853900	0.38493300
N	1.57837800	1.94810700	0.96688400
C	-1.85507800	2.45494500	0.55412200
N	-0.79004400	1.59141400	0.64841400
C	0.33434700	2.35856500	0.83757800
C	-0.01797000	3.76397900	0.86509000
C	-1.40021000	3.82623000	0.68041500
C	-6.08660500	1.31622600	0.04218600
C	-7.30219800	0.64670700	-0.04264400
C	-7.37330600	-0.75216100	0.07619600
C	-6.23097200	-1.51760900	0.28256800
C	0.75082600	4.91472000	0.99904200
C	0.08666200	6.13501800	0.93790500
C	-1.30440000	6.19806600	0.75388700
C	-2.06945800	5.04350200	0.62524900
C	4.34271200	-1.95943500	1.38091300
C	5.55941900	-1.28822300	1.44750400
C	5.62290200	0.11383100	1.37747200
C	4.47197900	0.88102100	1.23383700

Appendix D: Cartesian Coordinates

H	-3.66418600	-5.47113400	1.15967000
H	-2.51508700	-7.65277500	1.56705400
H	-0.06226800	-7.76149100	1.81042300
H	1.33119300	-5.69261300	1.65578400
H	-6.02344900	2.39950600	-0.04476100
H	-8.21827800	1.21305300	-0.20240300
H	-8.34334700	-1.24183800	0.00673100
H	-6.27923400	-2.60082400	0.38030300
H	1.82955300	4.85545600	1.13464800
H	0.65211100	7.06092400	1.02977400
H	-1.78928000	7.17180500	0.70685200
H	-3.14688300	5.08576400	0.47577400
H	4.28486500	-3.04479400	1.44401900
H	6.48164300	-1.85674000	1.56173700
H	6.59215400	0.60806000	1.43368900
H	4.51535300	1.96748000	1.17591000
Co	-0.87268600	-0.32966700	0.64707000
C	0.01081900	1.27710400	-2.42050900
C	-0.84077600	-0.74370900	-1.38745000
C	0.45662600	-1.17630700	-1.88322500
C	1.13435000	0.45019200	-2.65819000
C	-1.17789900	0.33566700	-2.44351700
C	0.58839400	-0.79822000	-3.30884700
C	-0.83219700	-0.44269200	-3.73717100
H	-1.58556400	-1.54597700	-1.32003500
H	1.17771400	-1.80768200	-1.36893100
H	-2.16857100	0.79450500	-2.38654100
H	1.25125400	-1.36871000	-3.95965700
H	-0.86657100	0.19119500	-4.63253900
H	-1.45922700	-1.33194300	-3.88551200
C	-0.07668600	2.66132400	-2.31172200
N	-0.19562500	3.82853900	-2.28840900
C	2.55653600	0.73424300	-2.46708200
C	3.00105200	1.99301800	-2.02349500
C	3.52430300	-0.25454100	-2.67892100
C	4.34241200	2.24130200	-1.80517500
H	2.28887900	2.79497600	-1.83546200
C	4.87586200	-0.02489600	-2.44040400
H	3.22696400	-1.24832800	-3.01395000
C	5.29012400	1.22959200	-1.99126300
H	4.68058400	3.21584600	-1.45599800
H	5.58598300	-0.83407600	-2.59252500
O	6.57208600	1.55584600	-1.69696600
C	7.56363000	0.56306200	-1.85626300
H	7.63013900	0.23004600	-2.90203100
H	8.50918500	1.02653000	-1.56519800
H	7.36732100	-0.30376200	-1.20736900

65

Co	9.23050000	1.98849000	-5.93270200
N	9.21157900	3.16199400	-4.40793800

Appendix D: Cartesian Coordinates

N	9.97366700	0.58645400	-4.84441300
N	8.48731800	3.39052300	-7.02098600
N	9.24938500	0.81497400	-7.45745700
C	8.77639600	4.46376400	-4.38916500
C	9.63074000	2.85197400	-3.13808000
C	10.27684800	0.66852900	-3.50812300
C	10.29858600	-0.68053200	-5.26099100
C	8.16243100	4.65751700	-6.60441600
C	8.18414900	3.30845100	-8.35728100
C	9.68452800	-0.48680800	-7.47622100
C	8.83016600	1.12497500	-8.72730100
C	8.91992600	5.01573000	-3.05643400
N	8.29076700	5.16442300	-5.39446900
C	9.45985800	3.99708500	-2.26577900
N	10.12358400	1.70667800	-2.71052500
C	10.81828800	-0.59347600	-3.04376500
C	10.83202100	-1.44604800	-4.15156900
N	10.17021500	-1.18744900	-6.47093000
C	7.62912300	5.42307700	-7.71387000
C	7.64283900	4.57049900	-8.82167100
N	8.33736500	2.27028700	-9.15486500
C	9.54098400	-1.03877900	-8.80894800
C	9.00103400	-0.02014000	-9.59959800
C	8.62827900	6.26899600	-2.52430500
C	9.72816900	4.19390900	-0.91369600
C	11.27040600	-1.01765800	-1.79694800
C	11.29837000	-2.75440200	-4.05365900
C	7.16289100	6.73147100	-7.81180800
C	7.19081800	4.99471700	-10.06851100
C	9.83263800	-2.29204300	-9.34107700
C	8.73271300	-0.21696800	-10.95167800
C	8.89508500	6.46855200	-1.17453100
H	8.20793400	7.05684000	-3.14690900
C	9.43801500	5.44424300	-0.37949700
H	10.14868400	3.39536800	-0.30499300
C	11.73665300	-2.32354100	-1.69604800
H	11.25632800	-0.34739900	-0.93928800
C	11.75045700	-3.18083900	-2.81000900
H	11.30567100	-3.41188100	-4.92123500
C	6.71088900	7.15793700	-9.05547800
H	7.15560000	7.38895200	-6.94423400
C	6.72467500	6.30063500	-10.16943600
H	7.20488000	4.32445300	-10.92616700
C	9.56580500	-2.49160800	-10.69084400
H	10.25299500	-3.07988400	-8.71847700
C	9.02285800	-1.46730600	-11.48587500
H	8.31218400	0.58156800	-11.56037900
H	8.68091200	7.43493500	-0.72091700
H	9.63350900	5.63774300	0.67400900
H	12.09876600	-2.69300600	-0.73797400
H	12.12298600	-4.19717500	-2.69246800
H	6.33844200	8.17430200	-9.17303900
H	6.36263100	6.67012400	-11.12752600

Appendix D: Cartesian Coordinates

H	9.77997200	-3.45799500	-11.14445800
H	8.82734600	-1.66081200	-12.53937600
C	-1.36958400	0.27237400	-2.21741500
C	-1.45885700	-0.50551700	-3.32931200
C	-1.46438200	-1.95189300	-2.81085000
C	-2.27462100	-1.74765400	-1.51252300
C	-1.30333100	-0.66690700	-0.99886300
C	0.01037400	-1.44406500	-1.11116300
C	-0.08604300	-2.21428100	-2.19857600
H	-1.83351700	-2.69880800	-3.51947200
H	-2.29807000	-2.64570900	-0.88329300
H	-3.29178400	-1.37265300	-1.68393700
H	-1.51480700	-0.19312000	-0.03650800
H	0.66887700	-2.86092100	-2.63763400
H	0.86298100	-1.31580300	-0.45044300
C	-1.22353500	1.66970200	-2.12249700
N	-1.10924100	2.82639900	-2.00656700
C	-1.47054200	-0.15377500	-4.73684900
C	-1.12015600	-1.10834400	-5.71066000
C	-1.81349500	1.13168400	-5.18086900
C	-1.09646700	-0.78881500	-7.05502200
H	-0.83883500	-2.11575600	-5.40643300
C	-1.80487600	1.46331400	-6.52920800
H	-2.10918100	1.89304600	-4.46088400
C	-1.44058800	0.50090000	-7.47642000
H	-0.81364800	-1.52388000	-7.80617500
H	-2.08579700	2.46982600	-6.82835800
O	-1.39527200	0.71906800	-8.80914400
C	-1.72275900	2.00808500	-9.29082900
H	-1.61235400	1.96278700	-10.37635100
H	-2.75962100	2.27360800	-9.04169600
H	-1.03970600	2.76815900	-8.88682900

Cu(CH₃CN)₄⁺:**SCF : -728.3473051**

Cu	-0.49518000	-0.31029800	-0.00045300
N	0.18068800	0.64584600	-1.65575900
C	0.56222800	1.18549300	-2.58998700
N	0.18118500	0.64567000	1.65490400
C	0.56291600	1.18519000	2.58912800
N	-2.52263500	-0.31046300	0.00023900
C	-3.66700400	-0.31048600	0.00065400
N	0.18083000	-2.22184300	-0.00054200
C	0.56220300	-3.30079000	-0.00060000
C	1.04714100	1.86983200	-3.77410400
H	2.13734100	1.87423400	-3.77926400
H	0.68879500	1.36082400	-4.66913400
H	0.68678200	2.89875100	-3.78115800
C	-5.11807900	-0.31043700	0.00106400
H	-5.48842300	-0.82426900	0.88841900
H	-5.48862900	0.71487800	0.00256400
H	-5.48894800	-0.82187300	-0.88745900

Appendix D: Cartesian Coordinates

C	1.04690400	1.86900800	3.77392700
H	0.68724900	1.36005900	4.66846600
H	2.13710000	1.87274800	3.78030200
H	0.68717000	2.89814700	3.78076200
C	1.04494200	-4.66920500	-0.00049800
H	2.13513000	-4.67757500	-0.00110800
H	0.68527700	-5.18899900	0.88778000
H	0.68428600	-5.18946900	-0.88810000

cis-67:

SCF: -687.3240708

N	-0.86375900	1.01821600	-1.07676200
C	-0.88046800	0.22307800	-2.27014500
C	-1.27072400	-1.11468000	-2.14708400
C	-1.39933900	-1.90755500	-3.28642700
C	-1.19190500	-1.35611200	-4.55255300
C	-0.85125300	-0.00576000	-4.67401900
C	-0.68731700	0.78495900	-3.54011100
H	-1.45604000	-1.51983600	-1.15699100
H	-1.67856800	-2.95238400	-3.18559400
H	-1.30973300	-1.96984900	-5.44061800
H	-0.70847300	0.43300300	-5.65744200
H	-0.41486600	1.83101000	-3.63016800
N	0.08150700	1.78462500	-0.77768900
C	1.32935600	1.81036000	-1.47376300
C	2.02755200	0.67092500	-1.89336700
C	3.29794900	0.78519300	-2.45110200
C	3.87731000	2.05169700	-2.61688100
C	3.18930400	3.19442100	-2.17851400
C	1.94377600	3.06771400	-1.58550200
H	1.58875000	-0.31217100	-1.77161200
H	3.82426400	-0.11196000	-2.75305400
H	3.66283100	4.16353600	-2.29523100
H	1.41641400	3.94034100	-1.21304000
O	5.09889900	2.27255600	-3.17039500
C	5.84210100	1.14843000	-3.62729600
H	6.77062300	1.55072100	-4.03395100
H	6.07147500	0.46056500	-2.80432900
H	5.30221000	0.60715900	-4.41384800

trans-67:

SCF: -687.3435354

N	-0.77953800	0.64697800	0.02023300
C	-0.80349000	-0.18586600	-1.12653500
C	-1.96560800	-0.95328600	-1.29015100
C	-2.09505900	-1.80802300	-2.38583700
C	-1.06323100	-1.89966500	-3.32355200
C	0.09955600	-1.13259400	-3.16067300
C	0.23544600	-0.27839200	-2.07057500
H	-2.75404100	-0.86517500	-0.54841300
H	-2.99785500	-2.40006200	-2.50718100
H	-1.16034600	-2.56380200	-4.17799100

Appendix D: Cartesian Coordinates

H	0.90138300	-1.20491800	-3.89078100
H	1.12950200	0.31936200	-1.93419800
N	0.26879900	1.33240300	0.16240000
C	0.30371400	2.16522600	1.29940100
C	-0.72633000	2.27653000	2.24799500
C	-0.59332800	3.12937800	3.33855300
C	0.58178700	3.88754400	3.49488200
C	1.61507900	3.78143800	2.54985000
C	1.47297300	2.92836400	1.46538600
H	-1.62860600	1.68899200	2.12034800
H	-1.40027200	3.20042700	4.05836100
H	2.51345000	4.37461400	2.68773500
H	2.26303200	2.83536000	0.72617000
O	0.80501700	4.74625900	4.52515500
C	-0.20547200	4.89809200	5.52104200
H	0.18939000	5.62438200	6.23195700
H	-1.13533300	5.27933200	5.08278500
H	-0.39837500	3.94810800	6.03338000

TS 67a:

SCF: -687.280496

Freq: *i*416.8413

N	-0.06399000	1.49839300	-1.06381700
C	-0.47434900	0.27651700	-1.39070000
C	-1.84344000	0.02702700	-1.68469900
C	-2.24903400	-1.25617100	-2.02807000
C	-1.34592000	-2.32147800	-2.09076600
C	-0.00143500	-2.07151000	-1.80041400
C	0.44864100	-0.80379400	-1.45497600
H	-2.55144300	0.84733200	-1.63921100
H	-3.30032400	-1.42193500	-2.25094000
H	-1.68012900	-3.31790400	-2.36007500
H	0.72286200	-2.88138400	-1.84354300
H	1.49414000	-0.61903700	-1.23367300
N	0.32488600	2.63066500	-0.78836700
C	0.30542500	3.00615900	0.59871400
C	-0.12483700	2.17136100	1.63544100
C	-0.10883600	2.62304700	2.94846700
C	0.34273000	3.92587600	3.23024000
C	0.77529300	4.76271100	2.18750400
C	0.75515600	4.30231300	0.88147900
H	-0.47136000	1.16878300	1.40419000
H	-0.44440700	1.96813300	3.74311300
H	1.11855800	5.76203200	2.43255900
H	1.08369700	4.92986600	0.05889700
O	0.39653100	4.46124800	4.47322600
C	-0.03075100	3.66551700	5.57571800
H	0.09552900	4.29215500	6.45892100
H	-1.08490100	3.38180300	5.47504300
H	0.58395400	2.76328000	5.67548500

TS 67b:

Appendix D: Cartesian Coordinates

SCF: -687.274875544

Freq: *i*455.3628

N	0.27618300	1.38726400	-0.99287000
C	-0.25470500	0.22327300	-1.36738300
C	-1.64883300	-0.01702200	-1.25467100
C	-2.21005600	-1.20144900	-1.72232300
C	-1.38858100	-2.22673900	-2.20787400
C	0.00047600	-2.02410100	-2.27293300
C	0.55818300	-0.81186000	-1.91313800
H	-2.28274400	0.76074900	-0.84199400
H	-3.28473500	-1.32875400	-1.66459000
H	0.62267600	-2.82783100	-2.65425500
H	1.62556000	-0.64336100	-2.00627200
N	0.77481500	2.47569000	-0.67735000
C	0.45970200	2.95752800	0.65137600
C	-0.34802700	2.27025600	1.56633000
C	-0.57211900	2.81728200	2.82508900
C	0.00603300	4.04455900	3.17354500
C	0.81241100	4.72494600	2.25897900
C	1.04181100	4.17948600	0.99655500
H	-0.78572500	1.31917700	1.27967100
H	-1.19809700	2.29126500	3.54040700
H	1.26075900	5.67638700	2.52949600
H	1.66648900	4.68052100	0.26319100
O	-1.83316400	-3.44380000	-2.63925700
C	-3.22981900	-3.69422000	-2.58900300
H	-3.36826400	-4.70418400	-2.97760100
H	-3.60957600	-3.64457400	-1.56039800
H	-3.78711700	-2.98400500	-3.21343300
H	-0.17379100	4.46669300	4.15801700

68_i:

SCF: -1282.909485

Cu	-0.67042700	-0.59832700	0.07320700
N	-0.11714400	0.72863600	1.53270900
C	0.15008400	1.76142800	1.98299100
N	-2.64088300	-0.90809300	0.16252400
C	-3.77989400	-1.11035800	0.18555700
N	0.37997100	-2.29782400	0.12969400
C	0.99783400	-3.27358300	0.06815100
C	-5.21264300	-1.36942300	0.21479600
H	-5.44230800	-2.09554900	1.00027900
H	-5.75614200	-0.44150400	0.41606400
H	-5.53661100	-1.77237800	-0.74935200
C	0.47167100	3.07699800	2.51536900
H	0.03030600	3.20119400	3.50844600
H	1.55641500	3.19746300	2.58800800
H	0.06928200	3.84089300	1.84205700
C	1.77513500	-4.50232700	-0.01306800
H	2.82998900	-4.28927700	0.18351900
H	1.41286900	-5.22317000	0.72587200
H	1.67866300	-4.93634500	-1.01280300

CX

Appendix D: Cartesian Coordinates

N	-0.11843200	0.46784300	-1.61496400
N	0.31802300	-0.16997100	-2.60706800
C	-0.11407100	1.89939700	-1.51669300
C	0.66455500	0.45526400	-3.83712100
C	1.03217300	2.65362200	-1.78334800
C	-1.24617300	2.52063800	-0.97224700
C	1.78548200	-0.06817100	-4.49457000
C	-0.13376400	1.42655900	-4.46408100
C	1.04477700	4.02408300	-1.53729700
H	1.92225600	2.17105800	-2.17097300
C	-1.25183500	3.88975500	-0.75580800
H	-2.11946500	1.92145800	-0.73585900
C	2.15459900	0.43240900	-5.74119900
H	2.35984500	-0.85131300	-4.00995400
C	0.21988700	1.88769200	-5.72772800
H	-1.02457100	1.80103300	-3.97363900
C	-0.10446300	4.65426600	-1.03413000
H	1.94694900	4.58787400	-1.73889000
H	-2.12882700	4.39323900	-0.36314200
C	1.37161400	1.40846800	-6.36134900
H	3.03905400	0.04522100	-6.23740200
H	-0.40417200	2.62656500	-6.22094600
O	-0.20059100	5.97807600	-0.76611600
H	1.64585600	1.78338000	-7.34247600
C	0.91636500	6.81369100	-1.06230400
H	0.60810600	7.82470600	-0.79616300
H	1.79348500	6.52953500	-0.46888900
H	1.16635100	6.77458400	-2.12869300

68_ii:

SCF: -1282.911119

Cu	-0.74638100	0.52491200	0.26826900
N	0.22746200	0.98818800	1.94983000
C	0.77869100	1.28500900	2.92278700
N	-2.73558300	0.57707000	0.51630800
C	-3.88529900	0.64405700	0.62351200
N	-0.15657000	-1.30887900	-0.43135800
C	0.36662000	-2.05000000	-1.15108200
C	-5.33306800	0.72409600	0.75913400
H	-5.64170700	0.28926200	1.71439200
H	-5.65321600	1.76949500	0.72285300
H	-5.81397800	0.17399600	-0.05508100
C	1.46834300	1.65831000	4.14992000
H	0.81843300	1.47619900	5.01096100
H	2.38083400	1.06480400	4.25982500
H	1.73269500	2.71953900	4.12062500
C	1.03651900	-2.95695200	-2.07102700
H	1.80587900	-3.52703600	-1.54185600
H	0.31344400	-3.65186300	-2.50779800
H	1.50655200	-2.37246000	-2.86812400
N	-0.82453900	2.82455700	-1.46742600
N	-0.21301600	1.73234600	-1.31164200

Appendix D: Cartesian Coordinates

C	-0.53058700	3.77892700	-2.45883700
C	0.75040200	1.21356400	-2.24598500
C	0.71977200	4.02965300	-3.05776200
C	-1.60975000	4.63784800	-2.75650100
C	2.02580600	0.87958300	-1.78443300
C	0.35878400	0.90144700	-3.55236900
C	0.87452900	5.08295300	-3.94838000
H	1.58410300	3.42938400	-2.80907500
C	-1.47369600	5.65981800	-3.67536000
H	-2.55599100	4.46623400	-2.25415600
C	2.93635800	0.28167300	-2.65630600
H	2.29495500	1.09703100	-0.75571600
C	1.26822300	0.28447600	-4.40917000
H	-0.64460700	1.14329400	-3.88675400
C	-0.22589500	5.89408200	-4.28171100
H	1.85106500	5.26890800	-4.37777500
H	-2.30415400	6.30999100	-3.92739000
C	2.56154300	-0.01654100	-3.96948800
H	3.93571700	0.04194700	-2.30616300
H	0.96712300	0.04191700	-5.42368900
O	-0.17935700	6.92473400	-5.14932900
H	3.26998000	-0.48662200	-4.64448400
C	1.06193100	7.23632200	-5.78183300
H	0.85761000	8.09176800	-6.42539000
H	1.82382200	7.50615900	-5.04189900
H	1.41665900	6.39566100	-6.38850600

MECP 68_i:

SCF: -1282.87841144

Cu	-0.66887100	-0.52292900	-0.16743400
N	-0.10685800	0.59991000	1.48976300
C	0.18627400	1.59193300	2.01055200
N	-2.65950200	-0.74793900	-0.07322800
C	-3.80480900	-0.89629000	-0.00568100
N	0.29898600	-2.27798000	-0.20236600
C	0.92754300	-3.24690600	-0.25893900
C	-5.24566200	-1.08588800	0.07953600
H	-5.49764100	-1.60055000	1.01155500
H	-5.75062700	-0.11557000	0.05865300
H	-5.59088300	-1.68775200	-0.76623200
C	0.54097100	2.86241200	2.62561700
H	0.09054400	2.94284900	3.61927600
H	1.62785400	2.94529400	2.71696500
H	0.16970600	3.67556900	1.99349200
C	1.72449300	-4.46295200	-0.33516000
H	2.77632600	-4.22826700	-0.14664100
H	1.37995400	-5.18479800	0.41125800
H	1.63071600	-4.90601300	-1.33116000
N	0.03075700	0.75196500	-1.59345600
N	0.97551100	0.20202300	-2.33711400
C	-0.02943500	2.12217300	-1.42257900
C	0.99278300	0.38491700	-3.69386700

Appendix D: Cartesian Coordinates

C	1.01890400	2.99325000	-1.79471200
C	-1.17094800	2.66555300	-0.78137700
C	2.10827500	-0.14457500	-4.39207600
C	-0.03559000	1.03887300	-4.42429800
C	0.94325700	4.35162600	-1.51950400
H	1.90306800	2.59037900	-2.27464400
C	-1.25384400	4.01747100	-0.52282700
H	-1.98245800	2.00060400	-0.50644200
C	2.20661200	0.00624200	-5.76622400
H	2.87778500	-0.65309500	-3.82058900
C	0.07694000	1.17270500	-5.79962700
H	-0.90483200	1.42010100	-3.90119700
C	-0.19079700	4.87668800	-0.87435500
H	1.76970100	4.99288600	-1.80120600
H	-2.12850200	4.44653900	-0.04556500
C	1.19525600	0.66690900	-6.47780900
H	3.06913600	-0.39140800	-6.29226100
H	-0.71221400	1.67016500	-6.35531200
O	-0.35549500	6.17515000	-0.54041000
H	1.27399800	0.78125000	-7.55427900
C	0.71337100	7.08565200	-0.79581700
H	0.37793400	8.04941800	-0.41376900
H	1.62308700	6.77634500	-0.26847100
H	0.91840400	7.16547900	-1.86906600

MECP 68_ii:

SCF: -1282.87942928

Cu	-0.66221600	-0.53534100	-0.13411600
N	-0.12899500	0.56018400	1.55987300
C	0.17869000	1.56234600	2.05317700
N	-2.65647700	-0.75824800	-0.06588600
C	-3.80285100	-0.90211400	-0.00484800
N	0.29565500	-2.29526100	-0.17199500
C	0.92610500	-3.26181000	-0.24360900
C	-5.24503700	-1.08665400	0.07528700
H	-5.50166600	-1.59837700	1.00770800
H	-5.74768500	-0.11513400	0.05092400
H	-5.59048000	-1.68946600	-0.76978300
C	0.55433700	2.84524500	2.62883900
H	0.09797400	2.96823000	3.61533800
H	1.64186600	2.90867700	2.72677900
H	0.20710500	3.64406800	1.96524500
C	1.72594400	-4.47484300	-0.33656500
H	2.77768900	-4.23900100	-0.14936700
H	1.38587900	-5.20500500	0.40364300
H	1.62972400	-4.90764700	-1.33679200
N	0.07248100	0.74314300	-1.52511600
N	1.00590000	0.21753500	-2.30375100
C	0.00931100	2.12141100	-1.35613200
C	0.97681300	0.39435400	-3.65174100
C	1.05471500	2.98779000	-1.74779100
C	-1.13833900	2.65676800	-0.72968000

Appendix D: Cartesian Coordinates

C	2.08377800	-0.09908000	-4.39954300
C	-0.09012000	1.01729600	-4.35503000
C	0.94104900	4.35340900	-1.51909700
H	1.94794800	2.57559400	-2.20185500
C	-1.24334600	4.02580000	-0.52270300
H	-1.93390500	1.98240700	-0.43232400
C	2.13899100	0.06811900	-5.76365000
H	2.88785300	-0.59138700	-3.86309800
C	-0.03616100	1.17629600	-5.72872600
H	-0.95601000	1.36852700	-3.80728100
C	-0.20463700	4.88221100	-0.91273600
H	1.75402100	5.01233600	-1.80964100
H	-2.13701200	4.43115900	-0.05761900
C	1.08526900	0.71702000	-6.44695400
H	2.98549500	-0.28577100	-6.34190700
H	-0.86361200	1.65521000	-6.23823300
O	1.24620100	0.84440800	-7.77875700
C	0.23593500	1.51337300	-8.53394100
H	0.59715300	1.52839300	-9.56182700
H	-0.71476700	0.97044100	-8.48597600
H	0.09692000	2.54061200	-8.17950400
H	-0.28981300	5.95134400	-0.74712200

68_i-T:

SCF: -1282.887572

Cu	-0.48744500	-0.02217300	0.11228800
N	0.05972400	0.23042000	2.02425100
C	0.45387300	0.43359800	3.09254200
N	-2.47836500	0.15524900	-0.15865600
C	-3.61137200	0.26954800	-0.36278200
N	0.08055900	-1.80375500	-0.67671400
C	0.49537700	-2.58994200	-1.41776500
C	-5.03658600	0.41718400	-0.62140400
H	-5.57571700	-0.45556700	-0.24119000
H	-5.41371400	1.31525500	-0.12315900
H	-5.21115000	0.50507200	-1.69787800
C	0.95264400	0.69012200	4.43618500
H	0.27140000	0.25864000	5.17543500
H	1.94259300	0.24007200	4.55574800
H	1.02767900	1.76866200	4.60388600
C	1.01494300	-3.56037700	-2.36894700
H	2.07365300	-3.74884500	-2.16884700
H	0.46020600	-4.49969800	-2.28902800
H	0.91187600	-3.15965800	-3.38187500
N	0.48755600	1.35994900	-1.05512400
N	1.58591600	0.86843100	-1.63159100
C	0.20336400	2.69419700	-1.17751500
C	1.47361600	0.22050000	-2.82755400
C	0.94746400	3.55922300	-2.01728400
C	-0.88628100	3.23228000	-0.44213100
C	2.65392700	-0.36774300	-3.35219400
C	0.25821300	0.10293000	-3.55488500

Appendix D: Cartesian Coordinates

C	0.60970600	4.89825300	-2.13389000
H	1.79299400	3.16390100	-2.56819200
C	-1.22165400	4.56272000	-0.56203100
H	-1.45113400	2.57870800	0.21261700
C	2.61981500	-1.03497800	-4.56719200
H	3.57243300	-0.27231300	-2.78247300
C	0.24171000	-0.57446100	-4.76482200
H	-0.64479700	0.54310600	-3.14687300
C	-0.48215100	5.41379000	-1.41149900
H	1.19702700	5.53694400	-2.78211100
H	-2.05152500	4.98598000	-0.00613600
C	1.41665300	-1.14364900	-5.28079200
H	3.52831400	-1.47501500	-4.96666900
H	-0.68839300	-0.66208400	-5.31874600
O	-0.89529300	6.69840300	-1.45608600
H	1.39411600	-1.66528700	-6.23243400
C	-0.18756400	7.61521400	-2.29015400
H	-0.69536800	8.57254800	-2.17405000
H	0.85655500	7.71116400	-1.97138500
H	-0.22621700	7.30289700	-3.33992400

68_ii-T:

SCF: -1282.887397

Cu	-0.13086400	0.51031500	-0.41075500
N	1.41210700	1.17626800	0.70434200
C	2.31068000	1.57690400	1.31307500
N	-1.73201400	1.69881100	-0.02648500
C	-2.52236500	2.53545300	-0.14787600
N	-0.50034100	-1.43587300	-0.10513900
C	-0.74118600	-2.56415600	-0.02197700
C	-3.50093200	3.59839700	-0.31757700
H	-3.80424100	3.99066400	0.65726800
H	-3.05718000	4.40191000	-0.91244400
H	-4.38045600	3.21472600	-0.84222400
C	3.44146600	2.08047700	2.08004200
H	3.08237300	2.69611000	2.91007800
H	4.02070600	1.24369800	2.48138300
H	4.08713600	2.68676800	1.43788500
C	-1.04934600	-3.98338000	0.08102700
H	-0.70101400	-4.37256300	1.04227500
H	-2.13044100	-4.13303500	0.00471100
H	-0.55473400	-4.53005600	-0.72728200
N	-0.80715800	1.32492500	-3.08038800
N	0.23451900	0.85234200	-2.40053900
C	-1.06977700	2.65510300	-3.09795400
C	1.38376000	0.52728200	-3.09134900
C	-0.24201900	3.63757400	-2.49034900
C	-2.25474900	3.08312500	-3.76256000
C	2.43079700	-0.10942500	-2.38375500
C	1.54984500	0.81612200	-4.46770000
C	-0.57629900	4.98142200	-2.54983100
H	0.65524400	3.32050900	-1.97064800

Appendix D: Cartesian Coordinates

C	-2.57884100	4.41924400	-3.82794500
H	-2.88771600	2.33136600	-4.22206200
C	3.61440800	-0.42878700	-3.03327200
H	2.28908100	-0.33894500	-1.33357000
C	2.73990200	0.48792900	-5.10121300
H	0.73959600	1.28513600	-5.01364900
C	-1.74308800	5.38806200	-3.22667000
H	0.07086600	5.71063100	-2.07752800
H	-3.47286700	4.75845500	-4.34009400
C	3.77818800	-0.13120600	-4.39243300
H	4.41426300	-0.91651100	-2.48428700
H	2.86314600	0.71060800	-6.15674200
O	-2.15055100	6.66902900	-3.35122900
H	4.70434700	-0.38652500	-4.89758500
C	-1.33632000	7.70342800	-2.80003000
H	-1.84367500	8.63778300	-3.03901900
H	-1.25000300	7.59933100	-1.71228100
H	-0.33779300	7.69941500	-3.25108300

TS (68-69)_i:

SCF: -1282.866124

Freq: i438.6393

Cu	-0.69024500	-0.20693100	0.39332200
N	0.08624700	0.31821100	2.14387400
C	0.57780900	0.61958000	3.14699200
N	-2.67474400	-0.04263500	0.25970500
C	-3.82155600	0.02553200	0.12216900
N	-0.09819000	-2.07593300	-0.20474900
C	0.38245800	-2.93956100	-0.80760000
C	-5.26446600	0.10988600	-0.05416800
H	-5.72691300	0.52602700	0.84573900
H	-5.49716500	0.75424200	-0.90727100
H	-5.67492700	-0.88745600	-0.23759000
C	1.19788000	0.99628900	4.40954600
H	0.69922000	0.48156000	5.23611000
H	2.25598100	0.71817700	4.40138500
H	1.11398600	2.07699800	4.55794200
C	0.99000000	-4.01499900	-1.57721900
H	1.98330200	-4.23901400	-1.17885100
H	0.36699400	-4.91261500	-1.52272400
H	1.09347300	-3.70131800	-2.62049200
N	0.24005500	0.79218600	-1.22985800
N	1.01197500	0.11185100	-1.90915800
C	-0.04029300	2.12866000	-1.63866700
C	1.60306900	-0.69750900	-2.79161200
C	-0.84192600	2.89554200	-0.78826400
C	0.45324700	2.67901800	-2.83642900
C	0.89377700	-1.11096000	-3.95138300
C	2.90712700	-1.20405600	-2.55918600
C	-1.16812700	4.20626000	-1.11839200
H	-1.20600800	2.45330200	0.13378500
C	0.13176500	3.97725200	-3.17209200

Appendix D: Cartesian Coordinates

H	1.07957800	2.07768100	-3.48692100
C	1.47330200	-2.03634300	-4.81337200
H	-0.10160300	-0.71913600	-4.13075300
C	3.47303900	-2.08601500	-3.47190500
H	3.44846400	-0.88413600	-1.67558400
C	-0.68005700	4.75507500	-2.31586000
H	-1.78861000	4.78925900	-0.44990300
H	0.49161500	4.43024100	-4.08947300
C	2.76456400	-2.52749600	-4.59461000
H	0.90822500	-2.36088800	-5.68302500
H	4.47957700	-2.45123200	-3.28783700
O	-0.92664700	6.00954000	-2.73782800
H	3.21187200	-3.23119600	-5.28822400
C	-1.73241700	6.86345000	-1.92494300
H	-1.78364000	7.81313500	-2.45678200
H	-2.74145300	6.45316200	-1.80470300
H	-1.27428100	7.01580400	-0.94130600

TS (68-69)_ii:

SCF: -1282.86252

Freq: i434.6152

Cu	-0.68704800	-0.19697500	0.34842800
N	0.28768300	0.28931400	2.01471500
C	0.87969800	0.62053800	2.95220100
N	-2.68084700	-0.04363300	0.54438300
C	-3.83316600	0.05117700	0.59254800
N	-0.31011900	-2.13204000	-0.26420500
C	-0.03568400	-3.04976900	-0.91412100
C	-5.28348500	0.17006400	0.65092300
H	-5.73778100	-0.82516500	0.65855300
H	-5.57785200	0.70316000	1.55978200
H	-5.64702600	0.72189300	-0.22107600
C	1.62567700	1.03817400	4.13114300
H	1.24023200	0.52561200	5.01753700
H	2.68422100	0.79115300	4.00740700
H	1.52590000	2.11873600	4.27078200
C	0.31634000	-4.19247200	-1.74546800
H	-0.53751100	-4.47870000	-2.36656400
H	1.15773000	-3.92236500	-2.39094600
H	0.60036900	-5.04144600	-1.11667800
N	0.09214500	0.72782600	-1.34393800
N	0.85940200	0.06347700	-2.05888600
C	-0.25898800	2.05886500	-1.77720000
C	1.63754000	-0.65926600	-2.86567600
C	-1.12321600	2.78181300	-0.94946000
C	0.25489300	2.63427400	-2.94605800
C	1.49369800	-0.61573900	-4.28356500
C	2.62391000	-1.52510300	-2.32227600
C	-1.49116200	4.07961200	-1.30030900
H	-1.49659900	2.31844500	-0.04182200
C	-0.11480400	3.93063600	-3.28841200
H	0.94251600	2.06950500	-3.56541500

Appendix D: Cartesian Coordinates

C	2.25309500	-1.43816200	-5.09144800
H	0.74072800	0.03482400	-4.71529500
C	3.45999400	-2.26659900	-3.14626300
H	2.74059400	-1.56167300	-1.24433100
C	-0.98980800	4.65516900	-2.46971500
H	-2.16427400	4.64220100	-0.66057900
H	0.27975700	4.38224600	-4.19352800
C	3.26133500	-2.25256400	-4.53882200
H	2.11897600	-1.44437000	-6.16808100
H	4.24013100	-2.87332700	-2.70274300
O	3.98044400	-2.97733900	-5.42370800
H	-1.27389200	5.66687900	-2.74242800
C	5.02586200	-3.81308400	-4.93147700
H	5.46456700	-4.28618700	-5.80983100
H	5.78958500	-3.22417900	-4.41066300
H	4.63177800	-4.58336700	-4.25798400

MECP 69_i:

SCF: -1282.886792

Cu	-0.44830600	-0.02231700	0.00393600
N	0.02520300	0.36228500	1.91783900
C	0.38465400	0.63687900	2.98257600
N	-2.43401400	0.11503400	-0.33942500
C	-3.55906800	0.23150400	-0.58240400
N	0.20420300	-1.81007300	-0.66693100
C	0.64564500	-2.63236400	-1.35097700
C	-4.97602500	0.37788500	-0.88296300
H	-5.52573100	-0.49050400	-0.50782000
H	-5.36538600	1.28158800	-0.40470300
H	-5.12203800	0.45430600	-1.96449200
C	0.84377300	0.98556400	4.31993700
H	0.34184700	0.35912600	5.06314500
H	1.92442800	0.82982600	4.39167400
H	0.62050900	2.03641800	4.52698800
C	1.20059900	-3.64920700	-2.23070600
H	2.28536100	-3.69947000	-2.10030800
H	0.76327500	-4.62529000	-2.00187300
H	0.98157500	-3.38349700	-3.26922100
N	0.48512800	1.37084100	-1.19585800
N	1.56214200	0.93578700	-1.84702500
C	0.23475800	2.71697500	-1.18575100
C	1.39002700	0.16454500	-2.95741900
C	0.94988000	3.62360500	-2.00704300
C	-0.80487300	3.22067700	-0.35985000
C	2.55402000	-0.40709600	-3.53475900
C	0.12878800	-0.06036900	-3.57341800
C	0.63642300	4.97256000	-2.01515400
H	1.74983100	3.24386900	-2.63132100
C	-1.11794700	4.56165900	-0.37242500
H	-1.35212400	2.53236200	0.27432700
C	2.45724000	-1.16456800	-4.69186700
H	3.50947100	-0.22340600	-3.05441000

Appendix D: Cartesian Coordinates

C	0.05074600	-0.82475400	-4.72719400
H	-0.75702400	0.37837600	-3.12838300
C	-0.40449300	5.45566300	-1.20053600
H	1.19814500	5.64197200	-2.65487300
H	-1.91348200	4.96020300	0.24828500
C	1.20842100	-1.37873400	-5.29561700
H	3.35296400	-1.58761000	-5.13578400
H	-0.91390400	-0.98544200	-5.19991200
O	-0.79332000	6.74636000	-1.13934400
H	1.13828700	-1.96426400	-6.20674700
C	-0.11868600	7.70304700	-1.95630400
H	-0.59518500	8.65969900	-1.74358100
H	0.94580400	7.75743900	-1.70201600
H	-0.23235600	7.46232800	-3.01932500

MECP 69_ii:

SCF: -1282.886543

Cu	-0.43755400	0.01205000	0.01350100
N	0.02503500	0.37476700	1.93435900
C	0.38734100	0.64419100	2.99945300
N	-2.42476300	0.12274000	-0.33004600
C	-3.55020200	0.23829200	-0.57207100
N	0.23459500	-1.77593700	-0.64950100
C	0.66477600	-2.61375600	-1.32166800
C	-4.96756800	0.38224500	-0.87267600
H	-5.51576300	-0.48772900	-0.49897900
H	-5.35930400	1.28444800	-0.39357700
H	-5.11341400	0.46004100	-1.95414500
C	0.84969600	0.98626800	4.33735100
H	0.34792900	0.35742000	5.07860800
H	1.93018600	0.82819700	4.40633000
H	0.62885100	2.03666100	4.54933700
C	1.19856700	-3.65378000	-2.18777500
H	2.28661800	-3.70053300	-2.08760100
H	0.76939400	-4.62343000	-1.91945700
H	0.94888700	-3.41966600	-3.22665600
N	0.48928200	1.40127400	-1.18879400
N	1.53782500	0.96912500	-1.88286400
C	0.24576300	2.75826300	-1.16221000
C	1.34576700	0.19363800	-2.97753800
C	0.95795500	3.66882900	-1.98085500
C	-0.77730700	3.24297500	-0.31242300
C	2.49415500	-0.38857300	-3.58777200
C	0.07287900	-0.04863600	-3.56223700
C	0.63881900	5.01842300	-1.95111600
H	1.74975100	3.29420500	-2.61924700
C	-1.08541400	4.59580200	-0.29896000
H	-1.31530300	2.54207000	0.31608300
C	2.37107900	-1.15971300	-4.72198200
H	3.46535000	-0.20043700	-3.14179600
C	-0.04784500	-0.82945900	-4.69987400
H	-0.80736200	0.38629500	-3.10215300

Appendix D: Cartesian Coordinates

C	-0.38237500	5.49107300	-1.11573400
H	1.18600200	5.71119700	-2.58318300
H	-1.87671800	4.96053700	0.34908600
C	1.09932700	-1.38864400	-5.29659900
H	3.23914100	-1.59741100	-5.20353000
H	-1.02900300	-0.99655700	-5.12716400
O	1.08680700	-2.15639600	-6.40746900
C	-0.14910900	-2.34826900	-7.09652200
H	0.08820000	-2.96435300	-7.96380100
H	-0.87851500	-2.86986900	-6.46590600
H	-0.56498600	-1.38972900	-7.42721800
H	-0.62421400	6.54903000	-1.09779800

69_i:

SCF: -1282.927314

Cu	-0.71400900	0.06892200	-0.80411200
N	-0.25511800	0.92036400	1.00367700
C	0.03874200	1.71685500	1.79033200
N	-2.67687700	-0.19946900	-1.02315700
C	-3.81445800	-0.35123700	-1.17145900
N	0.43425800	-1.55232500	-1.00767500
C	1.11195900	-2.45264600	-1.26682100
C	-5.24536200	-0.54688200	-1.35739100
H	-5.64040900	-1.17964400	-0.55704100
H	-5.75947100	0.41872600	-1.33657500
H	-5.43205700	-1.03004400	-2.32104000
C	0.39629500	2.75775100	2.74200500
H	-0.15127500	2.61899200	3.67863600
H	1.47043300	2.72725900	2.94635100
H	0.13777900	3.73124600	2.31268600
C	1.96476700	-3.58264400	-1.60329800
H	2.87393600	-3.22200600	-2.09224600
H	2.23311600	-4.13419600	-0.69749300
H	1.43606700	-4.24911600	-2.29053200
N	0.04397400	1.61604600	-2.10631200
N	0.88315700	1.41199600	-3.02841900
C	0.06433600	2.92015900	-1.55162300
C	0.82398100	0.14817200	-3.64612400
C	1.15937100	3.78661300	-1.67066700
C	-1.06700500	3.32862700	-0.82636700
C	2.03864600	-0.40145500	-4.07828200
C	-0.38422800	-0.52509800	-3.89008200
C	1.13650800	5.03719200	-1.06650600
H	2.03056700	3.46154600	-2.22696800
C	-1.10510400	4.58063400	-0.23565200
H	-1.91423800	2.65621600	-0.74336400
C	2.05207700	-1.65455100	-4.68657400
H	2.95499800	0.15546700	-3.91208100
C	-0.36307900	-1.76389600	-4.52345600
H	-1.32150400	-0.06342800	-3.60169200
C	0.00019100	5.44460100	-0.34423400
H	1.99881100	5.68600100	-1.15640100

CXX

Appendix D: Cartesian Coordinates

H	-1.97729700	4.91957400	0.31310300
C	0.85248800	-2.33911900	-4.90837600
H	2.99445300	-2.08923700	-5.00576900
H	-1.29650700	-2.28050600	-4.72574800
O	-0.11968800	6.63416700	0.28589200
H	0.86260400	-3.30456600	-5.40517500
C	0.95073200	7.57263000	0.18264100
H	0.62879800	8.45022800	0.74300700
H	1.87118100	7.17254600	0.62328400
H	1.13264400	7.84895100	-0.86192800

69_ii:

SCF: -1282.92815614

Cu	-0.80199400	0.05151700	-0.85179900
N	-0.28582900	0.89145500	0.94885100
C	0.07925900	1.70791200	1.68387500
N	-2.77525900	-0.12507000	-1.05677000
C	-3.92549700	-0.20719900	-1.15347600
N	0.27747300	-1.61739700	-1.07424400
C	0.91632300	-2.54427200	-1.34010400
C	-5.37312200	-0.31281700	-1.26983500
H	-5.76503300	-0.94033400	-0.46379000
H	-5.82572000	0.68083600	-1.20116100
H	-5.63850600	-0.75969300	-2.23248200
C	0.53336800	2.76903300	2.57004800
H	-0.08206600	2.79406400	3.47392100
H	1.57726500	2.60327200	2.85126500
H	0.44739100	3.72696500	2.04706900
C	1.72294700	-3.70711700	-1.68275600
H	2.76264800	-3.40080000	-1.82937500
H	1.67468000	-4.44738500	-0.87878200
H	1.35675800	-4.15266900	-2.61212900
N	0.00807400	1.63271100	-2.09386200
N	0.90677300	1.43511400	-2.95971000
C	0.01605100	2.93428200	-1.51257400
C	0.86431500	0.19243900	-3.60537000
C	1.15448600	3.75212600	-1.49556700
C	-1.17272200	3.36149000	-0.90913500
C	2.09359000	-0.38334600	-3.96772400
C	-0.33248800	-0.46646800	-3.92553200
C	1.09397400	4.99454000	-0.87177100
H	2.06675800	3.39948300	-1.96173500
C	-1.22964500	4.61439500	-0.30103800
H	-2.03886300	2.70837000	-0.92785000
C	2.12723100	-1.64371500	-4.53875900
H	3.01045700	0.15629500	-3.75485500
C	-0.30683900	-1.71120200	-4.54300900
H	-1.28051600	0.01175200	-3.70663200
C	-0.09617100	5.43165300	-0.27734000
H	1.97619100	5.62699700	-0.84827500
H	-2.15542200	4.95109600	0.15518500
C	0.92700400	-2.32359700	-4.81799500

Appendix D: Cartesian Coordinates

H	3.06594300	-2.12371600	-4.79320800
H	-1.23988900	-2.19706500	-4.79991900
O	1.06657300	-3.56261200	-5.34824500
C	-0.10878700	-4.27827900	-5.72629300
H	-0.66699400	-3.73744100	-6.49874600
H	0.24044200	-5.22987900	-6.12666700
H	-0.75802900	-4.45897800	-4.86154400
H	-0.13790500	6.40525300	0.20139100

70_i:

SCF: -1837.479112

Cu	-1.00334200	-1.57541700	-1.48558500
N	0.26677500	0.07123300	-1.33676900
N	1.41020400	-0.19416900	-0.88369000
C	-0.39126700	1.34174900	-1.23505300
C	2.29397700	0.80135200	-0.38468800
C	-0.34407100	2.14557800	-0.08927600
C	-1.29115500	1.66059100	-2.26415700
C	2.94965800	0.50080600	0.81568700
C	2.61247100	1.96602700	-1.09885800
C	-1.20005800	3.23418400	0.04265100
H	0.33092200	1.90495800	0.72026000
C	-2.11767700	2.76626300	-2.15683900
H	-1.33483600	1.02458600	-3.14074600
C	3.86610500	1.40752700	1.34461300
H	2.71342900	-0.42573800	1.32666200
C	3.55967700	2.84382800	-0.58041300
H	2.12948000	2.17072500	-2.04806500
C	-2.09771000	3.54921400	-0.98937700
H	-1.16742500	3.82293900	0.95083100
H	-2.80913600	3.03190400	-2.94950100
C	4.17402300	2.57894000	0.64842500
H	4.35578400	1.18699400	2.28839300
H	3.81910900	3.74019500	-1.13540300
O	-2.99284000	4.56317300	-0.94320700
H	4.90371100	3.27514300	1.05023800
C	-3.05364000	5.35924600	0.23880000
H	-3.84166600	6.09132400	0.06249200
H	-3.30655100	4.74670500	1.11232700
H	-2.10475900	5.87830300	0.41526900
N	-1.98942900	-1.04786900	0.29342800
N	-3.09797200	-0.46845700	0.16382000
C	-1.15001900	-0.99790600	1.45010200
C	-3.79892800	0.15694200	1.22807700
C	-1.02209000	0.11940600	2.28811300
C	-0.26393300	-2.07782200	1.60906000
C	-4.36022100	1.40965600	0.94566900
C	-4.06696500	-0.48321300	2.44741900
C	-0.02434900	0.16509900	3.25497000
H	-1.66984000	0.97556800	2.16400500
C	0.70508800	-2.05671500	2.59594800
H	-0.34428500	-2.92701800	0.93917000

Appendix D: Cartesian Coordinates

C	-5.12648100	2.05637200	1.91375100
H	-4.16542800	1.86769800	-0.01792500
C	-4.86438000	0.15669700	3.39153100
H	-3.65897400	-1.46856000	2.64411500
C	0.84836300	-0.92380600	3.41631300
H	0.07395800	1.05202600	3.86817100
H	1.38822200	-2.88788500	2.73244100
C	-5.38152900	1.43172500	3.13701400
H	-5.54239700	3.03716600	1.70340400
H	-5.08315200	-0.34006200	4.33181900
O	1.86469200	-0.96436500	4.30463900
H	-5.99519900	1.92649500	3.88323700
C	2.09600600	0.17761400	5.12869100
H	2.96846100	-0.06740800	5.73421100
H	2.30568100	1.06507700	4.52054600
H	1.23841500	0.37266400	5.78257800
C	0.62448600	-4.18029400	-2.04241400
N	-0.02742500	-3.25460200	-1.80442400
C	-3.66346400	-0.84640300	-2.73567700
N	-2.60974900	-1.33114400	-2.75737000
C	-4.97433100	-0.21787900	-2.69952700
H	-5.34512700	-0.23294200	-1.67074900
H	-4.89404200	0.82107300	-3.03378600
H	-5.67402100	-0.75051300	-3.35002000
C	1.44529100	-5.34353600	-2.34680600
H	2.12547600	-5.54728500	-1.51454300
H	0.80771200	-6.21716700	-2.51166800
H	2.03342300	-5.15464800	-3.24986600

70_ii:

SCF: -1837.478609

Cu	-1.03064700	-1.65218200	-1.50502200
N	0.16218500	0.03307400	-1.42893700
N	1.19308800	-0.06217000	-0.70830300
C	-0.48936100	1.27498800	-1.75073700
C	1.97015100	1.02787800	-0.27455200
C	-0.95325600	2.11770900	-0.73408300
C	-0.80764400	1.53125900	-3.08623700
C	2.67566500	0.78953800	0.92300000
C	2.18815100	2.23275900	-0.96766400
C	-1.72007800	3.23240200	-1.06339700
H	-0.70495000	1.90232400	0.29824700
C	-1.55291900	2.66567800	-3.40978600
H	-0.46850000	0.84471300	-3.85492400
C	3.50328300	1.75708500	1.45943600
H	2.52952400	-0.16036000	1.42553700
C	3.05571100	3.18903300	-0.45719400
H	1.70976300	2.41533600	-1.92101500
C	-2.01553300	3.51548800	-2.40095600
H	-2.08456300	3.88201300	-0.27333300
H	-1.78138700	2.87832900	-4.44968700
C	3.70149000	2.96936100	0.77310800

Appendix D: Cartesian Coordinates

H	4.03053600	1.59765500	2.39372100
H	3.22782900	4.09847400	-1.01898900
N	-1.95754100	-1.16926400	0.29505200
N	-2.94152900	-0.38362000	0.27650500
C	-1.14708300	-1.43024800	1.45434900
C	-3.53980000	0.16827300	1.42740500
C	-0.63106000	-0.38894200	2.23627500
C	-0.73780600	-2.74910500	1.67073500
C	-4.11296900	1.44266500	1.25105700
C	-3.72121800	-0.50190000	2.64883300
C	0.28395100	-0.67874300	3.24417600
H	-0.94350100	0.63294300	2.05802000
C	0.15644900	-3.03291800	2.70179200
H	-1.12407300	-3.53515100	1.03010800
C	-4.77175500	2.06825700	2.29354100
H	-3.99567400	1.93702200	0.29256700
C	-4.42345500	0.10211300	3.68367200
H	-3.33895100	-1.50622500	2.78440000
C	0.67349100	-1.99965500	3.48679200
H	0.69541600	0.13003700	3.84017800
H	0.45983600	-4.05944900	2.88301100
C	-4.93268500	1.40323800	3.52285700
H	-5.19085900	3.06243000	2.18262400
H	-4.57282600	-0.44201400	4.60781300
C	0.54894100	-4.28511700	-1.85725400
N	-0.09449300	-3.34768500	-1.76021100
C	-3.49762400	-0.43623400	-2.68268800
N	-2.63017000	-1.20465100	-2.73885200
C	-4.56466300	0.54790700	-2.60518400
H	-5.13487700	0.39232700	-1.68542300
H	-4.12268700	1.54935400	-2.58899900
H	-5.23177300	0.46078800	-3.46777700
C	1.37231900	-5.47940000	-1.97834300
H	2.07855100	-5.52809400	-1.14396000
H	0.73962800	-6.37199800	-1.96569500
H	1.93146600	-5.45177200	-2.91851000
O	-5.60154100	2.08498400	4.47674400
O	4.53882300	3.84803400	1.36208600
H	1.38236700	-2.22050800	4.27865500
H	-2.60341300	4.39214600	-2.65462000
C	-5.79761900	1.46750800	5.74834800
H	-6.33930700	2.19710900	6.34995500
H	-6.39370400	0.55263100	5.65493800
H	-4.83844700	1.23600500	6.22551700
C	4.80056400	5.08949500	0.70823700
H	5.48351400	5.62953400	1.36375300
H	5.27575000	4.92898300	-0.26610300
H	3.87910100	5.66864700	0.57879200